Seismic wave field, spatial variability and coherency of ground motion over short distances : near source and alluvial valley effects

Afifa Imtiaz

UNIVERSITÉ DE GRENOBLE

THÈSE

Pour obtenir le grade de

DOCTEUR DE L'UNIVERSITÉ DE GRENOBLE

Spécialité : **Sciences de la Terre, l'Universe et l'Environment**

Arrêté ministériel : 7 août 2006

Présentée par

Afifa Imtiaz

Thèse dirigée par **Pierre-Yves Bard** et
codirigée par **Cécile Cornou** et **Emmanuel Chaljub**

préparée au sein du **l'Institut des Sciences de la Terre**
dans **l'École Doctorale Terre, Universe, Environment**

Champ d'ondes, variabilité spatiale, et cohérence des mouvements sismiques : effets en champ proche et en vallée alluviale

Thèse soutenue publiquement le **06 Janvier 2015,**
devant le jury composé de :

M. Michel BOUCHON
Directeur de Recherches, CNRS, ISTerre Grenoble, Président
M. Didier CLOUTEAU
Professeur, Ecole Centrale Paris, Rapporteur
M. Donat FÄH
Professeur, ETH Zurich, Rapporteur
Mme. Aspasia ZERVA
Professeur, Drexel University, USA, Examinatrice
M. Matthias OHRNBERGER
Professeur Assistant, Université de Potsdam, Germany, Examinateur
M. Pierre-Yves BARD
Ingénieur Général des Ponts et Forets, UdG, ISTerre Grenoble, Directeur de thèse
Mme. Cécile CORNOU
Chargé de Recherche, IRD, ISTerre Grenoble, Co-directeur de thèse
M. Emmanuel CHALJUB
Physicien Adjoint, UdG, ISTerre Grenoble, Co-directeur de thèse

Université Joseph Fourier / Université Pierre Mendès France /
Université Stendhal / Université de Savoie / Grenoble INP

Seismic wave field, spatial variability, and coherency of ground motion over short distances: near source and alluvial valley effects

Champ d'ondes, variabilité spatiale, et cohérence des mouvements sismiques: effets en champ proche et en vallée alluviale

Summary

Spatial variation of earthquake ground motion over short distances significantly affects the dynamic response of engineered structures with large dimensions. In current practices, the ground motion excitation across the foundation of a structure is assumed to be spatially uniform, which becomes inadequate for spatially extended structures in the near-fault region or on sites with inhomogeneity in surface geology and geometry. This PhD thesis seeks to understand the key parameters that locally control the ground motion spatial variability with the intent of putting forth practical propositions for incorporating such effects in seismic design and hazard assessment.

The first part of the thesis addresses the within-event component of the standard deviation of ground-motion distribution in near source region by means of numerical simulation of ground motions for extended sources with realistic rupture kinematics. The results suggest that the within-event variability significantly depends on the rupture type, depicting an increase with distance for bilateral ruptures and a decrease for unilateral ruptures.

The second part deals with the characterization of seismic wave field at the Koutavos-Argostoli site, a small-size, shallow, alluvial valley located in the seismically active Cephalonia Island in Western Greece. The seismic wave field was investigated from the recordings of a dense seismological array for a set of 46 earthquakes, with magnitude 2 to 5 and epicentral distance up to 200 km. The MUSIQUE array analysis algorithm was used to extract the phase velocity, back-azimuth, type and polarization of the dominant waves crossing the array. The results clearly indicate dominant scattering of seismic surface waves, mainly from the valley-edge directions, beyond the fundamental frequency of the valley. While Love surface waves clearly dominate the wave field close to the resonance frequency, Rayleigh waves strongly dominate only in relatively narrow frequency bands at higher frequency. Besides, an excellent consistency is observed between the dominance of the identified surface wave type in the wave field and the site amplification.

The "lagged coherency" of the most energetic part of the ground motion has been quantified for each station-pair within the array. In general, spatial coherency estimated from the horizontal components exhibit decays with frequency and interstation distance. Estimates from the vertical component exhibit rather larger values at some higher frequencies. Although coherency does not show any consistent trend indicating dependence on the magnitude, back-azimuth or site-to-source distance of the event, it seems to be primarily controlled by the site geometry. Larger coherency is systematically observed when the station pair is oriented parallel to the valley axis, while lower values are observed in the perpendicular direction. This observation proves to be consistent with the MUSIQUE analysis results: the predominance of scattered surface waves propagating across the valley implies an in-phase motion along valley-parallel direction and out-of-phase motion along valley-perpendicular direction.

The findings of the present research are expected to contribute in enhancing our understanding of spatial variability of ground motion and improving the coherency models used in engineering. This work also opens up new insights and many questions in need of further investigation.

Key-words: earthquake, spatial variation, numerical simulation, seismic array, surface waves, coherency

Résumé

La variation spatiale du mouvement sismique a des effets significatifs sur la réponse dynamique des structures de génie civil de grandes dimensions. Dans la pratique courante, l'excitation du mouvement sismique le long de la fondation de la structure est considérée uniforme, approche cependant inadéquate pour les structures de large portance au sol localisées à proximité des failles ou sur des sites présentant une structure du sous-sol latéralement hétérogène. Cette thèse se propose donc de comprendre les facteurs clefs contrôlant localement la variabilité spatiale du mouvement sismique, avec en ligne de mire la mise en place de recommendations en vue d'incorporer ces effets dans l'estimation de l'aléa sismique et le dimensionnement des structures.

La première partie de cette thèse s'intéresse à la composante intra-évènement de l'écart-type de la distribution du mouvement sismique en champ proche à l'aide de simulations numériques du mouvement sismique pour des sources étendues présentnat une cinématique de rupture réaliste. Les résultats suggèrent que la variabilité intra-évènement dépend significativement du type de rupture, cette variabilité augmentant avec la distance pour les ruptures bilatérales et diminuant pour les ruptures unilatérales.

La seconde partie traite de la caractérisation de la composition du champ d'onde dans la vallée de Koutavos-Argostoli, qui est une vallée de petite dimension et d'épaisseur sédimentaire faible, située sur l'île – sismiquement active - de Céphalonie en Grèce. Les champs d'onde générés par 46 séismes, ayant des magnitudes variant entre 2 et 5 et des distances épicentrales jusqu'à 200 km, ont été analysés à partir de l'enregistrement par deux réseaux denses de capteurs sismologiques. L'algorithme de traitement d'antenne MUSIQUE est utilisé pour extraire la vitesse, l'azimut, le type et la polarisation des ondes dominantes se propageant à travers le réseau. Les résultats montrent clairement d'importantes diffractions d'ondes de surface aux bords de vallée au-delà de la fréquence de résonance de la vallée. Tandis que les ondes de Love dominent clairement le champ d'ondes proche de la fréquence de résonance, les ondes de Rayleigh dominent à plus haute fréquence dans des gammes de fréquences étroites. Par ailleurs, un excellent accord est observé entre les champs d'onde de surface diffractés localement et les caractéristiques d'amplification du site.

La "cohérence décalée" de la partie la plus énergétique du signal a été quantifiée pour chaque paire de stations du réseau. En général, la cohérence calculée sur les composantes horizontales diminue avec la distance entre stations et la fréquence. La cohérence sur la composante verticale indique des valeurs relativement fortes à haute fréquence. Les valeurs de cohérence apparaissent très faiblement corrélées à la magnitude, l'azimut et la distance épicentrale du séisme, mais sont au contraire liées aux caractéristiques géométriques de la vallée. La coherence est systématiquement plus forte pour les couples de capteurs orientés selon la direction parallèle à l'axe de la vallée, et moins forte pour des couples de capteurs orientés dans la direction perpendiculaires. Cette observation est en accord avec les résultats du traitement d'antenne: la prédominance d'ondes de surface diffractées sur les bords de la vallée conduit à des mouvements en phase le long de la direction parrallèle à l'axe de la vallée.

Les résultats de cette thèse apporte des elements de compréhension sur la variabilité spatiale du movement sismique et ouvrent de nombreuses perspectives d'application.

Mots-Clefs: *séisme, variation spatiale, simulation numérique, réseau dense, ondes de surface, cohérence*

Acknowledgements

This PhD thesis is the outcome of the guidance and help of a number of individuals who in one way or another contributed and extended their valuable assistance in the preparation and completion of the work.

First and foremost, I would like to express my sincerest gratitude to my thesis advisors, Prof. Pierre-Yves Bard, Dr. Cécile Cornou, and Dr. Emmanuel Chaljub, for their invaluable supervision, constructive suggestions, patience, and kindness throughout the three years of my PhD. Their active guidance, unwavering enthusiasm, and continuous motivation kept me engaged with my research and enabled successful completion of the PhD. The precious experience of working with such knowledgeable researchers has been hugely enriching for me. I would like to specially thank Dr. Cornou for her incessant support and mentorship, kindness and warmth, and for always being there to help me get over the difficulties.

My profound appreciation extends to Dr. Mathieu Causse and Prof. Fabrice Cotton, who have collaborated and contributed to the first chapter of this thesis. Their continuous guidance and kind efforts have added great value and diversity to this work. I appreciate all their contributions in terms of valuable time, ideas, funding, interest and helpful comments.

I am greatly indebted to Prof. Didier Clouteau and Prof. Donat Fäh for their kind willingness to review this work. I am heartily thankful to Prof. Aspasia Zerva and Dr. Matthias Ohrnberger, the examiners, and Prof. Michel Bouchon, the chairman, of my PhD committee. I am honored to have them in my jury. I really appreciate their time, kind participation and valuable comments. I specially thank Dr. Zerva for her constant engagement with my research, for her kind support and valuable advices.

I am sincerely grateful to Mickaël Langlais and Dr. Philippe Gueguen, the tutors of my complementary monitoring duty, for their generosity and understanding. It is their co-operation that enabled me to be involved in an additional load of work without interrupting my thesis. My cordial thanks to Dr. Manuel Hobiger for the MUSIQUE code, to Dr. Erwan Pathier for the GIS mapping tools, to Dr. Giovanna Cultrera, Tobias Boxberger, Dr. Nikos Theodoulidis, and the entire NERA Team for collaborating with information, data, and the results of common interest, and to EU-NERA project for funding my PhD. I express my deepest gratitude to Prof. Mehedi Ahmed Ansary, my mentor in Bangladesh, who convinced me to pursue earthquake engineering and guided my way up to here. Huge thanks to the entire ISTerre community, my colleagues and researchers, especially the administration and the IT departments, for their continuous support and assistance.

Last, but not the least, is my family and friends. I thank my mom Amena Imtiaz, dad Imtiaz Ahmed and brother Salman Imtiaz for always being my source of inspiration. I thank all my friends in Bangladesh, France and abroad for making me feel loved. Over the years of my stay in Europe, I have been fortunate enough to make a great many international friends, who have eventually become my family, especially, Con Lu, Christel Marchica, Hilal Tasan, Ismael Riedel, and Johanes Chandra. I gratefully acknowledge their affection, warmth, concern and care. Finally, I would like to acknowledge each and every one who extended their kind assistance but have not been named directly. I truly admire all their contributions and will remain grateful forever.

Table of Contents

List of Tables

List of Figures

List of Symbols/Abbreviations

$\bar{\gamma}_{jk}(\omega)$	Lagged coherency or coherency
δ	residual
Δ	steps
θ	Azimuth angle (Chapter 1), back-azimuth angle (Chapter 3, 4)
ρ	Amplitude parameter
σ_{tot}	Total ground motion variability (sigma)
σ_{SS}	Single station sigma
Σ	summation
τ	Between-event variability (Chapter 1), time (Chapter 4)
φ	Phase difference (Chapter 3)
ϕ	Within-event variability
ϕ_{SS}	Event corrected single station sigma
ω	Angular frequency
ω_m	Frequency smoothed

a	Steering vector of MUSIC functional
a_m	Weight of frequency smoothing
a_q	Modified steering vector of MUSIC functional
ATANH, $\tanh^{-1}$	Hyperbolic arc tangent
D_{ij}	Separation distance between stations i and j
E	Expectation value
E_{XX}	Energy; XX = different components
f	frequency
f_c	Central Frequency
f_s	Sampling frequency
FK	Frequency-wavnimuber
H, h	Hypocentral depth
H/V	Horizontal/Vertical
Im	Imaginary part

k	Wave number
k_c	Corner wave number
K	Degree of slip heterogeneity (Chapter 1), Number of strongest eigenvalues (Chapter 3)
l	Time sample
L	Length of fault
L_c	Characteristic rupture length
m	Time index
M	Earthquake magnitude
M_h	Number of points of Hamming window
M_L	Local magnitude
M_w	Moment magnitude
n	Number of observations
N	Number of sensors/signals
N_f	Number of frequency points
N_t	Number of time index
N_{st}	Number of stations
P	MUSIC functional
q	Quantile value
R, r	Epicentral distance
$\boldsymbol{R}$	Matrix of sensor position
Re	Real part
R_{hyp}	Hypocentral distance
R_{jb}	Joyner-Boore distance
R_{rup}	Rupture distance
s	Site category (Chapter 1), slowness (Chapter 3)
S(f)	Single covariance matrix
$\bar{S}_{jj}$	Smoothed auto power spectrum for station j
$\bar{S}_{jk}$	Smoothed cross power spectrum between stations j and k
t_c	Centre of time window
T_p	Time of peak velocity
v(l)	Taper window

U(l)	Ground motion time series
U(ω)	Ground motion Fourier spectrum
X	Complex data vector
T_R	Rise Time
v	Velocity of wave
V_R	Rupture velocity
Vs	Shear wave velocity
W	Width of fault

AI	Arias Intensity
AUTH	Aristotole University of Thessaloniki
BC	Before Christ
BSSA	Bulletin of the Seismological Society of America
CI	Confidence Interval
CTF	Cephalonia Transform Fault
DR	Directivity Ratio
EMSC	European-Mediterranean Seismological Centre
EU	European Union
FAS	Fourier Amplitude Spectum
GCMT	Global Centroid Moment Tensor
GFZ	German Research Centre for Geosciences
GIS	Geographical Information System
GMPE	Ground Motion Prediction Equation
GMT	Greenwich Mean Time
GPS	Global Positioning System
HUSN	Hellenic Unified Seismological Network
InSAR	Interferometric Synthetic Aperture Radar
INGV	Istituto Nazionale Geofisica e Vulcanologia
ISTerre	Institut des Sciences de la Terre
ITSAK	Institute of Engineering Seismology and Earthquake Engineering (Greece)
MUSIC	MUltiple SIgnal Characterization

NE	North East
NERA	Network of European Research Infrastructures for Earthquake Risk Assessment and Mitigation
PGV	Peak Ground Velocity
NW	North West
PSHA	Probabilistic Seismic Hazard Assessment
SE	South Easr
SNR	Signal to noise ratio
SSR	Standard Spectral Ratio
SVF	Slip velocity function
SVEGM	Spatial Variation of Earthquake Ground Motion
SW	South West
UTC	Coordinated Universal Time

General Introduction

Earthquake has been one of the deadliest natural hazards throughout the history of human civilization. In a seismically active region, ground shaking caused by earthquakes pose inevitable risk to the inhabitants and infrastructure subjected to it. To date, a number of urban centers have been developed near major earthquake faults. The trend of growing urbanization has been followed by the construction of significant numbers of large and extended structure. Hence, one key challenge in modern day engineering practices is to better understand the processes associated with ground shaking in order to mitigate the effects and to cope with the future earthquakes.

An earthquake occurs when rocks slip suddenly due to the stresses built up in the earth's outer layer. Energy radiates away from the source of this sudden movement and propagates as seismic waves rapidly through the earth's crust reaching the ground surface where they produce shaking, i.e. the ground motion. Accordingly, the factors that influence ground motion during earthquakes are attributed to the complexity of the source, propagation path, and site effects. Seismologists and engineers base their understanding on knowledge of these effects in order to estimate as well as to predict the level and nature of ground motion.

Generally speaking, the damage caused by earthquakes depends on the strength or intensity of the ground motion coupled with the quality of the engineering structure. The level of shaking is controlled by the proximity of the affected region or structure to the earthquake source as well as the type of geological structure that seismic waves pass through *en route*, especially those at or near the ground surface. On their travel path, seismic waves make their final way through the ground structure near the surface where they are greatly modified by the local geology and soil conditions. When the waves pass from rock to soil, they slow down in propagation speed but become larger in amplitude. The more intense shaking of the sedimentary layers cause greater energy movement and results in larger waves. Since geometry and soil conditions of the sedimentary layer often vary over short distances, nature and levels of ground shaking can vary significantly within a small area.

As a matter of fact, a number studies have reported large variations in the spatial distribution of ground motion during past major damaging earthquakes (e.g. Shabestari and Yamazaki, 2003). The degree of damage was often observed to vary from one location to another, even for similar structures located within short distances, which consistently suggest different levels of ground motion in addition to vulnerability variations linked with structural defaults. Some important issues raised by recent earthquakes and requiring elucidations are therefore:

- How do the seismic waves, radiated from the source, affect ground motion variability in the near-fault region?
- What are the physical properties of the source that contribute to this variability?
- To what extent is ground motion variability caused by the local geological structure?
- What type or characteristics of the seismic waves modify the nature and level of ground motion in such sites and within short distances?

Answering such issues is obviously required to improve our understanding of such complex source and site effects through a mix of experimental observations and numerical simulations.

By definition, spatial variation of earthquake ground motion refers to the differences in amplitude and waveform (phase) observed in the seismic time histories recorded over extended areas (e.g. within the dimension of a engineered structure) on the ground surface. It has significant effect on the dynamic response of engineered structures with large dimensions, such as dams, nuclear power plants, or multiple supports such as bridges and lifeline facilities. Usually, spatially uniform ground motion excitation is assumed in practice for seismic analysis. This assumption becomes inadequate for spatially extended structures constructed in the near-fault region or on large sites with inhomogeneity in surface geology and geometry, emphasizing the need to include spatial variability in earthquake-resistant design and analysis of such structures.

The effect of source characteristics on the ground motion is profound. In the near-fault region, shallow earthquakes can cause severe differences in ground motions depending on the direction of the fault rupture. The existing Empirical Ground Motion Prediction Equations (GMPEs) provide the distribution of ground-motion in terms of a median and

a standard deviation, but these equations are developed by means of regression techniques from recorded strong motion data, generally based on very simple parameterization with magnitude, distance and site category. On the other hand, the standard deviation of the ground motion distribution, commonly referred to as the aleatory variability "sigma", is a fundamental component in Probabilistic Seismic Hazard Assessment (PSHA) since it controls the hazard level at very low probabilities of exceedance. It is therefore imperative to accurately constrain "sigma" to perform reliable seismic hazard analyses. Though a few recent data analyses suggest that sigma is distance-dependent, development of models describing ground motion variability at short distances (<20 km) remains questionable due to the scarcity of near-source records of moderate to large events (Mw>6).

Furthermore, it is well known that engineering structures cross sites with irregular subsurface topography and ground types (e.g. sedimentary valleys). Such sites give rise to the formation of surface waves, which can lead to large amplifications, loss of correlation and significant ground strains in the wave field. Besides, seismic waves become trapped and amplified by sedimentary valleys during earthquakes. As a result strong ground motion of long duration and strong spatial variation in amplitude and phase occur, especially near the edges of the basins, which can substantially increase the seismic forces on structures and lifelines. Such effects could not be incorporated so far in routine seismic hazard assessment and risk mitigation due to their complexity as well as the limitations of geophysical investigations. The installation of dense seismic arrays worldwide initiated the comprehensive analysis of seismic ground motion. However, most of these arrays are located at uniform ground conditions, mostly at soil sites. In addition, most of the array analysis studies utilized a stochastic approach (coherency estimation) to model the spatial variation of the motions (Zerva, 2009). A purely stochastic approach, however, precludes any association of the spatial variation of the motions with the physical causes underlying it. Additional research efforts at such sites are, hence, necessary to fully capture the physical causes underlying the spatial variation of the seismic ground motions for engineering applications.

One of the main (long term) goals of this thesis is, then, to understand the key parameters that locally control the ground motion spatial variability, as well as to

investigate the relative contributions of scattering and local site effects, in view of aiding development and calibration of engineering oriented models, and to put forth practical propositions for incorporating the effects of such a variability in seismic design (building codes, microzonation studies, critical facilities). It includes two main parts. The first one addresses the spatial "aleatory" variability of ground motion related to the aleatory features of rupture kinematics in the near fault region, while the second one is dedicated to an analysis of the variability of ground motion over short distances in connection to the shallow underground structure at the site : although such a variability is usually considered as stochastic, our goal here is to investigate its "deterministic" relationship with the composition of the wave field, which includes both source and site signatures. The first part of the thesis is based on numerical simulations while the second on recorded data.

The PhD thesis begins with the analysis of potential distance dependency of the ground-motion variability “sigma” (**chapter 1**). The main goal is to quantify statistical properties of ground-motion variability in the near source region where it is poorly constrained due to the lack of available records, and look into the relative contributions of source complexity and wave propagation effects. Therefore, numerical simulations of ground motions were performed for strike-slip events. Synthetic velocity seismograms have been generated from a suite of finite-source rupture models of past earthquakes. Then the within-event component of the ground-motion variability, in terms of variance in peak ground velocity (PGV), was evaluated as a function of distance.

The second, experimental, part of the thesis deals with the identification of seismic wave field composition in a site with pronounced shallow underground heterogeneities, with the objective to improve the physical understanding and the engineering-oriented quantification of spatial variability of ground motion (i.e. spatial coherency). This part of the research is based on the temporary seismological experiment that took place at the Argostoli basin within the FP7 EU-NERA (Network of European Research Infrastructures for Earthquake Risk Assessment and Mitigation) 2010-2014 project. The chosen site Koutavos-Argostoli area is a relatively small-size shallow sedimentary basin, situated in the Cephalonia Island, Western Greece, where the seismic activity is high and dominated by the Cephalonia transform fault (**chapter 2**). The seismological wave field

generated by a significant number of earthquakes was investigated from dense array recordings of earthquake ground motion using an array analysis technique MUSIQUE (Hobiger et al., 2012) (**chapter 3**). Unlike the classical array processing methods (high-resolution frequency-wavenumber analysis [Capon, 1969], MUSIC [Schmidt, 1986]), MUSIQUE allows analysis of all three components of a seismic record together and identification of the surface wave types as well as retrieval of wave polarization along with resolving the wavenumber vector. Thus the results from MUSIQUE analysis provide us with slowness and back-azimuth of the dominant wave trains crossing the array, discrimination between Rayleigh and Love surface waves, plus, estimates of polarization parameters of Rayleigh waves.

Subsequently, the "lagged coherency" of the ground motion has also been quantified for each possible pair within the array and for the set of selected events **(chapter 4)**. This work focuses on observation of spatial variation of the waveforms over short distances, that is, within the dimension of a large structure. The final goal is to associate lagged coherency with the results obtained from wave field characterization and investigate the dependency of coherency on source parameters (such as magnitude, distance, source direction) as well as the site parameters (such as azimuth of station pairs, basin axis) based on statistical analyses.

The last section wraps up the main findings from each of the three major components of this work concerning the spatial variability of ground motion: even if it is most often described as stochastic, it does include some deterministic items. It thus identifies some perspectives that now seem at hand, given the data and results obtained here. The appendix gathers information that is not critical for the understanding of the main chapters, but may be of interest to curious readers or all those who would perform some similar studies or use the same data set for other purposes.

Thesis outline

The present work is an attempt to understand spatial variation of ground motion combining two aspects, analysis from numerical simulation and real data. The chapters are, therefore, organized in the following way:

- **Chapter 1** presents the study on near source variability of ground motion, in terms of amplitude variability, from finite source ruptures simulations. The single station within-event variability from peak ground velocities (PGVs) of a synthetic network of stations and for a suite of events is estimated. Then the distance dependence of this variability has been discussed.
- **Chapter 2** presents the description of the site Argostoli, where the seismological experiment of FP7 EU-NERA project (2011-2014) took place. A brief overview of the seismotectonics, seismicity, geology and geomorphology of the region is provided. Then, a preliminary description of the Argostoli valley followed by an overview of the seismological experiment is provided. The catalogue of the recorded earthquakes, the quality of the data, and the subset of the events used for the data analyses in Chapter 3 and 4, are discussed.
- In **Chapter 3**, an advanced array analysis technique, MUSIQUE, is used to investigate the seismological wave field with the data recorded from two dense seismic arrays (Arrya A and Array B) at Argostoli valley. For a subset of 46 earthquakes, the azimuthal energy distribution and the energy repartition between Love and Rayleigh waves are measured and dispersion curves of the valley are retrieved. Finally, the results of the analysis as well as the possible interpretations/implications regarding site effects are presented.
- **Chapter 4** presents the analysis of spatial coherency using earthquake data from the principle dense seismic array (Array A) located at Argostoli site. The chapter begins with a short overview of the available coherency models, the causes of incoherency along with the description of coherency and its evaluation procedure. Then a detailed description of the time window selection procedure for coherency analysis, and some test results have been provided. Finally, results from some individual events and the statistical analyses of the entire subset of events are presented.

Chapter 1: Ground-motion variability from finite-source ruptures simulations

This chapter represents the analysis of potential distance dependence of the ground motion variability "sigma", in the near source region, from numerical simulations of ground motions. The within event component of ground motion variability has been evaluated, from peak ground velocity (PGV), as a function of distance and the relative contributions of some source complexity and propagation effects in ground motion variability have been discussed. The chapter represents the article "Is ground-motion variability distance-dependent? : Insight from finite-source ruptures simulations", scheduled to be published at the Bulletin of the Seismological Society of America (BSSA) and co-authored by Afifa Imtiaz, Mathieu Causse, Emmanuel Chaljub, and Fabrice Cotton (Imtiaz et al., 2015).

Summary

The ground-motion variability “sigma” is a fundamental component in Probabilistic Seismic Hazard Assessment (PSHA) since it controls the hazard level at very low probabilities of exceedance. So far, most of the analyses based on empirical Ground-Motion Prediction Equations (GMPEs) do not consider any distance dependency of “sigma”. This study aims to analyze the potential distance dependency of ground-motion variability, especially in the near field region, where the variability is poorly constrained due to the lack of available records. We, therefore, investigate the distance dependency of “sigma” by performing numerical simulations of ground-motion for some strike-slip events. Synthetic velocity seismograms (up to 3 Hz) have been generated from a suite of finite-source rupture models of past earthquakes. Green’s functions were calculated for a 1D velocity structure using a discrete wavenumber technique (Bouchon, 1981). The within-event component of the ground-motion variability was then evaluated from the synthetic data as a function of distance. The simulations reveal that the within-event component of the ground-motion shows a distance-dependency, subject to the rupture type. For bilateral ruptures, the variability tends to increase with distance. On the contrary, in case of unilateral events, the variability decreases with distance.

1.1 Introduction

Empirical Ground-Motion Prediction Equations (GMPEs) are developed by means of regression techniques from recorded strong motion data, generally are based on very simple parameterization with magnitude (M), distance (d) and site category (s). The distribution of ground-motion for a given M, d and s is then represented in terms of a median and a standard deviation, referred to as the aleatory variability sigma, which is a fundamental component in Probabilistic Seismic Hazard Analysis (PSHA). Sigma exerts a strong influence on the seismic hazard level, especially for long return periods (Bommer and Abrahamson, 2006). It is therefore imperative to accurately constrain sigma to perform reliable seismic hazard analyses.

In seismic hazard studies two types of uncertainties, termed as aleatory variability and epistemic uncertainty, are considered. Aleatory variability is defined as the natural

randomness in a process and supposed to be irreducible. On the contrary, epistemic uncertainty refers to the scientific uncertainty in the model of the process caused by limited data and knowledge, which can theoretically be reduced to zero with models better explaining the data. Ideally, sigma should represent the aleatory ground-motion variability obtained from repeated events on the same fault and recorded at the same station. As such, it includes only the natural randomness of the source rupture process (Anderson and Brune, 1999). Nevertheless, the computation of sigma in GMPEs is typically performed from records at multiple stations from different earthquakes, and hence mixes various paths and site responses. In other words, the variability in ground-motion due to differences in paths and site response is typically considered as aleatory whereas it should be treated as epistemic uncertainty. This assumption is commonly referred to as ergodic (Anderson and Brune, 1999).

Thanks to the increasing availability of strong-motion records, several recent studies propose to refine ground-motion variability analyses by splitting sigma into various components (e.g. Chen and Tsai, 2002; Al-Atik et al., 2010 ; Rodriguez-Marek et al., 2011; Edwards and Fäh, 2013). Following the notation of Al-Atik et al. (2010), the total variability can then be expressed as:

$$\sigma_{tot} = \sqrt{\phi^2 + \tau^2} \tag{1.1}$$

where, ϕ refers to the within-event variability (due to the variability in site conditions and path effects for a given event recorded at various stations) and τ refers to the between-event variability (essentially due to the natural source randomness). The variability σ_{tot} can further be refined by extracting the contribution of site-specific effects from ϕ, to obtain the 'single-station' standard deviation (or 'single-station' sigma) defined as:

$$\sigma_{SS} = \sqrt{\phi_{SS}^{\ 2} + \tau^2} \tag{1.2}$$

The term ϕ_{SS} is then called the event-corrected 'single-station' sigma. A very recent work by Rodriguez-Marek et al. (2013) addresses the issue of the variation of 'single station'

sigma with respect to region, magnitude, and distance. First, it is remarkable from their work that the mean values of ϕ_{SS} appear to be stable (average $\phi_{SS} \approx 0.45$) across the different regions (California, Taiwan, Japan, Switzerland and Turkey). Second, the authors observe that ϕ_{SS} depends both on magnitude and distance. They propose various models to account for such potential dependencies for moment magnitude (M_w) 4.5 to 8 and for distances up to 200 km, opening some new insights for improving PSHA. Nevertheless, the reliability of such models at short distances (<20 km) remains questionable due to the scarcity of near-field records of moderate to large events (M_w>6) and potential large epistemic uncertainties associated to small event metadata (in particular depth).

The present paper addresses the issue of the ground-motion variability using near-field kinematic-rupture simulations. Our strategy is to evaluate sigma from synthetic data, as a function of distance. Our study focuses on the within-event component of sigma (ϕ) only. Various published kinematic source models of vertical strike-slip events are considered to represent the source process on the fault. Synthetic velocity time series are computed up to 3 Hz by convolving slip rate functions with 1D Green's functions at stations placed at various azimuths and distances from the source. For each source model, we then extract ϕ for Peak Ground Velocity (PGV) and study the variations of ϕ with respect to distance. It is important to note that the scope of our study is not to provide ground motion variability values, to be directly incorporated in seismic hazard analyses, which would require unreasonably large number of source models and computation time. We rather limited our selection by considering vertical strike slip events with $6 < M_w < 7$ only, in order to focus on the overall physical properties that are likely to influence the distance dependency of ϕ.

While a variety of distance definitions are available, this work will use R_{jb}, the Joyner-Boore distance, defined as the shortest distance from the receiver to the surface projection of the fault plane (Joyner and Boore, 1981), enabling us to represent the finiteness of the fault in the region of near fault plane. The R_{jb} distance is equivalent to the rupture distance R_{rup} (closest distance to the rupture surface) for vertical strike-slip events, especially when the rupture is very close to the surface as for our selected fault models.

1.2 Ground-motion simulations

1.2.1 Kinematic source models

A total of 11 kinematic source models (i.e., the spatio-temporal distribution of slip on the fault plane), with magnitudes ranging from M_w=5.8 to M_w=6.8, were generated for vertical strike slip events. 8 of the source models are based on published models of past events, obtained using kinematic inversion of strong-motion observations, sometimes combined with Global Positioning System (GPS) and/or Interferometric Synthetic Aperture Radar (InSAR) data. Although they were derived by using various inversion techniques, most of them assume uniformity in rupture velocity and rise time (Table 1.1). These models were extracted from a database of finite-source rupture models available online (Mai and Thingbaijam, 2014; see Data and Resources section). Among the 8 models, 6 correspond to bilateral rupture and 2 to unilateral rupture. The classification of the models into bilateral / unilateral rupture is based on McGuire et al. (2002) who proposed to quantify rupture directivity using a directivity ratio (DR) computed from the second moments of the slip space-time distribution (see Appendix A). Directivity ratio (DR) ranges from 0, for a 1D symmetric bilateral rupture with constant slip, to 1, for a unilateral rupture.

In order to properly compute ground-motion up to 3 Hz, a fine grid is required to represent the slip history on the fault plane. Since the considered kinematic source models are defined on coarse grids (~2 km x 2 km), they have been interpolated on a smaller grid (e.g., 200m x 200m), ensuring at least five points per minimum wavelength. The interpolation procedure assumes self-similarity of the static slip beyond the Nyquist wavenumber of the original model by imposing a k^{-2} slope of the slip spectrum. The resulting numbers of sub-faults are shown in Table 1.1.

These 8 source models were complemented by 3 synthetic models produced using a k^{-2} description of the final slip (e.g. Causse et al. 2009). The fault plane configuration and other kinematic parameters (rise-time and rupture velocity) are the same as the source model derived by Sekiguchi and Iwata (2002) for the 2000 Tottori earthquake (Table 1.1). The final slip on the fault plane is described in the wave number domain by a k^{-2}

asymptotic decay beyond a corner wavenumber $k_c = K/L_c$, where L_c is the characteristic rupture length, and K is a non-dimensional parameter. This parameter K can be considered as a measure of the degree of roughness of slip heterogeneity. Thus we generated 3 source models characterized by a smooth slip distribution (K=0.4), a rough one (K=1.6) and an intermediate one (K=0.8), so as to isolate the effect of the slip roughness on the ground-motion variability.

Source parameters and computed directivity ratios of the 8 models, extracted from the database of Finite-source Rupture Models, are listed in Table 1.1. The corresponding source parameter distributions are provided in Figure 1.1 and 1.2. The images of the k^{-2} slip models are shown in Figure 1.3. In Table 1.1, magnitude (M_w) and hypocentral depth (H) of each event along with the length (L) and width (W) of the source model are given. SVF indicates the slip-velocity function considered. Each extracted model from the database was interpolated to a finer grid of sub-faults, which is given by 'Nb. Sub-faults'. In case of constant rupture velocity (V_R) and rise time (T_R), the corresponding values are indicated. "Nb.TW" refers to the number of time windows used in the inversion (Nb.TW > 1 in case of multi-time window linear inversion; Hartzell and Heaton, 1983). Note that the Kagoshimaen-hoku-seibu source model has been derived assuming constant rise time but variable rupture velocity. Nevertheless, this model has been simplified, considering an average constant rupture velocity, due to unavailability of the rupture time distribution in the source model database. The Directivity Ratio (DR) indicates the rupture type. Imperial Valley and Coyote Lake models (DR>0.5) can be considered as unilateral and the rest (DR<0.5) as bilateral.

Table 1.1: Information on the kinematic source models from the database [1]

Event Name	Event Date	Author	M_w	H (km)	L (km)	W (km)	SVF	Nb. Sub-faults	V_R (km/s)	Nb. TW	T_R (s)	DR
Fukuoka	20.03.2005	Asano and Iwata (2006)	6.7	14	26	18	smooth ramp	10,248	2.1	6	3.5	0.06
Yamaguchi	25.06.1997	Miyakoshi et al. (2000)	5.8	8.2	16	14	triangle	5,751	2.5	2	0.75	0.39
Kagoshimaen-hoku-seibu	26.03.1997	Horikawa (2001)	6.1	7.6	15	10	triangle	15,251	2.5	1	0.3	0.10
Kagoshima	26.031997	Miyakoshi et al. (2000)	6.0	7.7	18	12	triangle	14,065	2.5	2	0.75	0.36
Tottori	06.10.2000	Semmane et al. (2005)	6.7	14.5	32	20	tanhyp	16,261	variable	1	variable	0.13
Tottori	06.10.2000	Sekiguchi and Iwata (2002)	6.8	7.8	34	17.6	tanhyp	15,390	1.8	6	3.5	0.11
Imperial Valley	15.10.1979	Archuleta (1984)	6.5	8.0	35	13	boxcar	211,031	variable	1	variable	0.95
Coyote Lake	06.08.1979	Liu and Helmberger (1983)	5.9	8.0	10	10	triangle	10,404	2.8	1	0.5	0.60

[1] M_w = magnitude, H= hypocentral depth, L= length, W= width of the sourcemodel, SVF = slip-velocity function, Nb. Sub-faults = number of sub-faults of the finer-grid fault-model, V_R = rupture velocity (V_R), T_R = rise time (T_R), Nb.TW = number of time windows used in the inversion, DR = Directivity Ratio (DR < 0.5 indicate bilateral and DR> 0.5 indicate unilateral rupture)

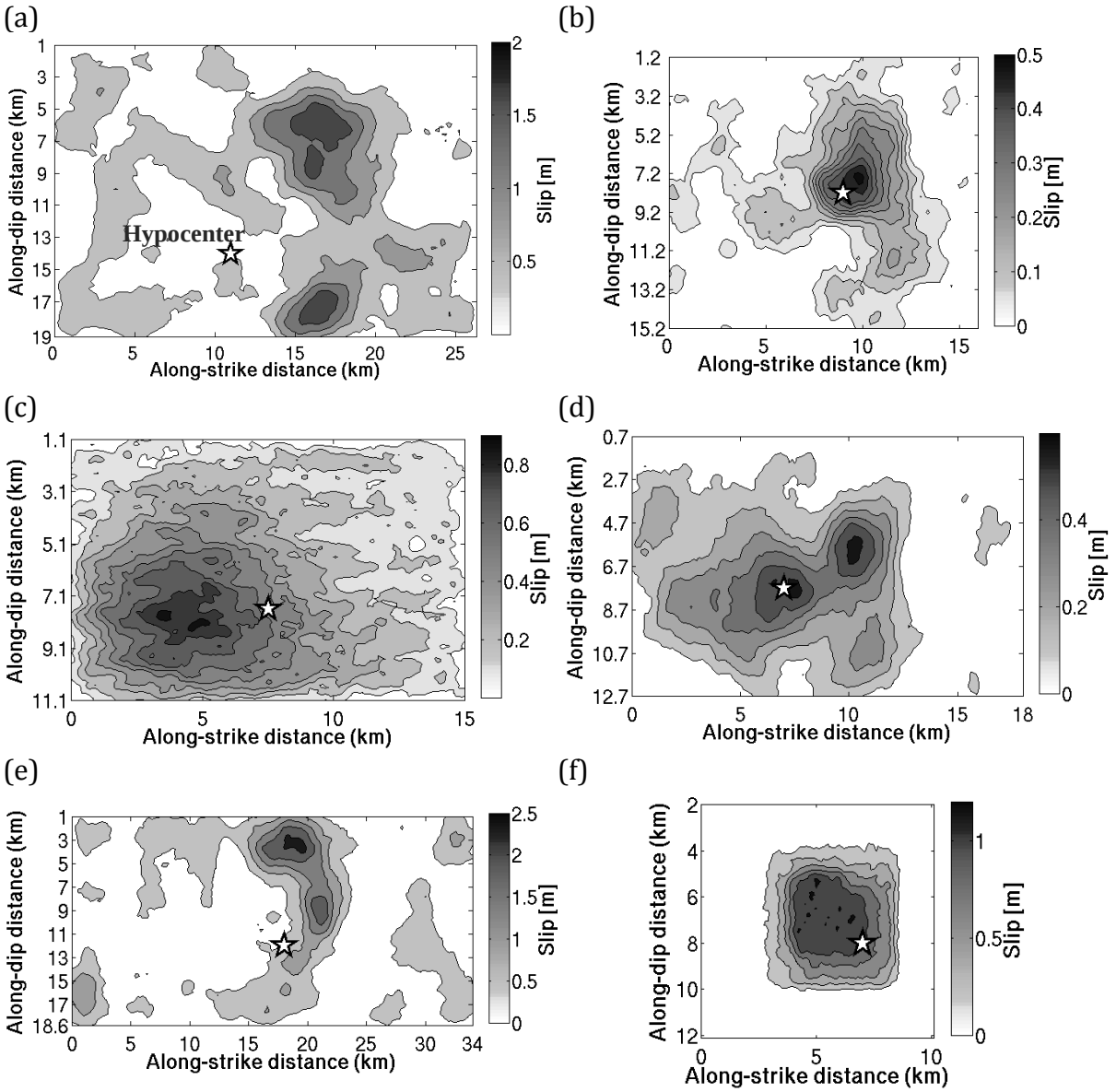

Figure 1.1: Slip images of the kinematic source models, having constant rupture velocity and rise time, extracted from the database of finite-source rupture models and interpolated to a finer grid. The models are (a) Fukuoka (2005), (b) Yamaguchi (1997), (c) Kagoshimaen-hoku-seibu (1997), (d) Kagoshima (1997), (e) Tottori (2000, Sekiguchi and Iwata), (f) Coyote Lake (1979). The symbol 'star' shows the location of the hypocenter. Contour lines represent lines of constant slip value.

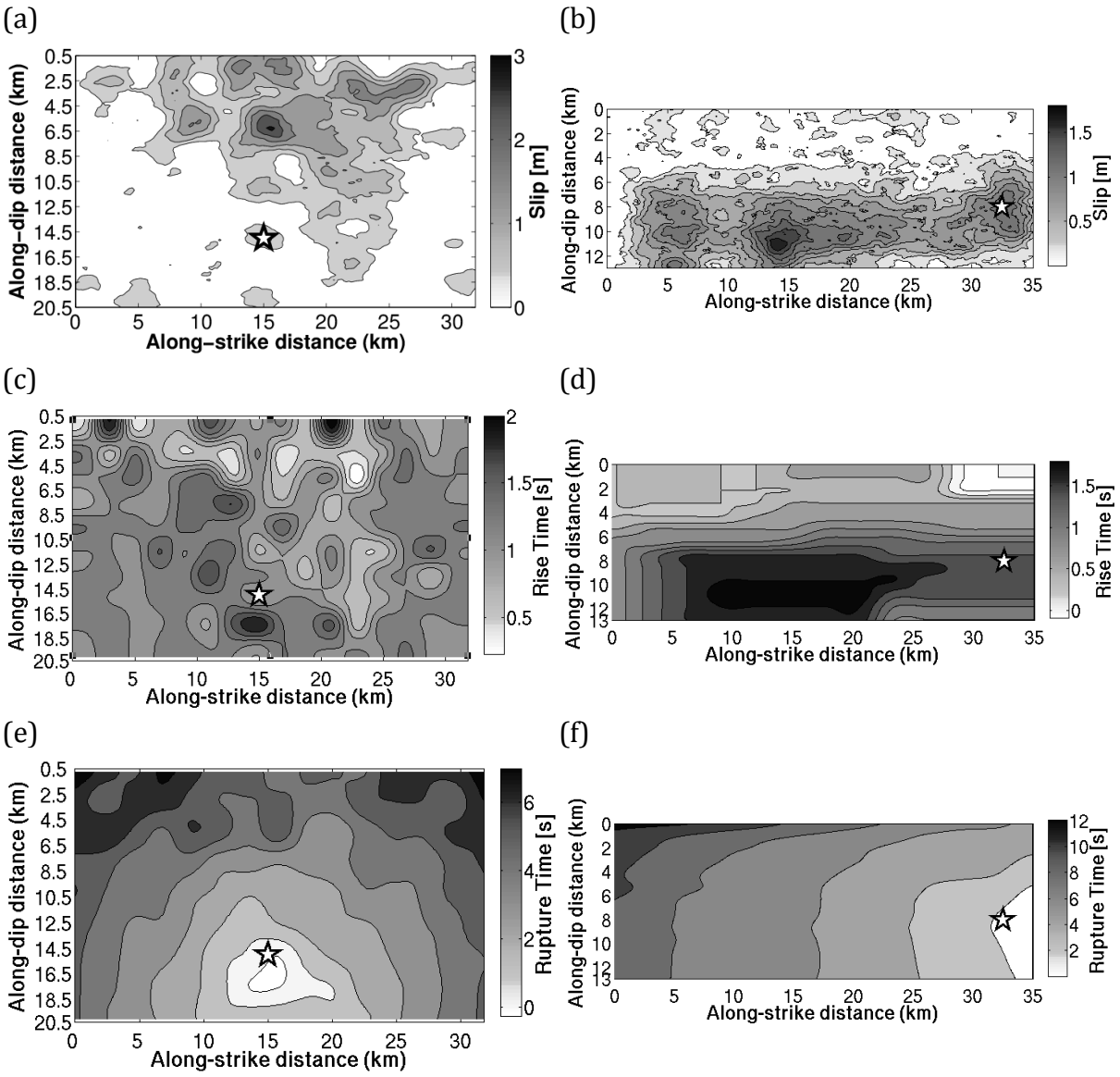

Figure 1.2: (a) Slip amplitude, (c) slip duration, (e) rupture front evolution images of Tottori (2000, Semmane et al.), and (b) slip amplitude, (d) slip duration, (f) rupture front evolution images of Imperial Valley (1979). Both kinematic source models have been extracted from the database of finite-source rupture models and then interpolated to a finer grid.

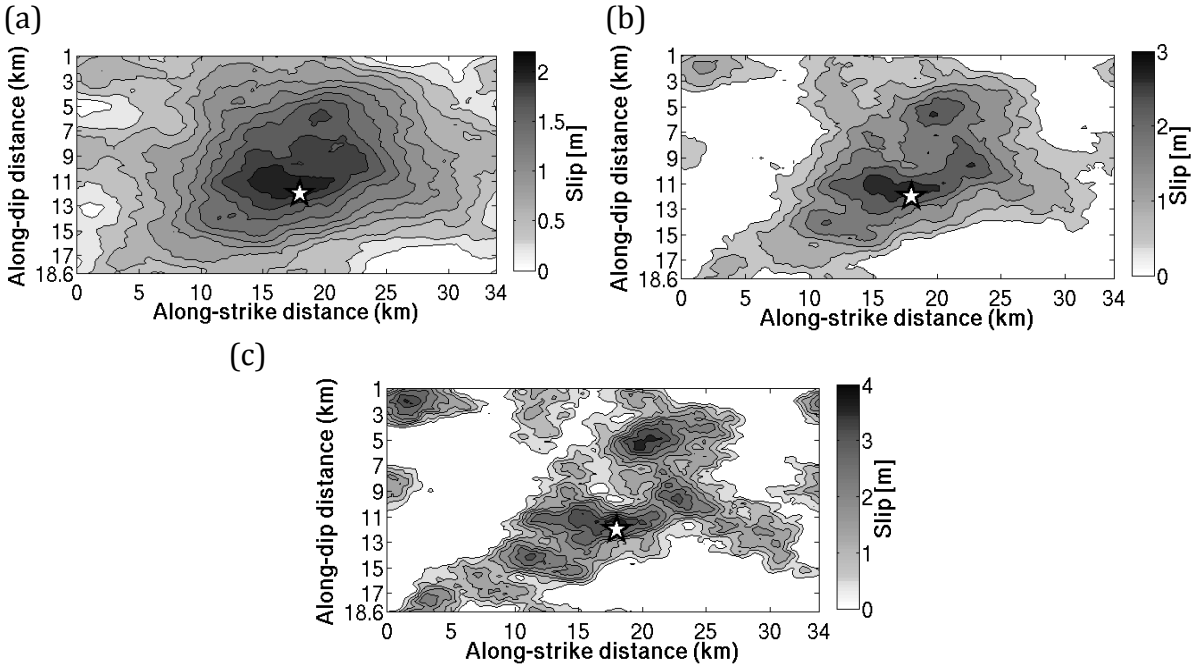

Figure 1.3: Slip images of the synthetic source models (a) k2-C04 (K=0.4), (b) k2-C08 (K=0.8), (c) k2-C16 (K=1.6), produced using k^{-2} descriptions of the final slip.

1.2.2 Station layout

A network of 135 hypothetical stations at various distances and azimuths was designed. The receiver configuration was set up for the R_{jb} (Joyner-Boore distance) distances 1, 3, 10, 20, 30, 60 and 100 km. We remind that R_{jb} and R_{rup} distances are the same for vertical strike-slip events with rupture reaching the surface. The receivers were positioned at the specified distances along a line parallel to the fault as well as beyond the ends of the fault extending radially outward. The locations of the stations were adapted to the respective rupture lengths of the source models. The station layout is illustrated in Figure 1.4 for the source model of the 2005 Fukuoka event (rupture length L = 26 km). The azimuth angle (θ) between the direction of the rupture propagation and the epicenter-receiver azimuth followed the definition provided in Somerville et al. (1997). Since we are considering strike-slip fault-models only, the angle θ is measured from the epicenter to the station in the horizontal plane as illustrated in Figure 1.4.

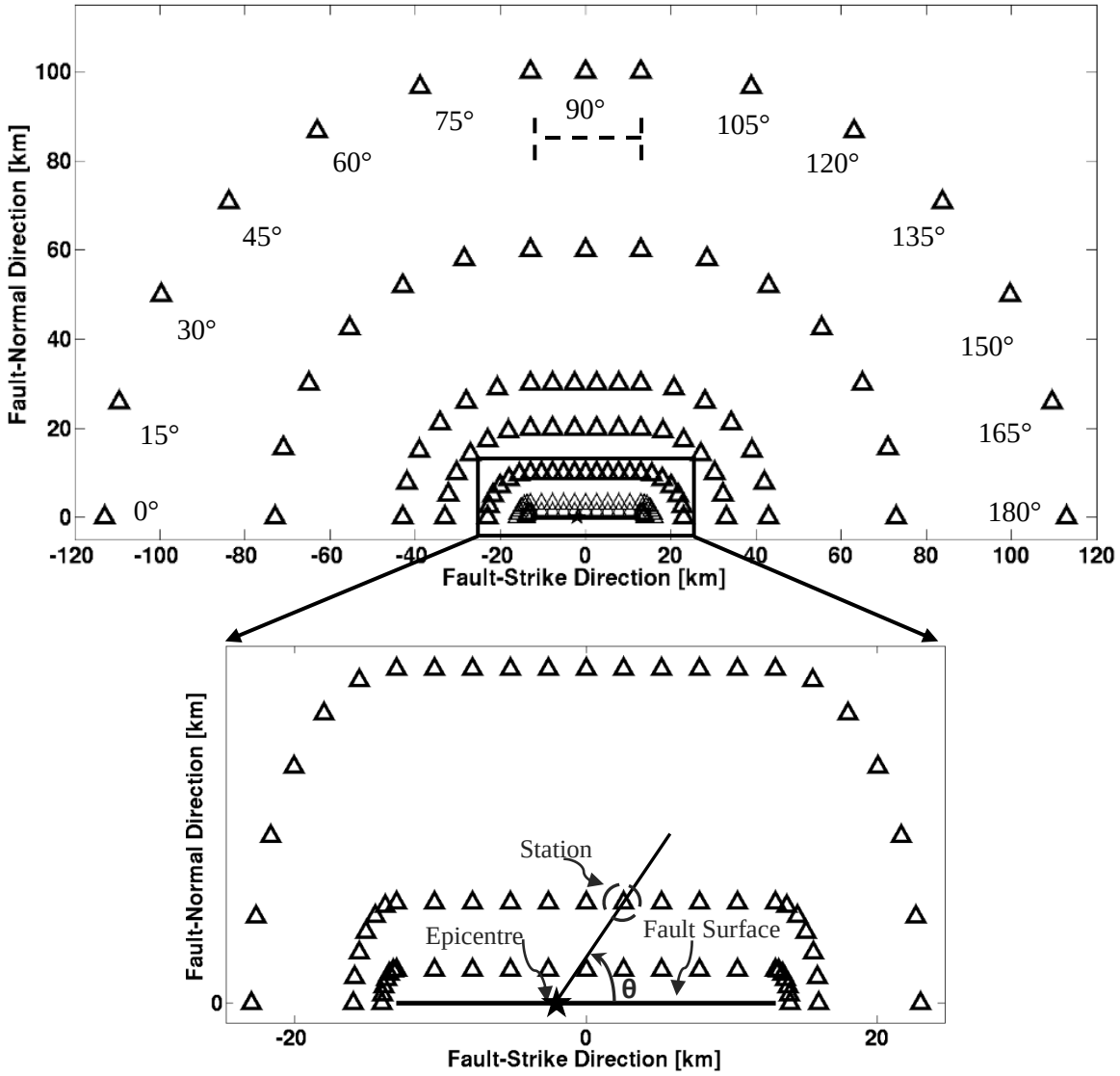

Figure 1.4: Station network for 2005 Fukuoka event with a zoom on the station very close to the fault (at 1, 3 and 10 km distance). The angle θ displayed on the zoomed plot represents the definition of azimuth angle between fault plane and ray path to site, according to Somerville et al. (1997). The radial angles (0° to 180°) on the top layout represent the alignment direction of the stations at different distances, i.e., the angle between the closest point on the fault and the station.

1.2.3 Synthetic ground-motion computation

Green's functions were computed considering 1D layered velocity structures (as used by the respective authors for source inversion, see Appendix B) using a discrete wavenumber technique (computer package AXITRA, Coutant 1989). For the 3 synthetic k^{-2} source models, the chosen velocity structure is the one used by Sekiguchi and Iwata (2002) to derive the source model of the 2000 Tottori event. Synthetic ground-motions are next computed by convolving the Green's functions with the slip history of all the sub-faults, as defined in the 11 considered kinematic source models. The source velocity functions (SVF) were the same as used by the authors. Finally 3-component velocity time series were obtained at each receiver location, by summing the contributions from the different sub-faults, for the respective source models. Because of the large extent of some of the faults considered in this study (Number of sub-faults, Table 1.1), the calculation of the ground motions were distributed on a computing grid in order to be achieved in a reasonable time. The principle of the decomposition of the computations is explained in Appendix C. The synthetics of the fault-normal component from the 2005 Fukuoka model have been illustrated in Figure 1.5.

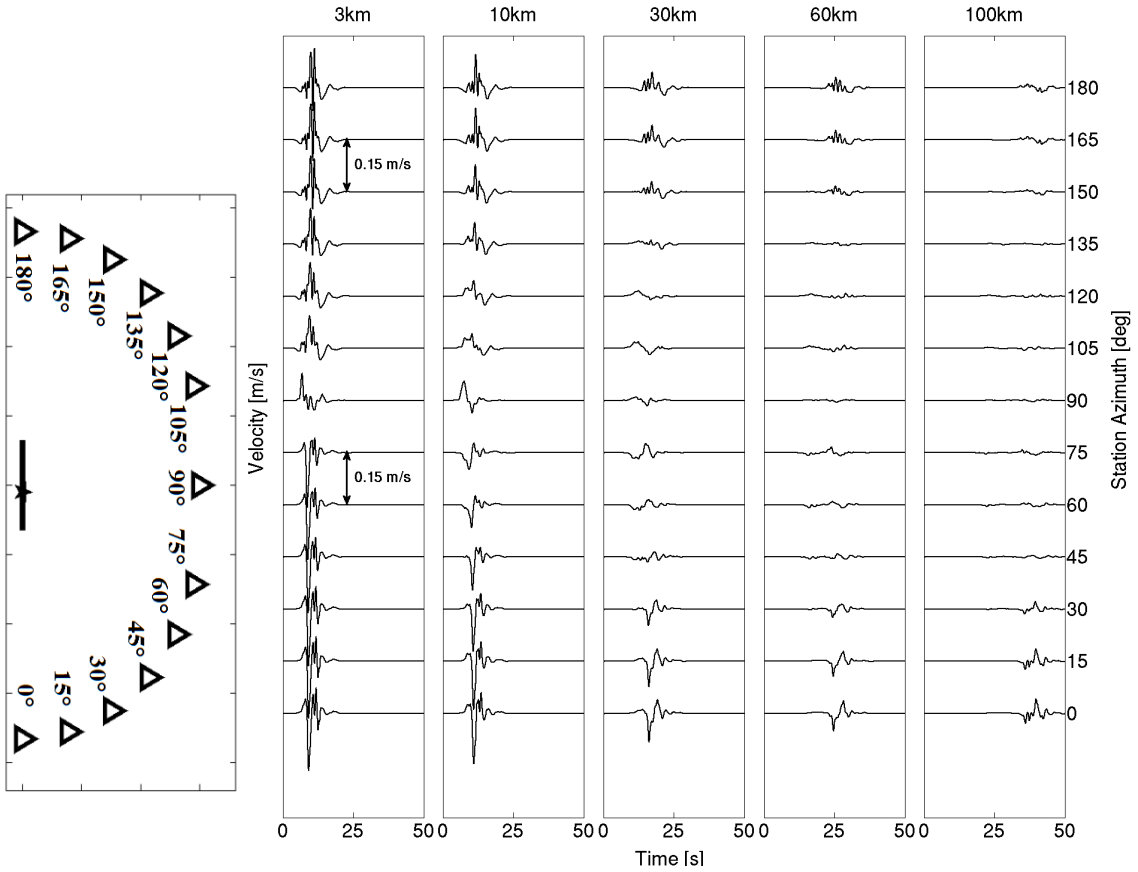

Figure 1.5: Synthetic velocity time series on the 'fault-normal' component of 2005 Fukuoka source model. Here station azimuth represents the station alignment (the angle between the closest point on the fault and the station) as illustrated in the station layout on the left.

1.2.4 PGV calculation

We computed the PGV values as proposed by Boore et al., 2006, using the GMRotD50 definition. GMRotD50 is an orientation-independent geometric mean using period-dependent rotation angles. The two orthogonal components of the synthetic time series have been rotated from 1° to 90° in 1° steps and the geometric mean for each pair of rotated time series were stored. Finally, PGV is taken as the median value of all the 90 geometric means. Ripperger et al. (2008) compared different PGV approximations from the two horizontal components and observed that GMRotD50 is a stable measure of the PGV showing a low dependence on the orientation of the horizontal components. Figure 1.6 shows mean (with standard deviation error bar) of ground motion in terms of natural log of PGV averaged over the different azimuths and along the R_{jb} distances for

the fault models considered in this study. It is interesting to notice that in Figure 1.6 (b), the PGV values at R_{jb} = 1 km seems to indicate a slight reduction compared to those at R_{jb} = 3km.

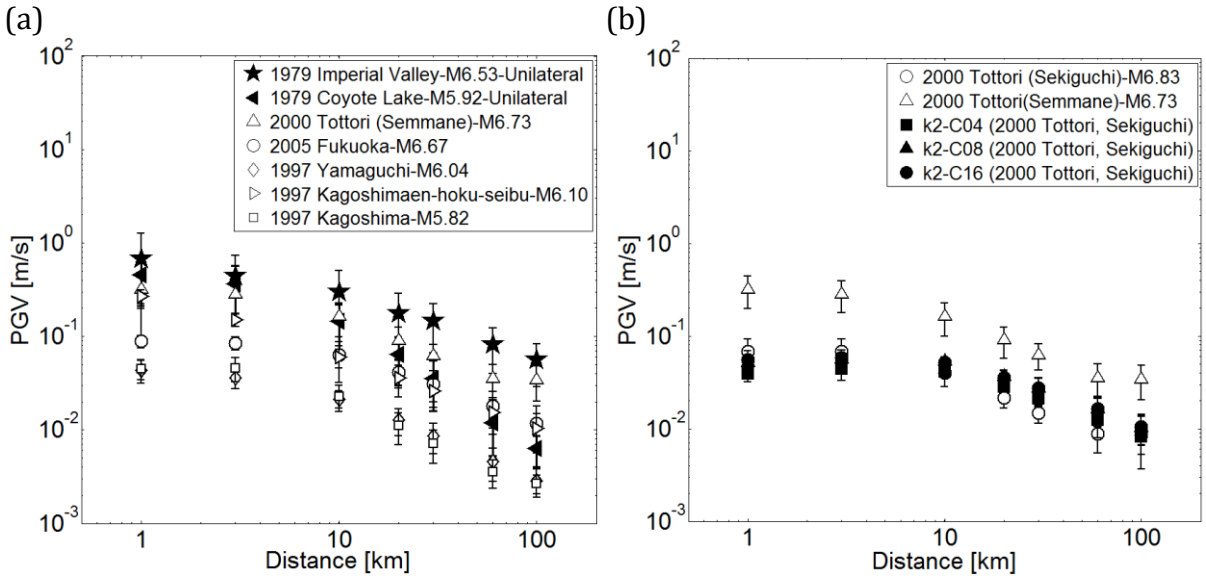

Figure 1.6: Mean ± std values (bars showing one standard deviation band) of peak ground velocity (PGV) with varying R_{jb} distances for (a) source models from the finite-source rupture model database and (b) k^{-2} source models and 2000 Tottori models.

1.3 Analysis of PGV within-event variability

We remind that we assessed the within-event component ϕ of the PGV variability (corresponding to a single source recorded at several stations) in this work. For each earthquake *e*, the variability at a distance *R* is calculated as the standard deviation of the residuals. The residuals are defined as:

$$\delta_{e,R} = \ln(PGV)_{e,R,\theta} - \overline{\ln(PGV)}_{\theta\, e,R}, \tag{1.3}$$

where $\ln(PGV)_{e,R,\theta}$ refers to the predictions for earthquake *e* at distance *R* and azimuth θ, and $\overline{\ln(PGV)}_{\theta\, e,R}$ denotes the average over azimuths.

Figure 1.7 (a) illustrates the within-event ground-motion variability ϕ with varying distances for the selected source models from finite-source rupture model database. Similarly, Figure 1.7 (b) compares the variability for the three k^{-2} source models along with the two 2000 Tottori models.

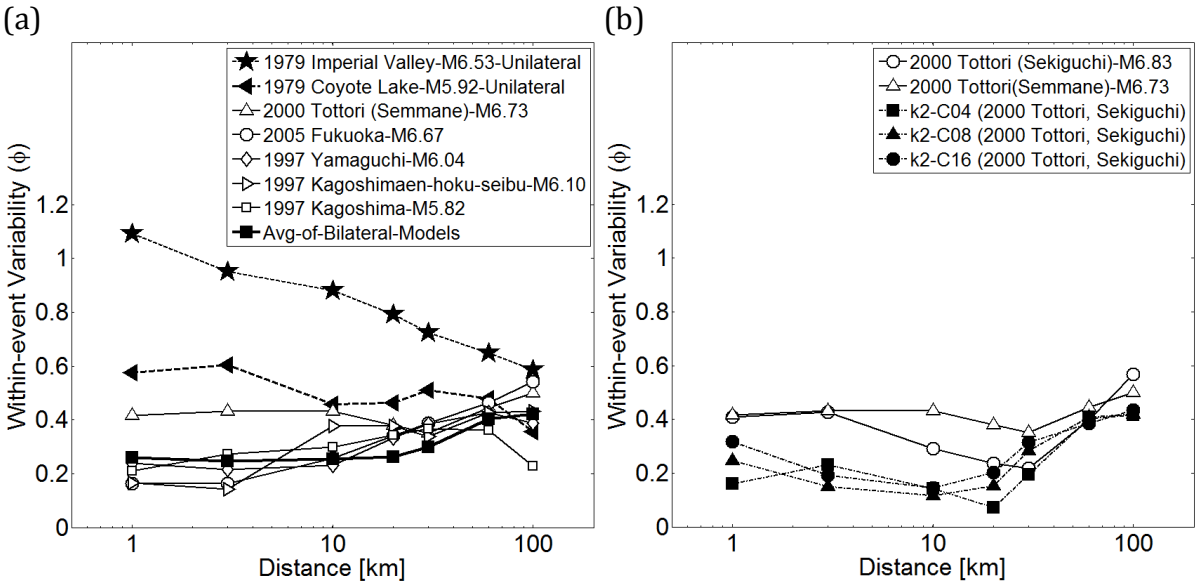

Figure 1.7: Within-event ground-motion variability (ϕ) with varying R_{jb} distances, for (a) source models from the finite-source rupture model database and (b) k^{-2} source models and 2000 Tottori event models.

We cannot ascertain any magnitude dependency of the variability due to the narrow magnitude range (M_w 5.82 to 6.83) considered. The most remarkable observation is that ϕ is dependent on distance. The distance-dependency of ϕ exhibits two main regimes depending on the rupture type, i.e., unilateral or bilateral (Figure 1.7, a.). The perceptible trends of the PGV-variability along with physical explanations on the origin of the variability are described below.

1.3.1 Variability considering bilateral ruptures only

We observe two main tendencies of ϕ considering bilateral rupture models only (*i.e.* with directivity ratio < 0.5), which could further be distinguished by the distance from the source.

1.3.1.1 Variability in the near field (below R_{jb} ~20 km)

Considering the tendency of average values of within-event variability computed from 9 bilateral models (the curve 'Avg-of-Bilateral-Models') in Figure 1.7 (a), variability ϕ demonstrates a fairly steady trend up to about 20 km from the source. However, the difference in the ϕ values among different rupture models is large (Figure 1.8). This is because at short distances ϕ is controlled by source parameters such as location of main slip area, rupture initiation point and hypocentral depth. A comparison of the results obtained for the Tottori event (models of Semmane et al., 2005, and Sekiguchi and Iwata, 2002) and the synthetic k^{-2} source models (Figure 1.7, b) highlights the effect of the position of the main slip area. The source model derived for Tottori (Figure 1.1, e and Figure 1.2, a) considers the main slip area to be more widespread on the upper part in comparison to the synthetic k^{-2} source models, which assume the main slip area to be on the middle of the fault plane (Figure 1.3). This may have caused the lower values of ϕ at 3 to ~20 km distance for the former models. Besides, the comparison between the three k^{-2} models (Figure 1.7, b) illustrates the effect of the different degrees of slip roughness (represented by the non-dimensional parameter K). According to Causse et al. (2010), the natural variability of K can be described by a lognormal distribution with $\sigma_{\log(K)}$=0.12. Thus, the values of K considered in our study (K=0.4, K=0.8 and K=1.6) are expected to cover a wide range of potential degree of slip roughness ([median - 1.5 std, median + 1.5 std], i.e. ~85% of the potential values). The comparison indicates that the degree of slip roughness alone has little influence on the ground motion variability in comparison to the position of the main slip area, except in the very near-field (*i.e.* at 1 km), where $\phi \sim 0.15$ for K=0.4 and $\phi \sim 0.35$ for K=1.6. Note that the sensitivity to slip roughness is likely to depend on other source parameters (rise, time, rupture velocity) and their potential correlations. For instance, large values of the rise time act as low pass filters and could contribute to smoothing the effects of slip heterogeneities. On the other hand, shorter values of rise time (*i.e.* < 3.5 s) may tend to increase the sensitivity to slip roughness.

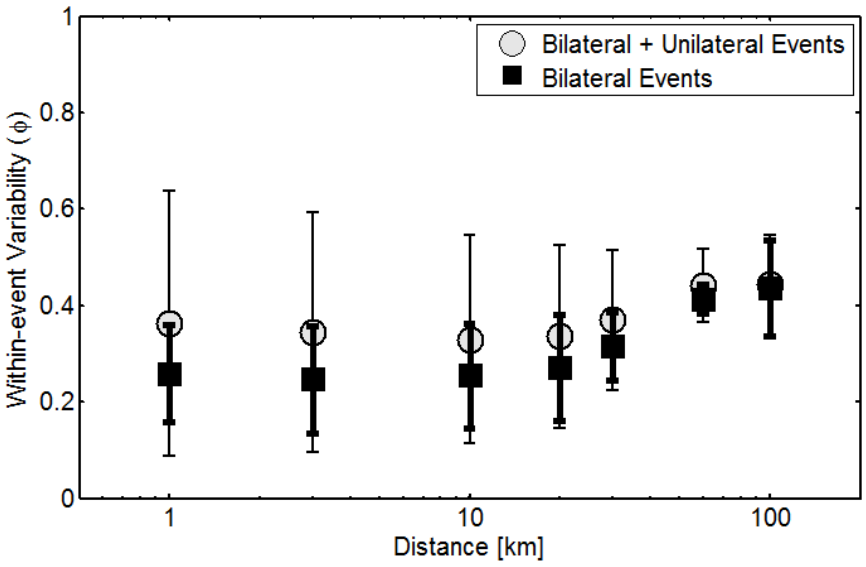

Figure 1.8: Mean ± std (bars showing one standard deviation band) of the values of within-event ground-motion variability (ϕ) with varying R_{jb} distances, for the cases (i) bilateral and unilateral events combined (ii) only bilateral events.

1.3.1.2 Variability in the far-field (beyond Rjb ~20 km)

Interestingly, the ϕ values for the bilateral events seems to increase gradually above ~20 km distance (Figure 1.7, a). This tendency can be explained by the fact that in the far field extended sources behave like point sources, and accordingly, ϕ is essentially controlled by the shape of radiation pattern of S waves and Love waves. This is further investigated by analysing the azimuth –and distance dependency of the PGV values for the 2005 Fukuoka and 2000 Tottori (Semmane et al., 2005) earthquakes. Figure 1.9 (a) represents the PGV values at each receiver station for the respective azimuth angle θ at different R_{jb} distances. Here, we remind that θ is the angle between the direction of rupture propagation and the epicenter-station azimuth (Somerville et al., 1997). For distances larger than ~30 km, the PGV values over various azimuths along the station-array form a 'W'-shape exhibiting radiation pattern effect. Following the SH-wave radiation pattern shape, we observe PGV maxima at azimuths 0°, 90° and 180° and PGV minima at 45° and 135°. The slower decay of PGV maxima compared to that of PGV minima, with increasing distance (featuring the elongation of 'W'–shape in Figure 1.9, a), eventually results in increased variability. Indeed PGV maxima are related to maximum SH-wave energy radiation at all distances, whereas the minima, i.e., ground

velocity at azimuths 45° and 135° are associated with a decrease of SH-wave energy radiation due to finite-source effects as distance increases.

1.3.2 Variability considering unilateral ruptures only

Turning now to the two unilateral rupture models (*i.e.* with directivity ratio > 0.5) of the 1979 Imperial Valley and 1979 Coyote Lake earthquakes, we can observe that unlike the bilateral models, the variability exhibits a decreasing tendency with distance (Figure 1.7 a), implying higher ϕ values at shorter distances due to the presence of directivity effects. For unilateral events, strong forward directivity effects (i.e. amplification of the PGV value) are expected for small values of the station-azimuth θ ($\theta < \sim 30°$). The dependence of directivity effects on θ is illustrated in Figure 1.9 (b), where the PGV values for the unilateral events are plotted against θ, at each R_{jb} distance. At short distances (< ~10 km) most of the stations are located in the 0°-30° azimuth region (15 out of 20 stations at 1 km) and thus associated with a strong PGV amplification due to forward directivity effects. The large proportion of high peaked PGV values results in large variability ϕ at shorter distances. As the distance increases, fewer stations remain in the forward directivity direction (3 out of 20 at 100 km) due to the smaller fault dimension relative to the fault-to-station distance, and hence the ϕ values decrease. Note that at 100 km, the values of ϕ are of the same order as for bilateral events, meaning that the directivity of the rupture propagation is a second order effect far away from the source (i.e., beyond 2-3 rupture lengths).

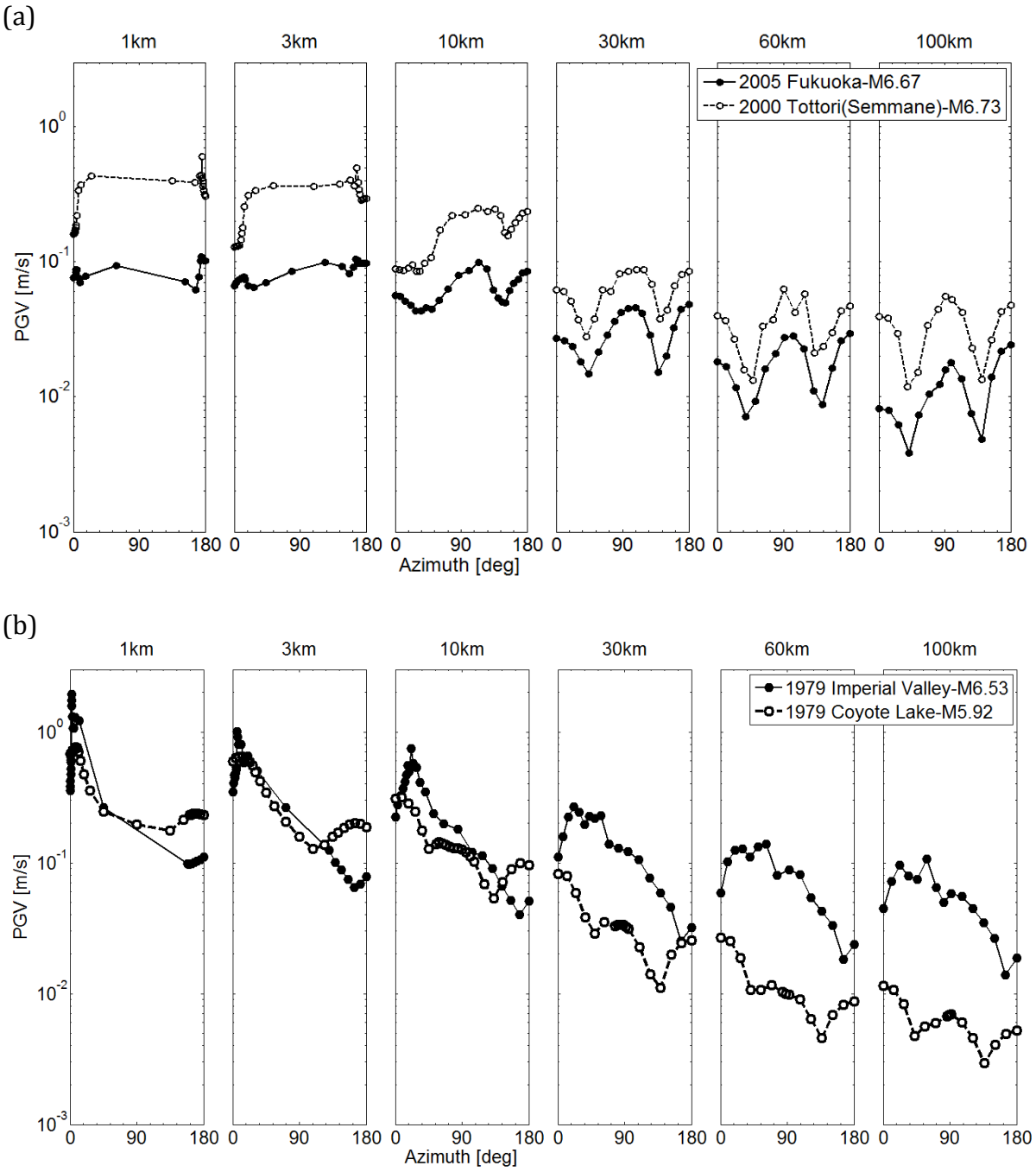

Figure 1.9: PGV values for the stations located at different azimuths along varying R_{jb} distances, for (a) bilateral and (b) unilateral events. Here azimuth represents θ, the angle between the epicenter and the station, as illustrated in Figure 1.4.

1.4 Discussion and conclusion

The ground-motion variability 'sigma' is a fundamental component of PSHA studies, because small variations in sigma values can largely influence seismic hazard analyses. So far GMPEs have considered sigma to be constant over distance. Though a few recent data analyses suggest that sigma is distance-dependent, such studies remain, however, affected by the lack of strong motion data recorded in the near source region (< 10-20 km). In this chapter we have analyzed sigma from the viewpoint of simulations to complement real data studies and to investigate the influence of different source parameters on the resulting ground-motion variability. Ground-motion, represented by the PGV, is computed from various kinematic source models and Green's functions computed for 1D-layered velocity models. Note that our study focuses on the within-event component ϕ of sigma. For simplicity we have limited our study to vertical strike-slip faults.

Our results suggest that the within-event variability ϕ significantly depends on the rupture type, with unilateral ruptures resulting in larger ϕ values than bilateral ruptures, especially in the near source region. Far away from the source (~100 km), this dependency vanishes and ϕ is steady ($\phi \sim$ 0.3-0.5) for both kind of ruptures. Thus the distance-dependency of ϕ presents two main behaviors: (1) ϕ increases with distance for bilateral events and (2) ϕ decreases with distance for unilateral events. Interestingly, the range of within-event variability values provided by our numerical simulations in far field is consistent with the 'single station' within-event variability (ϕ_{ss}) estimates obtained from real data by Rodriguez-Marek et al. 2013 ($\phi \sim 0.4$ at 100 km). It should be mentioned, however, that our ϕ estimations are not only 'single-station' but also 'single-path' since we assume a 1D velocity structure.

Using a global catalog of large shallow earthquakes, McGuire et al. (2002) found that approximately 80% of ruptures have directivity ratios larger than 0.5, pointing out the overall predominance of unilateral ruptures. This shows the importance of considering directivity effects in the estimation of the between-event variability of ground-motions. For a given earthquake scenario, prior knowledge about the rupture direction may contribute in refining the estimates of ϕ. Note that the large variability we obtained at

short distance for unilateral ruptures may, however, be strongly reduced if azimuth is considered as a predictor. This could be quantified by computing median ground motion from prediction models that account for directivity effects (*e.g.* Spudich and Chiou, 2008; Somerville et al. 1997), or simply by assessing the variability in various azimuth ranges.

Our simulations are performed up to 3 Hz for simple 1D media. The ϕ values inferred in far field are essentially controlled by the shape of the wave radiation pattern. Nevertheless the radiation pattern effect, that is clearly observed in our synthetics, might be limited to lower frequency range (<∼1 Hz) in real velocity structures. The theoretical four-lobe S-wave radiation pattern may be limited to low frequencies (<1 Hz), with a pattern getting isotropic at high frequency due to the scattering of seismic waves (e.g. Takemura et al. 2009; Takenaka et al. 2003; Liu and Helmberger 1985). In addition, according to Cho et al. (2010), observations suggest that far-field radiation patterns change from a distinct double couple pattern, with strong directivity effects at low frequencies (<1 Hz), to a more isotropic pattern with diminished directivity effects at high frequencies, putting forward the fact that directivity effects are also frequency dependent. This frequency dependence of directivity effects has been attributed to source incoherency by Bernard and Herrero (1994). Since our rupture models do not include any source of incoherency, the strong impact of directivity effects on the ϕ values computed from our synthetics may be weaker in the case of real earthquakes.

We remind that the results presented in this study are valid in a narrow magnitude range (∼6 < Mw < ∼7) and for vertical strike-slip events only. In addition, due to the small number of considered source models, the source variability may be underestimated and the inclusion of additional source models may then modify the observed overall trends. Considering additional unilateral rupture models would also strengthen the conclusions on the role of directivity effects. Finally, the cogency of our results relies on the validity of the inverted source models, which may be affected by uncertainties (*e.g.* Mai et al. 2007), due to the non-uniqueness of the inverse problem, errors in the forward model, etc. Source inversion models derived from incomplete datasets and the ground-motion prediction at a site that is not considered in the inversion can be significantly biased. This is especially true if the prediction site is

isolated as pointed out by Cirella and Spudich (2013). From a set of accelerograms recorded in the area of Niigata, the authors generated thousands of "good" source models (*i.e.* with a good level of data fit) of the 2007 Chuetsu earthquake, that they used to predict ground motion at the Kashiwazaki-Kariwa Nuclear Power Plant. They found that the ground motion scatter at the Power Plant is of the order of the empirically observed between-event variability. Part of this scatter arises from particular choices to parameterize the inversion process, which are inherently user dependent. For instance, two of the source models considered in our study account for variability in slip, rupture velocity and rise time, while the other models assume uniformity in rupture velocity and rise time (Table 1.1). These *a priori* choices partially constrain distributions and correlation patterns of source parameters, which may impact the ϕ values. However, the fact that we got nearly analogous estimation of ϕ from the two 2000 Tottori models, which were obtained by different authors / inversion parameterization, adds credibility to our results. Furthermore, our study is intended to focus only on the variability of ground motion rather than its absolute value. The overall observed trends of the ground motion variability have been related to global source features (rupture directivity, depth of the main slip area) that may still be captured by source inversions.

1.5 Data and resources

The eight finite-source rupture models used in this study have been extracted from the Finite-Source Rupture Model Database (Mai, 2004) available at http://equake-rc.info/SRCMOD/ (last accessed at 16:15, 21 March, 2014). This website is an online database of finite-fault rupture models of past earthquakes obtained using kinematic inversion of strong motion data, sometimes combined with geodetic and/or data. The database provides the complete description of the space-time distribution of the co-seismic slip, except from the model of Horikawa (2001) of the Kagoshimean-hoku-seibu event for which the rupture time distribution is not available.

Institut des Sciences de la Terre (ISTerre) is part of Labex OSUG@2020 (ANR10 LABX56). Most of the computations presented in this paper were performed using the Grenoble University High Performance Computing (HPC) centre, CIMENT, infrastructure (https://ciment.ujf-grenoble.fr, last accessed at 9:00, 20 March, 2014),

which is supported by the Rhône-Alpes region (GRANT CPER07_13 CIRA: http://www.ci-ra.org, last accessed at 9:00, 20 March, 2014) and France-Grille (http://www.france-grilles.fr, last accessed at 9:00, 20 March, 2014). For the parallel computations of a large number of single jobs, we exploited the available resources of a local grid of HPC clusters (totalizing more than 3000 computing cores) in a best-effort mode, the grid middleware "cigri" (http://ciment.ujf-grenoble.fr/cigri, last accessed at 9:00, 20 March, 2014). The results were stored on a distributed data grid operated by the IRODS system (https://www.irods.org, last accessed at 9:00, 20 March, 2014).

Chapter 2: Review of Argostoli site and dense array network

This chapter presents a very brief description of the site Argostoli, where the seismological experiment took place from September 2011 to April 202 within the framework of FP7 EU-NERA project (2011-2014). The chapter starts with an overview of the seismotectonics, seismicity, geology and geomorphology of the Cephalonia Island, where Argostoli basin is located in, and the surrounding region. Then, a short and preliminary description of the Argostoli site followed by an overview of the seismological experiment is provided. The catalogue of the recorded earthquakes, the quality of the data, and the subset of events used for the data analyses in Chapter 3 and 4, are discussed.

2.1 Introduction

The importance of spatial variability of earthquake ground motion has been recognized in earthquake-resistant design and analysis of horizontally extended structures for a long time. At least part of the ground motion variability is generally associated with a significant proportion of surface waves in the seismic wave field caused by lateral variation of material properties of the site (i.e. surface geology and geometry). Hence, recognition of the physical patterns of the wave field caused by the effects of subsurface geology and geometry is essential to fully capture the physical causes underlying the ground motion variation and incorporate it in engineering applications. Although many such instrumental and numerical investigations have been undertaken over the last decades, the complexity of the wave field combined with the limitations of geophysical investigation techniques and numerical simulation made it impossible till now to include effects of spatial variability in seismic hazard and risk assessment, except in very rare cases. Consequently, the vast majority of building codes do not have any provision for considering such effects.

To this end, one of the goals of the JRA1 & JRA3 work packages (Waveform modeling and site coefficients for basin response and topography; coherence of near-fault ground motion) of the FP7 EU-NERA 2010-2014 project (Network of European Research Infrastructures for Earthquake Risk Assessment and Mitigation) was to perform seismological experiment on basin effects and spatial variability of ground motion with the long term aim of proposing simple, engineering oriented models to incorporate such effects. The experiment took place in, Cephalonia Island situated in western Greece, one of the most active seismic sites in Europe. The instrumental setup was carried out at a small alluvial valley 'Koutavos-Argostoli', located in the south of the town Argostoli in Cephalonia. Four European institutions, ISTerre, INGV, ITSAK and GFZ participated in the experiment and deployed 64 seismological stations along two profiles (parallel and perpendicular to the major axis of the valley) for the period September 2011 to April 2012. Since seismic arrays are very useful to study the fine-scale structure of Earth's interior as well as the variations of the material properties, and the current development of data processing techniques have provided valuable means of

understanding seismic wave field, installation of two very dense arrays was also included in the experiment. In addition, specific geophysical and geological surveys have been performed on the site to constrain the basin geometry and the wave-velocity structure.

The experimental part of this thesis deals with the identification of seismic wave field composition and analysis of spatial variability of ground motion in Argostoli site based on array data acquired from this temporary seismological experiment of Argostoli. the French national pool of portable seismic instruments SISMOBRESIF, France, provided 25 seismological stations in the experiment. The principle array, Array-A, consisted of 21 SISMOB/INSU SISMOBRESIF stations equipped with broadband 30s velocimeters, with interstation distance ranging from 5 to 160 m and was located towards the south-western edge of the valley. Four stations were placed in the linear station-arrangement located on the station-profile crossing the valley. A smaller array, Array B, was deployed by the project partner German Research Centre for Geosciences (GFZ), close to the north-eastern edge. It consists of 10 stations, equipped with 1 Hz velocimeters, with interstation distance ranging from 5 to 60 m. In this thesis, earthquake data recorded by Array A has been used to perform seismic wave field analysis and spatial coherency estimation. For comparison purpose, Array B data of some events have been used in seismic wave field analysis. The aim of this chapter is thus to present a review on the Argostoli site and earthquake data recorded by Array A. At the same time, a brief description of the configuration of Array B has also been included. The detailed account of the entire seismological, geophysical and geological experiments held in Argostoli is, however, out of the scope of this chapter, and will be found in a forthcoming paper (Cultrera et al., 2014).

2.2 The site: Argostoli, Cephalonia

2.2.1 Seismotectonics

The island of Cephalonia falls in the north-westernmost boundary of the Aegean plate. It is located in a tectonically active region, mainly formed by the Apulian (Adriatic region) microplate (Figure 2.1). This microplate is bounded by three tectonic plates: the stable

continental Eurasian plate to the North, the Anatolian plate to the East, and the African plate to the South (Lagios et al., 2007). Plate motions showed in the Figure 2.1 indicates that the African plate is moving northward relative to Eurasia at a rate of about 10 mm/yr. The predominant motion between Africa and Arabia (~ 10 mm/yr) seems to be left-lateral motion along the Dead Sea transform fault. This northward motion of Arabia results in westward displacement of the Anatolian plate, counter-clockwise, relative to Eurasia. It is notable that the westward rotation of Anatolia (20-25 mm/yr) does not result in a compressional field in the Aegean area. Rather, an extensional stress field dominates the Aegean, which moves with much high velocity (~35 mm/yr) with respect to Eurasia.

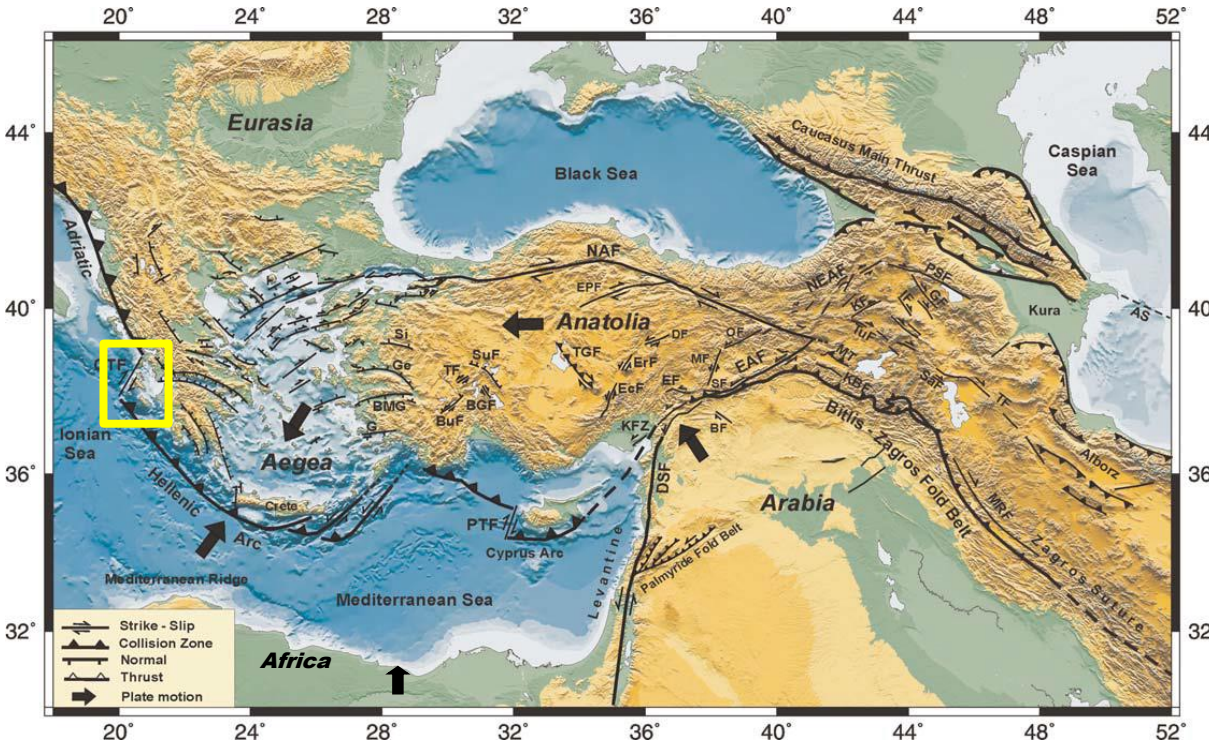

Figure 2.1: Tectonic-plate map of Greece (Taymaz et al., 2007). Yellow rectangle marks the study area Cephalonia.

The interaction between the African and the Eurasian tectonic plates where the Eastern Mediterranean lithosphere is being subducted beneath the Aegean lithosphere along the Hellenic Arc-Trench System, control the tectonic setting of western Greece (Le Pichon et al., 1995; Papazachos and Kiratzi, 1996; Lagios et al., 2007). Cephalonia, being one of the central Ionian Islands, lies in the western part of the subduction zone (Figure 2.1 and

2.2). Subduction results in high shallow seismicity along low-angle thrust faults of the Hellenic arc and in intermediate-depth seismicity along a well-defined Benioff zone in the southern Aegean (Papazachos, 1990). The western part of the Hellenic convergence zone, extending from Cephalonia to the south of Zakynthos, is also characterized by a positional change of the frontal thrust in this domain. The evolution here could be described as a continuation of the Alpine orogeny with a foreland-propagating fold and thrust belt of the Hellenides, the front of which jumped during the middle Miocene from its position at the Pindos thrust (east of Ionian zone) to the west of this zone at the Ionian thrust which is now clearly expressed to the east of Cephalonia and Zakynthos (Underhill, 1989; Hatzfeld et al., 1990, Lagios et al., 2007).

Faults of various directions and types (normal, reverse and strike-slip) traverse the Cephalonia area. An escarpment in the bathymetry northwest of the island indicates the existence of a strike-slip fault trending NE–SW (Finetti, 1976; Underhill, 1989; Tselentis et al., 1997). Underhill (1988, 1989) suggested that the strain accommodation within the main system of contraction results in this dextral strike-slip faulting. Figure 2.2 shows the NE-SW trending strike-slip fault system of Cephalonia, known as Cephalonia Transform Fault (CTF). CTF is a well-documented offshore active fault and limits the Island of Cephalonia to the west. This fault is a major right-lateral strike-slip fault, linking the continental collision to the subduction zone, between the Apulian microplate and the Hellenic foreland (Le Pichon et al., 1995; Sachpazi et al., 2000) and contributes significantly to the region's geodynamic complexity (Le Pichon et al., 1995; Louvari et al., 1999). The recent shallow seismic activity in the area is thus associated with this strike-slip mechanism. The deeper seismicity, due to mostly compressional mechanisms, is related to the subduction.

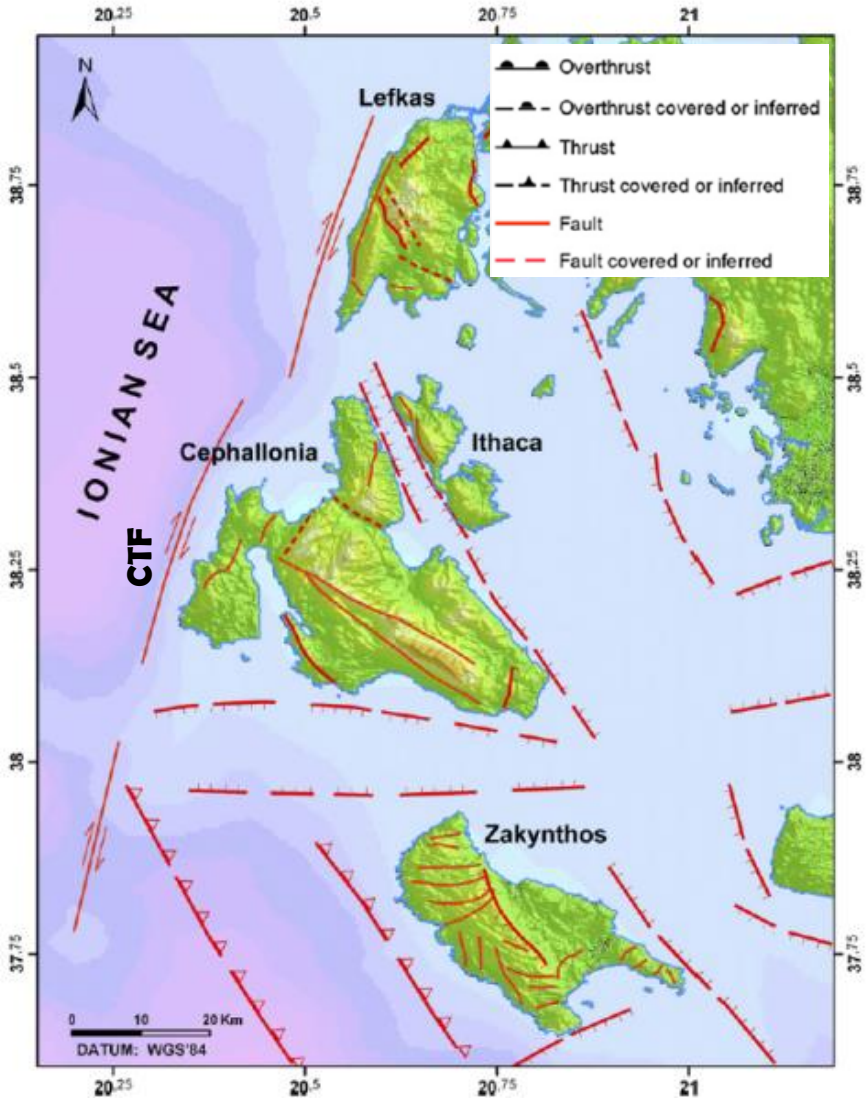

Figure 2.2: Main fault systems of the Cephalonia Island taken from the Seismotectonic Map of Greece (IGME) (Lekkas et al., 2001; Lagios et al., 2007). CTF: Cephalonia Transform Fault.

From different studies on the analyses of the earthquakes occurring on the fault, it is considered that the length of the Cephalonia transform fault is approximately 100 km, striking in an almost NNE–SSW direction (Papadimitriou et al., 2006). The slip direction of the CTF is N 213° and is in agreement with a south-westwards motion of the Aegean. The rate of seismic slip in the CTF varies from 7 to 30 mm/yr based on DGPS measurements (Anzidei et al., 1996; Hollenstein et al., 2006), which is consistent with seismological data and considered to be the highest observed in the whole Aegean area (Papazachos and Kiratzi, 1996).

2.2.2 Seismicity

Greece is currently considered as the highest seismic activity area in Europe and characterized by the occurrence of large earthquakes. Figure 2.3(a) shows the shallow seismicity (h≤40km) in the Aegean and surrounding region after Kiratzi et al., 2007. The plot includes historical seismicity from 464 BC to 1910 and instrumental seismicity from 1911 to 2005. The highly frequent occurrences of large magnitude (M_w> 6.5) earthquakes are quite evident from the plot, especially in and around Cephalonia. Figure 2.3(b) illustrates the significant seismicity in the Ionian Sea for the time period from 1964 to 2005 where epicentres and fault plane solutions of moderate to large events that occurred in this period are presented (Papadimitriou et al, 2012). Fault plane solutions of all major events reveal right-lateral strike-slip faulting with a small thrust component striking in a SW–NE direction and dipping in SE.

(a) (b)

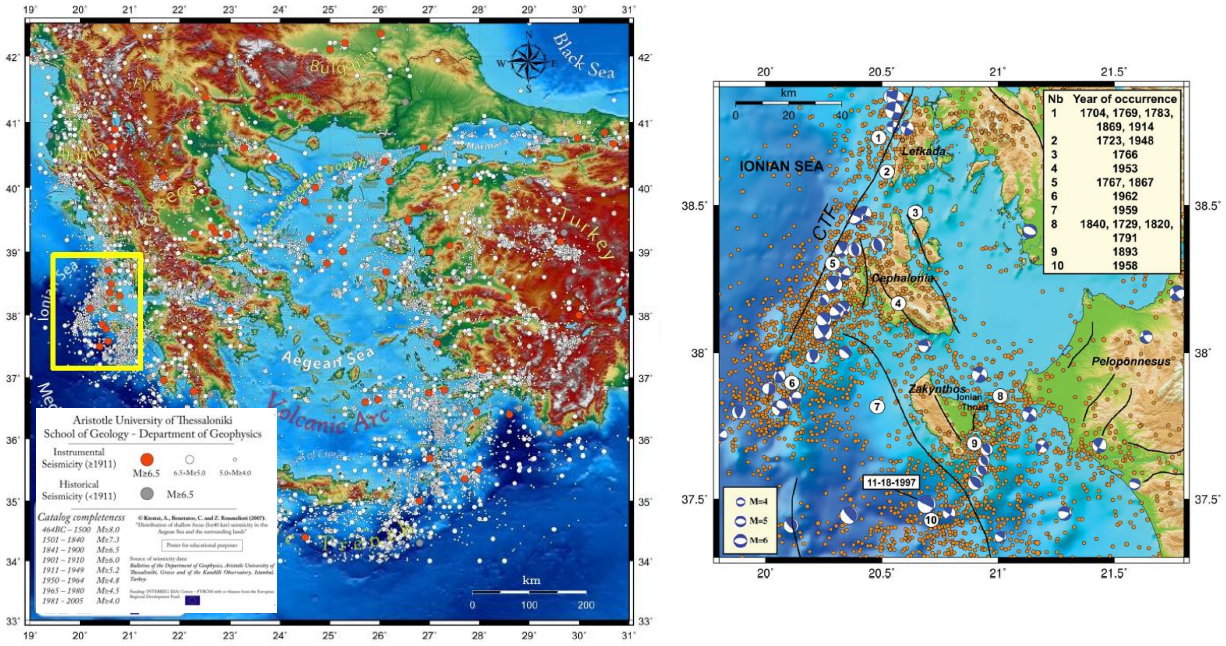

Figure 2.3: (a) Shallow seismicity (h ≤ 40 km) in Greece and surrounding region. Yellow rectangle shows Cephalonia area. (Kiratzi et al., 2007; taken from Pitilakis, 2014). (b) Seismotectonic map of Ionian Sea and surrounding area (Papadimitriou et al, 2012). Small circles represent epicentres with M_w > 3.6 for the time period from 1964 to 2005, large circles labelled 1–10 correspond to historical and instrumentally recorded strong (M_w > 6.0) events before 1964. The fault plane solutions of the events with M_w > 4.5 for the same time period are also shown. Black lines represent main active faults.

In view of the seismicity, Cephalonia Island is, hence, one of the most active seismo-tectonic regions in Greece. The area is included in the highest seismic hazard class of the Greek building code. High seismicity in the central Ionian Sea is considered to be the result of intense crustal deformation associated with right lateral strike–slip faulting along the CTF which supports earthquake magnitudes up to M = 7.4 (Louvari et al., 1999). Historical data show that seismicity rate of the strong (M ≥ 6.5) main shocks in this zone remained stable during the last four centuries with an average of about one such shock per decade (Papadimitriou and Papazachos 1985; Kokinou et al., 2006). More than 10 earthquakes of magnitudes between 6.5 and 7.5 occurred in the area between 1900 and 1998 causing major destruction. The past large events (1469-1983) in Cephalonia and surrounding areas plotted from Papazachos et al. (2000) and (2010) are shown in Figure 2.4(a). It is remarkable that these past large events often appear clustered in time (showed in different colors).

In 1953, the city of Argostoli was devastated by a sequence of three Ms > 6 earthquakes that took place within 4 days, destroying 80% of the houses, and killing more than 450 people. The largest event, M = 7.2, occurred on 12 August 1953, at an epicentral distance less than 20 km from the town. Another large magnitude event, M = 7.0, occurred on 17 January 1983, at an epicentral distance of about 30 km, with, however, a low damage impact on Argostoli. Some other recent strong events include M_w = 6.5 earthquake in August 14, 2003 to the west of Lefkas, a sequence of M_w = 5.6 earthquakes in October 2005 and M_w = 5.5–5.7 earthquakes in April 2006 to the south of Zakynthos. Smaller events of $4 < M_w < 5$ occur in the area in a regular interval and at least one event of $M_w \approx 5.0$ is expected in the broader region every year. Very recently, two strong earthquakes occurred on 26 January (M_w = 6.1) and 03 February 2014 (M_w = 6.0) in the western coast of Cephalonia, within 20 km distance from the city of Argostoli and damaged a significant number of structures. According to the Seismological Centre of the Aristotle University of Thessaloniki, the events were shallow crustal events with depth about 10 km. These two events were followed by a number of aftershocks up to M_w 5.5. The epicentres of the January 26 and February 3, 2014 strong events and the epicentre of the January 26 aftershock (M 5.5) are shown in the Figure 2.4(b). Focal mechanisms for these three events along with the typical focal mechanism of Cephalonia region are also provided. From the epicentre and the focal mechanism of the

main shocks of 2014 events, it could be deduced that the focal mechanism of Cephalonia earthquake sequence resembles to the typical mechanism of the region and thus related to the well-known Cephalonia Transform Fault (CTF) zone.

(a) (b)

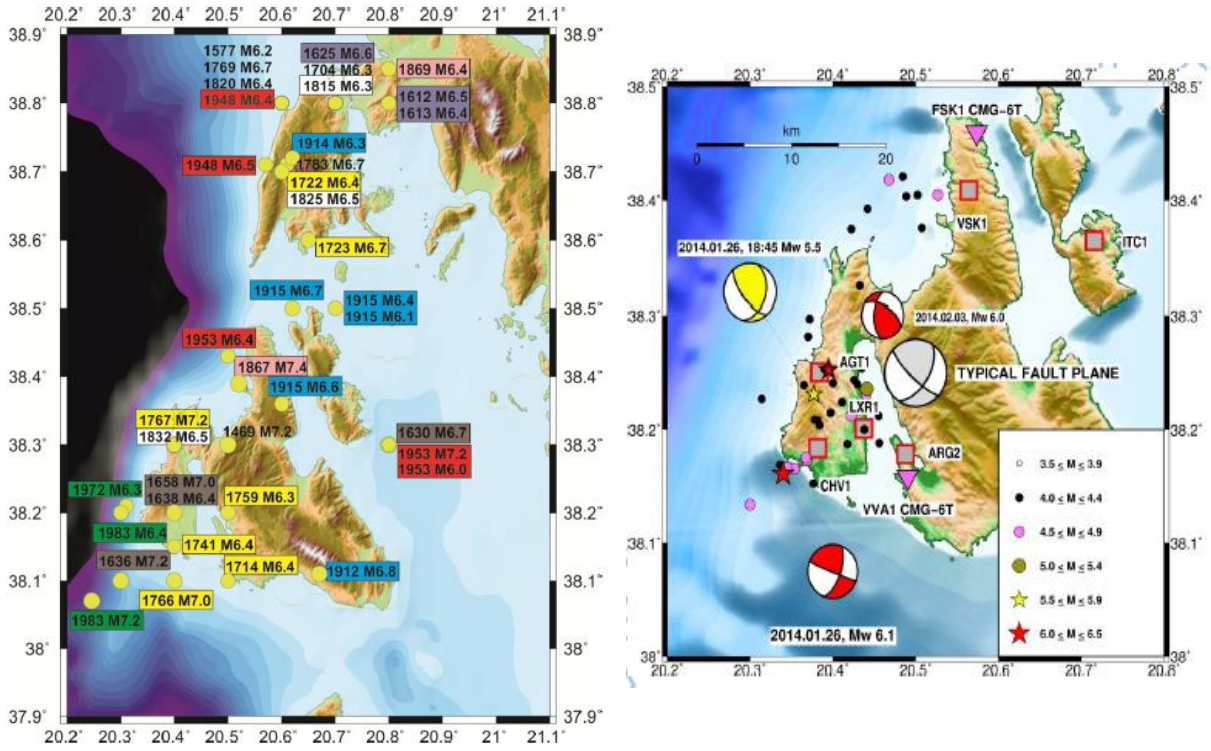

Figure 2.4: (a) The spatial distribution of epicenters of the large past earthquakes for the period 1469-1983 (Papazachos et al. (2000) and (2010); Pitilakis, 2014). (b) Epicenters and the faulting mechanisms of the January 26 and February 3, 2014 earthquakes. Red stars show the epicenters of the two main shocks. Yellow star shows the epicenter of the M = 5.6 aftershock of January 26, 2014 18:45 GMT. The aftershock distribution (M >= 4) of the seismic sequence in Cephalonia one month after the first event are also shown (source: Hellenic Unified Seismological Network-HUSN) The focal mechanisms of these events (source: GCMT solutions) are shown in respective color balloons. The typical focal mechanisms for Cephalonia area (Papazachos and Papazachou, 2003) is shown by the grey ballon. The grey squares and pink triangles denote the sites of accelerographs and seismographs (GEER Report, 2014)

2.2.3 Geology and geomorphology

Cephalonia comprises the western part of the fold-belt of the External Hellenides (Himmerkus et al., 2007; GEER Report, 2014). The island was formed during Tertiary times as a result of the convergence between the African and the Eurasian plates that initiated at the end of the Cretaceous (Kamberis et al., 1996). It mainly consists of Alpine Mesozoic and Cenozoic sedimentary rocks belonging to the External Hellenides, the Paxos or Pre-Apulian zone and the overthrusted Ionian zone (Lekkas et al., 2001). The Pre-Apulian zone forms the major part of Cephalonia. This rock unit (Pre-Apulian or Paxos) consists mainly of a thick sequence of carbonates (limestone and dolomite) of Triassic to Middle Miocene age, overlain by a much thinner fine clastic sequence of marl and pelite of Middle Miocene to Lower Pliocene age. The zone has experienced significant late Neogene and Quaternary shortening (Underhill, 1989). Figure 2.5 shows the geological formations of Cephalonia after Underhill (2006). The study area, Argostoli block (south and south-western part of the island) is seen to be mainly composed Pilocene-Pleistocene marine deposit and bounded by Cretaceous-Palaeocene formation in the east and west. According to Lekkas et al. (2001), the study area, Argostoli block (south and south-western part of the island) is seen to be mainly composed of Hollocene-Pleistocene alluvial deposit in the center and surrounded by Pilocene –Pleistocene marine deposit in the south-west and by carbonate sequence in the east.

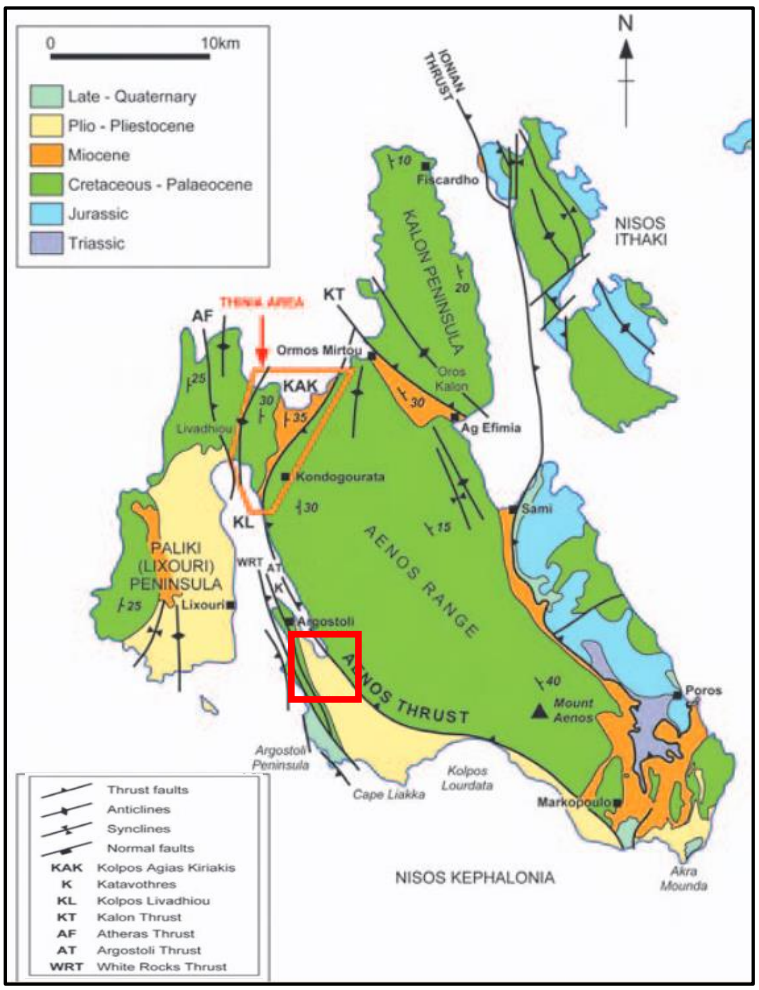

Figure 2.5: Geological formations of Cephalonia (Underhill, 2006). Red rectangle shows the study area at Argostoli.

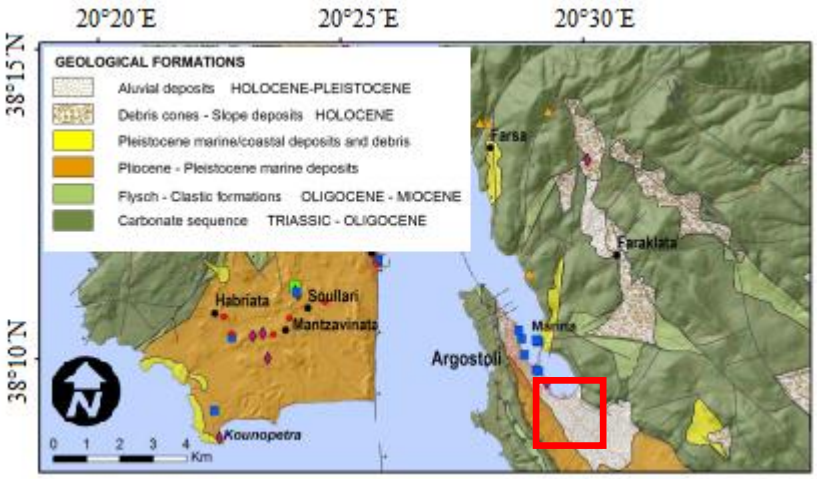

Figure 2.6: Geological formations of Argostoli area, after Lekkas et al. (2001) and modified from Valkaniotis, et al., 2014. Red rectangle shows the study area at Argostoli.

2.2.4 Argostoli Valley

Argostoli is a relatively small alluvium valley situated in the eastern part of the Gulf of Argostoli (Figure 2.7). The gulf opens towards the Ionian Sea in the south and extends to the entrance of the Bay of Argostoli. The Kutavos Bay branches off from the main gulf and extends approximately 5 km to the southeast. Kutavos Bay is surrounded by the Tilegrafos hills and the city of Argostoli to the west, the coastal plain of Krane to the south and the foothill of the Aenos mountain range to the east. The dense seismic arrays under Nera experiment were deployed at the Koutavos park, just to the south of the Bay.

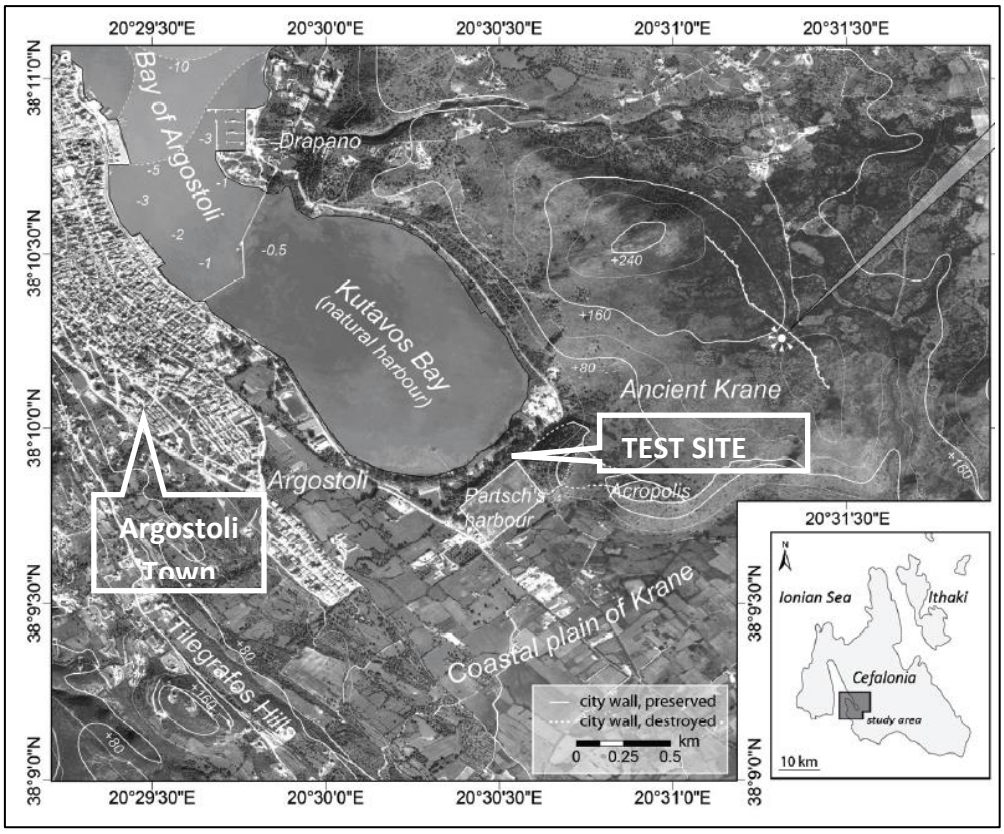

Figure 2.7: Topographical overview of the test site Argostoli (Hadler et al, 2011).

Existing literature demonstrates that 3 km long and 1.5 km wide Argostoli valley is surrounded by hills of limestone and marl, and covered by soft Neogene sediments up to 40-50 m depth (Protopapa et al., 1998). The NE-SW cross-section of the valley, proposed by Protopapa et al. (1998), is presented in Figure 2.8. The cross-section shows shear-wave velocities (V_s) ranging between 140 m/s and 500 m/s in the sedimentary core.

(a) (b)

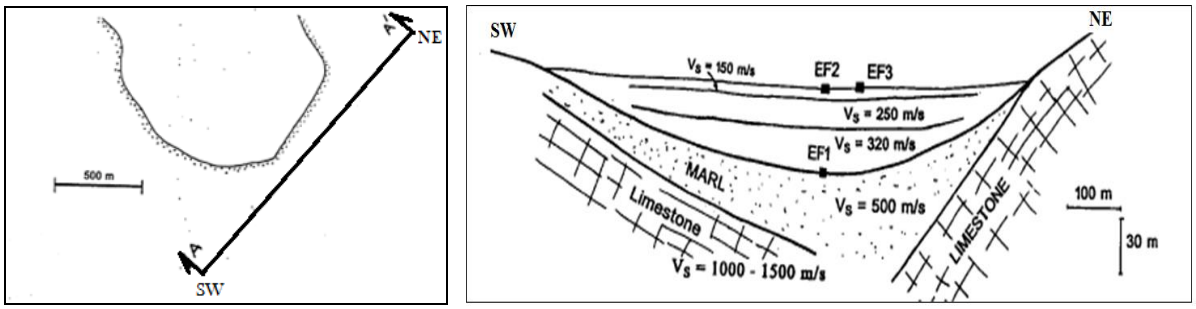

Figure 2.8: (a) The SW-NE cross-section and (b) 2D model of the SW-NE section of the Argostoli valley (Protopapa et al., 1998).

The available description of Argostoli valley is very preliminary. Therefore, further geological and geophysical studies have been carried out by NERA project for the better characterization of the basin. Prior to conducting NERA seismological experiment, H/V spectral ratio was calculated based on ambient noise recorded by Güralp CGM6TD acquisition unit at the centre of the valley (EF2 site in Figure 2.8,b). The H/V estimation outlined a very clear fundamental frequency of the site of about between 1.5-2 Hz (Figure 2.9).

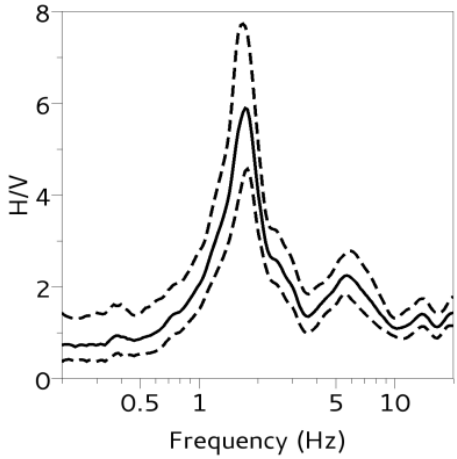

Figure 2.9: H/V average spectral ratios (±1σ) at the center of the valley, site EF2, based on ambient noise recordings of about 1 hour.

2.2 Seismological experiment

A total of 62 seismological stations were deployed in the Koutavos-Argostoli basin during NERA seismological experiment that took place on 20 September 2011, and were operational until 17 April 2012. Two more stations were installed in two distant sites in order to improve the hypocentral locations of the earthquakes recorded during the experiment. In addition, specific geophysical (single-station noise, passive and active surface waves measurements) and geological surveys have been performed to constrain the basin geometry and the wave-velocity structure. Other investigations have been performed within the SINAPSC project (founded by French research Agency ANR) and their data were made available to NERA partners under a specific formal agreement (Cultrera et al., 2014). Analyses of geological and geophysical data are going on presently in order to properly characterize the basin geology and geometry as well as the wave-velocity structure. However, providing details of the entire seismological, geological and geophysical experiments is beyond the scope of this thesis. Here, we will only focus on the array experiment.

Figure 2.10 shows H/V peak frequencies estimated at the instrumental sites during NERA and SINAPSC projects. R01 and R02 are the two reference stations and A00 and B01 are the central stations of the two arrays. Distance between R01 and R02 is about 2 km. Figure 2.11 shows locations of the NERA seismological stations only. The stations were distributed along two profiles (parallel and transversal to the major axis of the valley); the one crossing the basin had inter-station distances of about 50 meters, and included two very dense arrays, Array A and B (Cultrera et al., 2014). From Figure 2.10 we can consider the average fundamental frequency of the basin at the location of our seismological experiment as ~1.5 Hz. Preliminary results of geological and geophysical investigations showed that location of the arrays are on the soft Quaternary sediments.

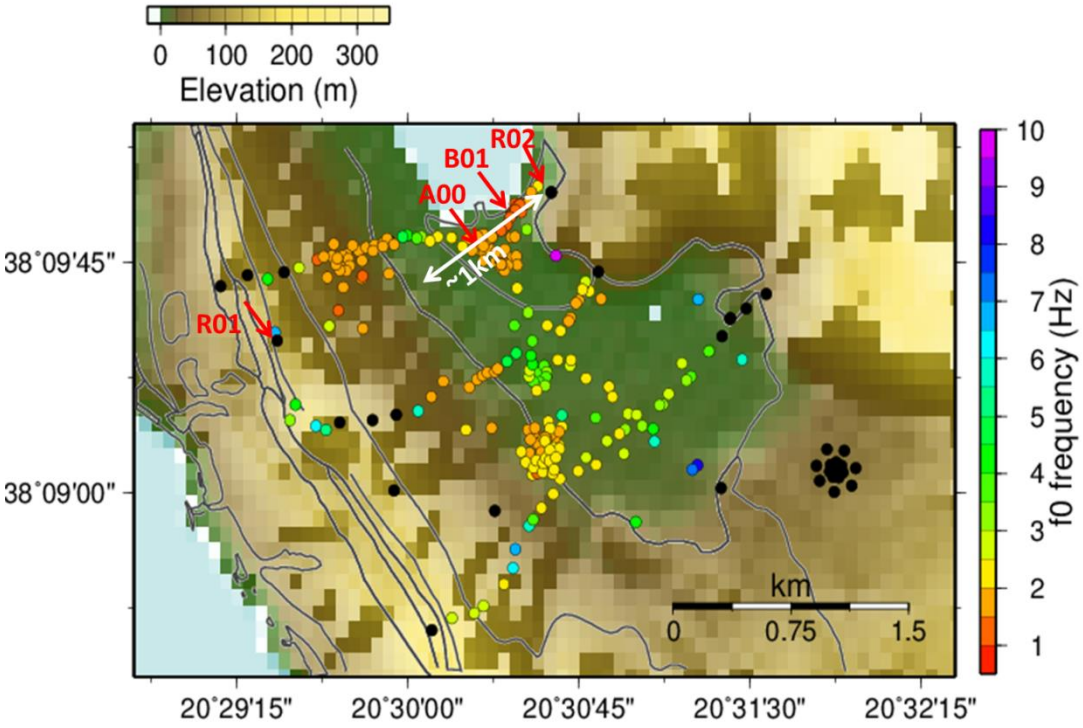

Figure 2.10: Map of fundamental frequency estimated at all the stations from seismological and geophysical investigations carried out by NERA and SINAPSC projects (Boxberger et al., 2014). Black dots indicate sites that do not exhibit any H/V peak.

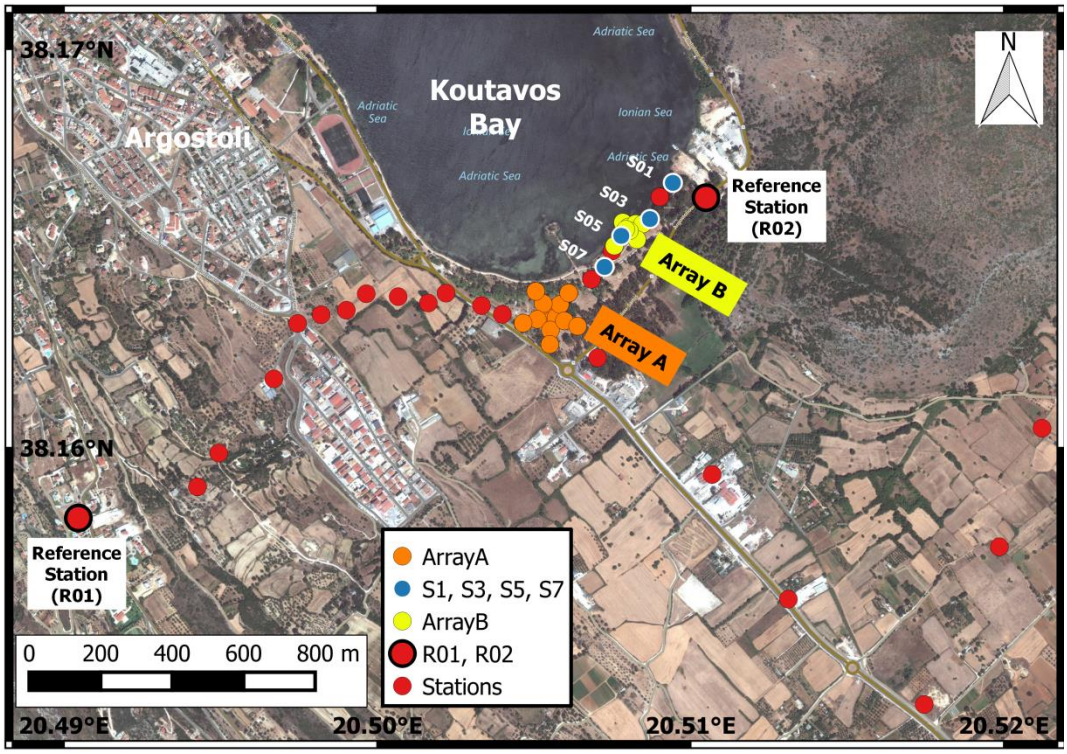

Figure 2.11: Location of NERA seismological stations. Circles of different colors indicate the location of the stations. S01, S03, S05, S07 and Array-A constitute the deployed stations by ISTerre.

Array A was deployed by the NERA project partner team from ISTerre (Institut Sciences de la Terre, Grenoble, France), located approximately 550 m away from R02 station (i.e. from the NE edge of the valley). It consists of 21 stations (Güralp CMG40T with eigenperiods between 30 and 60 s) connected to Nanometrics Taurus digitizers, belonging to the French mobile national seismological pool INSU/SISMOB. The stations are placed along four concentric circles, with radii of 5, 15, 40 and 80 m, around the central station A00 (Figure 2.12). All stations are located on the same geological unit. The other 4 stations installed by ISTerre are named as S01, S03, S05 and S07, and they are located on the linear profile of the stations between Array A and R02 (Figure 2.11). A smaller array was deployed by the project partner GFZ (German Research Centre for Geosciences), close to the north-eastern edge of the basin, named as Array B. It consists of 10 stations, Mark 1Hz sensor, with interstation distance ranging from 5 to 60 m. The central station B01 was located at about 260m from R02. Geometry of Array A and Array B are shown in the Figure 2.12 and 13, respectively. The coordinates of the stations of both arrays are given in Appendix D.

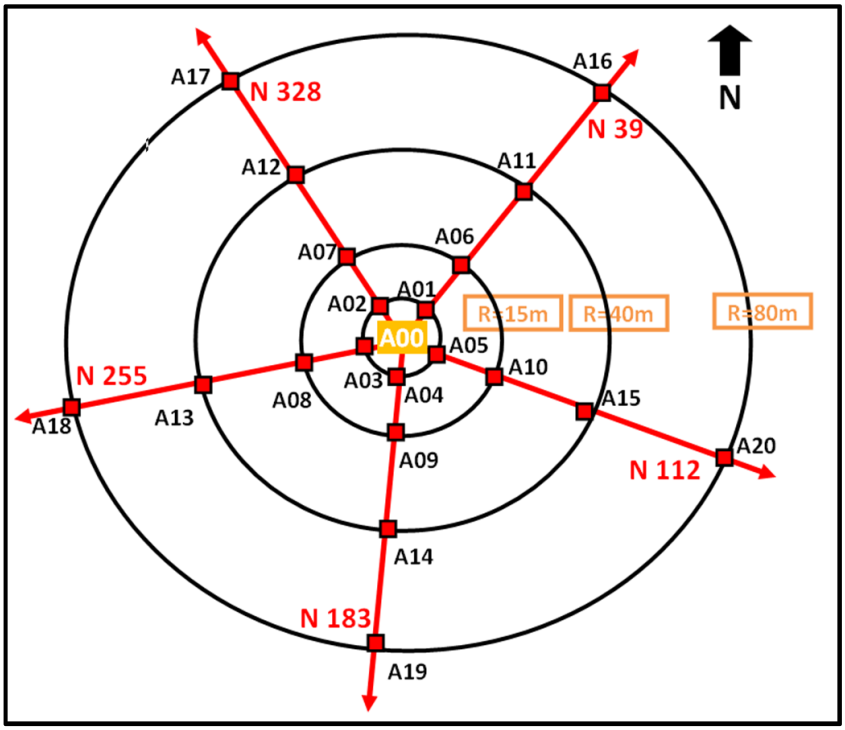

Figure 2.12: Geometry of Array A. A00 is the central station. Stations are located around A00 in four concentric circles at radii 5, 15, 40 and 80 m. Five stations are placed on each concentric circle. The stations branch off from A00 in five directions: N 39, N112, N183, N255 and N 328.

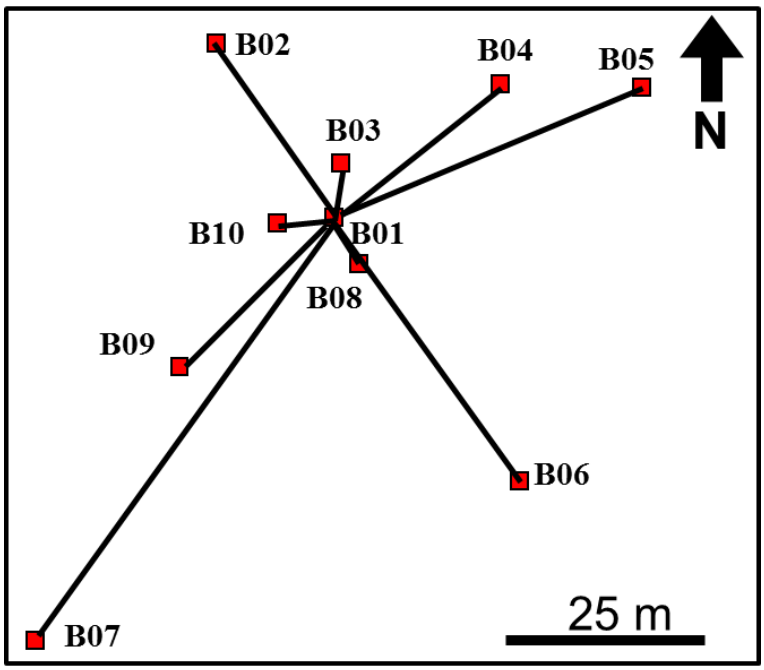

Figure 2.13: Geometry of Array B. B01 is the central station. Other stations are placed around B01 at distances ranging from 5 to 60 m.

2.3 Data acquisition

This section includes information about only the stations deployed by ISTerre, especially Array A. Figure 2.14 illustrates a typical instrumentation and Figure 2.15 shows a global picture of Array A stations. The stations were well maintained throughout the entire duration of the experiment. A routine-maintenance was performed every month in order to ensure better functioning of the stations. Although good quality data has been acquired by the stations, there are still data gaps due to some difficulties faced at the site. Our experiment site Koutavos Park is full of grown up trees which made it difficult to find enough solar power for the batteries. The weather conditions during winter worsened the power problem. Another issue was the behaviour of the CMG40T velocimeters. The sensors start malfunctioning (stepping the signals) after moderate earthquakes. Figure 2.16 shows the data status during the experiment duration.

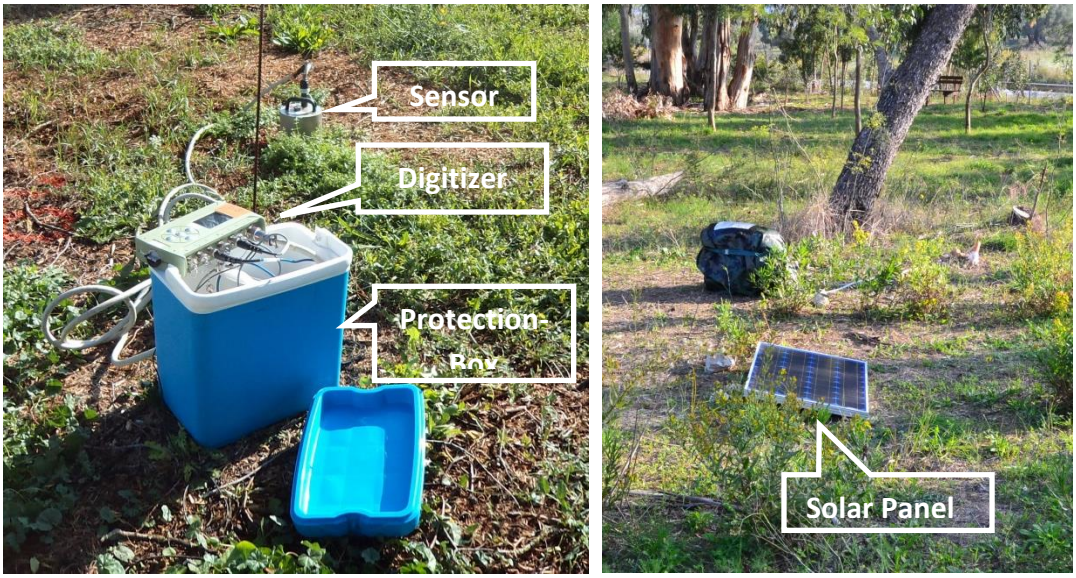

Figure 2.14: Typical set-up of a station.

Figure 2.15: A view of central part of the Array A stations.

(a)

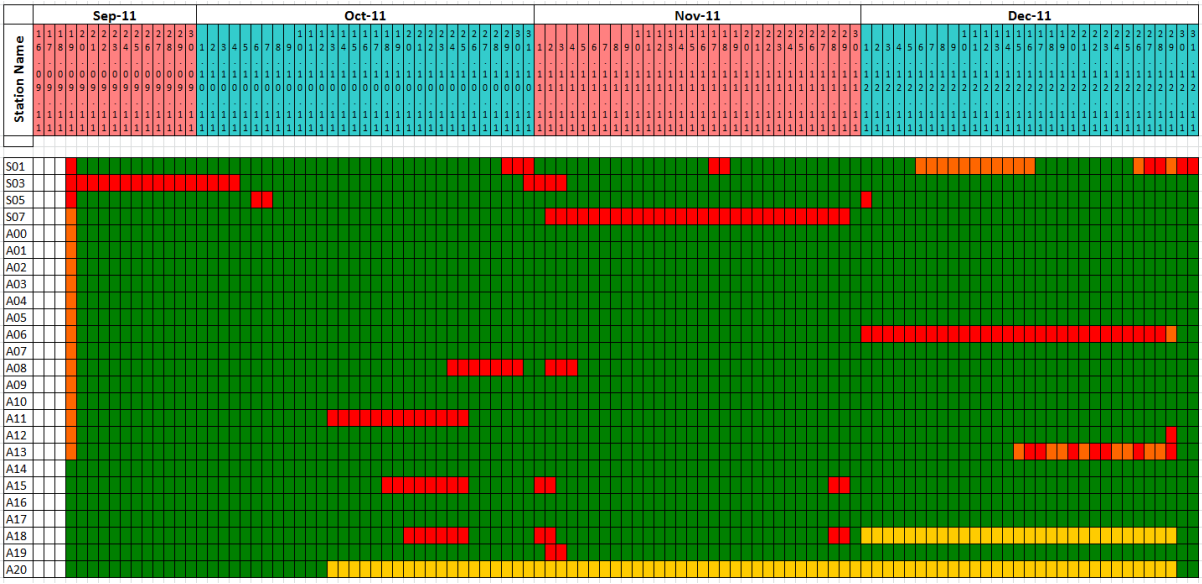

(b)

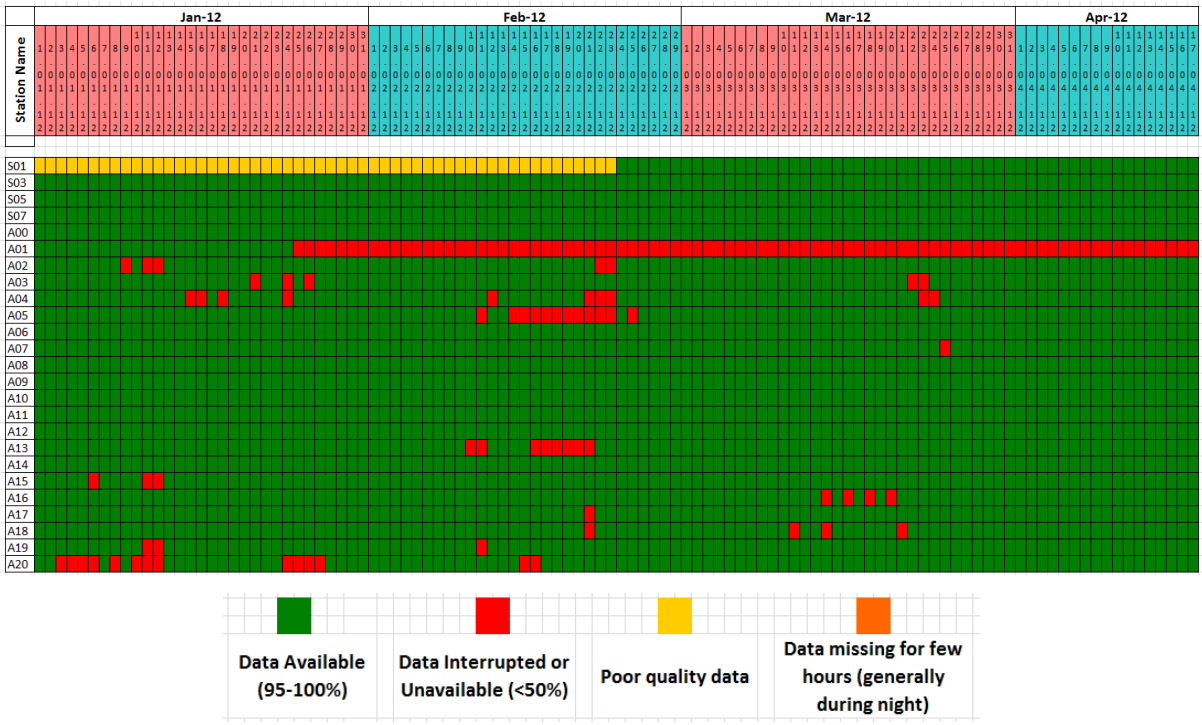

Figure 2.16: Day-by-day data availability of ISTerre stations for the period (a) September 2011 to December 2011, and (b) January 2012 to April 2012.

2.4 Catalogue preparation

Continuous records of about 7 months from the station A00 was considered for catalogue preparation. Probable seismic events were first identified from the continuous records through visual inspection. Then catalogues obtained from the earthquake data portal of NERA, school of geology at the Aristotle University of Thessaloniki (AUTH), and European-Mediterranean Seismological Centre (EMSC) were used to identify the origin time and characteristics of the events. Over the seven months of experiment in Argostoli, more than 3000 local, regional and teleseismic events, with $M \geq 2.0$, occurred in the broader Agean area and about 1700 events were detected from visual inspection. However, after careful inspection 711 events with high signal-to-noise ratio were selected for catalogue preparation. The catalogue of these events is given in Appendix E. It includes some large worldwide events such as Mw 7.2 Van earthquake on October 23, 2011, Mw 7.4 Mexico earthquake on March 20, 2012, Mw 8.6 and Mw 8.0 Sumatra earthquakes on April 11, 2012. From the catalogue, 461 events, within 80 km epicentral distance, have been re-localized (Appendix E.1) using the local network and the local crustal velocity model by AUTH seismological center (NERA Report, 2014). For the remaining 258 earthquakes, mainly regional and a few teleseismic events above epicentral distance 80 km (Appendix E.2), the best location solutions have been taken either from the Hellenic Unified Seismographic Network or from EMSC. In the next step 452 events were sorted out from the 711 events based on the quality of data and event parameters. Figure 2.17 (a) shows the locations of 452 good quality local, regional and teleseismic events recorded by station A00. A zoomed in view of the local and regional events is shown in Figures 2.17 (b) and (c). Magnitude and estimated peak ground velocity (PGV) of these 452 events are presented in Figures 2.18 (a) and (b), respectively. It can be observed from the figures that most of the recorded events have occurred within 200 km of hypocentral distance of the site having magnitudes about 1 to 5 and PGV 0.01 to 6 mm/s. There are also some $M > 5$ events within the hypocentral distance 200 and 10,000 km but their PGV values are around 0.1 mm/s or less. The distribution of PGV values of the events are shown in Figure 2.18 (c) where we can see that PGV of most of the recorded events range from 0.02 to 0.2 mm/s.

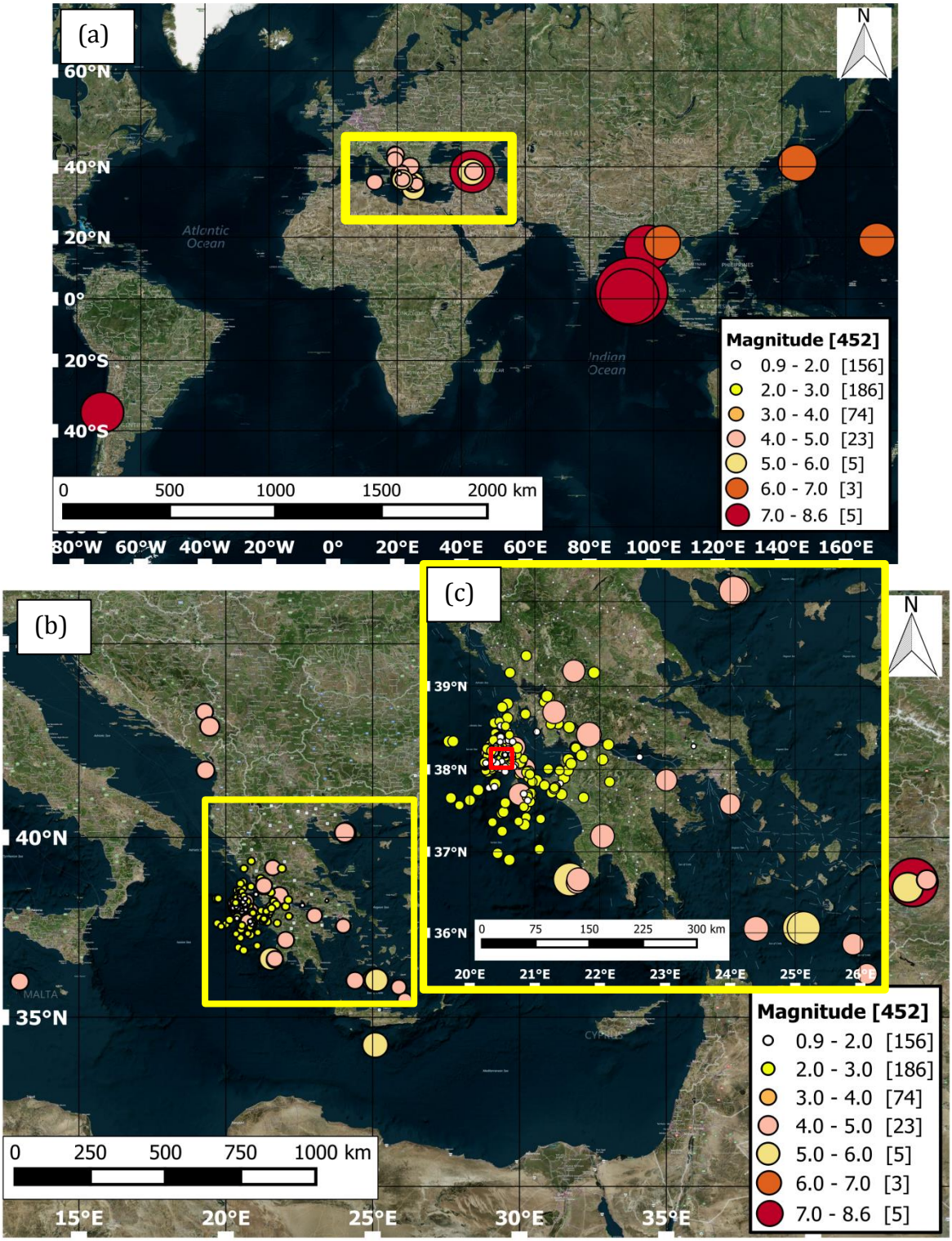

Figure 2.17: Location of (a) 452 good quality local, regional and teleseismic events. (b) Zoomed in view of the local and regional events from the area marked by yellow rectangle on the (a). (c) Zoomed in view of the events occurring around Argostoli site. Legend on the map represents event locations; the circle-sizes are proportional to the magnitude of the event. The red rectangle on (c) marks the location of the site.

(a)

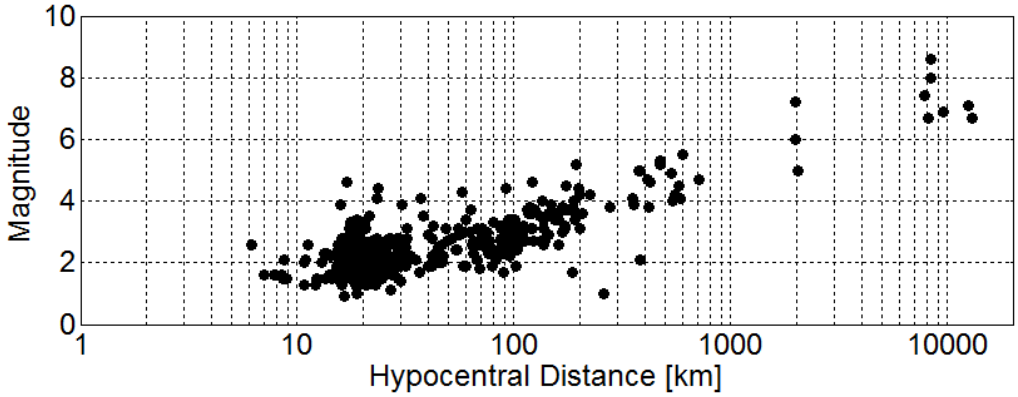

(b)

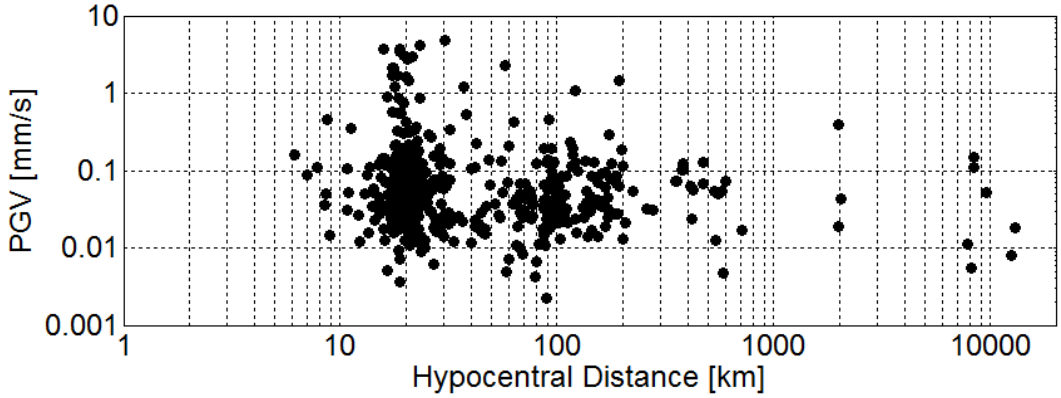

(c)

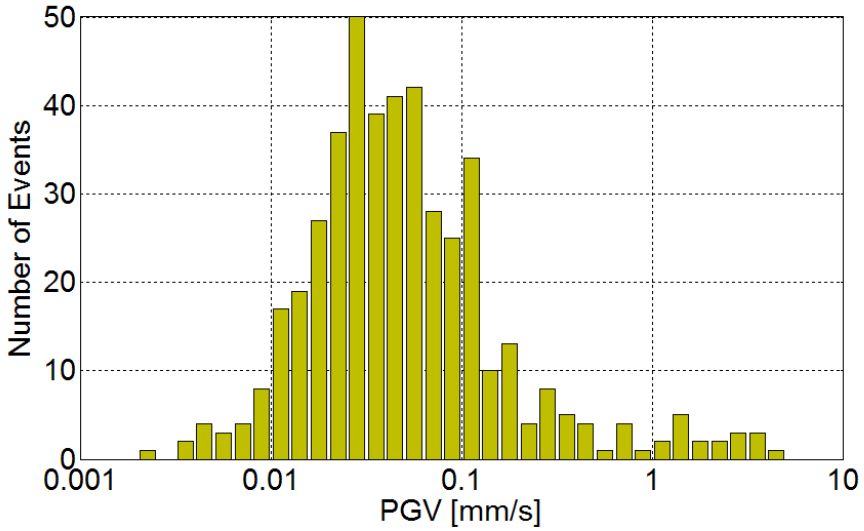

Figure 2.18: (a) Magnitude and (b) Peak ground velocity (PGV) over the hypocentral distance, and (c) Distribution of peak ground velocity (PGV) of the 452 good quality events.

2.5 Selection of subset of events

A subset of events with very good signal to noise ratio, recorded by more than 15 stations of Array A, was selected for the seismic wave field and coherency analyses (Chapter 3 and 4, respectively). A total of 46 events (Appendix F), within 200 km distance from the Array having magnitude 2 to 5, were selected. Most of the events are shallow and they were chosen such that a homogeneous distribution of epicentral distance, magnitude and azimuthal coverage can be achieved. Table 2.1 shows the number of selected events for each back-azimuth, epicentral distance and magnitude group analyzed for the arrays A. Origin date and time, latitude, longitude, peak ground velocity, magnitude as M_W or M_L, hypocentral depth, epicentral distance, hypocentral distance, and back-azimuth of the subset of events are given in Appendix F.1. Different parameters used in the analyses of the events, in Chapter 3 and 4, are listed in Appendix F.2. Since Array B data was used for seismic wavefield analysis (using MUSIQUE technique) in Chapter 3, the events for which Array B data was analyzed are indicated also in Appendix F.2. However, good set of recording was not available for all the events in case of Array B data. Thus 16 out of 46 events recorded by Array B were considered for seismic wavefield analysis (Table 2.1). Figure 2.19 (a) and (b) show the location of the subset of events selected from Array A and Array B, respectively. Time series of the events recorded at central station, A00, of Array A and rock stations, R01 and R02, are provided in Appendices G, H and I, respectively.

Table 2.1: Number of events selected for each back-azimuth, epicentral distance and magnitude group for the analysis of Array A and Array B data

Name	Back-azimuth	Nb. of Events	Range of epicentral distance (km)	Nb. of Events	Range of Magnitude (M_{WL})	Nb. of Events
Array A	NE	10	0-30	17	2-3	23
	NW	12	30-60	10	3-4	17
	SE	13	60-100	10	4-5	6
	SW	11	100-200	9		
	Total	46		46		46
Array B	NE	2	0-30	5	2-3	7
	NW	5	30-60	2	3-4	7
	SE	4	60-100	5	4-5	2
	SW	5	100-200	4		
	Total	16		16		16

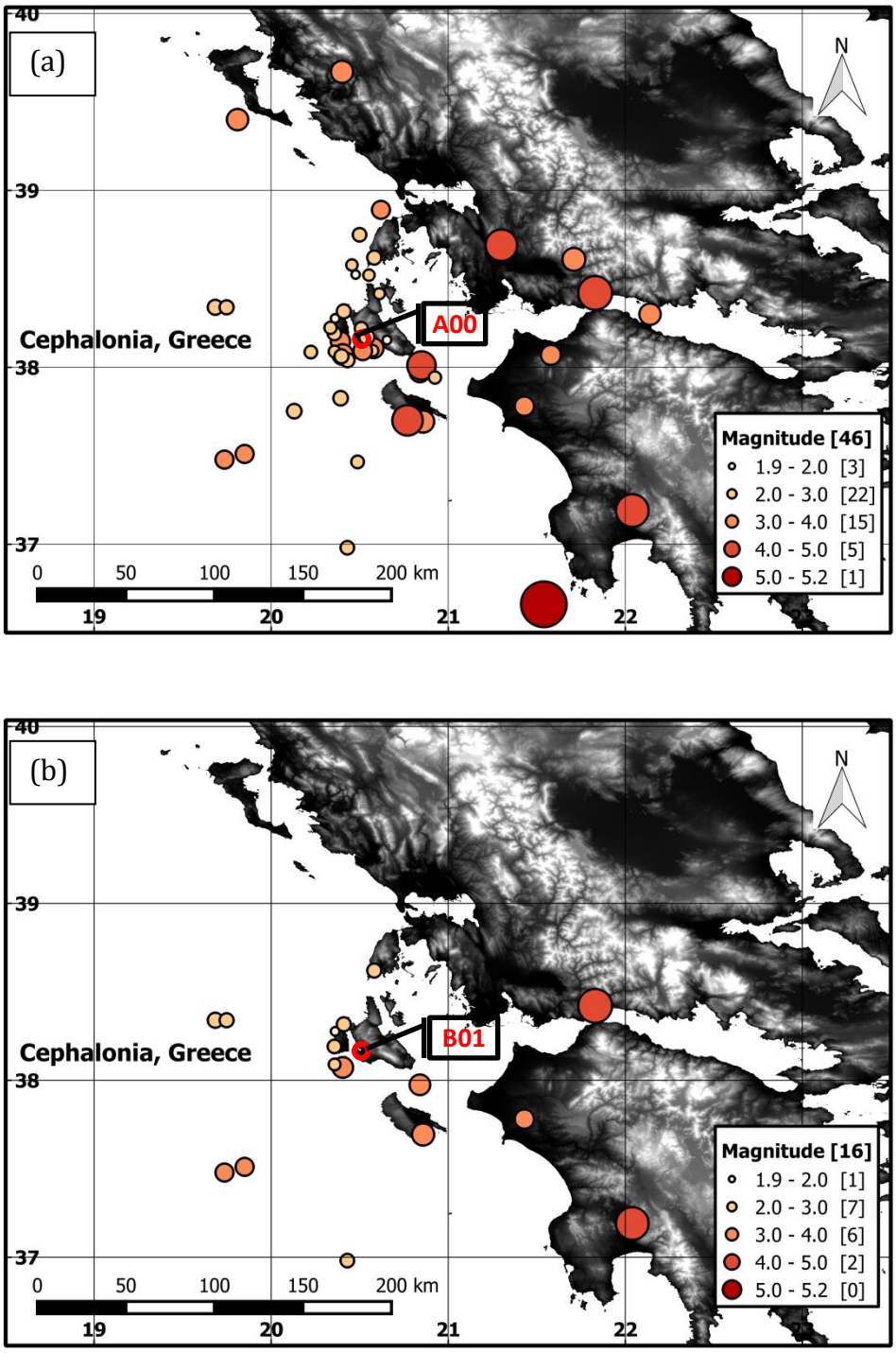

Figure 2.19: Map of the analyzed events from (a) Array A (46 events) and (b) Array B (16 events). Catalogue of the events are provided in Appendix F. Orange to red circles (legend) on the map represent event locations; the circle-sizes are proportional to the magnitude of the event. The red circles mark location of the central stations A00 and B01. The events are plotted on SRTM data-maps, available from http://srtm.csi.cgiar.org (Jarvis et al., 2008).

2.6 Example wave forms

In this section, some example waveforms from local and regional events are provided along with their respective Fourier spectra and signal-to-noise (S/N) ratios. We have selected three events at epicentral distances about 3, 56 and 190 km (no. 36, 31 and 46, respectively, in Appendix F.1). Figure 2.20 shows the locations of the events and the station A00. Magnitudes of the events are M 3, M 4.3 and M 5.2 and hypocentral depths are 18.5, 13 and 33 km, respectively. Time series recorded at station A00, Fourier amplitude spectra and signal-to noise-ratio (from the same station) of each event are given in Figures 2.21 to 2.23

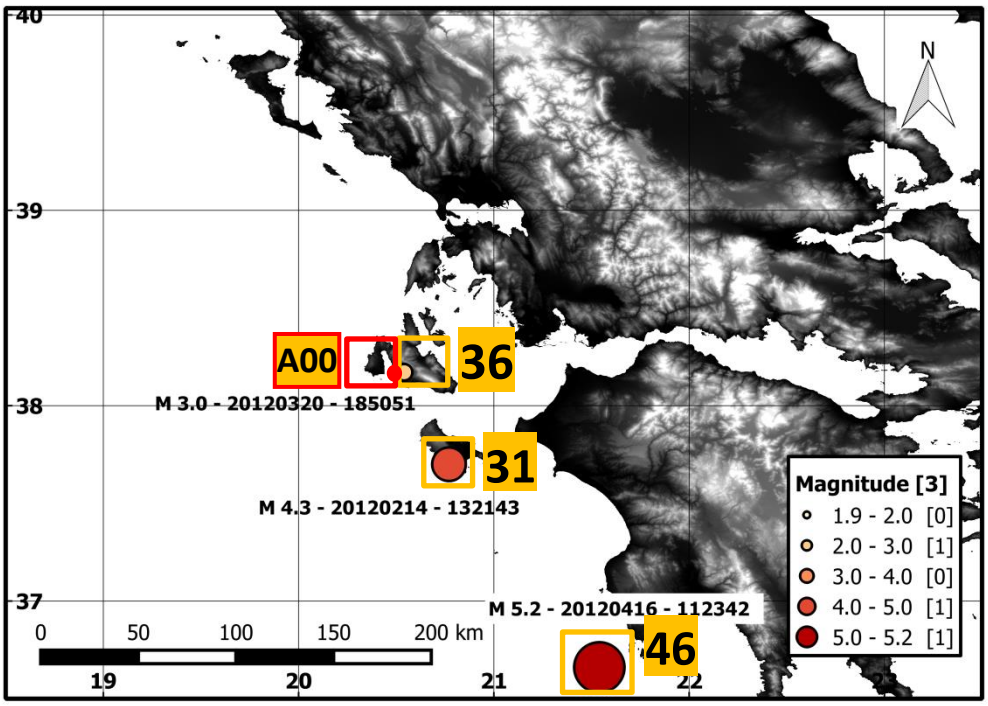

Figure 2.20: Location of the three example events, no. 36, 31 and 46 in Appendix F.1. Orange rectangles on the map mark the event locations and red one marks the central station A00.

(a)

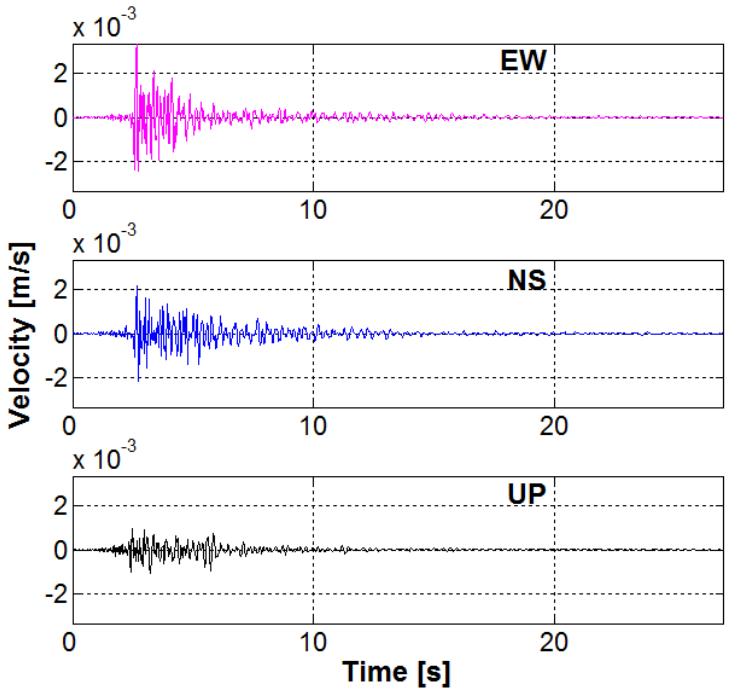

(b)

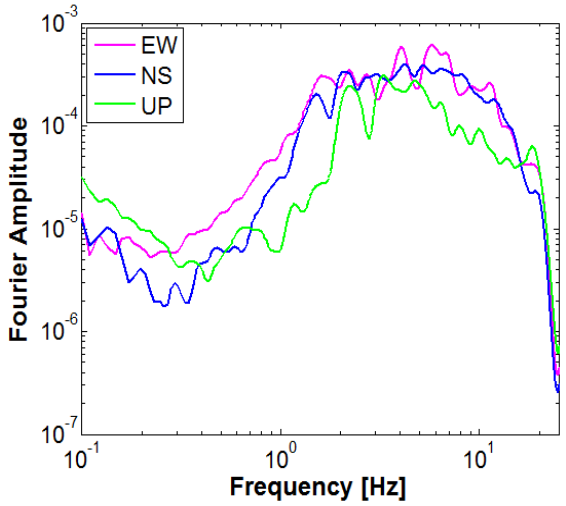

(c)

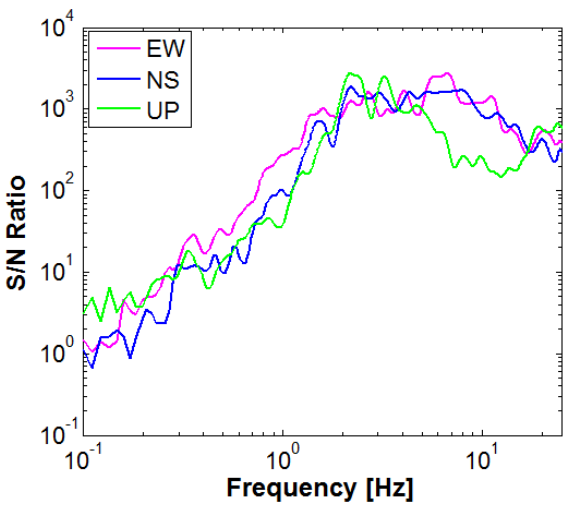

Figure 2.21: (a) Velocity time series (b) Fourier amplitude spectra and (c) signal-to-noise ratio, of the three components (EW, NS and UP) recorded at A00 station, for the event no. 36, occurred on March 20, 2012 at UTC 18:50:51. Magnitude, hypocentral depth and epicentral distance of the event are M 3, 18.5 km and 3.1 km, respectively.

(a)

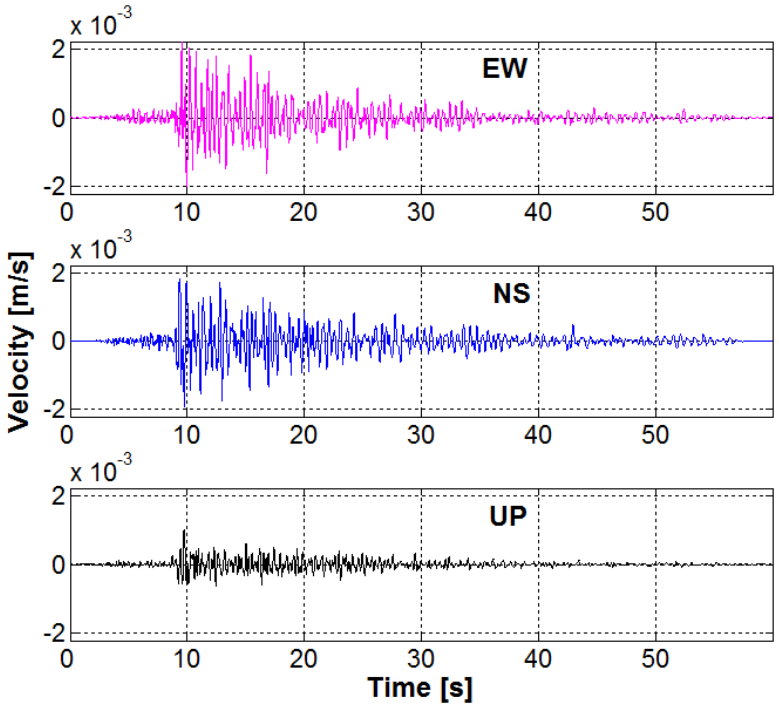

(b)

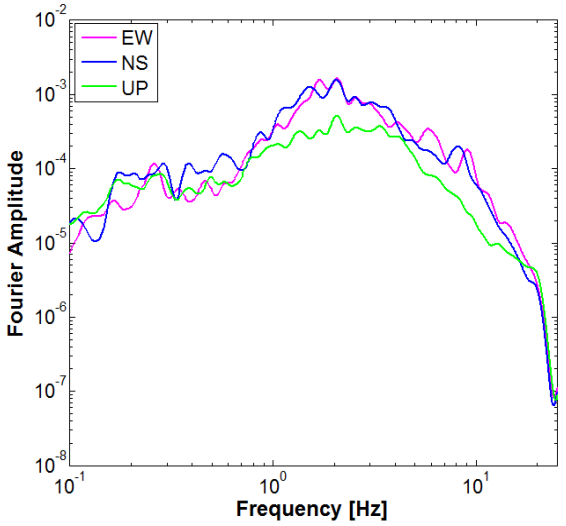

(c)

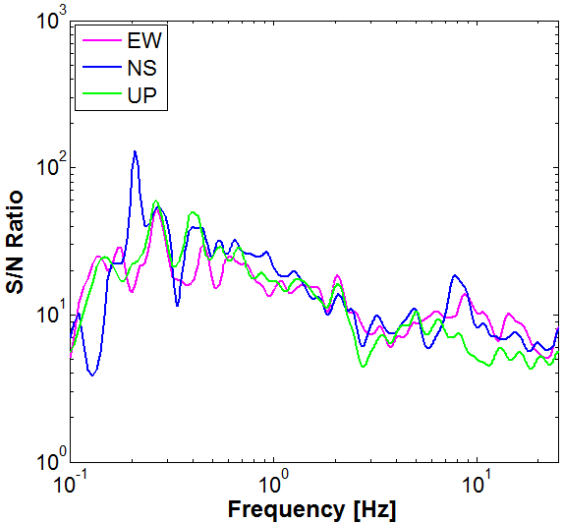

Figure 2.22: (a) Velocity time series (b) Fourier amplitude spectra and (c) signal-to-noise ratio, of the three components (EW, NS and UP) recorded at A00 station, for the event no. 31, occurred on February 14, 2012 at UTC 13:21:43. Magnitude, hypocentral depth and epicentral distance of the event are M 4.3, 13 km and 56 km, respectively.

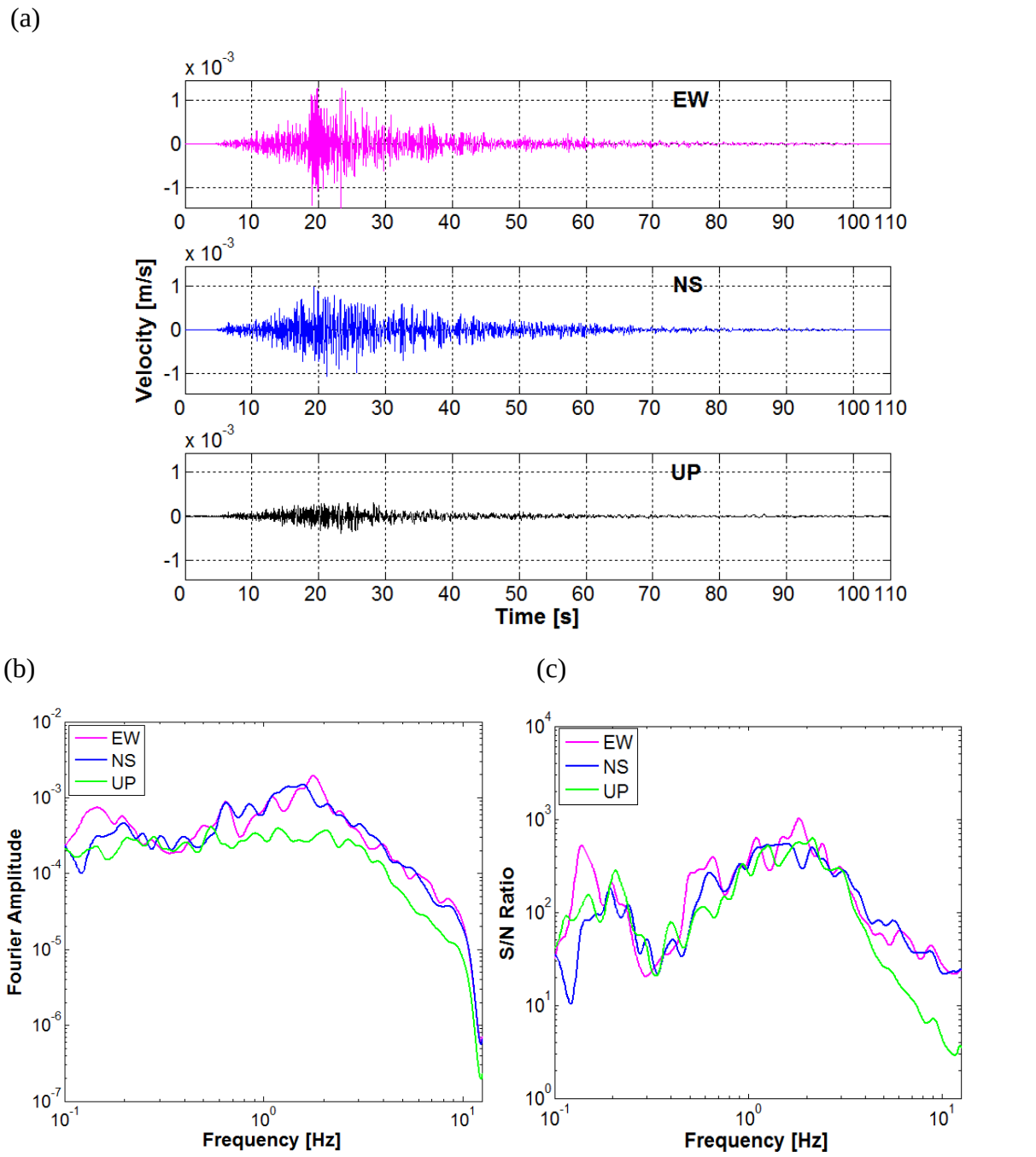

Figure 2.23: (a) Velocity time series (b) Fourier amplitude spectra and (c) signal-to-noise ratio, of the three components (EW, NS and UP) recorded at A00 station, for the event no. 46, occurred on April 16, 2012 at UTC 11:23:42. Magnitude, hypocentral depth and epicentral distance of the event are M 5.2, 33 km and 190 km, respectively.

Chapter 3: Seismic Wave Field Analysis of Argostoli Dense Array Network

This chapter presents the description of the seismic wave field analysis from dense seismic array data and the corresponding results. First, an overview of the seismic wave field analysis and relevant techniques has been provided. Then the two dense arrays (Array A and B) are presented. Next, the array analysis technique MUSIQUE, the methodology used in this part of the work, along with the data processing procedure has been described. Finally the post-processing criteria and the results of the analysis as well as the possible interpretations of the results have been provided.

3.1 Introduction

Site-specific characteristics of the observed ground motions are considered important for the estimation of seismic design parameters in engineering applications. Seismological observations have indicated that effects of surface geology and geometry (e.g. sedimentary valleys, topography) significantly contribute to ground-motion amplification and variability. These effects are generally associated with a substantial proportion of surface waves in the seismic wave field. Among them, the surface waves diffracted by the basin edges do contribute significantly to the site effects in modifying the wavefield and the resulting ground motion(e.g. Moczo and Bard, 1993; Field, 1996; Chavez-Garcia et al., 1999; Cornou and Bard, 2003; Bindi et al., 2009; Scandella and Paolucci, 2010). An understanding of the seismic wave field crossing the site, hence, is the key aspect to characterize and quantify these effects.

Studies investigating the properties of the wave field have shown that seismic arrays are very useful to characterize the fine-scale structure of Earth's interior and the variations of the material properties. A single seismometer is unable to determine both velocity and direction of the incident seismic waves while arrays of seismic sensors enable us to study the phase delays that normally cannot be identified in seismograms of single stations. Yet, a one dimensional seismic array can only determine the component of the wave vector which lies in the array direction. Therefore, two-dimensional arrays are needed to retrieve the back-azimuth and velocity of the incoming waves.

In this study, the two-dimensional dense seismic arrays, deployed during the seismological experiment in Argostoli basin, as a part of the FP7 EU-NERA (Network of European Research Infrastructures for Earthquake Risk Assessment and Mitigation) 2010-2014 project, was used to analyze the seismic wave field composition. As presented in Chapter 2, the principal dense array (Array A) was located close to the south-western edge of the basin and consisted of 21 velocimeters located in concentric circles with radii of 5 m, 15 m, 40 m and 80 m around the reference station. Another smaller array was deployed near the north-eastern edge and consisted of 10

velocimeters with interstation distances ranging from 5 to 60 meters. A subset of 46 events recorded by Array A was used for the MUSIQUE analysis. This subset was carefully selected so that the corresponding events are characterized by a homogeneous back-azimuth distribution, local magnitudes ranging between 2 and 5, and epicentral distances ranging between 3 and 200 km from the array center (see chapter 2).

Among the various available array techniques, we have chosen and applied the MUSIQUE algorithm (Hobiger et al., 2012) to analyze our selected events. This algorithm, combining the two algorithms MUSIC (MUltiple SIgnal Characterization; Schmidt, 1986; Goldstein and Archuleta, 1987) and quaternion-MUSIC (Miron et al., 2005; Miron et al., 2006), offers an advanced three-component seismic array processing technique. In addition to the estimation of slowness of the incoming waves, MUSIQUE allows identification of Love and Rayleigh waves, and estimation of the polarization parameters, i.e., ellipticity and sense of rotation of the Rayleigh wave particle motion. The array analysis was performed over a frequency range of 1 to 20 Hz considering entire duration of the signals. The present chapter focuses on the results of array analysis which include identification and characterization of the diffracted wave fields.

3.2 Seismic wave field analysis

When an earthquake occurs, seismic waves are generated as rupture occurs along the fault and propagate towards the site or point of observation after being diffracted, reflected, or scattered, through regional and local earth's structure. Especially, near-surface geology plays an important role in modifying earthquake ground motion and, hence, the damage distribution, as witnessed by most of the past destructive earthquakes (e.g. Mexico, 1985; Loma Prieta, 1989; Kobe, 1995; Izmit, 1999). Generally, four types of seismic waves form the seismic signal, namely, pressure (P) and shear (S) waves, Love and Rayleigh surface waves. P- and S-waves are linearly polarized. P-waves are compressional waves propagating along the wave propagation direction. S-waves propagate perpendicularly to the wave propagation direction and consists of two components, SH and SV. SH waves have a motion parallel to the horizontal plane while SV wave motion is perpendicular. Love and Rayleigh surface waves travel along the free surface of the earth and that is the reason they are known as surface waves. Love waves

are horizontally polarized shear waves resulting from the superposition of multiple reflected of SH waves at the free surface. Rayleigh waves originate from the superposition between P and SV waves at the free-surface. The coupled P-SV type displacement of Rayleigh waves results in a phase-shift of $\pm\pi/2$ between the horizontal and vertical components of particle motion which can be represented by an ellipse. The ratio of amplitudes between horizontal and vertical axes of the ellipse defines the ellipticity. In uniform half-space, at shallower depths (at and near the surface), horizontal movement advances the vertical movement by $\pi/2$ in phase and the motion (fundamental mode) becomes retrograde. Since P-wave component of the motion decays faster than the SV motion, at sufficiently greater depth, SV motion dominates, and the particle motion becomes prograde corresponding to a phase difference of $-\pi/2$. When the direction of wave propagation is from left to right, counter-clockwise particle motion is retrograde while clockwise is prograde. For multi-layered structure, ellipticity of Rayleigh waves depends on the velocity structure and frequency. Amplitude (energy) of surface waves decays exponentially with depth within a medium. Due to geometric spreading in 2-D, surface wave energy decays with distance r from the source as $1/r$ whereas it is $1/r^2$ for body waves making them less prominent on a seismogram. It is also to be noted that different types of waves travel at different velocities depending on the material characteristics of propagation media. P-waves are the fastest and marked by early arrival on a seismogram followed by the S-waves and then surface waves. Love and Rayleigh surface waves involve different mode of propagation (fundamental and higher modes) that propagate at different frequency-dependent velocities whose asymptotic values for the low and high frequencies are close to the shear-wave velocities, in the deep and surficial layers, respectively. The later arrivals on a seismogram are called coda waves that are caused by multipathing/scattering of waves through a heterogeneous structure. In terms of frequency content of a seismogram, the high frequency seismic wavetrain is usually dominated by the arrivals of P and S waves while the low frequency content is dominated by surface waves.

Although initially it was believed that the body wave trapped in the sedimentary layers are responsible for amplification of the ground motion, the contribution of locally generated surface waves in amplification, duration lengthening and spatial variation of ground motion and related damage has been recognized (Kawase, 1996). . At present

many urban areas have been developed on sedimentary basin structures, hence, the effects of surface waves need particular attention in the seismic hazard assessments and risk estimation of such sites. In other words, knowledge of the local soil structure and complex wave field propagation of a given site is of utmost importance in order to investigate the physical causes underlying spatial variation of earthquake ground motion and estimate associated risk.

The investigation of complex wave field in view of better understanding and better assessing spatial variation of ground motion is especially important in small or medium size (width smaller than a few hundred meters and thickness within tens of kilometers) valleys where direct S-waves and basin-edge induced waves are mixed, and ground motions are affected by both 1D and 2D/3D effects (Cornou et al., 2003a).

Seismic arrays of ground-motion recording stations are considered very handy for such purpose. It is a common practice in seismology to use dense seismic array analysis for source and path characterization of wave types and their polarization, investigation of heterogeneous ground-structure, and analysis of seismic ground strains. To date, many studies have been undertaken using analysis of very dense seismic arrays (Caserta et al., 1998; Gaffet et al., 1998; Chavez-Garcia et al., 1999; Rovelli et al., 2001; Cornou et al., 2003a, and 2003b) to characterize wave propagation from earthquake ground motion and identify the diffracted waves.

A seismic array is a combination of a set of seismographs distributed over an area of the earth's surface. The spacing among the seismographs or seismic stations within an array is generally small so that correlated signal waveforms could be recorded between adjacent seismometers. Three-component seismographs are made of three colocated sensors recording the ground motion in three orthogonal directions (output signal is a 3D vector-valued time series) aligned in north-south, east-west and vertical direction. Three-component stations are being used more and more in array configurations (Kværna and Doornboos, 1986) for many permanent as well as most of the temporary networks for their diverse usability. The single component arrays (vertical arrays) are unable to capture significant portions of P, SV, and Rayleigh waves as well as the entire SH and Love wave part of the wave field. On the contrary, addition of horizontal

components records in three-component arrays facilitates capturing this polarization information. Contrary to arrays of seismic sensors, a single three-component seismometer is unable to determine both the velocity and the direction of the incident seismic waves.

A one dimensional seismic array can only determine the component of the wave vector which lies in the array direction. Therefore, analysis of two-dimensional seismic arrays is needed to retrieve the wavenumber vector of any incident wave, in terms of back-azimuth (defined as the angle measured from north to the direction from which the energy arrives at a given station) and slowness. The basic principle of any array analysis technique is to measure the arrival time delays of an incident wave-front recorded at the different stations and then estimating the wave velocity v (or its inverse, the slowness s) and station-to-event azimuth (back-azimuth).

The underground earth-structure is heterogeneous and consists of different layers having different material properties. The vector velocity information of propagating incident wave helps to identify different seismic phases in the complex wave field, characterize waves from different seismic events and also to improve the signal-to-noise ratio by stacking the recorded waveforms with respect to the varying slowness of different phases. Therefore, analyzing the properties of different wave types, observed at a site, is particularly useful in obtaining insight into the local soil structure, material properties and topographic effects. The direct seismic waves, P and S-wave generally propagate at the actual velocity of the current medium. Use of these waves in the earthquake analysis is limited by the fact that the source location and time are needed to be determined if we want to acquire information on the entire propagating medium of the body waves (Hobiger et al., 2012). On the other hand, surface waves of varying wavelengths penetrate to different depths and travel at the velocity of the mediums they are travelling through. Thus, the velocity of these waves is directly linked to the underground structure that makes the analysis of surface waves a good means to investigate local underground structure. Now, short wavelengths correspond to high frequencies and only sample very superficial layers while the larger wavelengths (linked to lower frequencies) sample deep layers. Usually deeper layers are composed of stiffer materials which cause larger velocities compared to those at near-surface

layers. As a consequence, the larger wavelength (lower frequency) surface waves travel faster than the smaller wavelength (higher frequency) ones. This frequency dependent characteristic of wave propagation velocity is termed as dispersion and can be captured by the vector velocity information retrieved from the array analysis. The dispersion curve, i.e. the phase velocity as a function of frequency, of surface waves directly depends on the shear wave velocity profile of the soil structure and can be inverted to constrain local underground structure. In addition, polarization properties of Rayleigh waves are also closely linked to the underground structure, especially the ellipticity is complementary in inverting dispersion curves.

Estimation of polarization parameters helps us to better characterize different seismic phases. Distinction of the sense of particle motion at a given frequency can help in distinguishing between the fundamental and the higher harmonic modes of Rayleigh waves. Three-component array analysis of seismic data allows us to perform such ground motion decomposition at a site and acquire useful descriptions of propagating seismic wave field characteristics. Therefore, three-component 2D arrays were used in many studies for the analyses of P wave codas, polarization of waves, scattering, and the study of regional wave propagation (among others Jurkevics, 1988; Dainty, 1990; Wagner and Owens, 1993; Kuwahara et al., 1997; Wagner, 1997; Bear et al., 1999; Cornou et al., 2003a, and 2003b; Poggi and Fäh, 2010; Marano et al., 2012; Hobiger et al., 2012).

Various methods based on signal processing techniques are available for the analysis of dense seismic arrays. Three commonly used methods (Zerva and Zhang, 1996; Roulle and Chavez-Garcia, 2005; Wathelet et al., 2008) are: conventional f-k (frequency-wavenumber; Lacoss, 1969), high resolution f-k (Capon, 1969) and the Multiple Signal Characterization, MUSIC (Schmidt, 1981, 1986). The comparative studies among these methods suggested that MUSIC is less sensitive to noise. It has better resolving power in the case of multiple, closely spaced arrivals, and is able to handle difficult scenarios involving highly correlated (waves with different azimuths but the same frequency and phase content crossing the array at the same time) waves when applying an additional spatial smoothing technique (Goldstein and Archuleta, 1987, 1991; Krim and Viberg, 1996; Zerva and Zhang, 1996; Bokelmann and Baisch, 1999; Almendros et al., 2000;

Cornou et al., 2003a; Roulle and Chavez-Garcia, 2005). Goldstein and Archuleta (1987) showed that MUSIC is particularly well suited for frequency-wavenumber estimation with seimic arrays because (1) it has the ability to resolve multiple, closely spaced sources, (2) it works with both stationary and nonstationary signals, (3) it is most sensitive to the strongest sources and (4) it provides a unique solution to the wavenumber estimation problem. Roulle and Chavez-Garcia (2005) concluded that MUSIC is more useful in case of data with high coherence and small time delays. However, the limitation indicates that this method requires a number of parameters, including the number of signals, to be known a priori which may significantly affect its reliability in actual applications.

Keeping the aforementioned advantages of MUSIC technique in mind, we have chosen an advanced three-component seismic array processing technique, MUSIQUE (Hobiger et al., 2012), to analyze dense seismic array data in this study. This algorithm combines original MUSIC (Schmidt, 1981, 1986; Goldstein and Archuleta, 1987) with Quaternion-MUSIC (Miron et al., 2005, 2006). In addition to the estimation of slowness of the incoming waves, MUSIQUE allows the identification of Love and Rayleigh waves, and the estimation of polarization parameters, i.e., ellipticity and sense of rotation of the Rayleigh wave particle motion as a function of frequency. Hobiger et al. (2009, 2011) presented the application of MUSIQUE on synthetic seismic data and showed its potential in identifying different surface wave types as well as separating both Rayleigh wave polarizations. Hobiger et al. (2014) used MUSIQUE to analyze seismological data of Santa Clara valley and showed that this technique is capable of separating the contributions of Love and Rayleigh waves successfully.

3.3 Argostoli experiment and dense array characteristics

The experimental setup and dataset of Argostoli as well as the description of the site have been presented in the chapter 2. As mentioned in chapter 2, Array A consisted of 21 stations in four concentric circles, with radii of 5, 15, 40 and 80 m, around A00. All stations were located on the same geological unit. The configuration of the array and its location is recalled in Figure 3.1 (a). The minimum and maximum interstation distances are 5 m and 160 m, respectively, which indicates that the array can capture planar

waves with wavelengths from a few meters up to 360 m. Figure 3.1 (b) and (c) show the theoretical array response and the array resolution capability, respectively (Wathelet et al., 2008). Average FK dispersion curves and related standard deviation were derived from the phase velocity histograms (probability density functions) for wavenumbers above the classical array resolution (k_{min}), defined as the mid-height width of the main lobe peak in the array response function. For HRFK processing, the lower wavenumber limit is half the classical array resolution ($k_{min}/2$) (Asten & Henstridge 1984; Wathelet et al. 2008).

A smaller array was deployed by the project partner GFZ (German Research Centre for Geosciences), close to the north-eastern edge of the basin, named as Array B. It consists of 10 stations, with interstation distance ranging from 5 to 60 m. The central station B01 was located at about 0.29 km from A00 and 0.26 km from the northeastern valley-edge. The array configuration and resolution capability are shown in Figure 3.2.

(a)

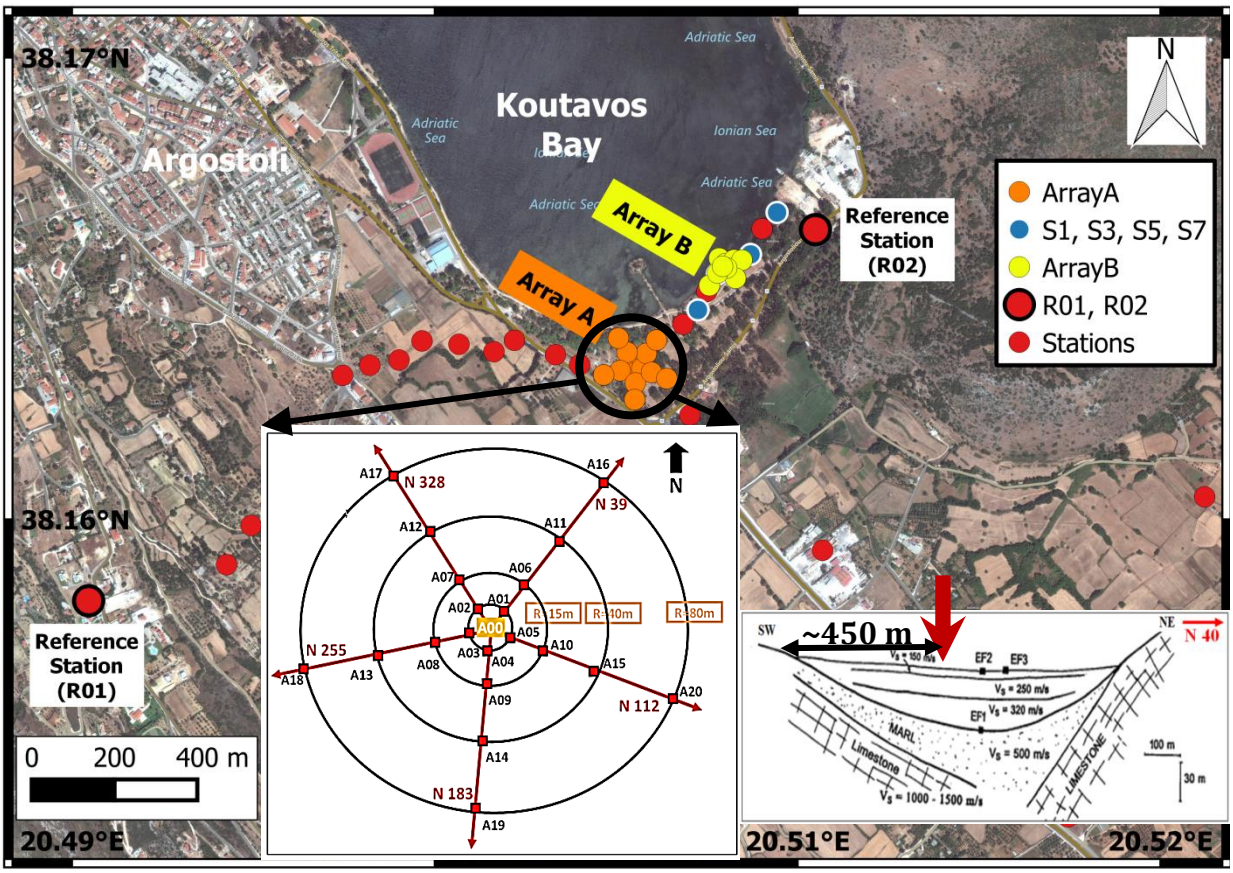

(b) (c)

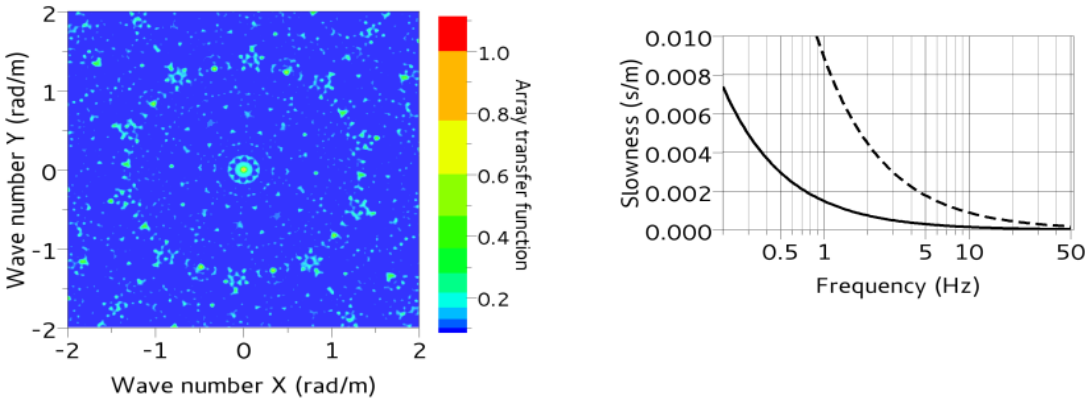

Figure 3.1: (a) Layout of the Argostoli Array A in the seismological experiment of NERA. (b) Theoretical array response function, and (c) resolution limit: the continuous and dashed black lines, respectively, correspond to the theoretical array resolution limit for the use of classical frequency wavenumber technique, and to half the classical array resolution using high-resolution frequency-wavenumber techniques (Lacoss et al., 1969; Asten & Henstridge, 1984; Cornou et al., 2006; Wathelet et al., 2008).

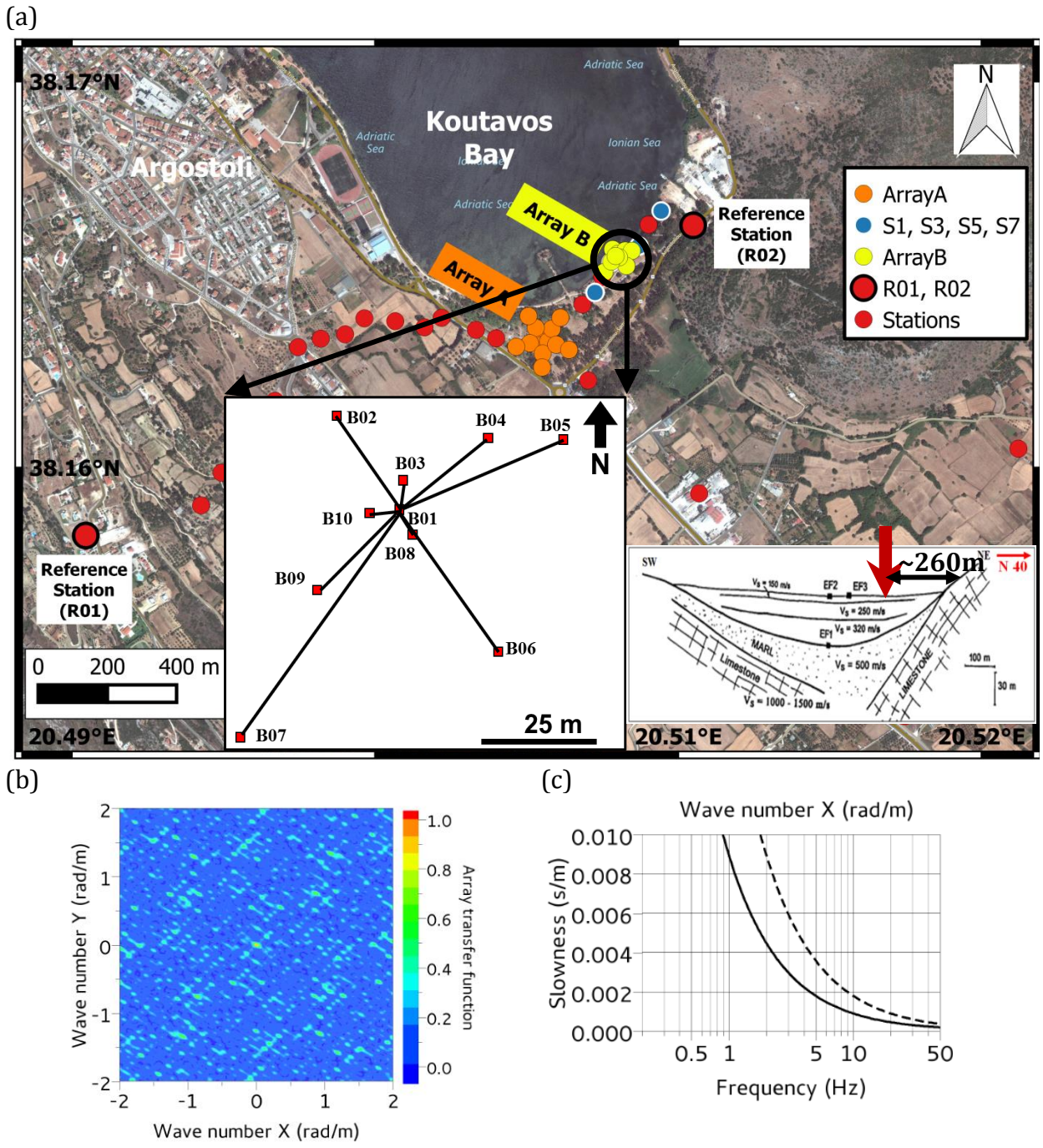

Figure 3.2: (a) Layout of the Array B in the seismological experiment of NERA. (b) Theoretical array response function and, (c) resolution limit: the continuous and dashed black lines, respectively, correspond to the theoretical array resolution limit for the use of classical frequency wavenumber technique, and to half the classical array resolution using high-resolution frequency-wavenumber techniques (Lacoss et al., 1969; Asten & Henstridge, 1984; Cornou et al., 2006; Wathelet et al., 2008).

3.3.1 Dataset

This study considers a subset of 46 events from the catalogue of Argostoli data, recorded by the dense array, Array A. Out of these 46 events, total 16 events have also been analyzed for Array B. Selected dataset has been discussed in chapter 2 and the catalogue with event parameters are given in Appendix F.1. Different parameters used in the MUSIQUE analysis are listed in Appendix F.2. Time series of the events recorded at central station, A00, of Array A are provided in Appendices G.

Figure 3.3 shows some example velocity time series, filtered within 1-5 Hz frequency band, recorded across the width of the valley for an event arriving from the south-east direction (back-azimuth = N134) of the site (event no. 15 in Appendix F). Hypocentral depth of the event is 16.5 km and epicentral distance is 9 km. Figure 3.3 (a) illustrates records for the vertical component. The waveform at 400 m corresponds to a station at stiffer site near the western border of the valley. Rock stations, R01 and R02, are shown at 0 m and 2000 m, respectively. We observe from the waveforms that apparantly surface waves are not visible at rock station. One can clearly identify the waves propagating from the southwest towards the northeast edge, associated to surface wave generations and diffractions the later arriving phases, especially between 1200 to 1600 m distances where the basin is supposed to be deeper. On the NS component records in Figure 3.3 (b), the complex mixing of surface waves is evident. We can also observe duration lengthening from the valley center towards the northeast edge.

(a)

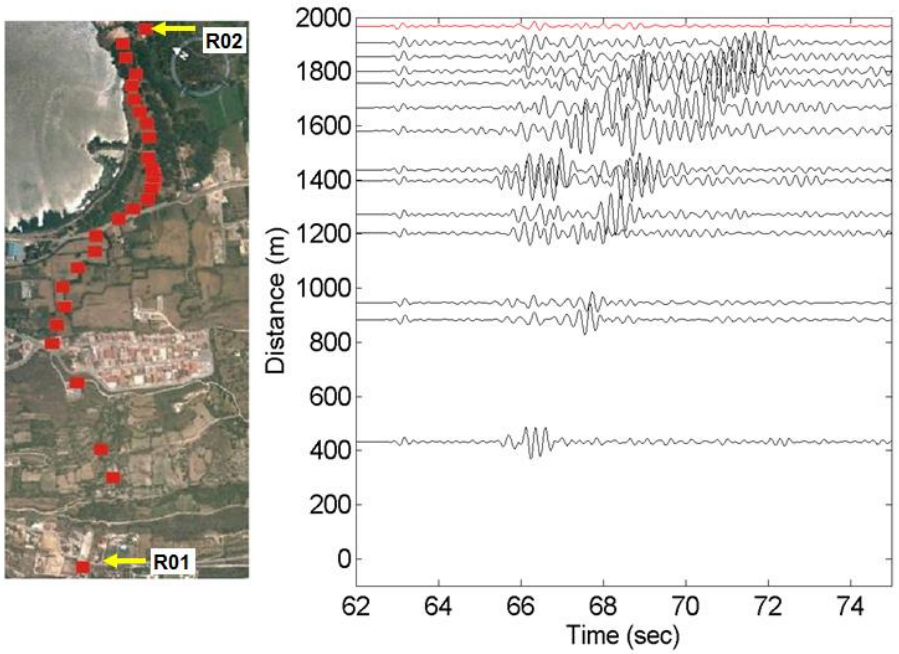

(b)

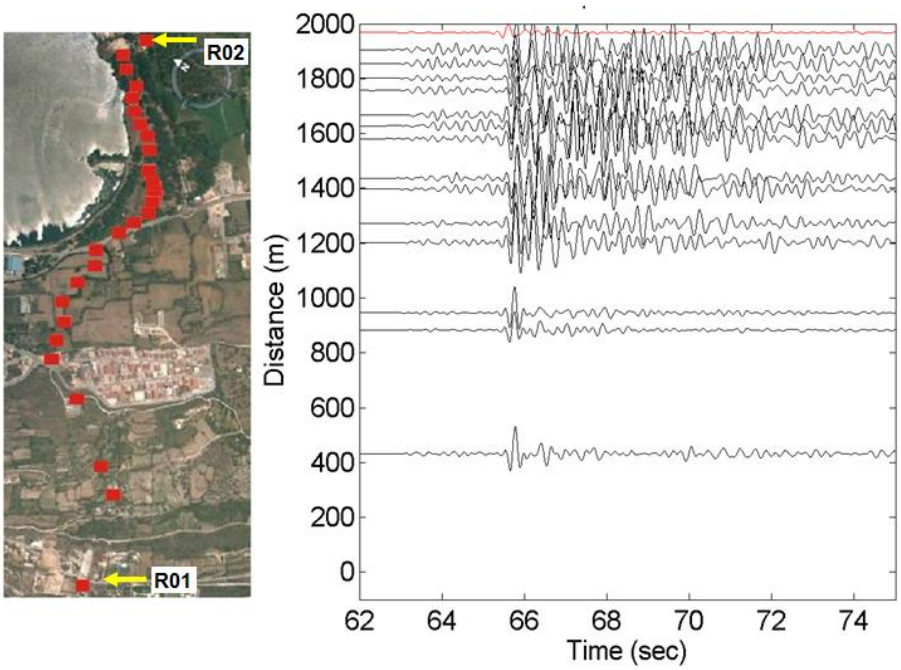

Figure 3.3: Band-pass filtered (1 to 5 Hz) velocity waveforms from (a) vertical component and (b) NS component, recorded across the width of Argostoli valley for an earthquake of M=3.4, Depth = 16.5 km, Back-azimuth=N 134 and Epicentral distance=9 km (event no. 15 in the table in Appendix F.1). Time series recorded at R02 rock site are displayed in red color. Records from R01 station were not available for this event. The corresponding arrangement of the stations on the site is shown at the left.

3.4 Methodology

We have used MUSIQUE technique (Hobiger, 2011; Hobiger et al., 2011, 2012 and 2014) in order to perform wave field characterization of the Argostoli array data. MUSIQUE consists of a combination of the "classical" MUSIC (Schmidt, 1986) and the quaternion-MUSIC (Miron et al., 2006) algorithms. First, it retrieves the azimuth and velocity (or slowness, respectively) of the wave with "classical" MUSIC. Then, the horizontal components are rotated to radial and transverse components and the polarization parameters between the vertical and the radial component are estimated by using the quaternion-MUSIC approach. The advantage of the quaternion formulation compared to other approaches is that the phase information and the sense of rotation of the particle motion is naturally preserved. MUSIQUE, thus, allows the distinction between retrograde and prograde Rayleigh wave motion. Hobiger (2011) has elaborately discussed the technique. Here we will only describe the principle of the technique.

3.4.1 MUSIC

The Multiple Signal Characterization (MUSIC) method is an array analysis technique based on the calculation of the eigenstructure of the cross-spectral matrix to determine signal parameters. It was originally developed by Schmidt (1986). Goldstein and Archuleta (1987) applied MUSIC in seismology and showed that it could resolve multiple, closely spaced sources. It works both with stationary and non-stationary signals and is more sensitive to the strongest sources (Roulle and Chavez-Garcia, 2005).

Basic principle of the method is to separate signal and noise subspace and then to estimate the signal parameters. Let us assume a dataset recorded by an array of N single-component sensors. As a first step, MUSIC calculates the cross-correlation matrix (in time domain) or cross spectral matrix (in frequency domain) for each frequency and time windows of interest, and defines the eigenstructure of the covariance matrix. The eigenvectors corresponding to the K strongest eigenvalues define the signal subspace ($K<N$) while the N-K weakest eigenvalues define the noise subspace. Then, from the set of array manifold vectors, the vectors that give the minimum projection onto the noise subspace are determined through the search of the maxima of the directional function (the so-called MUSIC spectrum). Once the signal vectors are determined, propagation

direction and phase velocity of the signals can be computed, as functions of time and frequency.

The extension of MUSIC algorithm for three-component signals is explained in Hobiger et al. (2014). Suppose we have an array composed of N three-component seismic sensors. Then three complex data vectors $X_i(f)$, of size N×1, can be used to store the data for frequency f, where i = 1 denotes the vertical, i = 2 the eastern and i = 3 the northern component. The covariance matrix (size N×N) calculated for each component is given by,

$$S_{i,jk}(f) = E\left[X_{i,k}(f)\, X_{i,j}{}^{*}(f)\right] \tag{3.1}$$

where E denotes the expectation value, j and k are the station indices, and *-operator denotes complex conjugation. The expectation value is realized by summing over a small number of frequencies around the central frequency, f. Then a covariance matrix, S(f), is derived by simply summing up the covariance matrices of the single components, and the eigenvectors and eigenvalues are calculated. The propagation back-azimuth (θ) and the slowness (s) of this dominant wave arrival are identified by maximizing the MUSIC functional P by a two dimensional grid search.

$$P = \frac{1}{a^{*}GG^{*}a} \tag{3.2}$$

where G denotes the noise subspace and a is the steering vector given by

$$a = \frac{\exp(-i\boldsymbol{R}\, k(f))}{\sqrt{N}} \tag{3.3}$$

here $\boldsymbol{R}$ is the matrix of the sensor positions , k(f) is the wave vector given by

$$k(f) = -2\pi.f.s(f)\,(\sin\theta, \cos\theta, 0)^{T} \tag{3.4}$$

Radial and transverse motions of the waves are determined by projecting the horizontal components ($X_2(f)$ and $X_3(f)$) of the signal into the identified back-azimuth direction θ, while the vertical signal ($X_1(f)$) remained unchanged:

$$X_{radial}(f) = -\sin\theta \,.\, X_2(f) - \cos\theta \,.\, X_3(f) \quad (3.5)$$

$$X_{transverse}(f) = \cos\theta \,.\, X_2(f) - \sin\theta \,.\, X_3(f) \quad (3.6)$$

$$X_{vertical}(f) = X_1(f) \quad (3.7)$$

The energies of the different components for each station are calculated by

$$E_{vertical}(f_c) = \sum_{f=f_c-\Delta}^{f=f_c+\Delta} \vec{X}_1^*(f)\ \vec{X}_1(f) \quad (3.8)$$

$$E_{east}(f_c) = \sum_{f=f_c-\Delta}^{f=f_c+\Delta} \vec{X}_2^*(f)\ \vec{X}_2(f) \quad (3.9)$$

$$E_{north}(f_c) = \sum_{f=f_c-\Delta}^{f=f_c+\Delta} \vec{X}_3^*(f)\ \vec{X}_3(f) \quad (3.10)$$

$$E_{radial}(f_c) = \sin^2\theta \,.\, E_{east}(f_c) + \cos^2\theta \,.\, E_{north}(f_c) \quad (3.11)$$

$$E_{transverse}(f_c) = \cos^2\theta \,.\, E_{east}(f_c) + \sin^2\theta \,.\, E_{north}(f_c) \quad (3.12)$$

where, f_c denotes the frequency to be analyzed and Δ is the number of frequency values around f_c.

An energy criterion is then considered to discriminate between Love and Rayleigh surface waves. If the transverse component carries more energy than the radial and transverse components together, the wave is identified as a Love wave. In the opposite case, it is considered as a possible Rayleigh wave and its identification is done based on the determination of polarization parameters in the next step.

3.4.2 Quaternion-MUSIC

In order to estimate polarization parameters, the data of radial and vertical components are stored in a single data matrix by using hyper-complex numbers, such as quaternions. Quaternions are indeed considered as an extension of complex numbers into four dimensions (e.g. Ward 1997). Two complex-valued data matrices

corresponding to different components can be stored in a single quaternion-valued data matrix (4 dimensions) or all three components of the seismic signals can be stored in a single biquaternion matrix (8 dimensions). Hobiger (2011) shows that since the polarization of a pure seismic wave is always confined to two components maximum, the quaternion-MUSIC (Miron et al. 2005, 2006) approach is sufficient to characterize the polarization parameters of an incident wave. This way, use of quaternions allows the algorithm to merge both the complex-valued data vectors of radial and vertical components into a single data vector and thus the polarization relation between both components remains naturally preserved in the data. The quaternion data matrix $X_q(f)$ is given by (Hobiger et al., 2014)

$$X_q(f) = \mathrm{Re}[X_{\mathrm{vertical}}(f)] + i.\,\mathrm{Re}[X_{\mathrm{radial}}(f)] + j.\,\mathrm{Im}[X_{\mathrm{vertical}}(f)] + k.\,\mathrm{Im}[X_{\mathrm{radial}}(f)] \quad (3.13)$$

where i, j and k are imaginary units such as $i^2 = j^2 = k^2 = ijk = -1$.

Following Equation 3.1, the quaternion-valued covariance matrix $S_q(f)$ is then built. The quaternion-MUSIC functional, which is maximized by the correct polarization parameters φ and ρ, remains analogous to Equation 3.2. The modified steering vector is then given by

$$a_q = [\cos\rho + i\sin\rho\,\exp(j\varphi)]\,.\exp(-j\boldsymbol{R}k)\,/\sqrt{N} \quad (3.14)$$

where, φ (with $0 \le \varphi \le 360°$) is the phase difference between the vertical and radial components and ρ (with $0 \le \rho \le 90°$) is the amplitude parameter. Quaternion-MUSIC approach uses a four-dimensional grid search for identifying four unknowns, azimuth, slowness, phase difference and amplitude parameter. In case of MUSIQUE algorithm, azimuth and slowness of the wave are estimated in the first step using classical MUSIC. Then only determination of the two polarization parameter is required which can be done in an analytical way rather than using the time consuming four-dimensional grid search.

3.5 Data processing

MUSIQUE code is written in Matlab programming language (Hobiger, 2011). The steps followed and parameters considered for the analysis of Argostoli array data are described in this section. Classical MUSIC is able to identify multiple sources. Due to the projection of the horizontal signals with respect to the identified wave back-azimuth for the estimation of polarization parameters, MUSIQUE code is limited to a single wave contribution, i.e. to the most dominant source (K=1). However, multiple sources can be identified by MUSIQUE if estimation of polarization parameters is excluded from the analysis. The single-source approach is suitable when the wave field is truly dominated by a single wave. If not the case, however, for example, if there are two dominating sources, assumption of single-source will cause a biased estimation of noise subspace and thereafter wave propagation parameters (velocity, azimuth, polarization characteristics). In this study we have, thus, performed two separate analyses based on single source (K=1) and double source (K=2) assumptions. For the double-source assumption, steps (1) to (4) have been performed while for the single-source case all the following steps have been considered.

(1) Our array analysis using MUSIQUE requires dividing the entire signal into smaller time windows within a certain frequency range of interest. From the array transfer function of Array A, the resolvable frequency range was found to be between 1 and 20 Hz for slownesses larger than 0.002 s/m. The same frequency range has been used for Array B data.. Therefore, we chose 200 log-based frequency bands between 1 to 20 Hz.

(2) The signals of all components and available stations are band-pass filtered using a Chebyshev filter with a bandwidth of 0.1 times the respective frequency. For instance, the signal is filtered between 0.18 and 0.22 Hz for a central frequency of 0.2 Hz.

(3) Then, for each frequency band, filtered signals are cut into time windows of duration equals to five periods the central frequency by considering also 50% overlapping of the windows. For example, at 1 Hz frequency the signal is divided into 5 s-long time windows while at 10 Hz it is 0.5 s with 2.5 s and 0.25 s overlapping, respectively. A 50 s

duration signal will, therefore, provide 19 windows at 1 Hz and 199 at 10 Hz, leading to an increase of time windows with frequency.

(4) The following processing is done for each time window and each frequency band. The "classical" MUSIC algorithm (Schmidt, 1986; Goldstein and Archuleta, 1987) is applied to the three components in order to identify back-azimuth and absolute slowness of the most energetic wave arrivals through a two-dimensional grid search on the values maximizing the MUSIC functional. To assure a well-conditioned covariance matrix, we consider spectral averaging over five frequencies samples centered on the central frequency.

(5) In the next step for each time window and each frequency band, radial and transverse components are computed by projecting the east-west and north-south components of the signals into the direction of the identified back-azimuth and its orthogonal direction. Here, an energy criterion is used to distinguish between Love and Rayleigh surface waves. Transverse energy will be larger than the sum of vertical and radial energies when predominant wave is a Love wave and smaller in case of Rayleigh waves. If the transverse energy is more than 70% of the total energy, the wave is identified as a Love wave (Equation 3.15):

$$E_{transverse} > 2.33 \times (E_{radial} + E_{vertical}) \tag{3.15}$$

Conversely, when the sum of radial and vertical energy is more than 70% of the total energy, the wave is treated as a possible Rayleigh wave and the analysis proceeds to the step (6) In case none of this energy criterion is fulfilled, no wave is identified for the analyzed frequency-time window signal block.

(6) The quaternion-valued covariance matrix is built by using the radial and vertical components and the quaternion-MUSIC functional is maximized to estimate the phase difference (φ) between vertical and radial components and the amplitude parameter (ρ). As azimuth and slowness parameters have already been estimated, the remaining two parameters, φ and ρ, are determined in an analytical way. As a final step, the retrograde and prograde particle motions are distinguished from the estimated φ

values. Theoretically a shift of φ=90° corresponds to a retrograde particle motion while φ=270° to a prograde one. In our analysis, φ values ranging from 45° to 135° is identified as retrograde motion and from 225° to 315° as prograde, the other values being neglected. The wave is identified as a Rayleigh wave if it satisfies either of these criteria, otherwise no wave is identified from the frequency-time window signal-block

3.6 Post-processing

Aside from retrieving the estimates of wave vector, slowness (s) and back-azimuth (θ), identified Love wave, and retrograde and prograde Rayleigh waves, energy for each frequency-time window [f_w, t_w] signal block is also estimated. In order to keep the most reliable and significant results, we then applied some filtering thresholds to keep only the most coherent part of the seismograms containing the most energetic signals. We thus compute the following quantities:

(1) The average Fourier amplitude spectra (FAS_{avg}), signal-to-noise ratio (SNRavg) at central frequency (f_c) of the frequency band (f_w) are estimated by using Fourier amplitude spectra computed over the entire signal length. For SNR computation, the entire length of the signal and 60 s duration of noise were considered and then their spectral ratio was estimated. To put equal weight to the different durations, both signal and noise spectra were corrected by dividing with square root of their respective lengths.

$$\mathrm{FAS_{avg}}(f_c) = \frac{1}{3N_{st}} \sum_{m=1}^{N_{st}} [\mathrm{FAS_E}(f_c, m) + \mathrm{FAS_N}(f_c, m) + \mathrm{FAS_Z}(f_c, m)] \tag{3.16}$$

$$\mathrm{SNR_{avg}}(f_c) = \frac{1}{3N_{st}} \sum_{m=1}^{N_{st}} [\mathrm{SNR_E}(f_c, m) + \mathrm{SNR_N}(f_c, m) + \mathrm{SNR_Z}(f_c, m)] \tag{3.17}$$

where, N_{st} is the number of stations, m is the sensor index. We denote the Fourier amplitude spectra and signal-to-noise ratio at three components by FAS and SNR with corresponding suffixes for north, east and vertical components, respectively.

(2) The lagged coherency is estimated (Equation 3.18) as modulus of the ratio of the smoothed cross-spectrum $(\bar{S}_{jk})$ of the time series between the stations j and k, to the geometric mean of the corresponding auto power spectra ($\bar{S}_{jj}$ and $\bar{S}_{kk}$) (details procedure is given in Chapter 4).

$$COH(t_c, f_c, j, k) = \frac{|\bar{S}_{jk}(t_c, f_c)|}{\sqrt{\bar{S}_{jj}(t_c, f_c)\bar{S}_{kk}(t_c, f_c)}} \tag{3.18}$$

The average coherency for each frequency-time signal block over all station pairs is then

$$COH_{avg}(t_c, f_c) = \frac{1}{3N_p}\sum_{m=1}^{N_p}[COH_E(t_c, f_c, m) + COH_N(t_c, f_c, m) + COH_Z(t_c, f_c, m)] \tag{3.19}$$

where, N_p is the number of station pairs, m is the sensor pair index, tc is the central time of the time window t_w. COH_E, COH_N and COH_Z are the coherencies computed on north, east and vertical components, respectively.

(3) For each component (E, N, Z), the energy (E_E, E_N, E_Z) carried in each time-frequency signal block is computed as the square absolute values of the Fourier amplitude spectrum (by using the time window length) evaluated at the central frequency. The window energy is then computed by summing up the three components' energies as,

$$E_{window}(t_c, f_c) = E_E(t_c, f_c) + E_N(t_c, f_c) + E_Z(t_c, f_c) \tag{3.20}$$

Here, at each frequency band, we eliminate MUSIQUE estimates obtained from the waves containing average SNR (SNR_{avg}) less than 5, energy less than the median energy of all available time windows, average lagged coherency (COH_{avg}) less than 0.5. We also considered only the results having slowness $0.0004 \leq s \leq 0.008$ s/m (i.e. apparent velocities between 125 m/s and 2500 m/s) to avoid misidentified results and aliasing.

In case of identified Love waves, retrograde and prograde Rayleigh motion, MUSIQUE uses 1 for the corresponding time-frequency signal block and 0 if no wave is identified;

the resulting matrices are denoted as L, R_{retro} and R_{pro}, respectively. Energies of the identified surface waves are then estimated (Equation 3.21 to 3.23) by using their identification index (1 or 0) and the energies computed from the radial, transverse and vertical components (Equation 3.5, 3.6 and 3.7.).

$$E_{Love}(t_c, f_c) = L(t_c, f_c) \times E_{transverse}(t_c, f_c) \tag{3.21}$$

$$E_{retro}(t_c, f_c) = R_{retro}(t_c, f_c) \times [E_{radial}(t_c, f_c) + E_{vertical}(t_c, f_c)] \tag{3.22}$$

$$E_{pro}(t_c, f_c) = R_{pro}(t_c, f_c) \times [E_{radial}(t_c, f_c) + E_{vertical}(t_c, f_c)] \tag{3.23}$$

$$E_{Rayleigh}(t_c, f_c) = \left[E_{retro}(t_c, f_c) + E_{pro}(vt_c, f_c)\right] \tag{3.24}$$

In each frequency band, percentage of the total analyzed surface wave energy compared to the total window energy is given by Equation 3.25,

$$E_{Wpercent}(f_c) = \sum_{m=1}^{N_t} \frac{E_W(m, f_c)}{E_{window}(m, f_c)} \times 100 \tag{3.25}$$

where, m is the time index, N_t is the number of time windows and W stands for different surface wave types: Love, Rayleigh, retrograde and prograde Rayleigh waves.

An estimation of normalized window energy is provided in Equations 3.26 and 3.28. The normalizing factor here is the squared Fourier amplitude spectra and the estimation is log scaled. This has been done to ensure equivalent weights to all the frequency-dependent windows and for the sake of clarity of the figures.

$$E_{norm}(t_c, f_c) = \log_{10}\left[\frac{E_{window}(t_c, f_c)}{(FAS_{avg}(f_c))^2}\right] \tag{3.26}$$

$$E_{Wnorm}(t_c, f_c) = \log_{10}\left[\frac{E_W(t_c, f_c)}{(FAS_{avg}(f_c))^2}\right] \tag{3.27}$$

Finally, in order to combine MUSIQUE estimates from different events and different wave types, energy at each time-frequency signal block for a given event is normalized by the maximum energy computed over all the time windows available for that event as,

$$\mathrm{SUME}_{\mathrm{Wnorm}}(t_c, f_c) = \sum_{\mathrm{m}=1}^{\mathrm{N}_{ev}} \log_{10}\left[\frac{\mathrm{E}_{\mathrm{Wnorm}}(t_c, f_c, \mathrm{m})}{\max\left(\mathrm{E}_{\mathrm{Wnorm}}(f_c, \mathrm{m})\right)}\right] \tag{3.28}$$

where, W denotes different wave types, N_{ev} is the number of events. This procedure leads to normalized energy values between 0 to 1 in order to perform an equally weighted summation over all the events.

3.7 Results from single dominant source : example event

We begin with results obtained based on the assumption that a single source dominates the wave field. First we will present the wave field characterization for one event and then combine and summarize results obtained from all the events.

3.7.1 Event characteristics

We consider the results obtained from the array analysis of an example event using Array A data. The event (index 12 in Appendix F) occurred 14th October 2011 at UTC 01:11:32 with a magnitude M_L=3.5, a hypocentral depth of 12 km, at an epicentral distance of 36 km and a back-azimuth of N125 from the central station A00. Figure 3.4 (a) and (b) display the waveforms recorded at the rock station R02 (northeast edge) and at the central station A00, respectively. From the comparison of the recordings of these two stations, amplification and locally generated surface wave-trains are evident on the seismograms of A00 station. Figure 3.5 shows the Fourier amplitude spectra (FAS) and signal-to-noise-ratio (SNR) of the velocities at A00 station. The SNR of this event between 1 to 20 Hz frequency range, which is the range considered for array analysis, is observed to be higher than 10.

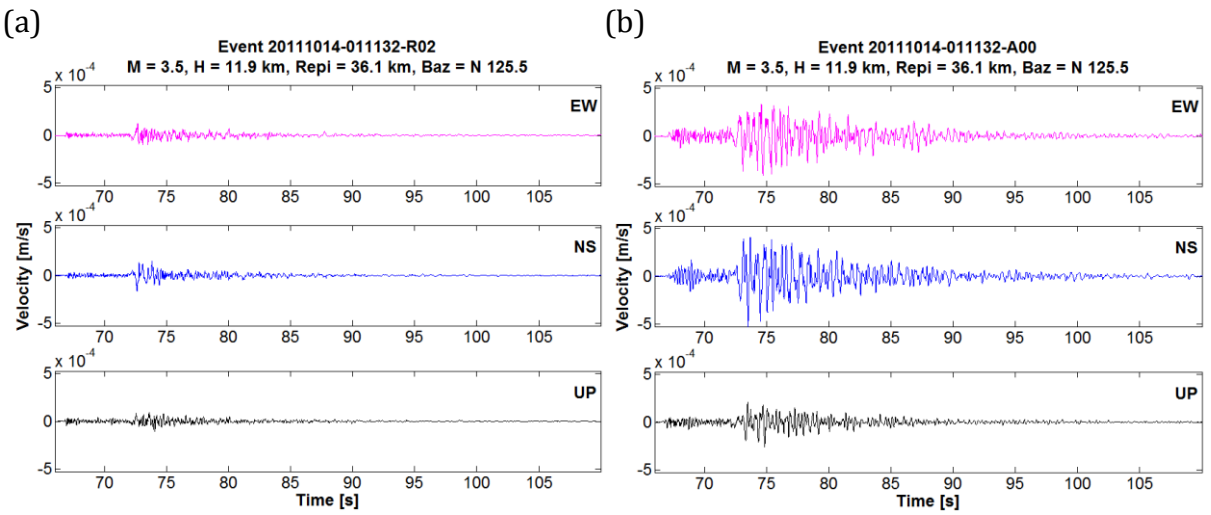

Figure 3.4: Velocity time series of the event no. 12 (ML=3.5) recorded (a) at rock station R02 and (b) at the central station, A00, of Array A.

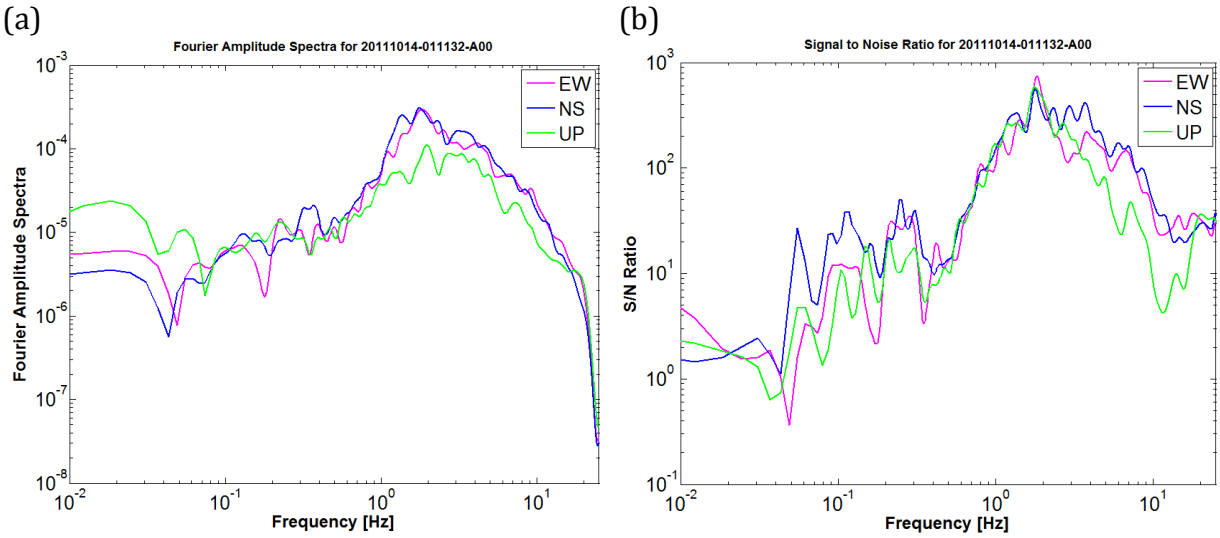

Figure 3.5: (a) FAS and (b) SNR for the event no. 12 (ML=3.5) at the central station, A00, of Array A.

3.7.2 MUSIQUE results

Figure 3.6 shows spectrogram of the identified waves from raw results. The colorbar indicates normalized energy calculated by Equation 3.26. Each point on the plot corresponds to the spectrogram value at a given time-window and a given frequency band. P- and S- wave onsets from the spectrogram occur at about 1s and 6 s, respectively. It is to be noted that the normalized energy estimation amplifies the lower energy results for achieving almost equivalent weighted over all the analyzed frequency

dependent windows. Therefore the energy values showed through the colorbar do not represent absolute energy of the windows.

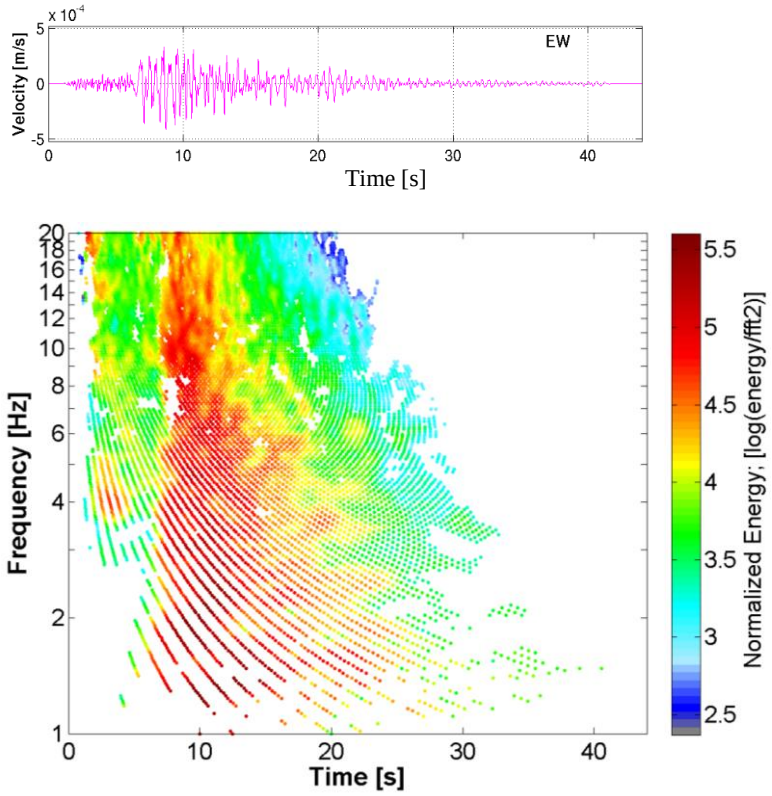

Figure 3.6: Velocity time series of the EW component (top) and spectrogram (bottom) of unfiltered results obtained for the identified dominant waves from array analysis of the event 12. Colorbar represents normalized window energy estimated by Equation 3.26.

In order to observe the effect of post-processing filtering on the results, we now present the filtered spectrograms in Figure 3.7 (a) and (b). Figure 3.7 (c) and (d) illustrate the filtered signal blocks which have been identified as Love or Rayleigh surface waves. Figure 3.7(a) presents the spectrogram after applying SNR, coherency and slowness filtering criteria on the results shown in Figure 3.6. By comparing these two spectrograms we observe that only a very small portion of the results has been left out. For this particular event, this is already partly explained by the very good SNR over the analyzed frequency range (Figure 3.5 (b)). Furthermore, since the array is very dense and the interstation distance is less than 100 m, the coherency is expected to be high for most of the station pairs. However, when we consider the energy filtering on the currently filtered results (Figure 3.7(a)), a significant change is observed as presented

in Figure 3.7 (b). We see that most of the high frequency (f > 10 Hz) time-frequency signal blocks, for which the absolute energy estimation is low, are discarded due to the application of post processing filtering.

Spectrograms in Figure 3.7 (c) and (d) show signal blocks for which the dominant source has been identified as Love and Rayleigh surface waves, respectively. Figure 3.7 (e) and (f) represent the signal blocks characterized as retrograde and prograde Rayleigh motion. From Figure 3.7(c) and (d), it appears that most of the lower-energy signal windows do not contribute to the wave identification and the dominant source is, primarily, a Love wave at lower frequencies (f < 3 Hz) and Rayleigh at higher frequencies (3 < f < 6 Hz). It can also be said that at around 3 to 4 Hz retrograde Rayleigh motion is prominent.

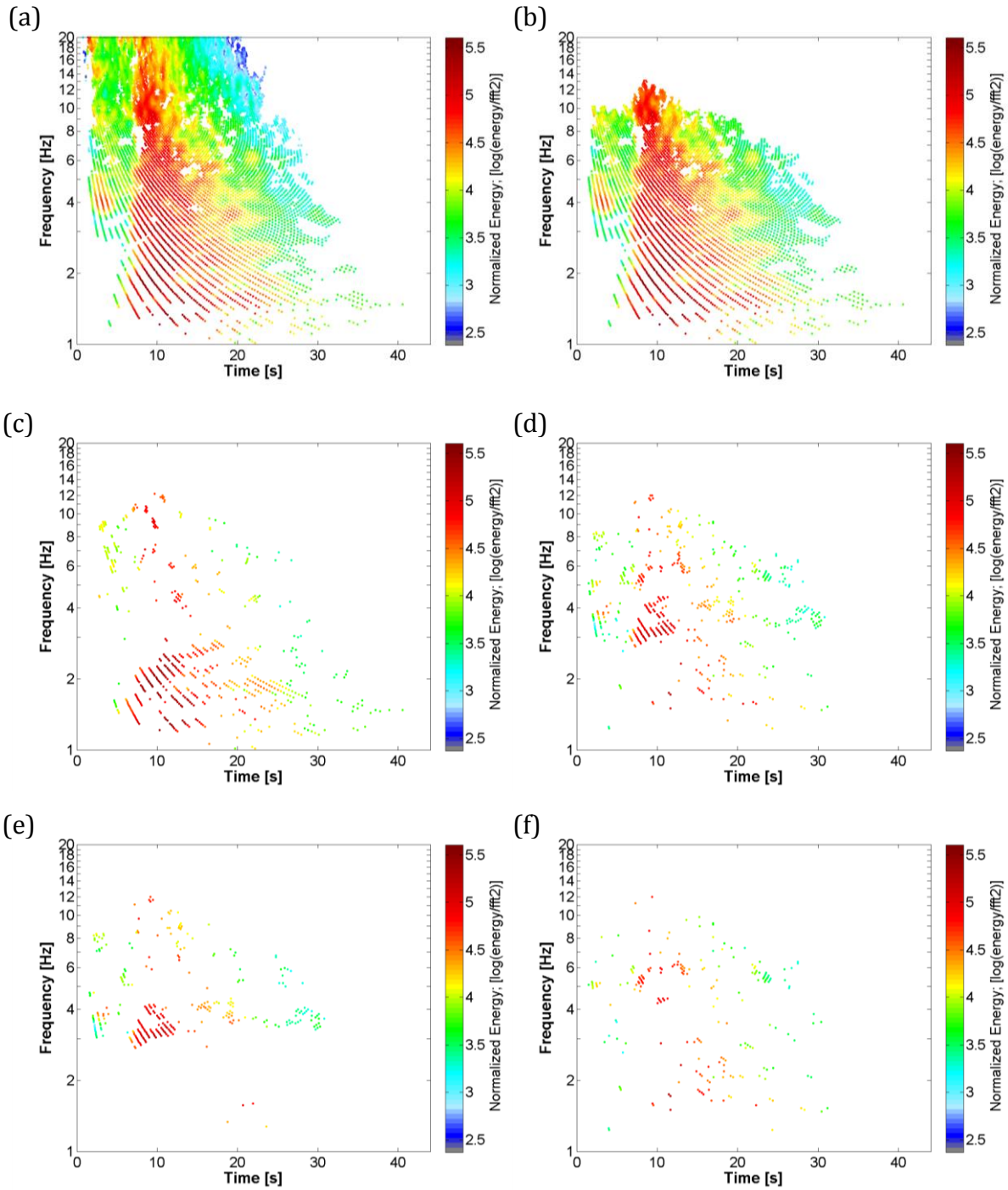

Figure 3.7: Spectrogram of the filtered results from the analysis of event no. 12, when (a) SNR, coherency and slowness filtering is applied and (b) energy filtering is added to the previous filtering. The identified dominant sources characterized as (c) Love (d) Rayleigh (e) retrograde Rayleigh and (d) prograde Rayleigh surface waves from the filtered results. Colorbar represents normalized window energy estimated by Equation 3.26.

3.7.3 Identified back-azimuth

Figure 3.8 shows identified back-azimuth distribution of the dominant sources as a function of time and frequency. When the dominant waves' back-azimuths are plotted against the time (Figure 3.8 (a)), direct S wave arrivals (the energetic data points close to the event's back-azimuth direction marked by a red line) are observed at the onset at ~6 s. Some diffracted waves are observed close to the east, while most diffracted wave trains appear very early in seismograms from south to south-west direction.

Figure 3.8 (b) shows the histogram of back-azimuth distribution over analyzed frequencies. The red line marks the event's back-azimuth. Here colorbar is the summed normalized windowenergy (Equation 3.26) for time-frequency signal block that provided back-azimuth estimates falling into specific frequency-backazimuth grid cell [fgrid1, θgrid]. For the back-azimuth histogram we have considered 72 grid points between 0° and 360° angles (i.e. interval = 5°). For frequency axis, we have considered 31 log-based grid-points between 1 and 20 Hz. The sum of normalized window energy is estimated by,

For $\theta_1 < \mathrm{BAZ}(t_c, f_c) < \theta_2$ and $f_{c1} < f_c < f_{c2}$:

$$\mathrm{SUME}_{\mathrm{normbaz}}(f_{\mathrm{grid1}}, \theta_{\mathrm{grid}}) = \sum_{m=1}^{N_t} \sum_{j=j_1}^{j_2} E_{\mathrm{norm}}(m, j) \tag{3.29}$$

where, m is in time index and N_t is the number of time windows, f_c is the central frequency of the time-frequency signal block, j_1 and j_2 and θ_1 and θ_2 are the minimum and maximum frequencies and back-azimuths of the grid cell [fgrid1, θgrid], respectively. $\mathrm{BAZ}(t_c, f_c)$ is the back-azimuth estimate for a given time-frequency signal block.

The back-azimuth distribution (Figure 3.8 (c)) outlines that, over the entire frequency range, most of the wave-energy is coming from the south-west direction (roughly N210±30° back-azimuth), which corresponds to the south-west edge of the valley.

(a)

Origin Date = 20111014

Origin Time = 01:11:32 UTC

ML = 3.5, Baz= N 125°

Repi = 36 km, H=11.9 km

(b)

(c)

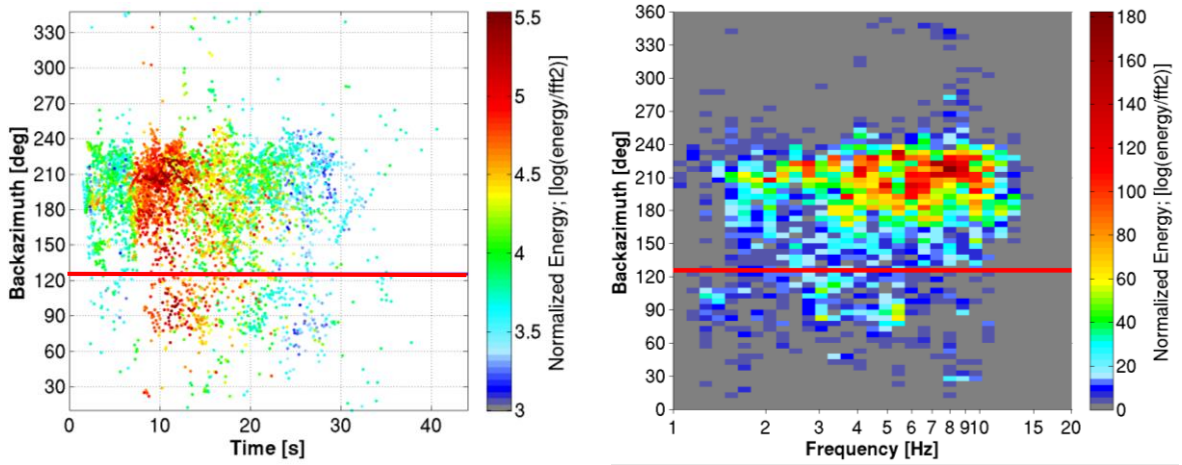

Figure 3.8: Identified back-azimuth distribution of the dominant waves, for event 12, propagating across the Array A. (a) Location of the event with respect to the central station A00. (b) Identified back-azimuths as function of time with colorbar indicating normalized energy as estimated in Equation 3.26. (c) Histogram of identified back-azimuths as a function of frequency with colorbar indicating the summation of normalized energy as estimated in Equation 3.29. Red line indicates the back-azimuth of the event.

3.7.4 Identified slowness

Figure 3.9 displays the histogram of slowness distribution over analyzed frequencies. Here colorbar is the summed normalized windowenergy (Equation 3.30) for time-frequency signal block that provide slowness estimates falling into specific frequency-slowness grid cell [f_{grid2}, S_{grid}]. For the histogram we have considered 100 grid-points for slownesses ranging between 0.0003 and 0.008 s/m. For the frequency axis, we have

considered 61 log-based grid-points between 1 and 20 Hz. The sum of normalized window energy is estimated by,

For $s_1 < S(t_c, f_c) < s_2$ and $f_{c1} < f_c < f_{c2}$

$$SUME_{normslowness}(f_{grid2}, S_{grid}) = \sum_{m=1}^{N_t} \sum_{j=j_1}^{j_2} E_{norm}(m, j) \quad (3.30)$$

where, m is in time index and N_t is the number of time windows, f_c is the central frequency of the time-frequency signal block, j_1 and j_2 and s_1 and s_2 are the minimum and maximum frequencies and slownesses of the grid cell [f_{grid2}, S_{grid}], respectively. $S(t_c, f_c)$ is the slowness estimate for a given time-frequency signal block.

From the slowness distribution (Figure 3.9) we can observed mostly dispersive phase velocities related to surface waves propagation characteristics with a possible fundamental mode within 1 to 3 Hz frequency and some indication of higher modes at higher frequencies.

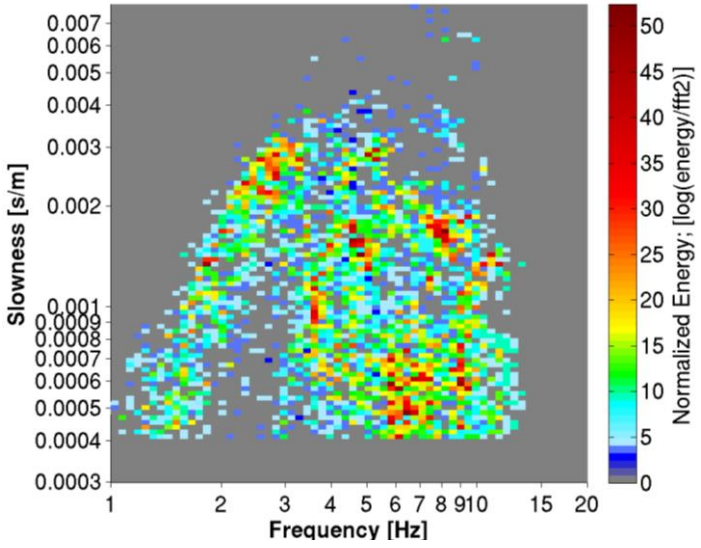

Figure 3.9: Histogram of identified slowness distribution of the dominant waves, for event no. 12, propagating across Array A. Colorbar indicates summation of normalized window energy estimated by Equation 3.30.

3.7.5 Energy repartition

Figure 3.10 provides the evolution of identified Love and Rayleigh wave energies for various frequency ranges for event no. 12. First we describe the estimation procedure of this normalized energy. We divided the identified back-azimuths into 36 bins of 10 degrees interval from N0 to N360. From the estimated window energy and identified back-azimuth, we sort out the time-frequency signal blocks having back-azimuths falling into each back-azimuth bin and then find out the corresponding energy. Then the energies of all available time windows, within our desired grouping, corresponding to each frequency are summed up to get the total energy contributions of Love and Rayleigh surface waves as $SUME_{ilove}$ (f_c, θ_i) and $SUME_{iray}$ (f_c, θ_i), respectively. We find out the minimum nonzero value between the total energy estimations as,

$$e_{min} = \min(SUME_{iray}(f_c, \theta_i) > 0, SUME_{ilove}(f_c, \theta_i) > 0) \tag{3.31}$$

Then the normalized energy for Love and Rayleigh waves are computed as,

$$NSUME_{ilove}(f, \theta_i) = \log_{10}\left[\frac{SUME_{ilove}(f_c, \theta_i)}{e_{min}}\right] \tag{3.32}$$

$$NSUME_{iray}(f, \theta_i) = \log_{10}\left[\frac{SUME_{iray}(f_c, \theta_i)}{e_{min}}\right] \tag{3.33}$$

We used log scale for the sake of clarity when plotting the energy distribution for various frequency bands. We indeed normalized the energy by the minimum value in order to ensure final values equal to or above 1 so that negative values can be avoided in our log scale.

Finally, for each frequency group of interest (values ranging from f_i to f_k), the normalized total energy estimations of a specific back-azimuth range falling into the frequency range are summed up as,

$$\mathrm{FNSUME_{ilove}}(\theta_i) = \sum_{m=f_i}^{f_k} \mathrm{NSUME_{ilove}}(m, \theta_i) \tag{3.34}$$

$$\mathrm{FNSUME_{iray}}(\theta_i) = \sum_{m=f_i}^{f_k} \mathrm{NSUME_{iray}}(m, \theta_i) \tag{3.35}$$

In the plots Figures 3.10 (a) to 3.10 (h), normalized energies for various frequency ranges as quantified by Equations 3.34 and 3.35 are plotted radially over the back-azimuth groups. The back-azimuth of the event is marked by a blue dot. Note that here the energy amplitudes not necessarily reflect the actual energy values. They rather correspond to the relative energy distribution among surface wave types where the smaller quantities are amplified for better visualization. These plots are more relevant for observing the evolution of propagating waves' back-azimuths.

From Figure 3.10 (a) and (b) we can observe that at frequencies below or close to the fundamental frequency of the valley (~1.5 Hz), although surface waves do propagate from the source direction (~N125), there is a significant proportion of energy arriving from the south-west (up to N240) and a relatively smaller proportion from the north-east (approximately N60-N90). These scattering directions can be attributed to the two edges of the valley structure, with the south-west edge being the dominant scatterer. As frequency increases (Figures 3.10, (c)-(h)), the principal scattering direction is still observed to be the south-west, with scattering contribution being relatively in a broader azimuthal range for the Rayleigh wave while Love wave seems to be arriving more from the source direction.

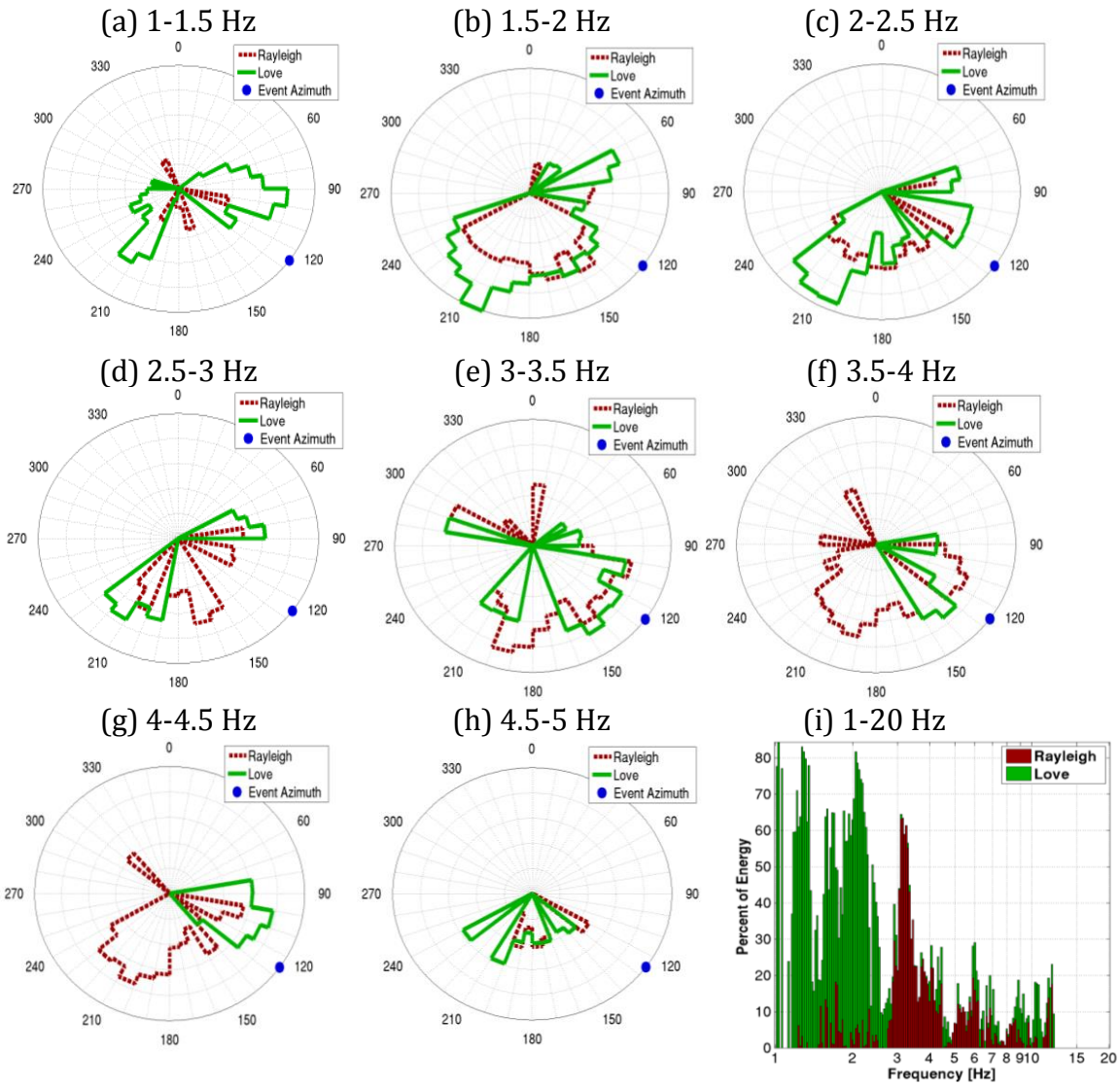

Figure 3.10: (a) to (h) Distribution of the estimated Love (green dashed line) and Rayleigh (red dashed line) surface-wave normalized energies over 10 degrees back-azimuth interval and various frequency ranges. The blue dot indicates back-azimuth of the event. The normalized energies have been estimated by using Equations 3.34 and 3.35. (f) Proportion of identified Love and Rayleigh surface wave energies (Equation 3.25) with respect to the total window energy as a function of frequency. The bar colors, red and green, indicate Rayleigh and Love waves, respectively.

The bar chart in Figure 3.10 (i) represents actual percentage of analyzed energy carried by the surface waves compared to the total energy estimated from all the time-windows over the frequencies considered (Equation 3.25). The bar colors, red and green, correspond to Rayleigh and Love surface wave energies, respectively, showing relative

contribution (%) of each wave in the total energy. We observe that, on an average, more than 50% of window energy has been explained up to a frequency about 3.5 Hz while about 20% for 3.5-4.5 Hz frequency band. Clearly, Love surface waves dominate the wave field within the 1 to 3 Hz frequency range, Rayleigh surface waves start providing very significant contributions to the analyzed wave field at 3 Hz, and the wave field becomes a mixture of Love and Rayleigh surface waves above 4 Hz. This outlines the frequency dependence of the partition of energy between Rayleigh and Love surface waves.

3.7.6 Results from Array B

We analyzed the same event (no. 12) for Array B data and the results are presented in Figure 3.11. The back-azimuth distribution over time and frequency are shown in Figure 3.11 (a) and (b), respectively. We can see that diffracted waves are arriving from northeast to southwest directions. This is more or less consistent with the previous observation from Array A results. However, the histogram shows that the dominant back-azimuth direction is more towards the east, within N60 to N120, especially at higher frequencies. This could be attributed to the northeast basin-edge effect.

The histogram of slownesses in Figure 3.11 (c) shows dispersive velocities with existence of fundamental and higher modes.. Figure 3.11 (d) represents the percentage of identified Rayleigh and Love surface wave energies compared to the total window energy. This bar chart reveals that lesser proportion of energy could be analyzed: on average 30% of the energy is indeed analyzed up to 5 Hz frequency, with the presence of some sparse higher proportions at some specific frequencies. Love surface waves dominate up to 1.5 Hz and in the 2 to 3 Hz frequency range, while both Rayleigh and Love surface waves are equally contributing at other frequencies.

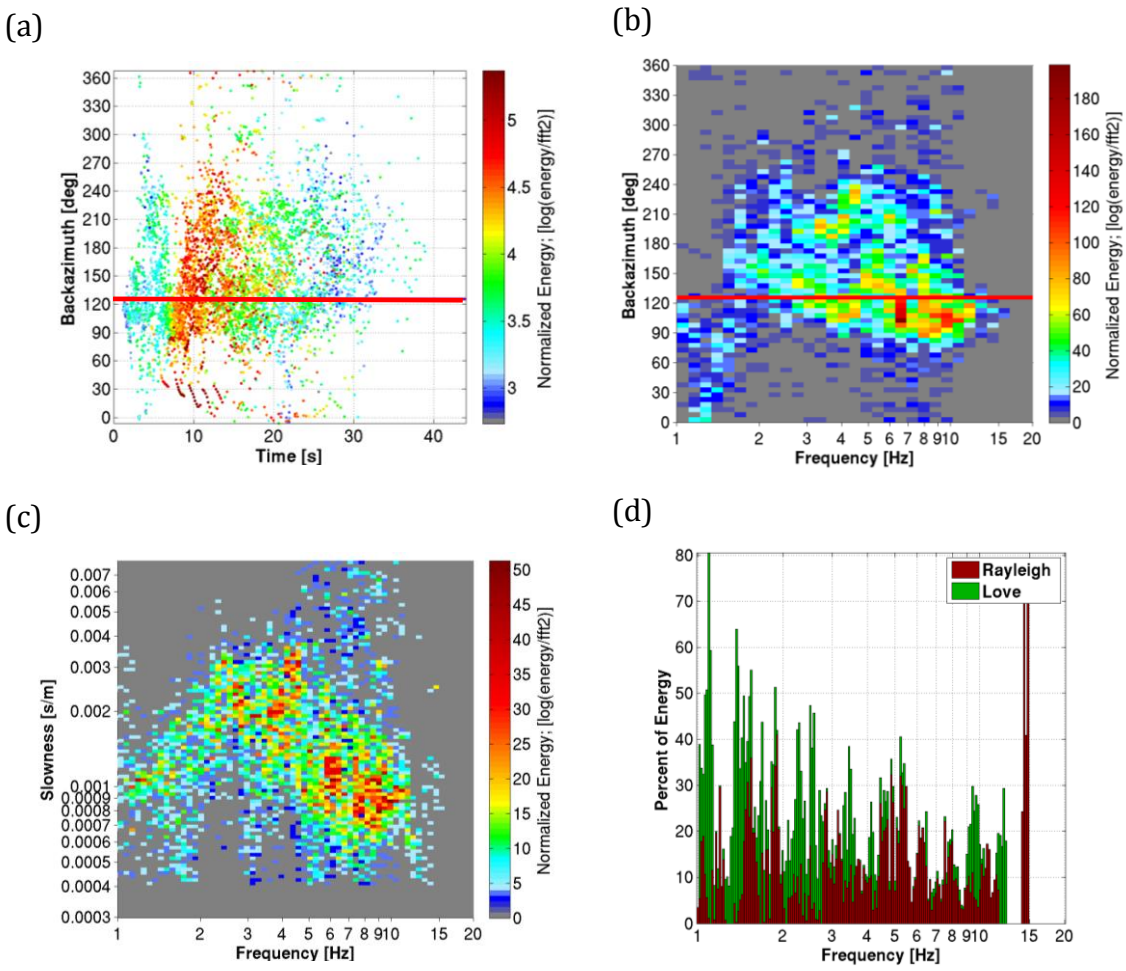

Figure 3.11: Main results from the analysis of Array B data for event no. 12. (a) Distribution of identified back-azimuths over time. Colorbar shows the normalized energy estimated by Equation 3.26. (b) Histogram of identified back-azimuths over frequency. Colorbar shows the normalized energy estimated using Equation 3.29. Red line indicates the back-azimuth of the event. (c) Histogram of identified slownesses over frequency. Colorbar shows the normalized energy estimated using Equation 3.30. (d) Proportion of identified Love and Rayleigh surface wave energies (Equation 3.25) with respect to the total window energy as a function of frequency. The bar colors, red and blue, indicate Rayleigh and Love surface waves respectively.

3.8 Robustness of the results

In order to investigate robustness of the MUSIQUE estimates, five events occurring in different azimuths for both arrays were selected. Figure 3.12 shows the location of the selected five events. The events are numbered as 6, 21, 24, 3 and 7 in Appendix F.

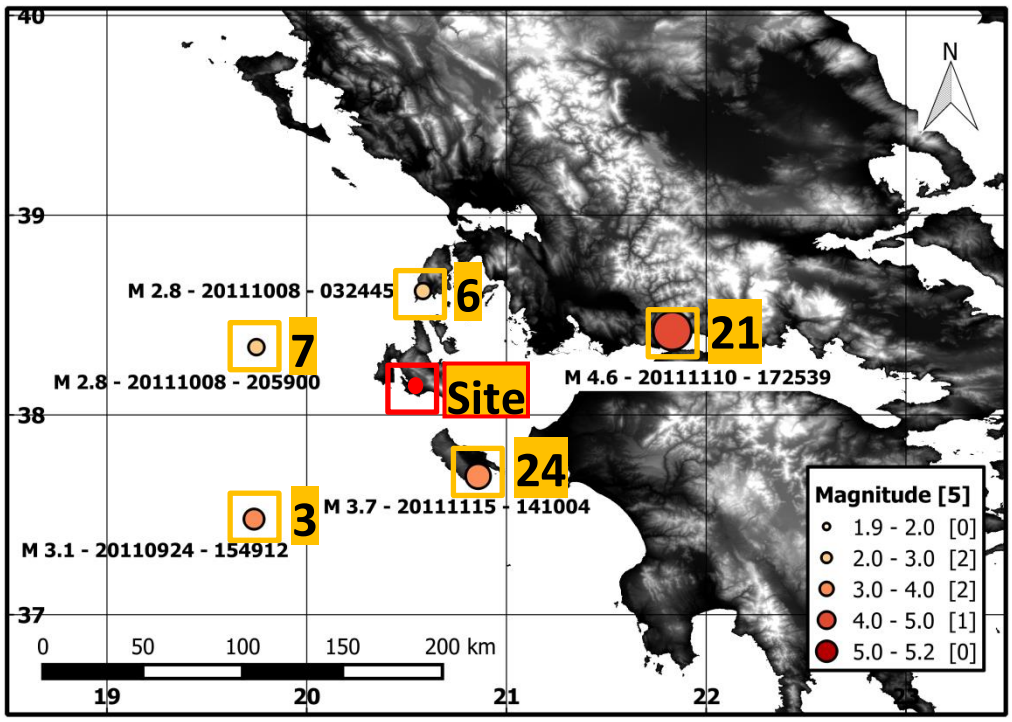

Figure 3.12: Locations of five example events occurred at different directions around the experiment site (Event no. 6, 21, 24, 3 and 7 in Appendix F.1).

Histograms of identified back-azimuth over frequency, from Array A and B results are compared in Figure 3.13. Figure 3.14 represents the corresponding bar charts of analyzed Love and Rayleigh surface wave energy proportions. From the identified back-azimuth, we observe a consistent trend whatever the event back-azimuth is. The dominant diffracted back-azimuth for Array A lies between N210 and N240 while it is ranging between N60 and N120 for Array B, corresponding to the southwestern and northeastern edges of the basin, respectively. We also observe diffracted waves coming from back-azimuths within these two dominant directions. Interestingly, though estimates from Array A do not indicate diffraction from the north-east, estimates from Array B indicate a second dominant diffracted wave field from the south-west direction. This observation is more evident when the event back-azimuth lies between the northeast and southeast directions as in case of event no. 21 and 24. One possible

implication from this observation is that the dominant diffraction of the wave field is controlled mostly by the southwestern basin-edge compared to the northeastern one. Figure 3.14 demonstrate that for Array A, Love surface wave is dominating at frequencies below 2.5-3 Hz while a mix of Love and Rayleigh surface waves are observed above ~3 Hz. A similar tendancy is observed for Array B except for events 6 and 24 where significant proportion of Rayleigh wave energy is observed at frequencies below 3 Hz.

(a) Array A

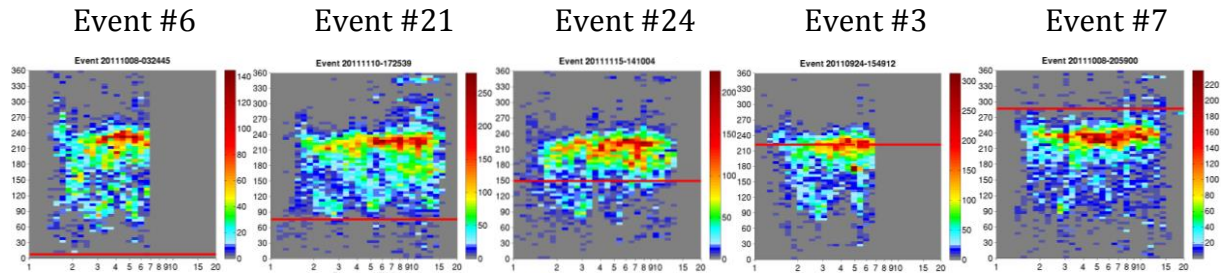

(b) Array B

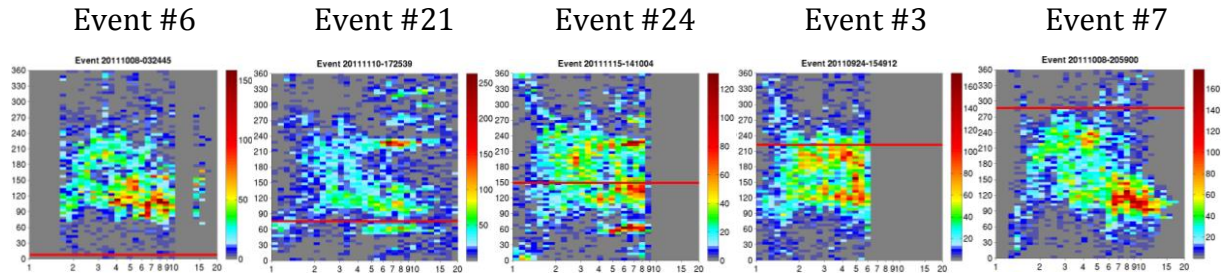

Figure 3.13: Histograms of identified back-azimuths for (a) Array A and (b) Array B data as a function of frequency for five earthquakes occurring in five different back-azimuths (Figure 3.12). Colorbar indicates the summation of normalized energy estimated by Equation 3.29. Red line indicates the back-azimuth of the event.

(a) Array A

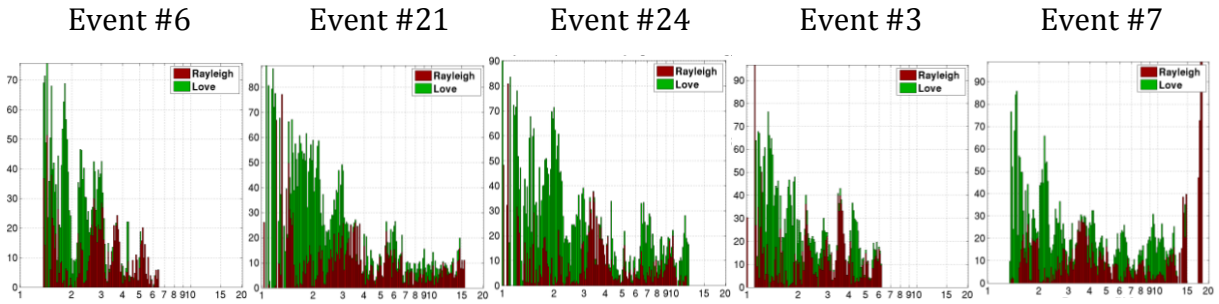

(b) Array B

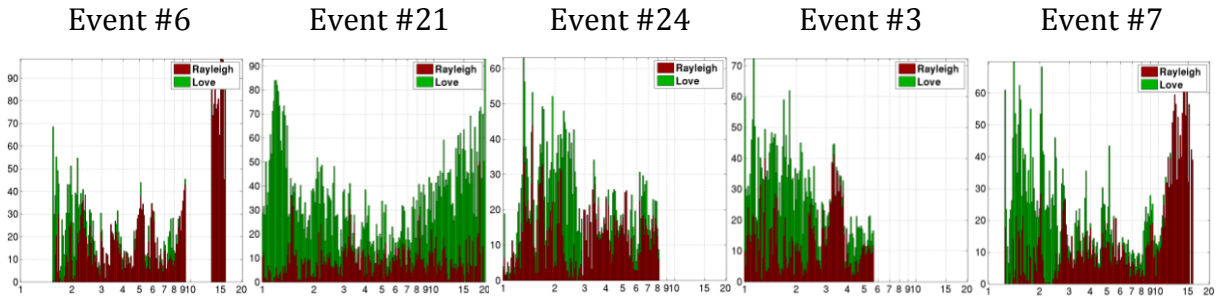

Figure 3.14: Proportion of identified Love and Rayleigh surface wave energies (estimated by Equation 3.25) with respect to the total window energy as a function of frequency, for (a) Array A and (b) Array B data. The bar colors, red and green, indicate Rayleigh and Love surface waves, respectively.

3.9 Summary results for all events

This section summarizes the main observations by combining results from all the events for both arrays. First, in order to focus on characteristics of diffracted wave field only, the contributions from direct arrivals were eliminated by removing the results corresponding to each event's back-azimuth ± 20°, as illustrated in Figure 3.15 (a). Then estimates from the single events were summed. Figure 3.15 (b) illustrates how the summation has been performed in order to get a summary plot of back-azimuth distribution. The same procedure has been followed to summarize the slownesses distribution and the proportion of analyzed Rayleigh and Love surface waves energy.

(a)

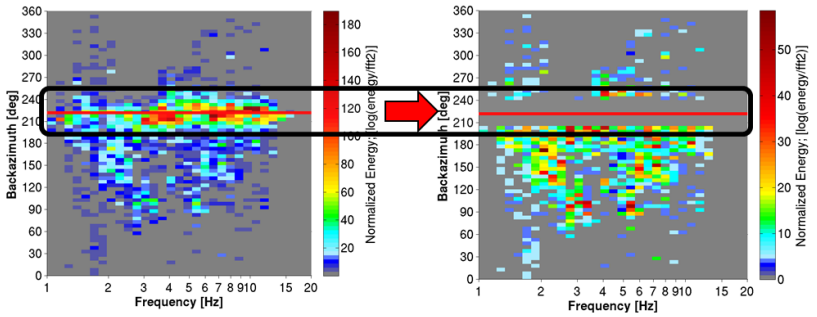

(b)

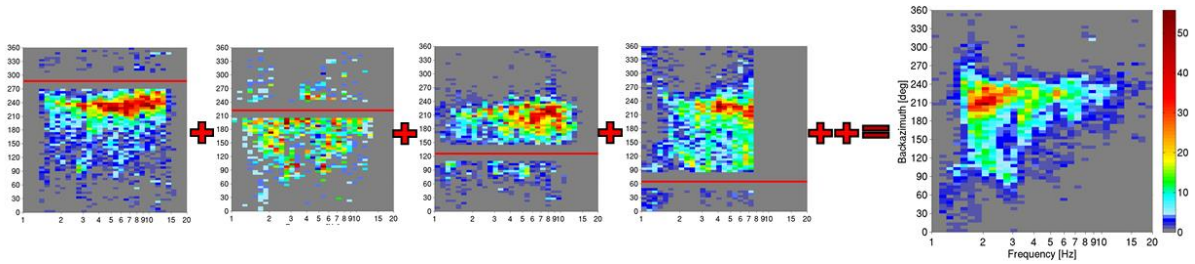

Figure 3.15: (a) Estimates corresponding to event back-azimuth ± 20° are removed for each event. (b) Then all the estimates from individual events are stacked together to obtain a summary plot. The red line indicates back-azimuth of the event. For all the individual plots, x-axis represents frequency (Hz) and y-axis indicates back-azimuth (degrees).

3.9.1 Back-azimuth distribution of the diffracted wave field

The identified back-azimuths obtained from Array A and Array B data for all events were combined into a single summary plot to retrieve the dominant tendency. The cumulative normalized energy totals the individual event's normalized energy (Equation 3.29) and is given by,

$$\mathrm{CSUME}_{\mathrm{normbaz}}(f_{\mathrm{grid1}}, \theta_{\mathrm{grid}}) = \sum_{m=1}^{N_{ev}} \mathrm{SUME}_{\mathrm{normbaz}}(f_{\mathrm{grid1}}, \theta_{\mathrm{grid}}, m) \tag{3.36}$$

where, N_{ev} is the number of events

Figure 3.16 (a) shows the combined results of all analyzed events from Array A. Normalized energy for each event is quantified by Equation 3.29 and then they are summed up to obtain the cumulative normalized energy as in Equation 3.36. The dominant wave scattering over the entire frequency range is observed from the south-

west direction (N210 ± 30°), as already been observed on the subset of 5 events. However, some scattering is also observed at low frequencies from the north-east (N70 ± 10° at 1-2 Hz) and south-east (N110 ± 10° at 2-3 Hz). After separating the contributions of Love and Rayleigh surface waves (Figures 3.16 (b) and (c)), Love surface wave arrivals are seen to dominate the low frequencies (1-3 Hz), while Rayleigh surface waves dominate the wave field between 3 and 5 Hz. Finally, Figure 3.16 (d) schematizes the main diffraction directions with respect to the location of Array A.

The summary plots for Array B (Figure 3.17 (a) to (d)) reflect the same conclusions that were drawn from the individual plots of Figure 3.8. The wave field is diffracted primarily from the northeast to eastern directions. The low frequency wave field (below 3 Hz) is mainly composed of Love surface waves and significant diffraction is observed from the east to southwestern directions as well. Interestingly, we observe (Figure 3.17 (b)) a significant Love surface wave diffraction from northeast to east direction and southwest direction below the resonance frequency of the site. This is also observed for estimates from Array A (Figure 3.16 (b)) even though corresponding energies are rather low. However, this could argue the presence of regional scatterers causing Love surface waves diffraction at long wavelengths.

(a) All Identified Waves

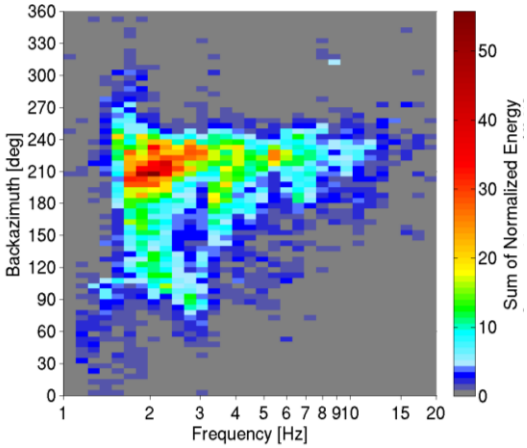

(b) Love Wave

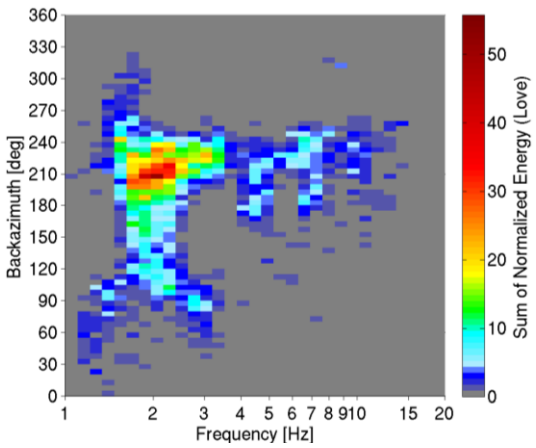

(c) Rayleigh Wave

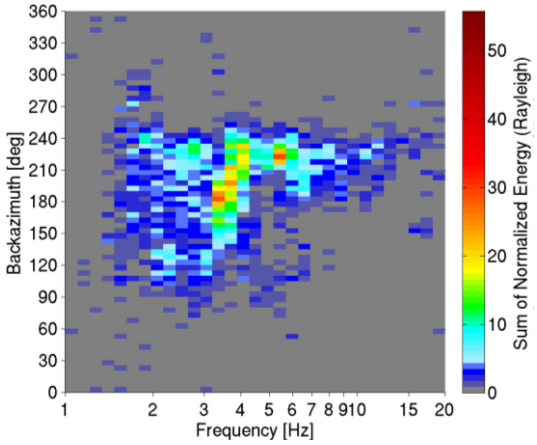

(d) Diffraction Directions

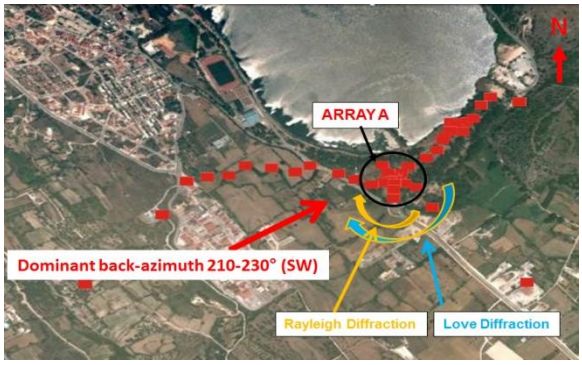

Figure 3.16: Overall cumulative distribution for the whole set of events of the diffracted wave field directions for Array A data, after removing the direct arrivals (event back-azimuth ± 20°). Contributions from (a) all waves, (b) Love waves, and (c) Rayleigh waves. Color bar represents the sum of the normalized energy, obtained by Equation 3.36. (d) Direction of dominant diffracted wave arrivals with respect to the array site location.

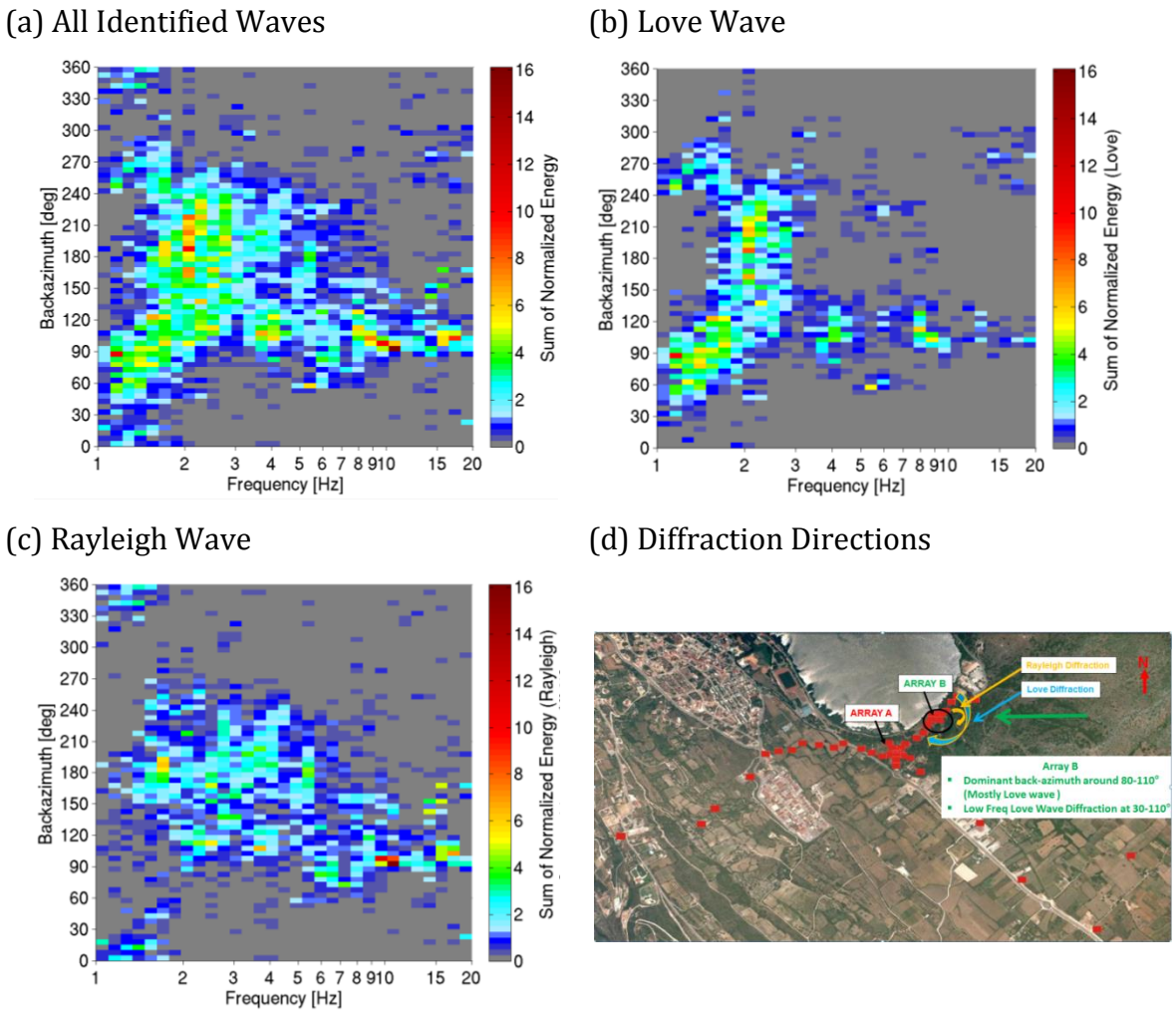

Figure 3.17: Overall cumulative distribution for the whole set of events of the diffracted wave field directions for Array B data, after removing the direct arrivals (event back-azimuth ± 20°). Contributions from (a) All waves, (b) Love waves, and (c) Rayleigh waves. Color bar represents the sum of the normalized energy, obtained by Equation 3.36. (d) Direction of dominant diffracted wave arrivals with respect to the array site location.

3.9.2 Dispersion curve (slowness)

Figure 3.18 (a) represents, for array A, the overall cumulative slownesses distribution for the whole set of events obtained from all the analyzed time windows after removing the direct arrivals (event-back-azimuth ± 20°). The extracted slowness values are frequency-dependent, confirming the surface-wave nature of the diffracted wave field. Figures 3.18 (b) and (c) provide slowness estimates for Love and Rayleigh surface waves, respectively, together with the dispersion curves obtained from classical array analysis performed on seismic ambient noise and active surface wave measurements

(Boxberger et al., 2014). The cumulative normalized energy sums up the individual event's normalized energy (Equation 3.30) and is given by

$$\mathrm{CSUME}_{\mathrm{normslowness}}(f_{\mathrm{grid2}}, s_{\mathrm{grid}}) = \sum_{m=1}^{N_{ev}} \mathrm{SUME}_{\mathrm{normslowness}}(f_{\mathrm{grid2}}, s_{\mathrm{grid}}, m) \tag{3.37}$$

Figure 3.18 (b) indicates that the very clear dispersion curve, at frequencies below 3 Hz, observed in Figure 3.18 (a), is dominated by the Love waves, and most probably the fundamental Love wave mode. Higher Love wave modes are observed at higher frequencies. On the other hand, the Rayleigh wave dispersion data (Figure 3.18 (c)) do not exhibit clear dispersion curve branches and seems to be a mixture of different propagation modes. The split of the dispersion estimates into retrograde and prograde Rayleigh wave particle motions (Figures 3.18 (d) and (e)) allows better distinction between the different mode branches, between 1.5 and 3 Hz, and 3 and 4 Hz, which is most likely to be corresponding to the fundamental and the first higher mode, respectively. From the H/V average spectral ratios (Figure 2.9, Chapter 2) indeed, the particle motion should be prograde between ~1.5 and 3 Hz, i.e. between the H/V peak and trough frequencies, for the fundamental mode of Rayleigh wave, and retrograde at higher frequency. Therefore, our observation of the fundamental mode corresponding to the prograde component fits perfectly. Given the estimated phase velocity range, the retrograde motion for higher frequencies is then probably the first harmonic mode.

The dispersion curves obtained from the analysis of Array B are shown in Figure 3.19. The dispersion curve at low frequency (Figure 3.19 (a)) is again observed to be dominated by the Love surface waves. The Rayleigh surface wave dispersion curve is a mixture of fundamental and higher harmonic modes, in consistence with observations at Array A. The split of the dispersion estimates into retrograde and prograde Rayleigh wave particle motions suggests a probable Rayleigh wave fundamental mode between 1 and 2 Hz (prograde particle motion) and a higher mode between 3 and 4 Hz (retrograde particle motion).

(a) All Identified Waves

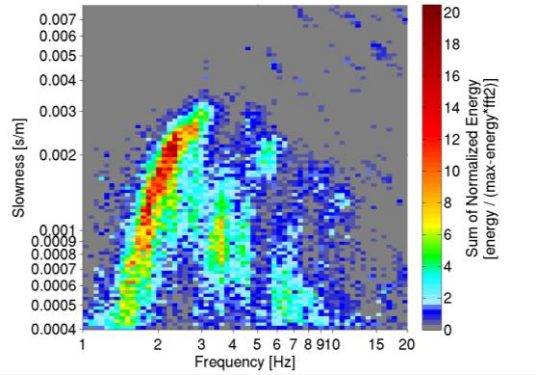

(b) Love Waves

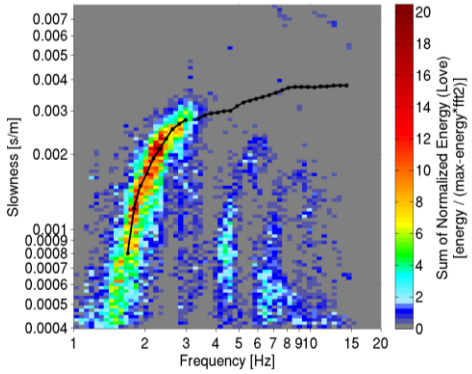

(c) Rayleigh Waves

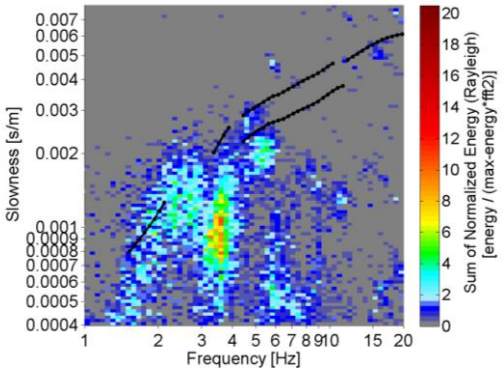

(d) Prograde Motion

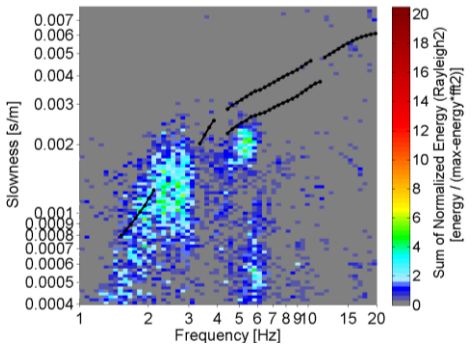

(e) Retrograde Motion

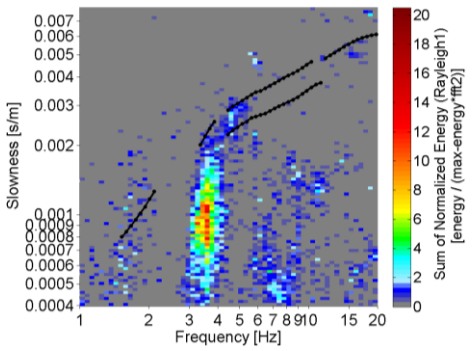

Figure 3.18: Overall cumulative slowness distribution for the whole set of events for Array A after removing the direct arrivals (event-back-azimuth ± 20°): (a) For all waves types, (b) Love waves, (c) Rayleigh waves, (d) Retrograde Rayleigh motion and (e) Prograde Rayleigh motion. The color bar represents the sum of normalized energy obtained by Equation 3.37. Black lines represent dispersion curves obtained from classical analysis of ambient noise recorded at Array A and from active surface wave measurements (Boxberger et al., 2014).

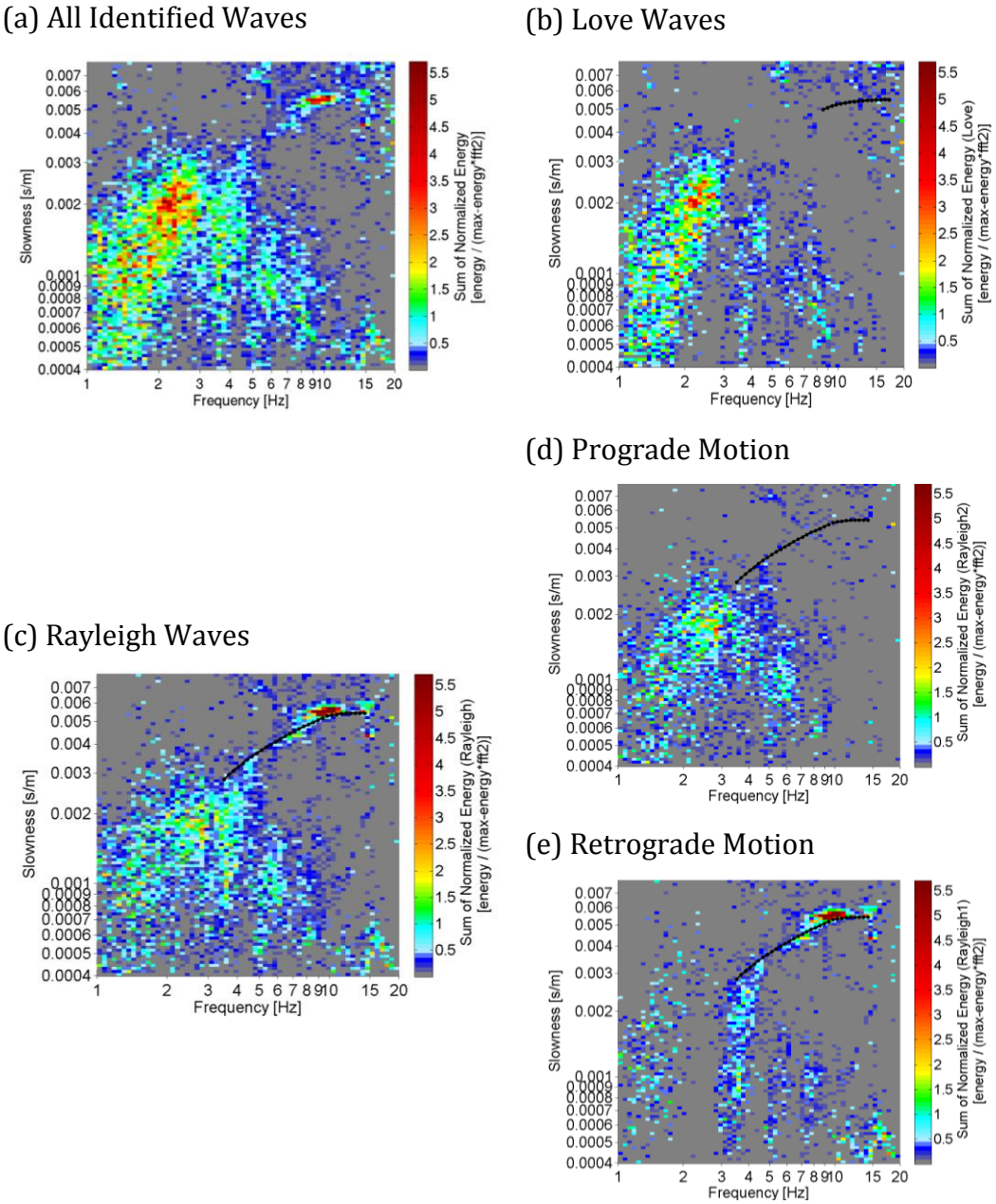

Figure 3.19: Overall cumulative slowness distribution for the whole set of events for Array B after removing the direct arrivals (event-back-azimuth ± 20°): (a) For all waves types, (b) Love waves, (c) Rayleigh waves, (d) Retrograde Rayleigh motion and (e) Prograde Rayleigh motion. The color bar represents the sum of normalized energy obtained by Equation 3.37. Black lines represent dispersion curves obtained from classical analysis of ambient noise recorded at Array B and active surface wave measurements (Boxberger et al., 2014).

3.9.3 Energy repartition between Rayleigh and Love surface waves

Figure 3.20 (a) and (b) show the arithmetic mean ±1σ of analyzed energy for Rayleigh and Love waves for all 46 events from Array A and 16 events for Array B, after removing the energies of the direct arrivals corresponding to the event-back-azimuth ± 20°. Once again, we observe the frequency dependency of the wave energy distribution, namely Love waves being dominant between 1 and 2.5 Hz for both arrays while Rayleigh waves is dominating between 3 and 4 Hz for Array A and above 3 Hz for Array B. The total of mean Rayleigh and Love energy (black line in Figure 3.20) indicates that we were able, in average, to explain about 80% of the total window energy up to about 6 Hz frequency, for both arrays.

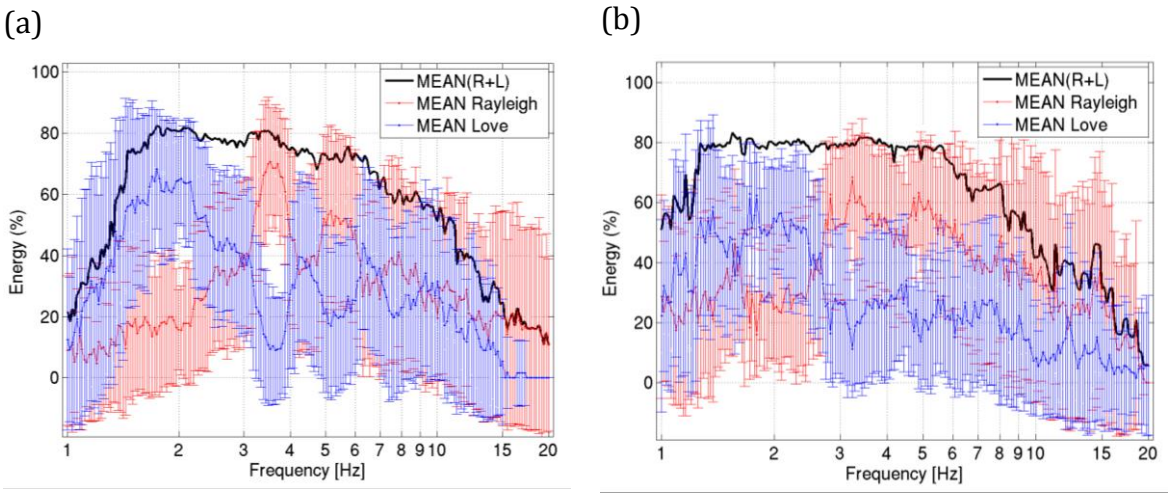

Figure 3.20: Arithmetic mean ±1σ distribution of analyzed energy for Rayleigh and Love waves as function of frequency, after removing the direct arrivals (event-back-azimuth ± 20°) from the estimates of each single event for (a) Array A and (b) Array B. The analyzed energy is expressed as the percentage of the total energy and estimated for each event using Equation 25. Then estimates from all the events are averaged. Red curve corresponds to Rayleigh waves while blue ones to Love waves. Black line shows the mean curve for the total of Rayleigh and Love energy.

3.10 Results from double source identification

So far we have presented the results obtained from MUSIQUE analysis by assuming that only a single source propagates throughout the array at a given time. This assumption would still be valid if more than one source is propagating across the array but only one is carrying most of the energy. However, if several sources carry almost equal proportion of energy, the assumption of a single dominating source will cause bias in the estimation of noise subspace and hence our final estimates. MUSIQUE, like MUSIC, algorithm is able to consider multiple sources for resolving the wavenumber vector velocity, that is, back-azimuth and slowness of the waves for a given time window and a given frequency band. In such a case however, it is not possible anymore to discriminate Love and Rayleigh surface waves since such discrimination relies on the projection of horizontal components on the identified back-azimuth direction, which can be done accurately if only a single wave contribution effectively propagates across the array. Therefore, with the assumption of two or more sources propagating at the same time across the array, only wavenumber vectors can be resolved. This is the reason why we have assumed a single dominant source in the previous analysis. In order to evaluate suitability of this assumption, we performed MUSIQUE analysis once again for all the events for both arrays by considering that two dominant sources are present in the wave field. The obtained back-azimuth and slowness estimates are discussed in the next sub-sections.

3.10.1 Array A results

Figure 3.21 shows the histogram of identified back-azimuths and slownesses for event 12. Plots in the left and right panels show the results from the first and the second dominant source, respectively. In both cases, colorbar shows the normalized window energy estimated using Equations 3.29 and 3.30. Note that this estimate of energy does not correspond to the respective energies carried by the two sources: it just provides an idea about the energy carried out by the signal blocks under consideration. From the back-azimuth distribution, as shown in Figure 3.21 (a) and (b) we observe a fairly similar trend of the dominant diffraction for the first and second source: the principal diffraction direction is always observed within N210 and N240. However, in case of the second source, a second direction of dense wave arrivals seems to appear around N60-

N120. The slowness distribution of the second source (Figure 3.21(b)) seems comparable with that of the first (Figure 3.21 (a)), estimates being, however, more scattered.

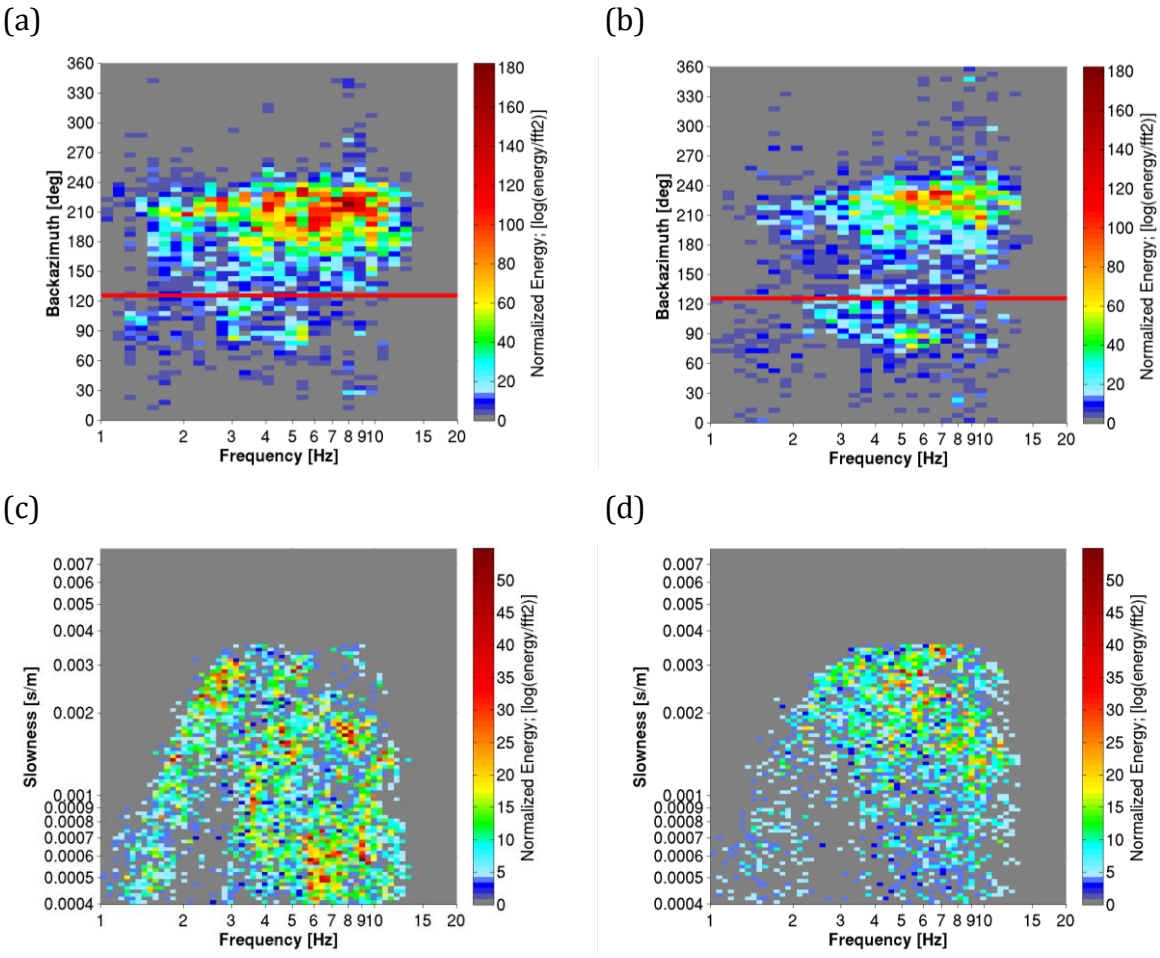

Figure 3.21: Histogram of back-azimuth distribution for event 12 for Array A from (a) the first source and (b) the second source. Red line marks the back-azimuth direction of the event. Colorbar indicates normalized window energy estimated by Equation 3.29. Histogram of slowness distribution for event 12 for (c) the first source and (d) the second source. Colorbar indicates normalized window energy estimated by Equation 3.30.

Figure 3.22 shows the summarized back-azimuth and slowness histograms for the first and second sources using estimates from the 46 events following the procedure described in sections 3.9.1 and 3.9.2. In case of the second source, the main diffraction direction (as seen in Figure 3.22 (b)) seems fairly identical with that from the first source (Figure 3.22(a)). However, a second dominant diffraction direction within N60 to N120 is well depicted. First, these observations confirm the previously identified main diffracted wave field from the southwest direction. Second, it outlines that diffracted waves, although carrying lesser energy, are also arriving from a second direction which corresponds to the northeastern border. However, the second direction was not very clear in the previous results obtained from MUSIQUE analysis considering single dominant source. It suggests that for some time-frequency signal blocks, inside which diffracted waves from the northeastern and southwestern borders are mixing, MUSIQUE algorithm may lead to slight bias in the estimates of wave propagation and polarization parameters when considering a single dominating source only (Cornou et al., 2003a). The summary of slowness histogram obtained for the second source (Figure 25(d)) is similar to the one obtained for the first source (Figure 25(c)), the latter exhibiting however clearer dispersion estimates.

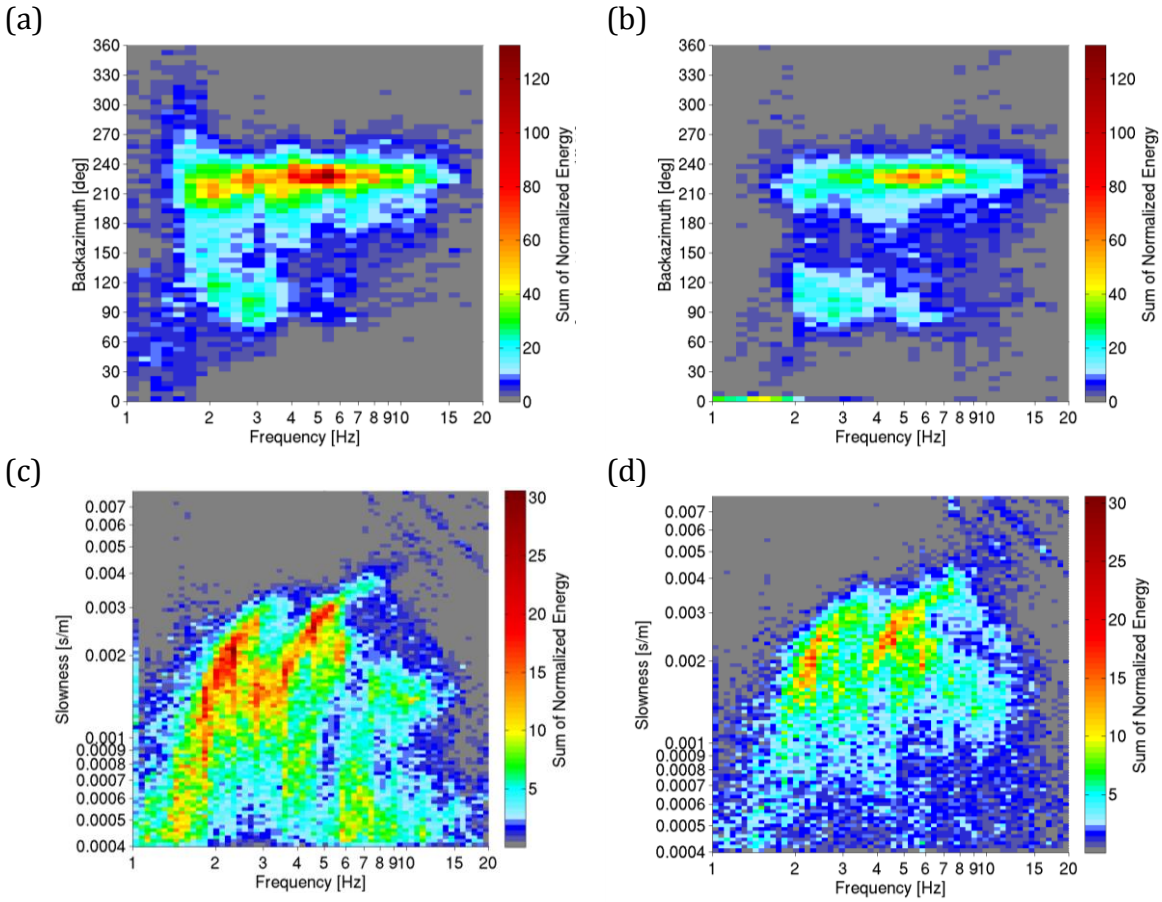

Figure 3.22: Histogram of cumulative back-azimuth distribution for Array A for (a) the first source and (b) the second source. Red line marks the back-azimuth direction of the event with colorbar indicating normalized window energy estimated by Equation 3.29. Histogram of cumulative slowness distribution for (c) the first source and (d) the second source with colorbar indicating normalized window energy estimated by Equation 3.30.

3.10.2 Array B results

Figure 3.23 shows the identified back-azimuth and slowness distributions extracted from estimates obtained at Array B data for event 12. We filtered out the results corresponding to the slowness values above 0.0035 s/m to avoid aliased estimates. The summarized results from all the 16 events are shown in Figure 3.24. Comparison of the estimates obtained from the first and second source indicates identical trends in both cases, with main diffracted wavefield coming from the eastern and southwestern direction (Figures 3.23(a), 3.23(b), 3.24(a), 3.24(b)), estimates from the second source

being, however, rather scattered. The summary of slownesses histogram (Figures 3.24 (c) and 3.24(d)) indicates rather clearer dispersion curves for the first source than the second one. These observations support the hypothesis of single source dominance.

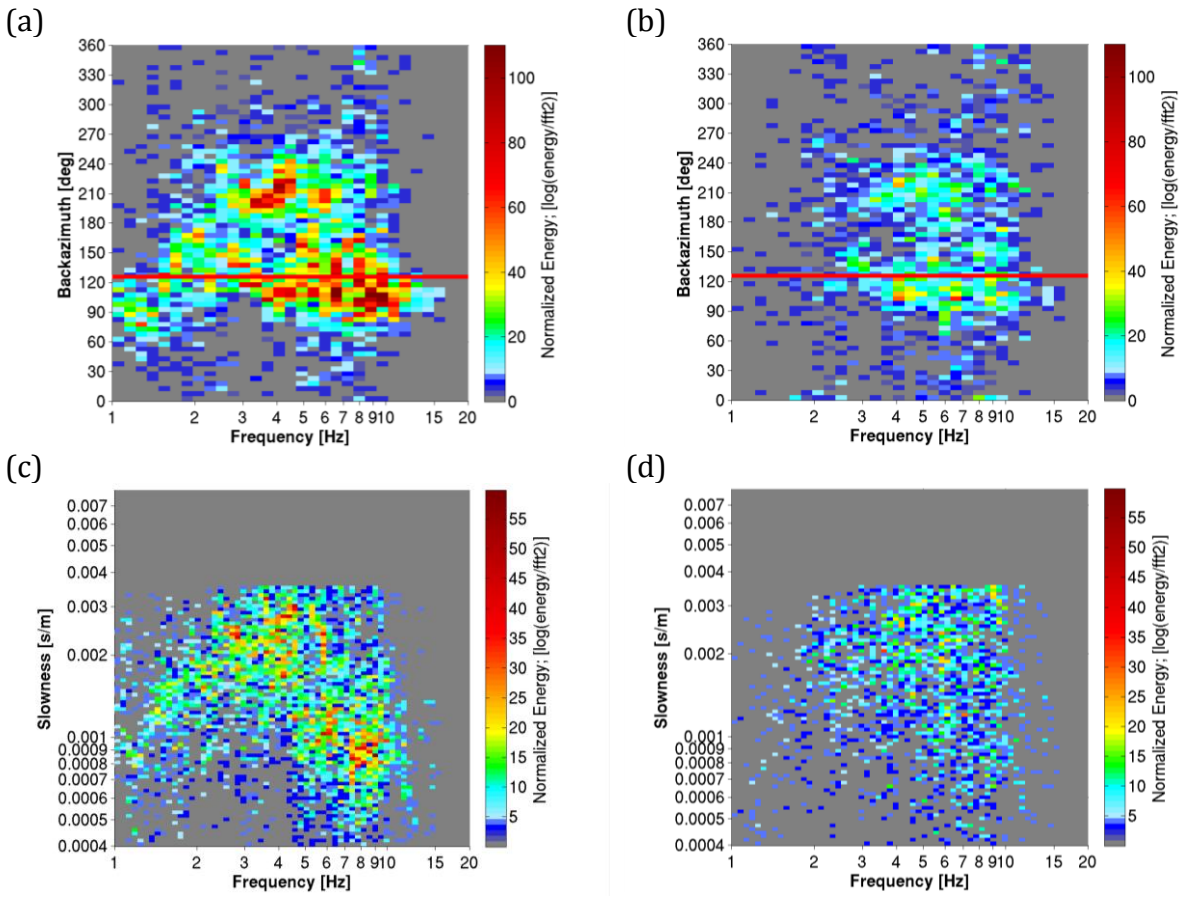

Figure 3.23: Histogram of back-azimuth distribution for event 12 from Array-B data for (a) the first source and (b) the second source. Red line marks the back-azimuth direction of the event. Colorbar indicates normalized window energy estimated by Equation 3.29. Histogram of slowness distribution from (c) the first source and (d) the second source. Colorbar indicates normalized window energy estimated by Equation 3.30.

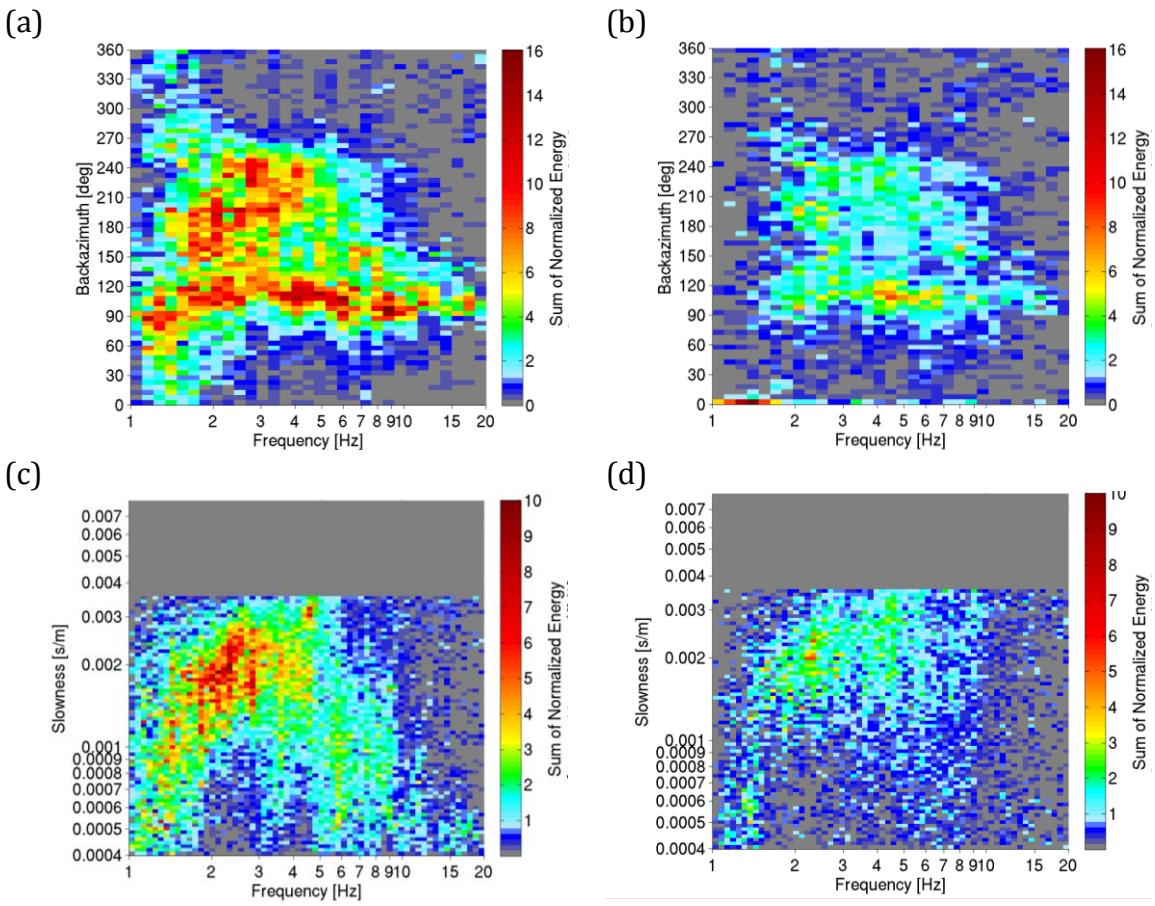

Figure 3.24: Histogram of cumulative back-azimuth distribution for Array B for (a) the first source and (b) the second source. Colorbar indicates normalized window energy estimated by Equation 3.36. Histogram of cumulative slowness distribution for (c) the first source and (d) the second source. Colorbar indicates normalized window energy estimated by Equation 3.37.

3.11 Interpretation of the energy partition between Rayleigh and Love waves

Shear-wave velocity structure at Array A and Array B were derived by inverting dispersion curves inferred from active and passive surface-waves measurements (Boxberger et al., 2014). Figure 3.25 (a) and (b) display the ensemble of inverted shear-wave velocity profiles that explain the observed dispersion data (Figures 3.18 and 3.19) within their uncertainty bound. From the ensemble of shear-wave velocity structure, we computed group velocities of Love and Rayleigh surface waves for the first 5 modes

(Figure 3.25 (c) and (d)). Group velocities indicate that the Airy phase occurs between 1.5 and 2 Hz for fundamental Love wave mode while between 3 and 4 Hz for the fundamental and first higher Rayleigh wave mode. Airy phase is defined as a local minimum on the group velocity curve that results in a large amount of energy arriving at the same time. Surface-waves trains within the range of frequency around Airy phase will travel with nearly the same velocity and arrive at a seismic station at about the same time, thus superimposing to large amplitudes. When we compare these group velocity curves with the results corresponding to energy repartition between Love and Rayleigh wave, shown in Figure 3.25 (c) and (d), we observe that Love wave energy dominates between 1.5-2 Hz which is consistent with the Love and Rayleigh wave partition inferred from MUSIQUE analysis at both arrays. For array A, the Airy phases of fundamental and, especially, the first higher mode of Rayleigh waves, that exhibit the lowest group velocity, occur within a narrow frequency range between 3.3 and 4 Hz. This is consistent with the high proportion of higher mode Rayleigh waves within that frequency band (Figure 3.18). Similar observations, much less striking though, can be made for Array B.

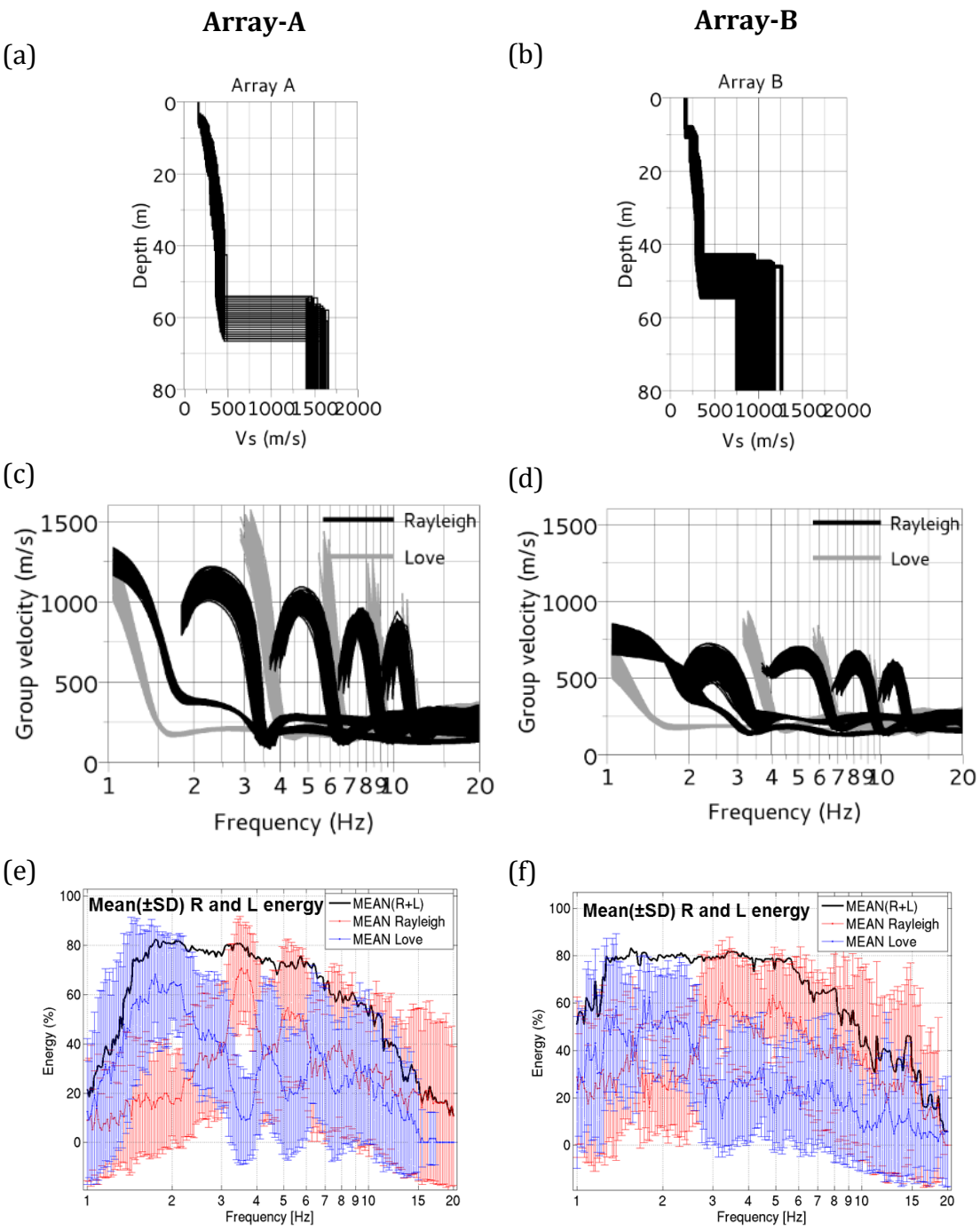

Figure 3.25: Ensemble of inverted shear-wave velocity profiles that explain the observed dispersion data within their uncertainty bound at (a) Array A and (b) Array B. Group velocities computed from the ensemble of shear-wave velocity profiles for the first 5 modes of Rayleigh (black lines) and Love (gray lines) waves for (c) Array A and (d) Array B. Mean ±1σ distribution of the cumulative analyzed energy for (e) Array A and (f) Array B (see Figure 3.20 for details).

3.12 Interpreting observed site amplification

It is also important to verify whether our results provide clues in interpreting observed site effects, such as amplification. We use here the Standard Spectral Ratio (SSR), a standard measure to characterize site amplification. SSR is defined as the ratio of Fourier amplitude spectra of a soil-site record to that of a nearby rock-site record from the same earthquake and component of motion. Assuming source and path effects are the same for both records, SSR reflects only the effect of local soil conditions at the site. Figure 3.26 (a) shows the geometrical average ± 1σ of SSR computed between the horizontal component recorded at sediment station A00 and at hard rock station, R02, from 164 events (Cultrera et al., 2014). The energy partition between Rayleigh and Love waves and the back-azimuth distribution as a function of frequency of Rayleigh and Love waves have been added in Figure 3.26 (c), (d) and (b), respectively. Amplification observed on the SSR plot between 1 and 2.5 Hz could be caused by the Love diffracted waves . Similarly, amplification between ~3 and 5 Hz frequency could be explained by the Rayleigh diffracted wave, which is likely to be the first harmonic mode corresponding to retrograde motion (Figure 3.18(e)).

For Array B, we selected a station, KES04, located 23 m away in the northeast direction from the central station B01. Mean ± 1σ of SSR computed between the horizontal component recorded at sediment station B01 and at rock station R02 are shown in Figure 3.27 (a). Energy repartition and back-azimuth distribution as a function of frequency of Love and Rayleigh wave are shown in Figure 3.27 (c), (b) and (d), respectively. Again, we can see that the observed amplifications between 1 and 2.5 Hz seems to be controlled by Love diffracted waves while amplifications between 3 and 6 Hz might be related to Rayleigh diffracted waves.

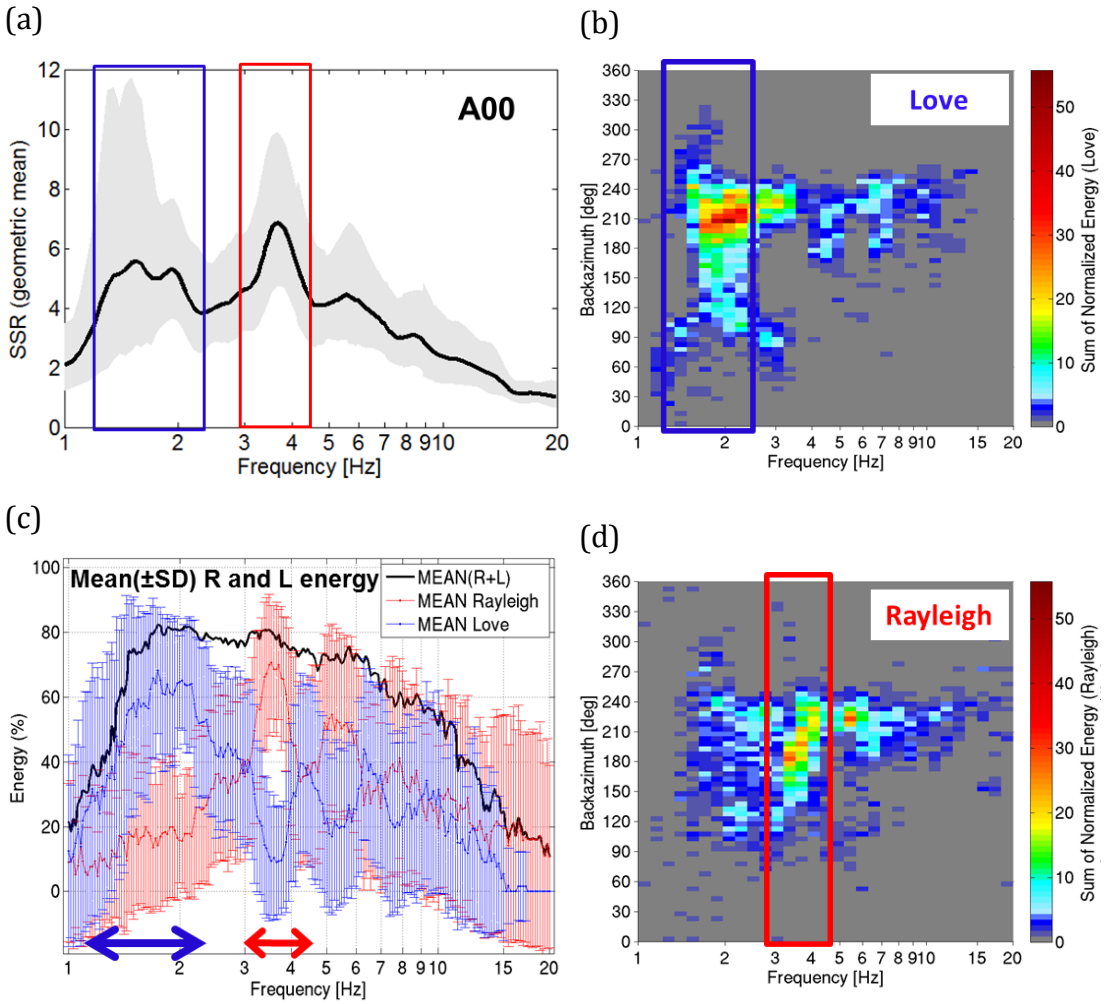

Figure 3.26: Comparison of estimated standard spectral ratio (SSR) with wave type and wave energy repartition for Array A. (a) Standard spectral ratio (SSR) from the horizontal components of A00 and R02 stations obtained by averaging SSRs from 164 events (Cultrera et al., 2014). Black line shows the geometric mean of SSR and grey-shaded region indicates ±1σ. (c) Mean ±1σ distribution of the cumulative analyzed energy for Array A as shown in Figure 3.20 (a). Histogram of back-azimuth distribution as a function of frequency for (b) Love and (d) Rayleigh waves as also shown in Figure 20 (b) and (c), respectively. In (b), (c) and (d) blue and red arrows and rectangle indicate frequency range dominated by Love and Rayleigh waves, respectively.

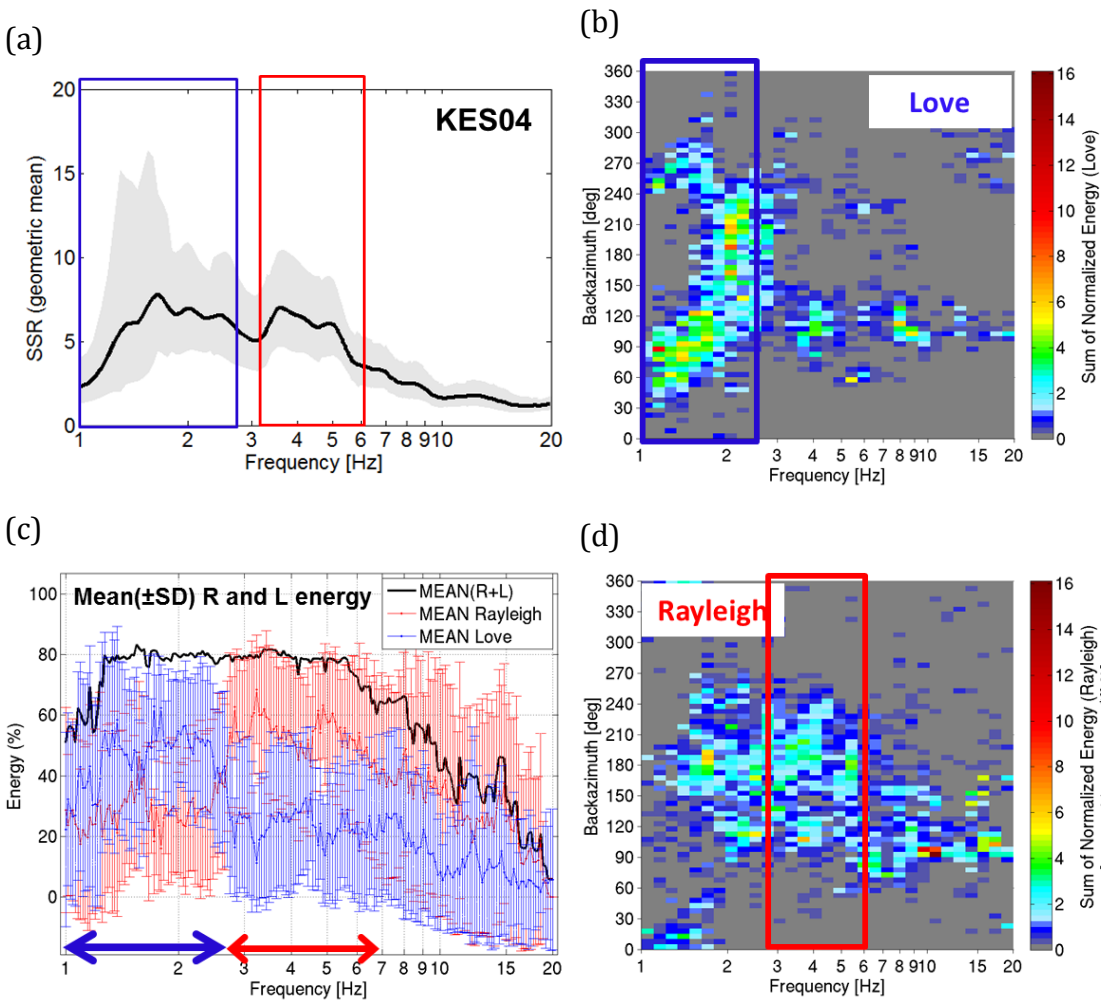

Figure 3.27: Comparison of estimated standard spectral ratio (SSR) with wave type and wave energy repartition for Array B. (a) Standard spectral ratio (SSR) from the horizontal components of KES04 and R02 stations obtained by averaging SSRs from 164 events (Cultrera et al., 2014). Black line shows the geometric mean of SSR and grey-shaded region indicates ±1σ. (c) Mean ±1σ distribution of the cumulative analyzed energy for Array B as shown in Figure 3.20 (b). Histogram of back-azimuth distribution as a function of frequency for (b) Love and (d) Rayleigh waves as also shown in Figure 20 (b) and (c), respectively. In (b), (c) and (d) blue and red arrows and rectangle indicate frequency range dominated by Love and Rayleigh waves, respectively.

3.13 Discussion and conclusion

This study presents results from the analysis of two arrays and explores the wave field characteristics generated by a set of local and regional earthquakes in the basin of Argostoli, Greece. MUSIQUE algorithm was utilized to estimate the apparent propagation characteristics of the waves, to identify the energies carried by Love and Rayleigh surface waves, and to distinguish the retrograde and prograde particle motion of the latter.

The results from array analysis clearly indicate significant scattering corresponding to 2D or 3D effects beyond the fundamental frequency (~1.5 Hz) of the valley. The identified back-azimuth distribution from Array A and Array B shows that whatever the back-azimuth of the earthquake, the wave field is dominated by scattered waves. In order to focus on the scattered wave field, for each event, all the waves coming from a direction lying within ±20° of the event's back-azimuth, were removed so that the direct arrivals from the source could be avoided. Then, meaningful statistics and robust conclusions were derived by "stacking" the results from each individual events for the whole set of 46 events and 16 events for Array A and B, respectively.

At array A, diffracted waves within 1.5 to 15 Hz are coming primarily from the south-west (N210-N240), which corresponds to the closest edge of the valley. The identified back-azimuth distribution from Array A shows that whatever the direction of the earthquake is, local scattering comes primarily from the south-west edge (N 210°-N 240°). Significantly higher proportion of Love waves dominate the wave field at lower frequencies whereas Rayleigh waves seem more scattered over all frequencies. However, the identified surface waves may also contain a small portion of body waves, especially SH waves since MUSIQUE algorithm is yet unable to separate SH waves from Love waves. The summary of energy repartition from all 46 events reveal that about 60% of the total energy between 1.5 to 2.5 Hz frequency is carried by Love waves while within the 3-4 Hz and 5-6 Hz frequency range, Rayleigh waves carry about 70% and 50% of the energy, respectively.

Likewise, the results from Array B data exhibit a relatively higher proportion of Love wave energy (50%) at about 1.5-2.5 Hz frequency and an invariably larger dominance of Rayleigh waves at frequencies above ~2.5 Hz containing about 40-50% of the energy. However, for this eastern array, the identified waves within 1.5 and 15 Hz come primarily from the northeastern edge (N60 - N120) of the valley.

Interestingly, from the resonance frequency (at about 1.5 Hz) to 2.5 Hz, although the dominant diffracted waves are coming from the south-western and north-eastern directions for Array A and B, respectively, some diffracted wave trains from the north-eastern direction for Array A and south-western direction for Array B, i.e. from the farthest valley edges from the arrays locations, are also observed.

The results from both arrays also show that at frequencies lower than the fundamental resonance frequency of the site, both Rayleigh and Love waves impinge the array from a range of back-azimuths (N30-N90), which probably manifests influence of some regional diffractors located outside the Argostoli basin.

Overall, from the analysis of both arrays about 80% of the total energy, within the frequency range approximately from 1.5 to 6 Hz, could be characterized as Rayleigh or Love surface waves. The dispersion estimates obtained from the analyses of two array data show that the fundamental mode (at 1-3 Hz) is evidently dominated by Love waves, while there is also some contribution (at 1.5-3 Hz) from the less energetic prograde Rayleigh waves. Within the frequency range from 3 to 4 Hz, dispersion estimates are most probably related to the first harmonic mode of Rayleigh wave with retrograde particle motion. These observations can be explained by the velocity structure beneath the arrays and related frequency of Rayleigh and Love Airy phases.

The estimated standard spectral ratios at two stations within the two array locations with respect to a nearby rock reference demonstrate that there is an excellent consistency between the dominance of the surface wave type identified in the wave field and the site amplification. The amplification between 1 and 2.5 Hz is controlled by Love diffracted surface waves while amplification between 3 and 5 Hz is most likely to be controlled by the first higher mode of Rayleigh diffracted waves. Alongside, the

characterization of wave types from MUSIQUE analysis shows that the various signal time windows throughout the duration of the event are usually complex mixture of different types of waves. The scattered waves apparently dominate the wave field composition of the most energetic part of the signal, even in the earlier time segments where a significant proportion of surface waves can be identified in the energetic windows classically considered as dominated by direct body waves.

Chapter 4: Coherency analysis of Argostoli dense array network

This chapter presents the analysis of spatial coherency using the earthquake data from the dense seismic array (Array A , discussed in Chapter 3) recorded at Argostoli site. The chapter begins with a short overview of the available coherency models, the causes of incoherency along with the description of coherency and its evaluation procedure. The dataset is briefly repeated after Chapter 3. Then a detailed description of the time window selection procedure for coherency analysis, and some test results have been provided. Finally, results from some individual events and the statistical analyses of the entire subset of events along with their interpretations are presented.

4.1 Introduction

The observed difference in seismic ground motions measured at different locations within a short distance (e.g. within the dimensions of typical large engineered structures) is simply termed as spatial variation of earthquake ground motions (SVEGM). It refers to the differences in amplitude and phase of seismic motions. This spatial variation of earthquake ground motion has an important effect on the response of large foundation (i.e. bridges, nuclear power facilities, and dams), multiple support (bridges), and very long (lifelines such as, pipelines, power lines, communication transmission systems, etc.) structures. Different supports of these long structures or continuous points along the foundations of a large structure may undergo different motions during an earthquake. Similarly, the behavior of large structures with rigid foundations can also be affected by ground motion variability, resulting in reduction of translational response at foundation level and increase in the rocking and torsional response (Abrahamson et al., 1991b). It may also induce increased localized deformations and strains in the structures with flexible foundations and/or with multiple supports (Luco and Wong, 1986).

In current engineering practices, generally the seismic ground motion excitations at the supports of the structures are assumed to be identical and excitations at all locations are considered to be coherent. In such cases, the presence of a non-negligible, not accounted for, differential motion can yield response beyond the design-expectations of the structure and can pose threat to structural safety. Therefore, spatially variable seismic ground motions are needed to be considered in the seismic response analysis and design of large and extended structures. At the same time, a better understanding of the physical causes underlying the spatial variability needs to be achieved in order to include it in the procedures applied in engineering practices. It might also be important for damage assessment and microzonation at a local scale.

The spatial variation of seismic ground motion was recognized as a potentially important component of the seismic wave field since the 1930s. But dense seismic arrays and extensive analyses of the corresponding ground-motion records are required for a quantitative estimation of this spatial variability of ground-motion. That is why

this scientific field started being investigated about three-four decades ago with the actual installation of several strong motion instrument arrays. Developing models capable of simulating broad-band earthquake process would also be ideal in predicting the ground-motion spatial variation. Nevertheless, this remains unachievable because of the difficulty in modeling both complexity of fault rupture mechanism and seismic wave propagation path at regional and local scale in the frequency of interest (from 0.5 to 20 Hz) in earthquake engineering (Harichandran, 1991).

The data recorded at dense seismograph arrays have provided valuable information in understanding and modelling spatial variation of the motions. Up to date, many permanent and temporary dense arrays have been installed at many sites around the world. One of the first few arrays was the Imperial Valley array (Bycroft, 1980); one of the most investigated arrays is SMART-1 array (Iwan, 1979). There are many other arrays such as Chiba array (Yamazaki and Turker, 1992), USGS Parkfield array (Abrahamson et al., 1991) and so on (for a review, see Zerva and Zervas, 2002). Most of these arrays are (or have been) located at uniform ground conditions, mostly at soil sites. Majority of the studies utilized a stochastic approach (coherency estimation) to model the spatial variation of the motions during the prominent strong-motion shear wave window. A purely stochastic approach, however, precludes any association of the spatial variation of the motions with the physical causes underlying it.

One of the difficulties in getting some insights on the physics of spatial variability is the identification and characterization of the different seismic phases contributing to the recorded signal (i.e. scattering in the vicinity of stations, source directivity, velocity and attenuation, ground structure, etc.). Second, it is difficult to compare results from different datasets, because of the various experimental setups (different coverage of interstation distances), site conditions, source mechanisms and data processing. Studies so far have observed a loss of coherency with increasing frequency and interstation distance. However, the frequency range to be characterized depends on the interstation distance. Interpretation of incoherency at high frequency (> 10 Hz) requires arrays with very short interstation distance (< 20 m) (Abrahamson, 1992a). Furthermore, it is well known that engineering structures cross sites with irregular subsurface topography and ground types. Such sites give rise to the formation of surface waves that can lead to

large amplifications, loss of correlation and significant ground strains in the wave-field (e.g. Bard and Bouchon, 1980; Moczo and Bard, 1993; Cornou et al., 2003; Scandella and Paolucci, 2010). A recent study (Zerva and Stephenson, 2011) also highlighted the significance of irregular subsurface topography and formation of surface waves in the physical understanding and modelling of the spatial variation of seismic ground motions.

In this context, the dense seismic array installed in Argostoli basin, as a part of the FP7 EU-NERA 2010-2014 project, gives us the opportunity to study the loss of coherency over a rather wide range of station separation distances, namely from 5 to 160 m, from a large number of closely located earthquakes. The deployed dense array was located in the western part of the inner, softer basin and consisted of 21 velocimeters in concentric circles with radii of 5 m, 15 m, 40 m and 80 m around the reference station. A subset of 46 events recorded by the array (named as Array A) was used for the analysis of spatial variation of ground motion in terms of spatial coherency. The selected events are characterized by a homogeneous back-azimuth distribution, local magnitudes ranging between 2 and 5, and epicentral distances ranging between 3 and 200 km from the array center. Lagged coherency of the most energetic part of the ground motion (beginning from S-wave onset) has been quantified for each possible pair within the array A. This chapter presents a comprehensive investigation on the sensitivity of the coherency (and its dependence on frequency and inter-station distance) to various potentially impacting factors : source characteristics (magnitude, distance, back-azimuth), component of ground motion (which may be oriented with respect to source: radial and transverse, or to site: parallel and perpendicular to valley axis), and orientation of the considered station pair with respect, once again, either to source or to site, main directions. A great attention has been put on the statistical meaning and the robustness of the results, which includes an analysis of the sensitivity to the choice of the time domain windows, and a careful averaging of the results associated to each individual event. Only robust results with possible significances for engineering practice should thus be considered.

4.2 Short review on coherency models

As mentioned earlier, spatial variation of earthquake ground motions (SVEGM) refers to the differences in amplitude and phase of seismic motions. This study focuses on the phase variation of ground motion. The spatial variation of the phase can be characterized by parameters such as correlation or coherency. Correlation is a time domain measure while coherency is a frequency domain measure. Previous studies have shown that the spatial variation of strong ground motion is strongly dependent on frequency (Loh et la., 1982; Smith et al., 1982; McLaughlin, 1983; Harada, 1984, Abrahamson, 1985). That is why coherency is commonly used to describe the spatial variation. In this study the spatial variation of ground-motion has been evaluated in terms of spatial coherency, which is the variation in Fourier phase, as functions of frequency and station separation distance.

An extensive number of studies investigated the effects of the SVEGM on the response of extended and large structures (Harichandran and Wang, 1990; Ramadan and Novak 1993; Zerva, 1994; Harichandran et al., 1996; Chen Harichandran, 2001; see Zerva and Zervas, 2002 for a review), and demonstrated the need to characterize these effects. In recent engineering practices, the effect of SVEGM has started to be considered. In the retrofitting of the great California bridges, as, e.g., the Coronado Bridge in San Diego, spatially variable seismic ground motions were utilized as excitations (Abrahamson, 1993). EUROCODE8 is presently providing provisions for its incorporation in the design of bridges, and Caltrans is seeking approaches for its incorporation in the design of California highway bridges (Liao, 2006). This emphasizes the importance of estimating and modeling spatial variability in a more realistic approach.

Dense array recordings are required to measure the spatial coherency. A review of some available seismic ground motion dense arrays has been provided in Liao (2006). Several dense arrays have recorded weak motions and a few have recorded strong ground motions. Among a number of weak-motion arrays some examples are the USGS Coaling temporary array (Schneider et al, 1992), the USGS/SCSD Anza Array (Fletcher et al., 1987), and the EPRI Parkfield array (Schneider et al, 1992). Examples of strong-motion arrays are the El Centro Differential array (one of the first arrays installed and recorded

the 1979 Imperial Valley earthquake (Spudich and Cranswick, 1984)) located in southern California and the SMART-1 array located in Lotung, Taiwan (Bolt et al, 1982).

The availability of dense seismic array data contributed to development of a large number of empirical functions to model the spatial variation of seismic motion, most often by using lagged coherency. Liao (2006) lists some of these coherency models. In these representations, coherency is generally modeled as exponential functions decaying with increasing frequency and separation distance between stations (e.g., Luco and Wong, 1986; Sommerville et al., 1988) or a double exponential decay (Harichandran and Vanmarcke, 1986). For frequencies lower than a specific distance dependent value, lagged coherency is observed to be approximately constant, while it decays with increasing frequency beyond a specific value, which can be treated as a 'corner' frequency (Harichandran and Vanmarcke, 1986). However, these empirical coherency models differ significantly depending from one site/array to another, even from one event to another recorded at the same site/array, mostly due to the complexity of propagating seismic wave-field and the inherent variance in the spectral estimation procedure adopted by different investigators. Moreover, these empirical models obtained by purely statistical approach generally do not refer to or account for the physical causes underlying the spatial variation of ground motion and hence cannot be reliably extrapolated to different sites and events. Some researchers also introduced analytical or semi-empirical models by combining functional forms from analytical consideration with parameter evaluation from spectral estimation of real data (e.g. Luco and Wong, 1986; Zerva et al., 1987; Der Kiureghian, 1996; Zerva and Harada, 1997). However, these models also may not capture the reality because of the simplified assumptions they are based on (Zerva and Zervas, 2002).

The SMART-1 array data has been used by various researchers to study spatial coherency (Harichandran, 1988; Harda, 1984; Harda and Shinzouk, 1988; Sawada and Kamada, 1988; Abrahamson, 1985, 1988). However, the smallest station separation in the SMART-1 array is about 100 m, which is larger than the dimensions of most engineered structures. A very dense and smaller scale three-dimesional free-field array, named as LSST array, was then installed within SMART-1 array. The spatial coherency of several events recorded by both SMART-1 and LSST array was studied by

Abrahamson (1988). The analysis of SMART-1 data yielded estimates of coherency at station separation distances from 100 to 4000 m while the LSST array analysis (Abrahamson, 1992b) extends the coherency estimates down to distances as small as 6 m. At a spacing of about 100 m, the coherencies computed from both arrays were in agreement. At separation distances greater than 1000 m, the coherency values were quite low. Abrahamson (1988) derived empirical coherency models using SMART-1 data and then extrapolate these models for short station separations (<100 m) in order to compare with the results from the LSST array. He observed that the coherencies predicted by these extrapolated models were larger than the coherencies measured using LSST array data, especially at frequencies greater than 5 Hz. This indicates that extrapolating empirically adjusted model would not produce reliable results when different separation distances are considered. From the results of LSST array data analysis Abrahamson concluded that, over the distance range of 6 to 85 m, coherency decays much faster with increasing frequency than with increasing separation distance. The author also examined the effects of earthquake magnitude, source distance, and source dimension on the coherency and observed that lagged coherency does not show a strong dependence on either earthquake magnitude or source distance.

4.3 Causes of incoherency

Spatial coherency refers to the similarity between ground motions in amplitude and waveform observed in the seismic time histories recorded over extended areas on the ground surface. Mathematical expression of coherency will be discussed in the next section. The ground motion at a given site can be affected by different factors that can be broadly grouped into source (magnitude, slip distribution etc.), path (site-to-source distance, travel path geology, attenuation etc.), and site effects (local geology and topography). However, in the literature three main causes of spatial incoherency have been recognized (Harichandran 1999; Hao et al. 1989), namely, wave passage effect, incoherence effect and site effects. Figure 4.1 and 4.2 illustrate schematically some of these principal physical causes underlying the spatial variation.

1. Wave passage effect: It is the most commonly recognized cause for the spatial incoherency of the motions defined as the systematic spatial variation due to difference

in arrival times of seismic waves over a short distance (e.g. across a foundation) due to inclined incidence of propagating plane body waves or horizontally propagating surface waves. As shown in Figure 4.1 (a), due to the inclined incidence of plane wave arriving at the site, seismic waves arrive at different times at different stations on the ground surface (stations 1 and 2). The wave passage time delay between two locations introduces a shift in the Fourier phases of earthquake ground motions, which is possible to estimate in a deterministic way. However, the coherency of signals with only travel time difference should be 1, unless the travel time depends on frequency (surface waves).

2. Incoherence effect: Spatial incoherency is caused by complex wave propagation. Differences in the way multiple waves are combined (a) arriving from an extended source, and (b) scattered by irregularities and local heterogeneities along the propagation paths of the incident wave and at the site, causes a loss of coherency. Figure 4.1 (b) presents the extended source effect, which illustrates, as rupture propagates along an extended fault, especially when the rupture kinematics is highly heterogeneous (variable slip, variable rake, rise time, rupture velocity), it transmits energy that arrives delayed on the ground surface, resulting in variability in the waveforms at the various locations. Figure 4.1 (c) shows the scattering effect where waves propagating away from the source encounter scatterers along their path that modify their waveforms and direction of propagation, and cause differences in the waveforms at the various locations on the ground surface. Complex waveform scattering occurs as the seismically generated body waves encounter heterogeneities along their source-to-site travel path. Scattering causes random Fourier phase and amplitude variations. Stochastic contributions dominate the phase variations at high frequencies and also cause a significant level of amplitude variability.

3. Local site effect: Differences in local soil conditions at each station may alter the amplitude, frequency content and duration of the bedrock motions differently. Local site effects refer to a set of different physical phenomena arising from the propagation of complex seismic waves in near-surface geological formations (shallow substructures) or in geometrically irregular configurations at the earth surface. Earthquake ground motion affected by these irregularities tend to increase in amplitude, and often also in

the duration. In case of sedimentary valleys, the seismic waves get trapped within the valley and surface waves develop at the basin edge leading to large amplification on the sediment sites compared to the rock site (e.g. Graves, 1993).

However, Abrahamson (1992b) suggests that for site conditions being assumed to be homogeneous, SVEGM would be caused by the wave passage effect and complex source-site wave scattering. This could be a result of deviations from 1-D plane layered velocity models or from scattering. According to the author, the incoherency observed over distances of tens of meters could be caused by scattering in the top 500 m though this requires confirmation from additional data and analysis of numerical simulations.

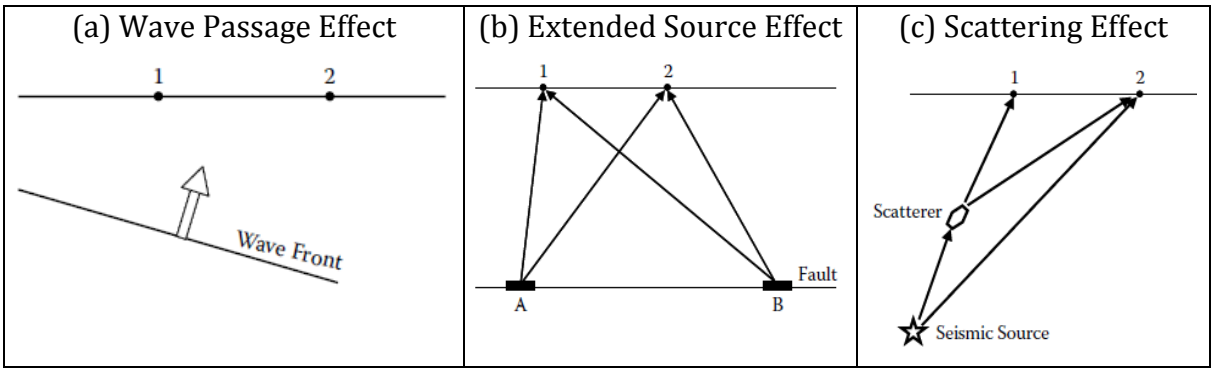

Figure 4.1: Illustration of the physical causes underlying the spatial variation of the seismic ground motion. The different parts of the figure show schematically (a) the wave passage effect, (b) the extended source affect (c) the scattering effect. The graphic illustrations are presented after Zerva (2009).

4.4 Coherency- a stochastic estimator

Here we follow the stochastic (or probabilistic) procedure for the estimation of spatial variability in terms of coherency from the seismic data recorded at our dense instrument array. This allows the estimation of deterministic or 'coherent' and stochastic or 'incoherent' part of the ground motion. The time histories recorded at the instrument stations are here considered as the realizations of a bivariate stochastic process (space-time random fields) and our preferred stochastic estimator 'coherency' is evaluated by applying signal processing techniques to the recorded time histories. The joint descriptors of the bivariate process, cross covariance function in the time

domain and the cross spectral density in the frequency domain, describe the joint characteristics of the time histories at two discrete locations on the ground surface. Hence, the spatial variation of the ground motion can be described by the parameters: correlation in time domain or coherency in frequency domain. Generally the second-order statistics (e.g. covariance function) between the seismograms recorded at different stations are used to characterize ground motion spatial variation in engineering practices. Because of its mathematical convenience in random vibration analysis, the frequency domain description of the second-order statistics, which is cross spectral density, is used in most cases (Matsushima, 1977; Abrahamson et al., 1990; Harichandran, 1991; Zerva and Zervas, 2002). It is, however, customary to work with the coherency of spatially variable ground motions rather than directly with the cross spectral density (Zerva, 2009). Coherency of the seismic motions is obtained from the smoothed cross spectrum of the time series between the two stations.

Zerva and Zervas (2002), describe the assumptions to be applied in order to extract valuable information from the available limited amount of data, such as the recorded time histories at the array stations during an earthquake. The assumptions are briefly:

a) The ground motion random field is homogenous in space, i.e. the probability distribution function and joint probability distribution function are functions of the separation distance between stations, but independent of absolute location. This assumption implies that the frequency content (amplitude) of the seismic motions at different recording stations does not vary significantly.

b) The seismograms are realizations of stationary random processes, i.e. the probability functions of the random process are only the functions of time lags.

c) The stationary random processes at stations are ergodic. In other words, the time averages of the recorded accelerograms are equal to the ensemble averages, i.e., the information contained in each realization is sufficient for the full description of the process.

Apparently such assumptions are strong. They could be adopted for continuous recordings of ambient vibrations but are less applicable for transient high amplitude signals. However, Zerva and Zervas (2002) argue that since majority of the dense

instrument arrays are located on fairly uniform soil conditions, the assumption of homogeneity is valid. The assumption of stationarity appears to be unrealistic, but it can be justified in the sense that most characteristics of seismic ground motions for engineering applications are evaluated from the strong motion shear (S-) wave window, which, in fact, can be viewed as a segment of an infinite time history with uniform characteristics through time. The assumption of ergodicity is considered as necessary by the authors since the description of the spatially variable seismic ground motions would require, ideally, recordings at the same site from many earthquakes with similar characteristic, so that averages of the ensemble of data can be evaluated; although in reality, there is only one set of recorded data at the array for an earthquake with specific characteristics. The authors point out that though reality does not fully conform to these assumptions, actual data recorded at dense instrument arrays during the strong motion S-wave window may be viewed as homogeneous, stationary, and ergodic in a limited or weak sense.

The mathematical formulation of coherency is described here following Abrahamson (2007). Let $U_j(t)$ be a recorded ground motion at location j. A taper window, v(t), is applied to $U_j(t)$ that envelopes the strong shaking. The tapered time series is, then, given by $U_j(t).v(t)$. The Fourier transform, $U_j(\omega)$, of the tapered time series is:

$$U_j(\omega) = \sum_{l=1}^{N_t} v(l)\, U_j(l)\, \exp(-i\omega l) \tag{4.1}$$

where N_t is the number of time samples, l is the time sample, and ω is the pulsation (in radians/sec). The cross-spectrum from recordings at sites j and k is a complex number given by $U_j(\omega)\ U_k^*(\omega)$, where the *-operator indicates the complex conjugate. For coherency estimates, the cross-spectrum is smoothed over a constant frequency band. The smooth cross-spectrum, $\bar{S}_{jk}$, is given by,

$$\bar{S}_{jk}(\omega) = \sum_{m=-M_h}^{M_h} a_m\, U_j(\omega_m)\, U_k^*(\omega_m) \tag{4.2}$$

where $2M_h+1$ is the number of discrete frequencies smoothed, $\omega_m = \omega + 2\pi m/N_t$ and a_m are the weights used in the frequency smoothing.

4.4.1 Complex coherency

The complex coherency of the seismic motion, $\bar{\gamma}_{jk}(\omega)$, is given by the ratio of the smoothed cross-spectrum of the time series between the stations j and k, to the geometric mean of the corresponding smoothed auto power spectra:

$$\bar{\gamma}_{jk}(\omega) = \frac{\bar{S}_{jk}(\omega)}{\sqrt{\bar{S}_{jj}(\omega)\bar{S}_{kk}(\omega)}} \tag{4.3}$$

The phase, termed as smoothed phase spectrum, $\bar{\varphi}_{jk}(\omega)$, is derived from the ratio between imaginary part, $\mathrm{Im}[\bar{\gamma}_{jk}(\omega)]$ and real part, $\mathrm{Re}[\bar{\gamma}_{jk}(\omega)]$, of the complex coherency. This is also same as the phase spectrum of the smoothed cross spectral estimator.

$$\bar{\varphi}_{jk}(\omega) = \tan^{-1}\frac{\mathrm{Im}[\bar{\gamma}_{jk}(\omega)]}{\mathrm{Re}[\bar{\gamma}_{jk}(\omega)]} = \tan^{-1}\frac{\mathrm{Im}[\bar{S}_{jk}(\omega)]}{\mathrm{Re}[\bar{S}_{jk}(\omega)]} \tag{4.4}$$

Finally, the complex function of coherency can also be expressed as (Zerva, 2009):

$$\bar{\gamma}_{jk}(\omega) = |\bar{\gamma}_{jk}(\omega)|\ \exp[i\ \bar{\varphi}_{jk}(\omega)] \tag{4.5}$$

where i denotes the complex number $\sqrt{-1}$. The complex term in the above equation, $\exp[i\ \bar{\varphi}_{jk}(\omega)]$, includes the wave passage effect, i.e., the delay in the arrival of the waveforms at the further away station caused by the propagation of the waveforms.

The complex coherency is obviously a complex number and the square of its modulus, termed as the coherence, is a real number assuming values $0 \leq |\bar{\gamma}_{jk}(\omega)|^2 \leq 1$ (Zerva, 2009):

$$|\bar{\gamma}_{jk}(\omega)|^2 = \frac{|\bar{S}_{jk}(\omega)|^2}{\bar{S}_{jj}(\omega)\bar{S}_{kk}(\omega)} \tag{4.6}$$

Figure 4.2 shows the typical shapes of an auto spectral density function, absolute coherency, and wrapped and unwrapped phase as a function of frequency (f), after Harichandran (1999).

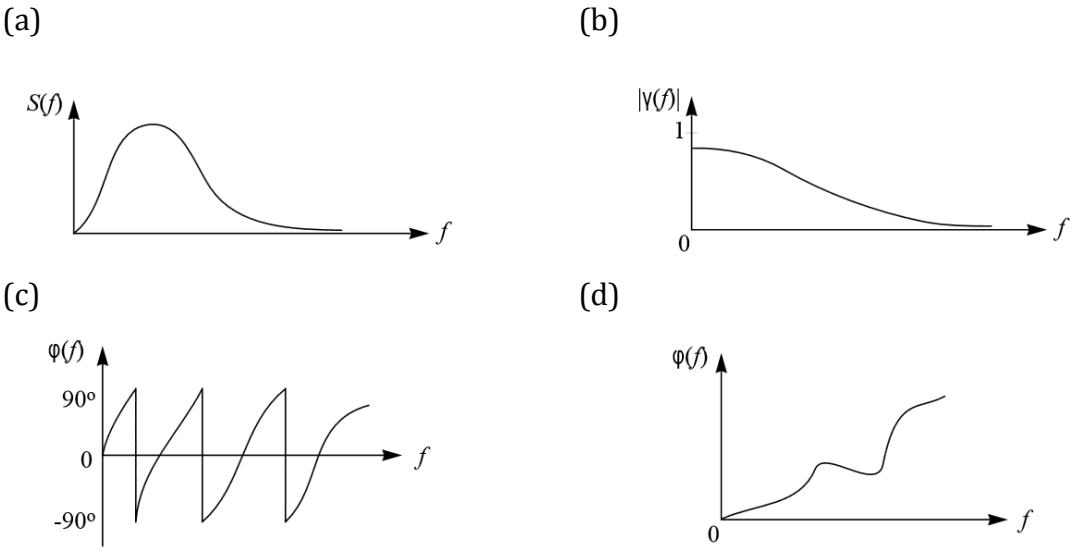

Figure 4.2: Typical shapes of (a) auto spectral density function, (b) absolute coherency, (c) wrapped phase, and (d) unwrapped phase, after Harichandran (1999).

Though the terminologies 'coherency' and 'coherence' are sometimes used interchangeably to indicate qualitatively the similarity between two time series, their mathematical expressions are not exactly the same. In this study, the term 'coherency' has been used throughout to avoid confusion. Coherency can be described in several ways, namely, lagged coherency, plane-wave coherency, and unlagged coherency. In this work we will focus on the lagged coherency and thus the other two measures of coherency will be introduced briefly.

4.4.2 Lagged coherency

The lagged coherency is the most commonly cited coherency measure. It indicates the degree of linear correlation (i.e. similarity) between the random processes recorded at the two stations under consideration. The two time histories are aligned using the time lag that leads to the largest correlation of the two ground motions. Thus this coherency measure is assumed to remove the effects of systematic delay due to the simple inclined plane wave propagation, often called as the wave-passage effect.

Let us consider two ground motions, $U_j(t)$ and $U_k(t)$, recorded at locations j and k, respectively, where $U_j(t)$ be a recorded ground motion at location j. The Fourier transform, $U_j(\omega)$, of the ground motion at location j is given in Equation (4.1). Now, if we align the ground motion at location k by Δl time samples, then Fourier transform can be expressed, following the former notations, as,

$$U_k(\omega) = \sum_{l=1}^{N_t} v(l + \Delta l)\, U_k(l + \Delta l)\, \exp(-i\omega(l + \Delta l)) \tag{4.7}$$

The lagged coherency between the stations j and k is given by the modulus of their complex coherency,

$$|\bar{\gamma}_{jk}(\omega)| = \frac{|\bar{S}_{jk}(\omega)|}{\sqrt{\bar{S}_{jj}(\omega)\bar{S}_{kk}(\omega)}} \tag{4.8}$$

The value of lagged coherency is zero for uncorrelated processes and it is equal to one for linearly correlated processes; thus, it is obvious that the value of lagged coherency ranges from 0 to 1. At low frequencies (large wavelengths) and small separation distances, the ground motions between two stations are supposed to be identical, which results in coherency estimates tending to unity; but the motions will become uncorrelated at higher frequencies (small wavelengths) and large separation distances, making the coherency tend to zero. Therefore, it is perceived that the value of coherency will decay with increasing frequencies and separation distances. Coherency analyses from recorded data have validated this expectation and the functional forms describing

the lagged coherency at any site and any event consider exponential decay with separation distance and frequency (Zerva and Zervas, 2002). However, the lagged coherency does not tend to zero at large separations and high frequencies due to the bias in the estimation. It also depends strongly on the selected frequency smoothing. The lagged coherency is always unity if no frequency smoothing is used. Zerva and Zervas (2002) refer to another important characteristic of lagged coherency, namely, that it is only minimally affected by the amplitude variability between the motions at the two stations. Spudich (1994) illustrated this characteristic with an example and concluded that the absolute value of the coherency is not sensitive to amplitude variations regardless of whether the motions at the various stations are multiples of each other or not.

4.4.3 Plane-wave coherency

The plane-wave coherency is also estimated after removing a time shift which is constrained to be the same (consistent with a single wave direction and apparent velocity) for each station (Abrahamson, 2007). The idea is to consider the deviations of the motions from a single plane wave at all frequencies where plane waves are accompanied by other wave components, such as scattered energy or noise, which is quite common in reality. It is estimated by taking the real part of the smoothed cross-spectrum after aligning the ground motions based on the best plane-wave velocity. However, such velocities are rarely directly measured at site, instead, only rough estimates are used. The value of the plane-wave coherency is less than or equal to the lagged coherency. Since real part of the smoothed cross-spectrum will have both positive and negative values, coherency estimates will approach zero at high frequencies and large separation distances.

4.4.4 Unlagged Coherency

Unlike lagged coherency, the unlagged coherency estimate considers no time lag between the pair of stations, which means, it includes the wave-passage effects. The wave-passage effect is absent in case of pure vertical wave propagation. Such a case is purely idealistic and almost never exists at frequencies of engineering interest. The real part of the complex coherency, $\mathrm{Re}[\bar{\gamma}_{jk}(\omega)]$, is referred to as the unlagged coherency. Its values are less than or equal to the plane-wave coherency and can range from -1 to 1.

The negative values result from the coherent part of the wave-passage effect and indicate out of phase ground motions between the pair of stations. For very short separations, a few hundred meters or less, the wave passage effects will not be significant because of the small travel time among the stations and the unlagged coherency will be similar to the plane-wave coherency (Abrahamson, 2007).

4.5 Evaluation of coherency

To evaluate coherency functions, the three items on the right side of Equation (4.8) need to be identified by applying spectral estimation techniques to recorded seismograms. The main techniques to estimate the spectra of time series are: Conventional Spectral Analysis, Maximum Likelihood Method and Maximum Entropy Method (Marple, 1987). Both Maximum Likelihood Method and Maximum Entropy Method can yield higher resolution than the Conventional Spectral Analysis method. For broadband seismic ground motions, however, the resolution of spectral estimate of the Conventional Spectral Analysis method is sufficient and appropriate for practical engineering application (Harichandran and Vanmarcke, 1986; Harichandran, 1991). Consequently, the current coherency estimation studies are mainly based on the Conventional Spectral Analysis (Zerva, 2009).

4.5.1 Smoothing parameter

It is important to define the frequency smoothing criteria for the estimation of coherency. The information about the differences in the phases of the motions at the stations is introduced in the estimate of the covariance function through the smoothing process. When no smoothing window is used, the phase difference terms disappear from the covariance spectra and the lagged coherency estimate will be unity for any frequency and any station-pair (Jenkins and Watts, 1968). Smoothing also controls the statistical properties (variance and bias) and resolution of the coherency estimates. The more frequencies are smoothed, the larger the decrease in uncertainty in the coherency estimation, but this in turn causes a corresponding loss of resolution in frequency.

According to Harichandran (1991) the common smoothing windows of different types yield similar results as long as the equivalent bandwidths of the spectral windows are

the same Therefore, selection of an appropriate equivalent bandwidth of spectral windows is more important than choosing smoothing spectral window types. Abrahamson et al. (1991) suggests that the selection of optimal smoothing parameters should not only depend on the statistical properties of the coherency, but also on the purpose for which the coherency is estimated. In order to use coherency estimates in structural analysis, for time windows less than approximately 2000 samples and for structural damping coefficient 5% of critical, an 11-point Hamming window (M_h=5 for the a_m in Equation 4.2) is suggested by the authors. This means, averaging the complex cross spectrum over 11 frequencies can provide with a reasonable trade-off between the frequency resolution and the bias and uncertainty. The Hamming window is a smoothed version of a triangle window, shown in the Figure 4.3.

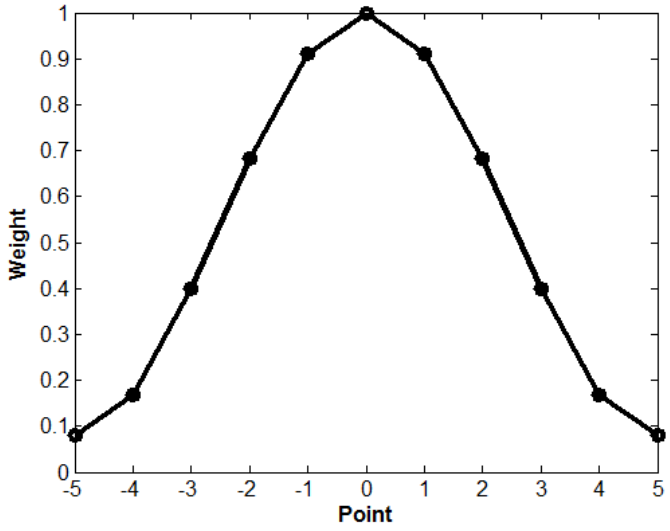

Figure 4.3: Example of an 11-point (M_h=5) Hamming Window

4.5.2 Selection of time window

With the assumption of homogeneity, stationarity and ergodicity, it is a common practice to choose some specific time windows, usually the shear (S-) wave part of the seismograms, to estimate the coherency function, because in most cases the shear wave carries the strongest energy in earthquake recordings and, generally, is the most damaging component from the engineering point of view. The selected time window is seen as a segment of a stationary process with limited duration. Different time window lengths have been used depending on specific earthquake events and the recorded time histories (for example: 5, 9, 10, 21 seconds [Hao et al., 1989]; 2 seconds [Schneider et al.,

1990]; 10 seconds [Harichandran, 1991; Boissieres and Vanmarcke, 1995a]). It is sometimes difficult to identify a clear S-wave part of the signal since it can be often accompanied by other wave components. In such cases there is actually no standard "rule" available for selecting the time windows. One idea could be to identify shear wave windows of one single main wave with unique velocity and back-azimuth. However, for a shallow sedimentary site like Argostoli, it is almost impossible to identify such windows. This would be further discussed in section 4.6.1 and in the conclusion (4.11) segments.

4.5.3 Statistical properties of coherency: distribution, bias and variance

Bias and variance are obvious in the estimation of coherency functions from finite-length time series by using spectral estimators. As discussed by Abrahamson (1992b), the statistical properties of coherency do not seem to be very straightforward. The uncertainty of the estimate increases as the coherency values decrease. When the lagged coherency, $|\bar{\gamma}_{jk}(\omega)|$, is not small, its $\tanh^{-1}$ (or, ATANH) transformation produces an approximately normal distribution with a bias that can be estimated and removed (Enochson and Goodman, 1965); this makes the uncertainty nearly constant. That is why, the statistical analyses of coherency are suggested to be performed on the $\tanh^{-1}|\bar{\gamma}_{jk}(\omega)|$ instead of $|\bar{\gamma}_{jk}(\omega)|$ (Harichandran, 1991; Abrahamson et al., 1991). Abrahamson (2007) shows through the estimated plane-wave coherency an example that the variability of the coherency is not constant; the variability is small for low frequencies and large for high frequencies (heteroscedastic). With the $\tanh^{-1}$ (or, ATANH) transformation, coherency values are observed to be approximately normally distributed about the median $\tanh^{-1}|\bar{\gamma}_{jk}(\omega)|$ curve and thus the scatter of coherency becomes independent of frequency (homoscedastic).

However, the assumption of normal distribution of $\tanh^{-1}|\bar{\gamma}_{jk}(\omega)|$ is a poor approximation when the coherency values are small. The statistical properties of coherency are dependent on the selection of frequency smoothing. Lagged coherency is affected by the number of frequencies smoothed for small values of M_h (as in Equation 4.2). The estimated lagged coherency values, $|\bar{\gamma}_{jk}(\omega)|$, that are not small, become biased

(Abrahamson et al, 1991; Abrahamson, 1992c). The expected value and variance of the estimated coherency are given by (Bloomfield, 1976; Abrahamson, 1992b, 1992c),

$$E[\tanh^{-1}|\hat{\gamma}_{jk}(\omega)|] \approx \tanh^{-1}|\gamma_{jk}(\omega)| + \frac{g^2}{2(1-g^2)} \tag{4.9}$$

$$VAR[\tanh^{-1}|\hat{\gamma}_{jk}(\omega)|] \approx \frac{g^2}{2} \tag{4.10}$$

where $|\hat{\gamma}_{jk}(\omega)|$ is the estimate of the 'true' coherency $|\gamma_{jk}(\omega)|$, g^2 includes mainly the effects the frequency smoothing (Abrahamson, 1992c),

$$g^2 = \sum_{m=-M_h}^{M_h} a_m^2 \tag{4.11}$$

When the chosen frequency smoothing is a Hamming window with $M_h = 5$, the bias and standard deviation of $\tanh^{-1}|\bar{\gamma}_{jk}(\omega)|$ are 0.08 and 0.26, respectively (Figure 4.4). The 50% and 90% confidence levels for "noise" (the coherency resolvability threshold) are 0.34 and 0.63, respectively for $\tanh^{-1}|\bar{\gamma}_{jk}(\omega)|$ (Figure 4.5(a)) while 0.33 and 0.57, respectively for $|\bar{\gamma}_{jk}(\omega)|$ (Figure 4.5(b)).

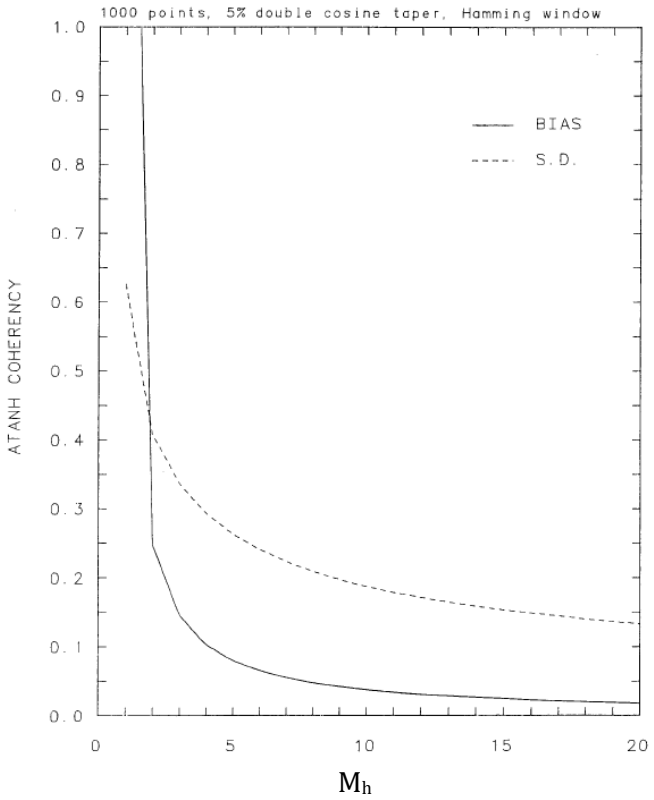

Figure 4.4: The bias and standard deviation of the coherency smoothing for different Hamming window frequency weights and a 1000 point 5% double cosine taper data window, after Abrahamson (1992b).

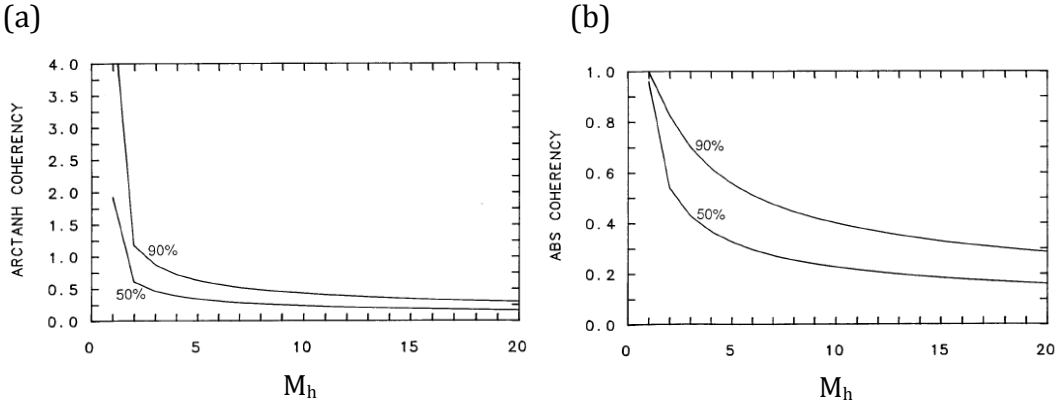

Figure 4.5: Example of the 50% and 90% confidence levels for different Hamming window frequency weights for (a) $\tanh^{-1}|\bar{\gamma}_{jk}(\omega)|$ and (b) $|\bar{\gamma}_{jk}(\omega)|$, after Abrahamson (1992b).

The underlying assumption in the statistics of $\tanh^{-1}$ (or, ATANH) transformation is that the spectra of the processes, $U_j(\omega)$ and $U_k(\omega)$, have approximately constant amplitude over the bandwidth of the frequency window; if this is not the case, then a second source of bias is introduced in the estimates. This bias is not easily quantifiable and it increases as the frequency band increases. It is not also not included in the equation 4.8, that is, in the estimation of the first bias. Abrahamson (1992a) mentions that this second bias can be reduced by using a triangular shaped smoothing window where the frequency weight, a_m, is subjective towards the central frequency of the window; but this essentially increases the first bias. Therefore, smoothing window type and sufficient number of frequencies are the key aspects in the statistical analysis of coherency.

Coherency functions can be considered as biased estimators since the estimation is performed over limited, finite segments of data. Some sources of bias are discussed here, after Zerva and Zervas (2002). Bias can be introduced due to the sensitivity characteristics of seismometers and the use of finite length series (Harichandran, 1991). Additional uncertainty is introduced by inaccuracies in recorder synchronization, and by imperfect elimination of time lags caused by wave passage effects. The time lags caused by the wave passage effect appear as deterministic. However, the wave passage effect also incorporates random, station dependent time delay fluctuations around these deterministic delays that affect the coherency and should be given proper consideration.

4.5.4 Prewhitening

The importance of prewhitening in coherency computation has been discussed here after Abrahamson (1992b). Prewhitening aims to make a time series contain equal-strength components at every possible frequency (i.e., a flat spectrum). In case of spectral leakage indeed at a given frequency, the coherency estimates may get biased by the more coherent energy at other frequencies. This leakage can be minimized by prewhitening the time series before performing the Fourier transform (Abrahamson, 1992b). This is particularly of interest when coherency is estimated at frequencies with a large dynamic range of Fourier amplitudes. However, Abrahamson (1992b) found that

the coherency estimates were not significantly affected by prewhitening for the LSST data and this was not performed for the present study.

4.6 Dataset

The experimental setup and dataset of Argostoli as well as the description of the site have been presented in the chapter 2. This study considers a subset of 46 events from the catalogue of Argostoli data, recorded by the dense array, Array A. Figure 4.6 represents the location and configuration of the array in the experimental setup at Argostoli. The coordinates of the array stations are given in Appendix D. Selected dataset for coherency analysis has been discussed in chapter 2 and the catalogue with event parameters are given in Appendix F.1. Figure 4.7 shows the magnitude distribution of the events over hypocentral distance. Different parameters used in the coherency analysis are listed in Appendix F.2. Time series of the events recorded at central station, A00, of Array A and rock stations, R01 and R02, are provided in Appendices G, H and I, respectively.

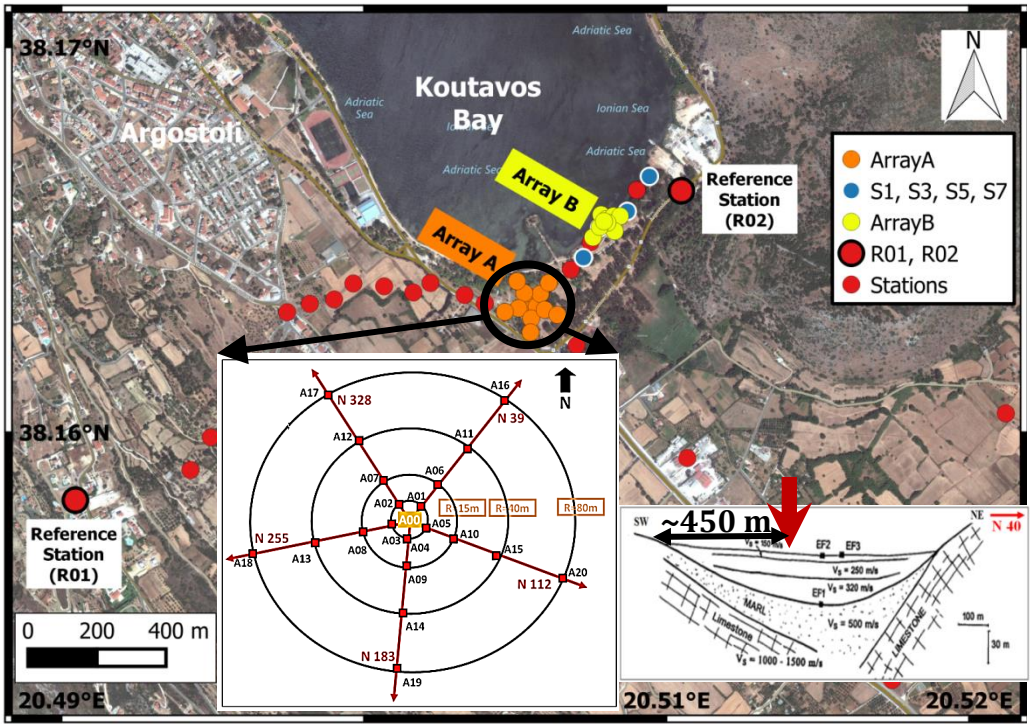

Figure 4.6: Layout of Array A in the seismological experiment at Argostoli. Distance between the rock stations R01 and R02 is about 2 km. The central station of the array, A00, is located about 550 m away from R02 station in the northeast and 450 m away from the southwest edge of the valley.

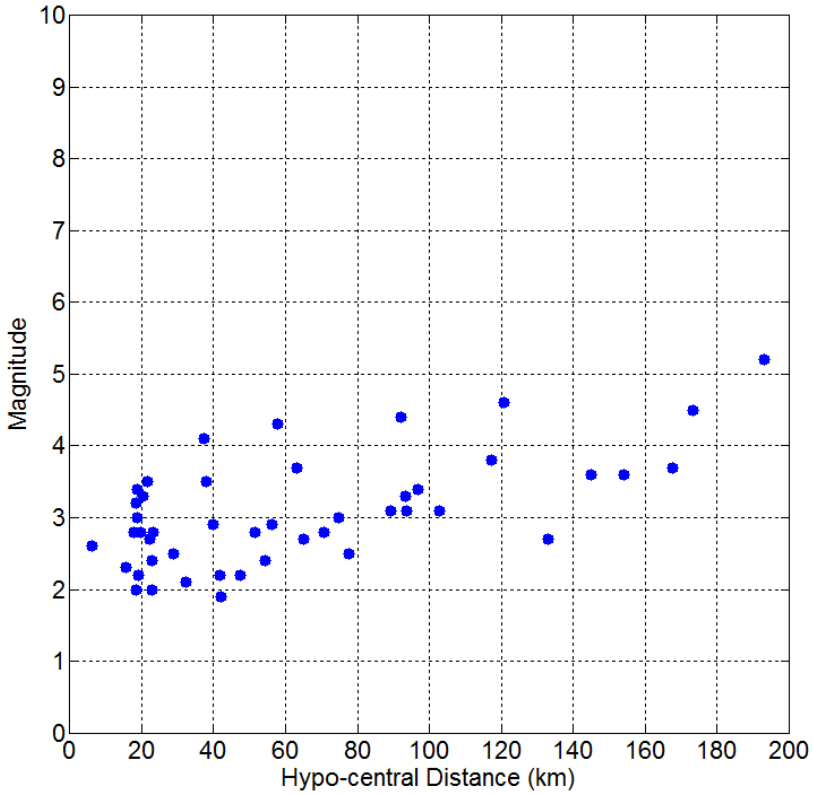

Figure 4.7: Magnitude-distance distribution of the selected subset of events

4.7 Selection of time-window for coherency estimation

From visual inspection of the recorded signals the most energetic part of the signal, from the onset of S-wave, has been selected as the time-window for coherency analysis. The duration (T_S) of the selected time windows are listed in Appendix F.2; TW-C1 marks the begin time and TW-C2 is the end time on the extracted time series. For the visual inspection, signals from the rock stations R01 and R02 (locations shown in Figure 4.6) have been considered since they are less contaminated by surface waves and located very close to the array. R02 is the hard-rock station located at a distance around 550 m northeast of A00 while R01 is the soft-rock station at about 1.45 km southwest of A00. For the selection of time window, dataset of R02 station has been used for 33 events while R01 was used for 13 events (when R02 is unavailable). This has been indicated in Appendix F.2 (column no. 12). During our visual inspection, the horizontal components, exhibiting the strongest shaking of the ground motion records were considered. Since we expect to include S-waves, the time windows were selected such as the energy of the

signal within the window is spread over a wide frequency range, and includes high frequencies. Therefore, our selected windows are supposed to include the most energetic phase that contains a mix of S-waves along with some converted body waves and surface waves. Begin and end time, and the duration of the selected time windows have also been listed in Appendix F.2 (column no. 10, 11 and 12, respectively. Selected time-window segments have been indicated on the time series of R01, R02 and A00 stations, and are provided in Appendices G, H and I. Figure 4.8 shows the distribution of durations of the selected time windows with their corresponding hypocentral distances and magnitudes.

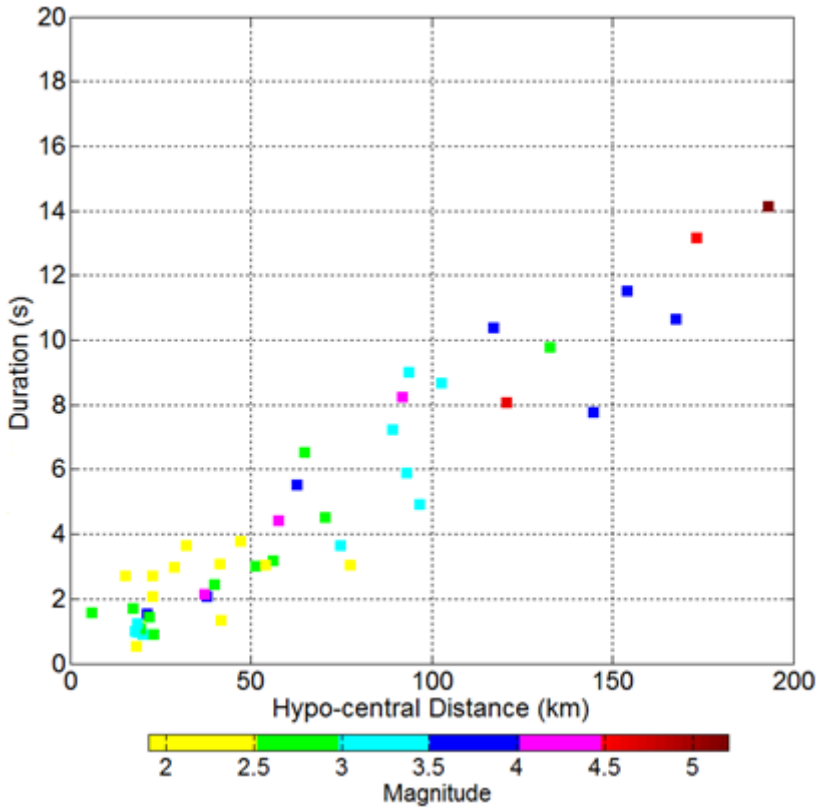

Figure 4.8: Duration of the selected time windows, from 46 events, plotted against the hypocentral distances of the respective events. The colorbar represents the magnitude of the events.

4.7.1 Sensitivity test of the time-window selection

In order to perform a sensitivity analysis on the selection of time windows, an automatic procedure has also been used. A new series of time windows were selected again based on the duration of the normalized Arias intensity of the two horizontal

components of velocity following Equation 4.12, as described in Abrahamson (2007). To estimate the normalized Arias intensity, an initial data window was applied that starts 10 seconds before the peak velocity and ends 10 seconds after the peak velocity. The peak velocity is defined as the largest velocity on either of the two horizontal components. The normalized Arias intensity (I) is then given by:

$$\mathrm{I}(\tau) = \frac{\int_{T_p-10}^{\tau}(V_1^2(t) + V_2^2(t))dt}{\int_{T_p-10}^{T_p+10}(V_1^2(t) + V_2^2(t))dt} \tag{4.12}$$

where, T_p is the time of the peak velocity, V_1 and V_2 correspond to the velocities of two horizontal components and τ indicates time. The final time-window was then estimated based on the time at which the normalized Arias Intensity (AI) reaches a value of 0.10 and 0.75, denoted as $T_{0.1}$ and $T_{0.75}$, respectively. The rock-station data used for visual inspection based time-window selection were primarily used to perform the AI-based time-window estimation. Afterwards, the sedimentary station (A00) data was also used for AI-based time-window estimation. Figure 4.9 shows the estimated Arias Intensity for all the rock station records and also marks the $T_{0.1}$ and $T_{0.75}$ lines to show the estimated durations.

The length of the time windows selected from visual inspection and automatic (AI-based) estimation have been compared in Figure 4.10 and 4.11. Figure 4.10 shows the time windows selected from rock station by using visual inspection and automatic estimation. Here almost all the windows from both methods seem to be overlapping, indicating a high consistency of the selection. Nevertheless, there is slight differences in the begin and end times of the windows. This discrepancy arises mainly because of the difference in the principle of these two methods. Moreover, considering two different rock stations located at different directions and distances may also cause slight shifts of the arrival times. During visual inspection, S-wave onset is considered as the begin time of the window and the end time is marked where the most energetic cycle of the signal seems to end. In case of AI estimation, on the other hand, begin and end times are considered, consecutively, with 20 s window starting 10 s earlier and ending 10 s later the peak velocity. This may automatically stretch the begin and end points of the

selected time window for very short duration signals (closer events). Similarly, the S-wave onset could be overlooked in case of longer duration (distant events). The maximum difference between the selection from visual inspection and automatic estimation is observed for the M 5.2 event (hypocentral distance 193 km) in Figure 4.10. The time-windows considering rock and sedimentary station (A00) records, estimated by automatic procedure (AI-based), have been compared in Figure 4.11. Though there are some exceptions, most of the window-lengths look consistent between rock and sediment records. The difference is caused by the location of peak velocity considered in AI estimation.

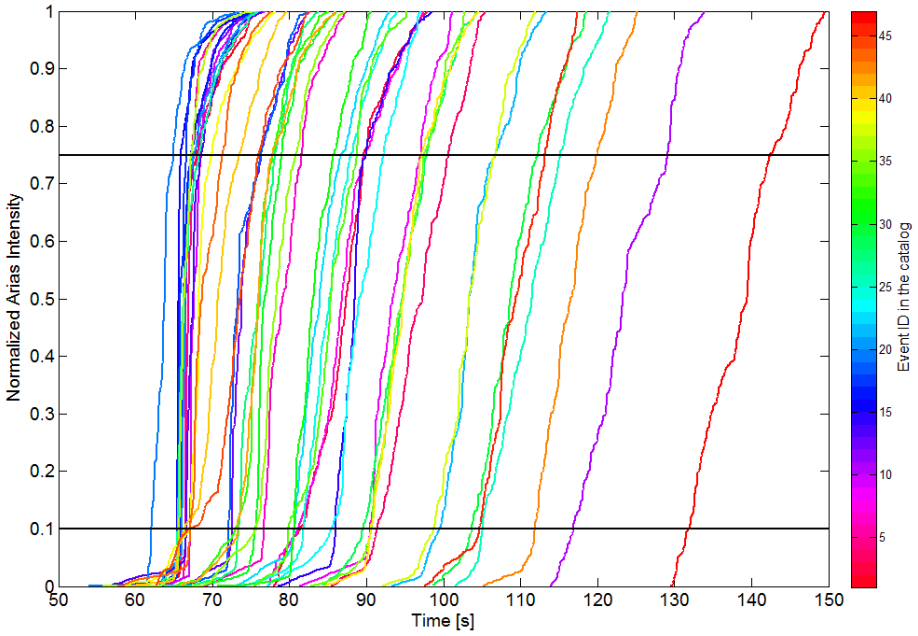

Figure 4.9: Time windows from the rock-stations based on normalized Arias Intensity estimations for the 46 events.

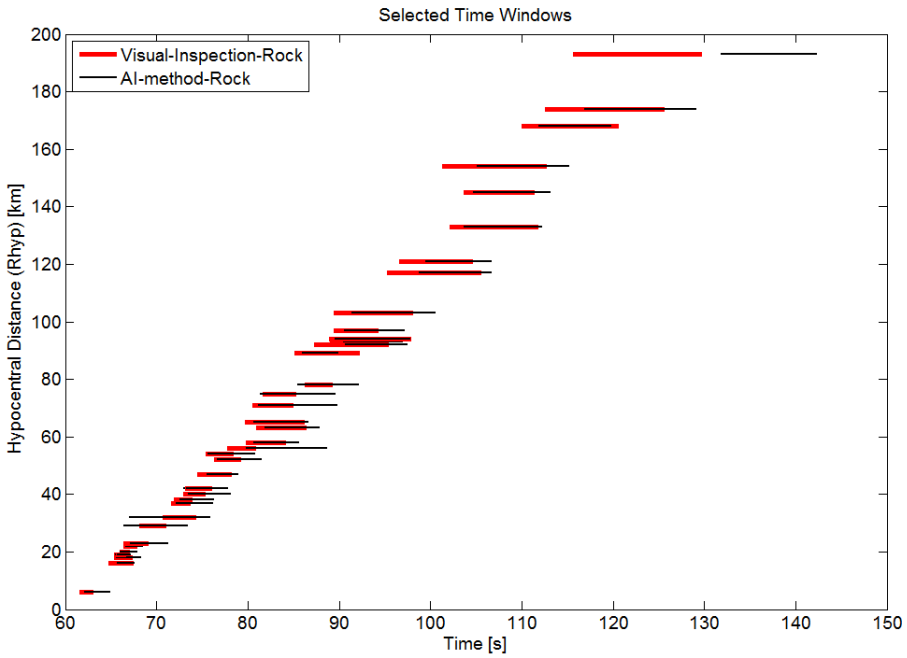

Figure 4.10: Comparison between the time windows based on visual inspection and AI method, from the rock-stations.

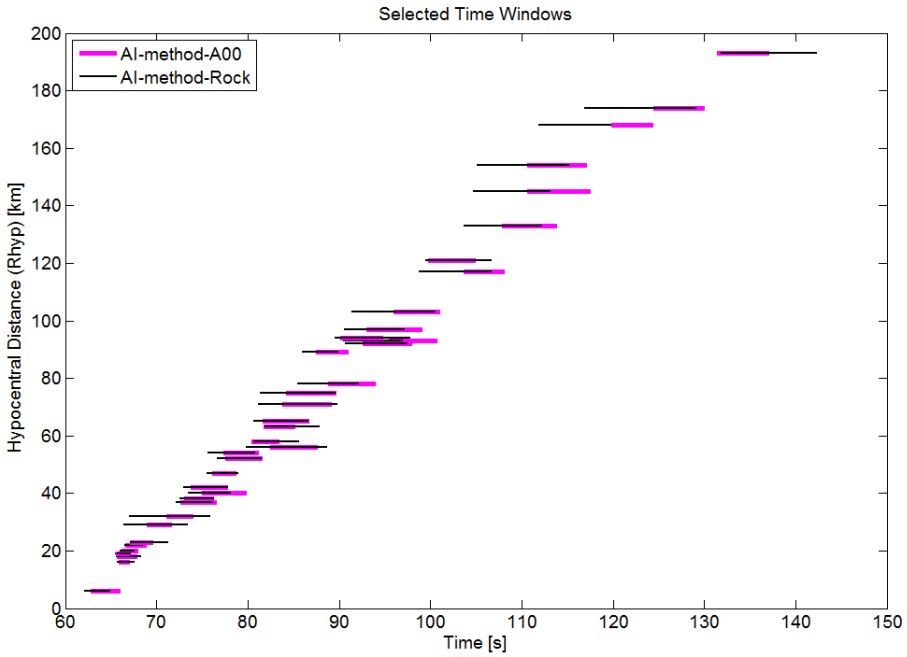

Figure 4.11: Comparison between the time windows from rock (R01, R02) and sedimentary (A00) stations based AI method.

Figure 4.12, 4.13 and 4.14 represent three examples showing the time window lengths selected using visual inspection and automatic method. The time series for the rock and sediment stations are plotted for the events 20110930_003052, 20111009_184220, 20120416_112342 (event index 5, 8 and 46 in Appendix F) having magnitudes 2, 3.3, 5.2, and the shortest, intermediate, the longest duration, respectively. The windows from visual inspection are selected starting from the S-wave onset; however, the S-wave onset for the event no. 46 is not very clear. From all the three cases we can observe the bias of automatic (AI-based) method towards the peak velocity segment of the time series.

(a)

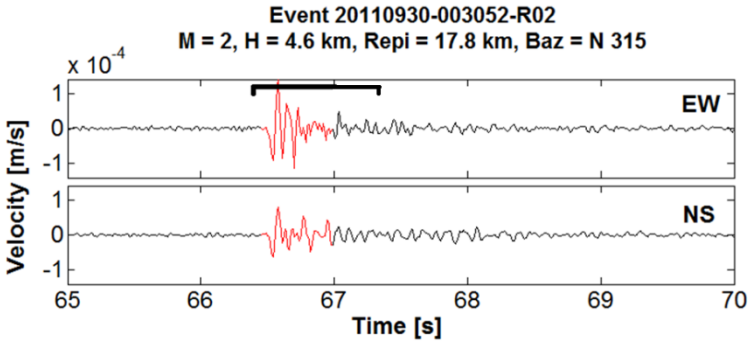

(b)

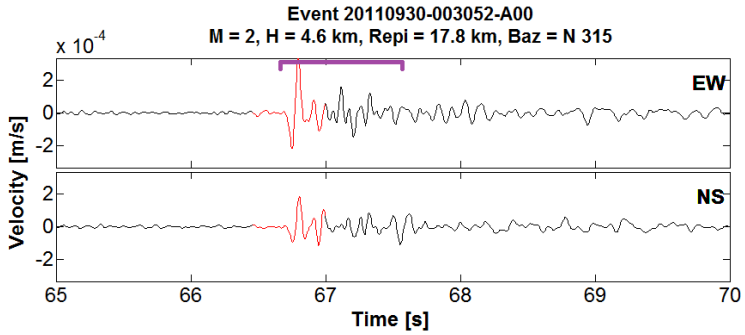

Figure 4.12: Time series of the horizontal components from (a) R02 and (b) A00 for the event no. 5 (Appendix F). The red segment of signal shows the visual selection on R02 seismogram (66.5-67 s) and corresponding window on A00. The brackets on R02 and A00 seismogram show the selections from AI-method on rock (66.5- 67.3 s) and sediment (66.7-67.6 s), respectively.

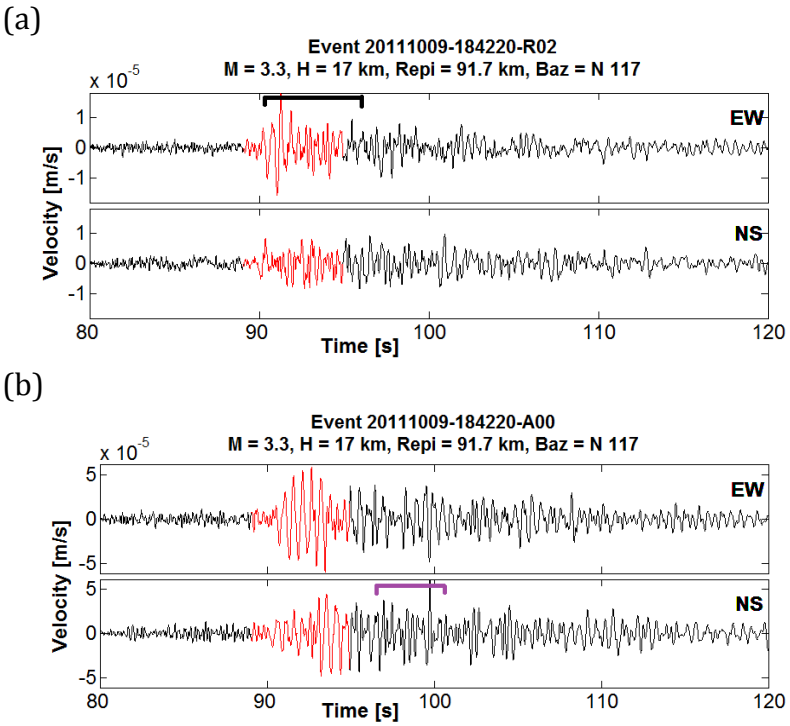

Figure 4.13: Time series of the horizontal components from (a) R02 and (b) A00 for the event no. 8 (Appendix F). The red segment of signal shows the visual selection on R02 seismogram (89- 95 s) and corresponding window on A00. The brackets on R02 and A00 seismogram show the selections from AI-method on rock (90.5-97 s) and sediment (95.5-100.8 s), respectively.

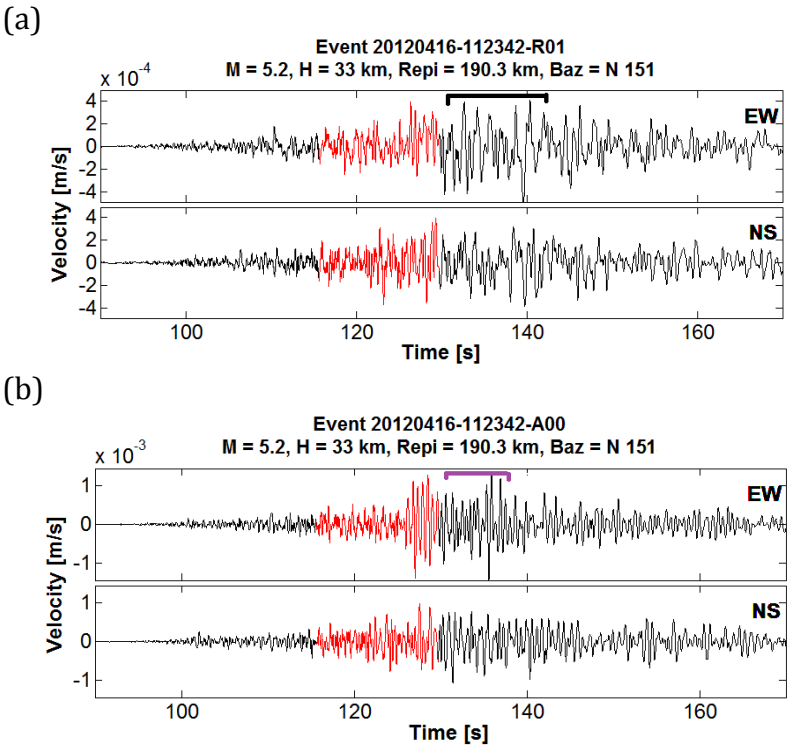

Figure 4.14: Time series of the horizontal components from (a) R02 and (b) A00 for the event no. 46 (Appendix F). The red segment of signal shows the visual selection on R02 seismogram (115.6-129.8s s) and corresponding window on A00. The brackets on R02 and A00 seismogram show the selections from AI-method on rock (131.9-142.5 s) and sediment (131.4-137.2 s), respectively.

Figure 4.15 represents the comparison of durations estimated from rock and sediment site records using visual inspection and automatic procedure along with 10 % error band. We can observe from Figure 4.15 (a) that the difference between two methods (from same site, rock stations) lies within the 10% error band except from a few closer events (30-50 km) whose duration is overestimated by the automatic method. On the other hand, Figure 4.15 (b) shows that difference due to sites (using same method, AI-based) appear mostly in case of the distant events (e.g., >80km). From the comparison between the selection methods (Figure 4.10 and 4.15, a) and recording sites (Figure 4.11 and 4.15, b), we can infer that the automatic system may be used for time window selection from a large dataset. However, in this study we have used the windows selected from the visual inspection based on rock data since we believe that our selection also includes precise judgments and, thus, is better suited for the analysis.

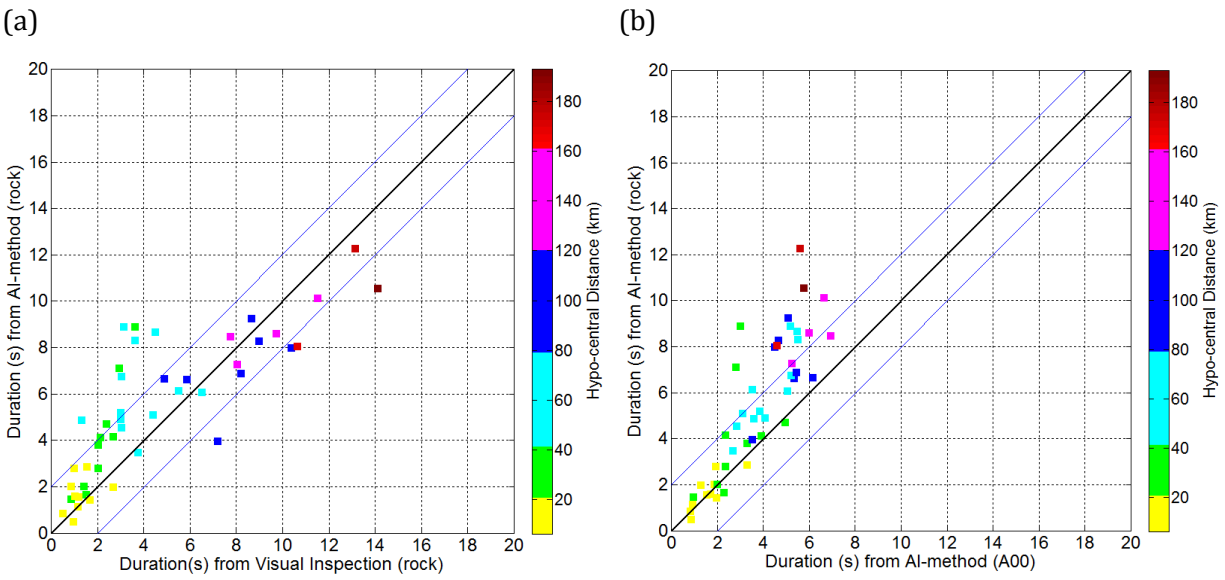

Figure 4.15: Comparison of the durations, estimated based on (a) rock station records using AI-method and visual inspection (b) rock and sediment station records using AI-method. Blue lines show the ±10% band of error. Colorbar shows the hypocentral distance.

4.8 Estimation of Coherency from the Array Data

Amongst the several techniques available to estimate the ground motion spectra, Conventional Spectral Analysis method is considered to be sufficient and appropriate for practical engineering application (Harichandran and Vanmarcke, 1986; Harichandran, 1991). Prior to that, the time series data of the recorded stations for all the events have been checked and corrected. The time windows to be analyzed for all the events have been selected by visual inspection from the rock station records (the procedure described in the previous section). Lagged coherency has been estimated for the vertical and two horizontal components of the recorded data and for each possible combination of pairs in the array (max. 210 pairs). The available number of pairs for each event has been listed in Appendix F.2 (column no. 13). The interstation distance and angles of the stations in each pair has been given in Appendix J. Since we have used lagged coherency estimates in this work, we have often used the terminologies 'lagged coherency' and 'coherency' interchangeably. The coherency has been estimated in the following way:

1) For lagged coherency estimation, arrival time perturbations have been removed from the data by aligning the records from each station in the array with respect to the reference station A00. The time lags in the alignment were determined by estimating the cross-correlation between stations and evaluating the positive maximum correlation coefficients (Boissieres and Vanmarcke, 1995a). In theory, the alignment operation does not affect the lagged coherency but the phase spectrum. However, since the concentric circles of station in Array have very small radii, ranging from 5 m to 80 m from the reference station A00, there is no significant time lag among the records. For an instance, in case of the event with longest duration from the subset (no. 46 Appendix F), maximum time lag estimated was 0.14 s at station separation distance 80 m for the time window of 14 s. This shows that the alignment operation has minimal effect on the phase arrivals in case of our data. Thus it can be said that the time windows considered for the coherency estimation represent almost absolute timescale and account for the realistic case of propagating wave field.

2) The time step for the recorded data is taken as 0.02s (sampling frequency, f_s = 50 Hz). The selected time windows have been segmented from the original time history by applying a 5% cosine bell window taper at each end. These windows are assumed to be the segments from infinite time histories with uniform characteristics through time (stationarity assumption).

3) The power spectral densities and cross-spectral density, as indicated in Eq. (4.8), were estimated. In order to estimate the respective discrete-form smoothed power-spectral densities, $\bar{S}_{jj}(\omega_n)$of the two stations (j=k), and the smoothed cross-spectrum between them, $\bar{S}_{jk}(\omega_n)$, Equations (4.13) and (4.14) have been followed (Zerva and Zervas, 2002).

$$\bar{S}_{jk}(\omega_n) = \sum_{m=-M_h}^{+M_h} W(m\Delta\omega)\, A_j^*(\omega_n + m\Delta\omega)\; A_k(\omega_n + m\Delta\omega) \tag{4.13}$$

$$\bar{S}_{jj}(\omega_n) = \sum_{m=-M_h}^{+M_h} W(m\Delta\omega)\, |A_j(\omega_n + m\Delta\omega)|^2 \tag{4.14}$$

where the duration of the time windows is T=NΔT, with time window length being 0 ≤ t ≤ T, N being the number of samples in the recorded time series for the window, and Δt the time step; *-operator indicates complex conjugate, ω being the angular frequency in rad/sec, Δω (= 2π/T) is the angular frequency step, W(ω) denotes spectral smoothing window and $2M_h+1$ is the number of point of the Hamming smoothing window. $A_j(\omega)$ and $A_k(\omega)$ are the scaled discrete Fourier transforms of the time histories $U_j(t)$ and $U_k(t)$, respectively, given by:

$$A_{j,k}(\omega_n) = \sqrt{\frac{\Delta t}{2\pi N}} \sum_{l=0}^{N-1} U_{j,k}(l\Delta t) exp^{-i\omega_n l\Delta t} \tag{4.15}$$

Where l is the time sample and $i = \sqrt{-1}$. It is to be noted that the Fourier spectra of the motions at different stations will not be identical but the assumption of homogeneity in the random field implies that the power spectrum of the motions is station independent. In this study we have used velocity time histories for the coherency analysis. In addition to that acceleration time histories and displacement time histories can also be used. Theoretically, due to stationarity, the coherency functions obtained from acceleration, velocity and displacement time histories are the same; nevertheless, there are minor differences between the estimated coherency functions due to the different dominant frequency ranges and the smoothing operations, but the general trend is similar in all cases.

4) The power-spectral and cross-spectral densities have been smoothed before being used in the coherency estimation. Considering the tradeoff between the bias and variance of the estimators, in this study, an 11 point (frequency weight M_h=5) Hamming window for smoothing has been used. The frequency band smoothed can be calculated as,

$$f_{smoothed} = 2M_h * \frac{f_s}{N_f} \tag{4.16}$$

where fs is the sampling frequency and N_f is the number of frequency points for the signal duration.

For our data, frequency sampling (f_s) is 50 Hz and time step (ΔT) 0.02s. Thus, for a 2.5 s time window (N = 250,) and N_f = 256 points, the smoothing corresponds to 1.95 Hz bandwidth of frequency smoothing. Equivalent number of smoothing points has been used for the longer durations of time windows so that the band of frequency smoothed remains constant.

5) Finally, the lagged coherency, $|\bar{\gamma}_{jk}(\omega)|$, values for frequency upto 25 Hz have been estimated as the ratio between cross spectrum of the pair of stations (j, k), normalized by the corresponding square root of the product of the power spectra at the stations by using Equation 4.8. No prewhitening of the time series has been performed. The bias and standard deviation of $\tanh^{-1}|\bar{\gamma}_{jk}(\omega)|$ for the smoothing considered above are given as 0.008 and 0.26, respectively, in Abrahamson et al. (1991). The 50% and 90% confidence level for noise are given as 0.34 and 0.63, respectively for $\tanh^{-1}|\bar{\gamma}_{jk}(\omega)|$by the authors.

4.8.1 Verification of the algorithms used for coherency estimation

The coherency code is written in MATLAB. The code has been verified by using SMART-1 array data and comparing the results with those of Zerva (2009). As illustrated in Figure 4.16, the results are almost identical.

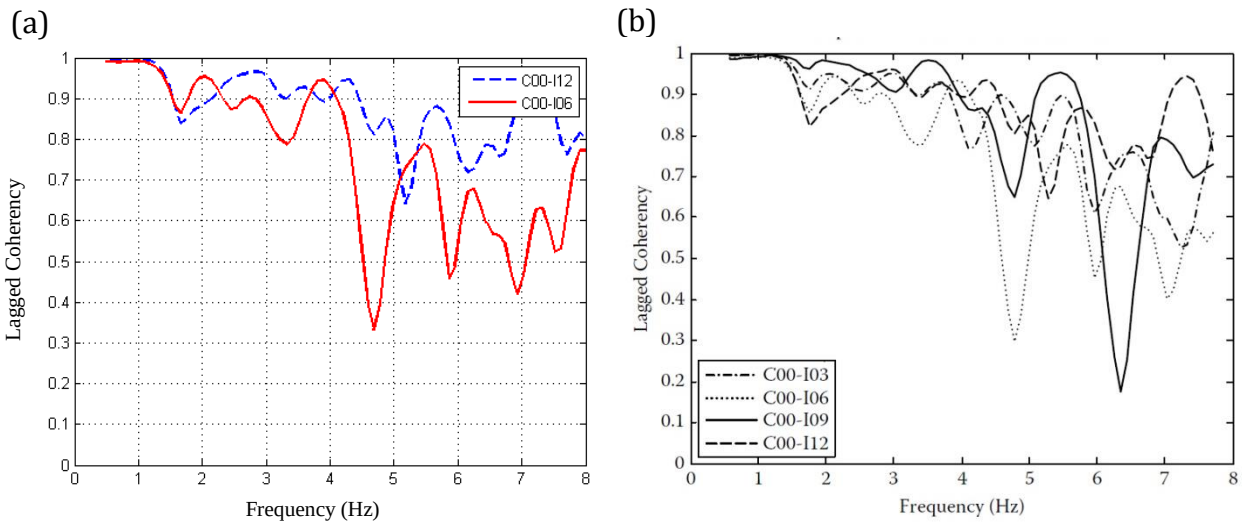

Figure 4.16: The lagged coherency estimation between the stations C00-I12 and C00-I06 for the Event-5 recorded by SMART-1 array. (a) Results of the estimation from this study (b) Results from Zerva (2009).

4.8.2 Sensitivity of lagged coherency to duration of time window

The effect of different considerations of time-window length is illustrated in Figure 4.17 using the event no. 46 (Appendix F), for which the selected time window is the largest and exhibits maximum difference between visual inspection and automatic selection procedures. This event has a magnitude of M 5.2 and hypocentral depth is about 193 km. The time series for the two horizontal components of station A00 and R01 are shown in Figure 4.14. We considered 6 different time lengths for testing. The first group, test 1 to 4 consider 4 different lengths (116-130s, 116-138s, 116-142s, 116-150s) of time windows starting from the begin time identified by visual inspection of R01. The second group, test 5 and 6 consider two different lengths (132-142s, 132-150s) with respect to the automatic time window estimation from R01 records. The plot shows the estimated coherency of the EW component for 5 station pairs having separation

distance 15 m (See Appendix K for the results at separation distances 40 m and 80 m). The plots reveal that in case of test 1 to 4 the estimated coherency is identical for all pairs despite the length of time windows is increasing. The same is observed in case of test 5 and 6. Therefore, it can be perceived from the results of this test that the estimated coherency is less sensitive to the window length. Abrahamson (1992a) also concludes that coherency is relatively insensitive to the window length provided that the strongest motions are included; he found that low amplitude motions contribute little to the coherency estimates. However, some discrepancies are observed between the two groups of time windows, especially at higher frequencies (>5 Hz). It is worth mentioning that the window lengths considered in test 1 to 4 include the time segment 116-132s while it is not considered for test 5 and 6.

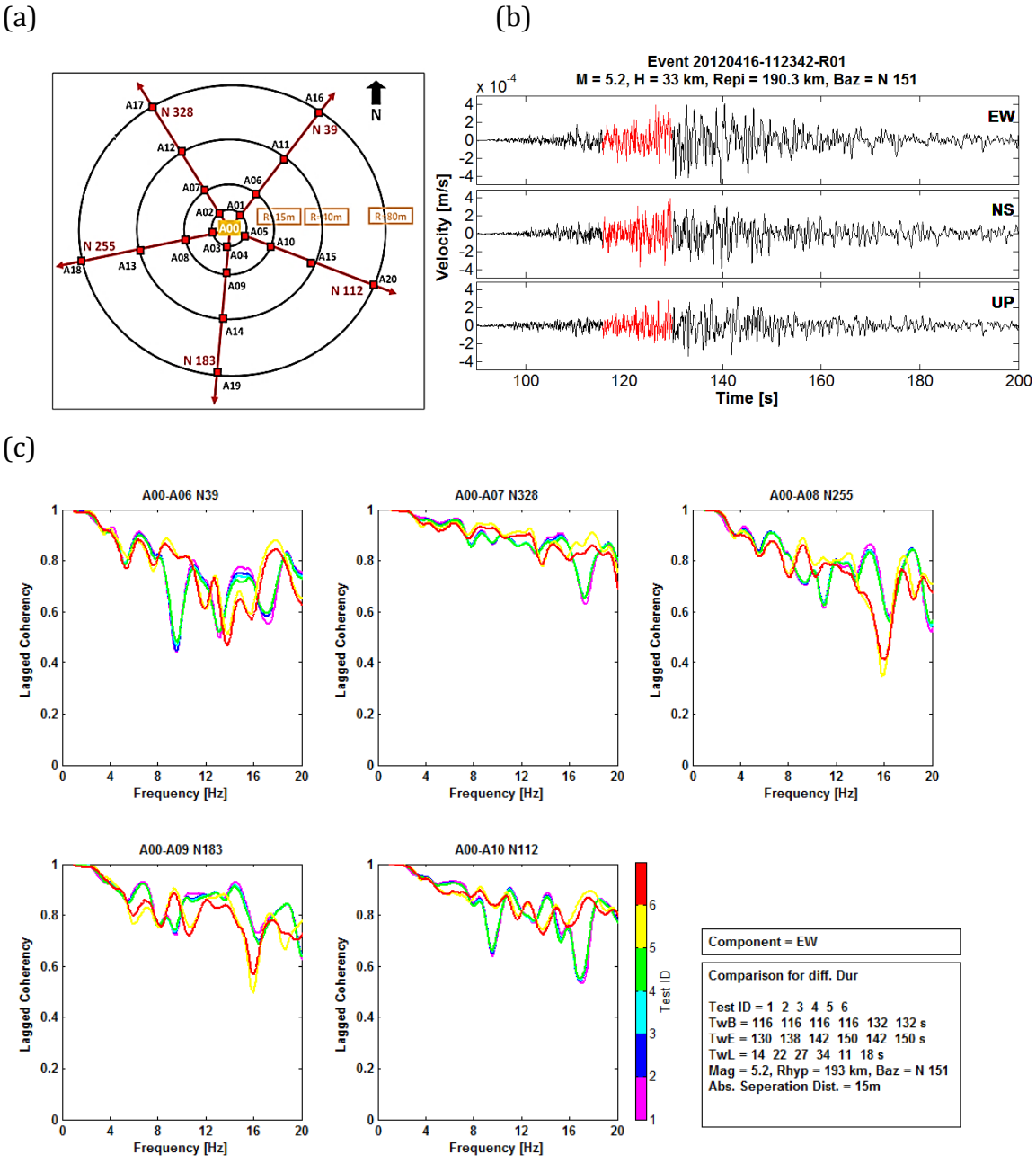

Figure 4.17: (a) Array A geometry, (b) velocity time series of event no. 46 (Appendix F) and (c) sensitivity of estimated lagged coherency to duration of selected time window. The plots represent the estimated coherency (EW component) between A00 and the stations on the 15m-radius circle of the Array A. The time histories from R01 are given in Figure 4.14 (a). The colorbar 'Test ID' indicates the index of the test time windows. Test 1 to 4 consider 4 different lengths (116-130s, 116-138s, 116-142s, 116-150s) of time windows starting from the begin time identified by visual inspection of R02. Test 5 and 6 consider two different lengths (132-142s, 132-150s) with respect to the automatic time window estimation from R02 records.

4.9 Results of coherency analysis from single events

First the coherency estimates from a single event are shown. We take the event occurred on October 9, 2011 at 18:42:20 UTC (M=3.3, R_{hyp}=93.3 km, Baz= N 117, S-tw=5.88s). Figure 4.18 shows the time history, Fourier amplitude and signal to noise ratio for the event. The estimated lagged coherency of the EW component has been plotted for the pairs along a single array direction (N 39) at 4 different separation distances (A00-A01, A00-A06, A00-A11 and A00-A16 at 5, 15, 40 and 80m inter-station distances, respectively). Figure 4.19 shows that the coherency decays with frequency as well as with increasing inter-station distances. As mentioned earlier, the resolvability threshold of coherency is considered to be 0.33 for the frequency smoothing applied here (M=5); hence coherency values below 0.33 bear no significance in terms of interpretation. The bumps in the coherency values above 0.33 appear when the spectra for the motions of two stations exhibit a simultaneous peak at similar frequency range. These peaks can be interpreted as to be dominated by coherent energy coming from direct waves. On the contrary, the troughs in the coherency estimates (low coherency values) could be dominated by incoherent energy coming from the scattered waves or destructive interference between two waves of comparable amplitude. When we compare this inter-station distance variability for all 5 array directions (Figure 4.20), we still observe the same tendency. The coherency plots at separation distance 15 m (the blue line) seem to be larger along directions N328 and N112.

Now for the same earthquake, Figure 4.21 shows the lagged coherency at 5 different array directions (pairs A00-A11, A00-A12, A00-A13, A00-A14, A00-A15 at N39, N328, N 255, N183, N112, respectively), located around 15 m radius from the central station A00. In this plot, the coherency is observed to decay faster, especially at N39 and N255 directions specific for this event at least. Again, when we compare the coherency estimates from 5 different directions over 4 different distances (the 4 concentric circles of the array), we find out that the previously observed trend is considerable only for the intermediate distances 15m and 40m (Figure 4.22). At 5m and 80 m, the directional variability appears to be less important.

(a)

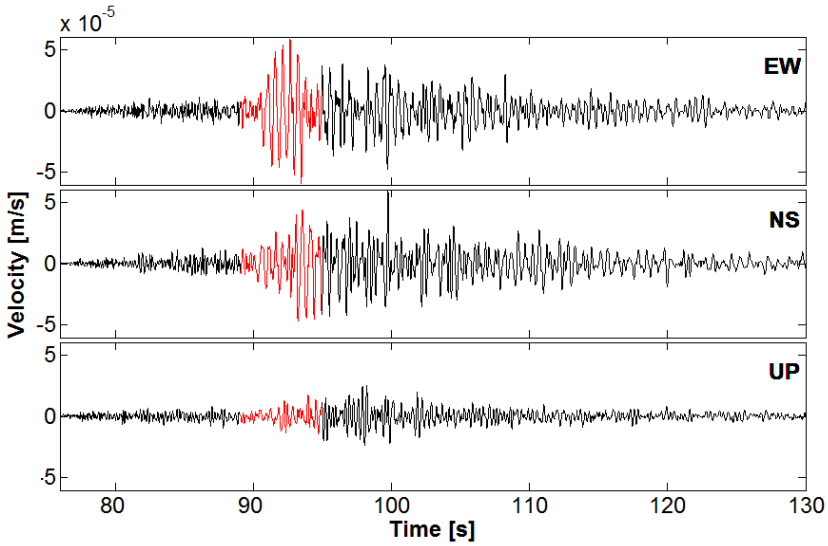

(b)

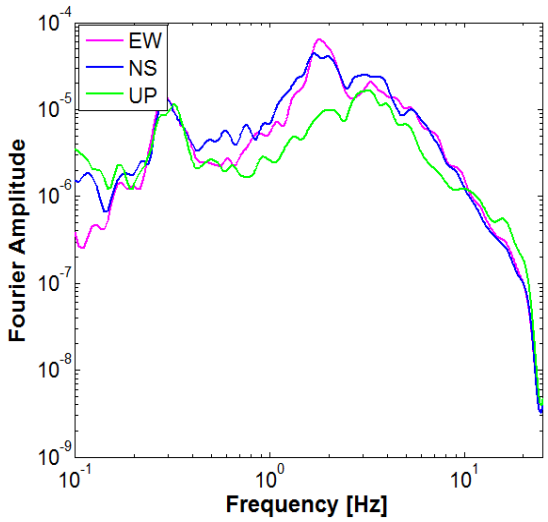

(c)

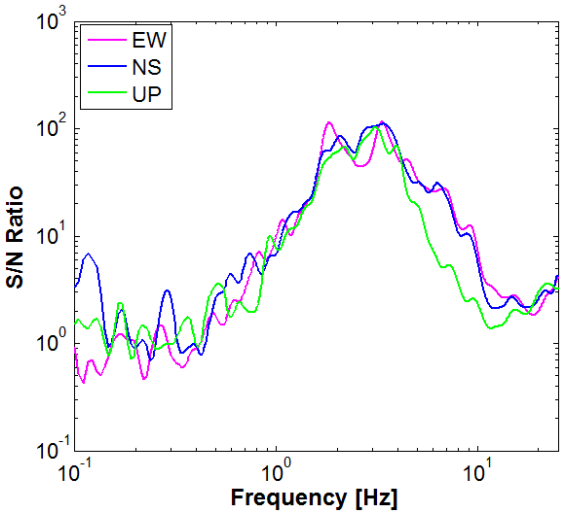

Figure 4.18: (a) Time history, (b) Fourier amplitude spectra and (c) signal to noise ratio for the event occurred on October 9, 2011 at 18:42:20 UTC (M=3.3, R_{hyp}=93.3 km, Baz= N 117, tw=5.88s). The event index is 8 in Appendix F. Red segment on the time history plot marks the window used for coherency estimation.

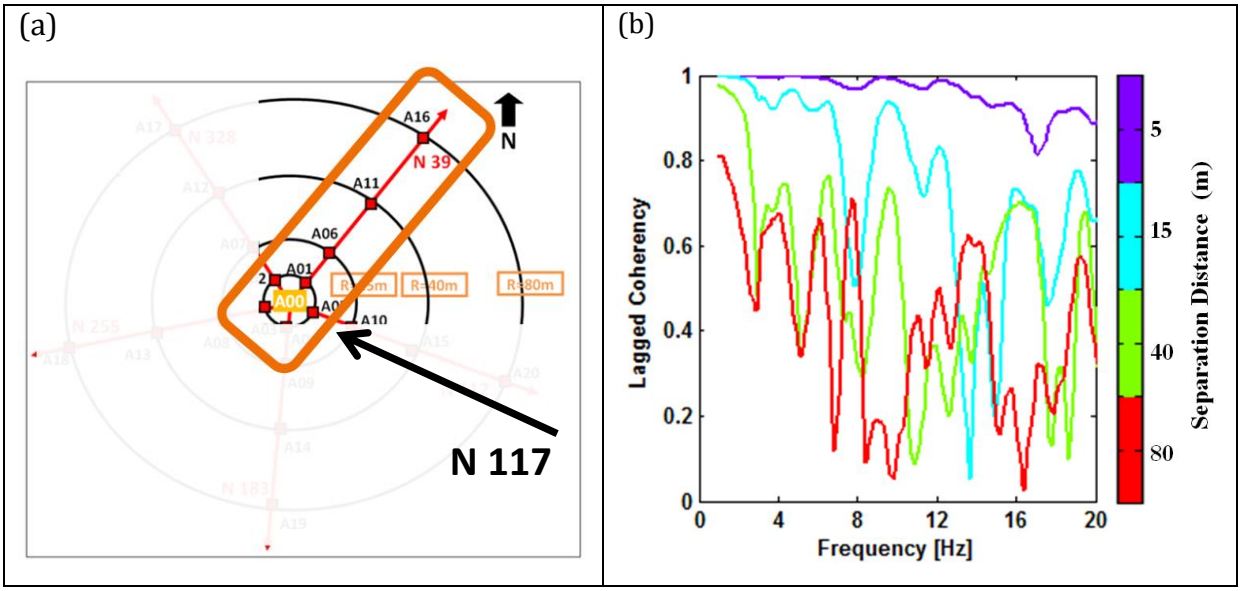

Figure 4.19: (a) Array configuration angle at N39 and (b) Lagged coherency (EW component) at interstation angle N39 for 4 inter-station distances (event no. 8). The black arrow shows the event back-azimuth.

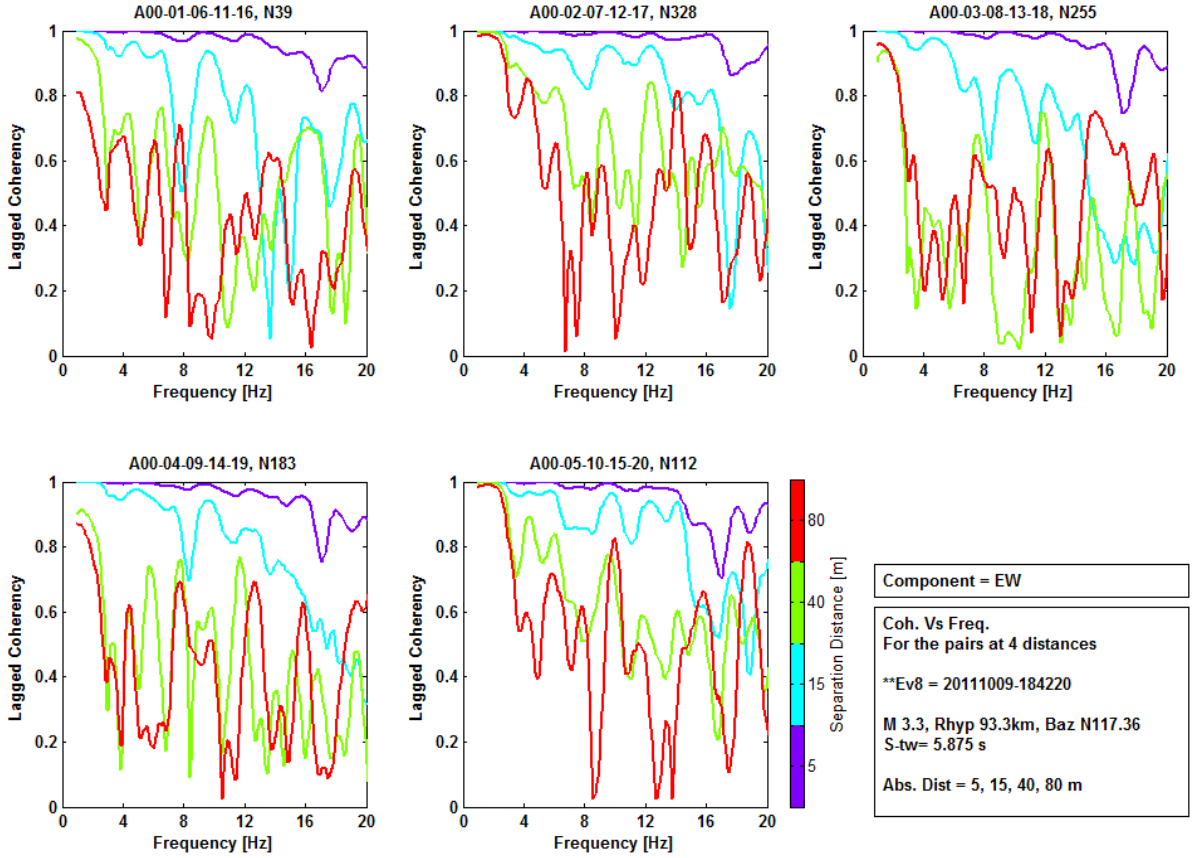

Figure 4.20: Lagged coherency variability (EW component) of event no 8. Each plot represents 4 interstation distances for the pairs lying in 5 array-branch directions.

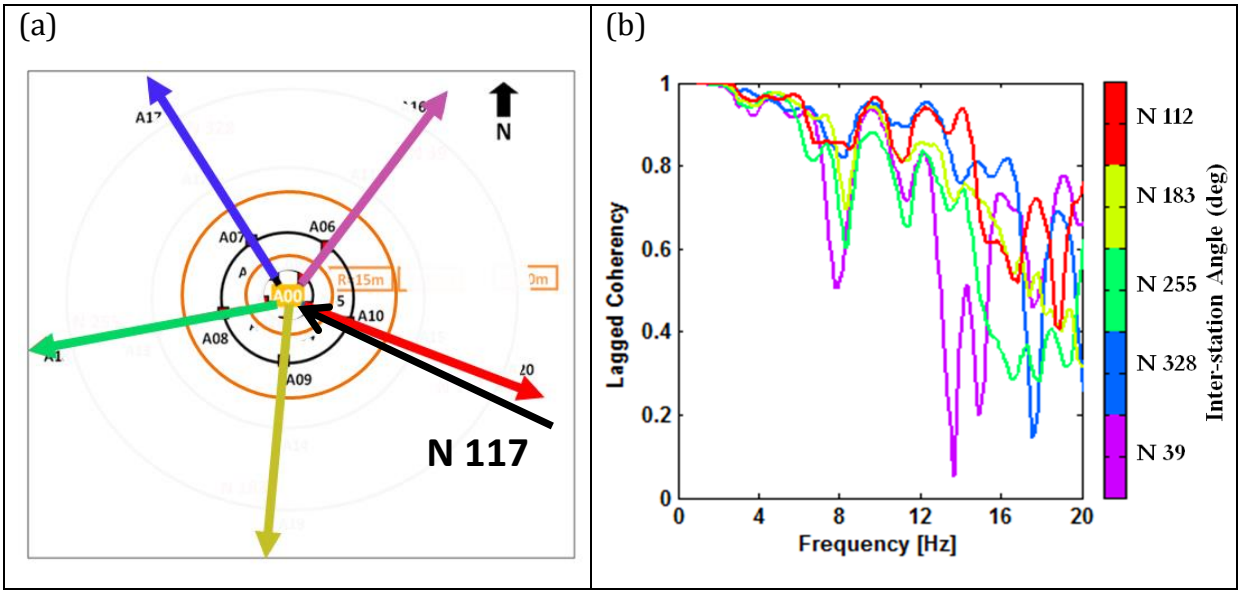

Figure 4.21: (a) Array configuration for 5 array directions and (b) Lagged coherency (EW component) of event no 8 at 5 array directions for inter-station distance 15m. The black arrow shows the event back-azimuth.

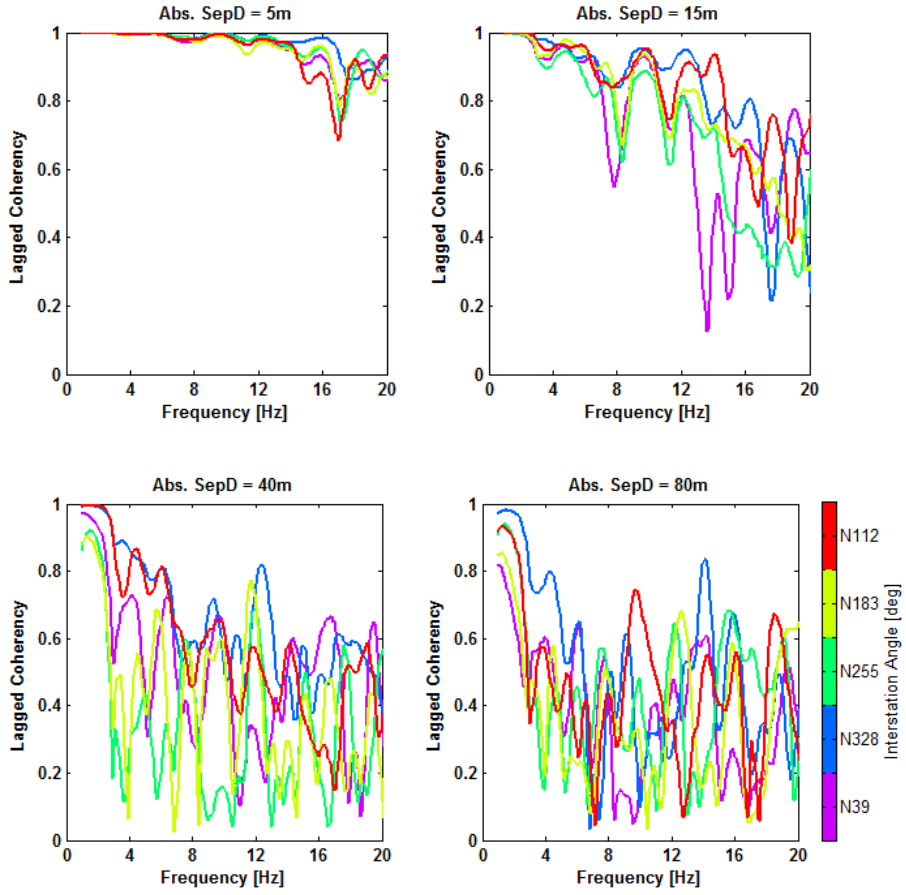

Figure 4.22: Lagged coherency variability (EW component) of event no 8. Each plot represents station pairs lying in 5 array branch directions at 4 interstation distances.

In order to investigate the variability in the coherency due to different source parameters (magnitude, hypocentral distance, R_{hyp}, and event back-azimuth), we choose one horizontal component (EW) of a group of events for which only one parameter varies and the rest two remain similar. Then we plot the estimated coherency for one pair at 5 array directions and 3 different inter-station distances (as in Figure 4.23, 4.24 and 4.25). Note that the coherency curves of some pairs are absent because some stations are missing for some of the events. The missing stations are listed in Table Appendix F.2.

In Figure 4.23, we have plotted 5 events (M~3.1, Baz~ N220) with hypocentral distances (R_{hyp},) 103, 22, 20, 94 and 56 km (event no. 3, 4, 20, 28, 33, respectively, in Appendix F). The magnitudes of the events are around 3.1 and back-azimuths are around N220. The figure shows that the decay of coherency with frequency is faster in case of the farthest event (R_{hyp}=103 km) at all the directions and inter-station distances. The other two distant events (R_{hyp}=93 and 56 km) seem to follow the trend of the farthest event, especially at larger separation distances.

Figure 4.24 shows the lagged coherency for events (M~2.8, R_{hyp}~20km) with different back-azimuths N334, N283, N206, N220, N74 (event no. 9, 13, 16, 20 and 36 in Appendix F). No clear event back-azimuth dependence is observed.

Figure 4.25 represents the lagged coherency for events (R_{hyp}~20km, Baz~N220) with three different magnitudes M 3.5, M 2.3 and M 2.8 (event no. 4, 11 and 20 in Appendix F). Again, no clear magnitude-dependence tendency is observed; however, the magnitude range considered here is too narrow to represent a good comparison.

Figure 4.26 illustrates one example of how the lagged coherency varies with different interstation distances at specific frequencies (~1, ~2.5, ~ 5 and ~7.5 Hz). We have taken the EW component of the event with M = 4.5, R_{hyp} = 173 km and Baz = N 128 (event no. 10, Appendix F) as an example. At each array direction, we have taken the pairs on the 4 array circles (e.g., for N 39 direction, the pairs taken are A00-A01, A00-A06, A00-A11 and A00-A16 at interstation distances 5, 15, 40 and 80 m, respectively). From the plots, it is evident that the coherency declines with increasing inter-station

distances for all the frequencies. The decay of coherency with distance seems smoother but slower than that of with frequency. The rate of decay also looks faster for higher frequencies. From the comparison among the five array directions, it seems that the coherency declines relatively faster in N39, N255 and N112 directions for this event. This could possibly be an indication that for this array, the assumption of isotropy may not be valid. At N39 direction low coherency is observed (<0.4) within separation distance 20 to 40 m. This might be event-specific, and corresponds to resolvability threshold of coherency estimate.

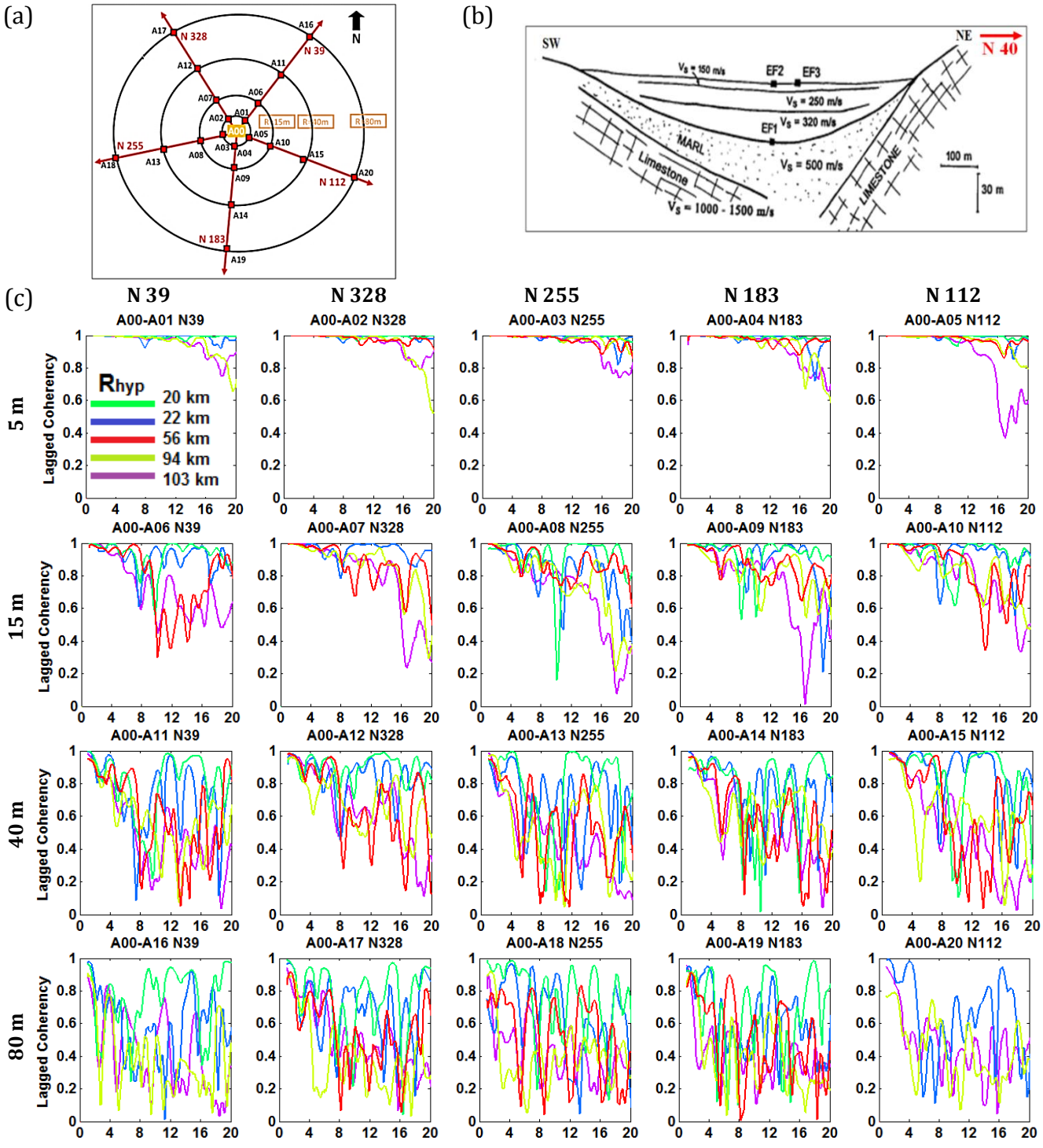

Figure 4.23: (a) Array configuration, (b) valley cross-section and (c) lagged coherency variability (EW component) from the events (M~3.1, Baz~ N220) with different hypocentral distances, at 5 array directions (indicated on the top of each panel) and 4 interstation distances (indicated at the left of each row of figures). Legend indicates the hypocentral distances.

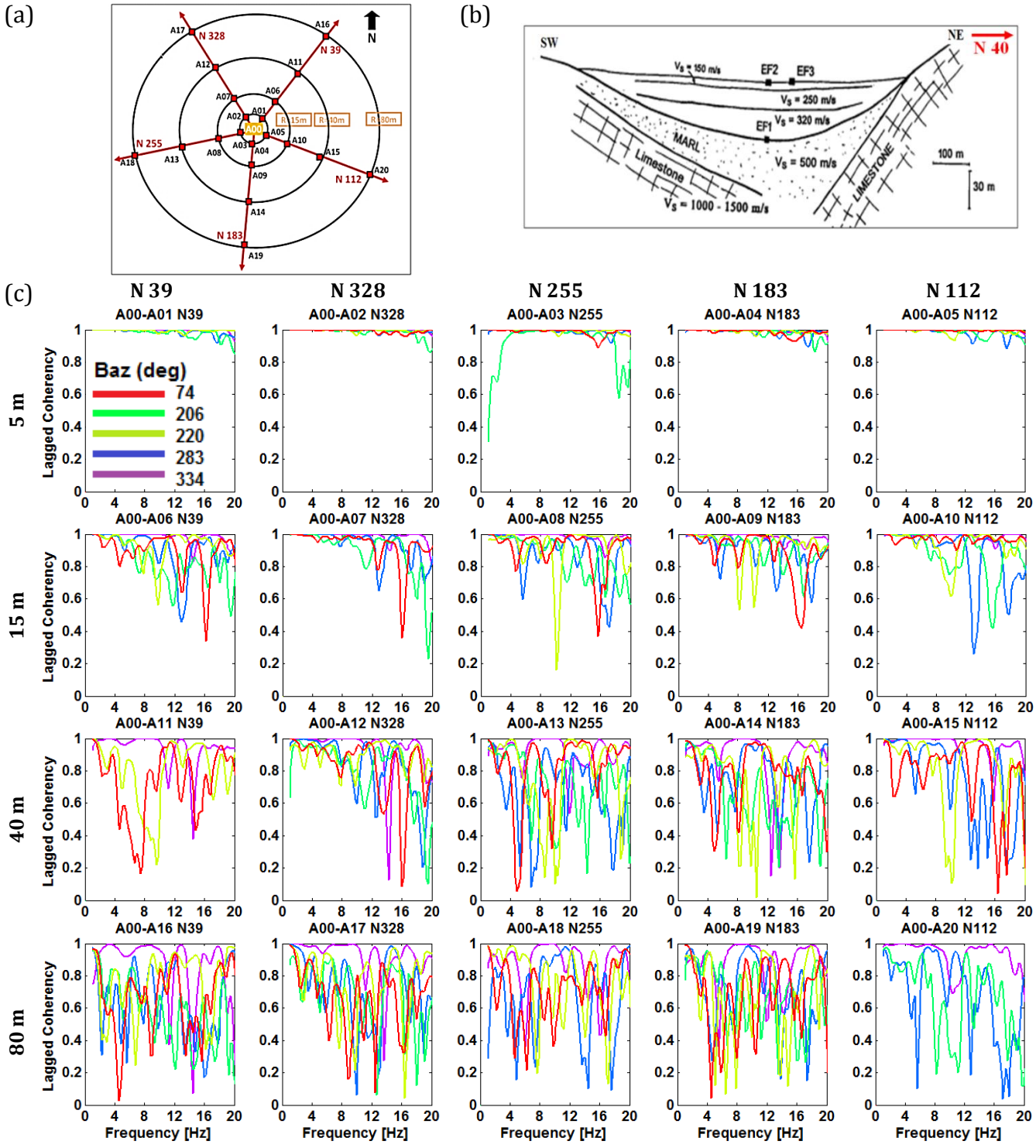

Figure 4.24: (a) Array configuration, (b) valley cross-section and (c) lagged coherency variability (EW component) for the events (M~2.8, R_{hyp}~20km) from different back-azimuths, at 5 array directions (indicated on the top of each panel) and 4 inter-station distances (indicated at the left of each row of figures). Legend indicates the event back-azimuths.

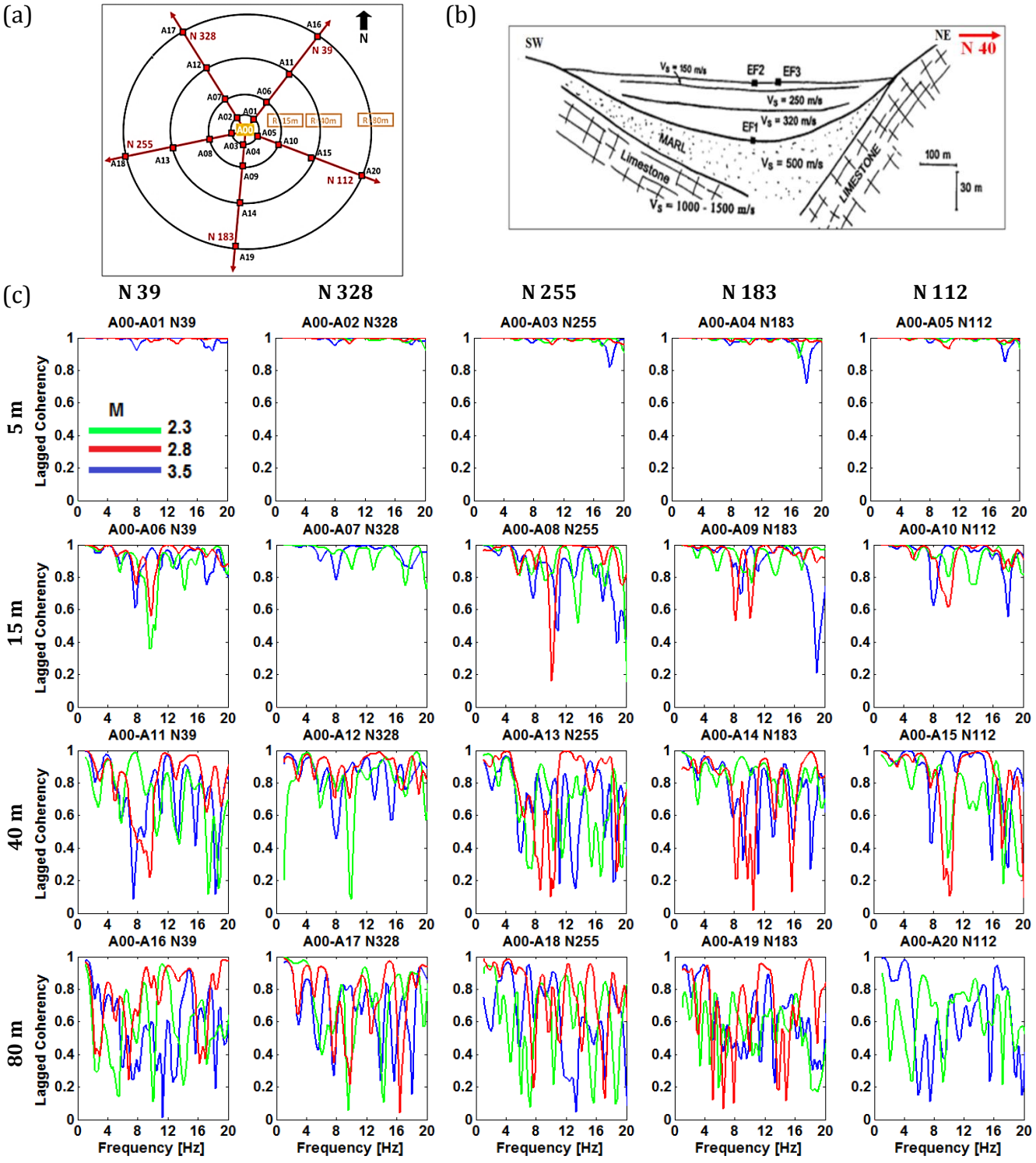

Figure 4.25: (a) Array configuration, (b) valley cross-section and (c) lagged coherency variability (EW component) of the events (R_{hyp}~20km, Baz~N 220) with different magnitudes, at 5 array directions (indicated on the top of each panel) and 4 inter-station distances (indicated at the left of each row of figures). Legend indicates the magnitudes of the events.

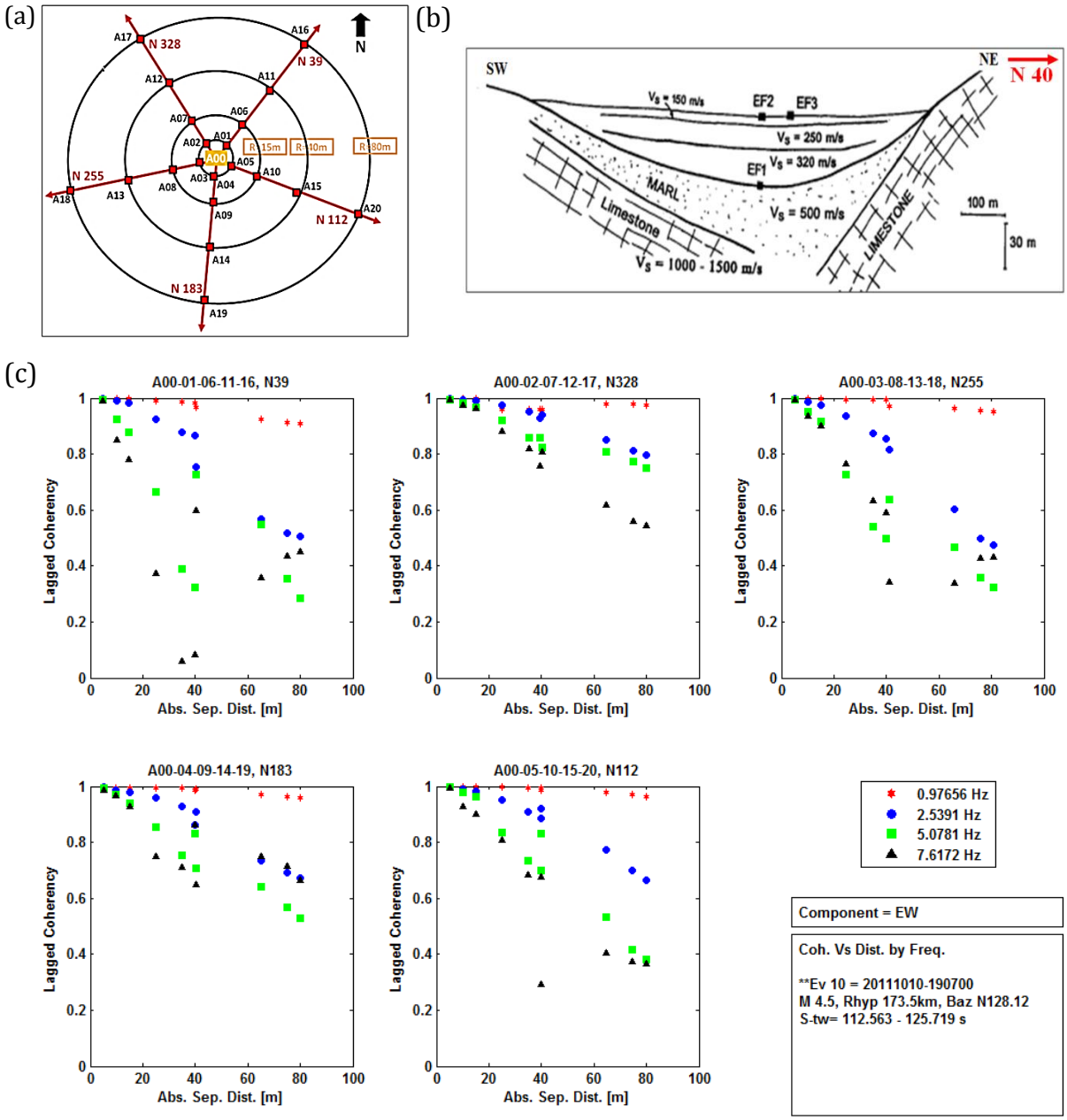

Figure 4.26: (a) Array configuration, (b) valley cross-section and (c) lagged coherency variability (EW component) with increasing interstation distances for different frequencies, at 5 array directions.

4.10 Statistical analysis considering all the events

It is evident from the figures above that lagged coherency (which ranges between 0 and 1) estimates exhibit a high variability. It is small for low frequencies and large for higher frequencies, that is, coherency variability is frequency dependent (heteroscedastic). Moreover, the observed variability may be significant from earthquake to earthquake, and it is difficult and dangerous to draw conclusions from observations on single earthquakes. Our main goal is thus to investigate the dependency of coherency on various site and source parameters on the basis of average values derived from a large and representative set of events. For such an averaging process, as for any kind of statistical analysis on the coherency estimates, normally distributed data is preferable. Therefore, a $\tanh^{-1}$ (or, ATANH) transformation is applied to the coherency to produce approximately normally distributed data about the median (Enochson and Goodman, 1965; Abrahamson, 2007). Abrahamson (2007) shows through an example how scatter of the coherency becomes independent of frequency (homoscedastic) with such a transformation. The author also shows that ATANH coherency distributions are skewed to the lower coherency values, and that the differences between mean and median estimates are small. Therefore, median coherency can be used as an estimate for the mean coherency for simplicity.

In this study, ATANH lagged coherency values have been used for statistical analysis in order to investigate the dependence of coherency on different source and site parameters. Four interstation distance ranges (5-10, 15-25, 35-40 and 65-80 m) have been chosen and the coherency estimates of the pairs available for each distance range have been used to derive the 'individual median' curve for a single event. The 'global median' of all the events at a given interstation distance range has also been derived by combining all the pairs available from 46 events. The residuals for each event have been computed from the difference between 'individual median' and 'global median'. Distribution of the ATANH coherency values at different interstation distances and frequency ranges has also been evaluated. The coherency estimates used for all the analyses, in this work, are based on the manual selection (from visual inspection) of time windows. However, in the subsection 4.9.3, coherency estimates from automatic

selection (AI-based method) of time windows have also been discussed and compared with those from manual selection.

Three cases have been considered for the direction of horizontal components of our ground-motion data: (1) EW and NS, (2) 'valley-perpendicular' and 'valley-parallel' where the originally recorded horizontal components (NS and EW) are rotated along the valley-perpendicular (or N40), and valley-parallel (or N130) directions, respectively, and (3) 'baz-parallel' and 'baz-perpendicular' where horizontal components are rotated with respect to the event-back-azimuth (i.e, radial component) and its perpendicular (i.e., transverse component) directions, respectively. Note that in the following segment the terminologies 'coherency' and 'lagged coherency' have been used interchangeably.

4.10.1 Estimation of Confidence Interval (CI)

In some of the following sub-sections we compared the median curves along with their 85% confidence intervals. Therefore, in this sub-section the estimation procedure of confidence interval (CI) has been described after Le Boudec (2011).

Confidence interval has been estimated for each curve in order to verify how precisely the median curves have been estimated. Here the interval has been considered at 85% confidence level. The underlying assumption is that all the values were independently and randomly sampled from the dataset and they are distributed according to a Gaussian distribution. We could say that there is an 85% chance that the 85% CI contains the true median of the dataset. In other words, if we generate many median coherence estimates from many samples, we can expect the 85% CI to include the actual median in 85% of the cases, and not to include the median in the other 15%.

When n coherency values are ranked in ascending order (from lower to higher values), the upper and lower limits of the 85% CI can be estimated from the j^{th} and k^{th} coherency estimates, derived from the following equations,

$$j = nq - \eta * \sqrt{(nq\,(1-q))} \quad (4.17)$$

$$k = nq + \eta * \sqrt{\left(nq\,(1-q)\right)} + 1 \quad (4.18)$$

where,

n = number of observations (number of available pairs from 46 events)

q = quantile-value, which is 0.5 for Median

η = reliability factor, which is 1.44 for 85% confidence level

The calculated j and k values are rounded to the next integer then the 85% CI is considered as the values between the j-th and k-th observations in the ordered dataset.

4.10.2 Coherency estimates from the subset of events

First we show the median estimates, 'individual' and 'global', of ATANH lagged coherency values from all the events (Figure 4.27) at four distances ranges (Dij) and for the three components EW, NS and Z. The corresponding lagged coherency values are also marked at the right-side axis of the figure. The time windows considered here are the ones selected manually from visual inspection using rock station records. We observe the decay of coherency with increasing interstation distance and frequency from Figure 4.27. Note that the median coherency resolvability threshold of ATANH coherency estimation is 0.34, hence not allowing the lower values to be interpreted. However, the estimated median curves in the plots are observed to be well above the coherency resolvability threshold (the limit has been marked by a blue line on the figure). The two horizontal components show very similar tendencies while the vertical component looks somewhat different. Coherency of the vertical component drops sharply between 0 and 5 Hz and an increasing trend is observed after 10 Hz at shorter distances (5-10 m and 15-25 m). This increase at higher frequencies could be attributed to the presence of P-waves in the vertical component. We also observe a significant dispersion of individual event's median from the global median. Figure 4.28 shows the corresponding residuals where we can clearly observe higher variation at interstation distance above 10 m and frequency above 5 Hz. Distribution of ATANH coherency values for EW component in different frequency bands and at different interstation distances (Dij) are shown in Figure 4.29. Similar figures for all three components are

provided in Appendix L.1. The distribution of ATANH coherency from EW component is clearly skewed to the lower values with increasing frequency and interstation distance.

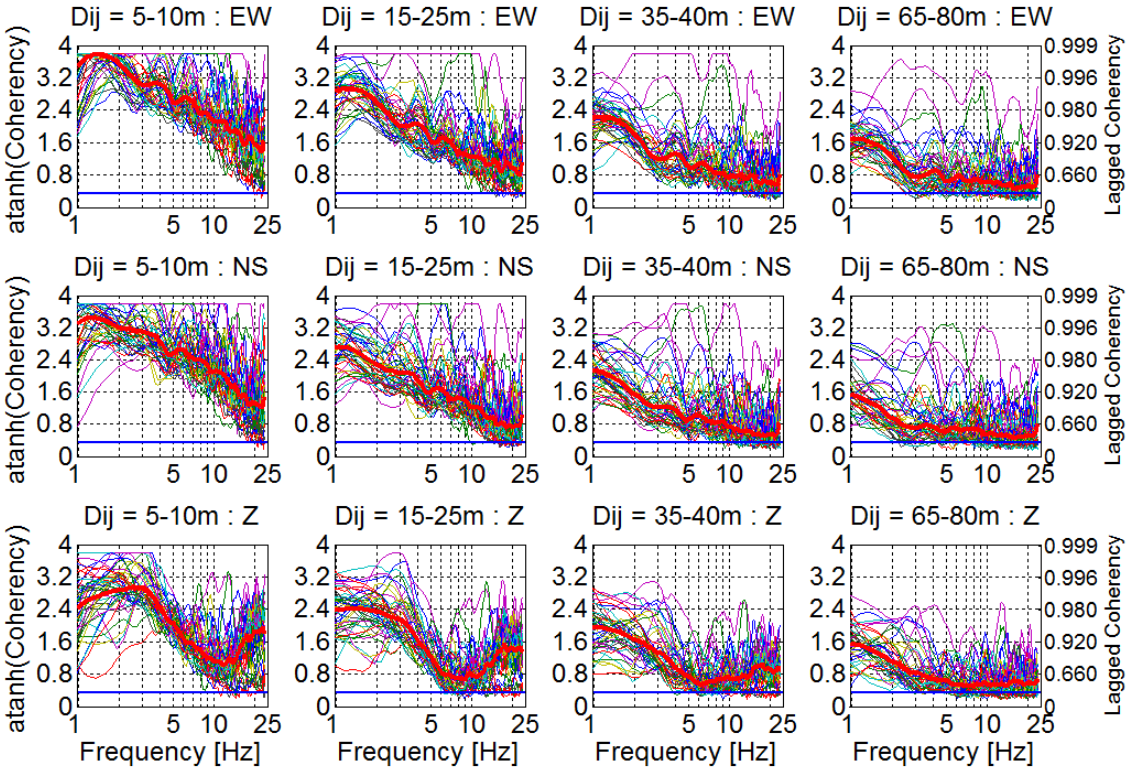

Figure 4.27: ATANH median curves of 46 events from the time windows selected visually from rock stations. The thick red curve shows the 'global median'. Dij stands for interstation distance and EW, NS, Z stand for the ground-motion components. Blue line marks the coherency resolvability threshold.

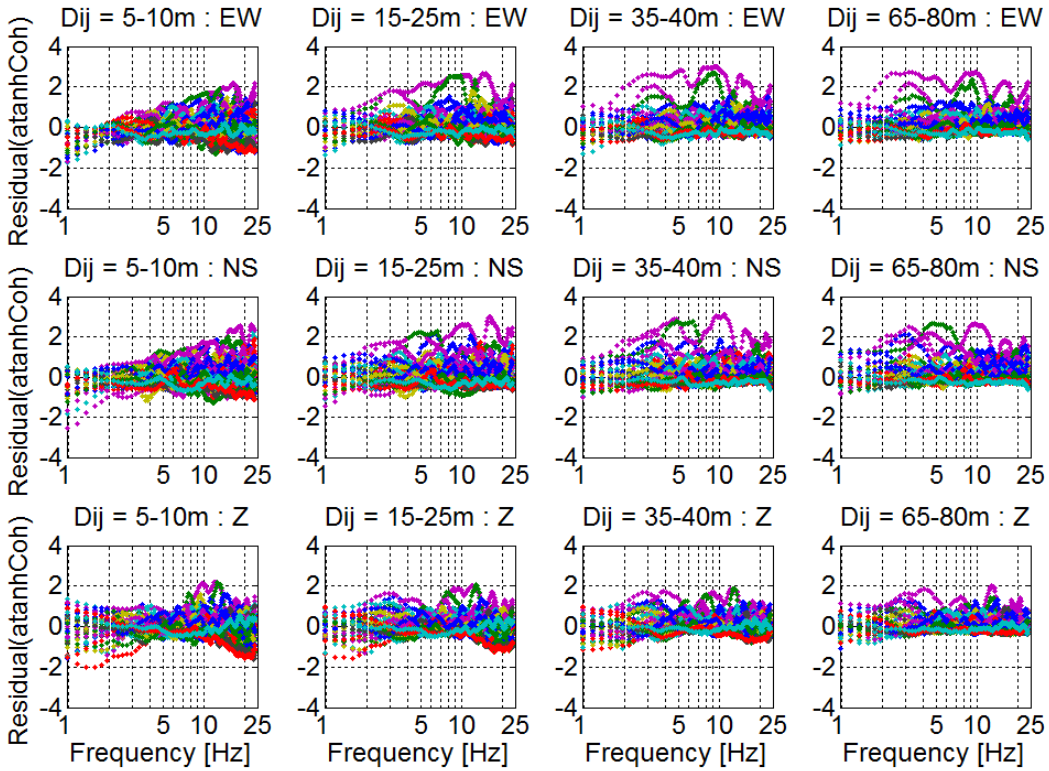

Figure 4.28: ATANH Coherency residuals of 'individual median' estimates with respect to the 'global median', from the time windows selected visually from rock stations. Dij stands for interstation distance and EW, NS, Z stand for the ground-motion components.

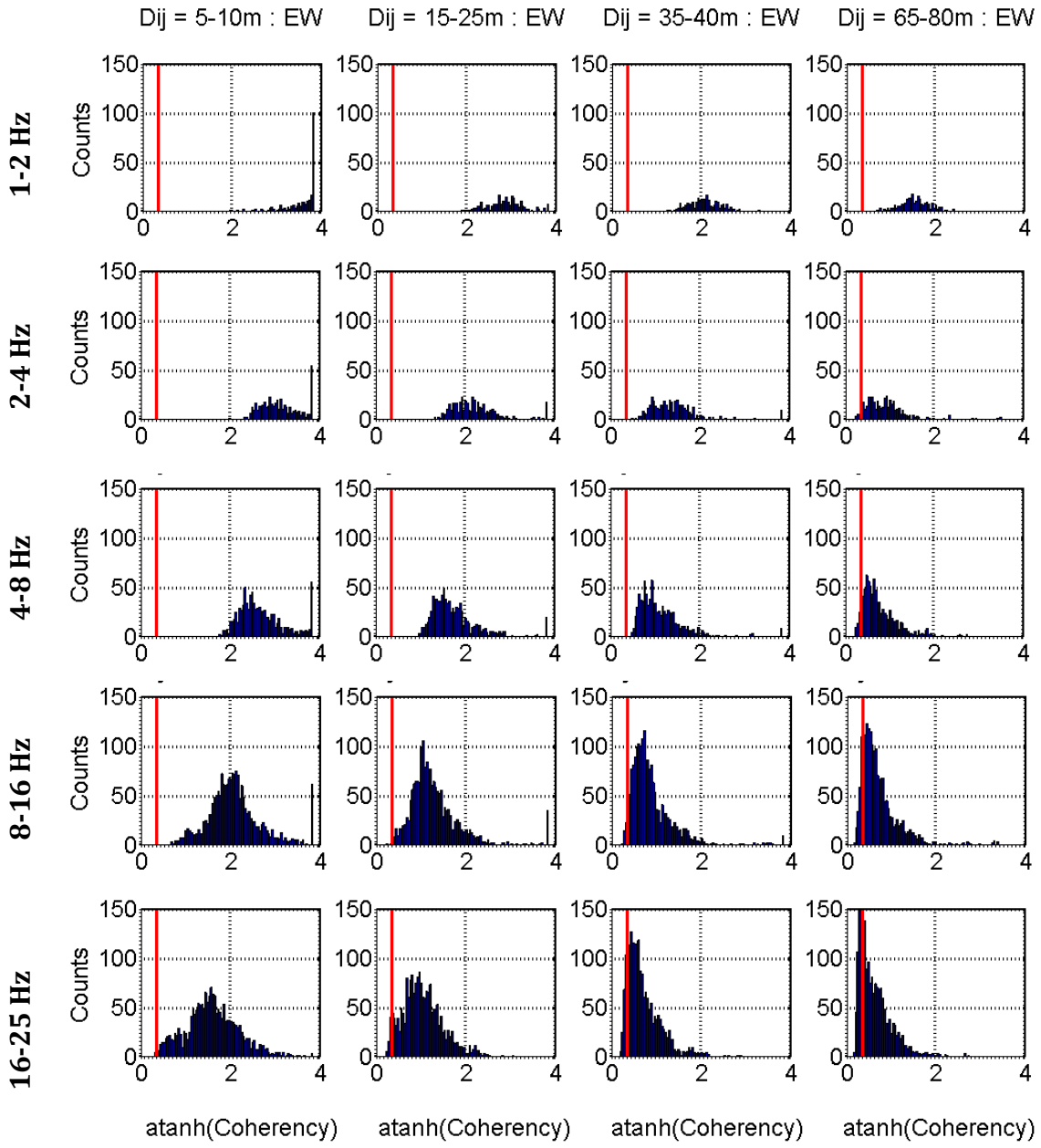

Figure 4.29: Distribution of ATANH estimates of 46 events (EW component), from the time windows selected visually from rock stations, at different distance and frequency ranges (indicated at the left of each row of figures). Red line shows the coherency resolvability threshold. Dij stands for interstation distance.

4.10.3 Variation from different time-window selection approaches

We evaluated lagged coherency from an automatic normalized-Arias-Intensity (AI) estimation based method using both rock station and sedimentary station (A00) records and then compared the results with the coherency estimates from on manually selected time window. Figure 4.30 shows the comparison of global median estimates of lagged coherency from three different time-window selection approaches (See Appendix L.2 for comparison from the ATANH coherency estimates). The individual median and residual plots (similar as Figure 4.27 and 4.28) of ATANH coherency estimated from both AI based window selections are provided in Appendix L.3 and L.4. The comparison shows that all three time selection procedure result in the same averaged values at all distances and frequencies. Thus it can be concluded that there is no significant difference between the estimates coming from time windows based on visual selection or automatic procedure, rock station or sedimentary station.

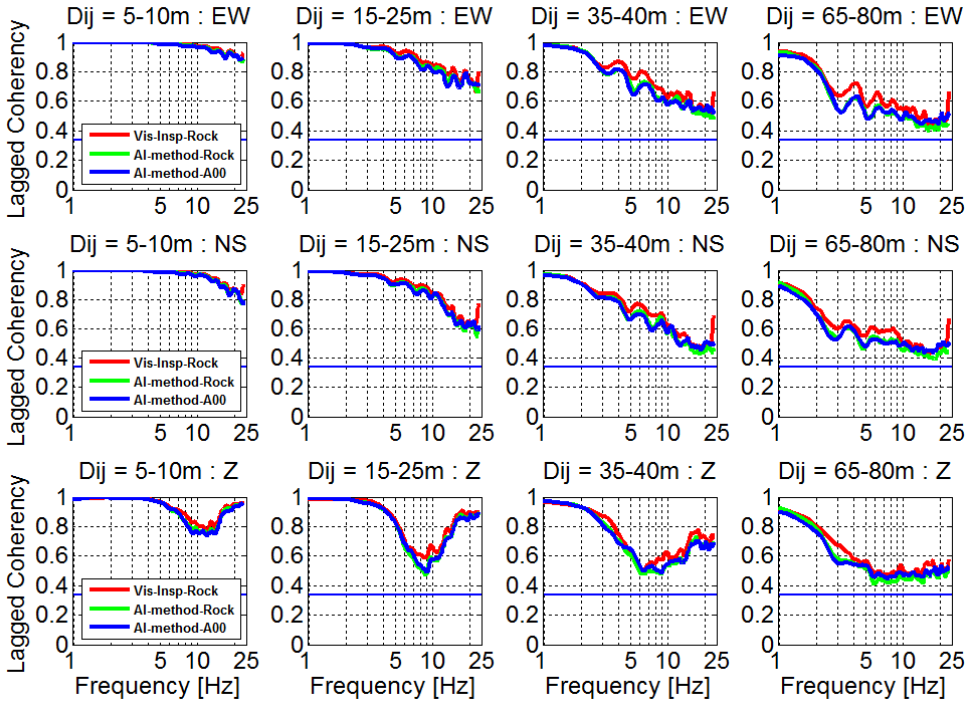

Figure 4.30: Global median estimates of lagged coherency from three different time-window selection approaches. Red, green and blue curves indicate the time windows selection from visual inspection on rock, AI-based estimation on rock and AI-based estimation on A00, respectively. Dij stands for interstation distance and EW, NS, Z stand for the ground-motion components. Blue line marks the coherency resolvability threshold.

4.10.4 Variation associated to the orientation of horizontal components

As mentioned in the beginning of the section, we considered three different pairs of orthogonal directions for the horizontal components of ground motion (manually selected windows) and compared the respective coherency estimates. Figure 4.31 shows comparison of ATANH coherency estimates between the two horizontal components, at four interstation distance ranges, of each direction pair : (a) EW and NS, (b) 'valley-perpendicular' and 'valley-parallel' where horizontal components are rotated along the valley-perpendicular or N 40°, and valley-parallel or N 130° directions, respectively, and (c) 'baz-parallel' and 'baz-perpendicular' where the horizontal components are rotated, for each event, along the event-back-azimuth ("radial" component) and its perpendicular directions (transverse component), respectively. In the figure, global medians of ATANH coherency, of both horizontal components, have been presented along with their respective 85% confidence intervals. Red and blue curves indicate the two horizontal components while 'purple' and 'cyan' indicate the 85% confidence intervals, respectively. It is observed that, whatever the direction pair considered, both horizontal components exhibit fairly similar values of ATANH coherency values, at all distances and frequencies. We also notice that the 85% confidence interval curves almost merge with the global median curves, indicating that 85% of the values in the distribution lie very close to the global median.

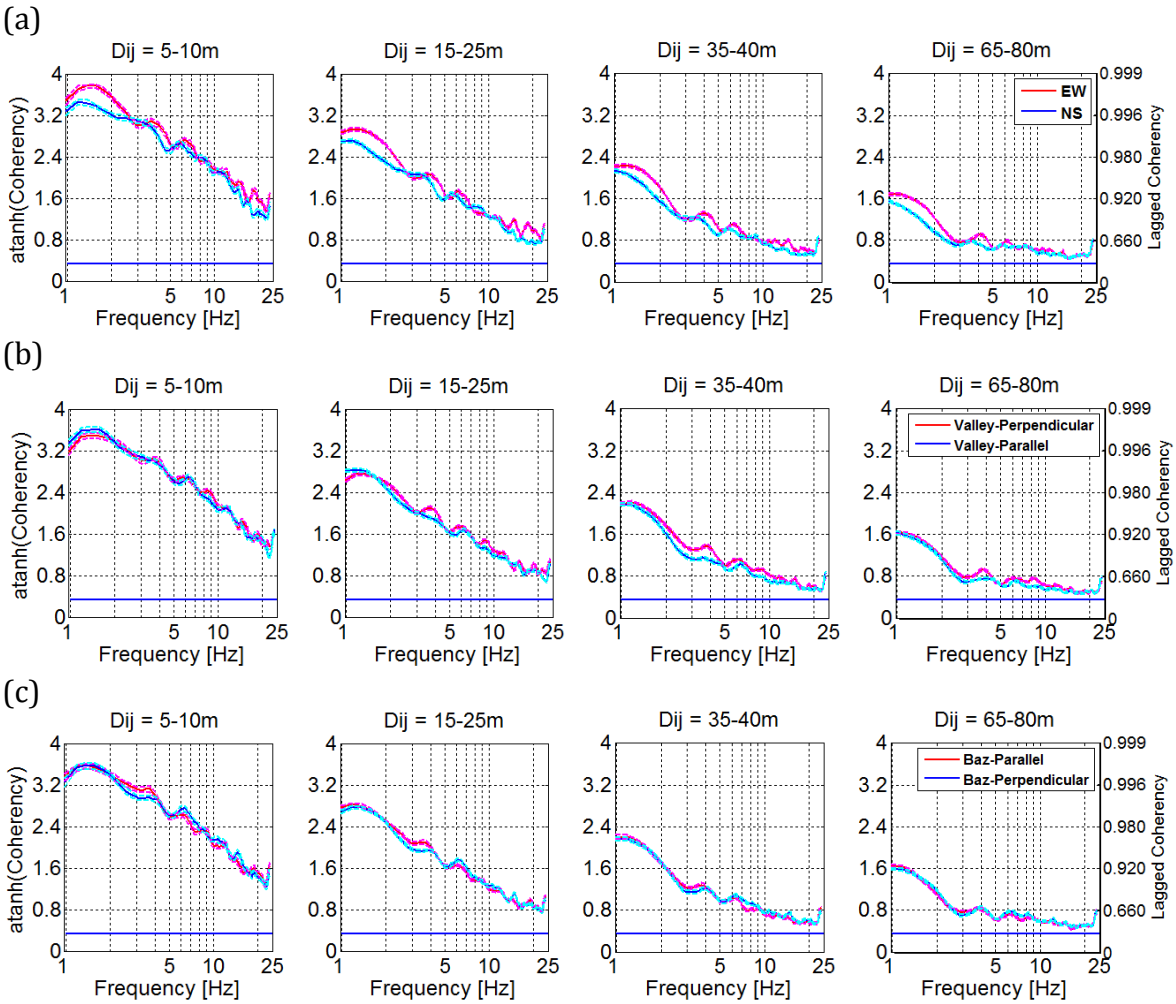

Figure 4.31: Comparison between horizontal components for (a) EW and NS, (b) valley-perpendicular (N40) and valley-parallel (N130), and (c) radial (baz-parallel) and transverse (baz-perpendicular) components of the ground motion, with their respective 85% confidence interval bound. On each figure, red and blue curves indicate the horizontal components and magenta and cyan curves indicate the respective 85% CI intervals. Dij stands for interstation distance. Blue line marks the coherency resolvability threshold.

We now consider one horizontal component from each case (EW, valley-perpendicular and baz-perpendicular components) and compare their respective ATANH coherency estimations in Figure 4.32. No remarkable difference is observed among the global median coherencies estimated from three different cases of horizontal-component orientation. This indicates that the coherency estimates are independent of the orientation of the horizontal component, whether such a component is related to the site or to the source.

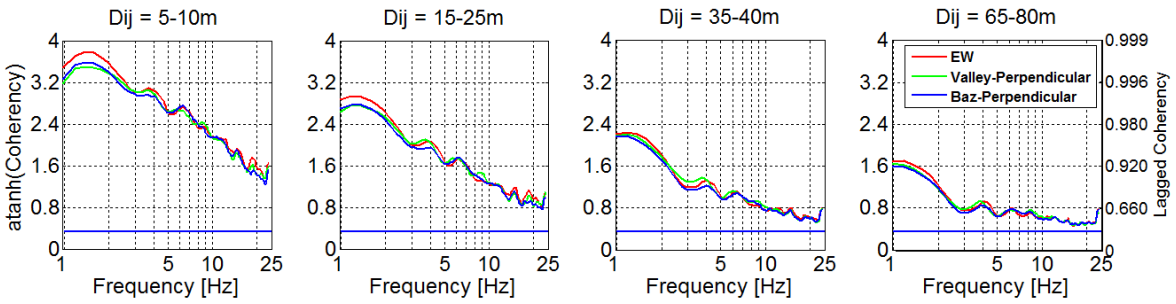

Figure 4.32: Comparison among horizontal components from different orientation definitions. On each figure, red, green and blue curves indicate EW, valley-perpendicular and baz-perpendicular components, respectively. Dij stands for interstation distance. Blue line marks the coherency resolvability threshold.

4.10.5 Variation from the array geometry

From the analysis of single events, the observed anisotropy indicates that there might be a dependence of coherency along the different station-profile branches of the array. Therefore, here we summarize the coherency estimates from all the events by grouping the pairs in five array-branch directions, N 39, N 112, N 183, N 328 and N255, as shown in Figure 4.33 (a). Once again, we consider the time windows selected manually from the rock station records. The horizontal components of the signals have been rotated with respect to the valley-parallel (N130) and valley-perpendicular (N40) axes of the site (Figure 4.33(b)). Median lagged coherency of all the events for five groups of station-pair direction and four interstation distances have been estimated. The global medians and residuals are also evaluated. Finally we present the global median estimates of five groups of station orientation at four interstation distance ranges and for three different components in Figure 4.34. Notably the pairs lying in N39 and N255 directions, which correspond to the two shortest dimension of the valley, have the lowest coherency for both horizontal components and at all distance ranges. Exception is seen at 5-10 m distance range, where median coherency in N39 direction has somewhat intermediate values. The highest coherency values are observed at N328 direction, which lies along the valley-parallel axis.

(a) (b) (c)

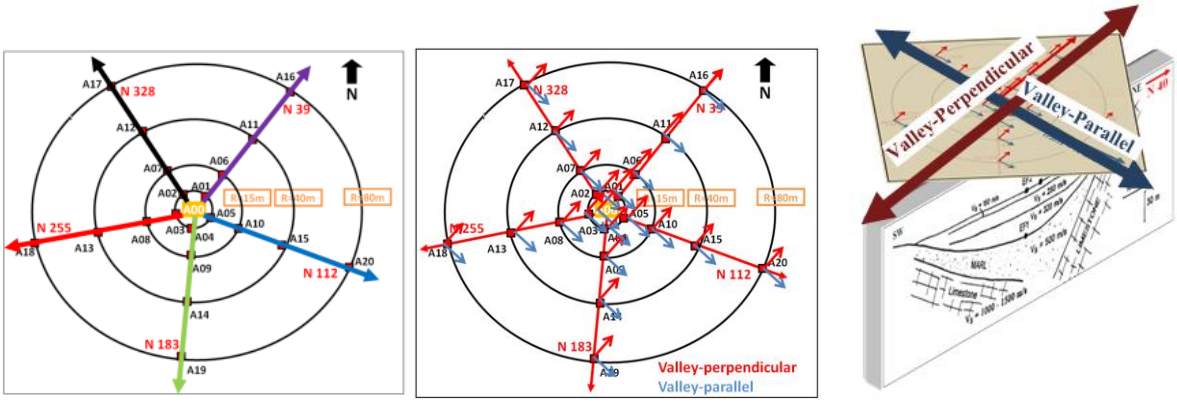

Figure 4.33: Graphic representation of (a) five array-branch directions (arrows in five colors), (b) orientation of horizontal ground-motion components (red small arrows indicate valley perpendicular and blue small arrows indicate valley-parallel orientations) and, (c) valley axes.

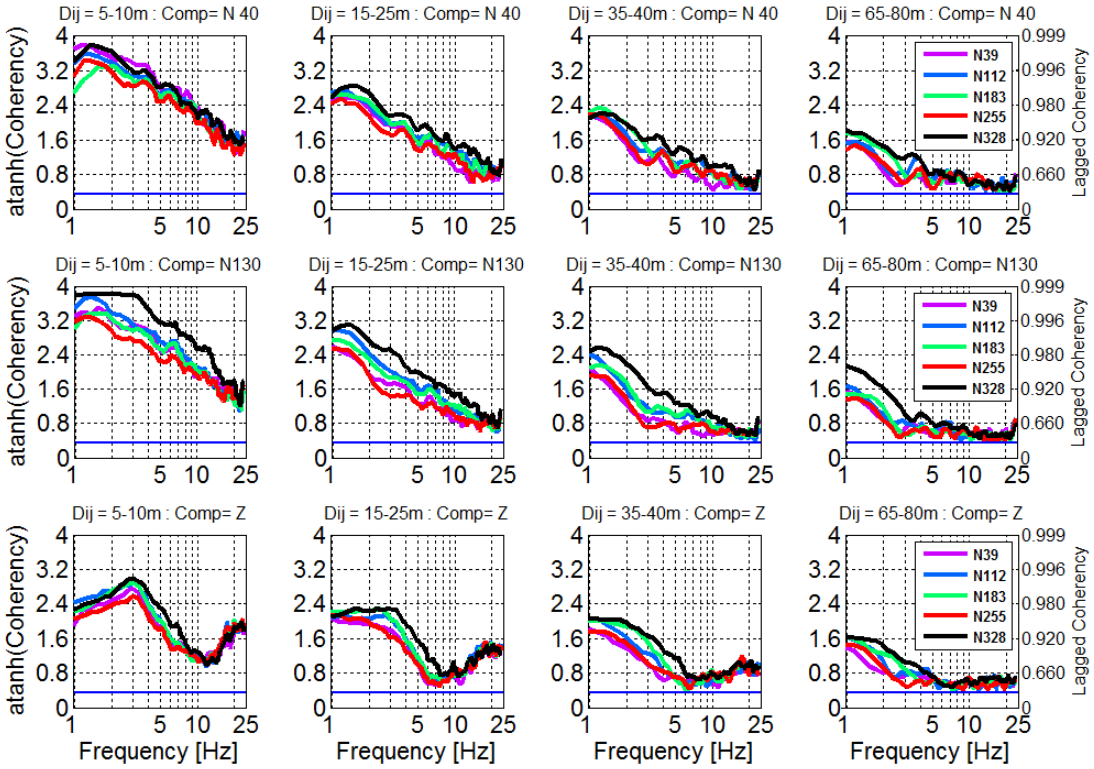

Figure 4.34: Comparison of median coherencies among the five directions of the array-branches for valley-perpendicular (N40), valley-parallel (N130), and vertical components. Dij stands for interstation distance, 'Comp' stands for the component of ground motion. Blue line marks the coherency resolvability threshold.

4.10.6 Variation from the site-axes orientation

In the previous sub-section, the two extreme ranges of the coherency estimates have been observed to be somewhat related to the main orientation of the valley. Therefore, now we group the station pairs in two groups corresponding to the valley principal axes. Note that, the time window and rotation of horizontal components are considered same as in section 4.9.5. Global medians of ATANH coherency from all available station-pairs lying in the valley-perpendicular (N40±10 and N220±10), and valley-parallel (N130±10 and N310±10) directions, have been estimated for the four distance ranges (given in Appendix L.5). The medians (along with 85% CI) for the three different ground motion components are shown in Figure 4.35.

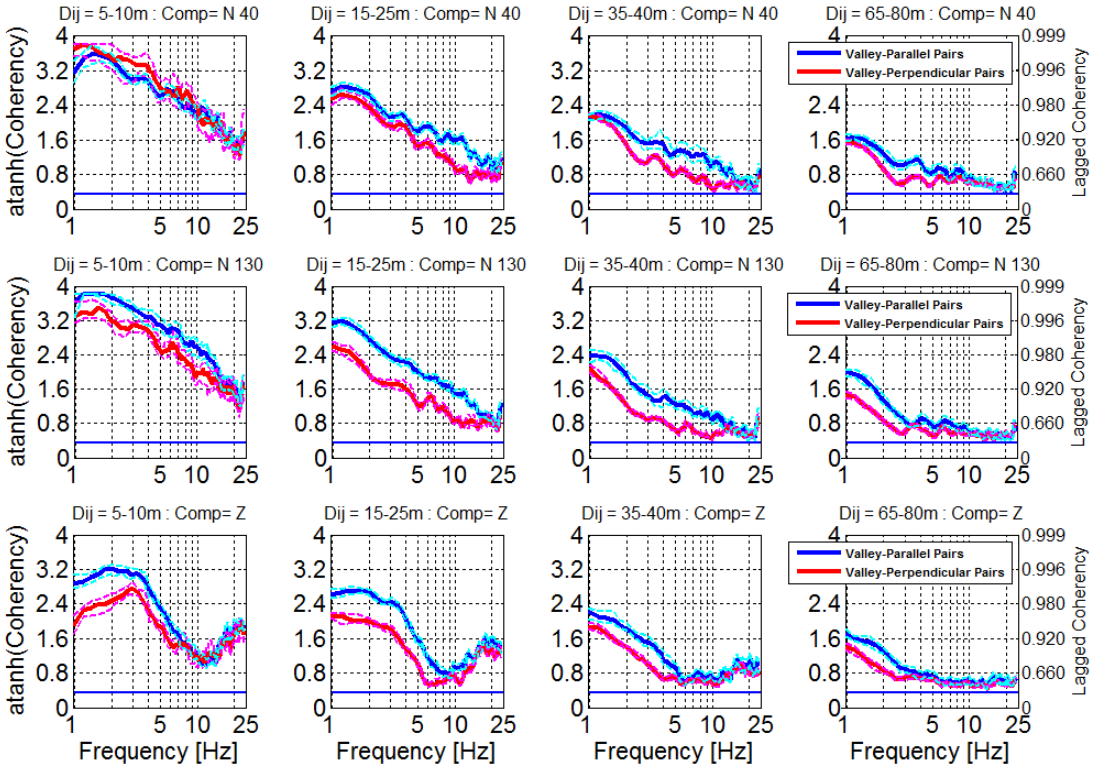

Figure 4.35: Comparison of median coherencies between Valley-perpendicular and Valley-parallel pairs for valley-perpendicular (N40), valley-parallel (N130) and Z components. Magenta and cyan curves indicate the corresponding 85% CI intervals. Dij stands for interstation distance comp stands for the component of ground motion. Blue line marks the coherency resolvability threshold.

Figure 4.35 reveals that coherency estimates are clearly higher for pairs in the valley-parallel direction, as compared to pairs in the valley-perpendicular direction, at all the distance ranges except the 5-10m range. This trend is consistent with observations from the Figure 4.34, where relatively lower coherency values have been observed at approximately valley-perpendicular array-branches (N39 and N255) and higher values at valley-parallel branch (N328). The difference between the coherency estimations along the two valley directions becomes particularly important at separation distances 15-25m and 35-40 m for the horizontal components. At 15-25 m inter-station distance, the coherency values up to 15 Hz frequency varies between a band of 0.66 and 0.92. This remarkable difference is consistent with the predominance of scattered waves propagating across the valley, i.e., along the valley-perpendicular direction: the associated ground motion is almost in phase for valley-parallel station pairs, it will exhibit significant phase changes between valley-perpendicular station pairs.

4.10.7 Variation from source back-azimuth

Now, we consider rotated horizontal components of the signals with respect to the event back-azimuth, which is along baz-parallel and baz-perpendicular directions, and then group the station pairs in the direction parallel (Baz±10 and Baz+180±10) and perpendicular (Baz+90±10 and Baz+270±10) to the event back-azimuth in order to examine the effect of source-direction on the coherency of ground motion. The global median of ATANH coherencies are estimated from all the events for the two groups of station pairs (given in Appendix L.6). Figure 4.36 shows the comparison of the global median estimates at four interstation distance ranges and for horizontal and vertical components in Figure 4.36. No systematic difference has been observed between the coherency estimates of baz-parallel and baz-perpendicular pairs for all three components.

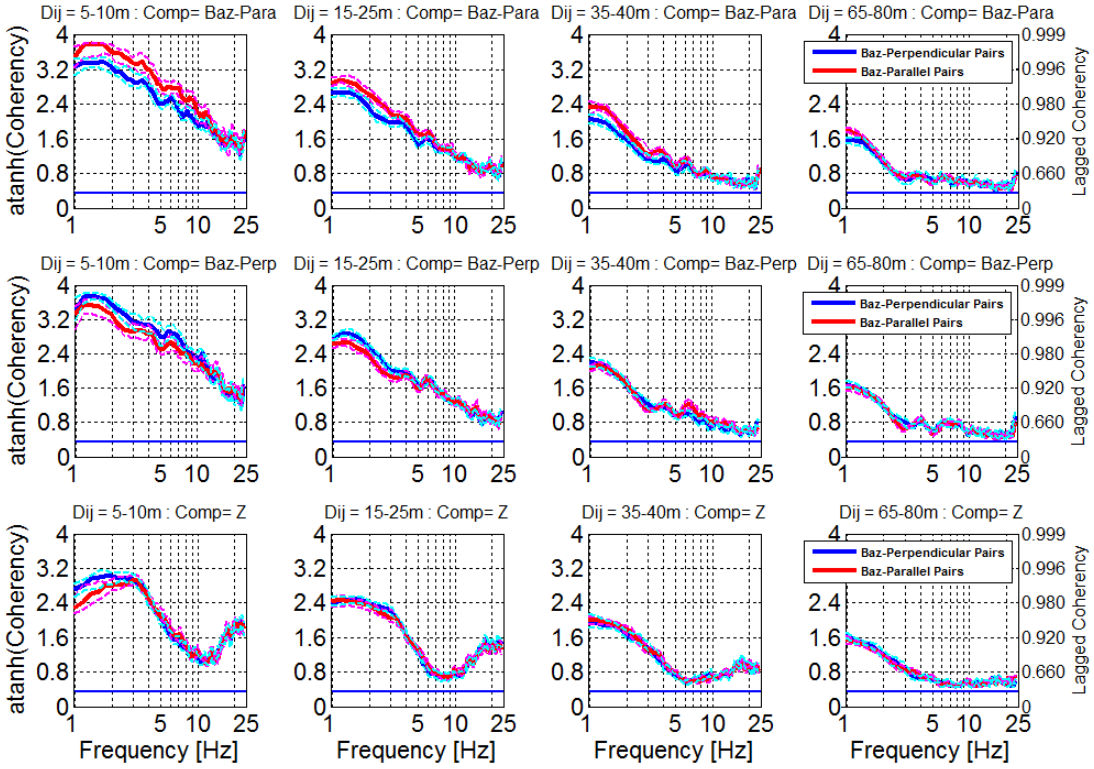

Figure 4.36: Global median estimates of ATANH coherency for the event back-azimuth oriented station pairs. Blue and red curves indicate the baz-perpendicular and baz-parallel pairs, respectively. Magenta and cyan curves indicate the respective 85% CI intervals Dij stands for interstation distance, comp stands for the component of ground motion. Blue line marks the coherency resolvability threshold.

4.10.8 Variability from coda windows

So far we have analysed coherency estimates from the most energetic window of the signal which contains a mix of S-waves with converted body waves and surface waves. In order to compare the coherencies from the pure surface wave windows, we have performed the analysis on the coda part of the signal. The lengths of the coda time windows are exactly as the 'most energetic' time windows (from manual selection) we have considered earlier. The onset of the S-wave and the starting point of the coda are taken as twice the time window length apart. No alignment has been done for both the time series of S- and coda wave windows. Figure 4.37 shows the global medians of ATANH unlagged coherency estimates from S- and coda-wave windows (median and residual plots given in Appendix L.7 and L.8). The results are presented for four interstation distances and the valley-perpendicular and valley parallel (rotated with

respect to N 40 and N 130, respectively), plus the vertical components of the ground motion. We observe that the median ATANH coherency values from coda windows are slightly lower than those of the 'most energetic' windows (Figure 4.37). The scatter of the median also seems to be lower for coda windows (Appendix L.7 and L.8). We then examine the variation of coherency for the station pairs lying along the two principal directions of the valley, as shown in Figure 4.38. Once again, from the analysis of coda windows, we observe the coherency to be roughly lower for the valley-perpendicular pairs at shorter interstation distances; however, the difference of coherency estimates between the two directions is not consistent always.

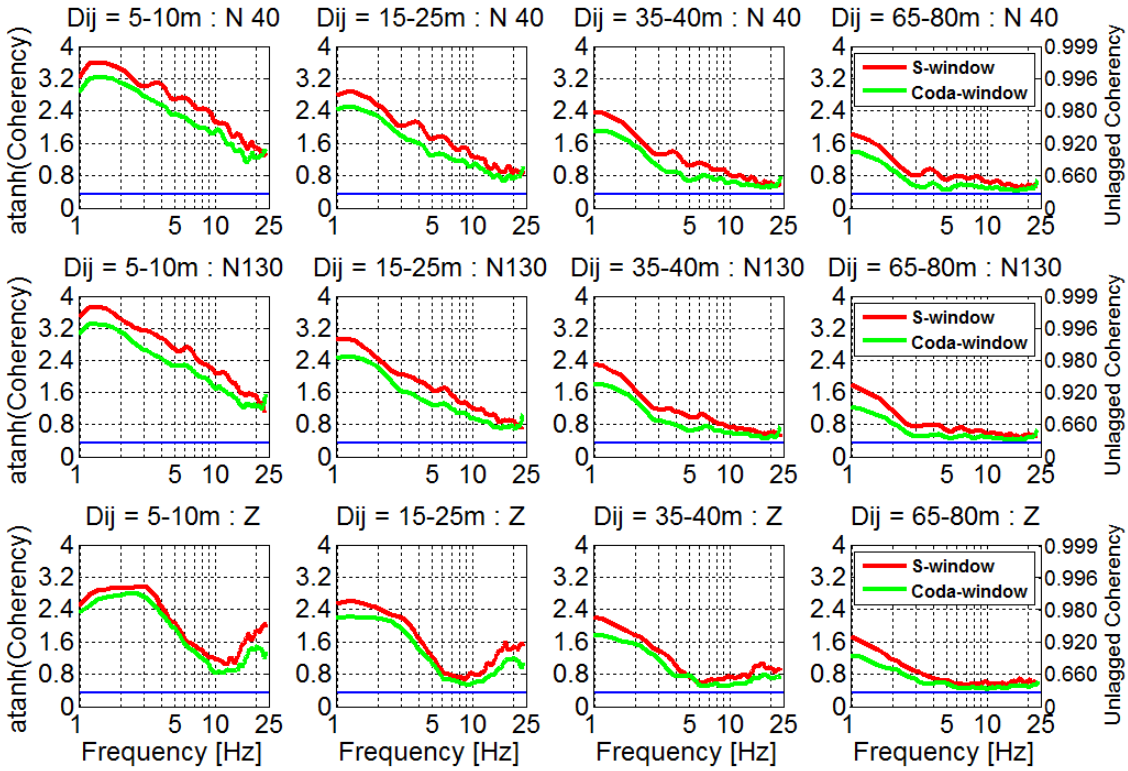

Figure 4.37: Comparison of unlagged ATANH coherency estimations from S- and coda wave windows Dij stands for interstation distance and N40, N130, Z stand for the ground-motion components. Blue line marks the coherency resolvability threshold.

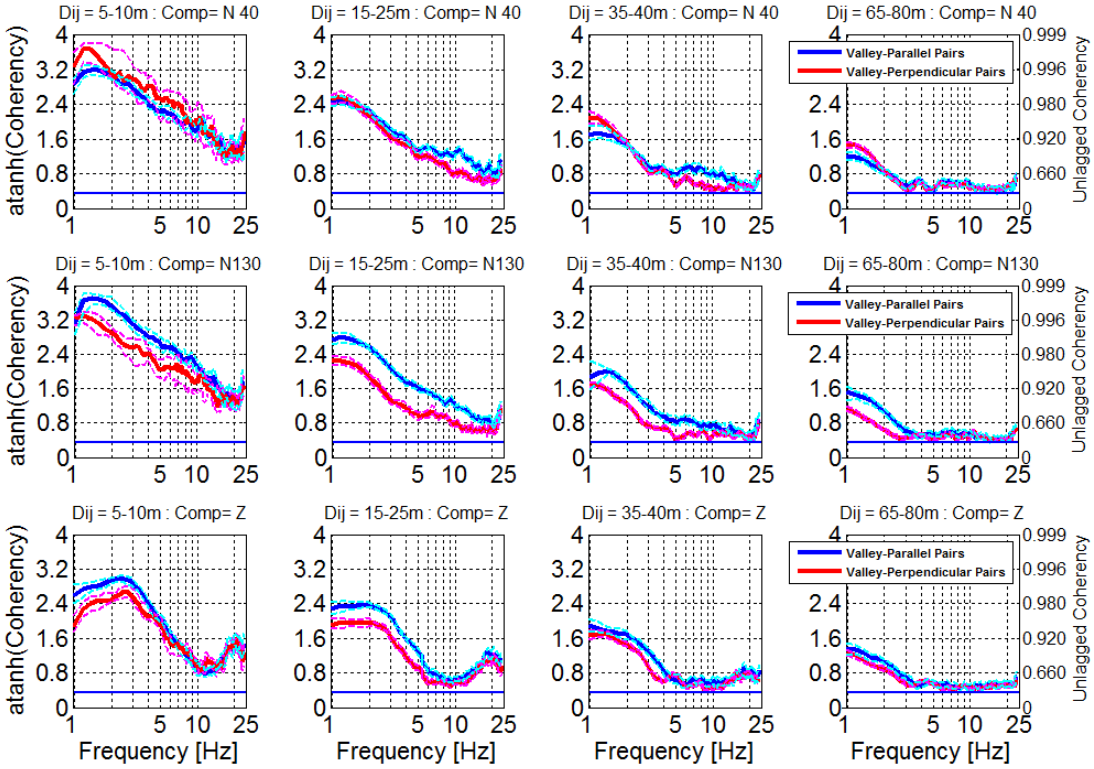

Figure 4.38: Global median estimates of ATANH coherency from coda wave window for the valley-axis oriented station pairs. Blue and red curves indicate the valley-parallel and valley-perpendicular pairs, respectively. Magenta and cyan curves indicate the respective 85% CI intervals Dij stands for interstation distance, comp stands for the component of ground motion. Blue line marks the coherency resolvability threshold.

4.10.9 Magnitude Dependence

In order to investigate the magnitude dependence, the events have been divided into two hypocentral distance groups, 0-60 km (27 events) and 60-200 km (19 events). Figure 4.39 and 4.40 show the residual plots of the ATANH coherency estimations of the Valley-perpendicular component against varying magnitudes, for different interstation distance groups and frequency ranges. No clear magnitude dependence is visible from both the plots. However, the residuals of the distant events (Figure 4.40) seem to have smaller scatter compared to those of nearer events (Figure 4.39). They also decrease with increasing separation distance (Figure 4.40). A possible explanation is that at greater distances the extended source effects diminish and the variability in coherence estimates among different events are mainly caused by the local site properties.

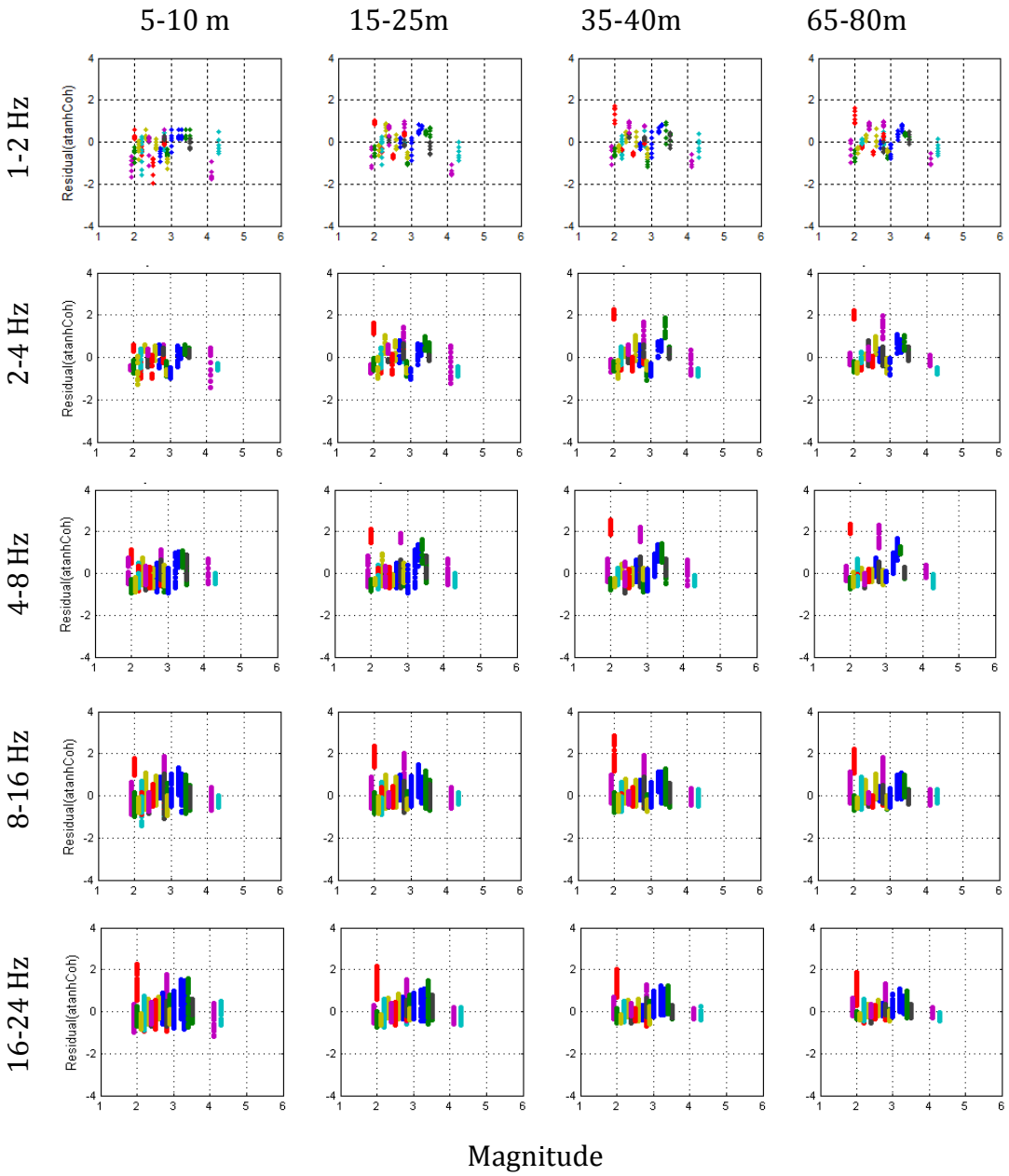

Figure 4.39: Residuals of ATANH coherency curves for the Valley-perpendicular component of the events coming from R_{hyp} 0-60km.

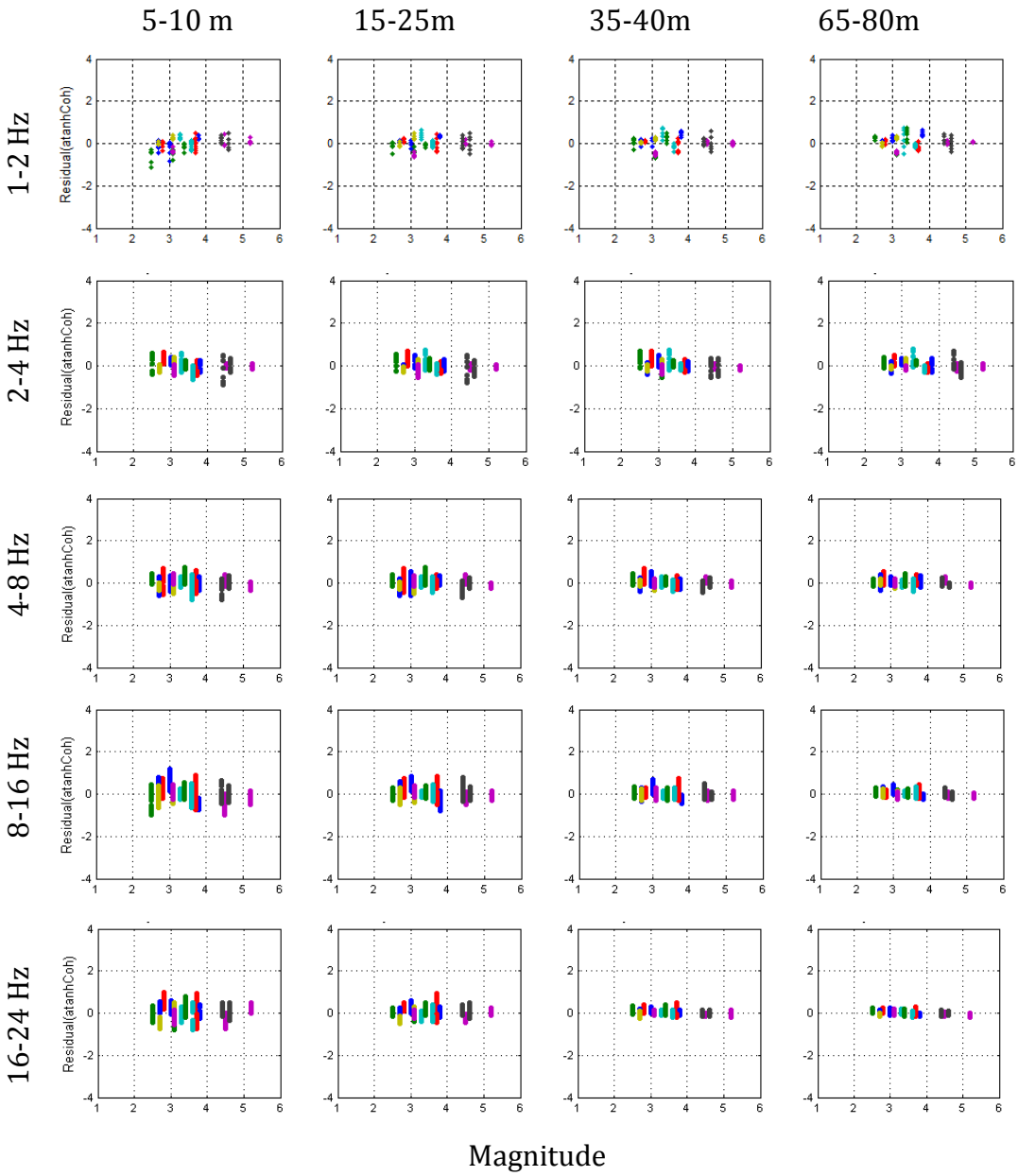

Figure 4.40: Residuals of ATANH coherency curves for the Valley-perpendicular component of the events coming from R_{hyp} 60-200km.

4. 10.10 Hypocentral Distance Dependence

Similarly, the events have been grouped into two magnitude ranges, M 2-3 (23 events) and M 3-5 (23 events) to examine the distance dependence. Like Figure 4.39 and 4.40, the residuals of ATANH coherency values (valley-perpendicular component) of the two magnitude groups of events have been plotted (Figure 4.41, 4.42) against the corresponding hypocentral distances for increasing interstation distances and frequency ranges. A somewhat larger variability is observed for the events located within 50 km hypocentral distance. In near source, the spatial incoherence can be

caused by a combined effect of nearby extended seismic source, source-site complex wave propagation and local soil properties, which in turn may cause larger scatter of the coherency estimates.

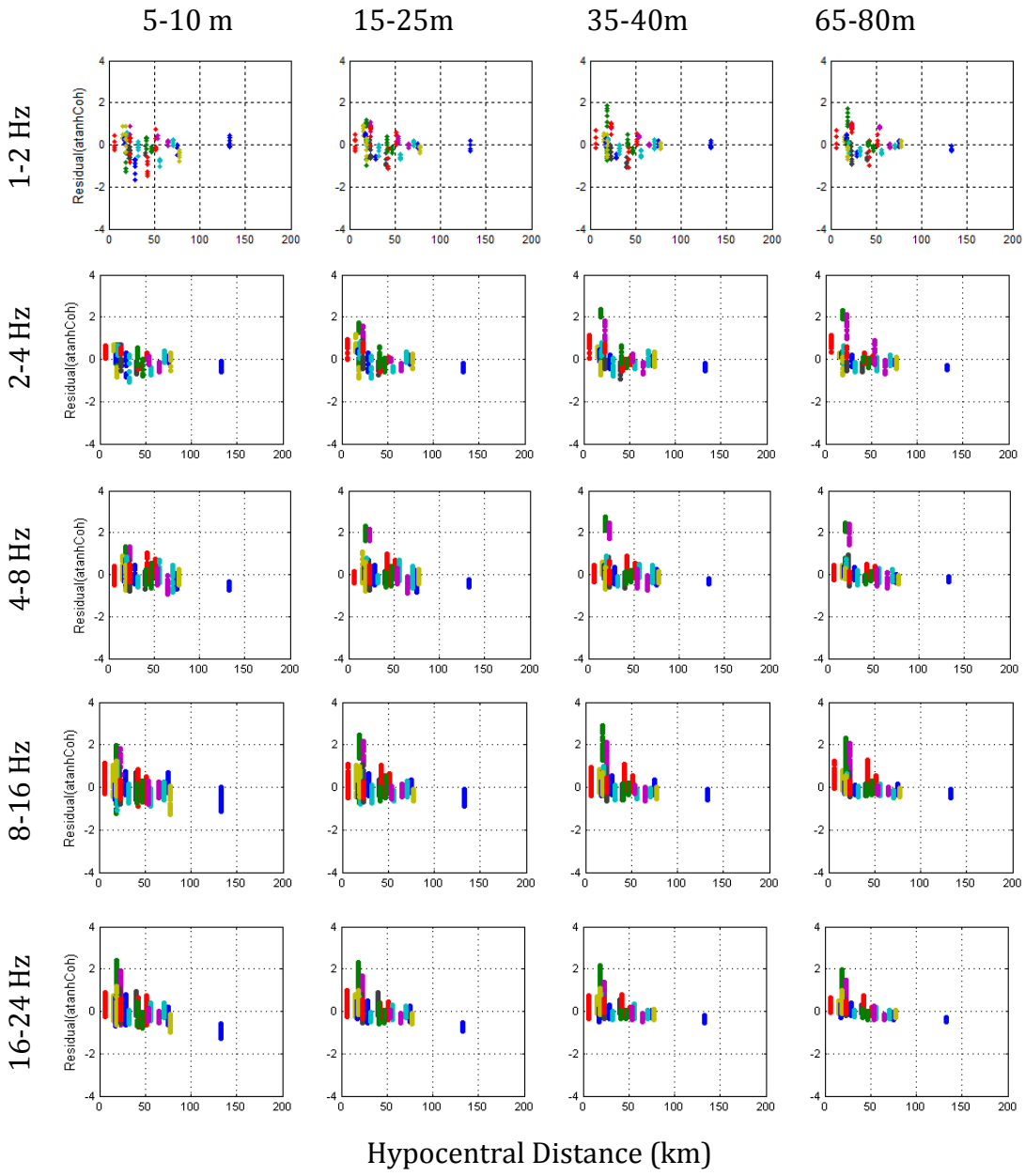

Figure 4.41: Residuals of ATANH coherency curves of the Valley-perpendicular component for the M 2-3 events.

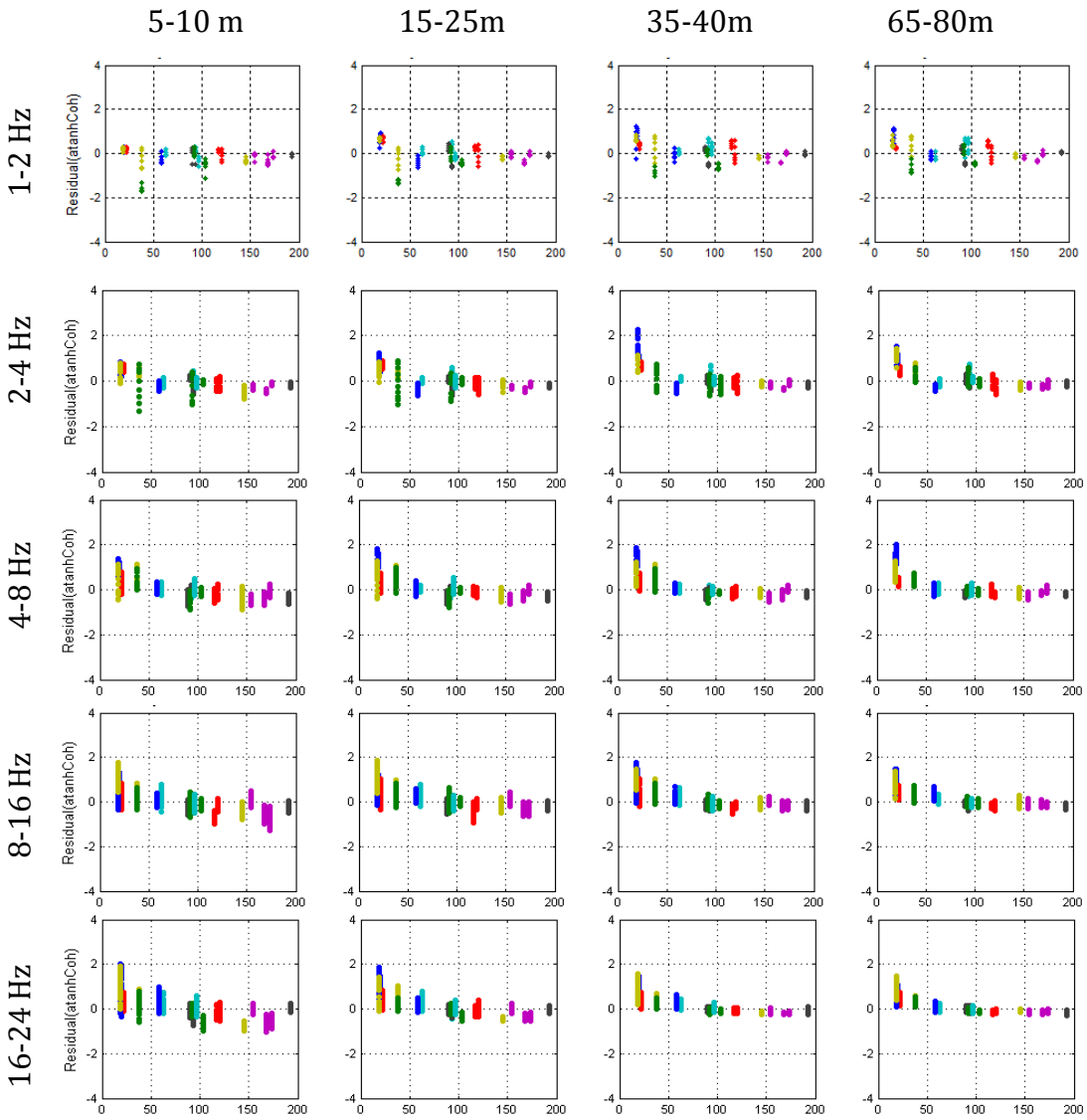

Figure 4.42: Residuals of ATANH coherency curves of the Valley-perpendicular component for the M 3-5 events.

4.11 Discussion and conclusion

The phase variability of the ground motion was investigated by estimating lagged coherency of the Array A data. It is to be noted that in the following section 'lagged coherency' has often been mentioned as 'coherency'. All possible station pairs with interstation distances 5-10, 15-25, 35-40 and 65-80 m have been considered and coherencies between the ground-motions in the pair have been computed from 1 to 25 Hz. A coherency value of 1 indicates perfect correlation while 0 theoretically indicates

no correlation between the ground motions (values below a value of 0.33 cannot however be discussed as they fall below a resolvability threshold).

The most energetic signal windows from the onset of S-wave have been carefully selected from visual inspection of the nearby rock station recordings for coherency estimation. Although, in the literature, coherency is usually estimated from the S-wave window of the signal, for the Argostoli array records it was challenging to clearly identify a time window dominated by S-wave. As a matter of fact, the seismic wave field analysis of array data indicates that the ground motions triggered at Argostoli basin are indeed composed of a complex mixture of different types of waves. A sensitivity test was thus performed to examine the influence of time window selection (manual or automatic selection) on the coherency estimates. We found that the statistics of coherency estimates derived from many events is only weakly sensitive to the selection of time windows, provided that the windows include the most energetic pulses.

In order to summarize the observed tendency of coherency estimated from all the pairs of an event and then from all the events, the median of the results were obtained and compared for different cases. For the statistical analyses a $\tanh^{-1}$ transformation was applied to the results to produce approximately normally distributed data about the median. As expected, spatial coherency estimates exhibit decay with increasing frequency and interstation distance. The frequency dependence seems more important and causes higher variability at larger interstation distances. No dependence of lagged coherency has been observed on the orientation of the considered horizontal ground-motion component. Whatever the component selection (source related: radial or transverse, and site related: parallel or perpendicular to valley axis), the two horizontal components exhibit similar behavior. However, the vertical component has a somewhat different trend, often including an increasing coherency at high frequencies. Slight or no systematic dependence of coherency was observed on the magnitude, back-azimuth or site-to-source distance of the event.

The key result of the sensitivity analysis is the variation of coherency estimates as a function of station-pair orientation. Specific coherency estimates along the five different directions of the array-branches yielded statistically different results. A careful

investigation showed that the largest coherency is observed for station pairs oriented parallel to the valley axis while the lowest one corresponds to the perpendicular direction (i.e. along the shortest valley cross-section). Difference between the coherency estimates along two valley directions is particularly important at separation distances 15-25m and 35-40 m. At 15-25 m inter-station distances and below 15 Hz frequency, the coherency values considerably vary between 0.66 and 0.92. Bearing in mind our results from the wave field analysis by MUSIQUE, we consider this difference as very consistent with the predominant propagation direction of locally scattered waves, which basically cross the valley along its shorter horizontal dimension: such waves have similar phases for valley-parallel pairs, while their phases are rapidly changing in the valley-perpendicular (i.e. edge) direction, especially as the wavelengths are comparable to the array size. The incoherence effect in this direction could be related to the wave scattering at the basin edges. In the light of these observations, we may draw our most important conclusion that the spatial lagged coherency estimates seem to be controlled by site dependent characteristics: the velocity profile of course, which controls the wavelength of surface waves, and also the geometry, which controls the predominant propagation direction of scattered waves.

Final Conclusions

Distance dependence of ground-motion variability from numerical simulation

In this study we have analyzed the within-event component (ϕ) of spatial variability "sigma" from numerical simulation of ground motions in order to complement real data studies and to investigate the influence of different source parameters on the resulting ground-motion variability. Ground-motion (up to 3 Hz), represented by the PGV, was computed from various kinematic source models and Green's functions was computed for 1D-layered velocity models. Hence, our ϕ estimations are not only 'single-station' but also 'single-path'. For simplicity we have limited our study to vertical strike-slip faults in a narrow magnitude range ($\sim 6 < Mw < \sim 7$). It is to be noted that our study does not focus on the absolute value of ground motion, but only on its variability and the overall observed trends of the ground motion variability have been related to global source features (rupture directivity, depth of the main slip area).

Our results suggest that the within-event variability ϕ significantly depends on the rupture type, with unilateral ruptures resulting in larger ϕ values than bilateral ruptures, especially in the near source region. At short distances ($< \sim 10$ km) most of the stations are located in the 0°-30° azimuth region of the epicentre and thus associated with a strong PGV amplification due to forward directivity effects. The large proportion of high peaked PGV values results in large variability (ϕ) at shorter distances. Far away from the source (~ 100 km), this dependency vanishes and ϕ is steady ($\phi \sim 0.3$-0.5) for both kind of ruptures. Thus the distance-dependency of ϕ represents two main behaviors: (1) an increases with distance for bilateral events and (2) a decrease with distance for unilateral events. Therefore, we conceive that prior knowledge about the rupture direction and type may contribute in refining the estimates of ϕ for a given earthquake scenario. Besides the large variability we obtained at short distance for unilateral ruptures may, however, be strongly reduced if azimuth is considered as a predictor. The radiation pattern effect, that is clearly observed in our synthetics, might be limited to lower frequency range ($<\sim 1$ Hz) in real velocity structures. Thus, the strong impact of directivity effects on the ϕ values computed from our synthetics may

be weaker in the case of real earthquakes. Interestingly, the range of within-event variability values provided by our numerical simulations in far field is consistent with the 'single station' within-event variability (ϕ_{ss}) estimates obtained from real data by Rodriguez-Marek et al., 2013 ($\phi \sim 0.4$ at 100 km).

Seismic wave field analysis from dense array data

The seismic wave field generated in the basin of Argostoli was analyzed from a subset of events recorded by two dense arrays. The 21-element dense array, Array A, was located between the center and the southwest edge of the basin and the data was analyzed based on a carefully selected subset of 46 events (magnitude range M 2-5, distance range 5–200 km, equally distributed back-azimuths). Array B, a smaller 10-element array, located near the northeast edge, was analyzed for 16 events. A quaternion-MUSIC algorithm, MUSIQUE, was used to process the seismic array data. MUSIQUE allows the simultaneous use of all three components of the records and extraction of the apparent propagation characteristics of the dominant waves, slowness and back-azimuth. Furthermore, it enables the characterization of Love and Rayleigh surface waves as well as identification of retrograde and prograde particle motion of the latter in the seismic wave field. This is of particular importance for a small and shallow basin like Argostoli where locally generated surface waves play an important role in modifying earthquake ground motion.

The results from array analysis clearly indicate significant scattering waves corresponding to 2D or 3D effects beyond the fundamental frequency (~1.5 Hz) of the valley. The identified back-azimuth distribution from Array A shows that, whatever the back-azimuth of the earthquake, local scattering comes primarily from the south-west edge (N210 -N240). Love waves are predominant in the scattered wave field at low frequencies (< 2.5 Hz) whereas Rayleigh waves can be seen over a broad range of frequencies, but dominating only in a relatively narrow band. The summary of energy repartition from all 46 events reveal that about 60% of the total energy between 1.5 to 2.5 Hz frequency is carried by Love waves while Rayleigh waves carry about 70% and 50% of the total energy at 3-4 Hz and 5-6 Hz frequencies, respectively. Likewise, the results from Array B data exhibit a relatively higher proportion of Love wave energy (50%) at about 1.5-2.5 Hz frequency and an invariably larger dominance of Rayleigh

waves at frequencies above ~2.5 Hz containing about 40-50% of the energy. However, this time the identified waves seem to arrive more from the northeast edge (N60 -N 120) of the valley. The results from both arrays show that at frequencies lower than the fundamental resonance frequency of the site, both Rayleigh and Love waves impinge the array from a range of back-azimuths (N30 - N90), which manifests influence of probable regional diffractors located outside the Argostoli basin.

Overall, from the analysis of both arrays about 80% of the total energy, within the frequency range approximately 1.5 to 6 Hz, could be characterized as Rayleigh or Love surface waves. The dispersion estimates obtained from the analyses of two array data show that the fundamental mode (at 1-2.5 Hz) is evidently dominated by Love waves, while there is also some contribution (at 1.5-3 Hz) from the less energetic prograde Rayleigh waves. The probable dispersion curve of the first harmonic mode (at 3-4 Hz) could be attributed to the retrograde Rayleigh waves. These observations can be explained by the velocity structure beneath the arrays and related frequency of Rayleigh and Love Airy phases. The estimated standard spectral ratios at two stations within the two array locations demonstrate that there is an excellent consistency between the dominance of the surface wave type identified in the wave field and the site amplification. Alongside, the characterization of wave types from MUSIQUE analysis shows that throughout the duration of the event, all signal time windows include complex mixtures of different types of waves. The scattered waves apparently dominate the wave field composition of the most energetic part of the signal, even in the earlier time segments where arrival of body waves are accompanied by significant proportion of surface waves.

Spatial coherency analysis from seismic array data

The phase variability of the ground motion was investigated by estimating lagged coherency of the Array-A data. It is to be noted that in the following paragraphs ‘lagged coherency’ has often been mentioned as ‘coherency’. All possible station pairs with interstation distance up to 80 m have been considered and coherencies between the ground-motions in the pair have been computed between 1 to 25 Hz. A coherency value of 1 indicates perfect correlation while 0 indicates no correlation between the ground

motions. It is however impossible in practical cases to discuss coherency values below a minimum threshold of 0.33 as they fall below a resolvability threshold.

The most energetic signal windows from the onset of S-wave have been carefully selected from visual inspection of the nearby rock station recordings for coherency estimation. Though in the literature coherency is usually estimated from the S-wave window of the signal, for the Argostoli array records it was challenging to clearly identify a time window dominated by S-wave only. As a matter of fact, the seismic wave field analysis of array data indicates that the ground motions triggered at Argostoli basin are indeed composed of a complex mixture of different types of waves. A sensitivity test was, however, performed to examine the influence of time window selection on the coherency estimates. Thereupon, an automatic procedure based on the Arias Intensity estimation of the time window around the most energetic signal was adopted and the selected time windows were used for the evaluation of coherency. The results of the test show that the statistics of coherency estimates derived from many events is less sensitive to the variation of time window selection as long as the windows include the most energetic pulses. Therefore, the time windows selected by visual inspection was used for the entire coherency analysis.

In order to summarize the observed tendency of coherency estimated from all the pairs of an event and then from all the events, the median of the results were obtained and compared in different cases. For the statistical analyses a $\tanh^{-1}$ transformation was applied to the results to produce approximately normally distributed data around the median. In general, spatial coherency estimates from horizontal components exhibit decays with frequency and interstation distance. The frequency dependence seems more important and causes higher variability at larger interstation distances. However, estimations on the vertical component exhibit larger coherency at some higher frequencies. No dependence of lagged coherency has been observed on the orientation of ground-motion component. Similar trends were systematically observed, on all kinds of orthogonal components, even when their orientation is related to source back-azimuth, site principal directions or random (e.g. NS and EW). Slight or no systematic dependence of coherency was observed on the magnitude, back-azimuth or site-to-

source distance of the event, at least for the range of magnitudes investigated here (M≤ 5).

Nevertheless, coherency estimates exhibit robust, consistent variations as a function of the orientation (azimuth) of station pairs: they vary when station pairs are aligned along the five different directions of the array-branches. Larger coherency is systematically observed when the orientation of station pairs is parallel to the valley length (i.e., NW-SE) as compared to the perpendicular direction (i.e. valley-edge direction, NE-SW). Such a difference between the two valley directions is particularly important at separation distances 15-25m and 35-40 m. At 15-25 m inter-station distances and up to 15 Hz frequency, the coherency values considerably vary between 0.66 (valley perpendicular direction) and 0.92 (valley parallel direction). This robust observation proves very consistent with MUSIQUE results showing the predominance of scattered surface waves propagating SW-NE in the wave field: as such waves seem to be in phase along valley-parallel pairs, and out of phase along valley-perpendicular (i.e. edge) direction. Thus, one can easily expect a larger coherency value for valley-parallel pairs. In the light of these observations our most important finding is that the spatial lagged coherency is primarily controlled by site dependent geometrical characteristics.

Perspectives

The distance dependency of within-event component of the aleatory variability “sigma”, observed from our numerical study brings some light on the nature of the variability and its apparent connection with some major source features. However, due to the small number of considered source models, the source variability may be underestimated, especially in case of the unilateral events. Therefore, inclusion of additional source models may contribute to improve the observed overall trends. Considering additional unilateral rupture models and fault type would definitely strengthen the conclusions on the role of directivity effects.

The characterization of wave types and their relative energy contributions, along with the extraction of apparent velocity and azimuth, in the seismic wave field through MUSIQUE algorithm seems very promising. In the next step, these results could be utilized to explain spatial variation of ground motion related to each wave type observed from coherency analysis. The identified wave types and polarization parameters could also be linked to the ground velocity model and geological structure of the valley in order to better understand the physical causes underlying the ground motion variability. Finally, use of recent promising three-component analysis algorithm (Marano et al., 2012) that allows wave polarization estimation even in case of simultaneous multiple waves may help improving accuracy of wave parameter estimates.

Our results from the estimation of spatial coherency indicate its dependence on site geometrical characteristics. This observation opens up new insights and possibilities for future studies. It would be of great interest to perform similar analysis for the seismic array data obtained from a hard-rock site. As such we could examine the spatial variation of ground motion in rock site condition and compare it with the tendencies observed from valley recordings. The current work on the spatial coherency would naturally be followed up by comparing the median coherency curves with the few available parametric models which include the short distance ranges considered in this study. Another interesting perspective would be to estimate unlagged coherency of the ground motions for the time windows and frequency ranges used in the MUSIQUE

analysis and then relate the results with the wave type and ground velocity structure. Finally, one more scientific question that might be of interest is, to what extent the observed ground motion variability would be affected when subjected to near-field condition, that is, in case of larger magnitude events that rupture the fault segment. One way to deal with this issue would be instrumenting a site near a large active fault with permanent dense seismic arrays and then perform similar analyses, which is totally dependent on probable earthquake occurrence on the fault in near future. However, another possibility is numerical simulation of ground motion for larger magnitude events using a representative site and the same dense array network. In fact, some of these issues can be tackled with the existing data set and the relevant work is already on the way.

Bibliography

Abrahamson, N. A. (1985). Estimation of Seismic Wave Coherency and Rupture Velocity Using the SMART-1 Strong Motion Array Recordings. *EERC Report No. EERC/UCB/85-02, Earthquake Engineering Research Center, University of California*.

Abrahamson, N. A. (1988). Statistical Properties of Peak Ground Accelerations Recorded by the Smart 1 Array. *Bulletin of the Seismological Society of America, 78*, 26-41.

Abrahamson, N. A. (1992a). Spatial Variation of Earthquake Ground Motion for Application to Soil-Structure Interaction. *Electrical Power Research Institute, Rpt. No. EPRI TR-100463, Tier 1*.

Abrahamson, N. A. (1992b). Spatial Variation of Earthquake Ground Motion for Application to Soil-Structure Interaction. *Electrical Power Research Institute, Rpt. No. EPRI TR-100463, Tier 2*.

Abrahamson, N. A. (1992c). Generation of Spatially Incoherent Strong Motion Time Histories. *Proceedings of Tenth World Conference on Earthquake Engineering, Madrid, Spain*.

Abrahamson, N. A. (1993). Spatial Variation of Multiple Support Inputs. *Proceedings of the First U.S. Seminar on Seismic Evaluation and Retrofit of Steel Bridges, University of California at Berkeley, Department of Civil Engineering and California Department of Transportation, Division of Structures, San Francisco*.

Abrahamson, N. A. (2007). Program on Technology Innovation: Effects of Spatial Incoherence on Seismic Ground Motions. *EPRI, Palo Alto, CA: 2007. 1015110.*

Abrahamson, N. A., Schneider, J. F., & Stepp, J. C. (1991a). Empirical Spatial Coherency Functions for Applications to Soil-Structure Interaction Analyses. *Earthquake Spectra, 7*(1-27).

Abrahamson, N. A., Schneider, J. F., & Stepp, J. C. (1991b). Spatial coherency of shear waves from the Lotung, Taiwan large-scale seismic test. *Structural Safety, 10*(1-3), 145-162.

Al-Atik, L., Abrahamson, N. A., & Kuehn, F. (2010). The variability of ground-motion prediction models and its components. *Seismological Research Letter, 81*, 794 – 801.

Almendros, J., J. M. Ibanez, G. A., & Blanco, M. J. (2000). A double seismic antenna experiment at Teide Volcano: existence of local seismicity and lack of evidences of volcanic tremors. *J. Volcanol Geoth. Res., 103*, 439-462.

Anderson, J. G., & Brune, J. N. (1999). Probabilistic seismic hazard assessment without the ergodic assumption. *Seismological Research Letters, 70*(1), 19-28.

Anzidei, M., Baldi, P. C., & Riguzzi, F. (1996). Repeated GPS surveys across the Ionian Sea: evidence of crustal deformations. *Geophysical Journal International, 127*(257–267).

Archuleta, R. J. (1984). A faulting model for the 1979 Imperial Valley earthquake. *J. Geophys. Res., 89*(B6), 4559-4585.

Asano, K., & Iwata, T. (2006). Source process and near-source ground motions of the 2005 West Off Fukuoka Prefecture earthquake. *Earth Planets Space, 58*, 93-98.

Asten, M. W., & Henstridge, J. D. (1984). Array estimators and the use of microseisms for reconnaissance of sedimentary basins. *Geophysics, 49*(11), 1828-1837.

Papazachos, B. & Papazachou, K. (2003). *The earthquakes of Greece.* Ziti Publ. Co., Thessaloniki, Greece, 286 pp.

Bard, P.-Y., & Bouchon, M. (1980). The seismic response of sediment-filled valleys. Part 1. The case of incident SH waves. *Bulletin of the Seismological Society of America, 70*(4), 1263-1286.

Bear, L. K., Pavlis, G. L., & Bokelmann, G. H. (1999). Multi-wavelet analysis of three-component seismic arrays: Application to measure effective anisotropy at Pinon Flats, California. *Bulletin of the Seismological Society of America, 89*(3), 693-705.

Bernard, P., & Herrero, A. (1994). Slip heterogeneity, body-wave spectra, and directivity of earthquake ruptures. *Annali Di Geofisica XXXVII*, 1679-1690.

Bindi, D., Parolai, S. C., & Rovelli, A. (2009). Site amplifications observed in the Gubbio Basin, Central Italy: hints for lateral propagation effects. *Bulletin of the Seismological Society of America, 99*(2A), 741-760.

Boissieres, H., & Vanmarcke, E. (1995a). Estimation of lags for a seismograph array: wave propagation and composite correlation. *Soil Dynamics and Earthquake Engineering, 14*, 5-22.

Boissieres, H., & Vanmarcke, E. (1995b). Spatial correlation of earthquake ground motion: non-parametric estimation. *Soil Dynamics and Earthquake Engineering, 14*, 23-31.

Bokelmann, G. H., & Baisch, S. (1999, February). Nature of narrow-band signals at 2.083 Hz. *Bulletin of the Seismological Society of America, 89*, 156-164.

Bokelmann, G. H., & Baisch, S. (1999). Nature of narrow-band signals at 2.083 Hz. *Bulletin of the Seismological Society of America, 89*(1), 156-164.

Bolt, B., Loh, C. P., & Yeh, Y. (1982). *Preliminary report on the SMART-1 strong motion array in Taiwan.* Tech. rep., Engineering Research Center Report No. UCB/EERC-82/13, Univ of California, Berkeley CA.

Bommer, J., & Abrahamson, N. A. (2006). Why do modern probabilistic seismic-hazard analyses often lead to increased hazard estimates? *Bull. Seismol. Soc. Am., 96*, 1967-1977.

Boore, D. M., Lamprey, J. W., & Abrahamson, N. A. (2006). Orientation-independent measures of ground motion. *Bull. Seismol. Soc. Am., 96*(4 A), 1502–1511.

Bouchon, M. (1981). A simple method to calculate Green's functions for elastic layered media. *Bull. Seismol. Soc. Am., 71*(4), 959–971.

Boxberger, T., Bindi, D., Cara, F., Cornou, C., Cultrera, G., Cushing, M., Dechamp, A., Delavaud, E., Di Giulio, G., Guyonnet-Benaize, C., Hollender, F., Imtiaz, A., Kuperminc, M., Parolai, S., Savvaidis, A., Theodoulidis, N., Vassallo, M., & Bard, P.-Y.(2014, 24-29 August). Effect of the underground structure on the wave-field: the high-resolution experiment in Cephalonia Island (Greece). Second European Conference on Earthquake Engineering and Seismology (2ECEES), Istanbul, Turkey.

Bycroft, G. N. (1980). *E1 Centro California differential ground motion array.* Tech. rep., U.S. Geol. Surv., Open-File, Rept. 80-919, 1-13.

Capon, J. (1969). High-resolution frequency-wavenumber spectrum analysis. *Proc. IEEE, 57*, 1408–1418.

Caserta, A., Marra, A., & Bellucci, F. (1998). Strong diffraction effects at the edge of the Colfiorito, Central I taly, basin. *Second International Symposium on the Effects of Surface Geology on Seismic Motion, Balkema, Yokohama, 2*, 435-440.

Causse, M., Chaljub, E. C., & Bard, P.-Y. (2009). New approach for coupling k-2 and empirical Green's functions: Application to the blind prediction of broadband ground-motion in the Grenoble basin. *Geophys. J. Int., 179*, 1627-1644.

Causse, M., Cotton, F., & Mai, M. (2010). Constraining the roughness degree of slip heterogeneity. *Journal of Geophysical Research*.

Chávez-García, F., Stephenson, W., & Rodríguez, M. (1999, June). Lateral Propagation Effects Observed at Parkway, New Zealand. A Case History to Compare 1D versus 2D Site Effects. *Bulletin of the Seismological Society of America, 89*(3), 718-732.

Chávez-García, F., Stephenson, W., & Rodríguez, M. (1999). Lateral propagation effects observed at Parkway, New Zealand. A case of history to compare 1D versus 2D site effects. *Bull Seismol Soc Am, 89*(3), 718–732.

Chen, M., & Harichandran, R. (2001). Response of an Earth Dam to Spatially Varying Earthquake Ground Motion. *." J. Eng. Mech, 127*(9), 932–939.

Chen, Y.-H., & Tsai, C.-C. P. (2002). A new method for estimation of the attenuation relationship with variance components. *Bull. Seismol. Soc. Am., 92*(5), 1984–1991.

Cho, H., Hu, J. K., & Dunham, E. M. (2010). Frequency dependence of radiation patterns and directivity effects in ground motion from earthquakes on rough faults. *Am. Geophys. Union, Fall Meeting 2010. abstract S51A:1914*.

Cirella, A., & Spudich, P. (2013). Aleatory and epistemic uncertainties in interpolated ground motions - Example from the Kashiwazaki-Kariwa Nuclear Powaer Plant recordings of the July 16, 2007, Niigata-ken Chuetsu-oki, Japan, earthquake. *Geophysical Research Abstract (15), EGU2013-5932*.

Cornou, C., Bard, P.-Y., & Dietrich, M. (2003a). Contribution of dense array analysis to the identification and quantification of basin-edge induced waves, part I: Methodology. *Bull. seism. Soc. Am., 93*, 2604–2623.

Cornou, C., Bard, P.-Y., & Dietrich, M. (2003b). Contribution of dense array analysis to basin-edge-induced waves identification and quantification, part II: Application to Grenoble basin, French Alps. *Bull. seism. Soc. Am., 93*(6), 2624–2648.

Cornou, C., Ohrnberger, M. B., & Bard, P.-Y. (2006, 30 August - 01 September). Using ambient noise array techniques for site characterisation: results from an international benchmark. *Proc. 3rd Int. Symp. on the Effects of Surface Geology on Seismic Motion, Grenoble*.

Coutant, O. (1989). *Program of numerical Simulation AXITRA.* Tech. rep., Research Reports LGIT, Université Joseph Fourier, Grenoble (in French).

Cultrera, G., Andreou, T., Bard, P.-Y., Boxberger, T., Cara, F., Cornou, C., Di Giulio, G., Hollender, F., Imtiaz, A., Kementzetzidou, D., Makra, K., Savvaidis, A., Theodoulidis, N. & The Argostoli Team (2014, 24-29 August). The Argostoli (Cephalonia, Greece) experiment. *Second European Conference on Earthquake Engineering and Seismology (2ECEES), Istanbul, Turkey*.

Dainty, A. M., & Toksöz, M. N. (1990). Array analysis of seismic scattering. *Bulletin of the Seismological Society of America, 80*(6B), 2242-2260.

Der Kiureghian, A. (1996). A Coherency Model for Spatially Varying Ground Motions. *Earthquake Engineering and Structural Dynamics, 25*, 99-111.

Edwards, B., & Fäh, D. (2013). A stochastic ground motion model for Switzerland. *Bull. Seismol. Soc. Am., 103*.

Enochson, L. D., & Goodman, N. R. (1965). Gaussian approximations to the distributions of sample coherence. *Tech Report, AFFDL-TR-65-57, Wright- Patterson Air Force Base*.

Field, E. H. (1996). Spectral amplification in a sediment-filled valley exhibiting clear basin-edge-induced waves. *Bulletin of the Seismological Society of America, 86*(4), 991-1005.

Finetti, I. (1976). Mediterranean Ridge. A Young Submerged Chain Associated with the Hellenic Arc. *Boll. Geofis. teor. applic., 15*, , 263–341.

Fletcher, J., Haar, L. H., & Brune, J. (1987). The digital array at Anza, California: Processing and initial interpretation of source parameters. *J. Geophys. Res., 92*(B1), 369–382.

Gaffet, S., C. Larroque, A. D., & Tressols, F. (1998). A dense array experiment for the observation of waveform perturbations. *Soil Dynamics and Earthquake Engineering, 17*, 475–484.

GEER Report (2014). GEER/EERI/ATC Earthquake Reconnaissance of Cephalonia, Greece 2014 V. 01. last accessed 10/10/2014. available at, http:// www.geerassociation.org/GEER_Post%20EQ%20Reports/Cephalonia_Greece_2014/index.html

Goldstein, P., & Archuleta, R. (1987). Array analysis of seismic signals. *Geophys. Res. Lett., I4*, 13-16.

Goldstein, P., & Archuleta, R. J. (1987). Array analysis of seismic signals. *Geophysical Research Letters, 14*(1), 13-16.

Goldstein, P., & Archuleta, R. J. (1991). Deterministic frequency-wavenumber methods and direct measurements of rupture propagation during earthquakes using a dense array: Data analysis. *Journal of Geophysical Research: Solid Earth, 96*(B4), 6187-6198.

Graves, R. (1993). Modeling Three-Dimensional Site Response Effects in the Marina District Basin, San Francisco, California. *Bulletin of the Seismological Society of America, 83*, 1042-1063.

Hadler, H., Andreas Vött, H. B., & Willershäuser, T. (2011). The harbour of ancient Krane, Kutavos Bay (Cefalonia, Greece) – an excellent geo-archive for palaeo-tsunami research. *Coastline Reports, 17*, 111-121.

Hao, H., Oliveira, C., & Penzien, J. (1989). Multiple-station ground motion processing and simulation based on SMART-I array data. *Nuclear Engineering and Design, 111*, 293-310.

Harada, T. (1984). Probabilistic Modeling of Spatial Variation of Strong Earthquake Ground Displacement. *Proceedings of Eighth World Conference on Earthquake Engineering, San Francisco*, 605-612.

Harichandran, R. (1991). Estimating the spatial variation of earthquake ground motion from dense array recordings. *Structural Safety, 10*, 219-233.

Harichandran, R. (1999). Spatial Variation of Earthquake Ground Motion. *Department of Civil and Environmental Engineering, Michigan State University, USA*.

Harichandran, R. S. (1988). Local Spatial Variation of Earthquake Ground Motion. *Earthquake Engineering and Soil Dynamics II - Recent Advances in Ground-Motion Evaluation, J. L. Von Thun (ed.), American Society of Civil Engineers, New York*, 203-217.

Harichandran, R., & Vanmarcke, E. (1986). Stochastic variation of earthquake ground motion in space and time, Journal of Engineering Mechanics. *ASCE, 112*, 154-174.

Harichandran, R., Hawwari, A., & Sweidan, B. (1996). Response of long-span bridges to spatially varying ground motion. *Journal of Structural Engineering, 122*, 476–484.

Hartzell, S., & Heaton, T. (1983). Inversion of strong ground motion and teleseismic waveform data for the fault rupture history of the 1979 Imperial Valley, California, earthquake. *Bull. Seismol. Soc. Am., 73*, 1553-1583.

Hatzfeld, D., Pedotti, G. H., & Makropoulos, K. (1990). The strain pattern in the western Hellenic arc deduced from a microearthquakes. *Geophys. J. Int., 101*, 181–202.

Himmerkus, F. a., & Kostopoulos, D. 2. (2007). Gondwana-derived terranes in the northern Hellenides. *Geological Soc.of America Memoirs, 200*, 379-390.

Hobiger, M. (2011). *Polarization of surface waves : characterization, inversion and application to seismic hazard assessment.* Ph.D. dissertation, Université de Grenoble.

Hobiger, M., Cornou, C., Bard, P.-Y., & Le Bihan, N. (2011). MUSIQUE: A quaternion-based array processing technique for surface wave polarization analysis. *IEEE Signal Processing Workshop (SSP)*.

Hobiger, M., Cornou, C., Bard, P.-Y., & Le Bihan, N. (2014). *Analysis of seismic waves crossing the Santa Clara Valley using the three-component MUSIQUE array algorithm.* Tech. rep., Geophys. J. Int.

Hobiger, M., Le Bihan, N. C., & Bard, P.-Y. (2012). Multicomponent Signal Processing for Rayleigh Wave Ellipticity Estimation Application to Seismic Hazard Assessment. *IEEE Signal Processing Magazine, 29*(3), 29–39.

Hobiger, M., N. Le Bihan, C. C., & Bard, P.-Y. (2009, 24-28 August). Rayleigh wave ellipticity estimation from ambient seismic noise using single and multiple vector-sensor techniques. *17th European Signal Processing Conference, Glasgow, UK*.

Hobiger, M., P.-Y. Bard, C. C., & Bihan, N. L. (2009). Single station determination of Rayleigh wave ellipticity by using the random decrement technique (RayDec). *Geophys. Res. Lett., 36*(L14303).

Hollenstein, C., Geiger, A. K.-G., & Veis, G. (2006). CGPS timeseries and trajectories of crustal motion along theWest Hellenic Arc. *Geophys. J. Int., 164*, 182–191.

Horikawa, H. (2001). Earthquake doublet in Kagoshima, Japan: Rupture of asperities in a stress shadow. *Bull. Seis. Soc. Am., 91*(1), 112-127.

Imtiaz, A., Causse, M., Chaljub, E., and Cotton, F (2015). Is ground-motion variability distance-dependent? Insight from finite-source ruptures simulations. *Bulletin of the Seismological Society of America (BSSA), Volume 105*, Issue 2a, doi:10.1785/0120140107.

Iwan, W. D. (1979). The deployment of strong-motion earthquake instrument arrays. *Earthquake Engineering and Structural Dynamics, 7*(5), 413-426.

Jarvis A., Reuter, H. I., Nelson, A., and Guevara, E. (2008). Hole-filled seamless SRTM data V4, *International Centre for Tropical Agriculture (CIAT)*, available from http://srtm.csi.cgiar.org, accessed on January 02, 2015.

Jenkins, G., & Watts, D. (1968). Spectral analysis and its application. *Holden-Day, San Francisco*.

Joyner, W. B., & Boore, D. M. (1981). Peak horizontal acceleration and velocity from strong-motion records including records from the 1979 Imperial Valley, California, earthquake. *Bull. Seism. Soc. Am., 71*(6), 2011–2038.

Jurkevics, A. (1988). Polarization Analysis of Three Component Array Data. *Bulletin of Seismological Society of America, 78*, 1725-1743.

Kamberis, E., Marnelis, F. L., & Group, S. (1996). Structure and deformation of the External Hellenides based on seismic data from offshoreWestern Greece. *Wessely, G., Liebl,W. (Eds.), Oil and Gas in Alpidic Thrustbelts and Basins of Central and Eastern Europe. EAGE Special Publication, 5*, 207–214.

Kawase, H. (1996). The cause of the damage belt in Kobe: "the basin-edge effect", constructive interference of the direct S-wave with the basin-induced diffracted/Rayleigh waves. *Seism. Res. Lett., 67*, 25-34.

Kawase, H. (1996). The cause of the damage belt in Kobe:“The basin-edge effect,” constructive interference of the direct S-wave with the basin-induced diffracted/Rayleigh waves. *Seismological Research Letters, 67*(5), 25-34.

Kiratzi, A., Sokos, E. G., & G-A., T. (2008). The April 2007 earthquake swarm near Lake Trichonis and implications for active tectonics in western Greece. *Tectonophysics, 452*(51-65).

Kokinou, E., . Papadimitriou, E. K., & Vallianatos, F. (2006). The Kefalonia Transform Zone (offshore Western Greece) with special emphasis to its prolongation towards the Ionian Abyssal Plain. *Mar Geophys Res, 27*, 241-252.

Krim, H., & Viberg, M. (1996). Two decades of array signal processing research: the parametric approach. *IEEE Signal Processing Magazine, 13*(4), 67-94.

Kuwahara, Y., Ito, H. K., & Kiguchi, T. (1997). Crustal heterogeneity as inferred from seismic coda wave decomposition by small-aperture array observation. *Physics of the earth and planetary interiors, 104*(1), 247-256.

Kværna, T., & Doornboos, D. J. (1986). An integrated approach to slowness analysis with arrays and three-component stations. *Rep. NORSAR 2-85/86, Norw. Seismic Array, Kjeller, Norway*.

Lacoss, R. T., Kelly, E., & Toksöz, M. (1969). Estimation of seismic noise structure using arrays. *Geophysics, 34*, 21-38.

Lagios, E., Sakkas, V., Papadimitriou, P., Parcharidis, I., Damiata, B., Chousianitis, K., et al. (2007). Crustal deformation in the Central Ionian Islands (Greece): Results from DGPS and DInSAR analyses (1995–2006). *Tectonophysics, 444*(1-4), 119-145.

Le Boudec, J.-Y. (2011). *Performance Evaluation Of Computer And Communication Systems.* EPFL Press.

Le Pichon, X., Chamot-Rooke, N. L., & Veis, G. (1995). Geodetic determination of the kinematics of Central Greece with respect to Europe: implications for Eastern Mediterranean tectonics. *Journal of Geophysical Research, 100*, 12675-12690.

Liao, S. (2006). *Physical characterization of seismic ground motion spatial variation and conditional simulation for performance-based design.* Ph.D. dissertation, Drexel University, Philadelphia, USA.

Liu, H., & Helmberger, D. V. (1983). The near-source ground motion of the 6 August 1979 Coyote Lake, California, earthquake. *Bull. Seis. Soc. Am, 73*(1), 201-218.

Liu, H., & Helmberger, D. V. (1985). The 23:19 aftershock of the 15 October 1979 Imperial valley earthquake: more evidence for an asperity. *Bull. seism. Soc. Am., 75*, 689–708.

Loh, C. H. (1985). Analysis of the Spatial Variation of Seismic Waves and Ground Movements from SMART-1 Array Data. *Earthquake Engineering and Structural Dynamics, 13*, 561–581.

Loh, C. H., Penzien, J., & Tsai, Y. B. (1982). Engineering Analysis of SMART-1 Array Accelerograms. *Earthquake Engineering Structural Dynamics, 10*, 575-591.

Louvari, E., Kiratzi, A., & Papazachos, B. (1999). The Cephalonia Transform fault and its extension to western Lefkada Island (Greece). *Tectonophysics, 308*, 223–236.

Luco, J., & Wong, H. (1986). Response of a rigid foundation to a spatially random ground motion. *Earthquake Engineering and Structural Dynamics, 14*, 891-908.

Mai, P.M., and Thingbaijam, K. K. S. (2014). SRCMOD: An Online Database of Finite- Fault Rupture Models, *Seis. Res. Lett., Volume 85*, Number 6, November/December 2014, doi: 10.1785/0220140077.

Mai, P., Burjanek, J. D.-H., & Zahradnik, J. (2007). Source-inversion blindtest: initial results and further developments. *Eos Trans. AGU, 88(52), Fall Meet. Suppl.*

Maranò, S., Reller, C. L., & Fäh, D. (2012). Seismic waves estimation and wavefield decomposition: application to ambient vibrations. *Geophysical Journal International, 191*(1), 175-188.

Marple, S. (1987). *Digital spectral analysis with applications.* Prentice-Hall.

Matsushima, Y. (1977). Stochastic response of structure due to spatially variant earthquake excitations. *Proceedings of Sixth World Conference on Earthquake Engineering, Sarita Prakashan, Meerut, India, II*, 1077-1082.

McGuire, J., Zhao, L., & Jordan, T. (2002). Predominance of Unilateral Rupture for a Global Catalog of Large Earthquakes. *Bull. Seismol. Soc. Am., 92*(8), 3309–3317.

McLaughlin, K. L. (1983). *Spatial Coherency of Seismic Waveforms.* Ph.D. dissertation, University of California, Berkeley.

Miron, S., Bihan, N. L., & Mars, J. (2005). High resolution vector-sensor array processing using quaternions. *IEEE International Conference on Statistical Signal Processing, Bordeaux, France*.

Miron, S., Bihan, N. L., & Mars, J. (2005). Vector-sensor MUSIC for polarized seismic sources localization. *EURASIP J. Appl. Signal Process.*, 74–84.

Miron, S., Le Bihan, N., & Mars, J. (2006). Quaternion-MUSIC for vector-sensor array processing. *IEEE Trans. Signal Process, 54*, 1218–1229.

Miyakoshi, K., Kagawa, T. S., & Irikura, K. (2000). Source characterization of inland earthquakes in Japan using source inversion results. *Paper read at Proc. 12th World Conf. Earthq. Eng., at Auckland, New-Zealand*, Year 2000.

Moczo, P., & Bard, P.-Y. (1993). Wave diffraction, amplification and differential motion near strong lateral discontinuities. *Bull. seism. Soc. Am., 83*, 85-106.

Morikawa, H., Sawada, S., & Akamatsu, J. (2004). A method to estimate phase velocities of Rayleigh waves using microseisms simultaneously observed at two sites. *Bull. Seismol. Soc. Am., 94*, 961–976.

NERA Report (2014). Report on Array Measurement. NERA JRA1, Task 11.4, Deliverable No. D 11.4.

Papadimitriou, E., & Papazachos, B. (1985). Evidence for precursory seismicity patterns in the Ionian islands (Greece). *Earth. Pred. Res., 3*, 95–103.

Papadimitriou, P., Chousianitis, K. A., & Makropoulos, K. (2012). The spatially extended 2006 April Zakynthos (Ionian Islands, Greece) seismic sequence and evidence for stress transfer. *Geophys. J. Int., 190*(2), 1025-1040.

Papazachos, B. (1990). Seismicity of the Aegean and surrounding area. *Tectonophysics, 178*, 287-308.

Papazachos, B. C., Comninakis, P. E., & Papazachos, C. B. (2010). A catalogue of earthquakes in the Mediterranean and surrounding area for the period 1901 - 2010. *Publ. Geophys. Laboratory, University of Thessaloniki*.

Papazachos, B., & Papazachou, K. (2003). *The Earthquakes of Greece* (3rd ed.). Ziti Publishing Co.,Thessaloniki Greece.

Papazachos, C., & Kiratzi, A. 1. (1996). A detailed study of the active crustal deformation in the Aegean and surrounding area. *Tectonophysics, 253*, 129–153.

Papazachos, C., & Kiratzi, A. (1996). A detailed study of the active crustal deformation in the Aegean and surrounding area. *Tectonophysics, 253*, 129-153.

Papazachos, C., B., Comninakis, P. E., & Scordilis, E. M. (2000). A catalogue of earthquakes in Greece and surrounding area for the period 550BC-1999. *Publ. Geophysical Research Letters, 1*, 333.

Papazachos, C., Karakaisis, G. S., & Papazachos, B. (2004). Probabilities of activation of seismic faults in critical regions of the Aegean area. *Geophys. J. Int., 159*, 679–687.

Papazachos, C., Karakaisis, G. S., & Papazachos, B. (2004). Probabilities of activation of seismic faults in critical regions of the Aegean area. *Geophysical Journal International, 159*, 679–687.

Pitilakis, K., Pitilakis, D. R., & Pistolas, A. (2014). *January 26, 2014 and February 03, 2014 Earthquakes in Cephalonia, Greece Preliminary Report.* unpublished.

Poggi, V., & Fäh, D. (2010). Estimating Rayleigh wave particle motion from three-component array analysis of ambient vibrations. *Geophysical Journal International, 180*(1), 251-267.

Protopapa, E., Papastamatiou, D. M., & Gazetas, G. (1998). The Ionianet Accelerometer Array: Early Results and Analysis. *Proceedings of the 11th European Conference on Earthquake Engineering Balkema,Rotterdam*.

Ramadan, O., & Novak, M. (1993). Response of long gravity dams to incoherent seismic ground motions, Transactions on the Built Environment. *WIT Press, 3*.

Ripperger, J., Mai, P. M., & Ampuero, J.-P. (2008). Variability of near-field ground motion from dynamic earthquake rupture simulations. *Bull. Seismol. Soc. Am., 98*(3), 1207-1228.

Rodriguez-Marek, A., Cotton, F. A.-A., & M., D. (2013).). A model for single-station standard deviation using data from various tectonic regions. *Bull. Seismol. Soc. Am., 103, 3149-3163*.

Rodriguez-Marek, A., Montalva, G. C., & Bonilla, F. (2011). Analysis of single-station standard deviation using the KiK-net data. *Bull. Seismol. Soc. Am.*

Rost, S., & Thomas, C. (2002). ARRAY SEISMOLOGY: METHODS AND APPLICATIONS. *Reviews of Geophysics, 40*(3), 2-1--2-27.

Roullé, A., & Chávez García, F. J. (2005). Comparison of three methods to study the wavefield in the valley of Mexico using data from dense arrays. *Revista de Ingeniería Sísmica, 73*.

Rovelli, A. L., Scognamiglio, F. M., & Caserta, A. (2001). Edgediffracted 1-sec surface waves observed in a small-size intramountain basin (Colfiorito, central Italy). *Bulletin of Seismological Society of America, 91*, 1851-1866.

Sachpazi, M., Hirn, A. C.-C., & Ansorge, J. (2000). Western Hellenic subduction and Cephalonia Transform: local earthquakes and plate transport and strain. *Tectonophysics, 319*, 301–319.

Sawada, T., & Kamada, H. (1988, August 2-9). Modeling of nonstationary cross spectrum for multivariate earthquake motions by multifilter technique. *Proc. Nineth World Conf. Earthquake Eng., II Tokyo, Japan*, 795-800.

Scandella, L., & Paolucci, R. (2010). Earthquake induced ground strains in the presence of strong lateral soil heterogeneities. *Bulletin of Earthquake Engineering, 8*(6), 1527-1546.

Schmidt, R. (1981). *A signal subspace approach to multiple emitter location and spectral estimation.* Ph.D. dissertation, Stanford University, Stanford, CA.

Schmidt, R. (1986). Multiple emitter location and signal parameter estimation. *IEEE Trans. Antennas and Propagation, 34*, 276–280.

Schneider, J., Abrahamson, N. S., & Stepp, J. (1990). Spatial variation of ground motion from EPRI's dense accelerograph array at Parkfield, California. *Proceeding of Fourth U.S. National Conference on Earthquake Engineering, EERI, Palm Springs*, 375-384.

Schneider, J., Stepp, J., & Abrahamson, N. (1992). The spatial variation of earthquake ground motion and effects of local site conditions. *Proceedings of the Tenth World Conference on Earthquake Engineering, A. A. Balkema, Rotterdam, 2*, 967-972.

Sekiguchi, H., & Iwata, T. (2002). Source process and near-fault ground motion of the 2000 Tottori-ken Seibu earthquake. *Monthly Chikyu, special issue, 38*(182-188).

Semmane, F., Cotton, F., & Campillo, M. (2005). The 2000 Tottori earthquake: A shallow earthquake with no surface rupture and slip properties controlled by depth. *J. Geophys. Res., 110*(B3).

Shabestari, K. T., & Yamazaki, F. (2003). Near-fault spatial variation in strong ground motion due to rupture directivity and hanging wall effects from the Chi-Chi, Taiwan earthquake. *Earthquake Engng. Struct. Dyn., 32*, 2197–2219.

Smith, S. W., Ehrenberg, E., & Hernandez, E. N. (1982). Analysis of the El Centro Differential Array for the 1979 Imperial Valley Earthquake. *Bulletin of Seismological Society of America, 72*, 237– 258.

Somerville, P. G., McLaren, J. P., & Saikia, C. K. (1988). Site-specific estimation of spatial incoherence of strong ground motion. *Earthquake Engineering and Soil Dynamics II, Recent advances in ground motion evaluation., Geotechnical Special Publication, No.20., ASCE, New York*.

Somerville, P., Smith, N. G., & Abrahamson, N. (1997). Modification of empirical strong ground motion attenuation relations to include the amplitude and duration effects of rupture directivity. *Seismological Research Letters, 68*, 199-222.

Spudich, P. (1994). *Recent Seismological Insights in to the Spatial Variation of Earthquake Ground Motions, New Developments in Earthquake Ground Motion Estimation and Implications for Engineering Design Practice, ATC 35-1.* Tech. rep.

Spudich, P., & Chiou, B.-J. (2008). Directivity in NGA earthquake ground motion: Analysis using isochrone theory. *Earth. Spectra, 25*, 279-298.

Spudich, P., & Cranswick, E. (1984). Direct observation of rupture propagation during the 1979 Imperial Valley earthquake using a short baseline accelerometer array. *Bull. Seismol. Soc. Am., 74*, 2083–2114.

Takemura, S. F., & Saito, T. (2009). Distortion of the apparent S-wave radiation pattern in the high-frequency wavefield: Tottori-Ken Seibu, Japan, earthquake of 2000. *Geophys. J. Int., 178*, 950–961.

Takenaka, H., M. Y., & Futamure, H. (2003). Near-source effect on radiation pattern of high-frequency S waves: strong SH-SV mixing observed from aftershocks of the 1997 northwestern Kagoshima, Japan, earthquakes. *Ph. Earth P. Int., 137*(1-4), 31–43.

Taymaz, T., Yilmaz, Y., & Y., D. (2007). The geodynamics of the Aegean and Anatolia: introduction. *Geological Society, London, Special Publications, 291*, 1-16.

Tselentis, G., Melis, N. S., & Beltas, P. (1997). The winter 1991-1992 earthquake sequence at Cephalonia island, Western Greece. *Pure Appl. Geophys, 150*(75-89).

Underhill, J. (2006). Quest for Ithaca. *Geoscientist, 6*(9), 4-17.

Underhill, J. R. (1988). Triassic evaporites and Plio-Quaternary diapirism in western Greece. *Journal of the Geological Society, 145*, 269282.

Underhill, J. R. (1989). Late Cenozoic deformation of the Hellenic foreland, Western Greece. *Bull. Geol. Soc. Am., 101*, 613–634.

Wagner, G. S. (1997). Regional wave propagation in southern California and Nevada: Observations from a three component seismic array. *Journal of Geophysical Research: Solid Earth (1978–2012), 102*(B4), 8285-8311.

Wagner, G. S., & Owens, T. J. (1993). Broadband bearing time records of three component seismic array data and their application to the study of local earthquake coda. *Geophysical Research Letters, 20*(17), 1823-1826.

Ward, J. P. (1997). *Quaternions and Cayley Numbers: Algebra and Applications.* Kluwer Academic Publishers.

Wathelet, M., Jongmans, D. O., & Bonnefoy-Claudet, S. (2008). Array performances for ambient vibrations on a shallow structure and consequences over Vs inversion. *Journal of Seismology, 12*(1), 1-19.

Yamazaki, F., & Shimizu, Y. (2000). Super Dense Real-time Monitoring of Earthquakes for a City Gas Network in Japan. *Proceedings of the 17th International Symposium on Automation and Robotics in Construction*, 581-586.

Zerva, A. (1994). On the spatial variation motions of seismic ground motions and its effects on lifelines. *Engg Struct, 16*(7), 534-546.

Zerva, A. (2009). *Spatial Variation of Seismic Ground Motions.* CRS Press, Boca raton, Florida, USA, 468 pp.

Zerva, A., & Harada, T. (1997). Effect of Surface Layer Stochasticity on Seismic Ground Motion Coherence and Strain Estimates. *Soil Dynamics and Earthquake Engineering, 16*, 445-457.

Zerva, A., & Stephenson, W. R. (2011). Stochastic Characteristics of Seismic Excitations at a Non-Uniform (Rock and Soil) Site. *Soil Dynamics and Earthquake Engineering, 31*, 1261-1284.

Zerva, A., & Zervas, V. (2002). Spatial variation of seismic ground motions: an overview. *Applied Mechanics Review, ASME, 55*(3), 271-297.

Zerva, A., & Zhang, O. (1996). Estimation of signal characteristics in seismic ground motions . *Probabilistic Engineering Mechanics, 11*(4), 229-242.

Zerva, A., Ang, A. H-S., & Y.K.Wen. (1987). Development of differential response spectra for lifeline seismic analysis. *Probabilistic Engineering Mechanics, 1*, 208-218.

APPENDIX A

Computation of directivity ratios

For each source model, we compute the directivity ratio as proposed by McGuire et al. (2002). From the space-time slip distribution, we first compute the second spatial moment $\hat{\mu}^{(2,0)}$, the second temporal moment $\hat{\mu}^{(0,2)}$, and the mixed moment $\hat{\mu}^{(1,1)}$ defined as:

$$\hat{\mu}^{(2,0)} = \iint \dot{M}(\vec{r},t)(\vec{r}-\vec{r}_0)(\vec{r}-\vec{r}_0)^T dVdt \quad \text{(A1)}$$

$$\hat{\mu}^{(0,2)} = \iint \dot{M}(\vec{r},t)(t-t_0)^2 dVdt \quad \text{(A2)}$$

$$\hat{\mu}^{(1,1)} = \iint \dot{M}(\vec{r},t)(\vec{r}-\vec{r}_0)(t-t_0) dVdt \quad \text{(A3)}$$

where $\dot{M}(\vec{r},t)$ is the space-time moment rate function, and $\vec{r}_0$ and t_0 refer to the spatial and temporal centroids. Next we determine the characteristic duration, expressed as:

$$\tau_c = 2\sqrt{\hat{\mu}^{(0,2)}/M_0)} \quad \text{(A4)}$$

and the characteristic dimension in a direction $\vec{n}$, expressed as:

$$x_c(\vec{n}) = 2\sqrt{\vec{n}^T(\hat{\mu}^{(2,0)}/M_0)\vec{n}} \quad \text{(A5)}$$

where M_0 denotes the seismic moment. The characteristic rupture length L_c is defined as $x_c(\vec{n}_1)$, the maximum value of $x_c(\vec{n})$, $\vec{n}_1$ being the Eigen vector associated to the largest eigen value. The ratio:

$$v_c = L_c/\tau_c \quad \text{(A6)}$$

then represents the characteristic rupture velocity.

Finally, we compute the average velocity of the instantaneous spatial centroid:

$$v_0 = \hat{\mu}^{(1,1)}/\hat{\mu}^{(0,2)} \quad \text{(A7)}$$

The directivity ratio is defined as the ratio v_0/v_c.

APPENDIX B

Velocity models used for ground motion computation

All the considered velocity models are the ones that have been used to perform source inversions, except for the Imperial Valley earthquake, for which the model has been slightly simplified to reduce computation-time. The velocity models considered in the ground-motion simulation are given in Table B1 for the bilateral models, and in Table B2 and B3 for unilateral models; V_p and V_s indicate the velocity and Q_p and Q_s the quality factor of P and S-wave, respectively and D indicates density of the material in the layer.

Note that for Imperial Valley (1979) event, Archuleta (1984) assumes a model with velocity gradient as presented in Table B2. For the Green's function computation with Axitra program, different sub-layers of the given velocity model were considered, which involved linear interpolation of the values. For example, the 2nd layer (between 0.4 km and 5 km) was divided into N=5 sub-layers of thickness dh=1150 m each and values of the other parameters were taken at the middle of each sub-layer. Similarly, the 3rd layer (between 5 km and 11 km depth) was divided into N=6 sub-layers of thickness dh=1000 m. The 4th layer (between 11 km and 11.1 km) marks the discontinuity. Finally, the 5th layer (between 11.1 km and 12 km depth) was divided into N=2 sub-layers of thickness dh=450 m. The final velocity model adopted is given in Table B3.

Table B1: Velocity models of the bilateral events

Event Name	Depth(m)	V_p(m/s)	V_s(m/s)	D (kg/m^3)	Q_p	Q_s
Fukuoka (2005)	0	5500	3200	2600	∞	∞
	5000	6000	3460	2700	∞	∞
	18000	6700	3870	2800	∞	∞
Yamaguchi (1997)	0	5600	3300	2600	400	400
	3000	6000	3500	2700	450	450
	30000	6600	3800	2900	500	500
Kagoshimaen-hoku-seibu (1997)	0	2800	1620	2100	80	40
	500	4900	2830	2300	300	150
	5000	6000	3460	2700	300	150
	15000	6700	3870	3100	500	250
	35000	7800	4500	3400	1000	500
Kagoshima (1997)	0	3100	1800	2300	200	200
	500	4400	2500	2500	350	350
	3000	5900	3400	2700	450	450
	22000	7000	4000	3000	500	500
Tottori (2000, Semmane et al.)	0	5500	3180	2600	500	200
	2000	6050	3490	2700	500	200
	16000	6600	3810	2800	200	200
	38000	8030	4620	3100	500	200
Tottori (2000, Sekiguchi and Iwata)	0	5500	3179	2600	500	200
	2000	6050	3497	2700	500	200
	16000	6600	3815	2800	500	200
	38000	8000	4600	3000	500	200
	20000	8100	4620	3300	500	200

Table B2: Initial Velocity Model of Imperial Valley (1979) from Database

Event Name	Depth(m)	V_p(m/s)	V_s(m/s)	D (kg/m^3)	Q_p	Q_s
Imperial Valley (1979), Initial Model	0	1700	400	1800	∞	∞
	400	1800	700	1800	∞	∞
	5000	5650	3200	2500	∞	∞
	11000	5850	3300	2800	∞	∞
	11100	6600	3700	2800	∞	∞
	12000	7200	4150	2800	∞	∞

Table B3: Velocity models of the unilateral events

Event Name	Depth(m)	V_p(m/s)	V_s(m/s)	D (kg/m^3)	Q_p	Q_s
Imperial Valley (1979), Interpolated Model	0	1700	400	1800	∞	∞
	400	1800	700	1800	∞	∞
	1550	2281	1013	1888	∞	∞
	2700	3243	1638	2063	∞	∞
	3850	4206	2263	2238	∞	∞
	5000	5169	2888	2413	∞	∞
	6000	5667	3208	2525	∞	∞
	7000	5700	3225	2575	∞	∞
	8000	5733	3242	2625	∞	∞
	9000	5767	3258	2675	∞	∞
	10000	5800	3275	2725	∞	∞
	11000	5833	3292	2775	∞	∞
	11100	6225	3500	2800	∞	∞
	11550	6750	3813	2800	∞	∞
	12000	7050	4038	2800	∞	∞
Coyote Lake (1979)	0	3000	1500	2400	∞	∞
	500	5000	2800	2700	∞	∞
	3000	5700	3300	2780	∞	∞
	12000	6900	3300	3000	∞	∞
	60000	8100	4670	3200	∞	∞

APPENDIX C

Computations of the synthetic ground motions for large faults

The principle of the decomposition of the computations of ground motions for the large faults considered in this study is as follows:

Let F stand for one of those faults. F is further decomposed into N_s sub-faults, such that the typical length of each sub-fault is a fifth of the minimum wavelength on F. Let N_r (here N_r=135) be the number of receivers, then the computation of the ground motions is done in three steps: (1) the components of all Green functions relating the N_s sub-faults to the N_r receivers are computed with the Axitra code (Coutant, 1989) (2) each Green function is convolved in space and time to account both for the magnitude and focal mechanism of the sub-fault and for the imposed rupture kinematics; (3) the contributions of the N_s sub-faults are summed at each of the Nr receivers.

The N_s*N_r calculations needed by step (1) were done in parallel on the number of sub-faults, i.e. for each sub-fault the calculations at all receivers were gathered in a single job. For this purpose, we exploited the available resources of a local grid of HPC clusters (totalizing more than 3000 computing cores) in a best-effort mode thank to the grid middleware “cigri”. The results, consisting of one binary file per sub-fault, were stored on a distributed data grid operated by the Integrated Rule-Oriented Data System (IRODS). The convolutions needed by step (2) were also distributed on the computing grid and stored again on the data grid. Finally the reduce operation needed in step (3) was done for all receivers by successive grouping of the sources by packets, the size of which was controlled by the maximum number of binary files that would fit in the random access memory (RAM) of each computing node. For the example of the Imperial Valley calculations, each binary file containing the contribution of a single sub-fault at all receivers was about 16 Mbytes, and the size of the source packets was 200 so that the summation could be done in a RAM of size 4 Gbytes. For this event, which was the most demanding of all cases, the total time needed to compute the Green's functions was about 4000 hours of a single CPU core on an Intel E5-2670 with frequency 2.6 Ghz.

Appendix D

Coordinates of the Array Stations

D.1.1 Coordinates of Array A stations

(1)	(2)	(3)	(4)	(5)	(6)
Index	**Station Name**	**Latitude (deg)**	**Longitude (deg)**	**Northing (m)**	**Easting (m)**
1	A00	38.163317	20.505549	4224051.089	456684.827
2	A01	38.163351	20.505583	4224054.838	456687.879
3	A02	38.163355	20.505519	4224055.406	456682.206
4	A03	38.163303	20.505492	4224049.607	456679.870
5	A04	38.163271	20.505545	4224046.007	456684.495
6	A05	38.163301	20.505603	4224049.273	456689.525
7	A06	38.163422	20.505654	4224062.676	456694.092
8	A07	38.163432	20.505457	4224063.905	456676.873
9	A08	38.163281	20.505382	4224047.260	456670.165
10	A09	38.163182	20.505541	4224036.115	456684.087
11	A10	38.163266	20.505708	4224045.379	456698.782
12	A11	38.163596	20.505833	4224081.955	456709.890
13	A12	38.163621	20.505299	4224084.970	456663.120
14	A13	38.163222	20.505109	4224040.833	456646.264
15	A14	38.162955	20.505529	4224010.974	456682.860
16	A15	38.163185	20.505973	4224036.244	456721.953
17	A16	38.163884	20.506111	4224113.734	456734.438

(1)	(2)	(3)	(4)	(5)	(6)
Index	**Station Name**	**Latitude (deg)**	**Longitude (deg)**	**Northing (m)**	**Easting (m)**
18	A17	38.163925	20.505060	4224118.762	456642.385
19	A18	38.163129	20.504656	4224030.694	456606.484
20	A19	38.162596	20.505509	4223971.109	456680.906
21	A20	38.163052	20.506396	4224021.327	456758.891

D.1.2 Relative Coordinates of Array A stations from A00

(1)	(2)	(2)	(3)	(4)
Index	**Reference Station**	**Station Name**	**Distance (m)**	**Azimuth (deg)**
1	A00	A01	4.83363	39.1478
2	A00	A02	5.04982	328.734
3	A00	A03	5.17382	253.354
4	A00	A04	5.09322	183.737
5	A00	A05	5.03663	111.142
6	A00	A06	14.8352	38.6472
7	A00	A07	15.084	328.173
8	A00	A08	15.1538	255.362
9	A00	A09	14.9924	182.829
10	A00	A10	15.0779	112.253
11	A00	A11	39.7593	39.0764
12	A00	A12	40.2386	327.353
13	A00	A13	39.9034	255.107
14	A00	A14	40.1636	182.807

(1)	(2)	(2)	(3)	(4)
Index	**Reference Station**	**Station Name**	**Distance (m)**	**Azimuth (deg)**
15	A00	A15	39.984	111.795
16	A00	A16	79.9093	38.377
17	A00	A17	79.8807	327.906
18	A00	A18	80.9542	255.408
19	A00	A19	80.076	182.807
20	A00	A20	79.8199	111.892

D.2.1 Coordinates of Array B stations

(1)	(2)	(3)	(4)	(5)	(6)
Index	**Station Name**	**Latitude (deg)**	**Longitude (deg)**	**Northing (m)**	**Easting (m)**
1	B01	38.165482	20.508014	4224290.1479	456902.0415
2	B02	38.165655	20.507837	4224309.4176	456886.6889
3	B03	38.165540	20.508018	4224296.5815	456902.4226
4	B04	38.165620	20.508249	4224305.4147	456922.7688
5	B05	38.165616	20.508467	4224304.8410	456941.8176
6	B06	38.165225	20.508291	4224261.5276	456926.2031
7	B07	38.165067	20.507568	4224244.3538	456862.7704
8	B08	38.165446	20.508047	4224286.1312	456904.9716
9	B09	38.165337	20.507795	4224274.1943	456882.7797
10	B10	38.165481	20.507933	4224290.0668	456894.9532

D.2.2 Relative Coordinates of Array B stations from B01

(1)	(2)	(2)	(3)	(4)
Index	**Reference Station**	**Station Name**	**Distance (m)**	**Azimuth (deg)**
1	B01	B02	24.6378	321.455
2	B01	B03	6.44489	3.38951
3	B01	B04	25.7428	53.6262
4	B01	B05	42.4031	69.726
5	B01	B06	37.4553	139.829
6	B01	B07	60.3269	220.615
7	B01	B08	4.97185	143.891
8	B01	B09	25.0107	230.367
9	B01	B10	7.08885	269.344

Appendix E

Full Catalogue of Argostoli Events

E.1 Catalogue of Re-localized Events (Repi <80 km)

Index	YYYYMMDD	HH MM SS	LAT (N)	LON (E)	DEPTH (km)	M_L	LOCATION
1	20110921	01:25:31.5	37.82	20.38	1.0	1.9	Central IONIAN sea- W. GREECE
2	20110921	13:29:16.2	38.25	20.37	15.9	2.4	CEPHALONIA Isl.- W. GREECE
3	20110921	14:24:18.1	37.72	20.64	14.3	2.4	ZAKYNTHOS Isl.- W. GREECE
4	20110921	15:59:23.1	38.00	20.43	0.7	2.3	CEPHALONIA Isl.- W. GREECE
5	20110922	10:43:35.6	38.33	20.53	9.0	1.7	CEPHALONIA Isl.- W. GREECE
6	20110922	15:15:09.0	38.15	20.39	17.6	3.3	CEPHALONIA Isl.- W. GREECE
7	20110923	22:10:47.5	38.06	20.35	8.7	1.2	CEPHALONIA Isl.- W. GREECE
8	20110924	03:08:34.4	38.34	19.68	7.0	0.0	Central IONIAN sea- W. GREECE
9	20110924	12:59:16.7	38.10	19.69	0.0	2.6	Central IONIAN sea- W. GREECE
10	20110924	15:49:12.7	37.48	19.74	14.4	3.1	
11	20110928	07:40:45.1	38.07	20.40	16.9	3.5	CEPHALONIA Isl.- W. GREECE
12	20110930	00:30:52.4	38.28	20.36	4.6	2.0	CEPHALONIA Isl.- W. GREECE
13	20110930	06:54:30.6	38.15	20.46	10.4	2.6	CEPHALONIA Isl.- W. GREECE
14	20111003	15:26:11.3	37.85	21.14	17.8	3.1	West PELOPONNESE- SW GREECE
15	20111008	03:24:45.4	38.62	20.58	6.1	2.8	LEFKADA Isl.- W. GREECE
16	20111008	20:59:00.5	38.34	19.75	14.8	2.8	Central IONIAN sea- W. GREECE
17	20111010	02:57:43.9	38.32	20.41	13.7	2.8	CEPHALONIA Isl.- W. GREECE
18	20111011	12:50:50.3	38.20	20.34	14.1	2.5	CEPHALONIA Isl.- W. GREECE
19	20111011	13:04:54.6	38.16	20.37	11.5	2.4	CEPHALONIA Isl.- W. GREECE
20	20111011	13:20:13.5	38.21	20.35	18.9	4.4	CEPHALONIA Isl.- W. GREECE
21	20111011	18:45:21.0	38.17	20.36	16.8	2.5	CEPHALONIA Isl.- W. GREECE
22	20111011	18:52:12.8	37.68	21.07	16.8	2.5	W of PELOPONNESE- SW GREECE
23	20111012	04:54:43.5	38.09	20.36	2.2	2.3	CEPHALONIA Isl.- W. GREECE
24	20111012	18:09:07.6	38.23	20.36	16.3	2.6	CEPHALONIA Isl.- W. GREECE
25	20111014	01:11:32.3	37.97	20.84	11.9	3.5	ZAKYNTHOS Isl.- W. GREECE
26	20111015	16:24:22.4	37.98	20.28	13.6	2.8	Central IONIAN sea- W. GREECE
27	20111016	03:14:03.6	37.84	20.43	1.9	2.1	CEPHALONIA Isl.- W. GREECE
28	20111016	10:01:37.9	38.19	20.36	17.6	2.7	CEPHALONIA Isl.- W. GREECE
29	20111019	23:25:43.7	38.18	20.59	4.3	1.5	CEPHALONIA Isl.- W. GREECE
30	20111020	06:18:20.4	38.11	20.58	16.5	3.4	CEPHALONIA Isl.- W. GREECE
31	20111020	07:35:37.5	38.04	20.43	9.2	2.8	CEPHALONIA Isl.- W. GREECE
32	20111020	17:46:00.7	38.00	20.34	0.0	2.3	CEPHALONIA Isl.- W. GREECE
33	20111020	20:40:20.3	38.09	20.57	16.5	2.2	CEPHALONIA Isl.- W. GREECE
34	20111020	22:01:43.0	38.16	20.36	14.5	2.0	CEPHALONIA Isl.- W. GREECE
35	20111020	22:24:18.6	38.20	20.47	9.6	2.1	CEPHALONIA Isl.- W. GREECE

Index	YYYYMMDD	HH MM SS	LAT (N)	LON (E)	DEPTH (km)	M_L	LOCATION
36	20111021	20:25:30.1	38.56	20.38	9.4	2.6	Central IONIAN sea- W. GREECE
37	20111022	21:01:58.2	37.94	20.76	12.0	2.1	ZAKYNTHOS Isl.- W. GREECE
38	20111023	02:12:09.8	37.67	20.83	6.1	3.0	ZAKYNTHOS Isl.- W. GREECE
39	20111023	10:37:52.8	38.43	20.44	17.2	2.4	CEPHALONIA Isl.- W. GREECE
40	20111023	21:39:58.4	38.13	20.57	21.0	1.9	CEPHALONIA Isl.- W. GREECE
41	20111024	16:36:50.5	38.79	20.58	13.4	2.9	LEFKADA Isl.- W. GREECE
42	20111024	18:04:13.1	38.08	20.38	0.3	2.2	CEPHALONIA Isl.- W. GREECE
43	20111025	00:10:19.3	38.08	20.39	13.2	2.2	CEPHALONIA Isl.- W. GREECE
44	20111025	08:36:29.7	38.68	20.55	9.6	2.9	LEFKADA Isl.- W. GREECE
45	20111025	22:33:04.7	38.01	20.85	13.9	4.1	CEPHALONIA Isl.- W. GREECE
46	20111028	01:15:23.5	37.59	20.48	7.0	1.9	South IONIAN sea- W. GREECE
47	20111028	13:01:43.6	38.17	20.68	7.8	2.0	CEPHALONIA Isl.- W. GREECE
48	20111031	07:22:50.3	38.22	20.51	0.1	2.6	CEPHALONIA Isl.- W. GREECE
49	20111031	20:40:35.6	38.06	20.40	13.1	2.8	CEPHALONIA Isl.- W. GREECE
50	20111101	07:04:39.7	38.09	20.57	17.0	2.3	CEPHALONIA Isl.- W. GREECE
51	20111101	12:52:48.6	38.18	20.39	14.4	2.9	CEPHALONIA Isl.- W. GREECE
52	20111101	13:14:02.4	38.17	20.38	15.8	3.1	CEPHALONIA Isl.- W. GREECE
53	20111101	13:25:34.1	38.14	20.35	16.7	2.6	CEPHALONIA Isl.- W. GREECE
54	20111101	15:29:46.4	38.17	20.37	15.6	3.3	CEPHALONIA Isl.- W. GREECE
55	20111101	15:47:28.6	38.11	20.37	8.4	2.8	CEPHALONIA Isl.- W. GREECE
56	20111101	15:55:36.1	38.09	20.39	0.0	2.3	CEPHALONIA Isl.- W. GREECE
57	20111101	16:06:52.8	38.20	20.39	13.4	3.1	CEPHALONIA Isl.- W. GREECE
58	20111101	16:49:46.2	38.21	20.40	12.4	2.8	CEPHALONIA Isl.- W. GREECE
59	20111101	17:01:07.5	38.15	20.38	14.9	2.3	CEPHALONIA Isl.- W. GREECE
60	20111101	17:13:50.4	38.08	20.36	10.6	2.3	CEPHALONIA Isl.- W. GREECE
61	20111105	21:55:23.1	38.09	20.55	14.3	2.4	CEPHALONIA Isl.- W. GREECE
62	20111105	22:37:57.8	38.44	20.39	9.6	2.2	CEPHALONIA Isl.- W. GREECE
63	20111107	06:07:59.6	38.07	20.44	15.2	2.4	CEPHALONIA Isl.- W. GREECE
64	20111109	01:50:38.8	38.13	20.46	15.1	1.3	CEPHALONIA Isl.- W. GREECE
65	20111110	23:10:28.4	38.75	20.50	2.9	2.7	LEFKADA Isl.- W. GREECE
66	20111112	04:51:48.0	37.47	20.49	0.5	2.5	South IONIAN sea- W. GREECE
67	20111113	00:36:13.9	38.27	20.63	0.0	1.8	CEPHALONIA Isl.- W. GREECE
68	20111113	23:44:21.6	38.22	20.61	19.5	2.3	CEPHALONIA Isl.- W. GREECE
69	20111114	03:33:29.3	37.78	20.30	4.2	2.0	Central IONIAN sea- W. GREECE
70	20111114	16:47:37.7	38.08	20.31	11.1	2.2	CEPHALONIA Isl.- W. GREECE
71	20111114	19:36:20.6	38.09	20.30	13.8	1.9	CEPHALONIA Isl.- W. GREECE
72	20111115	14:10:04.9	37.69	20.86	16.8	3.7	ZAKYNTHOS Isl.- W. GREECE
73	20111116	02:16:18.2	38.17	20.32	14.8	2.3	CEPHALONIA Isl.- W. GREECE
74	20111117	00:02:19.4	38.26	20.37	12.6	3.3	CEPHALONIA Isl.- W. GREECE
75	20111117	01:33:04.6	38.25	20.35	12.1	2.4	CEPHALONIA Isl.- W. GREECE
76	20111117	02:06:32.9	38.20	20.33	15.4	1.4	CEPHALONIA Isl.- W. GREECE
77	20111117	04:14:02.7	38.20	20.44	10.3	1.5	CEPHALONIA Isl.- W. GREECE
78	20111117	18:32:53.2	37.63	20.00	0.0	2.8	Central IONIAN sea- W. GREECE

Index	YYYYMMDD	HH MM SS	LAT (N)	LON (E)	DEPTH (km)	M_L	LOCATION
79	20111118	23:14:15.2	38.10	20.78	19.8	2.5	CEPHALONIA Isl.- W. GREECE
80	20111120	01:48:39.9	38.09	20.40	13.0	2.0	CEPHALONIA Isl.- W. GREECE
81	20111121	06:11:15.1	37.96	20.85	12.2	2.4	ZAKYNTHOS Isl.- W. GREECE
82	20111122	19:41:31.8	38.27	20.69	9.2	2.3	CEPHALONIA Isl.- W. GREECE
83	20111123	12:32:34.1	38.58	20.30	23.3	2.9	Central IONIAN sea- W. GREECE
84	20111125	13:19:01.1	38.18	20.38	17.7	1.9	CEPHALONIA Isl.- W. GREECE
85	20111125	20:51:01.8	37.67	20.95	10.2	2.6	ZAKYNTHOS Isl.- W. GREECE
86	20111127	00:28:06.8	38.09	20.30	9.4	2.1	CEPHALONIA Isl.- W. GREECE
87	20111127	16:27:05.0	38.23	20.36	12.8	1.7	CEPHALONIA Isl.- W. GREECE
88	20111127	23:33:47.0	38.08	20.51	14.0	2.9	CEPHALONIA Isl.- W. GREECE
89	20111127	23:34:40.6	38.11	20.52	20.0	2.2	CEPHALONIA Isl.- W. GREECE
90	20111127	23:40:21.0	38.10	20.52	16.9	2.8	CEPHALONIA Isl.- W. GREECE
91	20111127	23:42:55.0	38.27	20.36	7.8	2.7	CEPHALONIA Isl.- W. GREECE
92	20111128	03:18:49.2	38.07	20.51	12.8	2.4	CEPHALONIA Isl.- W. GREECE
93	20111128	03:21:41.4	38.09	20.52	13.5	2.0	CEPHALONIA Isl.- W. GREECE
94	20111128	03:23:08.6	38.09	20.52	16.5	3.2	CEPHALONIA Isl.- W. GREECE
95	20111129	05:40:23.5	37.77	21.26	16.9	3.0	West PELOPONNESE- SW GREECE
96	20111129	15:12:41.7	38.09	20.39	1.3	2.0	CEPHALONIA Isl.- W. GREECE
97	20111129	15:58:27.8	37.74	21.05	21.6	2.7	ZAKYNTHOS Isl.- W. GREECE
98	20111129	20:36:38.4	38.23	20.58	16.2	2.0	CEPHALONIA Isl.- W. GREECE
99	20111130	10:27:08.5	38.08	20.79	3.4	2.8	CEPHALONIA Isl.- W. GREECE
100	20111130	11:51:06.8	37.65	20.61	11.9	2.4	ZAKYNTHOS Isl.- W. GREECE
101	20111130	17:21:23.2	38.03	20.33	0.0	2.3	CEPHALONIA Isl.- W. GREECE
102	20111130	21:27:02.6	38.03	20.33	4.7	1.9	CEPHALONIA Isl.- W. GREECE
103	20111201	03:51:34.0	38.47	20.59	12.4	1.7	CEPHALONIA Isl.- W. GREECE
104	20111201	04:58:20.6	38.16	20.55	7.5	1.6	CEPHALONIA Isl.- W. GREECE
105	20111202	01:45:31.6	38.21	20.31	10.5	1.7	CEPHALONIA Isl.- W. GREECE
106	20111202	13:06:41.8	38.20	20.51	14.9	1.7	CEPHALONIA Isl.- W. GREECE
107	20111202	14:37:57.8	38.12	20.54	21.1	1.7	CEPHALONIA Isl.- W. GREECE
108	20111203	07:02:35.5	38.28	20.36	12.2	1.6	CEPHALONIA Isl.- W. GREECE
109	20111203	12:53:57.4	38.19	20.32	8.7	1.6	CEPHALONIA Isl.- W. GREECE
110	20111203	18:49:00.8	38.22	20.60	11.2	1.5	CEPHALONIA Isl.- W. GREECE
111	20111203	21:49:10.1	38.07	20.41	11.5	1.3	CEPHALONIA Isl.- W. GREECE
112	20111204	02:08:28.8	38.09	20.60	0.0	1.1	CEPHALONIA Isl.- W. GREECE
113	20111205	08:16:03.1	38.11	20.49	14.5	3.9	CEPHALONIA Isl.- W. GREECE
114	20111205	08:20:40.9	38.11	20.49	16.5	1.9	CEPHALONIA Isl.- W. GREECE
115	20111205	08:22:53.9	38.11	20.49	17.4	1.8	CEPHALONIA Isl.- W. GREECE
116	20111205	08:22:54.3	38.19	20.51	17.0	1.7	CEPHALONIA Isl.- W. GREECE
117	20111205	08:33:43.8	38.07	20.49	14.3	1.8	CEPHALONIA Isl.- W. GREECE
118	20111205	08:46:56.9	38.10	20.48	14.5	1.9	CEPHALONIA Isl.- W. GREECE
119	20111205	12:30:28.2	38.11	20.50	16.0	4.6	CEPHALONIA Isl.- W. GREECE
120	20111205	13:00:27.2	38.09	20.49	14.2	1.5	CEPHALONIA Isl.- W. GREECE
121	20111205	14:27:49.5	38.12	20.49	17.6	1.7	CEPHALONIA Isl.- W. GREECE

Index	YYYYMMDD	HH MM SS	LAT (N)	LON (E)	DEPTH (km)	M_L	LOCATION
122	20111205	16:17:54.2	38.12	20.51	16.9	1.9	CEPHALONIA Isl.- W. GREECE
123	20111205	16:20:46.7	38.08	20.50	12.4	1.9	CEPHALONIA Isl.- W. GREECE
124	20111205	23:29:54.1	38.11	20.50	17.8	1.9	CEPHALONIA Isl.- W. GREECE
125	20111206	02:20:47.2	38.10	20.48	16.2	2.1	CEPHALONIA Isl.- W. GREECE
126	20111206	10:18:38.5	38.11	20.60	16.5	2.8	CEPHALONIA Isl.- W. GREECE
127	20111206	10:42:03.3	38.07	20.62	14.1	1.8	CEPHALONIA Isl.- W. GREECE
128	20111207	00:50:06.0	38.11	20.50	17.1	1.8	CEPHALONIA Isl.- W. GREECE
129	20111207	18:23:17.3	37.97	20.55	23.5	2.0	CEPHALONIA Isl.- W. GREECE
130	20111208	09:09:35.0	37.83	20.39	9.7	2.9	CEPHALONIA Isl.- W. GREECE
131	20111208	18:51:55.2	37.90	20.91	17.8	2.7	ZAKYNTHOS Isl.- W. GREECE
132	20111209	00:28:51.7	38.26	20.35	13.2	1.7	CEPHALONIA Isl.- W. GREECE
133	20111209	19:19:22.9	38.10	20.50	18.0	1.3	CEPHALONIA Isl.- W. GREECE
134	20111209	20:18:16.5	38.26	20.33	12.4	1.9	CEPHALONIA Isl.- W. GREECE
135	20111209	22:12:19.8	37.66	19.71	6.0	2.8	Central IONIAN sea- W. GREECE
136	20111210	00:28:36.1	38.30	20.35	9.7	1.4	CEPHALONIA Isl.- W. GREECE
137	20111210	02:00:41.8	38.28	20.70	7.2	1.8	CEPHALONIA Isl.- W. GREECE
138	20111210	16:18:26.8	38.11	20.52	16.9	1.4	CEPHALONIA Isl.- W. GREECE
139	20111210	18:41:03.7	38.02	20.28	20.5	1.8	Central IONIAN sea- W. GREECE
140	20111211	15:42:04.9	38.26	20.35	13.7	2.0	CEPHALONIA Isl.- W. GREECE
141	20111211	21:19:12.3	38.10	20.51	15.8	1.7	CEPHALONIA Isl.- W. GREECE
142	20111211	21:25:39.8	36.50	21.53	11.3	3.6	SW of PELOPONNESE- SW GREECE
143	20111211	22:10:52.8	38.11	20.50	15.9	1.7	CEPHALONIA Isl.- W. GREECE
144	20111211	22:15:41.2	38.10	20.50	15.6	2.3	CEPHALONIA Isl.- W. GREECE
145	20111211	22:15:41.2	38.10	20.50	15.6	2.3	CEPHALONIA Isl.- W. GREECE
146	20111212	02:23:24.4	38.32	20.45	12.5	2.2	CEPHALONIA Isl.- W. GREECE
147	20111212	05:35:42.6	38.27	20.69	11.1	2.5	CEPHALONIA Isl.- W. GREECE
148	20111212	08:04:52.1	38.29	20.71	7.0	2.3	CEPHALONIA Isl.- W. GREECE
149	20111212	08:13:39.1	38.27	20.70	11.0	4.1	CEPHALONIA Isl.- W. GREECE
150	20111212	08:31:34.2	38.27	20.71	2.5	2.3	CEPHALONIA Isl.- W. GREECE
151	20111212	09:52:29.9	38.24	20.73	10.4	2.1	CEPHALONIA Isl.- W. GREECE
152	20111212	10:36:31.2	38.28	20.69	4.6	2.2	CEPHALONIA Isl.- W. GREECE
153	20111212	11:16:08.1	38.26	20.70	7.7	2.1	CEPHALONIA Isl.- W. GREECE
154	20111212	11:33:24.6	38.27	20.74	4.5	1.9	CEPHALONIA Isl.- W. GREECE
155	20111212	13:36:31.4	38.28	20.70	3.1	2.2	CEPHALONIA Isl.- W. GREECE
156	20111212	17:00:03.8	38.28	20.70	8.7	1.6	CEPHALONIA Isl.- W. GREECE
157	20111212	17:04:49.3	42.91	19.45	7.0	4.9	
158	20111212	17:12:06.5	38.25	20.71	18.6	1.9	CEPHALONIA Isl.- W. GREECE
159	20111212	17:42:16.4	38.29	20.68	10.9	1.6	CEPHALONIA Isl.- W. GREECE
160	20111212	22:21:48.2	38.01	21.21	16.9	2.6	West PELOPONNESE- SW GREECE
161	20111213	04:01:06.8	37.98	20.84	8.3	0.0	ZAKYNTHOS Isl.- W. GREECE
162	20111213	04:59:51.5	38.28	20.69	8.2	1.6	CEPHALONIA Isl.- W. GREECE
163	20111213	07:29:16.6	38.60	20.61	9.6	2.0	LEFKADA Isl.- W. GREECE
164	20111213	17:45:40.8	38.34	20.51	21.9	1.5	CEPHALONIA Isl.- W. GREECE

Index	YYYYMMDD	HH MM SS	LAT (N)	LON (E)	DEPTH (km)	M_L	LOCATION
165	20111213	19:55:33.8	38.29	20.69	4.6	1.9	CEPHALONIA Isl.- W. GREECE
166	20111213	19:57:33.3	38.29	20.67	8.2	1.6	CEPHALONIA Isl.- W. GREECE
167	20111213	20:51:23.8	38.29	20.69	3.8	1.6	CEPHALONIA Isl.- W. GREECE
168	20111213	22:55:46.5	38.12	20.69	10.4	1.4	CEPHALONIA Isl.- W. GREECE
169	20111213	23:39:58.3	38.29	20.69	8.3	1.4	CEPHALONIA Isl.- W. GREECE
170	20111214	00:51:30.3	38.27	20.71	9.4	1.3	CEPHALONIA Isl.- W. GREECE
171	20111214	11:17:02.7	38.26	20.72	8.0	2.5	CEPHALONIA Isl.- W. GREECE
172	20111214	11:24:29.9	38.25	20.72	10.5	2.1	CEPHALONIA Isl.- W. GREECE
173	20111214	20:02:51.4	37.98	20.91	17.7	2.5	ZAKYNTHOS Isl.- W. GREECE
174	20111215	02:22:49.0	38.11	20.48	15.6	1.7	CEPHALONIA Isl.- W. GREECE
175	20111215	15:36:37.9	37.52	20.51	5.8	2.8	South IONIAN sea- W. GREECE
176	20111215	16:08:13.6	38.19	20.46	13.3	1.6	CEPHALONIA Isl.- W. GREECE
177	20111215	16:18:32.4	38.20	20.45	14.1	2.6	CEPHALONIA Isl.- W. GREECE
178	20111215	23:24:11.0	38.12	20.52	17.5	2.5	CEPHALONIA Isl.- W. GREECE
179	20111215	23:25:40.4	38.12	20.50	14.3	1.8	CEPHALONIA Isl.- W. GREECE
180	20111216	07:05:53.9	37.95	21.13	9.7	2.3	West PELOPONNESE- SW GREECE
181	20111216	08:11:34.8	38.19	20.66	18.9	1.8	CEPHALONIA Isl.- W. GREECE
182	20111218	00:58:39.1	38.65	20.56	11.0	3.1	LEFKADA Isl.- W. GREECE
183	20111218	11:10:14.2	37.42	20.51	14.5	2.1	South IONIAN sea- W. GREECE
184	20111218	11:42:03.2	38.09	20.50	15.1	1.7	CEPHALONIA Isl.- W. GREECE
185	20111218	12:18:49.0	38.53	20.50	14.7	2.3	LEFKADA Isl.- W. GREECE
186	20111219	01:59:23.1	38.28	20.71	3.9	1.5	CEPHALONIA Isl.- W. GREECE
187	20111219	20:40:16.3	38.17	20.56	16.9	1.4	CEPHALONIA Isl.- W. GREECE
188	20111219	20:41:59.2	38.13	20.54	15.8	1.7	CEPHALONIA Isl.- W. GREECE
189	20111220	04:48:58.1	38.31	21.99	22.8	2.7	CORINTHIAKOS Gulf- C. GREECE
190	20111220	07:13:52.0	38.25	20.28	12.2	1.8	CEPHALONIA Isl.- W. GREECE
191	20111220	09:18:03.9	38.21	20.40	14.1	1.7	CEPHALONIA Isl.- W. GREECE
192	20111220	20:15:10.8	38.09	20.42	17.2	2.1	CEPHALONIA Isl.- W. GREECE
193	20111220	22:05:28.7	38.39	20.46	12.5	2.5	CEPHALONIA Isl.- W. GREECE
194	20111221	04:04:14.9	38.31	20.44	7.0	1.1	CEPHALONIA Isl.- W. GREECE
195	20111221	06:01:05.8	38.26	20.43	14.8	1.8	CEPHALONIA Isl.- W. GREECE
196	20111221	08:22:54.5	37.93	20.94	14.0	3.1	ZAKYNTHOS Isl.- W. GREECE
197	20111221	12:43:26.6	38.16	20.69	13.9	2.5	CEPHALONIA Isl.- W. GREECE
198	20111221	17:11:48.0	38.31	20.31	5.2	2.1	CEPHALONIA Isl.- W. GREECE
199	20111222	15:46:46.5	38.09	20.48	15.8	1.5	CEPHALONIA Isl.- W. GREECE
200	20111222	22:46:40.3	38.09	20.38	15.6	1.8	CEPHALONIA Isl.- W. GREECE
201	20111223	16:47:32.5	38.26	20.32	4.7	1.9	CEPHALONIA Isl.- W. GREECE
202	20111223	17:20:34.4	37.87	21.03	17.3	3.0	Central IONIAN sea- W. GREECE
203	20111224	13:40:02.4	38.79	20.58	13.6	3.1	LEFKADA Isl.- W. GREECE
204	20111225	00:23:13.7	38.27	20.67	14.7	2.3	CEPHALONIA Isl.- W. GREECE
205	20111225	00:27:08.2	38.27	20.68	12.4	1.5	CEPHALONIA Isl.- W. GREECE
206	20111225	02:22:24.7	38.22	20.43	15.5	2.2	CEPHALONIA Isl.- W. GREECE
207	20111225	03:57:52.2	38.23	20.43	14.5	2.9	CEPHALONIA Isl.- W. GREECE

Index	YYYYMMDD	HH MM SS	LAT (N)	LON (E)	DEPTH (km)	M_L	LOCATION
208	20111225	05:13:03.3	38.19	20.28	10.6	2.2	CEPHALONIA Isl.- W. GREECE
209	20111225	07:27:02.2	38.26	20.30	4.7	1.8	CEPHALONIA Isl.- W. GREECE
210	20111225	07:30:20.9	38.27	20.44	12.4	1.4	CEPHALONIA Isl.- W. GREECE
211	20111225	08:40:33.3	38.26	20.32	3.2	1.8	CEPHALONIA Isl.- W. GREECE
212	20111225	11:44:44.3	37.99	20.25	10.7	2.2	Central IONIAN sea- W. GREECE
213	20111226	02:34:44.9	37.92	21.18	19.5	2.1	West PELOPONNESE- SW GREECE
214	20111226	11:41:33.7	38.12	20.41	14.4	2.1	CEPHALONIA Isl.- W. GREECE
215	20111226	21:16:39.2	38.53	20.52	14.6	1.8	LEFKADA Isl.- W. GREECE
216	20111227	10:26:32.2	38.26	20.30	2.9	2.3	CEPHALONIA Isl.- W. GREECE
217	20111227	21:17:02.1	37.81	20.41	5.4	1.6	ZAKYNTHOS Isl.- W. GREECE
218	20111228	00:34:34.8	38.11	20.37	7.9	1.7	CEPHALONIA Isl.- W. GREECE
219	20111228	00:49:46.1	38.27	20.32	8.2	1.0	CEPHALONIA Isl.- W. GREECE
220	20111228	02:52:57.8	38.22	20.34	14.2	2.0	CEPHALONIA Isl.- W. GREECE
221	20111228	19:18:09.3	38.02	20.41	11.7	1.5	CEPHALONIA Isl.- W. GREECE
222	20111229	14:05:02.4	38.14	20.51	10.3	2.0	CEPHALONIA Isl.- W. GREECE
223	20111229	14:06:23.8	38.23	20.49	1.3	1.6	CEPHALONIA Isl.- W. GREECE
224	20111229	14:35:18.8	38.11	20.50	6.4	1.5	CEPHALONIA Isl.- W. GREECE
225	20111229	19:21:54.8	38.20	20.41	7.4	1.3	CEPHALONIA Isl.- W. GREECE
226	20111230	00:45:39.3	38.23	20.55	1.3	2.1	CEPHALONIA Isl.- W. GREECE
227	20111230	17:43:59.3	38.17	20.27	10.2	2.1	CEPHALONIA Isl.- W. GREECE
228	20111230	22:04:29.1	38.28	20.34	4.8	1.5	CEPHALONIA Isl.- W. GREECE
229	20111231	08:55:25.1	38.39	20.43	13.4	2.3	CEPHALONIA Isl.- W. GREECE
230	20111231	16:25:33.0	38.28	20.33	8.4	1.8	CEPHALONIA Isl.- W. GREECE
231	20111231	16:48:28.4	38.25	20.33	9.5	1.6	CEPHALONIA Isl.- W. GREECE
232	20111231	17:09:51.4	37.99	20.45	6.9	1.5	CEPHALONIA Isl.- W. GREECE
233	20111231	23:24:12.6	38.05	20.40	18.1	1.6	CEPHALONIA Isl.- W. GREECE
234	20120101	11:45:58.3	37.55	20.87	3.5	2.6	ZAKYNTHOS Isl.- W. GREECE
235	20120101	14:35:12.0	38.05	20.77	13.1	1.9	CEPHALONIA Isl.- W. GREECE
236	20120102	19:29:36.4	38.05	20.52	13.0	1.4	CEPHALONIA Isl.- W. GREECE
237	20120103	18:19:11.6	38.26	20.73	12.5	1.8	CEPHALONIA Isl.- W. GREECE
238	20120103	19:43:09.3	38.10	20.49	15.1	1.6	CEPHALONIA Isl.- W. GREECE
239	20120103	23:11:54.7	38.14	20.55	17.6	1.5	CEPHALONIA Isl.- W. GREECE
240	20120107	11:04:44.4	38.14	20.35	12.8	1.9	CEPHALONIA Isl.- W. GREECE
241	20120108	01:29:51.9	38.16	20.51	10.8	1.3	CEPHALONIA Isl.- W. GREECE
242	20120110	00:42:52.5	38.31	20.55	7.0	1.3	CEPHALONIA Isl.- W. GREECE
243	20120110	06:46:24.4	38.18	20.38	11.5	1.8	CEPHALONIA Isl.- W. GREECE
244	20120112	05:16:52.1	38.36	20.46	13.5	1.7	CEPHALONIA Isl.- W. GREECE
245	20120112	14:47:13.2	38.16	20.59	18.3	2.6	CEPHALONIA Isl.- W. GREECE
246	20120114	10:00:38.0	38.23	20.42	8.8	1.6	CEPHALONIA Isl.- W. GREECE
247	20120115	13:10:12.6	38.07	20.39	22.6	2.8	CEPHALONIA Isl.- W. GREECE
248	20120115	16:03:40.9	38.07	20.64	9.3	2.0	CEPHALONIA Isl.- W. GREECE
249	20120116	05:34:14.6	38.21	20.36	14.8	2.0	CEPHALONIA Isl.- W. GREECE
250	20120116	05:59:00.7	38.23	20.32	5.1	2.0	CEPHALONIA Isl.- W. GREECE

Index	YYYYMMDD	HH MM SS	LAT (N)	LON (E)	DEPTH (km)	M_L	LOCATION
251	20120116	12:22:44.8	38.22	20.33	6.1	1.8	CEPHALONIA Isl.- W. GREECE
252	20120116	15:38:58.9	38.22	20.30	5.1	1.9	CEPHALONIA Isl.- W. GREECE
253	20120117	04:58:47.2	38.20	20.32	2.8	1.5	CEPHALONIA Isl.- W. GREECE
254	20120117	14:48:50.3	37.48	20.52	18.6	2.7	South IONIAN sea- W. GREECE
255	20120118	04:48:57.2	38.14	20.34	26.1	1.4	CEPHALONIA Isl.- W. GREECE
256	20120119	10:39:43.0	38.26	20.70	13.1	1.6	CEPHALONIA Isl.- W. GREECE
257	20120119	12:50:51.5	38.08	20.77	14.0	2.8	CEPHALONIA Isl.- W. GREECE
258	20120119	23:46:08.7	38.58	20.46	10.0	2.2	LEFKADA Isl.- W. GREECE
259	20120120	05:57:35.9	38.23	20.40	20.0	1.5	CEPHALONIA Isl.- W. GREECE
260	20120120	06:42:16.6	38.16	20.37	12.7	1.6	CEPHALONIA Isl.- W. GREECE
261	20120120	13:57:17.8	38.25	20.38	14.6	1.6	CEPHALONIA Isl.- W. GREECE
262	20120120	19:38:17.2	38.38	20.44	7.0	2.2	CEPHALONIA Isl.- W. GREECE
263	20120121	17:04:01.8	38.14	20.40	19.2	1.4	CEPHALONIA Isl.- W. GREECE
264	20120121	23:24:23.0	38.14	20.40	18.4	1.3	CEPHALONIA Isl.- W. GREECE
265	20120122	02:22:48.4	38.11	20.42	12.6	1.5	CEPHALONIA Isl.- W. GREECE
266	20120122	03:30:13.9	38.35	20.60	4.3	1.8	CEPHALONIA Isl.- W. GREECE
267	20120123	00:32:18.1	38.70	20.52	4.3	1.9	LEFKADA Isl.- W. GREECE
268	20120124	11:17:06.3	38.06	20.24	13.4	2.8	Central IONIAN sea- W. GREECE
269	20120124	20:33:26.9	38.22	20.37	10.9	1.6	CEPHALONIA Isl.- W. GREECE
270	20120125	16:34:35.9	38.24	20.59	13.6	1.6	CEPHALONIA Isl.- W. GREECE
271	20120126	15:19:46.2	37.89	21.04	22.3	3.4	Central IONIAN sea- W. GREECE
272	20120127	13:24:12.8	38.01	20.47	4.5	1.9	CEPHALONIA Isl.- W. GREECE
273	20120127	22:40:06.6	37.55	20.97	6.9	3.3	W of PELOPONNESE- SW GREECE
274	20120128	08:16:46.4	38.16	20.40	17.1	2.1	CEPHALONIA Isl.- W. GREECE
275	20120129	13:45:59.6	37.85	20.96	12.8	2.4	ZAKYNTHOS Isl.- W. GREECE
276	20120130	07:31:47.4	37.95	21.14	26.6	2.6	West PELOPONNESE- SW GREECE
277	20120131	07:44:49.2	38.26	20.51	7.8	2.3	CEPHALONIA Isl.- W. GREECE
278	20120131	16:33:06.4	38.24	20.34	12.6	1.7	CEPHALONIA Isl.- W. GREECE
279	20120201	20:12:54.8	38.20	20.52	19.8	2.0	CEPHALONIA Isl.- W. GREECE
280	20120202	01:52:56.0	37.81	21.15	2.0	2.6	West PELOPONNESE- SW GREECE
281	20120202	21:29:45.9	38.08	20.53	18.5	1.3	CEPHALONIA Isl.- W. GREECE
282	20120204	01:25:07.2	38.08	20.61	18.6	2.1	CEPHALONIA Isl.- W. GREECE
283	20120204	06:11:19.5	38.18	20.69	8.3	2.0	CEPHALONIA Isl.- W. GREECE
284	20120205	05:58:09.6	38.26	20.47	10.1	1.9	CEPHALONIA Isl.- W. GREECE
285	20120206	03:28:39.0	37.79	20.38	12.7	2.0	Central IONIAN sea- W. GREECE
286	20120211	15:41:01.8	38.29	20.44	16.3	2.5	CEPHALONIA Isl.- W. GREECE
287	20120211	23:14:55.8	38.17	20.69	13.3	1.5	CEPHALONIA Isl.- W. GREECE
288	20120213	23:46:24.5	38.12	20.49	16.4	2.6	CEPHALONIA Isl.- W. GREECE
289	20120214	09:28:21.1	38.24	20.50	14.4	1.6	CEPHALONIA Isl.- W. GREECE
290	20120215	08:17:35.4	38.15	20.90	3.7	2.4	Central IONIAN sea- W. GREECE
291	20120217	03:11:34.0	37.82	20.39	13.3	3.2	Central IONIAN sea- W. GREECE
292	20120217	03:59:04.6	38.64	21.32	48.1	3.4	Western GREECE
293	20120218	14:02:40.8	38.13	20.82	11.6	3.9	CEPHALONIA Isl.- W. GREECE

Index	YYYYMMDD	HH MM SS	LAT (N)	LON (E)	DEPTH (km)	M_L	LOCATION
294	20120218	15:46:13.5	37.75	21.18	14.8	2.7	West PELOPONNESE- SW GREECE
295	20120218	22:10:17.8	38.35	20.51	15.5	1.4	CEPHALONIA Isl.- W. GREECE
296	20120219	05:29:00.2	38.12	20.64	16.5	2.1	CEPHALONIA Isl.- W. GREECE
297	20120219	06:17:03.2	38.41	20.48	11.6	2.0	CEPHALONIA Isl.- W. GREECE
298	20120219	11:21:37.6	38.26	20.35	14.0	1.8	CEPHALONIA Isl.- W. GREECE
299	20120220	18:08:35.2	37.71	20.95	14.5	2.6	ZAKYNTHOS Isl.- W. GREECE
300	20120220	23:15:24.3	38.20	20.56	16.5	1.5	CEPHALONIA Isl.- W. GREECE
301	20120222	00:01:40.0	38.40	20.50	2.5	1.9	CEPHALONIA Isl.- W. GREECE
302	20120222	00:25:35.2	38.13	20.83	11.9	2.1	CEPHALONIA Isl.- W. GREECE
303	20120224	20:13:26.8	38.16	20.62	12.0	2.4	CEPHALONIA Isl.- W. GREECE
304	20120225	20:46:03.8	38.25	20.40	12.5	2.1	CEPHALONIA Isl.- W. GREECE
305	20120225	21:19:26.0	38.19	20.48	5.7	1.6	CEPHALONIA Isl.- W. GREECE
306	20120226	06:17:15.7	38.32	20.40	9.8	0.9	CEPHALONIA Isl.- W. GREECE
307	20120226	16:53:50.6	38.23	20.56	18.0	1.5	CEPHALONIA Isl.- W. GREECE
308	20120226	21:18:57.5	38.40	20.45	6.7	1.6	CEPHALONIA Isl.- W. GREECE
309	20120228	04:39:22.0	37.97	20.88	13.9	2.8	ZAKYNTHOS Isl.- W. GREECE
310	20120301	18:24:48.8	38.04	20.39	4.8	1.7	CEPHALONIA Isl.- W. GREECE
311	20120302	02:56:17.2	38.22	20.42	15.3	2.3	CEPHALONIA Isl.- W. GREECE
312	20120302	19:44:11.6	38.38	20.54	18.0	1.2	CEPHALONIA Isl.- W. GREECE
313	20120303	07:49:43.3	38.54	21.25	3.2	2.5	Western GREECE
314	20120303	23:04:30.8	38.52	20.48	12.6	1.9	LEFKADA Isl.- W. GREECE
315	20120304	19:37:17.9	37.60	20.55	13.1	2.6	South IONIAN sea- W. GREECE
316	20120305	17:46:56.0	38.22	20.66	11.7	2.0	CEPHALONIA Isl.- W. GREECE
317	20120306	18:52:53.6	38.09	20.47	12.5	2.2	CEPHALONIA Isl.- W. GREECE
318	20120307	22:50:21.4	37.69	20.89	17.1	2.3	ZAKYNTHOS Isl.- W. GREECE
319	20120307	22:55:52.0	37.55	20.83	15.9	2.3	ZAKYNTHOS Isl.- W. GREECE
320	20120307	23:18:02.4	37.67	20.88	23.4	2.1	ZAKYNTHOS Isl.- W. GREECE
321	20120307	23:30:48.7	37.67	20.89	19.4	2.6	ZAKYNTHOS Isl.- W. GREECE
322	20120309	17:09:23.0	38.06	20.45	10.5	2.3	CEPHALONIA Isl.- W. GREECE
323	20120310	03:57:54.6	38.35	20.37	7.3	2.5	CEPHALONIA Isl.- W. GREECE
324	20120311	07:02:23.0	38.67	20.86	30.9	2.6	LEFKADA Isl.- W. GREECE
325	20120314	01:13:38.3	38.06	20.43	3.0	1.5	CEPHALONIA Isl.- W. GREECE
326	20120314	17:34:49.2	38.04	20.55	1.4	1.5	CEPHALONIA Isl.- W. GREECE
327	20120314	21:44:43.0	37.75	20.13	0.0	2.9	Central IONIAN sea- W. GREECE
328	20120314	22:17:36.5	38.05	20.70	10.5	1.8	CEPHALONIA Isl.- W. GREECE
329	20120315	01:07:11.7	38.11	20.48	16.0	1.7	CEPHALONIA Isl.- W. GREECE
330	20120315	06:26:12.9	38.06	20.37	8.4	1.9	CEPHALONIA Isl.- W. GREECE
331	20120317	02:36:59.4	37.94	20.93	31.2	2.4	ZAKYNTHOS Isl.- W. GREECE
332	20120317	22:37:44.6	38.08	20.36	8.5	1.9	CEPHALONIA Isl.- W. GREECE
333	20120318	13:52:21.8	38.04	20.25	17.5	3.1	Central IONIAN sea- W. GREECE
334	20120318	14:23:29.5	38.06	20.24	18.5	1.9	Central IONIAN sea- W. GREECE
335	20120318	17:35:19.6	38.24	20.56	15.9	1.6	CEPHALONIA Isl.- W. GREECE
336	20120318	18:11:21.9	38.18	20.72	17.2	2.3	CEPHALONIA Isl.- W. GREECE

Index	YYYYMMDD	HH MM SS	LAT (N)	LON (E)	DEPTH (km)	M_L	LOCATION
337	20120319	15:34:31.2	38.15	20.60	17.2	1.6	CEPHALONIA Isl.- W. GREECE
338	20120319	19:59:43.6	38.20	20.60	18.6	1.5	CEPHALONIA Isl.- W. GREECE
339	20120320	02:02:19.0	38.39	20.50	9.1	1.1	CEPHALONIA Isl.- W. GREECE
340	20120320	16:41:50.3	38.19	20.55	16.8	3.3	CEPHALONIA Isl.- W. GREECE
341	20120320	16:45:16.9	38.07	20.53	4.3	1.6	CEPHALONIA Isl.- W. GREECE
342	20120320	16:46:36.9	38.07	20.52	7.0	1.3	CEPHALONIA Isl.- W. GREECE
343	20120320	16:49:43.7	38.22	20.27	9.1	1.9	CEPHALONIA Isl.- W. GREECE
344	20120320	16:53:24.1	38.12	20.54	13.7	1.7	CEPHALONIA Isl.- W. GREECE
345	20120320	18:50:51.6	38.17	20.54	18.5	3.0	CEPHALONIA Isl.- W. GREECE
346	20120320	19:07:39.0	38.18	20.54	17.1	1.7	CEPHALONIA Isl.- W. GREECE
347	20120320	19:23:41.1	38.17	20.56	16.8	1.6	CEPHALONIA Isl.- W. GREECE
348	20120320	19:53:09.7	38.18	20.55	17.6	1.5	CEPHALONIA Isl.- W. GREECE
349	20120320	20:06:02.8	38.18	20.54	17.1	1.6	CEPHALONIA Isl.- W. GREECE
350	20120320	21:22:39.6	38.14	20.54	14.7	1.1	CEPHALONIA Isl.- W. GREECE
351	20120320	22:07:47.6	38.19	20.55	17.3	2.0	CEPHALONIA Isl.- W. GREECE
352	20120320	22:09:10.7	38.07	20.53	3.9	1.2	CEPHALONIA Isl.- W. GREECE
353	20120320	22:09:34.0	38.23	20.56	16.4	1.3	CEPHALONIA Isl.- W. GREECE
354	20120320	23:44:39.9	38.20	20.56	17.4	1.3	CEPHALONIA Isl.- W. GREECE
355	20120320	23:55:26.6	38.18	20.55	17.2	2.0	CEPHALONIA Isl.- W. GREECE
356	20120321	00:13:30.4	38.18	20.55	17.3	1.5	CEPHALONIA Isl.- W. GREECE
357	20120321	00:52:17.3	38.22	20.55	17.4	1.0	CEPHALONIA Isl.- W. GREECE
358	20120321	00:53:24.1	38.18	20.54	16.0	0.9	CEPHALONIA Isl.- W. GREECE
359	20120321	02:11:18.0	38.21	20.55	15.7	0.8	CEPHALONIA Isl.- W. GREECE
360	20120321	22:15:25.8	38.23	20.47	12.3	0.8	CEPHALONIA Isl.- W. GREECE
361	20120321	22:15:36.0	38.33	20.44	5.0	1.5	CEPHALONIA Isl.- W. GREECE
362	20120321	22:17:25.8	38.28	20.44	14.9	1.5	CEPHALONIA Isl.- W. GREECE
363	20120321	22:19:35.4	38.29	20.44	12.5	1.7	CEPHALONIA Isl.- W. GREECE
364	20120321	22:32:54.1	38.29	20.43	13.2	3.1	CEPHALONIA Isl.- W. GREECE
365	20120321	22:56:19.6	38.22	20.37	19.2	1.7	CEPHALONIA Isl.- W. GREECE
366	20120322	02:28:35.2	38.10	20.22	14.8	1.9	Central IONIAN sea- W. GREECE
367	20120322	02:47:47.4	38.29	20.42	12.3	1.7	CEPHALONIA Isl.- W. GREECE
368	20120322	03:35:16.3	37.63	20.89	6.6	1.8	ZAKYNTHOS Isl.- W. GREECE
369	20120323	13:25:06.0	38.42	20.49	14.2	1.5	CEPHALONIA Isl.- W. GREECE
370	20120323	21:49:14.0	38.06	20.53	4.4	0.9	CEPHALONIA Isl.- W. GREECE
371	20120323	22:34:37.9	38.18	20.74	18.5	0.4	CEPHALONIA Isl.- W. GREECE
372	20120324	11:44:09.3	38.13	20.32	9.6	1.5	CEPHALONIA Isl.- W. GREECE
373	20120324	16:36:14.3	38.12	20.65	18.5	1.6	CEPHALONIA Isl.- W. GREECE
374	20120324	21:44:50.8	37.71	20.83	14.6	1.9	ZAKYNTHOS Isl.- W. GREECE
375	20120326	09:01:26.6	38.42	20.50	7.5	1.8	CEPHALONIA Isl.- W. GREECE
376	20120326	10:04:22.7	38.48	20.57	16.8	2.2	CEPHALONIA Isl.- W. GREECE
377	20120326	10:07:13.4	38.48	20.60	17.4	1.7	CEPHALONIA Isl.- W. GREECE
378	20120326	21:47:04.9	38.03	20.68	13.0	1.5	CEPHALONIA Isl.- W. GREECE
379	20120327	14:33:02.3	38.15	20.65	18.8	2.0	CEPHALONIA Isl.- W. GREECE

Index	YYYYMMDD	HH MM SS	LAT (N)	LON (E)	DEPTH (km)	M_L	LOCATION
380	20120328	05:11:34.2	38.24	20.37	5.9	1.5	CEPHALONIA Isl.- W. GREECE
381	20120328	07:15:00.3	38.40	20.50	9.4	1.4	CEPHALONIA Isl.- W. GREECE
382	20120328	09:32:52.7	38.11	20.49	15.6	1.5	CEPHALONIA Isl.- W. GREECE
383	20120328	18:21:15.2	38.12	20.43	15.4	2.1	CEPHALONIA Isl.- W. GREECE
384	20120328	22:51:44.9	38.10	20.50	13.2	1.5	CEPHALONIA Isl.- W. GREECE
385	20120328	23:42:27.9	38.16	20.43	37.9	1.4	CEPHALONIA Isl.- W. GREECE
386	20120330	11:32:41.9	38.25	20.74	12.4	1.7	CEPHALONIA Isl.- W. GREECE
387	20120330	11:58:09.5	38.27	20.73	13.1	2.6	CEPHALONIA Isl.- W. GREECE
388	20120330	12:20:32.9	38.26	20.73	12.1	2.7	CEPHALONIA Isl.- W. GREECE
389	20120331	06:11:59.4	37.90	21.00	12.7	2.5	Central IONIAN sea- W. GREECE
390	20120331	23:17:26.5	38.06	20.23	14.6	1.9	Central IONIAN sea- W. GREECE
391	20120401	21:53:08.4	38.27	20.41	12.7	1.4	CEPHALONIA Isl.- W. GREECE
392	20120401	23:48:49.6	38.18	20.65	18.9	1.9	CEPHALONIA Isl.- W. GREECE
393	20120402	00:48:37.4	38.23	20.40	16.0	1.6	CEPHALONIA Isl.- W. GREECE
394	20120402	11:48:32.2	38.20	20.55	17.5	1.6	CEPHALONIA Isl.- W. GREECE
395	20120402	15:59:47.7	38.30	20.62	17.1	1.8	CEPHALONIA Isl.- W. GREECE
396	20120402	17:38:17.5	38.24	20.37	3.3	1.1	CEPHALONIA Isl.- W. GREECE
397	20120402	20:22:41.0	38.25	20.37	0.9	0.9	CEPHALONIA Isl.- W. GREECE
398	20120402	20:22:54.7	38.24	20.37	0.8	1.1	CEPHALONIA Isl.- W. GREECE
399	20120402	23:31:16.1	38.45	21.03	16.9	1.9	Western GREECE
400	20120402	23:34:59.7	37.58	20.91	0.7	1.6	ZAKYNTHOS Isl.- W. GREECE
401	20120402	23:41:57.8	37.99	21.38	14.3	2.4	West PELOPONNESE- SW GREECE
402	20120403	07:19:53.4	38.25	20.26	8.1	2.3	CEPHALONIA Isl.- W. GREECE
403	20120404	00:49:31.7	38.09	20.26	13.0	2.1	Central IONIAN sea- W. GREECE
404	20120405	03:52:29.5	38.26	20.42	16.0	2.2	CEPHALONIA Isl.- W. GREECE
405	20120406	09:35:07.4	38.20	20.39	15.9	2.1	CEPHALONIA Isl.- W. GREECE
406	20120406	15:07:46.1	38.20	20.40	15.8	1.7	CEPHALONIA Isl.- W. GREECE
407	20120406	18:42:49.0	38.22	20.39	16.5	1.4	CEPHALONIA Isl.- W. GREECE
408	20120406	18:50:24.9	38.15	20.39	13.9	1.2	CEPHALONIA Isl.- W. GREECE
409	20120406	20:48:17.8	38.26	20.38	17.1	1.4	CEPHALONIA Isl.- W. GREECE
410	20120406	21:07:11.5	38.21	20.40	15.6	1.6	CEPHALONIA Isl.- W. GREECE
411	20120406	22:12:27.6	38.24	20.32	10.4	2.0	CEPHALONIA Isl.- W. GREECE
412	20120406	23:12:11.1	38.25	20.35	8.9	1.5	CEPHALONIA Isl.- W. GREECE
413	20120407	00:20:25.6	38.39	20.48	14.4	2.0	CEPHALONIA Isl.- W. GREECE
414	20120407	00:35:33.5	38.24	20.38	15.6	1.4	CEPHALONIA Isl.- W. GREECE
415	20120407	02:31:22.9	38.27	20.35	4.9	0.9	CEPHALONIA Isl.- W. GREECE
416	20120407	07:26:41.8	38.23	20.40	14.9	1.4	CEPHALONIA Isl.- W. GREECE
417	20120407	07:33:08.2	38.13	20.32	15.3	1.6	CEPHALONIA Isl.- W. GREECE
418	20120407	07:43:01.4	38.21	20.39	15.7	1.6	CEPHALONIA Isl.- W. GREECE
419	20120407	11:24:25.1	38.20	20.28	13.3	1.1	CEPHALONIA Isl.- W. GREECE
420	20120407	13:09:56.3	38.22	20.42	18.2	1.4	CEPHALONIA Isl.- W. GREECE
421	20120407	13:54:26.3	38.37	20.69	17.6	1.5	CEPHALONIA Isl.- W. GREECE
422	20120407	18:52:02.5	38.17	20.76	13.8	1.6	CEPHALONIA Isl.- W. GREECE

Index	YYYYMMDD	HH MM SS	LAT (N)	LON (E)	DEPTH (km)	M_L	LOCATION
423	20120407	19:55:40.4	38.13	20.23	19.9	1.7	Central IONIAN sea- W. GREECE
424	20120408	06:31:54.5	38.11	20.37	18.3	2.0	CEPHALONIA Isl.- W. GREECE
425	20120409	07:57:53.0	38.08	20.23	16.3	2.1	Central IONIAN sea- W. GREECE
426	20120409	18:52:45.6	38.06	20.22	12.4	2.2	Central IONIAN sea- W. GREECE
427	20120410	00:26:07.1	38.33	20.47	15.2	1.5	CEPHALONIA Isl.- W. GREECE
428	20120410	00:39:57.1	38.25	20.40	13.5	1.5	CEPHALONIA Isl.- W. GREECE
429	20120410	02:39:07.1	38.27	20.40	13.2	1.6	CEPHALONIA Isl.- W. GREECE
430	20120410	02:43:42.1	38.22	20.38	15.1	2.0	CEPHALONIA Isl.- W. GREECE
431	20120410	09:41:07.8	38.22	20.38	15.6	1.9	CEPHALONIA Isl.- W. GREECE
432	20120410	13:33:38.7	38.07	20.23	11.4	2.6	Central IONIAN sea- W. GREECE
433	20120410	13:45:45.0	38.09	20.22	12.4	2.5	Central IONIAN sea- W. GREECE
434	20120410	14:24:35.8	38.09	20.24	11.9	2.0	Central IONIAN sea- W. GREECE
435	20120410	14:48:45.1	38.22	20.38	16.4	2.3	CEPHALONIA Isl.- W. GREECE
436	20120410	14:53:55.4	38.22	20.40	15.8	1.9	CEPHALONIA Isl.- W. GREECE
437	20120410	15:21:50.9	38.21	20.39	16.2	1.6	CEPHALONIA Isl.- W. GREECE
438	20120410	15:33:16.7	38.23	20.39	15.6	2.7	CEPHALONIA Isl.- W. GREECE
439	20120410	17:43:23.1	38.08	20.23	13.9	2.6	Central IONIAN sea- W. GREECE
440	20120410	18:29:54.6	38.27	20.40	12.5	1.4	CEPHALONIA Isl.- W. GREECE
441	20120410	19:07:47.9	38.28	20.41	9.8	1.3	CEPHALONIA Isl.- W. GREECE
442	20120410	21:55:35.7	38.52	20.55	11.8	2.2	LEFKADA Isl.- W. GREECE
443	20120410	23:50:49.4	38.21	20.37	16.4	2.0	CEPHALONIA Isl.- W. GREECE
444	20120410	23:54:23.0	38.20	20.38	16.8	1.8	CEPHALONIA Isl.- W. GREECE
445	20120411	00:09:02.8	38.09	20.23	12.3	2.3	Central IONIAN sea- W. GREECE
446	20120411	07:52:19.4	38.21	20.39	15.7	1.7	CEPHALONIA Isl.- W. GREECE
447	20120411	15:30:59.9	38.20	20.39	17.2	2.1	CEPHALONIA Isl.- W. GREECE
448	20120411	17:03:01.9	38.28	20.40	11.6	1.5	CEPHALONIA Isl.- W. GREECE
449	20120411	22:08:08.7	38.21	20.40	15.8	1.7	CEPHALONIA Isl.- W. GREECE
450	20120413	00:27:04.6	38.21	20.38	17.3	1.3	CEPHALONIA Isl.- W. GREECE
451	20120413	02:51:10.9	38.08	20.41	16.5	2.0	CEPHALONIA Isl.- W. GREECE
452	20120413	03:46:36.0	38.08	20.25	12.8	1.7	Central IONIAN sea- W. GREECE
453	20120413	04:03:40.1	38.21	20.38	17.3	2.4	CEPHALONIA Isl.- W. GREECE
454	20120413	06:58:03.8	38.11	20.36	15.2	1.5	CEPHALONIA Isl.- W. GREECE
455	20120413	16:28:39.5	38.20	20.39	16.0	1.8	CEPHALONIA Isl.- W. GREECE
456	20120415	13:25:43.3	38.22	20.34	16.0	2.4	CEPHALONIA Isl.- W. GREECE
457	20120415	22:19:04.9	38.42	20.61	13.1	2.1	CEPHALONIA Isl.- W. GREECE
458	20120416	00:33:17.0	38.24	20.59	17.4	1.8	CEPHALONIA Isl.- W. GREECE
459	20120416	15:46:38.5	38.24	20.40	6.6	1.7	CEPHALONIA Isl.- W. GREECE
460	20120416	20:53:52.3	38.34	20.66	9.1	1.8	CEPHALONIA Isl.- W. GREECE
461	20120417	06:50:17.0	38.43	20.49	1.5	1.9	CEPHALONIA Isl.- W. GREECE

E.2 Catalogue of Events that are Not Re-localized (Repi >80 km)

Index	YYYYMMDD	HH MM SS	LAT(N)	LON(E)	DEPTH(km)	M_L
1	20110922	00:41:48.1	38.23	22.22	54.0	2.5
2	20110922	03:11:01.3	37.20	22.02	10.0	3.1
3	20110922	21:31:47.7	37.18	22.01	14.0	3.2
4	20110923	20:59:43.0	40.55	21.43	24.0	3.8
5	20110924	13:10:21.1	38.32	21.80	18.0	2.9
6	20111004	09:26:28.3	39.18	21.60	20.0	4.3
7	20111009	18:42:20.4	37.78	21.43	17.0	3.3
8	20111010	13:22:31.7	38.89	20.28	27.0	3.2
9	20111010	19:07:00.5	37.19	22.04	11.0	4.5
10	20111011	01:10:08.8	37.19	22.01	15.0	3.7
11	20111013	12:43:50.2	38.01	21.68	19.0	1.8
12	20111014	20:12:44.6	37.17	22.04	7.0	3.3
13	20111015	01:13:19.1	37.19	22.01	8.0	2.4
14	20111015	22:06:38.3	37.17	22.07	13.0	3.7
15	20111017	10:00:04.4	38.89	20.62	37.0	3.1
16	20111019	19:39:10.5	39.26	20.83	9.0	3.7
17	20111019	20:49:34.1	37.34	20.81	25.0	2.6
18	20111019	23:19:39.4	37.18	22.06	3.0	3.0
19	20111020	17:24:08.4	39.79	20.45	20.0	3.1
20	20111020	17:50:08.2	38.21	21.65	10.0	1.9
21	20111020	22:35:23.2	38.20	21.65	23.0	2.0
22	20111023	10:41:23.4	38.78	43.40	10.0	7.2
23	20111023	17:51:15.9	37.08	21.54	36.0	3.4
24	20111023	20:45:37.4	38.64	43.22	10.0	6.0
25	20111024	14:31:15.8	38.76	21.84	5.0	3.4
26	20111026	19:11:46.2	37.24	22.04	2.0	3.3
27	20111027	03:23:11.8	39.01	19.73	31.0	2.7
28	20111028	03:41:13.5	37.14	21.07	9.0	3.3
29	20111028	08:01:52.6	37.54	20.65	25.0	2.2
30	20111028	16:22:16.5	37.23	20.41	22.0	2.2
31	20111029	14:07:18.6	37.08	20.95	15.0	2.6
32	20111031	17:49:51.9	37.39	20.52	25.0	1.8
33	20111101	00:21:38.0	38.22	21.96	12.0	2.6
34	20111101	13:01:44.6	37.85	22.15	63.0	2.6
35	20111103	19:34:54.5	37.89	22.01	22.0	3.4
36	20111104	19:58:41.6	37.80	22.06	23.0	2.9
37	20111105	05:10:41.7	38.01	21.66	27.0	2.5
38	20111106	03:18:31.4	39.16	20.62	12.0	2.7
39	20111107	18:51:01.4	37.42	20.87	9.0	2.4
40	20111108	14:49:36.5	38.96	21.19	13.0	2.5
41	20111108	20:41:48.0	39.22	19.53	36.0	2.7

Index	YYYYMMDD	HH MM SS	LAT(N)	LON(E)	DEPTH(km)	M_L
42	20111110	00:36:12.7	37.66	21.75	15.0	2.7
43	20111110	17:25:39.6	38.42	21.83	19.0	4.6
44	20111112	18:28:08.9	37.23	22.00	12.0	3.8
45	20111113	22:24:34.8	38.12	22.04	53.0	2.9
46	20111115	00:28:36.0	37.55	21.83	19.0	3.1
47	20111115	11:39:38.6	37.33	20.84	26.0	2.9
48	20111116	03:53:02.1	37.33	20.53	9.0	2.0
49	20111116	04:43:27.0	37.70	21.44	18.0	2.1
50	20111116	07:08:05.5	38.11	21.54	24.0	3.3
51	20111116	07:09:47.0	38.11	21.55	21.0	2.7
52	20111116	08:20:39.2	38.12	21.52	23.0	3.0
53	20111117	00:04:17.8	37.60	21.51	24.0	2.4
54	20111117	03:45:52.2	38.02	21.97	22.0	2.6
55	20111118	17:39:40.7	38.85	43.87	2.0	5.0
56	20111118	19:23:55.7	38.51	21.53	16.0	3.0
57	20111118	19:51:12.6	37.03	21.15	29.0	3.0
58	20111118	20:43:46.9	39.50	20.66	23.0	2.7
59	20111120	04:05:52.6	37.14	21.04	19.0	2.5
60	20111120	05:13:30.6	37.28	21.93	7.0	2.2
61	20111120	06:26:01.4	39.49	20.63	10.0	2.7
62	20111120	07:08:36.6	37.14	20.95	14.0	2.5
63	20111120	07:13:52.8	37.18	21.10	13.0	2.2
64	20111120	07:38:01.0	37.10	21.02	15.0	2.3
65	20111120	22:14:14.0	38.17	22.56	21.0	3.5
66	20111123	12:17:50.7	34.20	25.09	10.0	5.5
67	20111123	20:29:45.9	37.14	22.08	16.0	3.7
68	20111124	04:09:23.0	39.40	19.81	36.0	3.6
69	20111126	16:41:22.6	38.34	21.80	18.0	3.4
70	20111127	11:17:38.3	38.93	19.75	26.0	2.5
71	20111127	15:09:13.4	38.34	21.79	18.0	3.4
72	20111127	21:00:23.7	37.82	21.89	25.0	3.2
73	20111127	21:12:35.0	37.81	21.88	22.0	2.7
74	20111128	12:13:07.6	38.78	19.69	24.0	2.8
75	20111128	15:01:45.4	37.97	21.52	27.0	3.1
76	20111128	15:10:19.8	37.95	21.51	25.0	2.5
77	20111129	16:55:58.0	37.58	24.00	158.0	4.1
78	20111129	16:55:57.1	37.56	24.05	161.0	3.9
79	20111130	18:36:47.5	37.23	21.99	14.0	3.0
80	20111130	20:07:29.6	37.24	21.99	15.0	2.8
81	20111130	20:10:19.6	37.32	22.37	17.0	3.2
82	20111130	21:46:10.1	37.25	21.99	11.0	3.0
83	20111201	06:44:33.1	37.26	21.97	8.0	2.8
84	20111202	11:53:28.7	38.35	21.78	20.0	3.0

Index	YYYYMMDD	HH MM SS	LAT(N)	LON(E)	DEPTH(km)	M_L
85	20111202	20:25:06.1	37.26	22.02	3.0	2.8
86	20111202	20:56:25.0	37.21	22.01	14.0	2.5
87	20111203	04:21:23.6	39.23	21.50	23.0	2.4
88	20111203	20:18:47.8	38.36	21.80	18.0	3.3
89	20111203	21:53:25.1	39.32	20.30	14.0	2.0
90	20111203	22:14:36.8	37.50	19.97	34.0	2.6
91	20111205	01:18:02.4	38.07	21.57	13.0	2.3
92	20111205	03:59:38.6	37.91	21.47	29.0	2.3
93	20111205	04:22:26.8	37.90	21.45	22.0	2.9
94	20111209	07:18:55.8	38.37	21.85	12.0	3.1
95	20111209	22:32:53.6	38.02	21.68	28.0	3.1
96	20111211	15:46:33.6	39.73	20.41	14.0	2.9
97	20111211	20:25:31.1	38.39	21.86	12.0	2.6
98	20111212	17:04:43.5	43.29	19.28	3.0	4.5
99	20111212	18:06:20.5	38.35	21.68	15.0	1.3
100	20111215	00:07:42.8	37.51	19.85	14.0	3.1
101	20111215	05:34:52.0	37.98	22.00	16.0	2.5
102	20111215	06:43:58.0	38.55	21.36	9.0	2.7
103	20111215	17:05:49.1	36.98	20.43	20.0	2.7
104	20111217	04:01:12.3	37.32	20.86	27.0	2.3
105	20111218	15:01:03.0	36.02	12.98	10.0	4.7
106	20111218	19:54:04.7	38.34	21.83	12.0	2.6
107	20111219	20:05:47.9	37.67	21.74	16.0	2.8
108	20111219	20:24:21.4	38.41	21.92	12.0	2.4
109	20111220	02:47:47.3	38.34	22.05	9.0	2.4
110	20111220	04:47:54.0	38.35	22.04	14.0	3.3
111	20111220	13:30:19.2	40.18	20.68	14.0	3.3
112	20111221	02:39:28.8	40.10	19.65	2.0	3.0
113	20111221	04:02:31.9	39.44	21.01	8.0	2.6
114	20111221	07:22:59.7	39.95	20.66	5.0	2.9
115	20111221	09:01:21.8	37.70	21.41	19.0	2.9
116	20111221	09:43:47.2	35.86	25.89	117.0	4.2
117	20111222	04:49:29.9	36.97	21.55	18.0	3.2
118	20111222	23:26:17.6	41.77	19.17	15.0	3.8
119	20111223	14:14:48.1	38.09	22.15	56.0	3.4
120	20111224	14:51:10.1	38.52	21.66	20.0	2.6
121	20111225	14:02:18.7	37.51	20.20	19.0	2.3
122	20111226	13:50:44.7	38.38	21.88	10.0	2.5
123	20111226	14:36:45.0	38.38	21.87	9.0	2.6
124	20111226	19:06:03.1	39.34	21.90	24.0	2.8
125	20111226	19:19:57.3	38.26	21.64	26.0	1.9
126	20111228	01:27:20.3	37.07	20.47	24.0	3.1
127	20111228	18:53:21.2	37.83	21.39	24.0	1.7

Index	YYYYMMDD	HH MM SS	LAT(N)	LON(E)	DEPTH(km)	M_L
128	20111229	15:19:35.3	38.34	22.03	14.0	4.0
129	20111230	01:02:39.4	37.99	21.51	25.0	2.8
130	20111230	02:09:46.1	38.87	21.23	23.0	2.5
131	20111230	20:50:40.3	40.74	27.38	27.0	2.4
132	20120101	19:19:15.6	39.36	20.87	21.0	2.7
133	20120102	01:52:59.4	38.81	21.14	20.0	2.4
134	20120102	02:52:19.9	38.81	21.14	22.0	2.3
135	20120102	08:59:37.9	37.85	21.40	25.0	2.6
136	20120102	18:43:15.0	38.31	22.03	11.0	2.7
137	20120103	01:19:48.4	37.40	21.09	12.0	2.4
138	20120104	03:08:18.3	37.94	21.69	28.0	3.2
139	20120105	20:25:49.3	38.99	22.26	22.0	3.7
140	20120105	22:59:15.0	37.25	20.50	23.0	2.6
141	20120107	23:00:09.8	38.58	21.71	17.0	3.6
142	20120108	03:07:24.3	37.37	20.75	29.0	2.2
143	20120109	00:59:02.8	37.51	21.26	24.0	2.2
144	20120109	16:44:24.4	37.50	20.86	15.0	2.1
145	20120109	21:57:21.1	39.16	21.91	23.0	3.0
146	20120110	13:31:08.5	38.03	21.93	27.0	2.7
147	20120112	18:38:47.4	39.31	20.29	8.0	2.5
148	20120112	22:10:59.6	39.30	20.30	8.0	2.3
149	20120113	10:33:41.5	39.27	20.27	7.0	2.7
150	20120113	12:31:23.2	39.29	20.30	6.0	2.7
151	20120114	19:40:19.4	37.59	21.34	18.0	2.5
152	20120116	04:01:15.8	34.78	25.85	23.0	1.5
153	20120116	10:05:56.9	37.61	20.93	18.0	2.5
154	20120116	10:18:23.7	38.15	21.63	23.0	3.0
155	20120117	08:14:45.3	40.20	19.65	10.0	3.2
156	20120118	19:49:23.2	38.95	22.46	24.0	3.5
157	20120120	00:44:22.2	37.36	20.35	9.0	2.3
158	20120120	14:09:18.2	38.12	21.94	26.0	2.7
159	20120121	01:55:01.5	38.38	21.86	17.0	3.1
160	20120121	19:24:52.8	38.36	22.09	11.0	3.1
161	20120122	04:28:34.9	39.07	21.93	20.0	3.4
162	20120122	12:58:49.3	35.63	26.88	23.0	3.3
163	20120122	21:40:41.7	37.78	21.28	18.0	2.1
164	20120124	21:40:27.9	36.78	21.72	22.0	4.0
165	20120125	00:44:17.7	37.35	20.89	29.0	2.1
166	20120125	07:49:41.2	38.18	21.71	23.0	3.1
167	20120125	13:34:33.2	36.79	21.74	21.0	3.7
168	20120126	04:24:58.3	36.06	25.07	29.0	5.3
169	20120127	01:33:23.4	36.06	25.13	31.0	5.2
170	20120127	01:40:58.3	38.97	21.85	21.0	3.9

Index	YYYYMMDD	HH MM SS	LAT(N)	LON(E)	DEPTH(km)	M_L
171	20120128	11:47:20.7	37.39	20.44	15.0	3.1
172	20120129	21:25:41.8	36.66	21.41	14.0	3.1
173	20120130	03:46:27.3	36.41	21.09	18.0	3.1
174	20120201	09:37:42.9	40.16	24.06	20.0	2.1
175	20120203	13:22:38.5	39.19	20.60	12.0	3.7
176	20120205	16:08:13.4	38.18	21.71	22.0	3.1
177	20120205	16:11:25.8	38.18	21.73	22.0	3.1
178	20120211	04:47:07.0	37.71	21.41	13.0	3.1
179	20120211	14:03:47.5	37.37	20.73	27.0	2.4
180	20120213	18:39:22.4	37.19	22.00	8.0	3.2
181	20120214	01:34:38.7	40.13	24.09	24.0	5.0
182	20120214	12:08:12.3	40.11	24.06	24.0	3.5
183	20120217	03:39:35.1	40.12	24.03	17.0	2.1
184	20120217	06:55:56.6	40.16	24.01	14.0	2.2
185	20120217	08:05:04.3	37.87	23.02	17.0	4.2
186	20120218	01:57:40.2	37.54	21.89	21.0	3.5
187	20120219	15:06:03.2	38.88	21.19	19.0	3.0
188	20120220	08:46:36.8	37.19	20.29	16.0	3.2
189	20120225	21:48:32.6	37.42	20.71	13.0	1.9
190	20120226	00:58:04.0	36.30	21.52	30.0	2.3
191	20120226	16:17:06.4	38.32	22.08	7.0	1.7
192	20120302	00:53:14.4	38.27	21.63	23.0	1.9
193	20120302	15:53:21.0	37.03	21.07	17.0	2.6
194	20120304	01:15:43.3	38.27	21.62	27.0	2.8
195	20120304	03:31:07.8	40.13	24.05	24.0	5.0
196	20120304	05:35:32.9	38.26	21.64	28.0	2.2
197	20120304	14:43:59.4	40.16	24.00	18.0	2.1
198	20120305	16:37:36.4	38.26	21.63	27.0	2.2
199	20120305	21:43:41.1	38.25	21.64	28.0	1.9
200	20120305	22:01:15.5	38.28	23.44	20.0	1.0
201	20120306	20:40:06.7	38.27	21.62	25.0	2.6
202	20120307	06:42:44.8	38.27	21.62	23.0	2.3
203	20120307	21:51:36.9	38.27	21.63	24.0	2.5
204	20120308	03:55:50.8	38.12	23.72	18.0	2.5
205	20120308	18:54:24.2	38.70	21.32	17.0	3.4
206	20120308	19:30:47.9	38.69	21.30	19.0	3.0
207	20120308	19:39:27.8	38.69	21.26	21.0	3.2
208	20120309	07:09:53.6	19.10	169.71	29.0	6.7
209	20120309	20:29:51.8	38.69	21.29	17.0	3.1
210	20120309	22:12:25.1	38.27	21.64	24.0	2.4
211	20120311	16:30:44.2	38.26	21.65	20.0	2.6
212	20120313	10:59:36.8	38.60	21.72	17.0	3.8
213	20120313	22:54:18.8	38.15	22.61	13.0	1.7

Index	YYYYMMDD	HH MM SS	LAT(N)	LON(E)	DEPTH(km)	M_L
214	20120314	09:08:35.0	40.95	144.91	10.0	6.9
215	20120314	09:13:08.0	38.62	21.70	18.0	3.3
216	20120314	16:35:30.3	38.26	21.63	25.0	2.6
217	20120315	05:40:58.1	38.69	21.30	15.0	4.4
218	20120318	04:44:37.8	38.25	21.67	26.0	1.8
219	20120320	01:46:44.2	35.24	23.93	41.0	3.6
220	20120320	18:02:49.6	16.69	98.24	19.0	7.4
221	20120320	23:51:09.2	36.05	24.40	67.0	4.6
222	20120321	05:50:47.7	38.61	21.71	16.0	3.8
223	20120322	00:38:12.1	35.49	26.10	30.0	4.1
224	20120324	05:55:09.4	35.92	24.05	44.0	3.9
225	20120326	01:14:49.7	37.76	23.60	19.0	1.1
226	20120326	03:00:17.6	41.78	19.31	10.0	4.7
227	20120328	02:32:33.0	38.38	21.76	16.0	2.0
228	20120328	06:05:33.0	34.54	25.47	0.0	2.4
229	20120328	17:21:50.1	36.56	21.43	5.0	3.0
230	20120328	19:47:22.3	38.42	21.83	18.0	3.6
231	20120328	23:17:04.8	38.55	15.04	243.0	4.0
232	20120329	13:14:01.2	39.98	19.61	13.0	2.9
233	20120329	20:44:30.6	38.27	22.15	11.0	2.6
234	20120401	22:13:17.6	39.20	20.80	18.0	3.1
235	20120402	00:04:10.0	38.51	15.79	98.0	3.1
236	20120402	23:36:52.1	38.02	21.38	15.0	1.9
237	20120403	19:54:30.1	38.17	21.72	25.0	2.9
238	20120404	01:45:30.6	38.07	21.58	19.0	3.4
239	20120404	02:34:51.3	38.24	21.67	19.0	2.2
240	20120409	23:10:09.5	38.07	21.56	17.0	2.8
241	20120411	06:18:51.9	39.67	20.40	9.0	3.7
242	20120411	06:21:33.9	39.67	20.35	12.0	3.2
243	20120411	08:38:35.9	2.37	93.17	10.0	8.6
244	20120411	10:43:09.3	0.81	92.45	10.0	8.0
245	20120411	22:55:11.2	18.29	102.74	20.0	6.7
246	20120412	20:07:01.6	36.97	22.07	13.0	3.4
247	20120412	22:55:08.7	37.72	21.26	29.0	2.7
248	20120412	23:01:42.3	37.79	21.32	27.0	2.5
249	20120412	23:04:31.4	37.77	21.30	28.0	2.8
250	20120412	23:19:12.9	37.78	21.30	28.0	2.3
251	20120413	21:31:06.3	36.90	20.61	17.0	2.9
252	20120416	03:19:47.8	38.30	22.13	15.0	2.9
253	20120416	08:40:22.2	38.30	22.14	17.0	3.6
254	20120416	11:23:42.4	36.66	21.54	33.0	5.2
255	20120416	12:02:16.1	36.62	21.65	36.0	4.2
256	20120416	12:47:57.8	38.30	22.13	10.0	3.0

Index	YYYYMMDD	HH MM SS	LAT(N)	LON(E)	DEPTH(km)	M_L
257	20120416	15:06:54.4	36.66	21.67	34.0	4.4
258	20120417	00:41:11.4	37.77	21.32	28.0	2.1

Appendix F

List of Selected Subset of 46 Events

F.1 List of event parameters calculated with respect to station A00

List of the selected subset of events used for MUSIQUE and Coherency analyses are given. The table below presents the information: (1) event index, (2) origin date and time, (3) Latitude, (4) Longitude, (5) peak ground velocity, (6) magnitude as M_W or M_L, (7) hypocentral depth, (8) epicentral distance, (9) hypocentral distance, and (10) back-azimuth. The event parameters given in column no. 5 to 10 are calculated with respect to the station A00.

(1)	(2)	(3)	(4)	(5)	(6)	(7)	(8)	(9)	(10)
Indx	**YYYYMMDD_ HHMMSS**	**Lat (deg)**	**Lon (deg)**	**PGV (m/s)**	**M_{WL}**	**H (km)**	**R_{epi} (km)**	**R_{hyp} (km)**	**Baz (deg. N)**
1	20110922_151509	38.147	20.391	0.00271	3.3	17.6	10.2	20.3	260
2	20110924_030834	38.339	19.684	0.00005	3.0	7.0	74.5	74.8	285
3	20110924_154912	37.478	19.736	0.00004	3.1	14.4	101.9	102.9	222
4	20110928_074045	38.072	20.404	0.00299	3.5	16.9	13.5	21.6	221
5	20110930_003052	38.276	20.361	0.00033	2.0	4.6	17.8	18.4	315
6	20111008_032445	38.62	20.582	0.00003	2.8	6.1	51.1	51.5	7
7	20111008_205900	38.339	19.748	0.00003	2.8	14.8	69.1	70.7	287
8	20111009_184220	37.78	21.43	0.00006	3.3	17.0 0	91.7	93.3	117
9	20111010_025743	38.316	20.41	0.00086	2.8	13.7	18.9	23.3	334
10	20111010_190700	37.19	22.04	0.00029	4.5	11.0	173.2	173.5	128
11	20111012_045443	38.089	20.358	0.00010	2.3	2.2	15.3	15.5	238

(1)	(2)	(3)	(4)	(5)	(6)	(7)	(8)	(9)	(10)
Indx	**YYYYMMDD_ HHMMSS**	**Lat (deg)**	**Lon (deg)**	**PGV (m/s)**	**M_{WL}**	**H (km)**	**R_{epi} (km)**	**R_{hyp} (km)**	**Baz (deg. N)**
12	20111014_011132	37.974	20.84	0.00041	3.5	11.9	36.1	38.0	126
13	20111016_100137	38.191	20.357	0.00017	2.7	17.6	13.4	22.1	283
14	20111017_100004	38.89	20.62	0.00008	3.1	37.0	81.3	89.3	7
15	20111020_061820	38.108	20.578	0.00367	3.4	16.5	8.8	18.7	134
16	20111020_073537	38.04	20.431	0.00013	2.8	9.2	15.2	17.7	206
17	20111020_204020	38.094	20.573	0.00003	2.2	16.5	9.7	19.1	14
18	20111025_223304	38.01	20.849	0.00117	4.1	13.9	34.6	37.3	119
19	20111031_072250	38.219	20.509	0.00014	2.6	0.1	6.2	6.2	3
20	20111031_204035	38.062	20.397	0.00014	2.8	13.1	14.7	19.7	220
21	20111110_172539	38.42	21.83	0.00101	4.6	19.0	119.3	120.8	76
22	20111110_231028	38.749	20.499	0.00001	2.7	2.9	65.0	65.1	360
23	20111112_045148	37.465	20.488	0.00002	2.5	0.5	77.5	77.5	181
24	20111115_141004	37.693	20.858	0.00042	3.7	16.8	60.7	63.0	149
25	20111124_040923	39.4	19.81	0.00007	3.6	36.0	149.1	154.3	336
26	20111128_032308	38.093	20.517	0.00117	3.2	16.5	7.9	18.3	173
27	20111208_090935	37.825	20.392	0.00011	2.9	9.7	38.9	40.0	195
28	20111215_000742	37.51	19.85	0.00006	3.1	14.0	92.7	93.7	219
29	20111215_170549	36.98	20.43	0.00002	2.7	20.0	131.5	133.0	183
30	20120119_234608	38.578	20.456	0.00003	2.2	10.0	46.2	47.3	355
31	20120214_132143	37.7	20.77	0.00227	4.3	13.0	56.4	57.9	156
32	20120303_230430	38.524	20.477	0.00002	1.9	12.6	40.1	42.0	356

(1)	(2)	(3)	(4)	(5)	(6)	(7)	(8)	(9)	(10)
Indx	**YYYYMMDD_ HHMMSS**	**Lat (deg)**	**Lon (deg)**	**PGV (m/s)**	**M_{WL}**	**H (km)**	**R_{epi} (km)**	**R_{hyp} (km)**	**Baz (deg. N)**
33	20120314_214443	37.752	20.13	0.00005	2.9	0.0	56.3	56.3	216
34	20120315_054058	38.69	21.3	0.00043	4.4	15.0	90.7	92.0	50
35	20120317_023659	37.942	20.925	0.00003	2.4	31.2	44.3	54.2	124
36	20120320_185051	38.171	20.54	0.00343	3.0	18.5	3.1	18.8	74
37	20120321_055047	38.61	21.71	0.00017	3.8	16.0	116.3	117.4	64
38	20120327_143302	38.154	20.654	0.00003	2.0	18.8	13.1	22.9	95
39	20120404_014530	38.07	21.58	0.00008	3.4	19.0	94.8	96.7	96
40	20120410_134545	38.086	20.224	0.00007	2.5	12.4	26.1	28.9	251
41	20120410_215535	38.521	20.552	0.00002	2.2	11.8	39.9	41.6	6
42	20120411_061851	39.67	20.4	0.00005	3.7	9.0	167.5	167.8	357
43	20120415_132543	38.223	20.335	0.00008	2.4	16.0	16.3	22.9	294
44	20120415_221904	38.416	20.611	0.00002	2.1	13.1	29.5	32.3	18
45	20120416_084022	38.3	22.14	0.00007	3.6	17.0	143.9	144.9	83
46	20120416_112342	36.66	21.54	0.00144	5.2	33.0	190.3	193.2	151

F.2 List of event parameters used for MUSIQUE and Coherency analyses

List of the parameters of the subset of events used for MUSIQUE and Coherency analyses are given. The table below presents the information: (1) event index, (2) origin date and time, (3) begin time (4) end time and (5) duration of the window for MUSIQUE analysis, (6) missing stations of Array A, (7) if the event was analyzed for Array B: Yes/NA , (8) missing stations of Array B, (9) begin time (10) end time and (11) duration of the window for Coherency analysis, (12) which rock station was considered for window selection, (13) number of pairs available for Array A.

(1)	(2)	(3)	(4)	(5)	(6)	(7)	(8)	(9)	(10)	(11)	(12)	(13)
Indx	**YYYYMMDD_ HHMMSS**	**MUSIQUE ANALYSIS**						**COHERENCY ANALYSIS**				
		TW-M1 (s)	**TW-M2 (s)**	**T_M (s)**	**Missing Array A Stations**	**Array-B Analyzed**	**Missing Array B Stations**	**TW-C1 (s)**	**TW-C2 (s)**	**T_S (s)**	**Rock**	**Nb. of Pairs Array A**
1	20110922_ 151509	63	93	30	-	NA	NA	65.94	66.83	0.89	R02	210
2	20110924_ 030834	72	140	68	-	Yes	B01, B09	81.70	85.33	3.63	R02	210
3	20110924_ 154912	77	150	73	-	Yes	B01, B09	89.42	98.09	8.67	R02	210
4	20110928_ 074045	63	90	27	-	Yes	-	66.41	67.93	1.52	R02	210
5	20110930_ 003052	63	90	27	-	Yes	-	66.47	67.00	0.54	R02	210
6	20111008_ 032445	69	120	51	A02	Yes	-	76.30	79.32	3.01	R02	190
7	20111008_ 205900	72	130	58	A02	Yes	-	80.48	85.00	4.51	R02	190
8	20111009_ 184220	76	150	74	-	Yes	-	89.08	94.95	5.88	R02	210
9	20111010_ 025743	64	90	26	-	Yes	-	66.92	67.79	0.88	R02	210
10	20111010_ 190700	89	220	131	-	Yes	-	112.56	125.72	13.16	R02	210
11	20111012_ 045443	62	80	18	A01	Yes	B06	64.77	67.48	2.71	R02	190
12	20111014_ 011132	66	110	44	A11	Yes	-	71.93	73.97	2.04	R02	190
13	20111016_ 100137	63	93	30	A11	Yes	B04	66.52	67.94	1.43	R02	190

(1)	(2)	(3)	(4)	(5)	(6)	(7)	(8)	(9)	(10)	(11)	(12)	(13)
Indx	YYYYMMDD_HHMMSS	MUSIQUE ANALYSIS						COHERENCY ANALYSIS				
		TW-M1 (s)	TW-M2 (s)	T_M (s)	Missing Array A Stations	Array-B Analyzed	Missing Array B Stations	TW-C1 (s)	TW-C2 (s)	T_S (s)	Rock	Nb. of Pairs Array A
14	20111017_100004	75	130	55	A07	NA	NA	85.11	92.33	7.22	R02	190
15	20111020_061820	63	83	20	A11, A15, A18	NA	NA	65.34	66.31	0.97	R02	153
16	20111020_073537	63	88	25	A11, A15, A18	NA	NA	65.70	67.40	1.70	R02	153
17	20111020_204020	63	78	15	A11, A15, A18, A20	NA	NA	65.47	66.63	1.16	R02	136
18	20111025_223304	66	116	50	A08, A20	NA	NA	71.63	73.76	2.13	R02	171
19	20111031_072250	61	81	20	A07, A20	NA	NA	61.61	63.16	1.55	R02	171
20	20111031_204035	63	88	25	A07, A20	NA	NA	66.07	67.11	1.04	R02	171
21	20111110_172539	79	179	100	A07	Yes	B03, B04, B07, B08, B10	96.62	104.68	8.06	R02	190
22	20111110_231028	73	120	47	A07, A20	NA	NA	79.73	86.25	6.52	R02	171
23	20111112_045148	75	120	45	A07, A18	NA	NA	86.25	89.29	3.04	R02	171
24	20111115_141004	70	130	60	-	Yes	B03, B04, B05, B08, B10	80.90	86.42	5.52	R02	210
25	20111124_040923	83	170	87	A07, A20	NA	NA	101.27	112.79	11.52	R02	171
26	20111128_032308	63	90	27	A07, A20	NA	NA	65.34	66.34	0.99	R02	171
27	20111208_090935	67	120	53	A06	NA	NA	72.96	75.37	2.42	R02	190
28	20111215_000742	75	140	65	A06	Yes	B03, B04, B05, B10	88.91	97.91	8.99	R02	190
29	20111215_170549	85	160	75	A06, A13	Yes	B03, B04, B05, B10	102.09	111.84	9.75	R02	171
30	20120119_234608	68	120	52	A18, A20	NA	NA	74.51	78.27	3.76	R02	171
31	20120214_132143	71	131	60	A01, A05, A19, A20	NA	NA	79.79	84.21	4.41	R01	136
32	20120303_230430	67	110	43	A01, A20	NA	NA	73.31	74.63	1.32	R01	171
33	20120314_214443	70	130	60	A01, A16, A20	NA	NA	77.81	80.97	3.16	R02	153

(1)	(2)	(3)	(4)	(5)	(6)	(7)	(8)	(9)	(10)	(11)	(12)	(13)
Indx	YYYYMMDD_HHMMSS	MUSIQUE ANALYSIS						COHERENCY ANALYSIS				
		TW-M1 (s)	TW-M2 (s)	T_M (s)	Missing Array A Stations	Array-B Analyzed	Missing Array B Stations	TW-C1 (s)	TW-C2 (s)	T_S (s)	Rock	Nb. of Pairs Array A
34	20120315_054058	74	150	76	A01, A16, A18, A20	NA	NA	87.26	95.47	8.21	R02	136
35	20120317_023659	68	120	52	A01, A16, A18, A20	NA	NA	75.45	78.47	3.02	R02	136
36	20120320_185051	63	90	27	A01, A20	NA	NA	65.54	66.76	1.21	R01	171
37	20120321_055047	79	170	91	A01, A12, A18, A20	NA	NA	95.27	105.65	10.38	R01	136
38	20120327_143302	63	90	27	A01, A20	NA	NA	67.12	69.16	2.04	R01	171
39	20120404_014530	75	150	75	A01, A20	NA	NA	89.44	94.34	4.90	R01	171
40	20120410_134545	64	120	56	A01, A03, A20	NA	NA	68.12	71.09	2.97	R01	153
41	20120410_215535	67	110	43	A01, A03, A20	NA	NA	73.11	76.17	3.05	R01	153
42	20120411_061851	89	200	111	A01, A03, A20	NA	NA	110.00	120.65	10.65	R01	153
43	20120415_132543	63	90	27	A01, A20	NA	NA	66.38	69.06	2.68	R01	171
44	20120415_221904	65	100	35	A01, A03, A20	NA	NA	70.71	74.36	3.65	R01	153
45	20120416_084022	83	180	97	A01, A03, A20	NA	NA	103.72	111.46	7.75	R01	153
46	20120416_112342	89	300	211	A01, A20	NA	NA	115.64	129.76	14.12	R01	171

Appendix G

Velocity time series from A00 station

Available velocity time series from the reference array station A00 are shown here for the selected subset of events (Appendix E). The time window shown here represents the duration used for MUSIQUE analysis in Chapter 3. The window begins from the onset of P-wave and ends at the end of signal. The segment of signal shown in 'red' color represents the selected window, from visual inspection and based on the rock station records, used for Coherency analysis in Chapter 4.

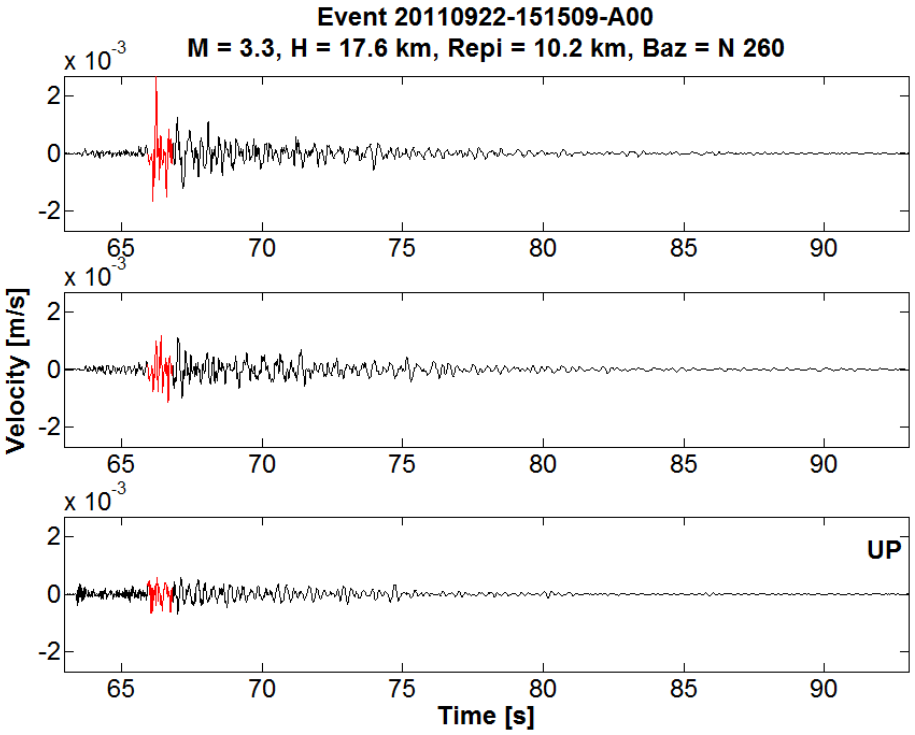
Event 20110922-151509-A00
M = 3.3, H = 17.6 km, Repi = 10.2 km, Baz = N 260
x 10^-3
2
0
-2
65
70
75
80
85
90
Velocity [m/s]
UP
Time [s]

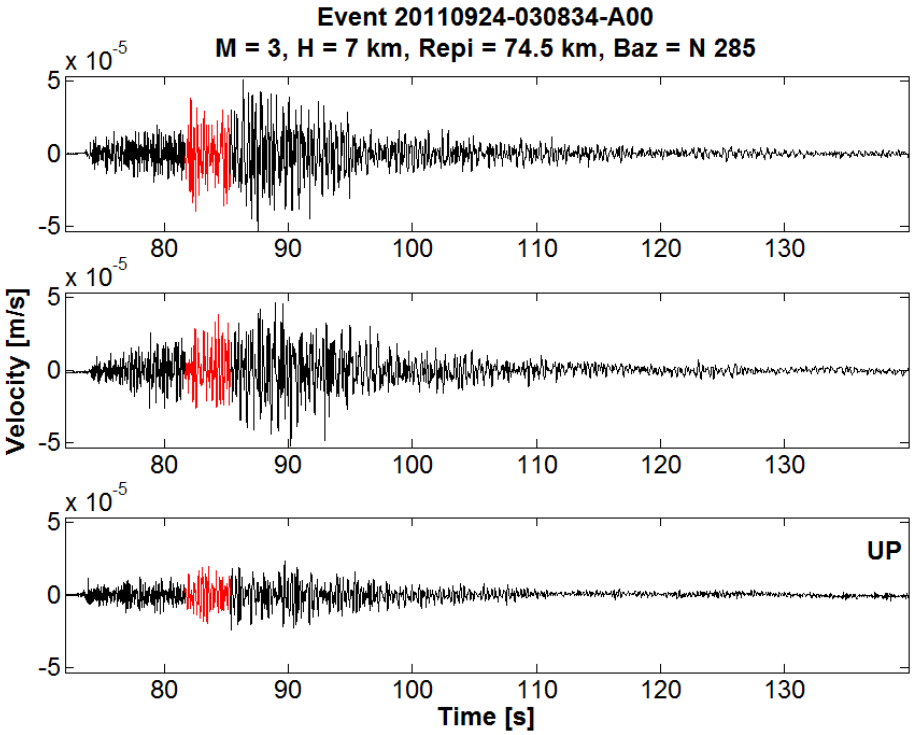
Event 20110924-030834-A00
M = 3, H = 7 km, Repi = 74.5 km, Baz = N 285
x 10^-5
5
0
-5
80
90
100
110
120
130
Velocity [m/s]
UP
Time [s]

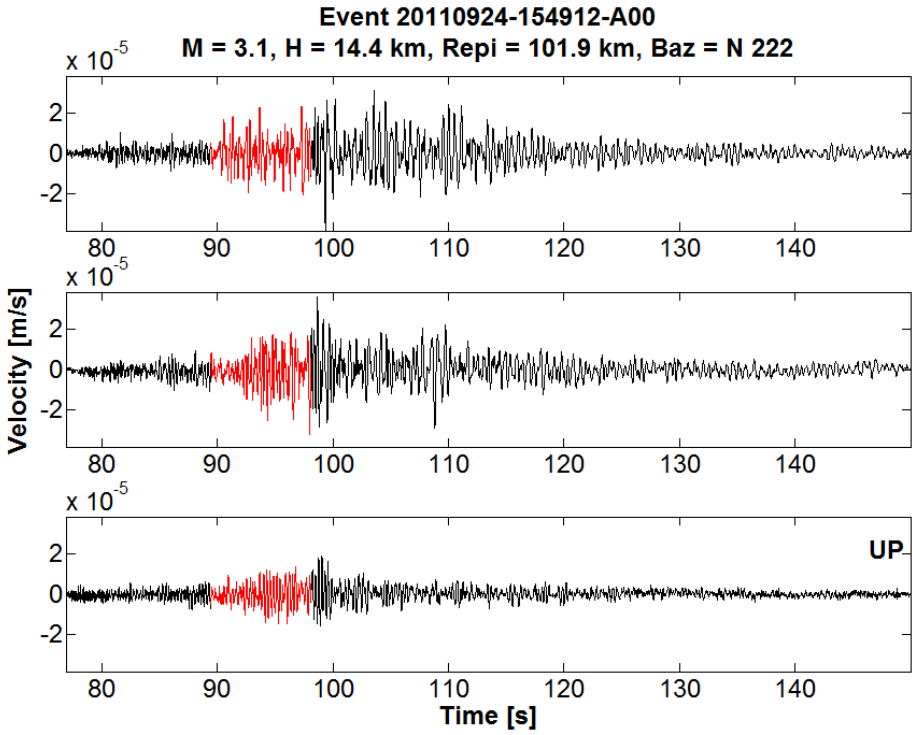
Event 20110924-154912-A00
M = 3.1, H = 14.4 km, Repi = 101.9 km, Baz = N 222
x 10^-5
2
0
-2
80
90
100
110
120
130
140
Velocity [m/s]
UP
Time [s]

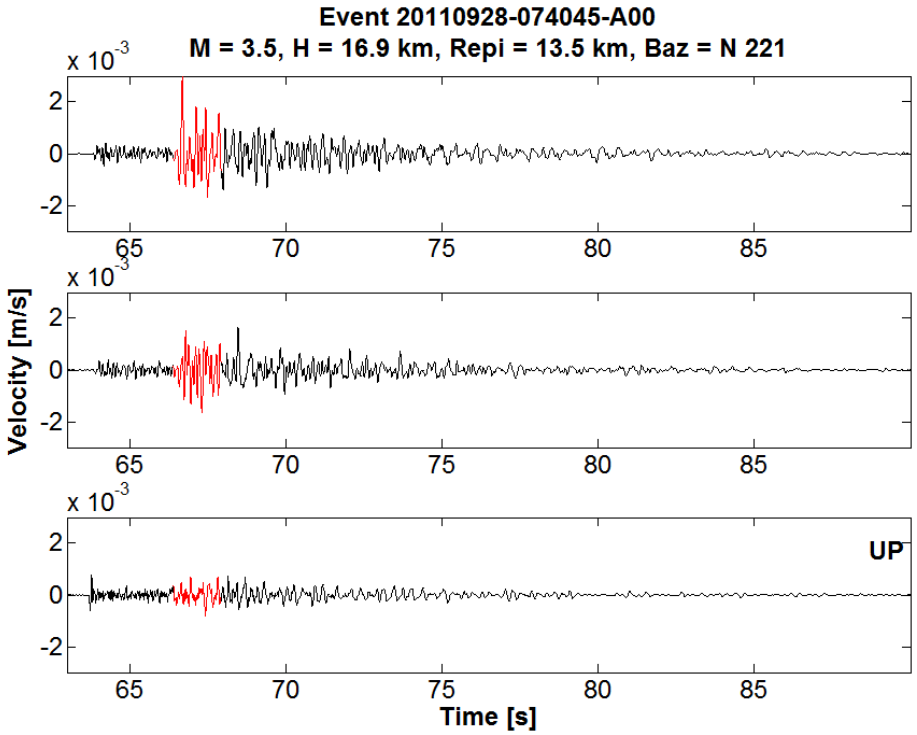
Event 20110928-074045-A00
M = 3.5, H = 16.9 km, Repi = 13.5 km, Baz = N 221
x 10^-3
2
0
-2
65
70
75
80
85
Velocity [m/s]
UP
Time [s]

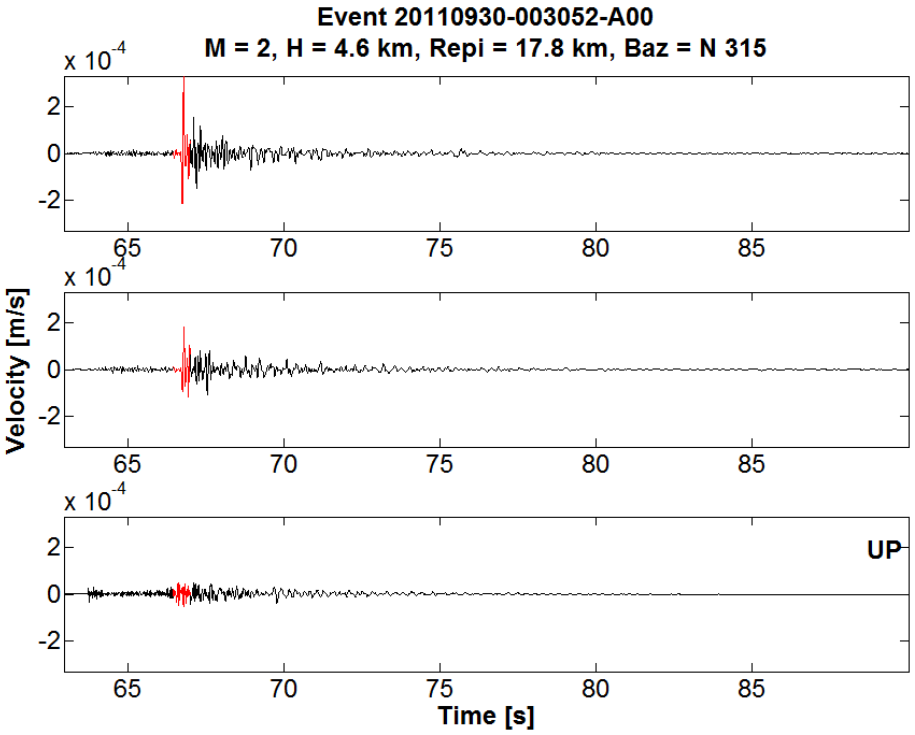
Event 20110930-003052-A00
M = 2, H = 4.6 km, Repi = 17.8 km, Baz = N 315
x 10^-4
2
0
-2
65
70
75
80
85
Velocity [m/s]
UP
Time [s]

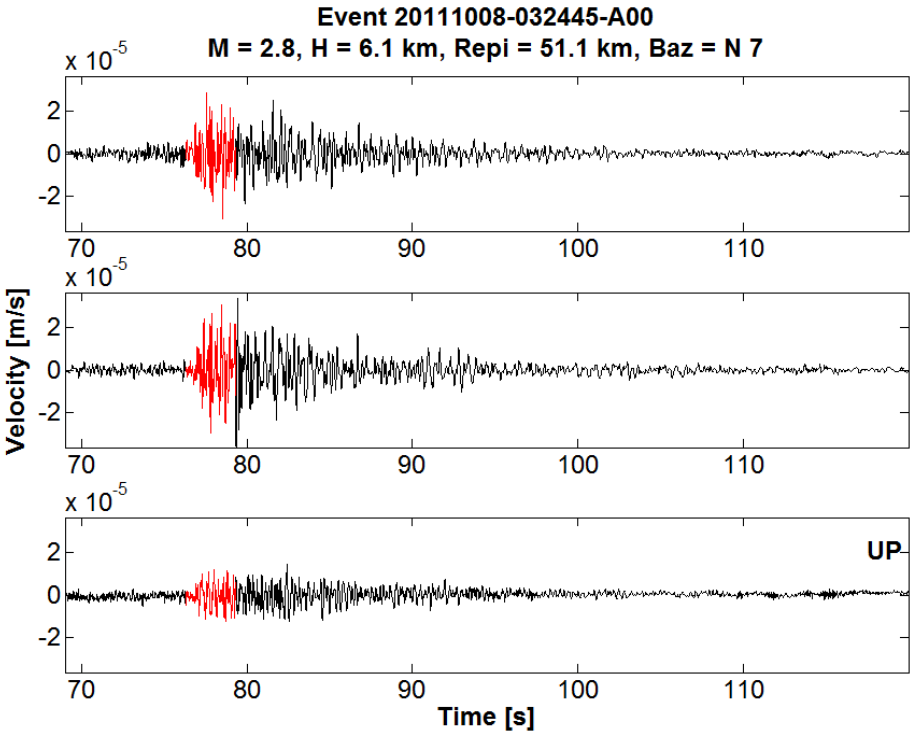
Event 20111008-032445-A00
M = 2.8, H = 6.1 km, Repi = 51.1 km, Baz = N 7
x 10^-5
2
0
-2
70
80
90
100
110
Velocity [m/s]
UP
Time [s]

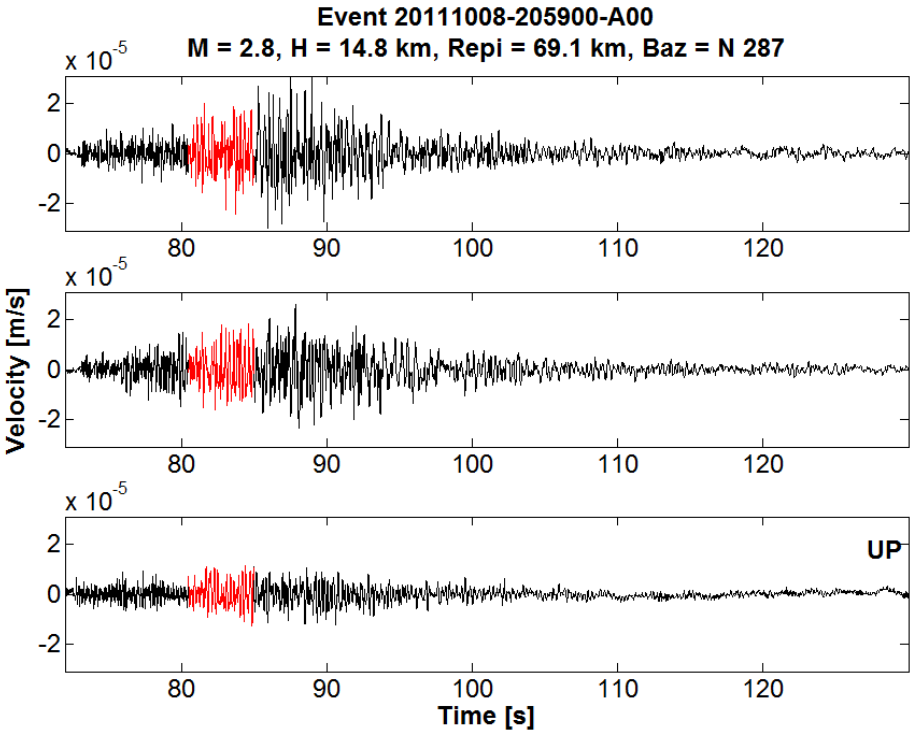
Event 20111008-205900-A00
M = 2.8, H = 14.8 km, Repi = 69.1 km, Baz = N 287
x 10^-5
Velocity [m/s]
UP
Time [s]

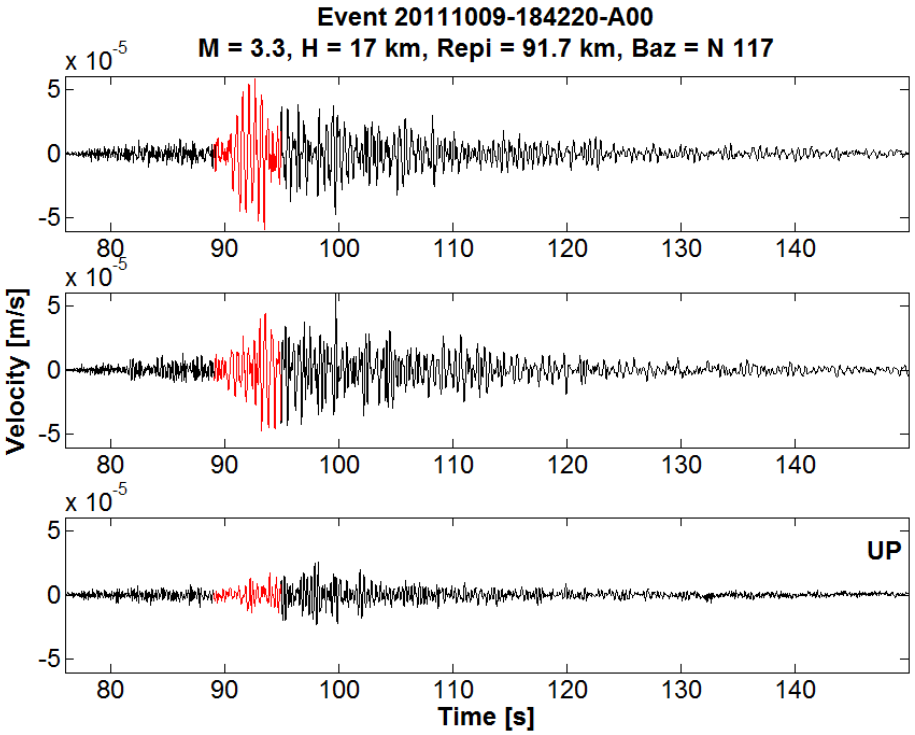
Event 20111009-184220-A00
M = 3.3, H = 17 km, Repi = 91.7 km, Baz = N 117
x 10^-5
Velocity [m/s]
UP
Time [s]

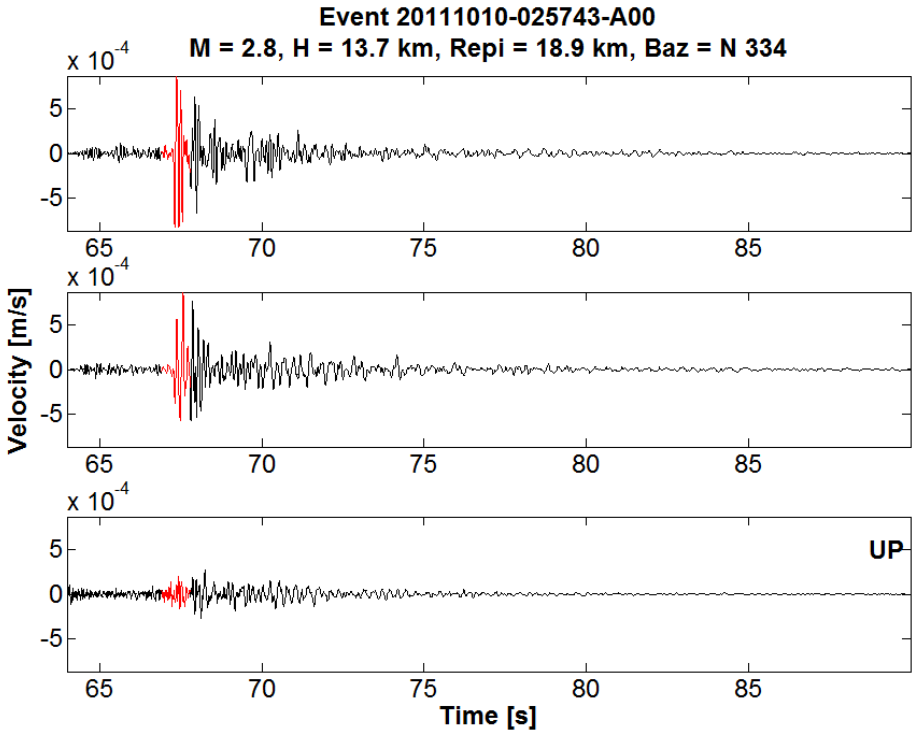
Event 20111010-025743-A00
M = 2.8, H = 13.7 km, Repi = 18.9 km, Baz = N 334
x 10^-4
5
0
-5
65
70
75
80
85
Velocity [m/s]
UP
Time [s]

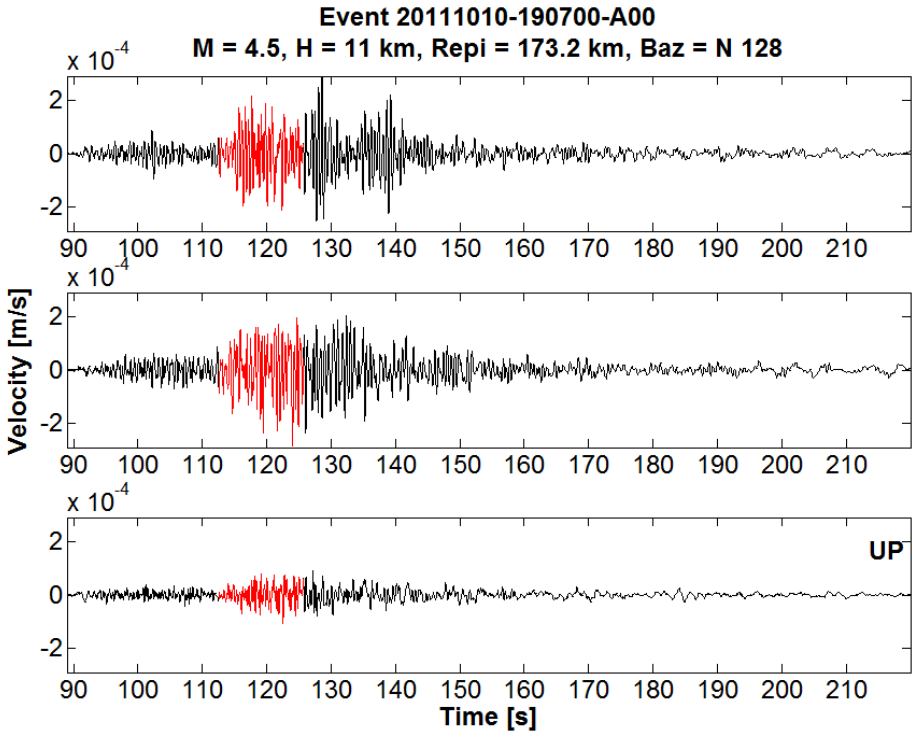
Event 20111010-190700-A00
M = 4.5, H = 11 km, Repi = 173.2 km, Baz = N 128
x 10^-4
2
0
-2
90
100
110
120
130
140
150
160
170
180
190
200
210
Velocity [m/s]
UP
Time [s]

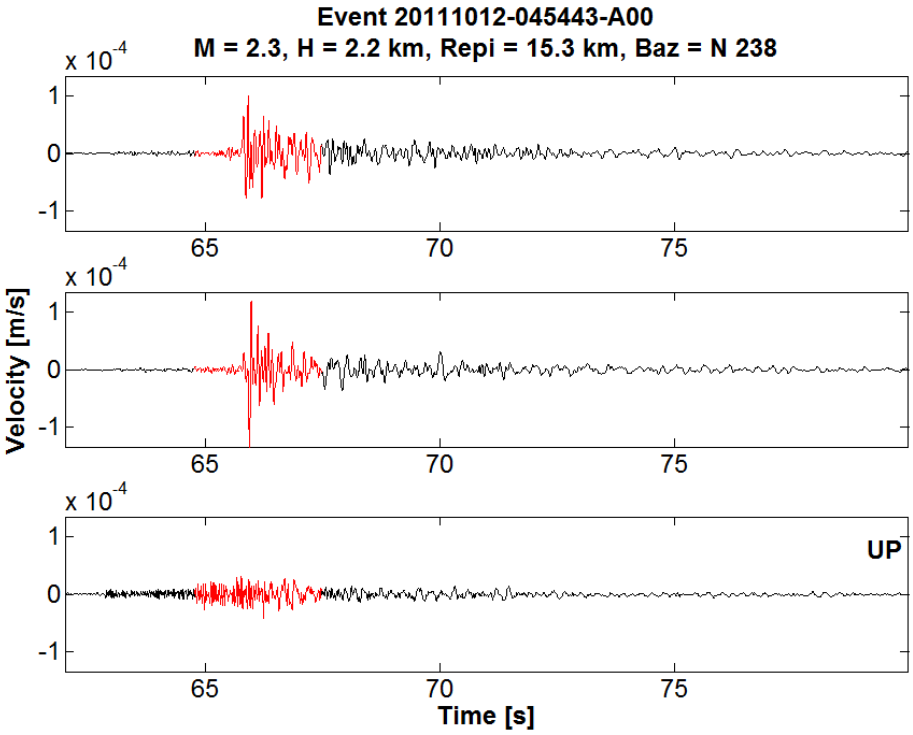
Event 20111012-045443-A00
M = 2.3, H = 2.2 km, Repi = 15.3 km, Baz = N 238
x 10^-4
1
0
-1
65
70
75
Velocity [m/s]
UP
Time [s]

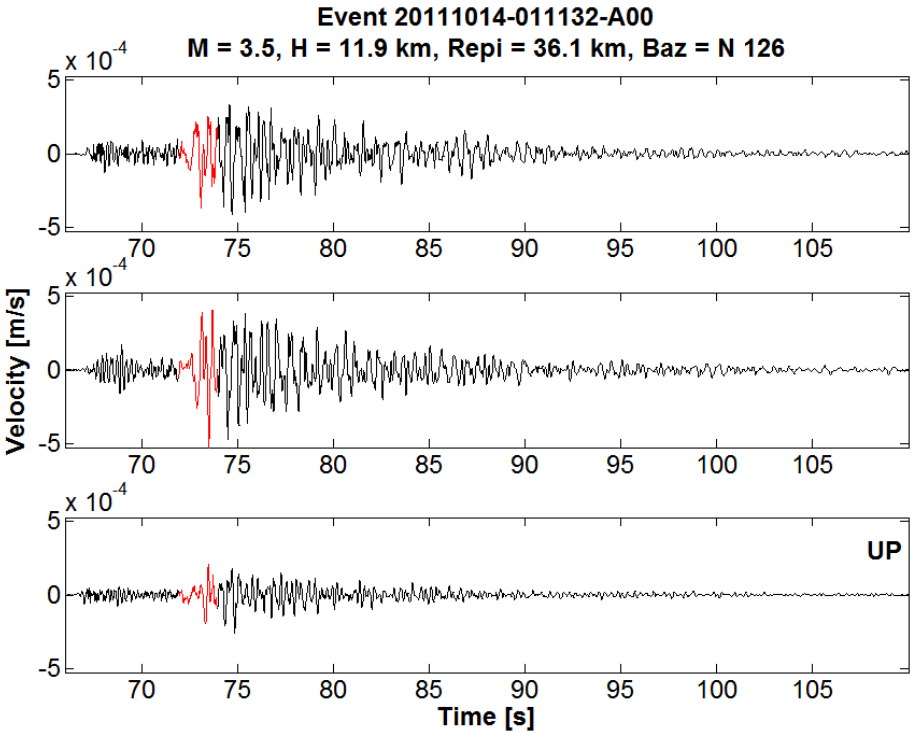
Event 20111014-011132-A00
M = 3.5, H = 11.9 km, Repi = 36.1 km, Baz = N 126
x 10^-4
5
0
-5
70
75
80
85
90
95
100
105
Velocity [m/s]
UP
Time [s]

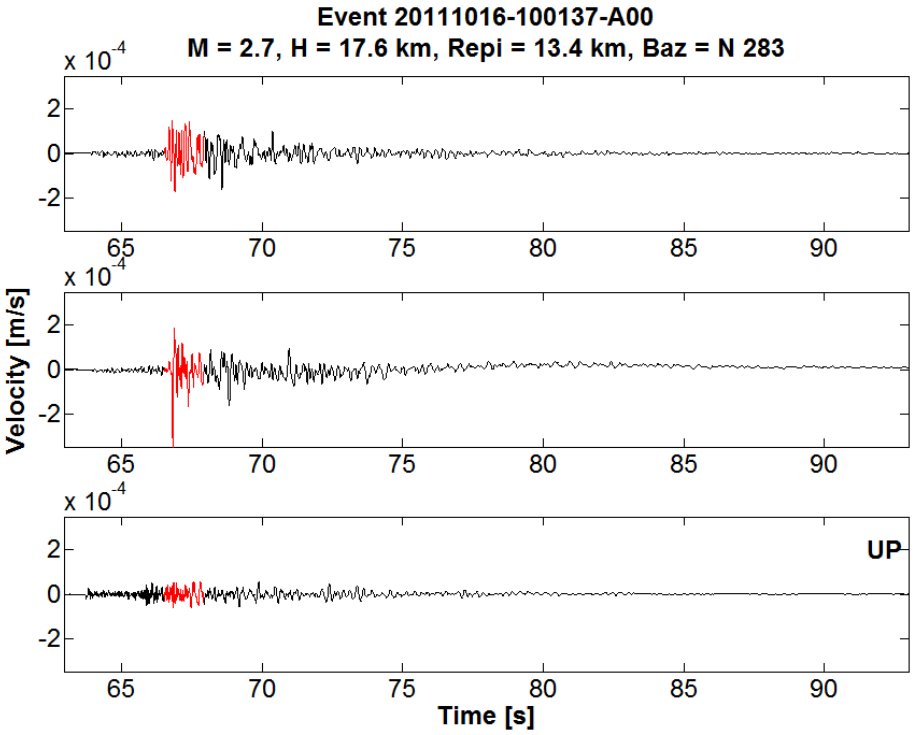
Event 20111016-100137-A00
M = 2.7, H = 17.6 km, Repi = 13.4 km, Baz = N 283
x 10^-4
2
0
-2
65
70
75
80
85
90
Velocity [m/s]
UP
Time [s]

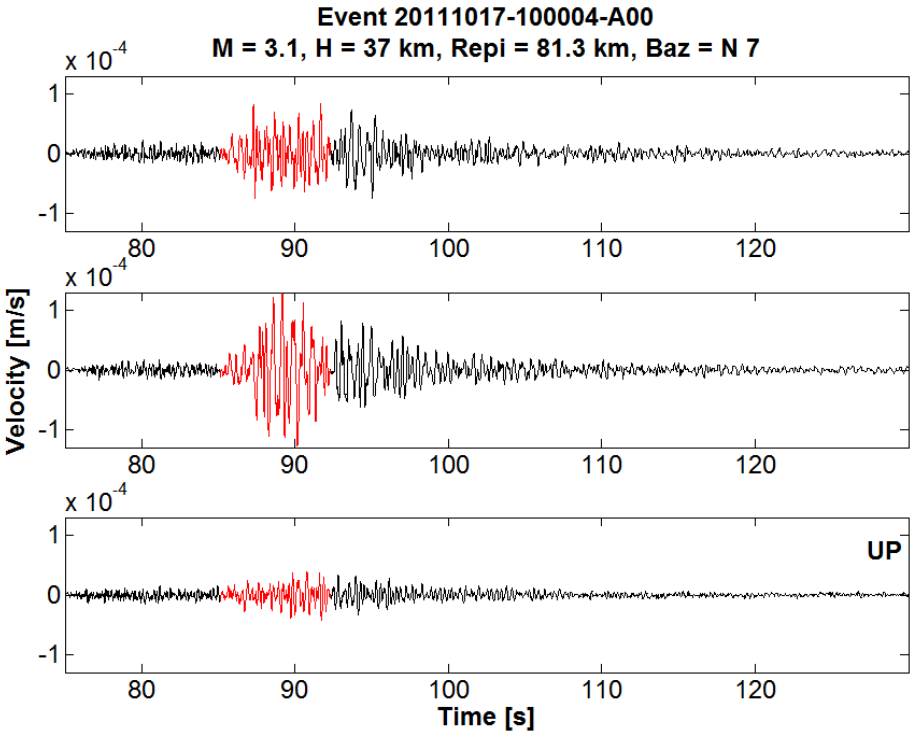
Event 20111017-100004-A00
M = 3.1, H = 37 km, Repi = 81.3 km, Baz = N 7
x 10^-4
1
0
-1
80
90
100
110
120
Velocity [m/s]
UP
Time [s]

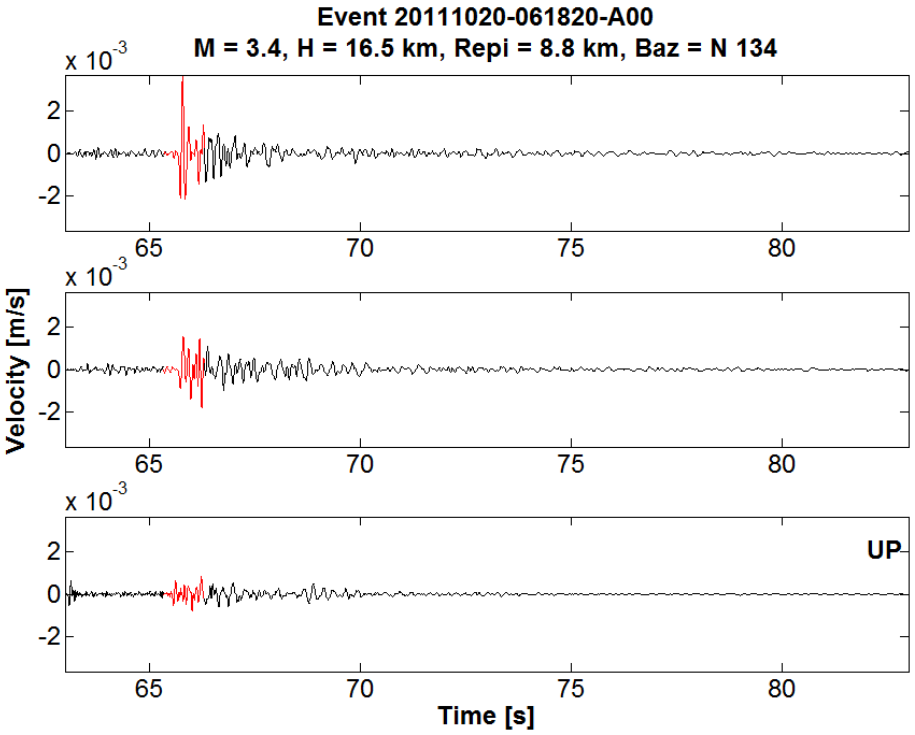
Event 20111020-061820-A00
M = 3.4, H = 16.5 km, Repi = 8.8 km, Baz = N 134
x 10^-3
2
0
-2
65
70
75
80
Velocity [m/s]
UP
Time [s]

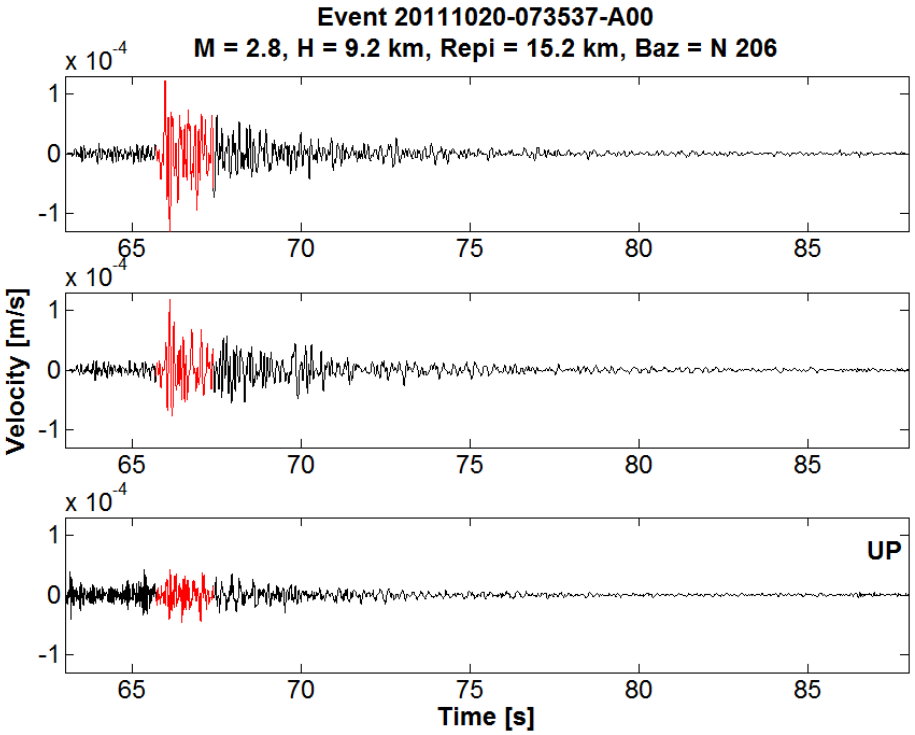
Event 20111020-073537-A00
M = 2.8, H = 9.2 km, Repi = 15.2 km, Baz = N 206
x 10^-4
1
0
-1
65
70
75
80
85
Velocity [m/s]
UP
Time [s]

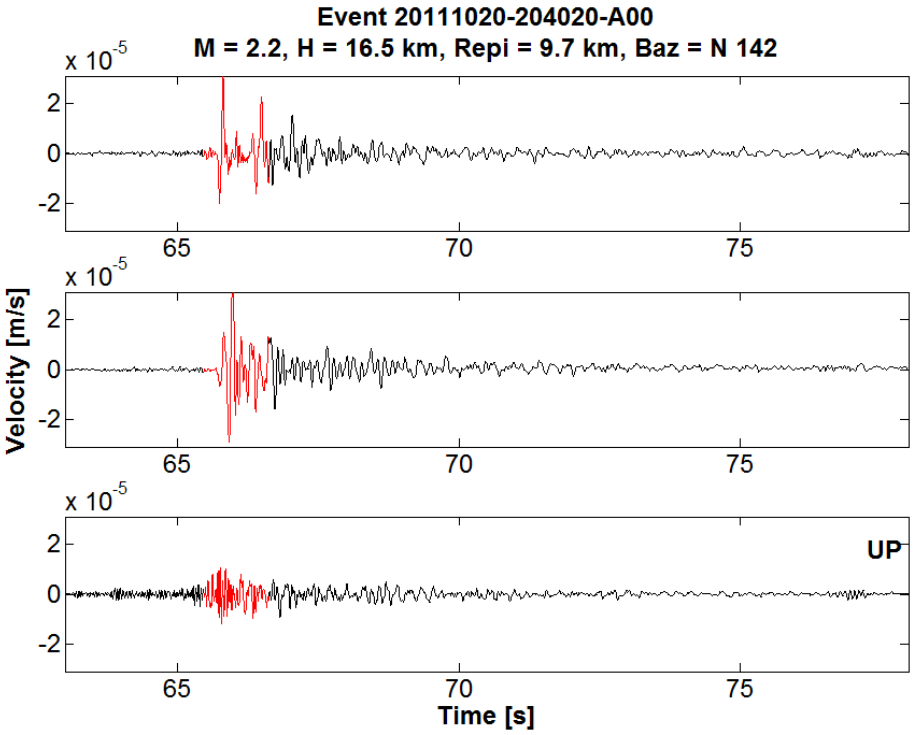
Event 20111020-204020-A00
M = 2.2, H = 16.5 km, Repi = 9.7 km, Baz = N 142
x 10^-5
2
0
-2
65
70
75
Velocity [m/s]
UP
Time [s]

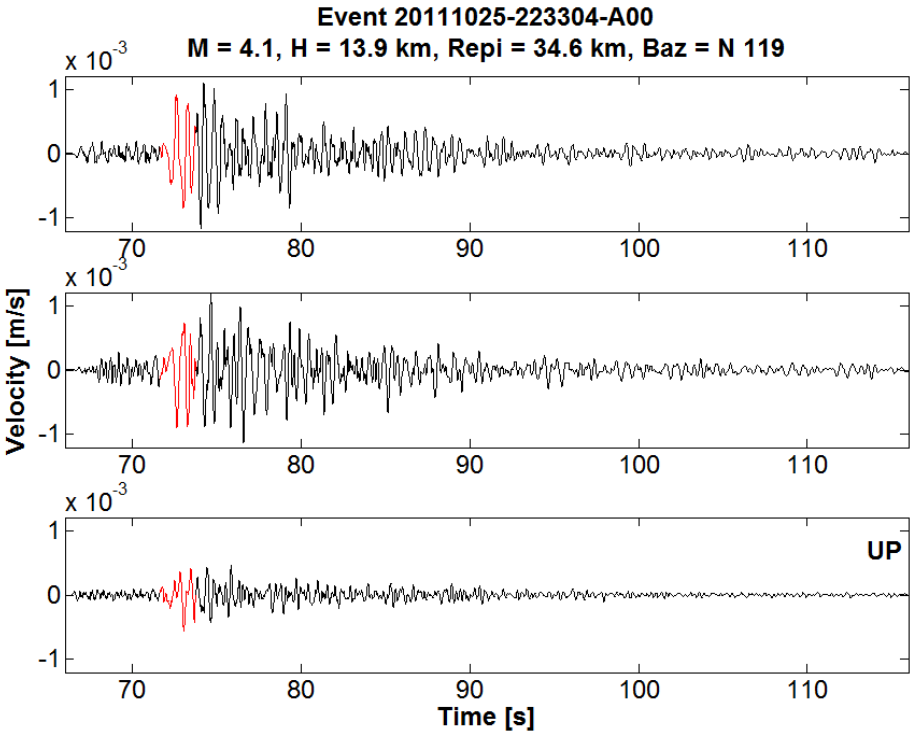
Event 20111025-223304-A00
M = 4.1, H = 13.9 km, Repi = 34.6 km, Baz = N 119
x 10^-3
1
0
-1
70
80
90
100
110
Velocity [m/s]
UP
Time [s]

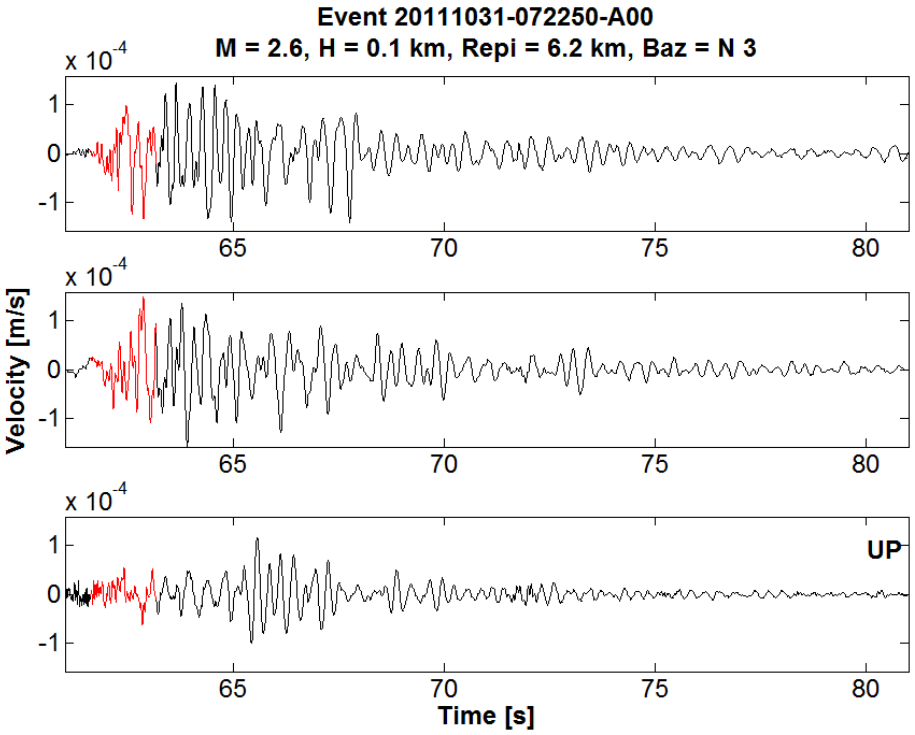
Event 20111031-072250-A00
M = 2.6, H = 0.1 km, Repi = 6.2 km, Baz = N 3
x 10^-4
Velocity [m/s]
UP
Time [s]

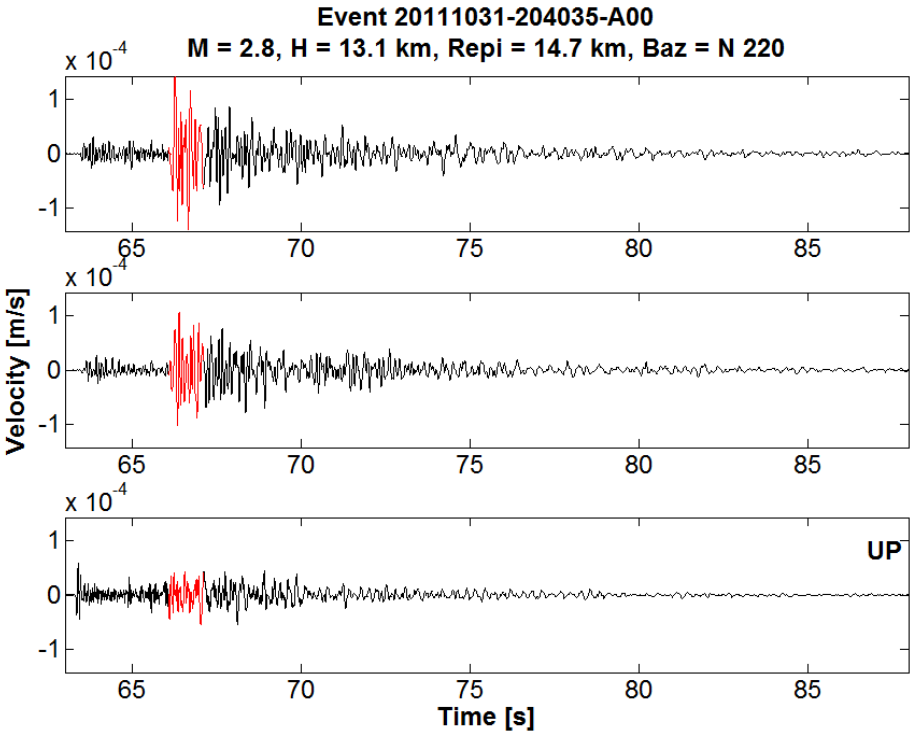
Event 20111031-204035-A00
M = 2.8, H = 13.1 km, Repi = 14.7 km, Baz = N 220
x 10^-4
Velocity [m/s]
UP
Time [s]

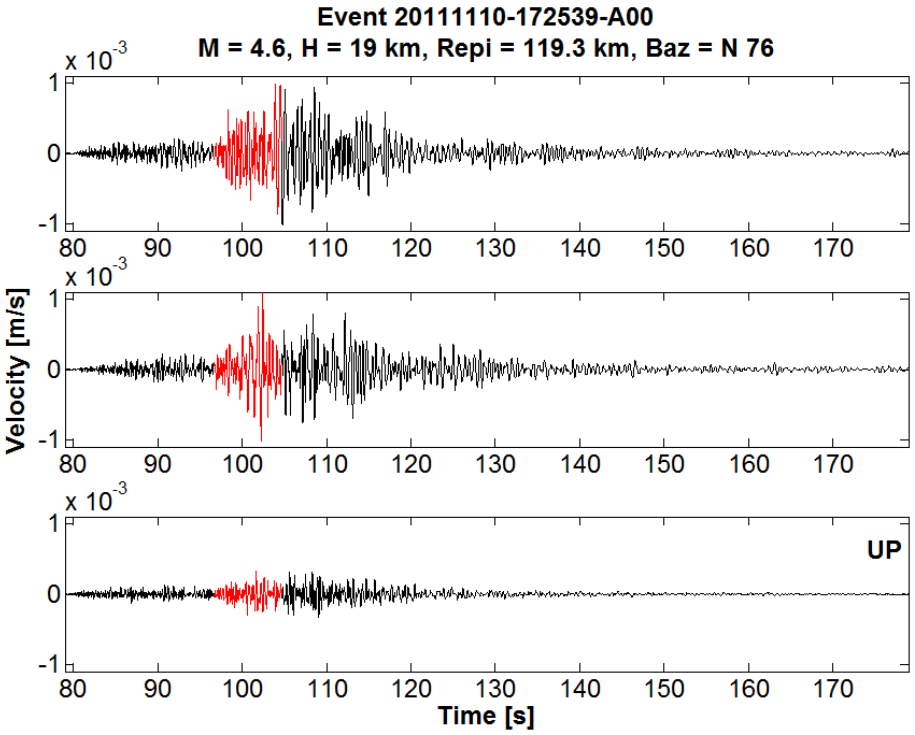
Event 20111110-172539-A00
M = 4.6, H = 19 km, Repi = 119.3 km, Baz = N 76
x 10^-3
Velocity [m/s]
UP
Time [s]

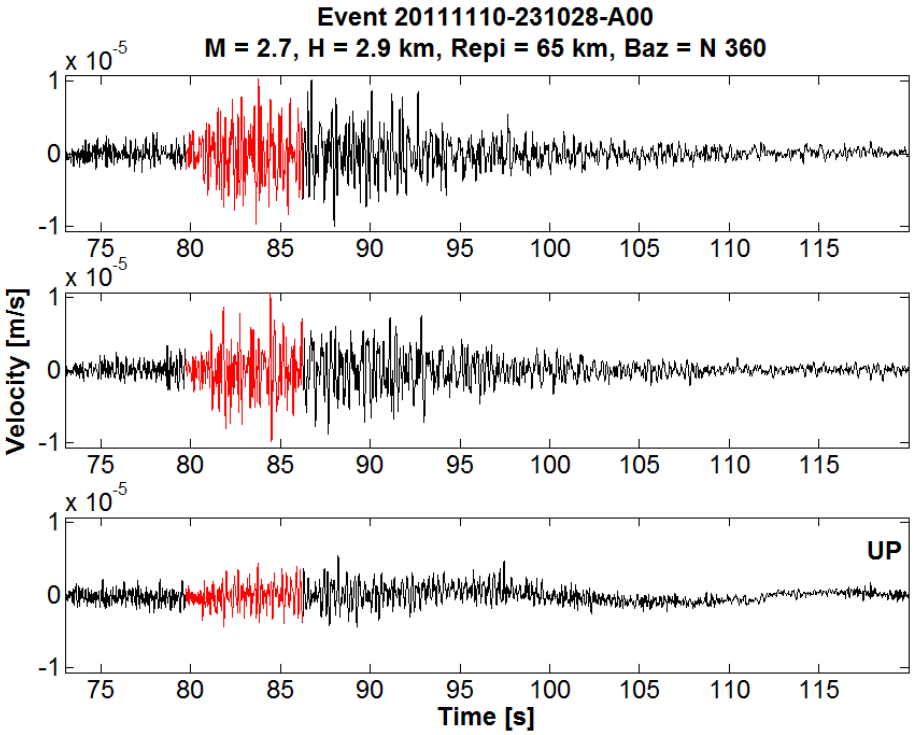
Event 20111110-231028-A00
M = 2.7, H = 2.9 km, Repi = 65 km, Baz = N 360
x 10^-5
Velocity [m/s]
UP
Time [s]

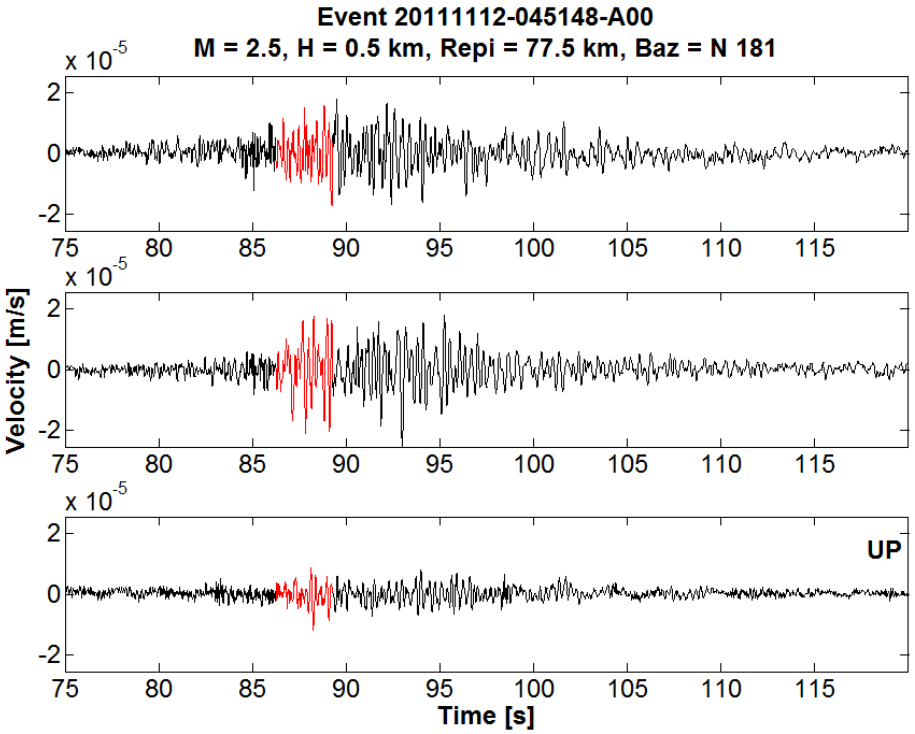
Event 20111112-045148-A00
M = 2.5, H = 0.5 km, Repi = 77.5 km, Baz = N 181
x 10^-5
Velocity [m/s]
UP
Time [s]

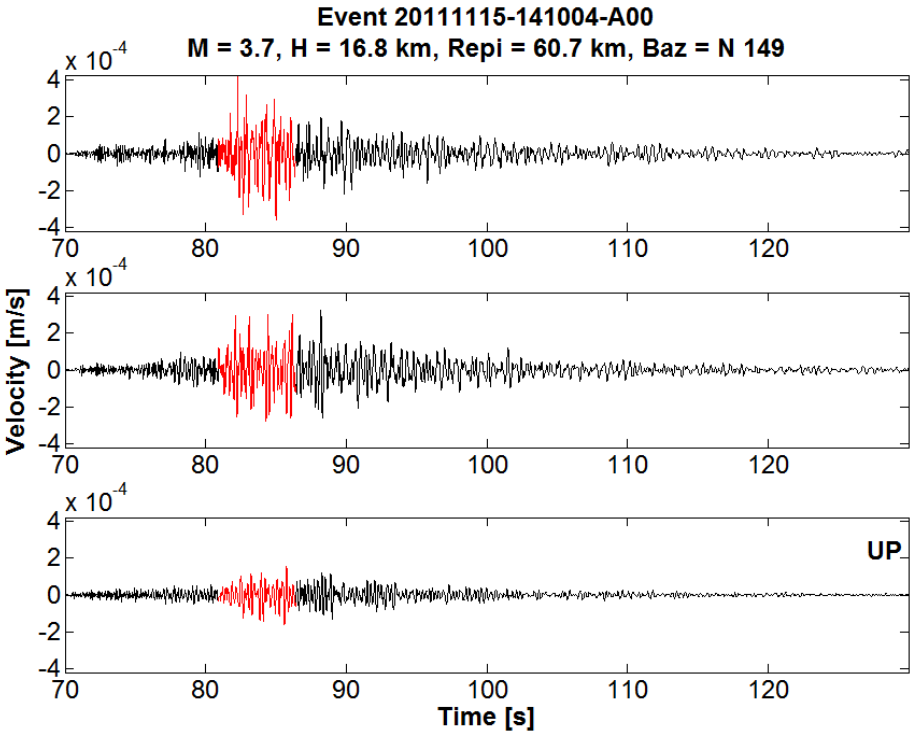
Event 20111115-141004-A00
M = 3.7, H = 16.8 km, Repi = 60.7 km, Baz = N 149
x 10^-4
Velocity [m/s]
UP
Time [s]

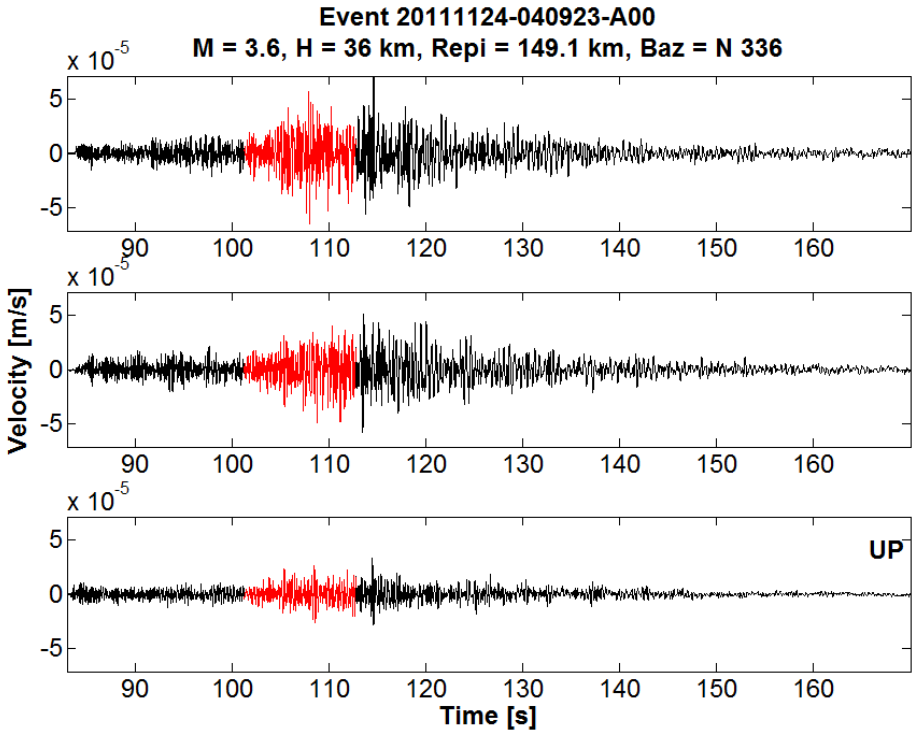
Event 20111124-040923-A00
M = 3.6, H = 36 km, Repi = 149.1 km, Baz = N 336
x 10^-5
5
0
-5
90
100
110
120
130
140
150
160
Velocity [m/s]
UP
Time [s]

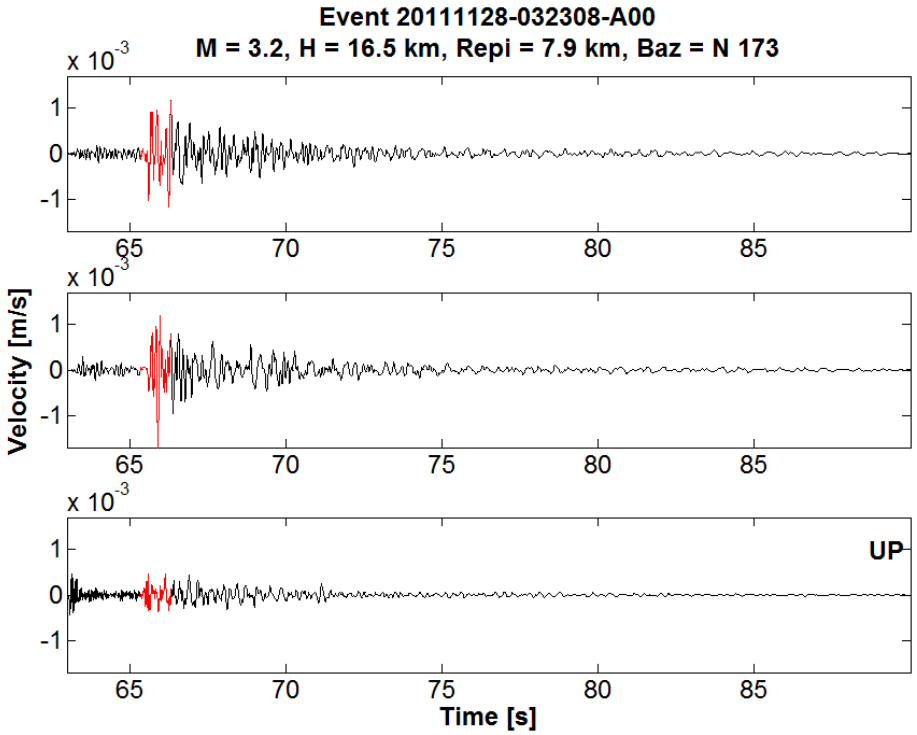
Event 20111128-032308-A00
M = 3.2, H = 16.5 km, Repi = 7.9 km, Baz = N 173
x 10^-3
1
0
-1
65
70
75
80
85
Velocity [m/s]
UP
Time [s]

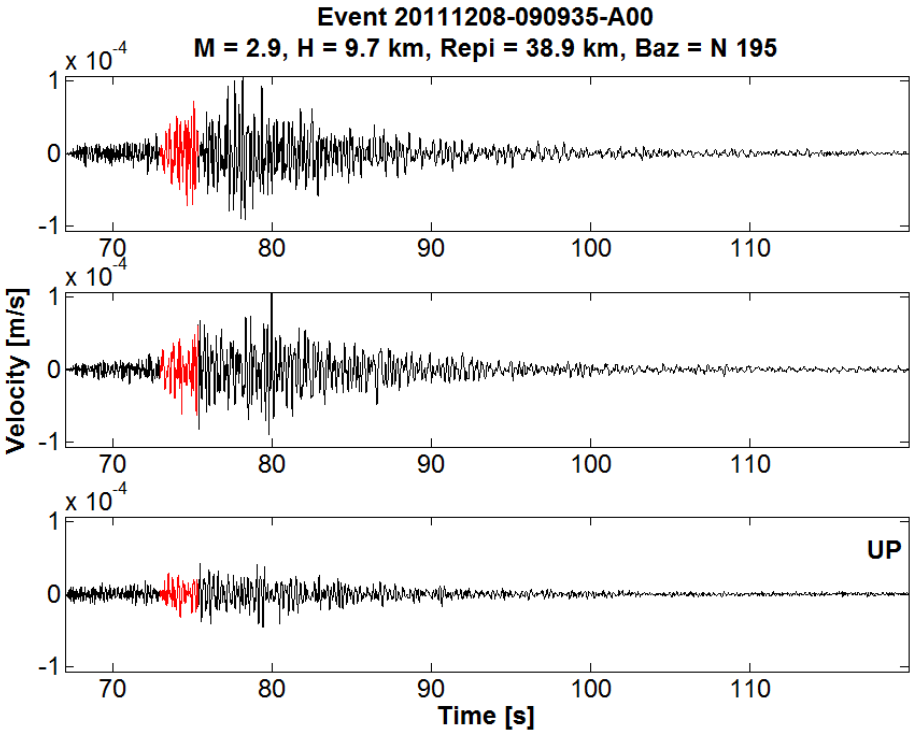
Event 20111208-090935-A00
M = 2.9, H = 9.7 km, Repi = 38.9 km, Baz = N 195
x 10^-4
1
0
-1
70
80
90
100
110
Velocity [m/s]
UP
Time [s]

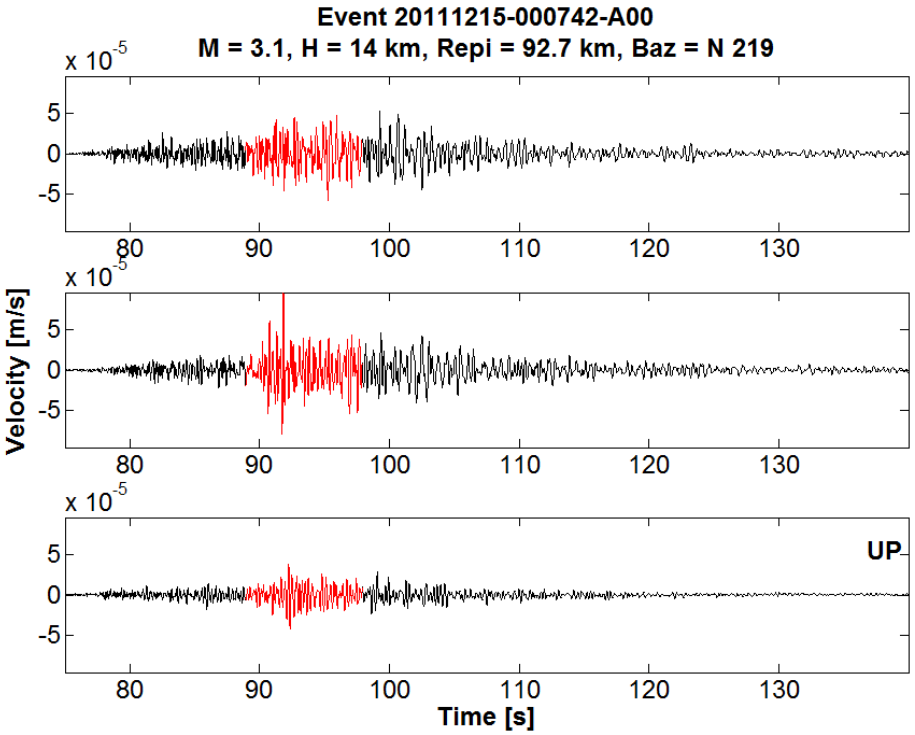
Event 20111215-000742-A00
M = 3.1, H = 14 km, Repi = 92.7 km, Baz = N 219
x 10^-5
5
0
-5
80
90
100
110
120
130
Velocity [m/s]
UP
Time [s]

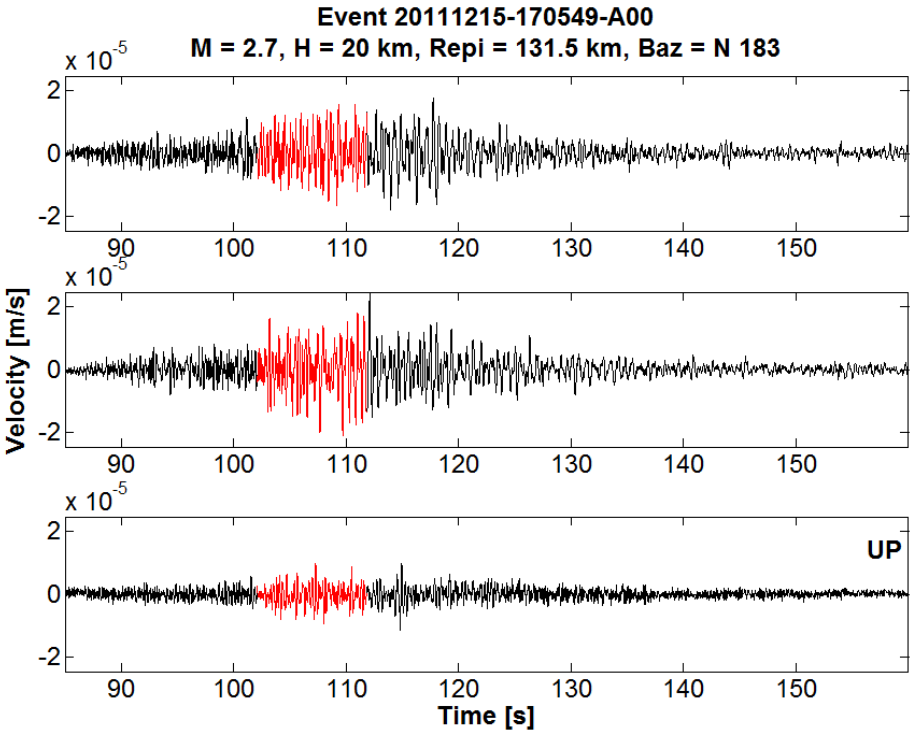
Event 20111215-170549-A00
M = 2.7, H = 20 km, Repi = 131.5 km, Baz = N 183
x 10-5
Velocity [m/s]
UP
Time [s]

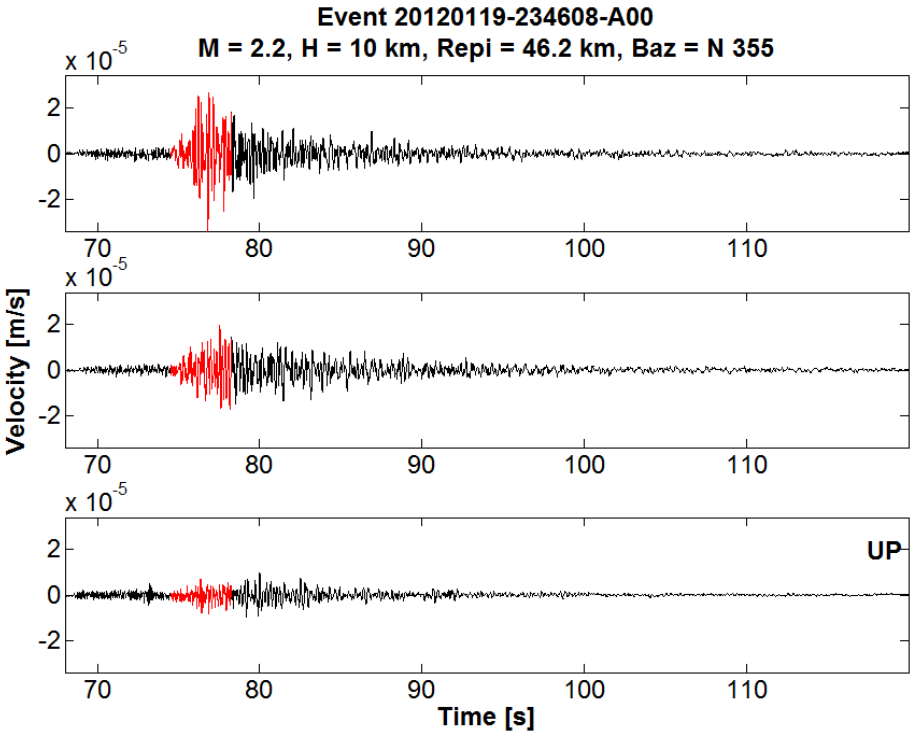
Event 20120119-234608-A00
M = 2.2, H = 10 km, Repi = 46.2 km, Baz = N 355
x 10-5
Velocity [m/s]
UP
Time [s]

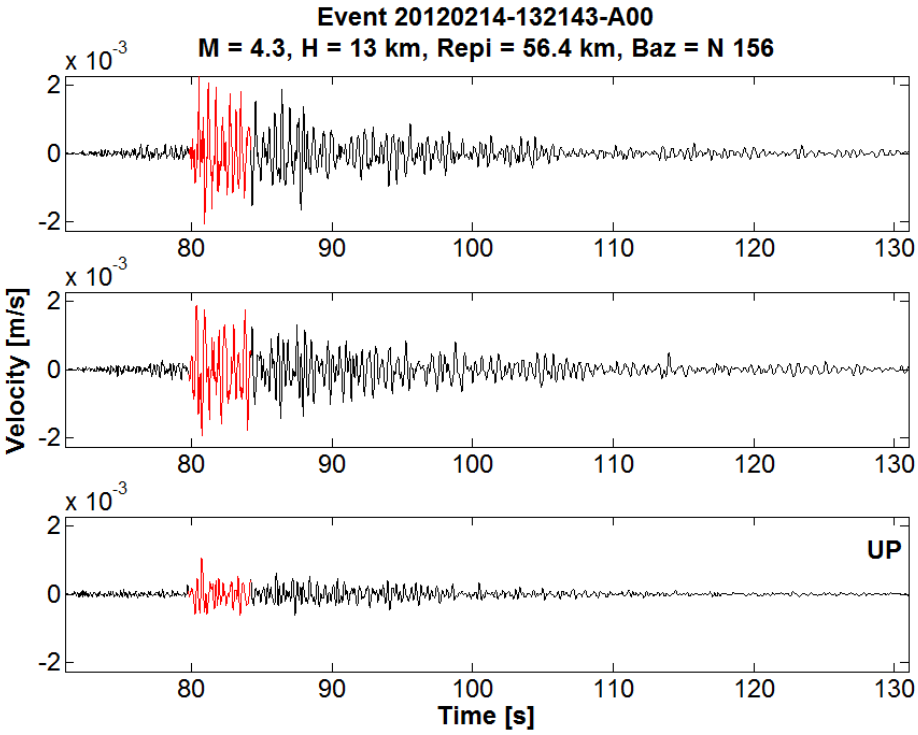
Event 20120214-132143-A00
M = 4.3, H = 13 km, Repi = 56.4 km, Baz = N 156
x 10^-3
2
0
-2
80
90
100
110
120
130
Velocity [m/s]
UP
Time [s]

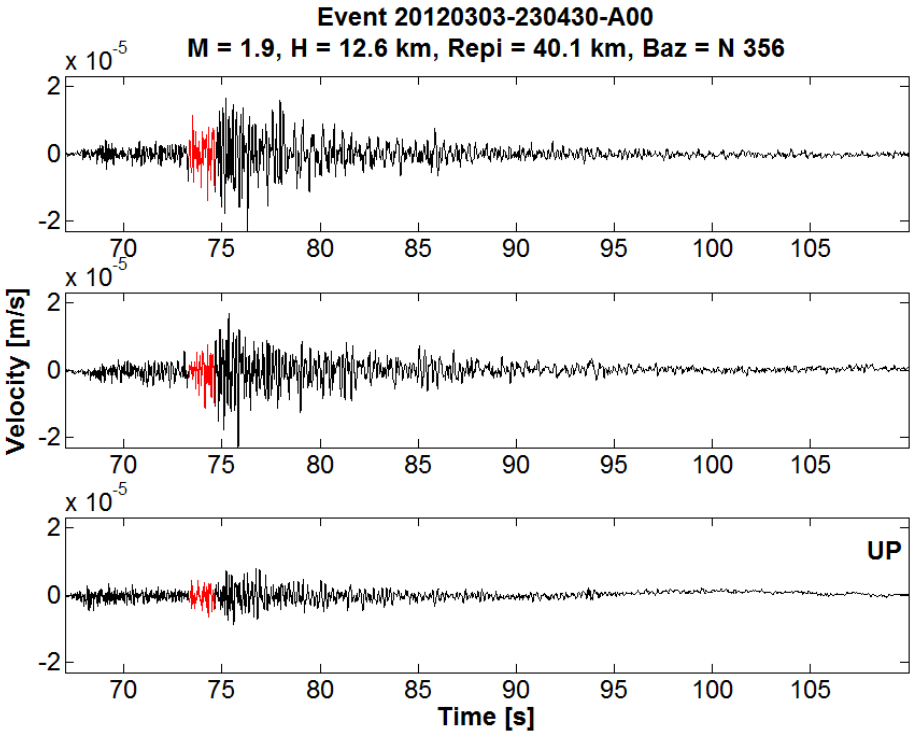
Event 20120303-230430-A00
M = 1.9, H = 12.6 km, Repi = 40.1 km, Baz = N 356
x 10^-5
2
0
-2
70
75
80
85
90
95
100
105
Velocity [m/s]
UP
Time [s]

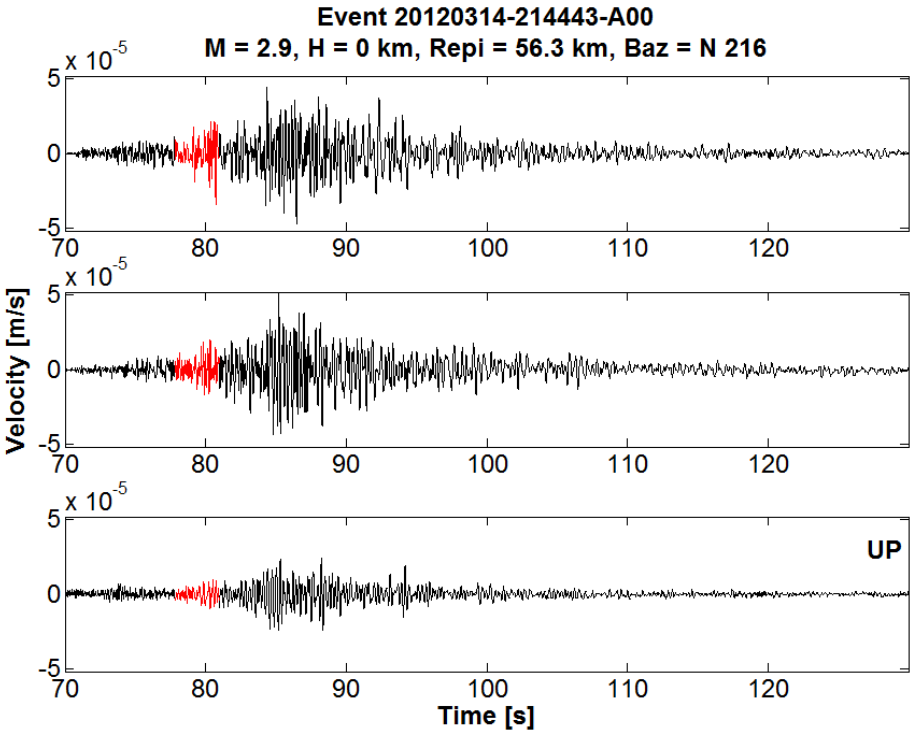
Event 20120314-214443-A00
M = 2.9, H = 0 km, Repi = 56.3 km, Baz = N 216
x 10^-5
Velocity [m/s]
UP
Time [s]

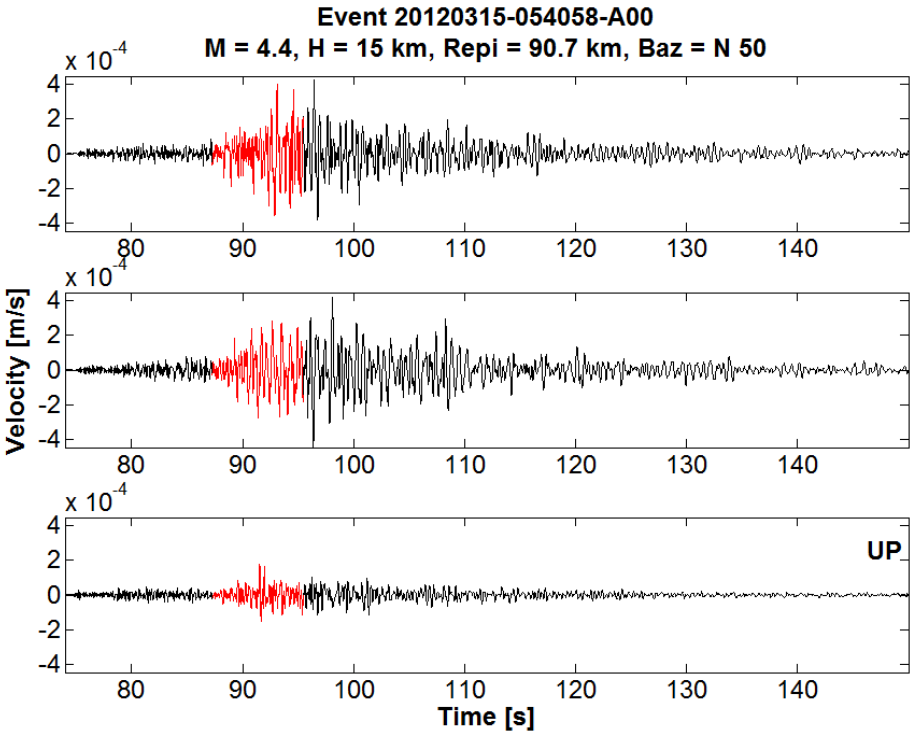
Event 20120315-054058-A00
M = 4.4, H = 15 km, Repi = 90.7 km, Baz = N 50
x 10^-4
Velocity [m/s]
UP
Time [s]

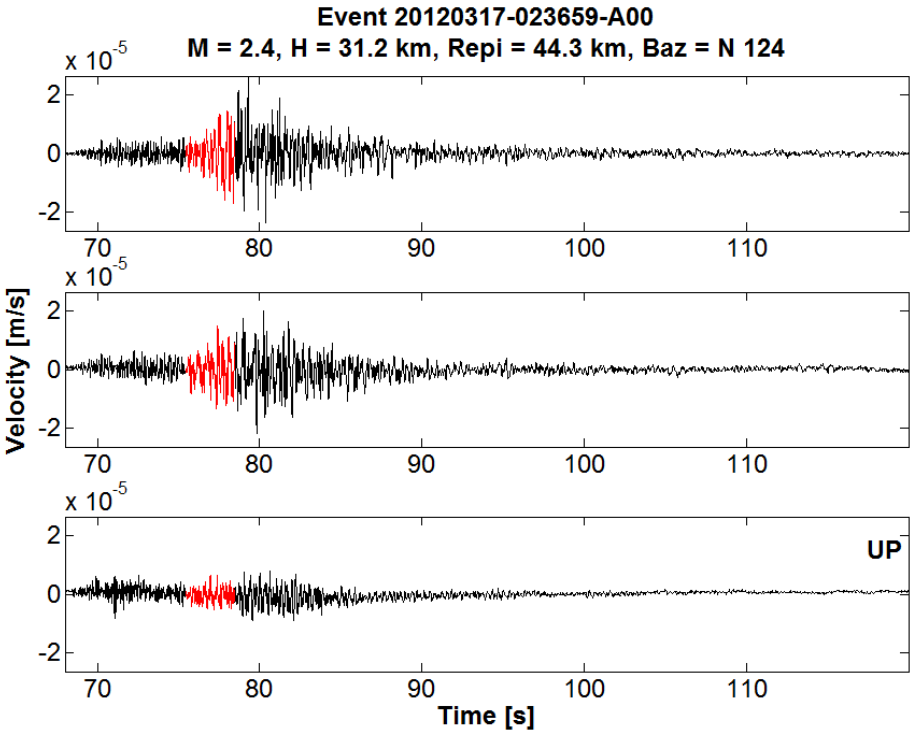
Event 20120317-023659-A00
M = 2.4, H = 31.2 km, Repi = 44.3 km, Baz = N 124
x 10^-5
Velocity [m/s]
UP
Time [s]

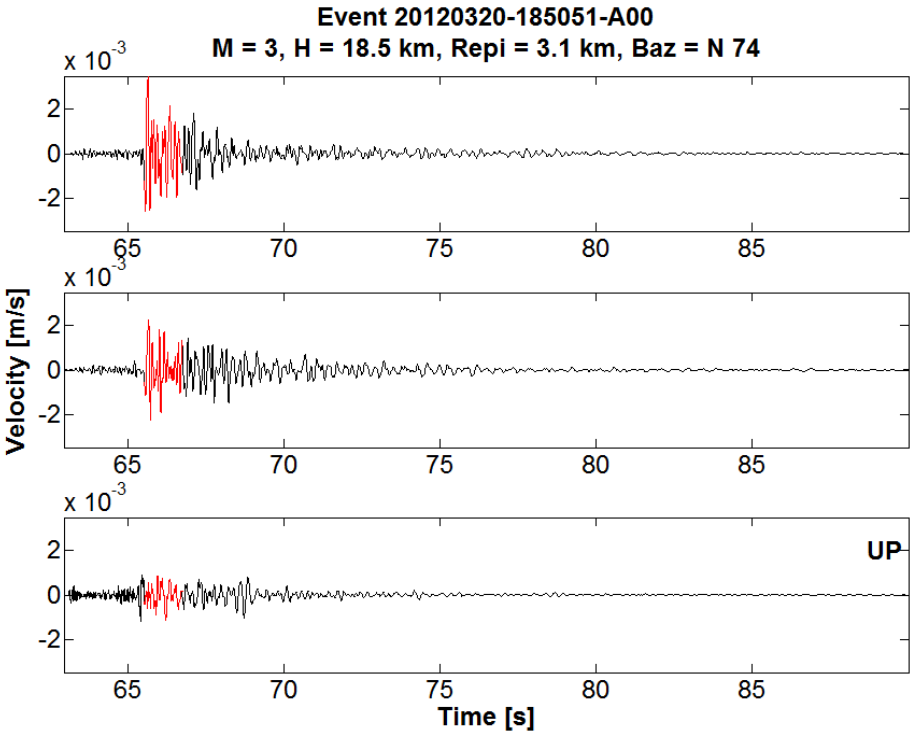
Event 20120320-185051-A00
M = 3, H = 18.5 km, Repi = 3.1 km, Baz = N 74
x 10^-3
Velocity [m/s]
UP
Time [s]

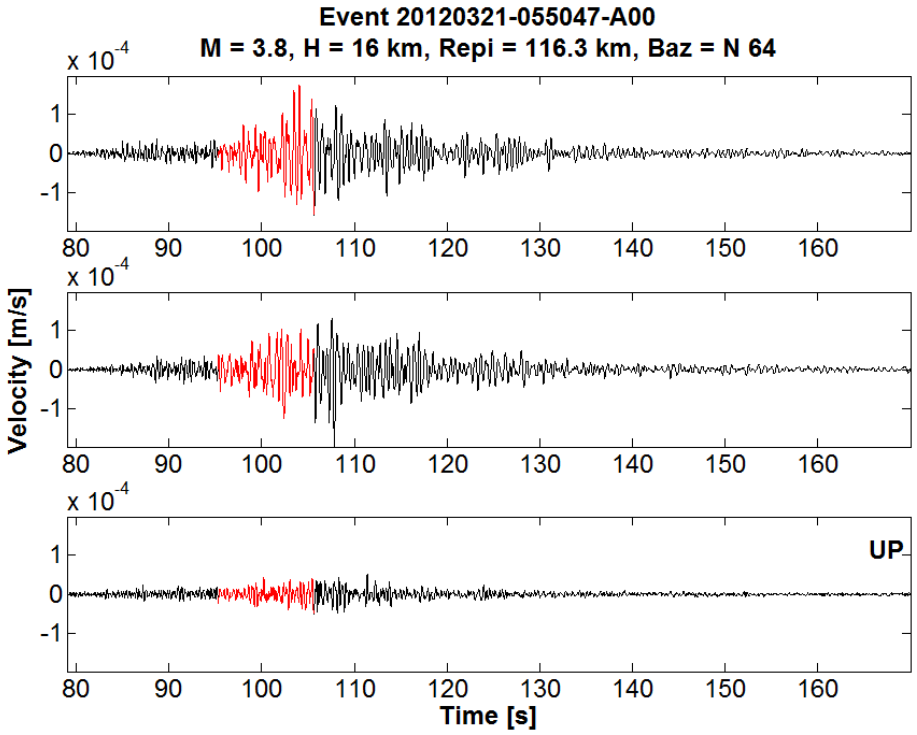
Event 20120321-055047-A00
M = 3.8, H = 16 km, Repi = 116.3 km, Baz = N 64
x 10^-4
Velocity [m/s]
UP
Time [s]

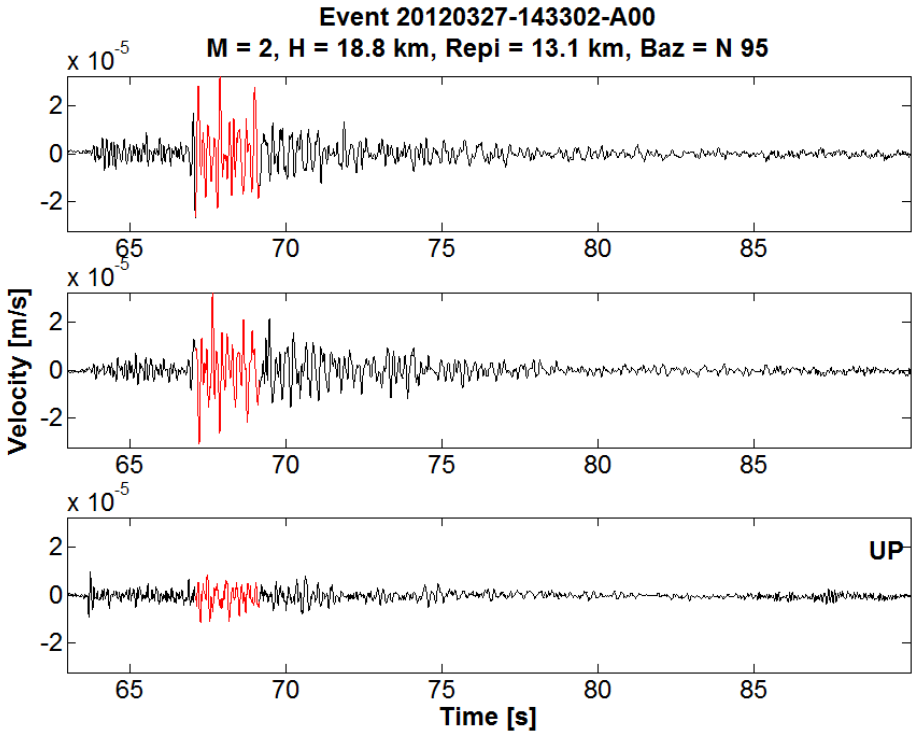
Event 20120327-143302-A00
M = 2, H = 18.8 km, Repi = 13.1 km, Baz = N 95
x 10^-5
Velocity [m/s]
UP
Time [s]

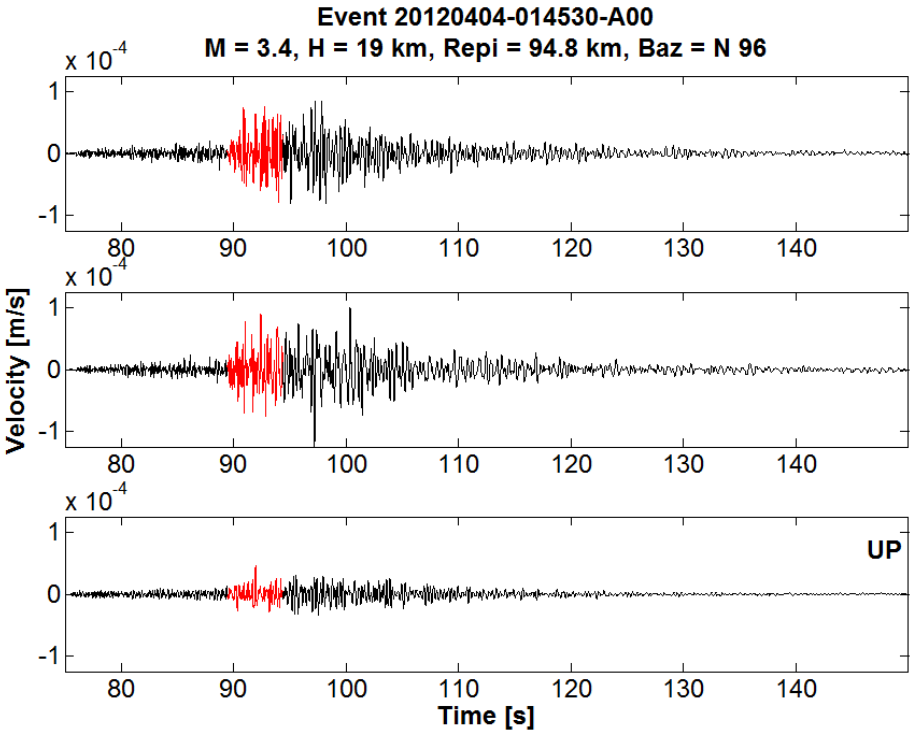
Event 20120404-014530-A00
M = 3.4, H = 19 km, Repi = 94.8 km, Baz = N 96
x 10^-4
Velocity [m/s]
UP
Time [s]

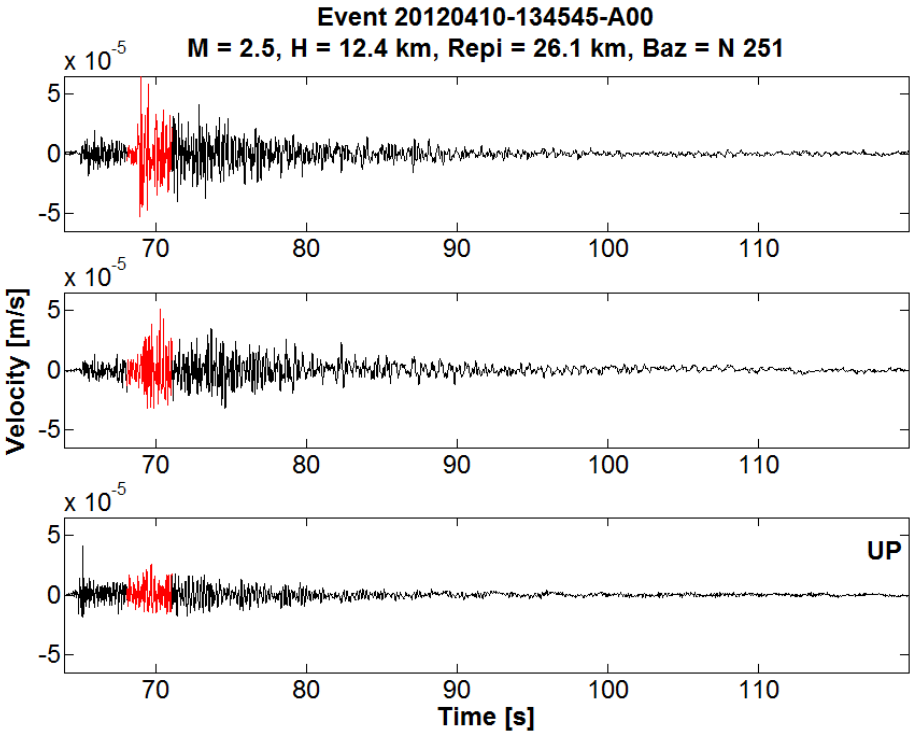
Event 20120410-134545-A00
M = 2.5, H = 12.4 km, Repi = 26.1 km, Baz = N 251
x 10^-5
Velocity [m/s]
UP
Time [s]

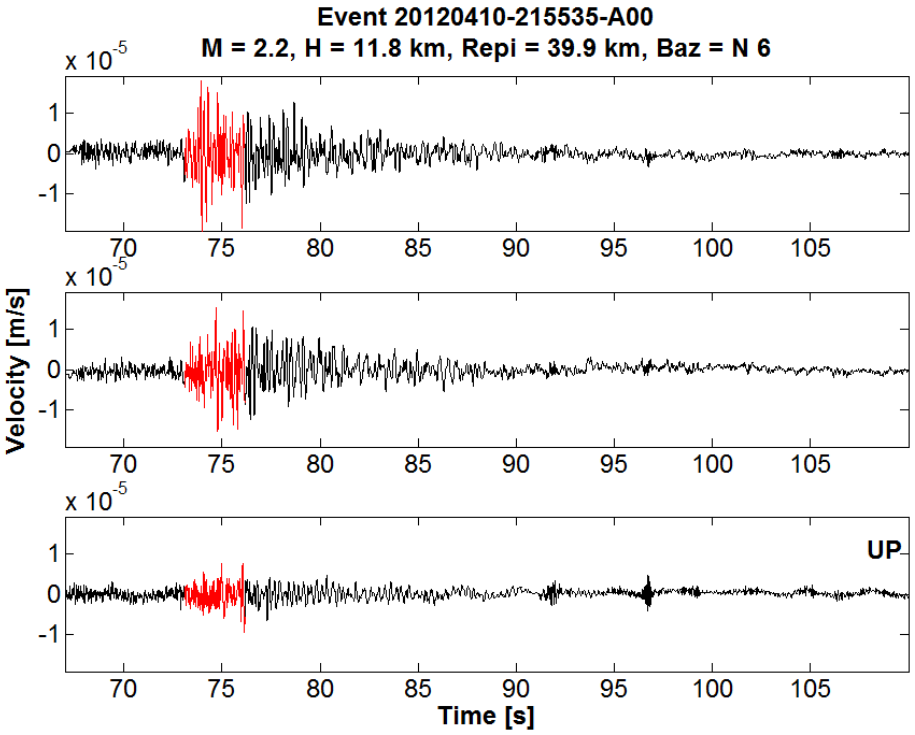
Event 20120410-215535-A00
M = 2.2, H = 11.8 km, Repi = 39.9 km, Baz = N 6
x 10^-5
Velocity [m/s]
UP
Time [s]

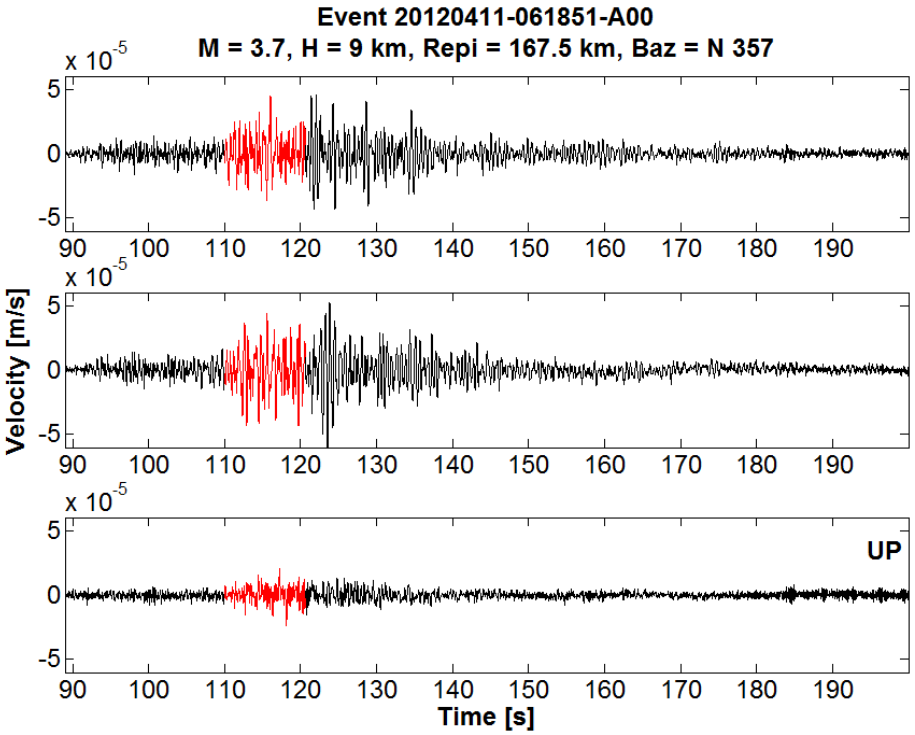
Event 20120411-061851-A00
M = 3.7, H = 9 km, Repi = 167.5 km, Baz = N 357
x 10^-5
Velocity [m/s]
UP
Time [s]

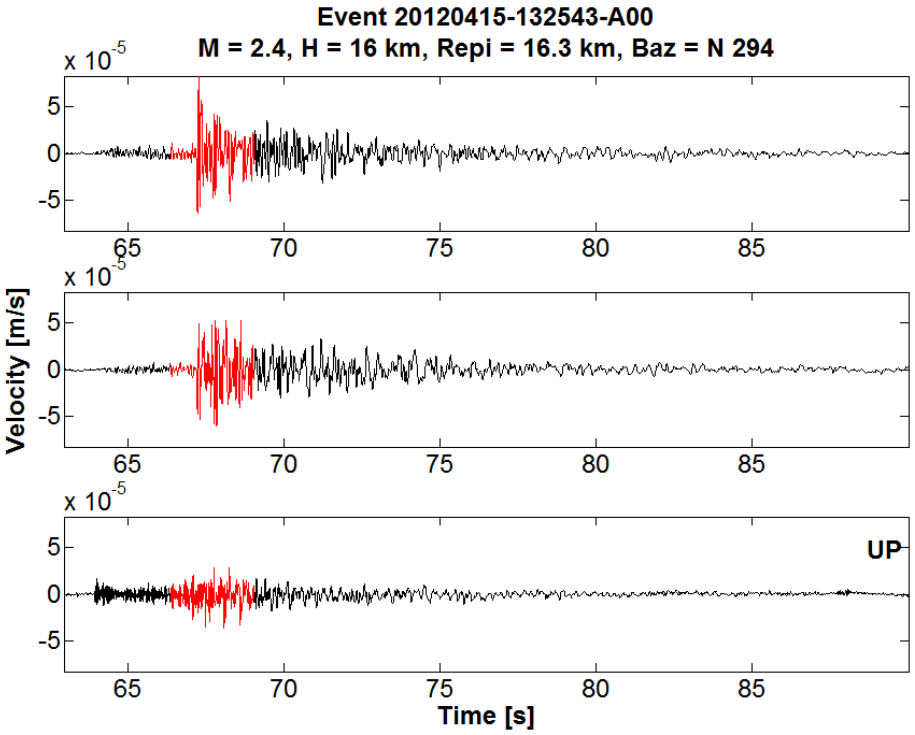
Event 20120415-132543-A00
M = 2.4, H = 16 km, Repi = 16.3 km, Baz = N 294
x 10^-5
5
0
-5
65
70
75
80
85
Velocity [m/s]
UP
Time [s]

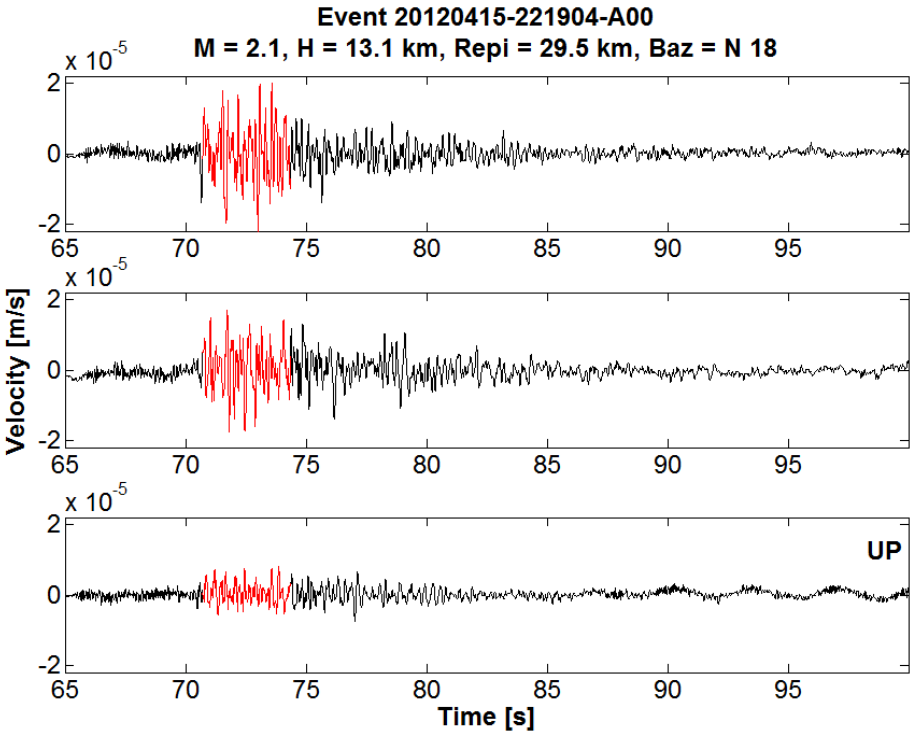
Event 20120415-221904-A00
M = 2.1, H = 13.1 km, Repi = 29.5 km, Baz = N 18
x 10^-5
2
0
-2
65
70
75
80
85
90
95
Velocity [m/s]
UP
Time [s]

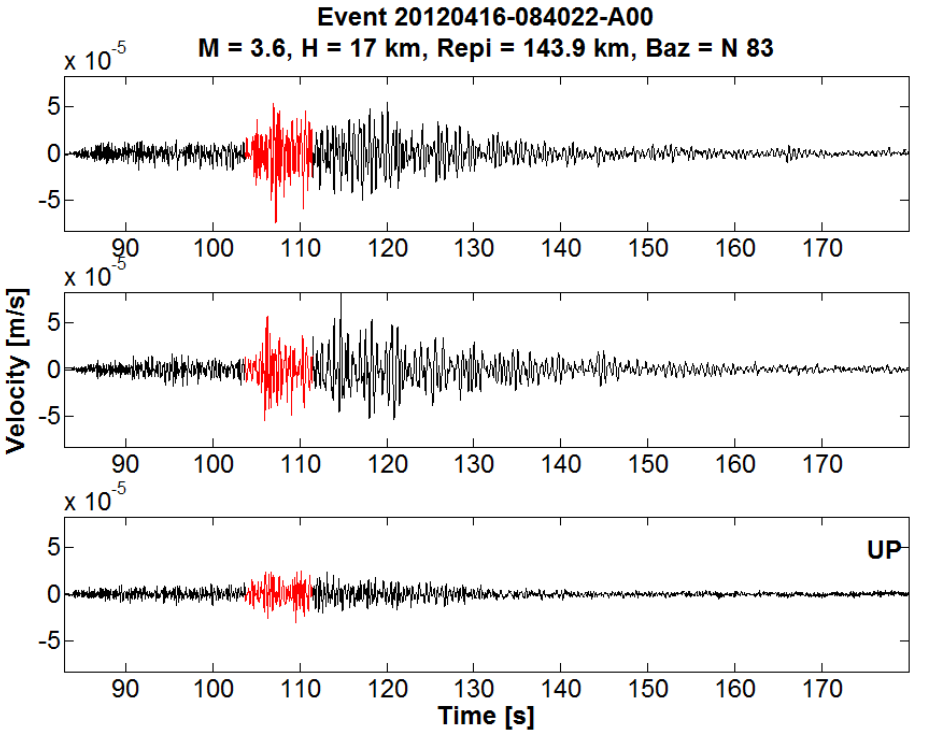
Event 20120416-084022-A00
M = 3.6, H = 17 km, Repi = 143.9 km, Baz = N 83
x 10^-5
5
0
-5
90 100 110 120 130 140 150 160 170
Velocity [m/s]
UP
Time [s]

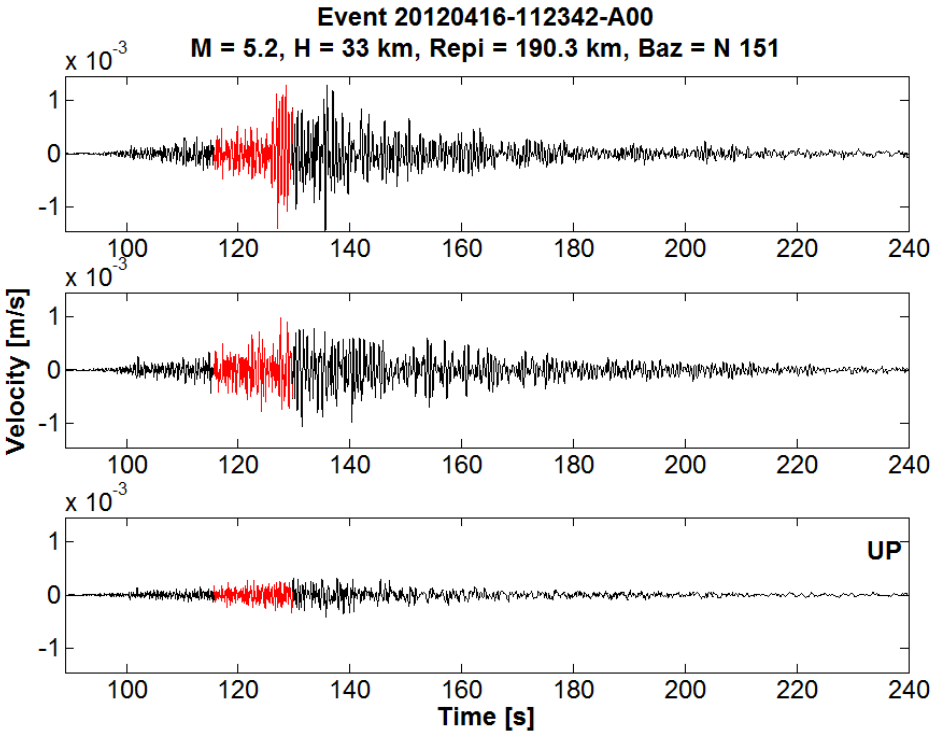
Event 20120416-112342-A00
M = 5.2, H = 33 km, Repi = 190.3 km, Baz = N 151
x 10^-3
1
0
-1
100 120 140 160 180 200 220 240
Velocity [m/s]
UP
Time [s]

Appendix H

Velocity time series from R01 station

Available velocity time series from rock station R01 are shown here for the selected subset of events (Appendix E). The time window represents the duration from the onset of P-wave till the end of the signal. The segment of signal shown in 'red' color represents selected window from visual inspection based on which Coherency analysis of Array A stations have been performed in Chapter 4. It is to be noted that R01 is the soft-rock station. Records from R01 have been used in case R02 records were unavailable. That's why the selected window for coherency, in red curve, is shown for those events only.

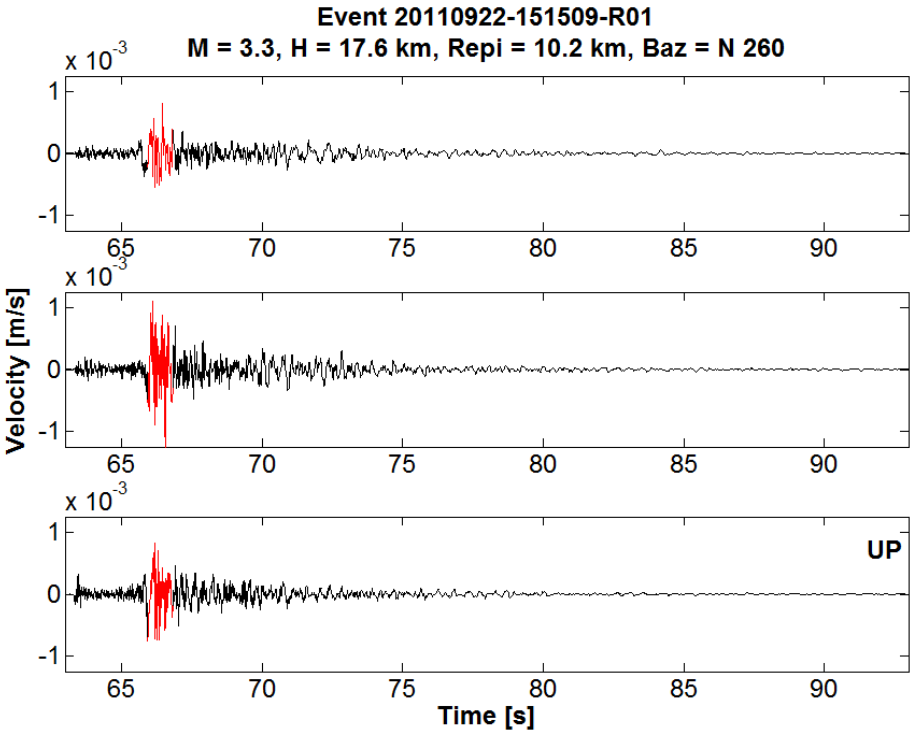
Event 20110922-151509-R01
M = 3.3, H = 17.6 km, Repi = 10.2 km, Baz = N 260
x 10^-3
Velocity [m/s]
UP
Time [s]

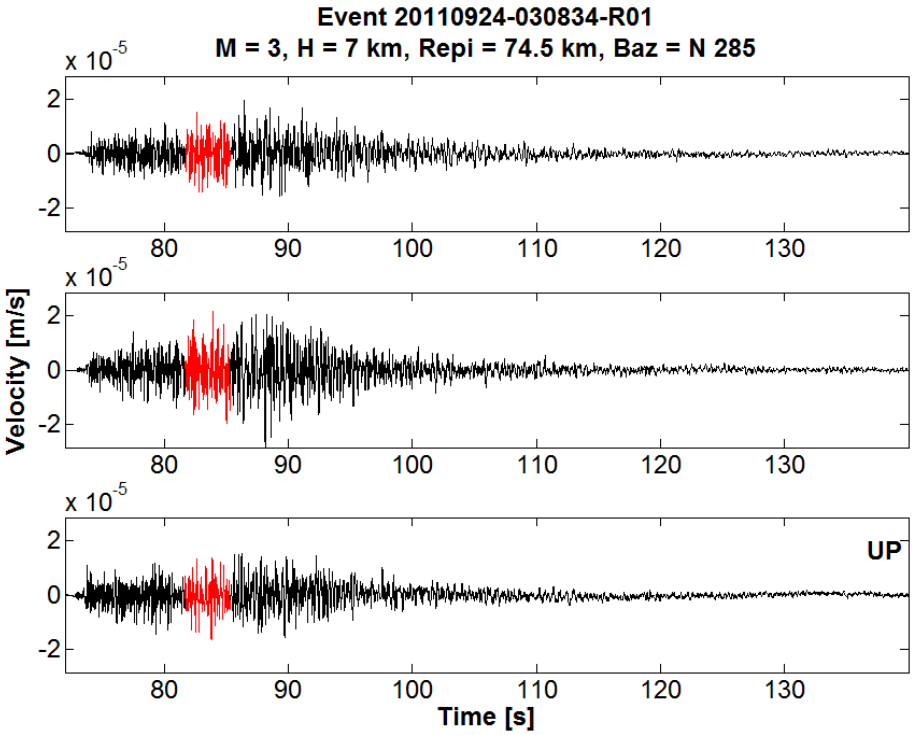
Event 20110924-030834-R01
M = 3, H = 7 km, Repi = 74.5 km, Baz = N 285
x 10^-5
Velocity [m/s]
UP
Time [s]

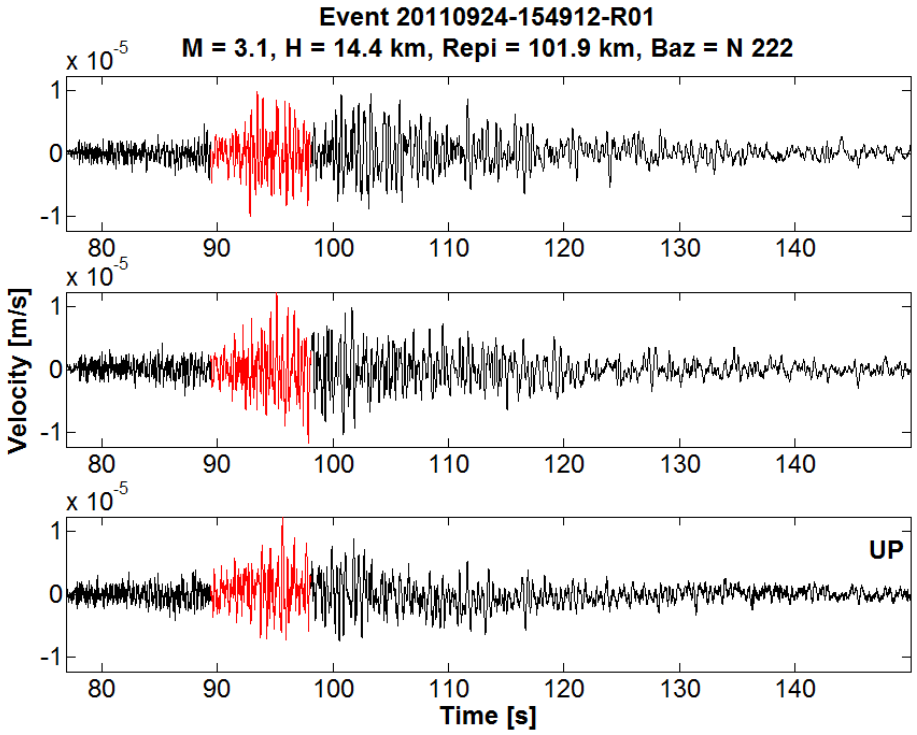
Event 20110924-154912-R01
M = 3.1, H = 14.4 km, Repi = 101.9 km, Baz = N 222
x 10-5
x 10-5
x 10-5
UP
Velocity [m/s]
Time [s]

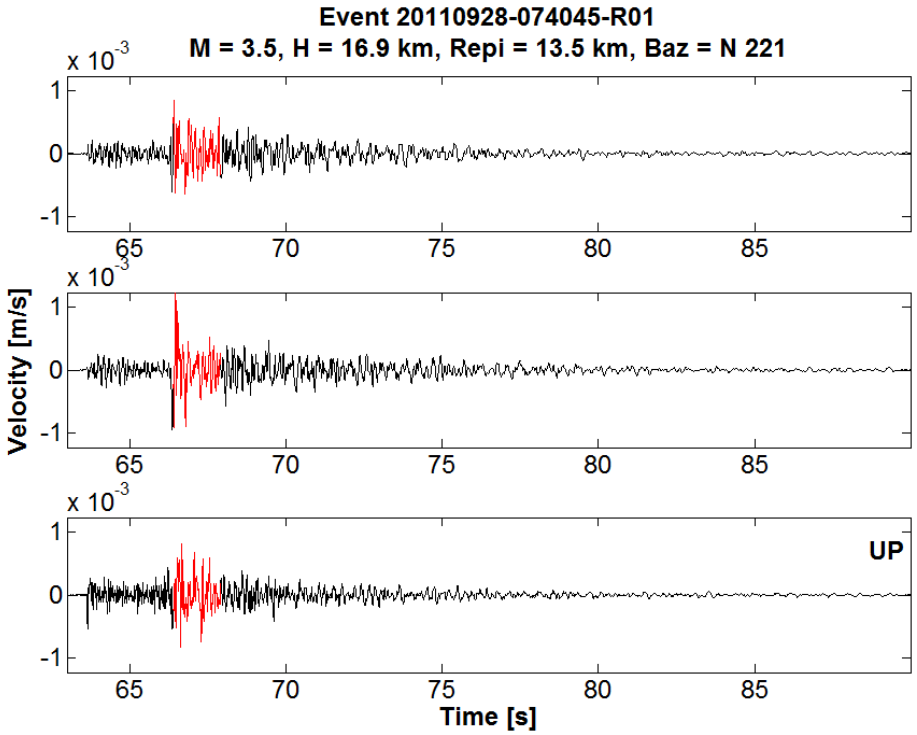
Event 20110928-074045-R01
M = 3.5, H = 16.9 km, Repi = 13.5 km, Baz = N 221
x 10-3
x 10-3
x 10-3
UP
Velocity [m/s]
Time [s]

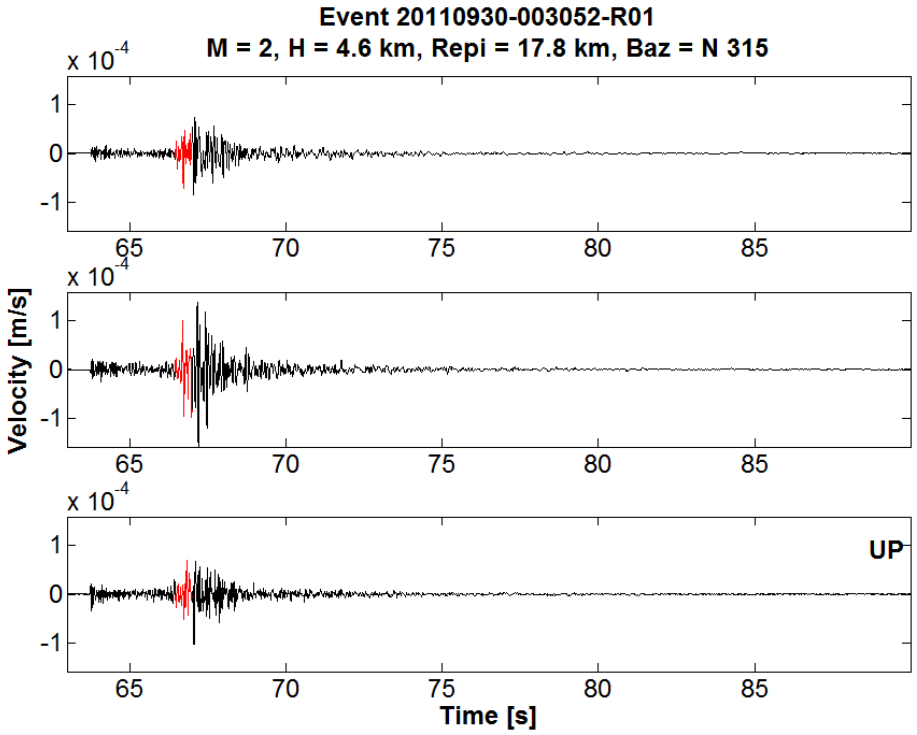
Event 20110930-003052-R01
M = 2, H = 4.6 km, Repi = 17.8 km, Baz = N 315
x 10^-4
Velocity [m/s]
UP
Time [s]

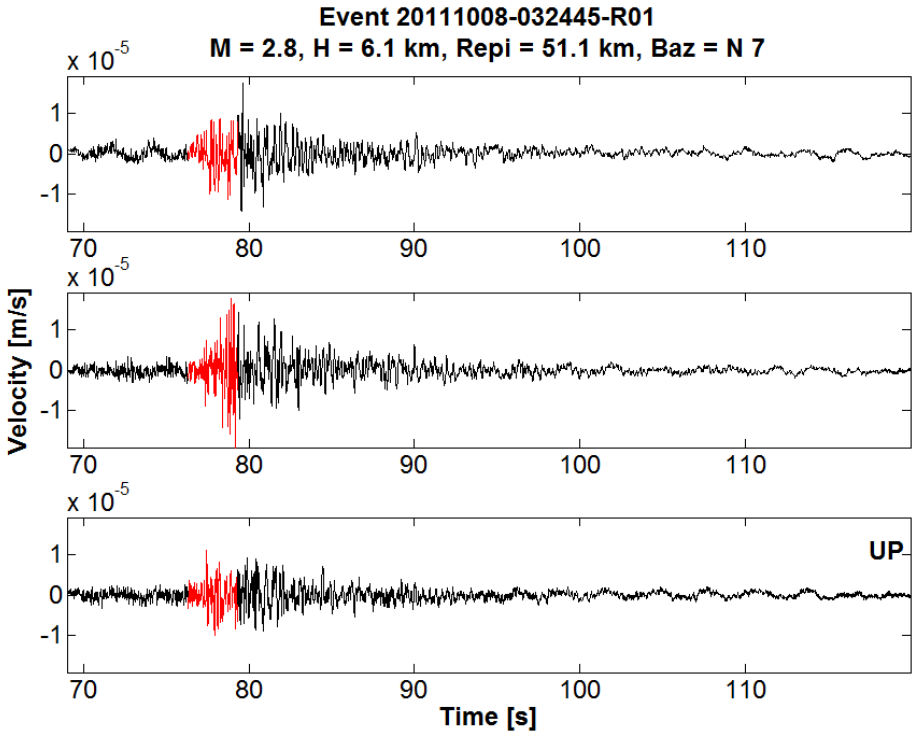
Event 20111008-032445-R01
M = 2.8, H = 6.1 km, Repi = 51.1 km, Baz = N 7
x 10^-5
Velocity [m/s]
UP
Time [s]

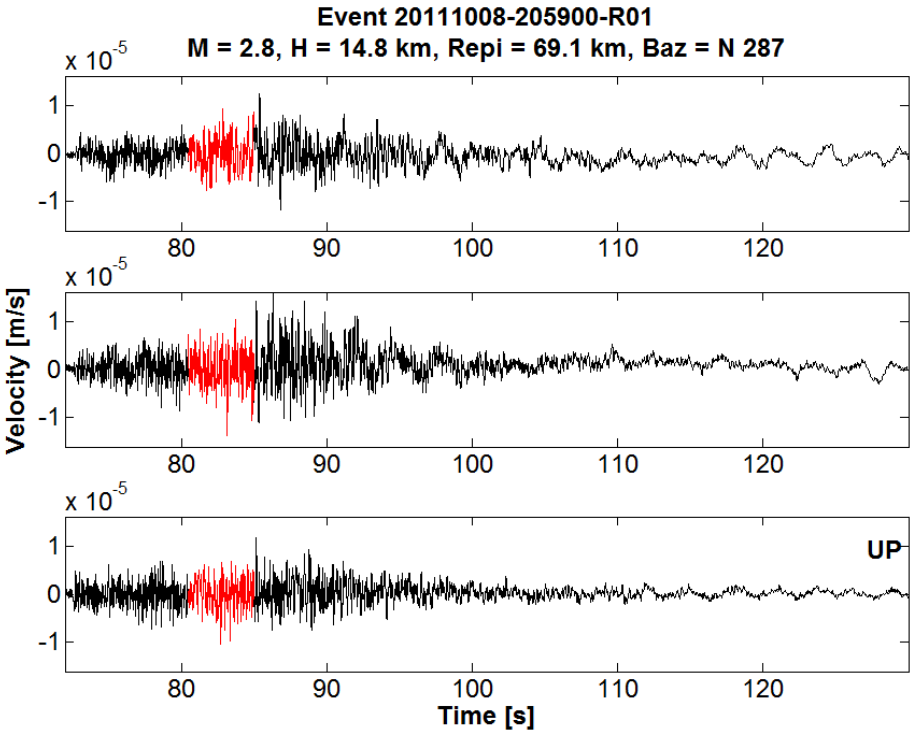
Event 20111008-205900-R01
M = 2.8, H = 14.8 km, Repi = 69.1 km, Baz = N 287
x 10^-5
Velocity [m/s]
UP
Time [s]

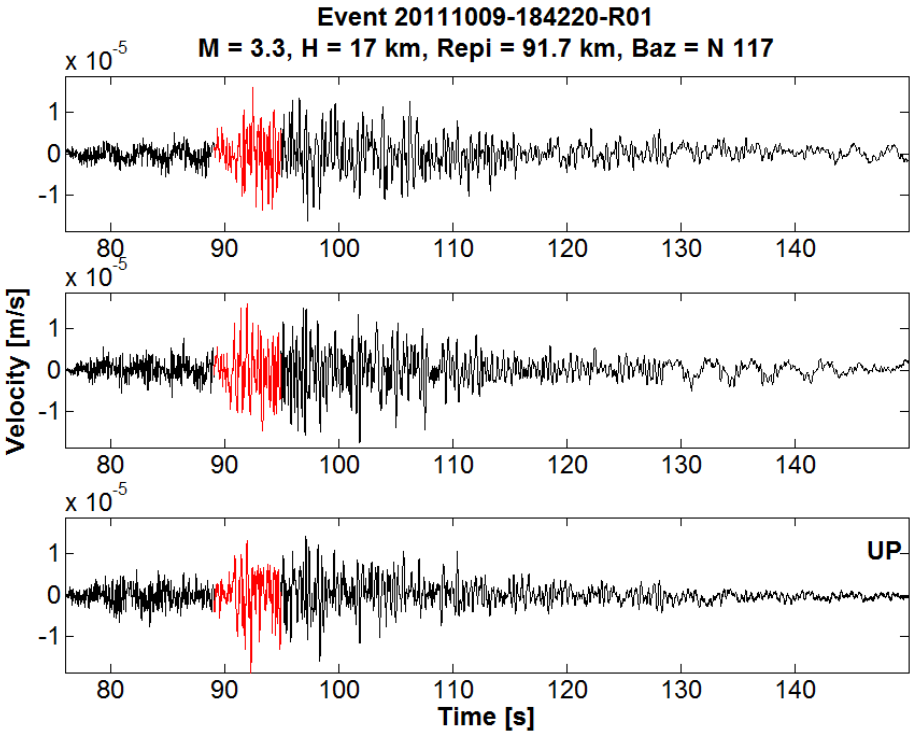
Event 20111009-184220-R01
M = 3.3, H = 17 km, Repi = 91.7 km, Baz = N 117
x 10^-5
Velocity [m/s]
UP
Time [s]

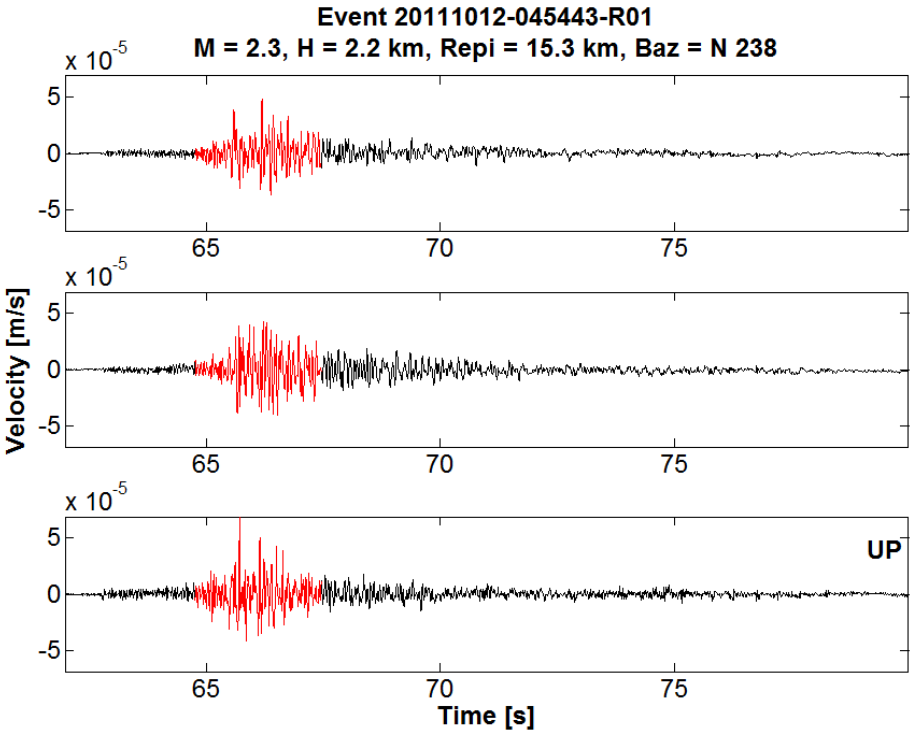
Event 20111012-045443-R01
M = 2.3, H = 2.2 km, Repi = 15.3 km, Baz = N 238
x 10-5
5
0
-5
65
70
75
Velocity [m/s]
UP
Time [s]

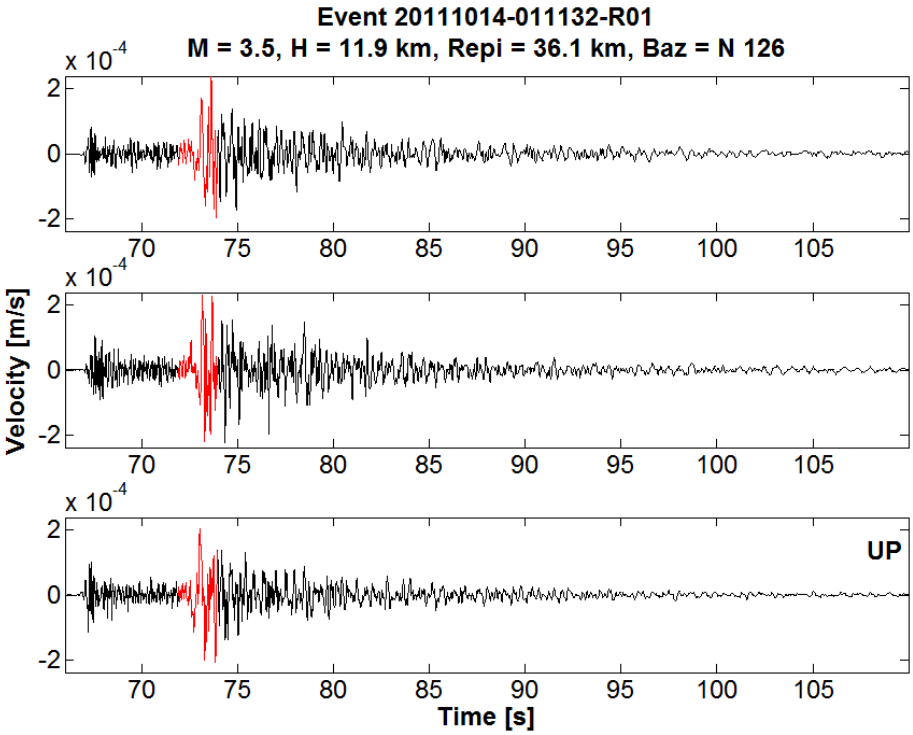
Event 20111014-011132-R01
M = 3.5, H = 11.9 km, Repi = 36.1 km, Baz = N 126
x 10-4
2
0
-2
70
75
80
85
90
95
100
105
Velocity [m/s]
UP
Time [s]

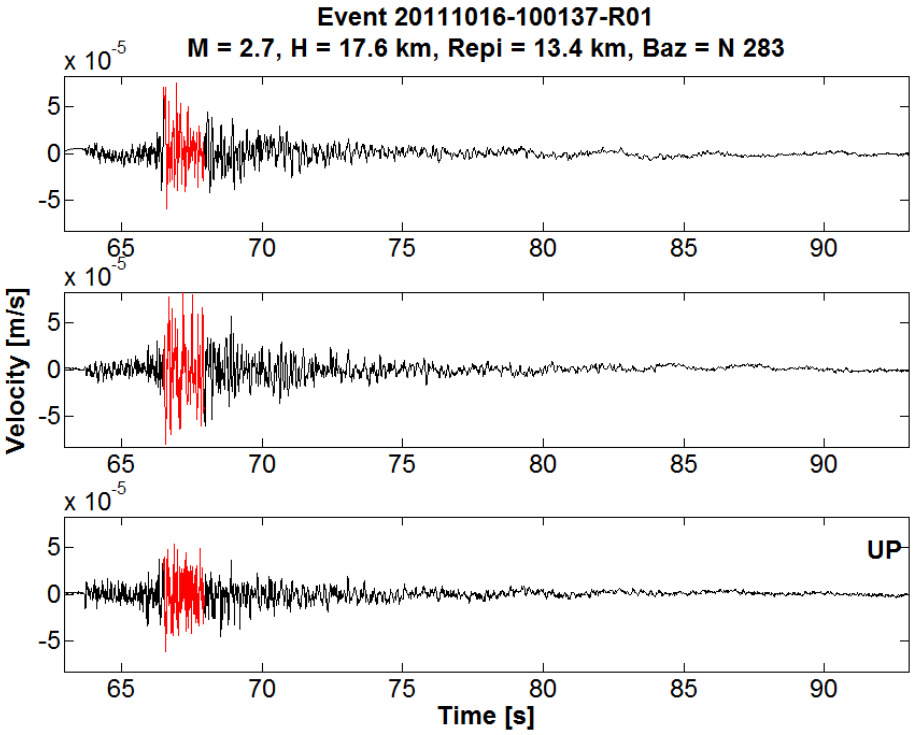
Event 20111016-100137-R01
M = 2.7, H = 17.6 km, Repi = 13.4 km, Baz = N 283
x 10^-5
Velocity [m/s]
UP
Time [s]

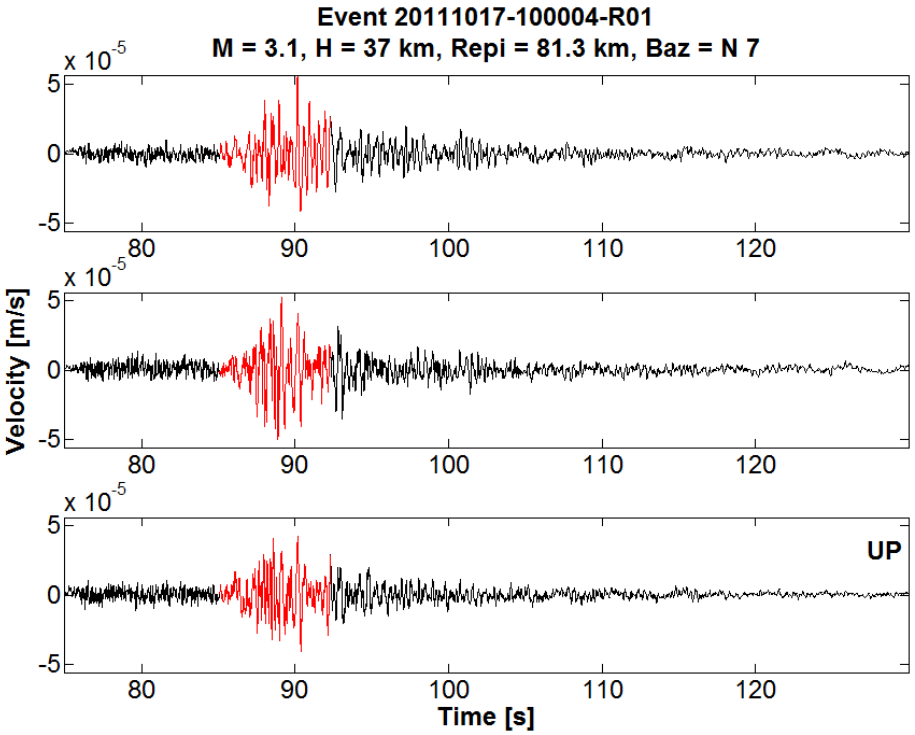
Event 20111017-100004-R01
M = 3.1, H = 37 km, Repi = 81.3 km, Baz = N 7
x 10^-5
Velocity [m/s]
UP
Time [s]

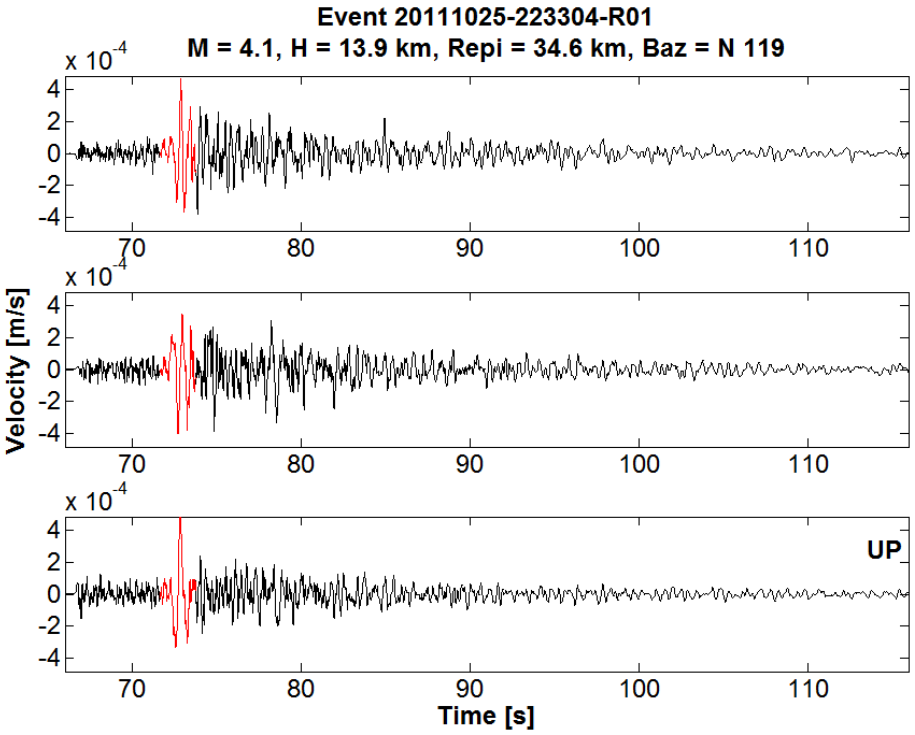
Event 20111025-223304-R01
M = 4.1, H = 13.9 km, Repi = 34.6 km, Baz = N 119
x 10^-4
Velocity [m/s]
UP
Time [s]

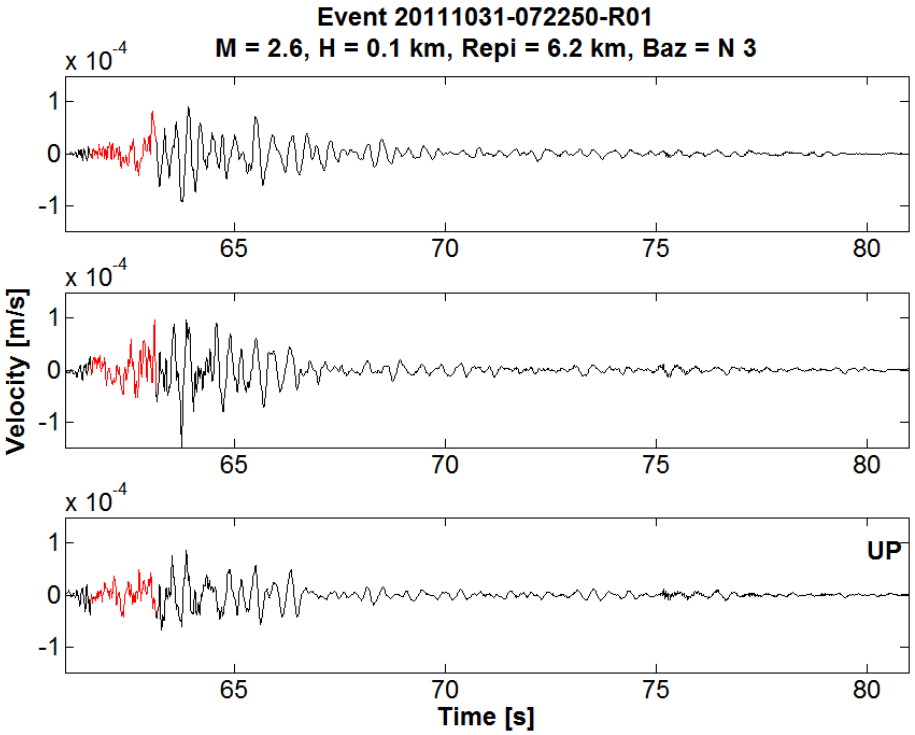
Event 20111031-072250-R01
M = 2.6, H = 0.1 km, Repi = 6.2 km, Baz = N 3
x 10^-4
Velocity [m/s]
UP
Time [s]

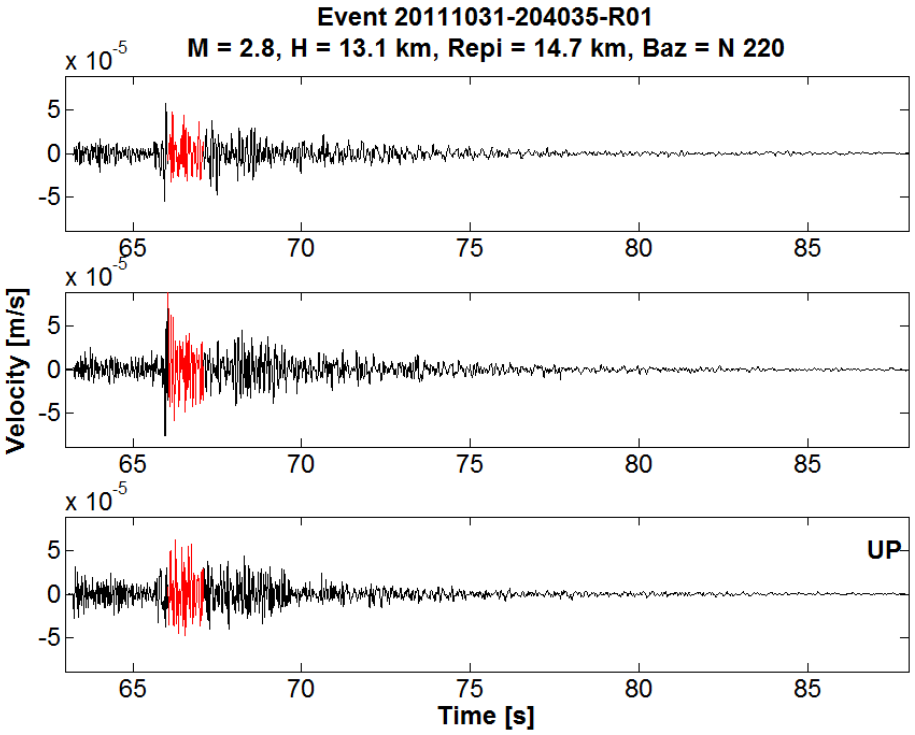
Event 20111031-204035-R01
M = 2.8, H = 13.1 km, Repi = 14.7 km, Baz = N 220
x 10^-5
5
0
-5
65
70
75
80
85
Velocity [m/s]
UP
Time [s]

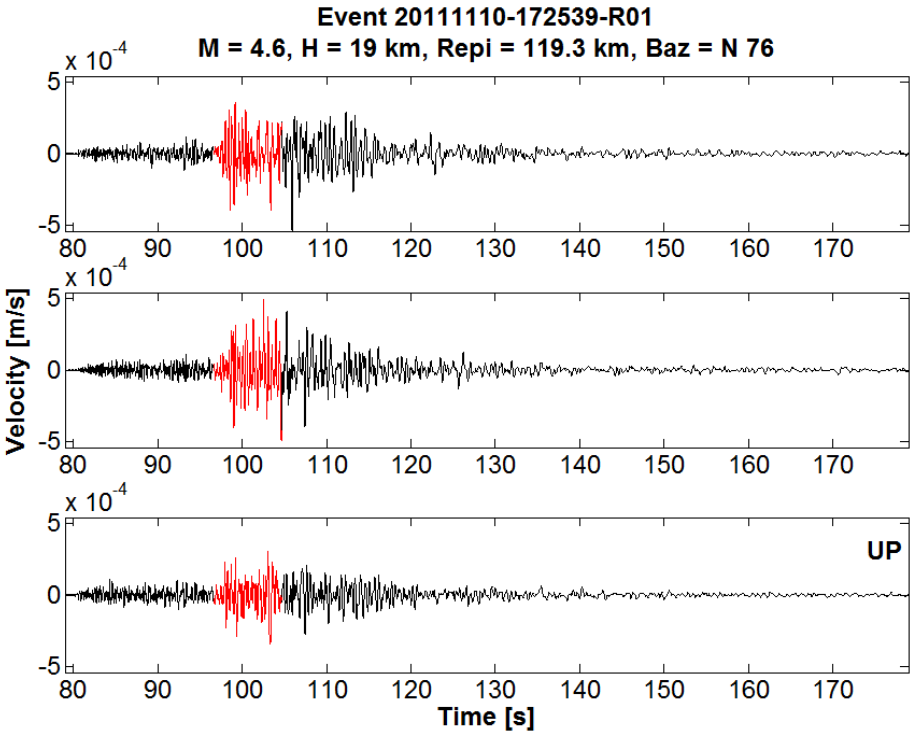
Event 20111110-172539-R01
M = 4.6, H = 19 km, Repi = 119.3 km, Baz = N 76
x 10^-4
5
0
-5
80
90
100
110
120
130
140
150
160
170
Velocity [m/s]
UP
Time [s]

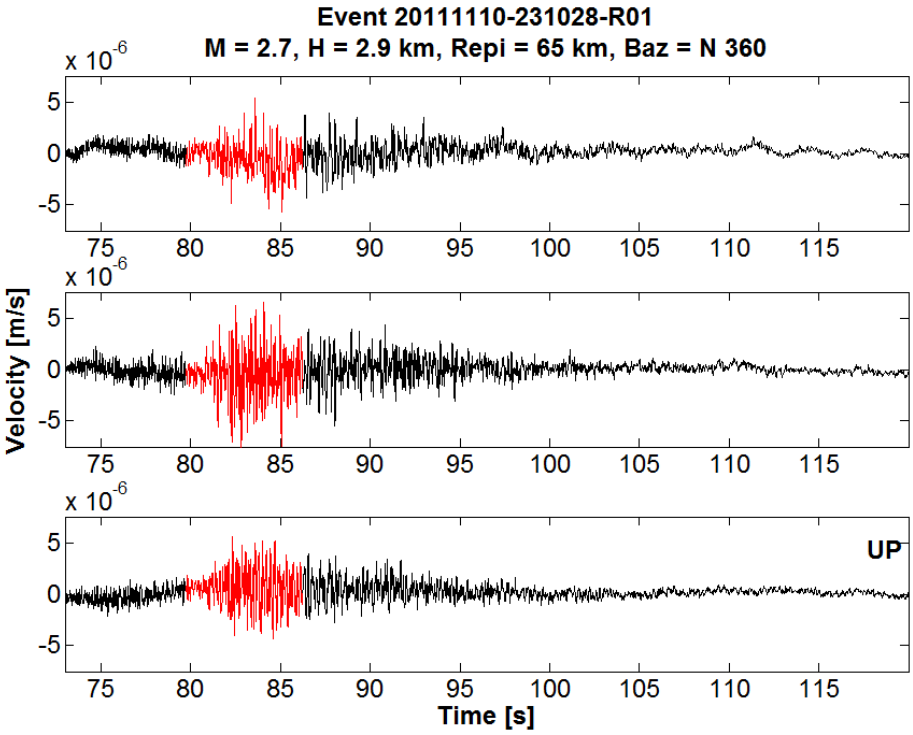
Event 20111110-231028-R01
M = 2.7, H = 2.9 km, Repi = 65 km, Baz = N 360
x 10^-6
5
0
-5
75 80 85 90 95 100 105 110 115
Velocity [m/s]
UP
Time [s]

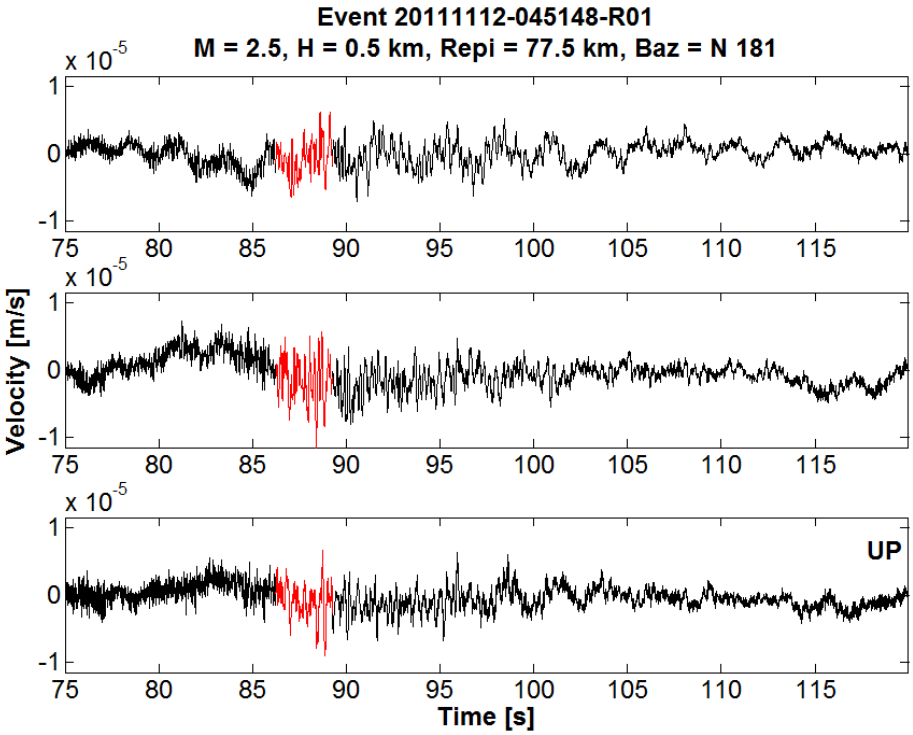
Event 20111112-045148-R01
M = 2.5, H = 0.5 km, Repi = 77.5 km, Baz = N 181
x 10^-5
1
0
-1
75 80 85 90 95 100 105 110 115
Velocity [m/s]
UP
Time [s]

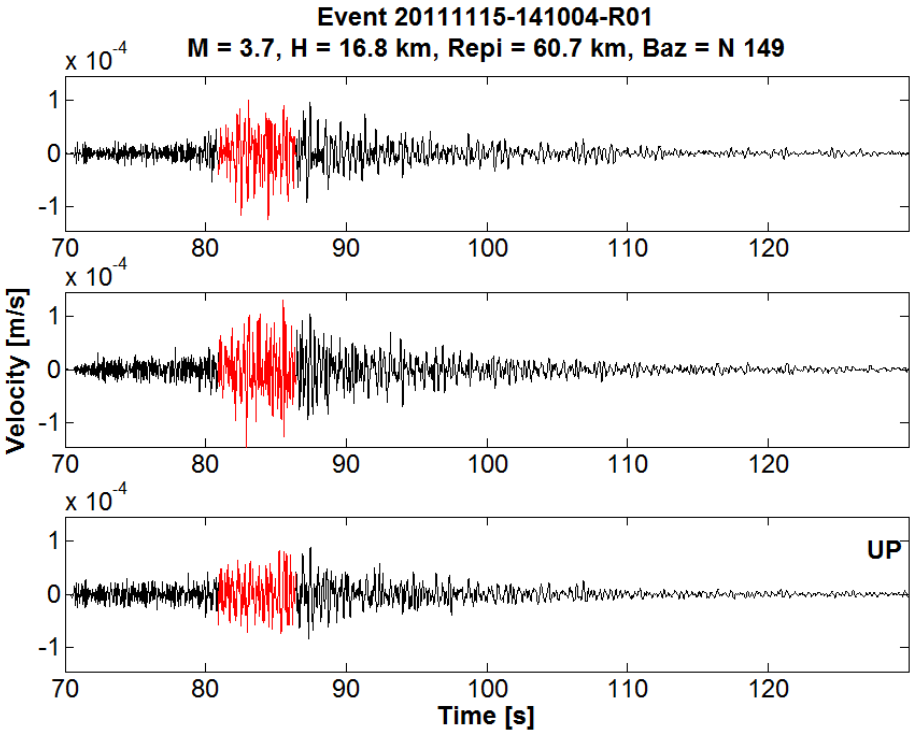
Event 20111115-141004-R01
M = 3.7, H = 16.8 km, Repi = 60.7 km, Baz = N 149
x 10^-4
Velocity [m/s]
UP
Time [s]

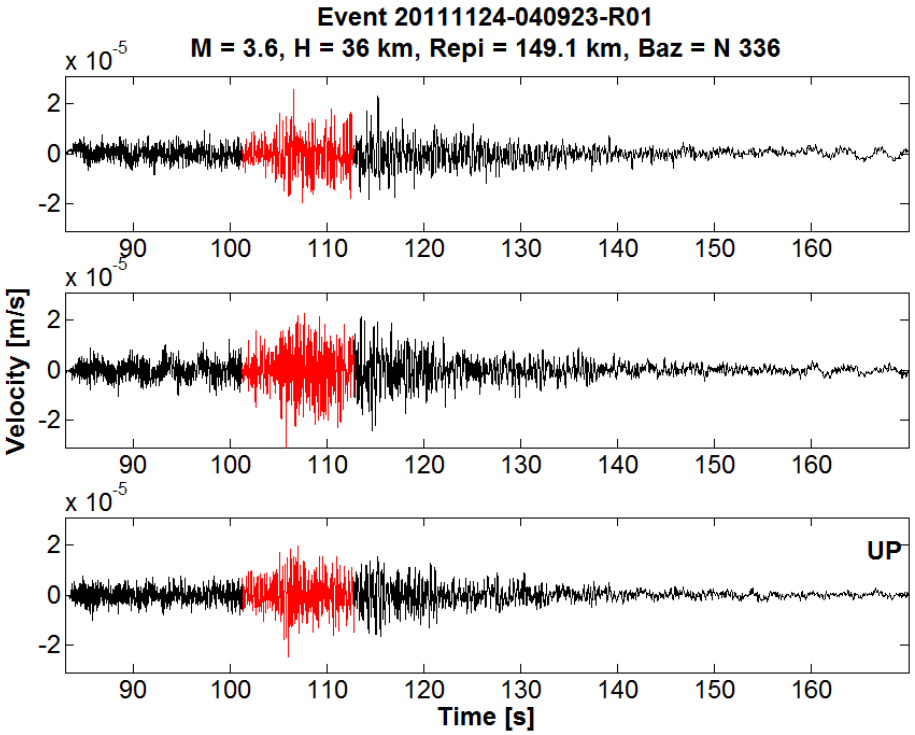
Event 20111124-040923-R01
M = 3.6, H = 36 km, Repi = 149.1 km, Baz = N 336
x 10^-5
Velocity [m/s]
UP
Time [s]

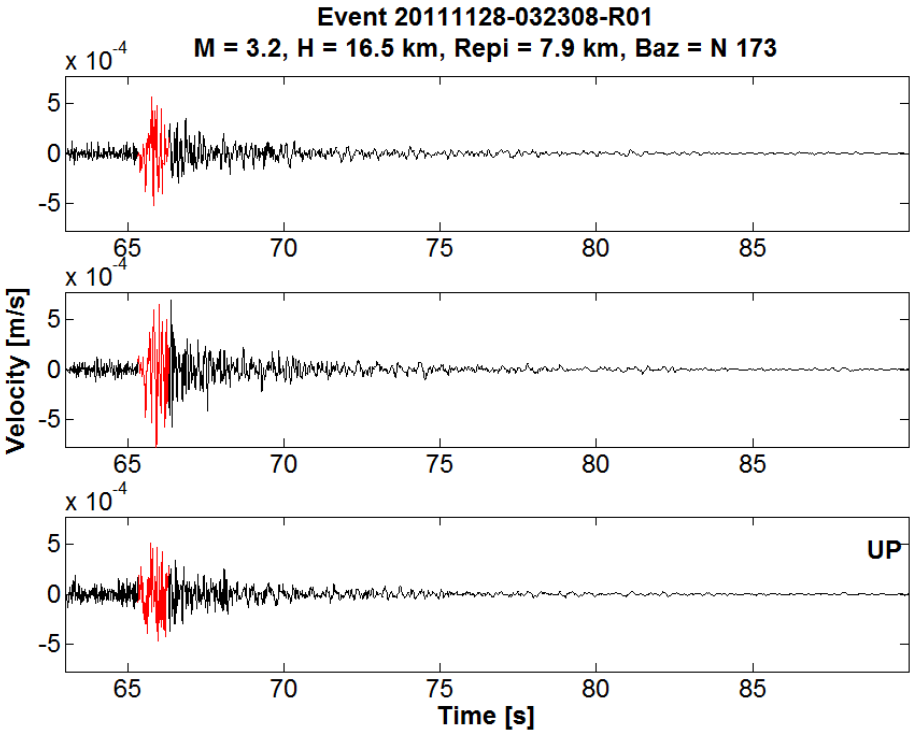
Event 20111128-032308-R01
M = 3.2, H = 16.5 km, Repi = 7.9 km, Baz = N 173
x 10^-4
5
0
-5
65
70
75
80
85
Velocity [m/s]
UP
Time [s]

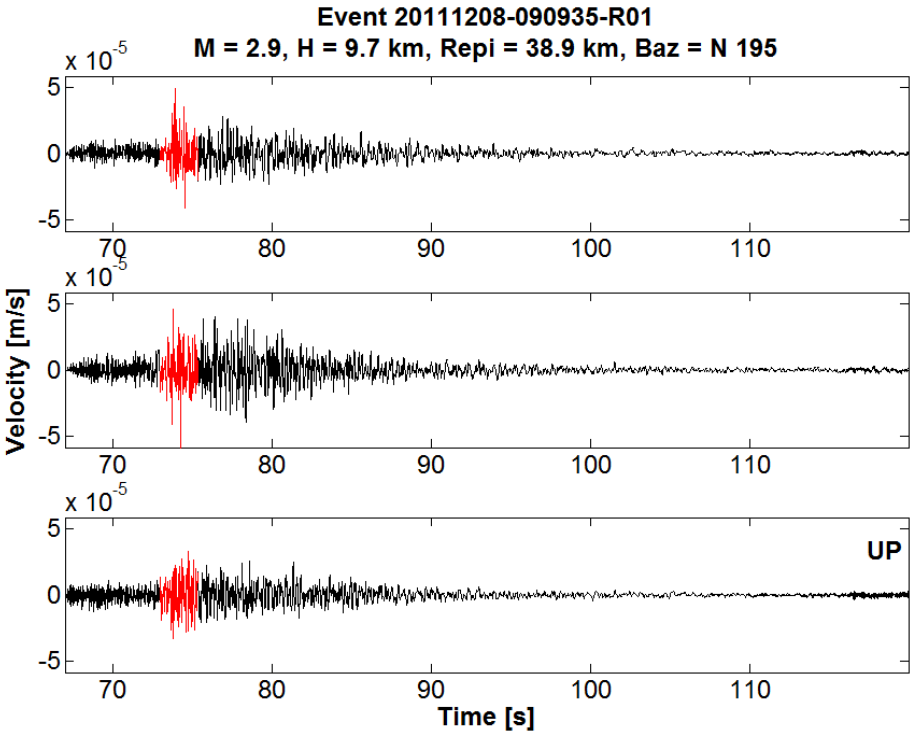
Event 20111208-090935-R01
M = 2.9, H = 9.7 km, Repi = 38.9 km, Baz = N 195
x 10^-5
5
0
-5
70
80
90
100
110
Velocity [m/s]
UP
Time [s]

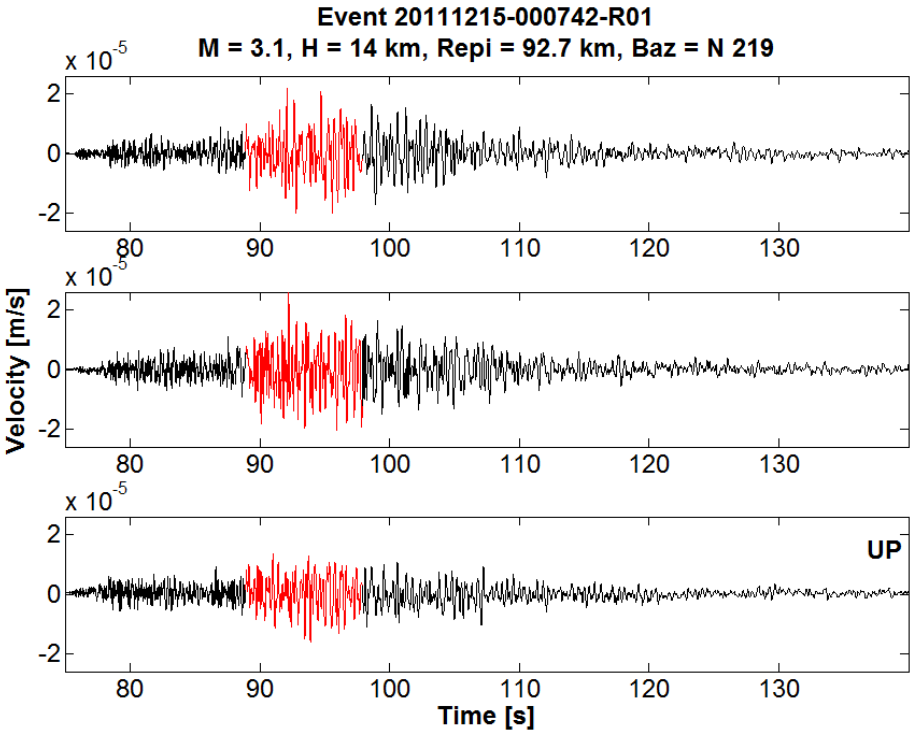
Event 20111215-000742-R01
M = 3.1, H = 14 km, Repi = 92.7 km, Baz = N 219
x 10-5
2
0
-2
80
90
100
110
120
130
Velocity [m/s]
UP
Time [s]

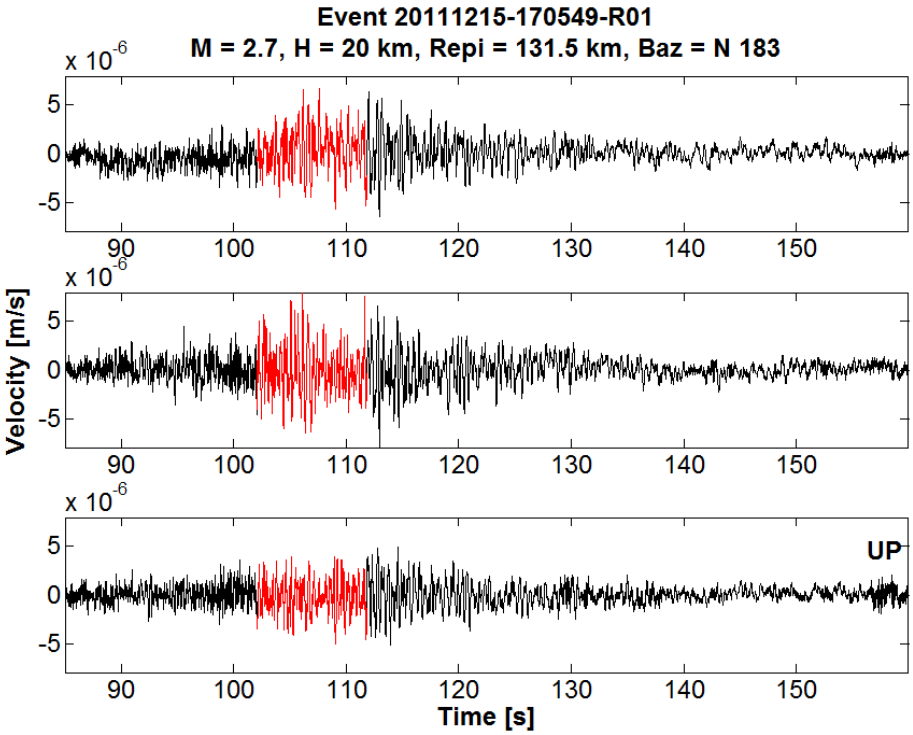
Event 20111215-170549-R01
M = 2.7, H = 20 km, Repi = 131.5 km, Baz = N 183
x 10-6
5
0
-5
90
100
110
120
130
140
150
Velocity [m/s]
UP
Time [s]

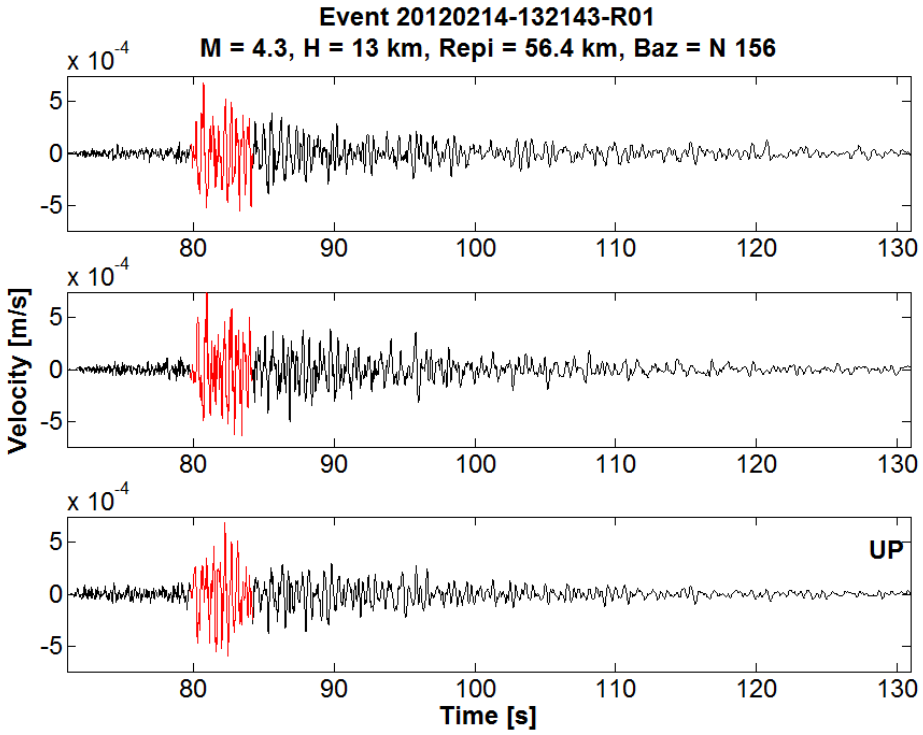
Event 20120214-132143-R01
M = 4.3, H = 13 km, Repi = 56.4 km, Baz = N 156
x 10^-4
5
0
-5
80
90
100
110
120
130
Velocity [m/s]
UP
Time [s]

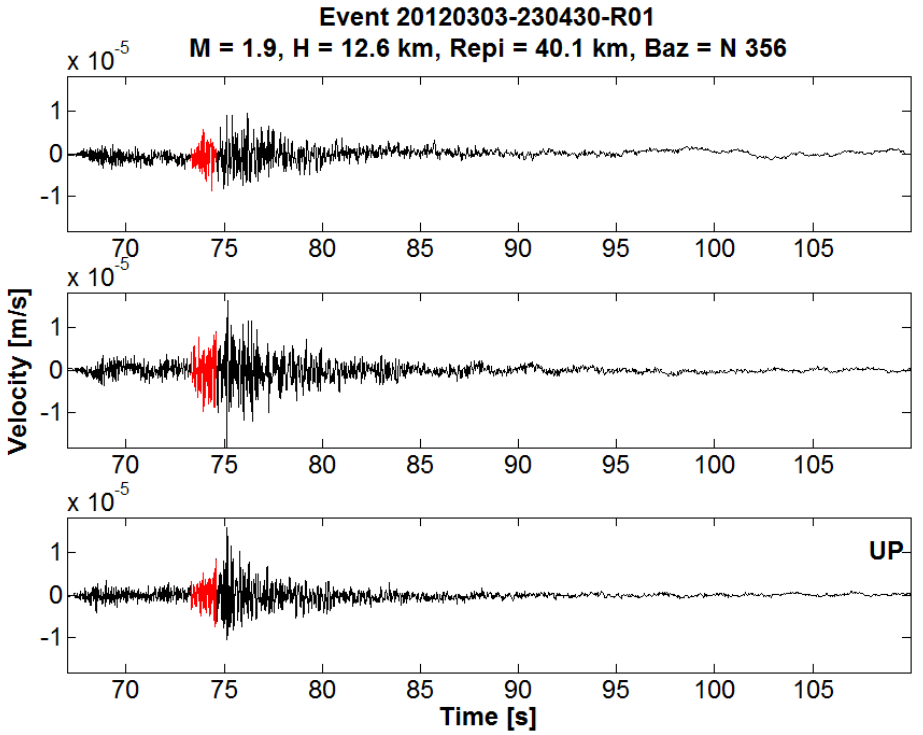
Event 20120303-230430-R01
M = 1.9, H = 12.6 km, Repi = 40.1 km, Baz = N 356
x 10^-5
1
0
-1
70
75
80
85
90
95
100
105
Velocity [m/s]
UP
Time [s]

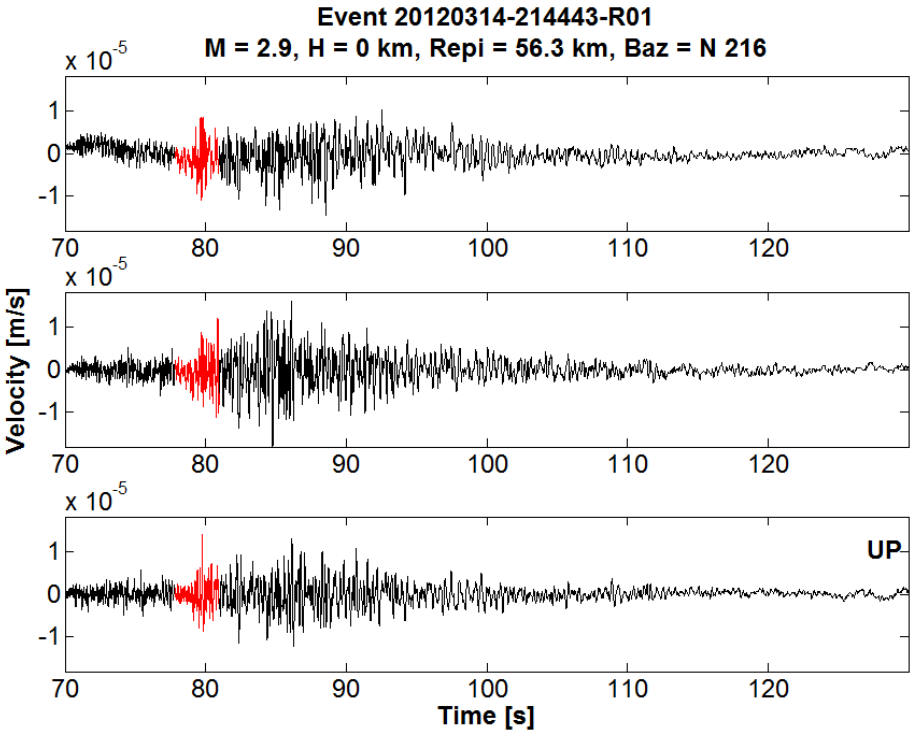
Event 20120314-214443-R01
M = 2.9, H = 0 km, Repi = 56.3 km, Baz = N 216
x 10^-5
Velocity [m/s]
UP
Time [s]

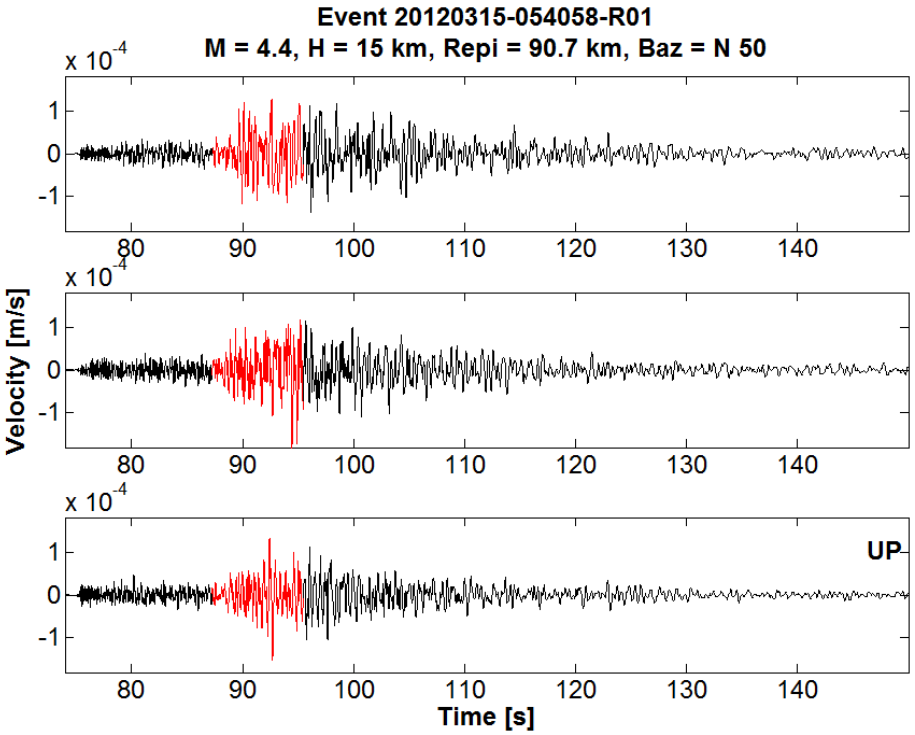
Event 20120315-054058-R01
M = 4.4, H = 15 km, Repi = 90.7 km, Baz = N 50
x 10^-4
Velocity [m/s]
UP
Time [s]

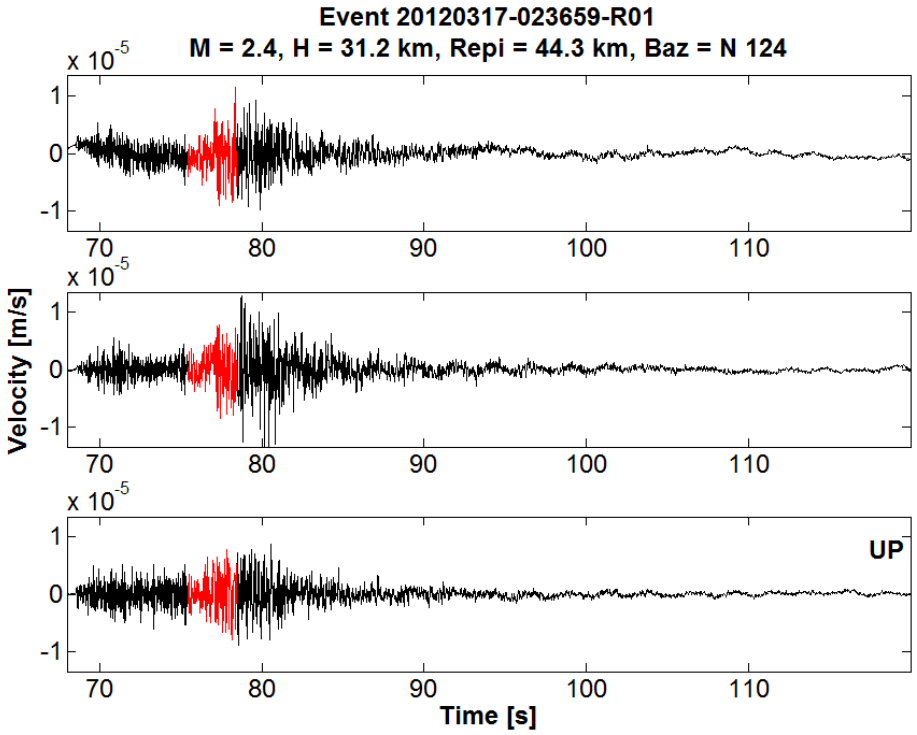
Event 20120317-023659-R01
M = 2.4, H = 31.2 km, Repi = 44.3 km, Baz = N 124
x 10^-5
Velocity [m/s]
UP
Time [s]

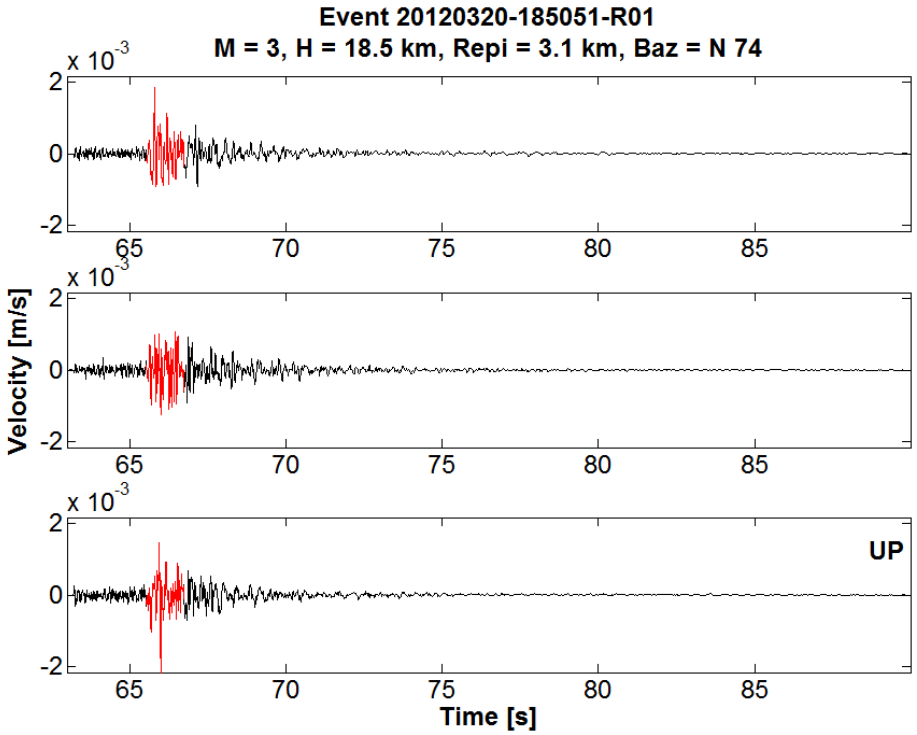
Event 20120320-185051-R01
M = 3, H = 18.5 km, Repi = 3.1 km, Baz = N 74
x 10^-3
Velocity [m/s]
UP
Time [s]

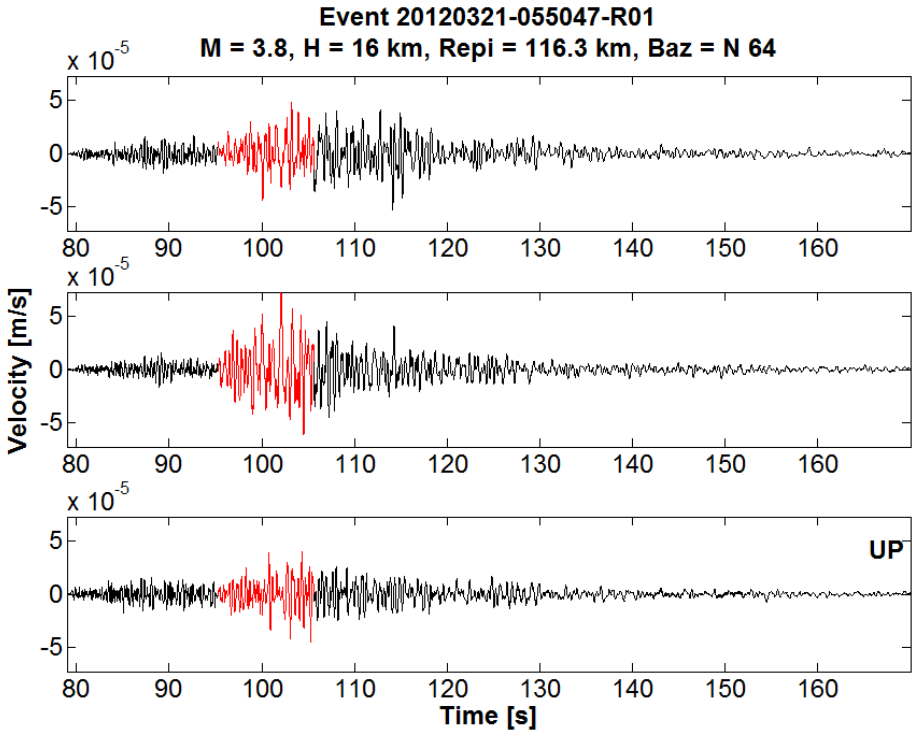
Event 20120321-055047-R01
M = 3.8, H = 16 km, Repi = 116.3 km, Baz = N 64
x 10^-5
Velocity [m/s]
UP
Time [s]

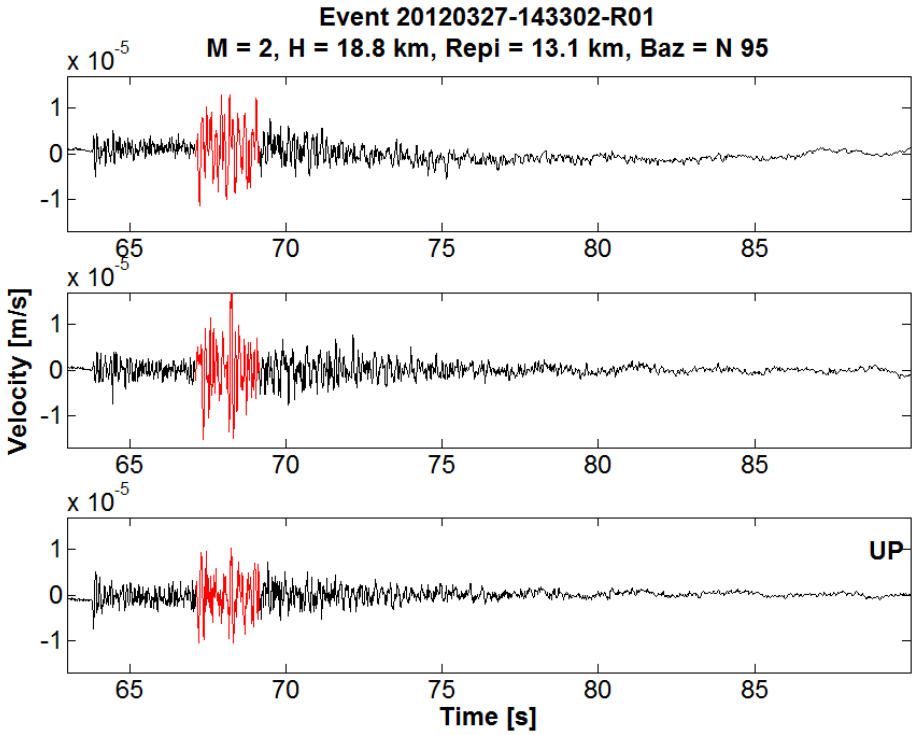
Event 20120327-143302-R01
M = 2, H = 18.8 km, Repi = 13.1 km, Baz = N 95
x 10^-5
Velocity [m/s]
UP
Time [s]

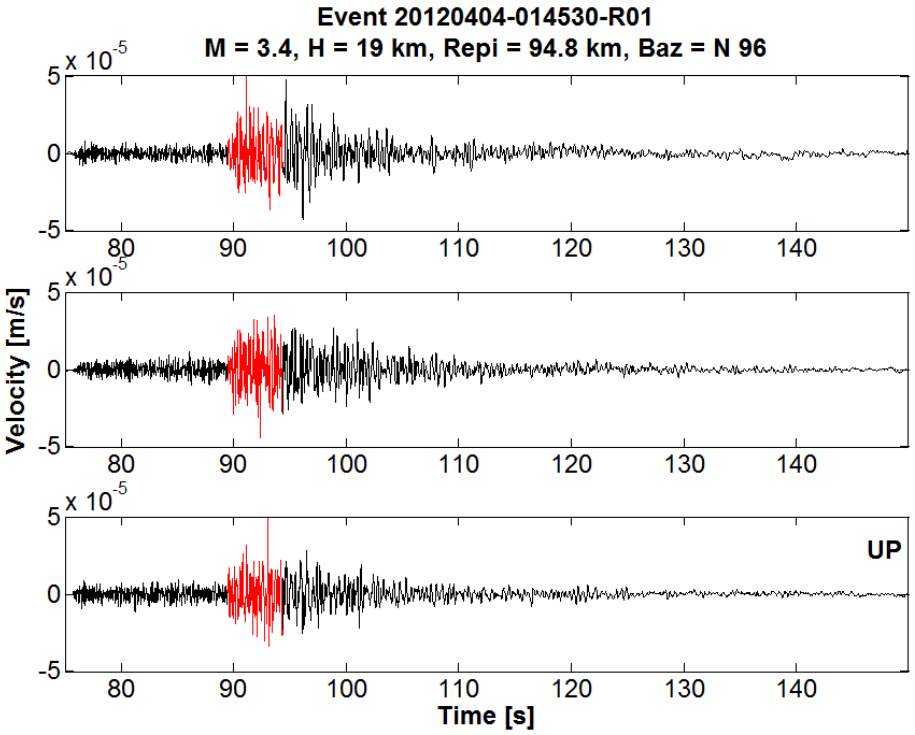
Event 20120404-014530-R01
M = 3.4, H = 19 km, Repi = 94.8 km, Baz = N 96
x 10^-5
5
0
-5
80
90
100
110
120
130
140
Velocity [m/s]
UP
Time [s]

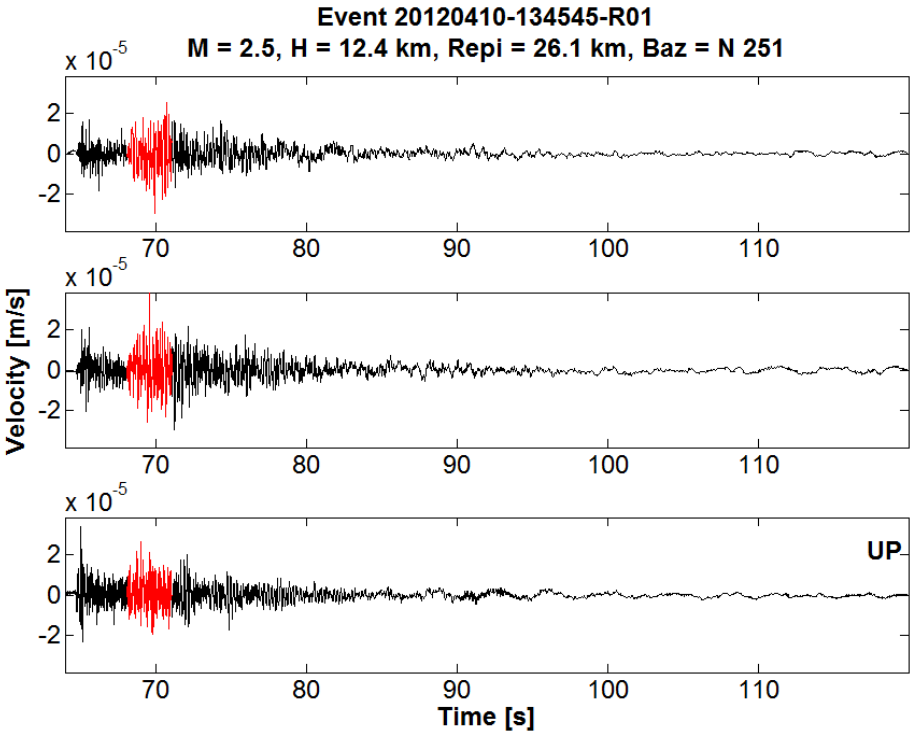
Event 20120410-134545-R01
M = 2.5, H = 12.4 km, Repi = 26.1 km, Baz = N 251
x 10^-5
2
0
-2
70
80
90
100
110
Velocity [m/s]
UP
Time [s]

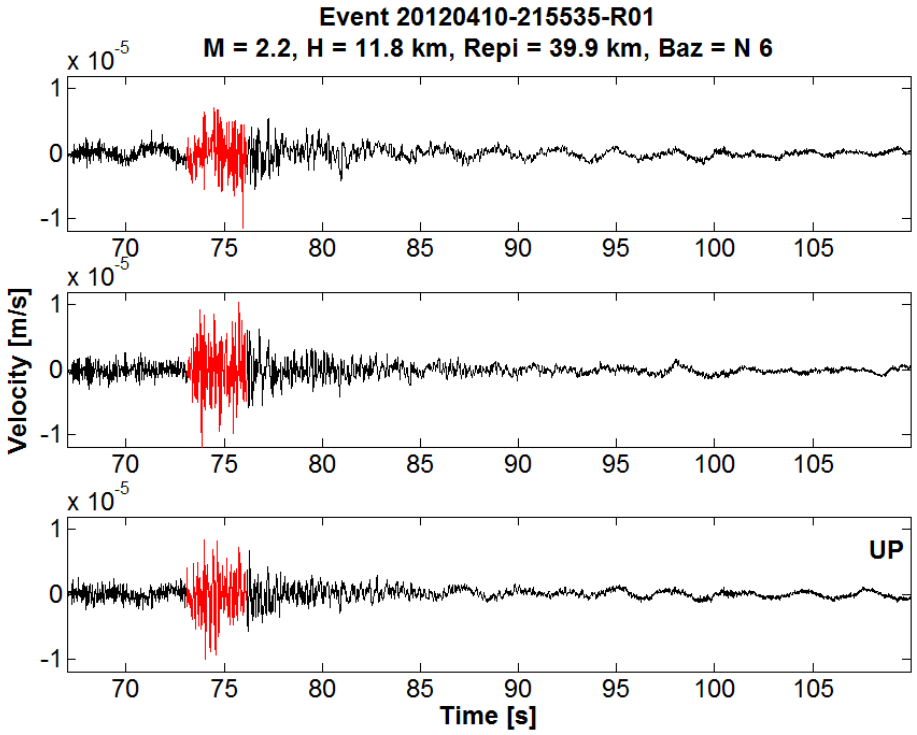
Event 20120410-215535-R01
M = 2.2, H = 11.8 km, Repi = 39.9 km, Baz = N 6
x 10^-5
Velocity [m/s]
UP
Time [s]

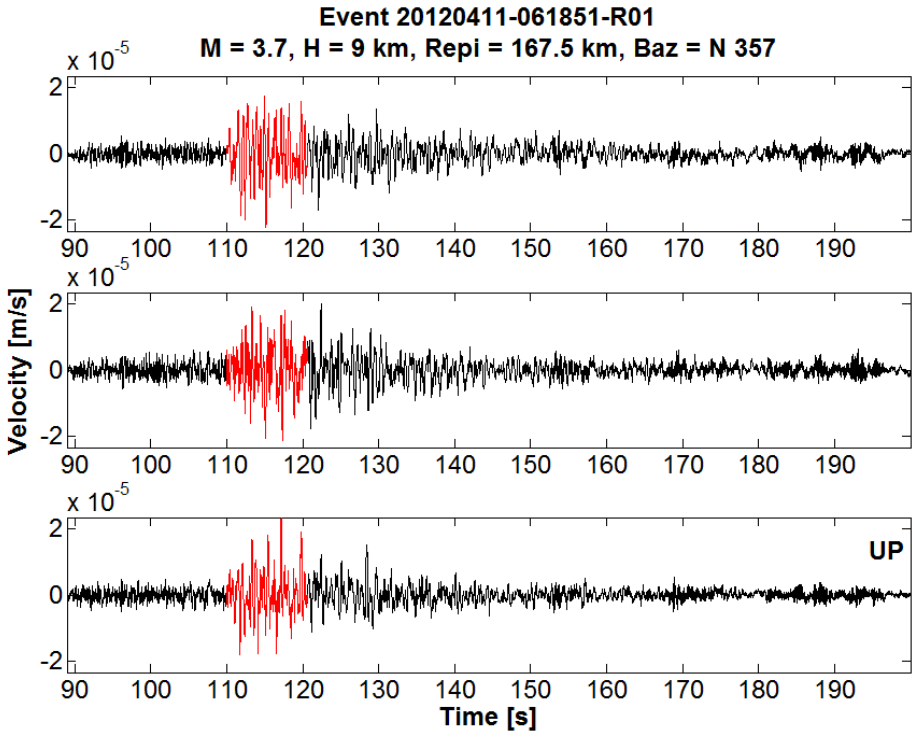
Event 20120411-061851-R01
M = 3.7, H = 9 km, Repi = 167.5 km, Baz = N 357
x 10^-5
Velocity [m/s]
UP
Time [s]

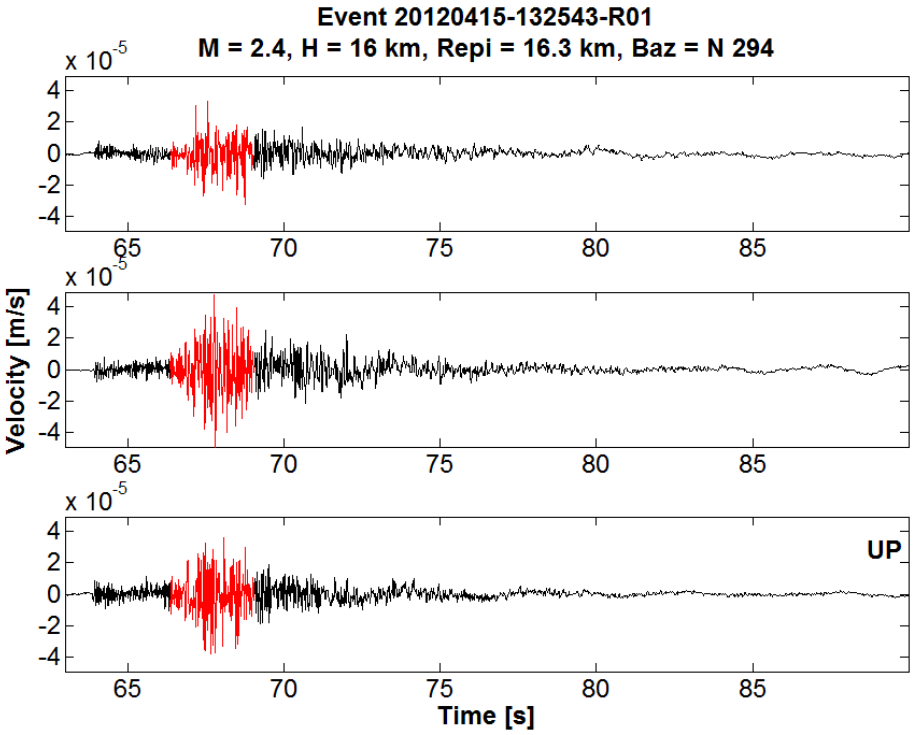
Event 20120415-132543-R01
M = 2.4, H = 16 km, Repi = 16.3 km, Baz = N 294
x 10^-5
Velocity [m/s]
UP
Time [s]

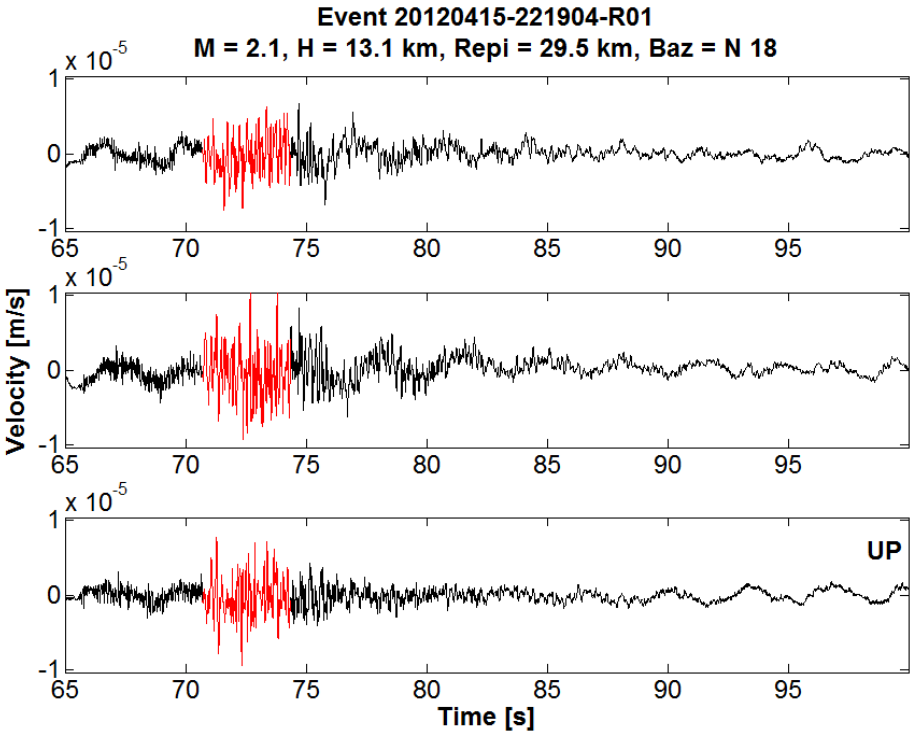
Event 20120415-221904-R01
M = 2.1, H = 13.1 km, Repi = 29.5 km, Baz = N 18
x 10^-5
Velocity [m/s]
UP
Time [s]

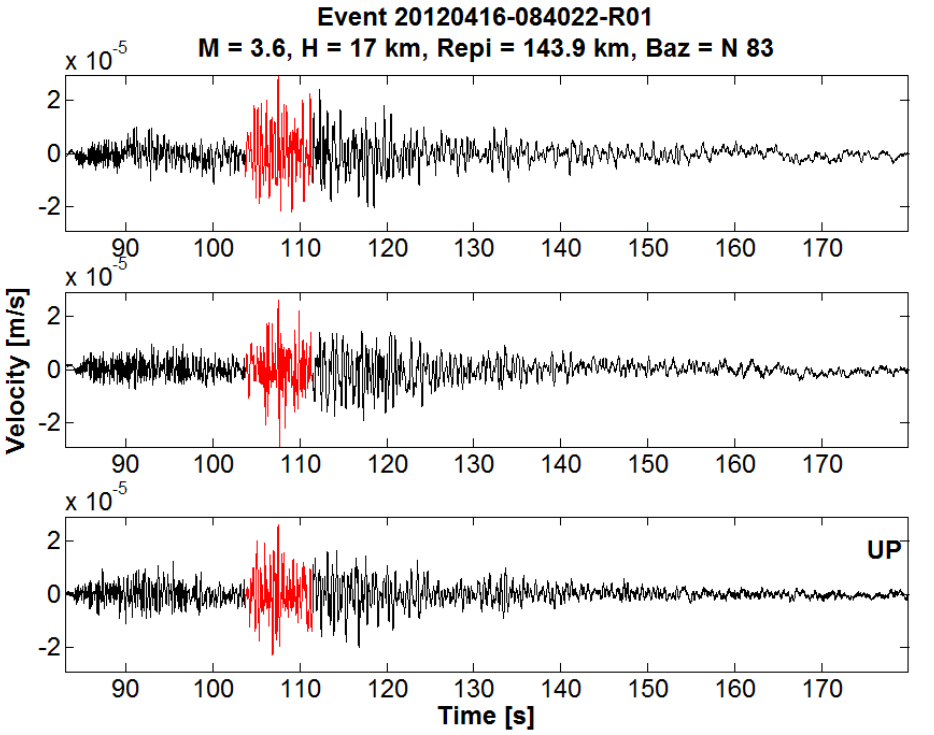
Event 20120416-084022-R01
M = 3.6, H = 17 km, Repi = 143.9 km, Baz = N 83
x 10-5
2
0
-2
90 100 110 120 130 140 150 160 170
Velocity [m/s]
UP
Time [s]

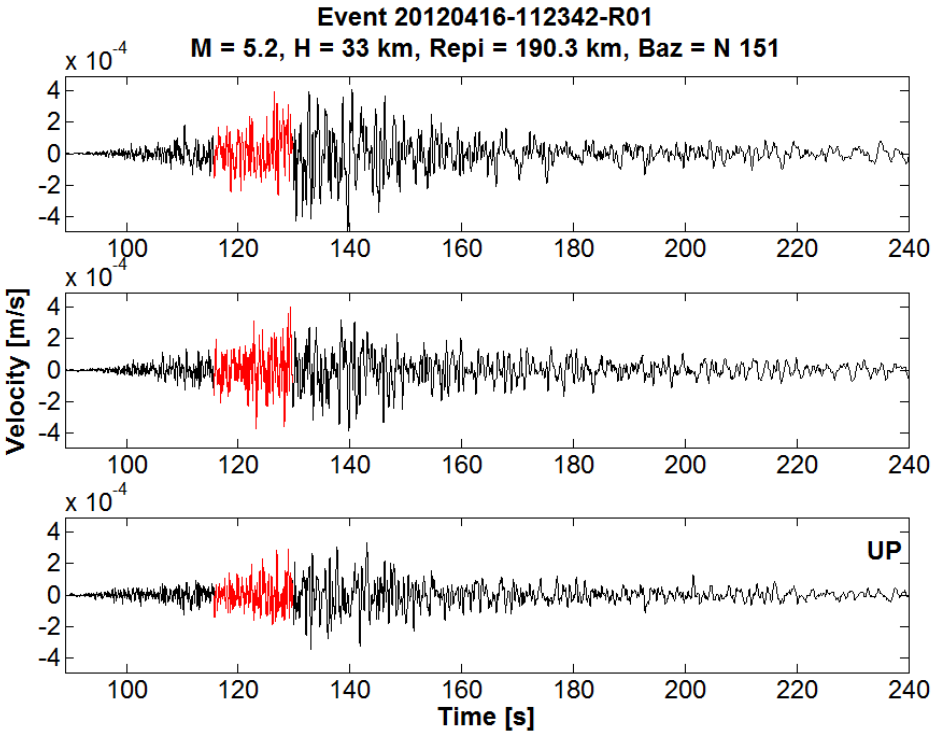
Event 20120416-112342-R01
M = 5.2, H = 33 km, Repi = 190.3 km, Baz = N 151
x 10-4
4
2
0
-2
-4
100 120 140 160 180 200 220 240
Velocity [m/s]
UP
Time [s]

Appendix I

Velocity time series from R02 station

Available velocity time series from rock station R02 are shown here for the selected subset of events (Appendix E). The time window represents the duration from the onset of P-wave till the end of the signal. The segment of signal shown in 'red' color represents selected window from visual inspection based on which Coherency analysis of Array A stations have been performed in Chapter 4. It is to be noted that R02 is the hard-rock station. All the available records from R02 have been used for the selection of time window.

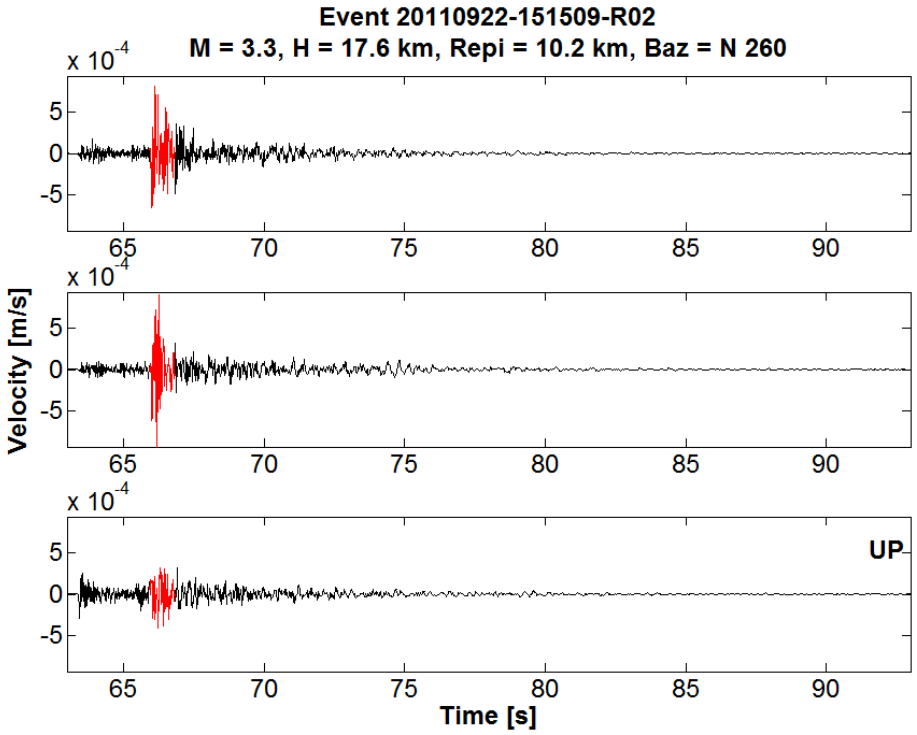
Event 20110922-151509-R02
M = 3.3, H = 17.6 km, Repi = 10.2 km, Baz = N 260
x 10^-4
5
0
-5
65
70
75
80
85
90
Velocity [m/s]
UP
Time [s]

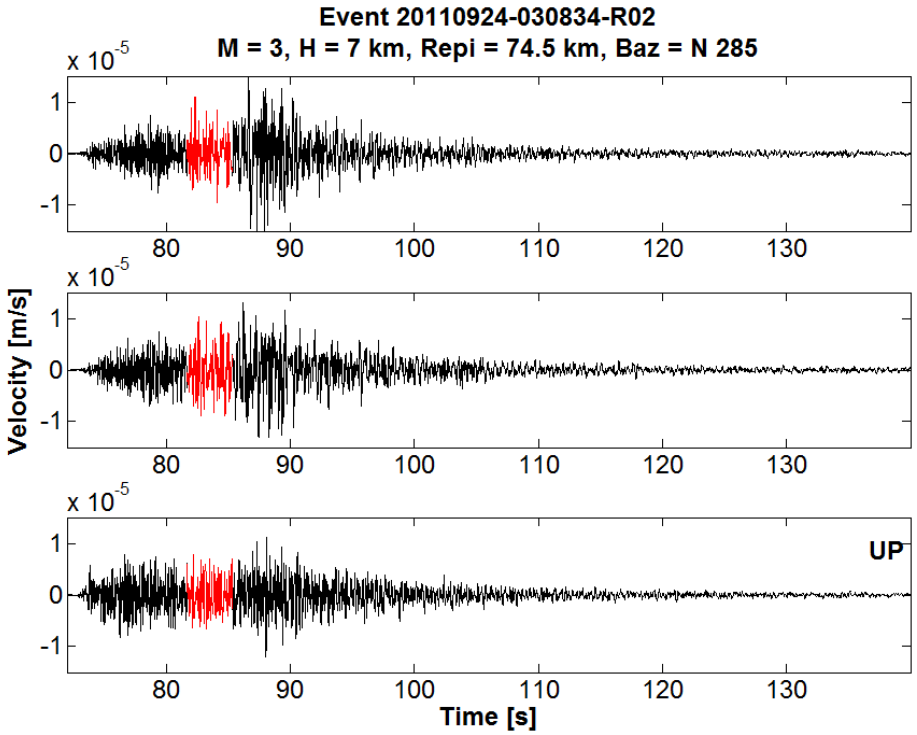
Event 20110924-030834-R02
M = 3, H = 7 km, Repi = 74.5 km, Baz = N 285
x 10^-5
1
0
-1
80
90
100
110
120
130
Velocity [m/s]
UP
Time [s]

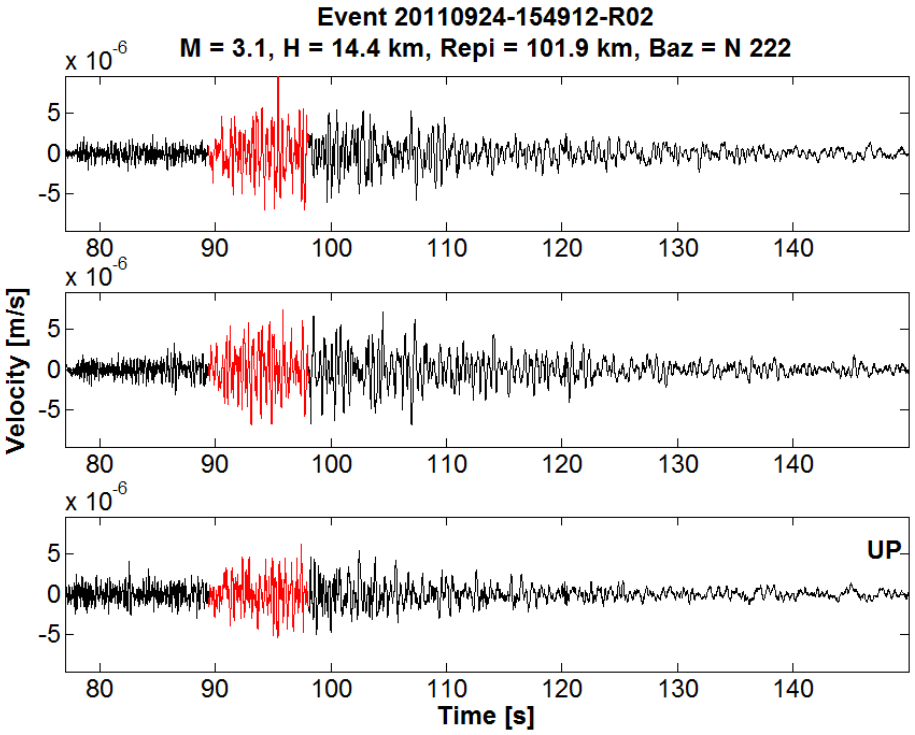
Event 20110924-154912-R02
M = 3.1, H = 14.4 km, Repi = 101.9 km, Baz = N 222
x 10^-6
5
0
-5
80
90
100
110
120
130
140
Velocity [m/s]
UP
Time [s]

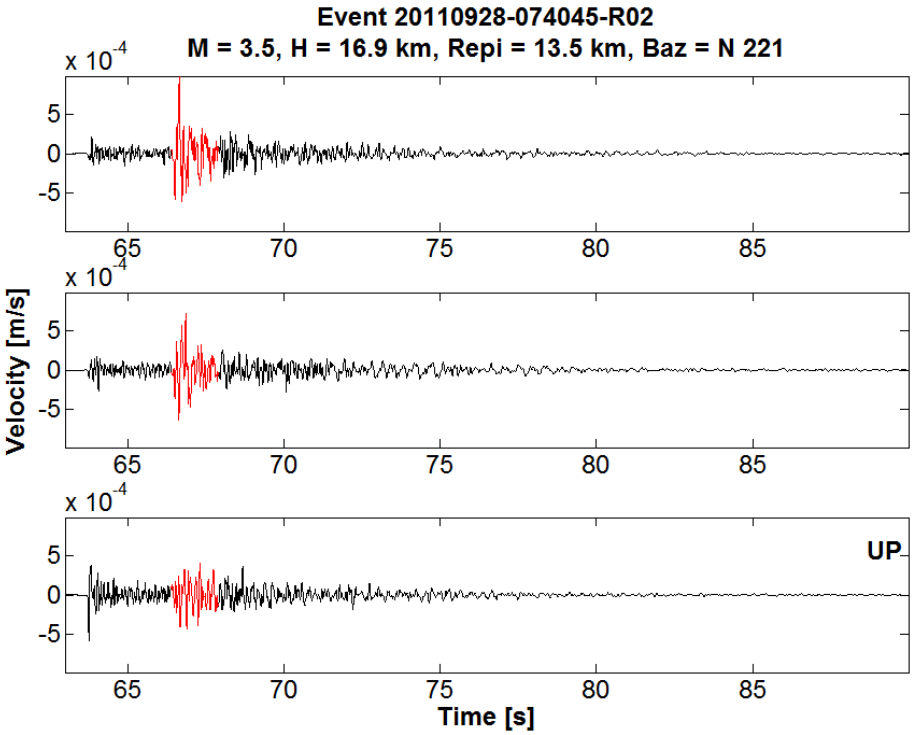
Event 20110928-074045-R02
M = 3.5, H = 16.9 km, Repi = 13.5 km, Baz = N 221
x 10^-4
5
0
-5
65
70
75
80
85
Velocity [m/s]
UP
Time [s]

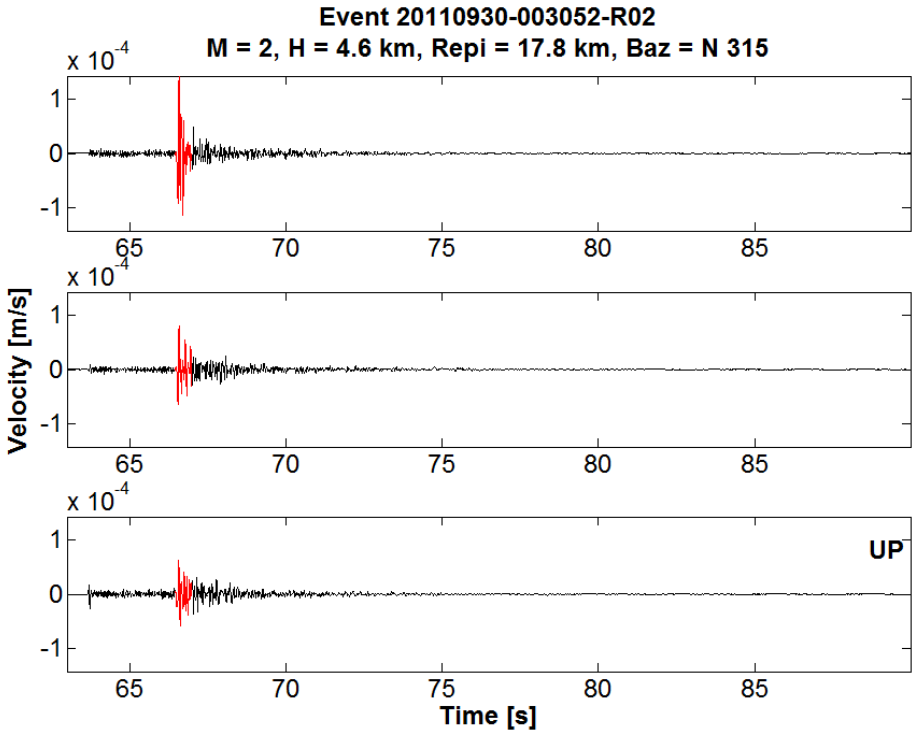
Event 20110930-003052-R02
M = 2, H = 4.6 km, Repi = 17.8 km, Baz = N 315
x 10^-4
1
0
-1
65
70
75
80
85
Velocity [m/s]
UP
Time [s]

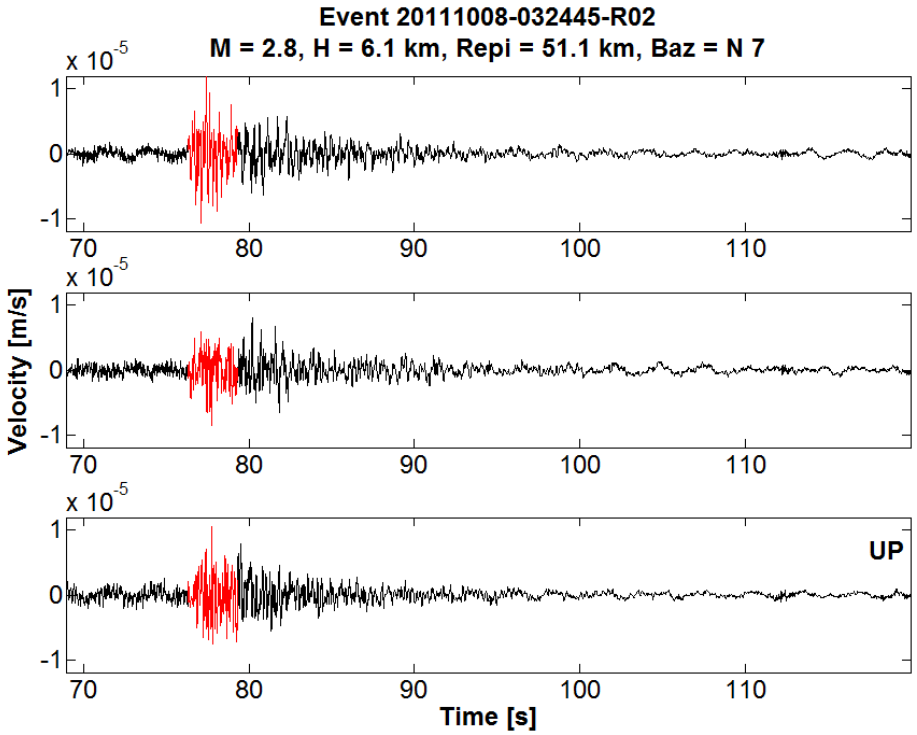
Event 20111008-032445-R02
M = 2.8, H = 6.1 km, Repi = 51.1 km, Baz = N 7
x 10^-5
1
0
-1
70
80
90
100
110
Velocity [m/s]
UP
Time [s]

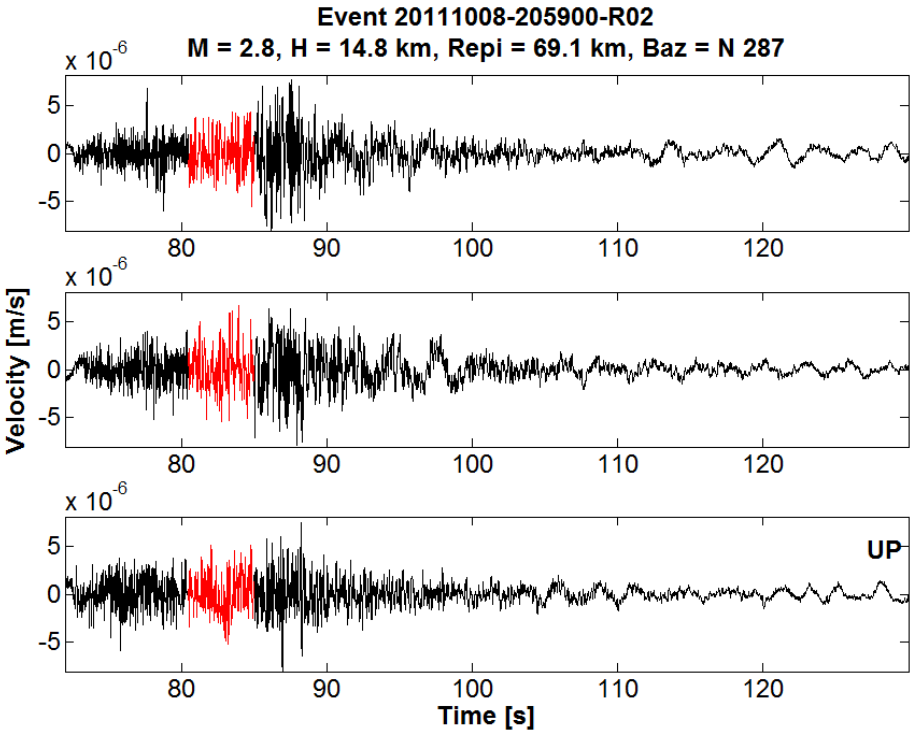
Event 20111008-205900-R02
M = 2.8, H = 14.8 km, Repi = 69.1 km, Baz = N 287
x 10-6
5
0
-5
80
90
100
110
120
Velocity [m/s]
UP
Time [s]

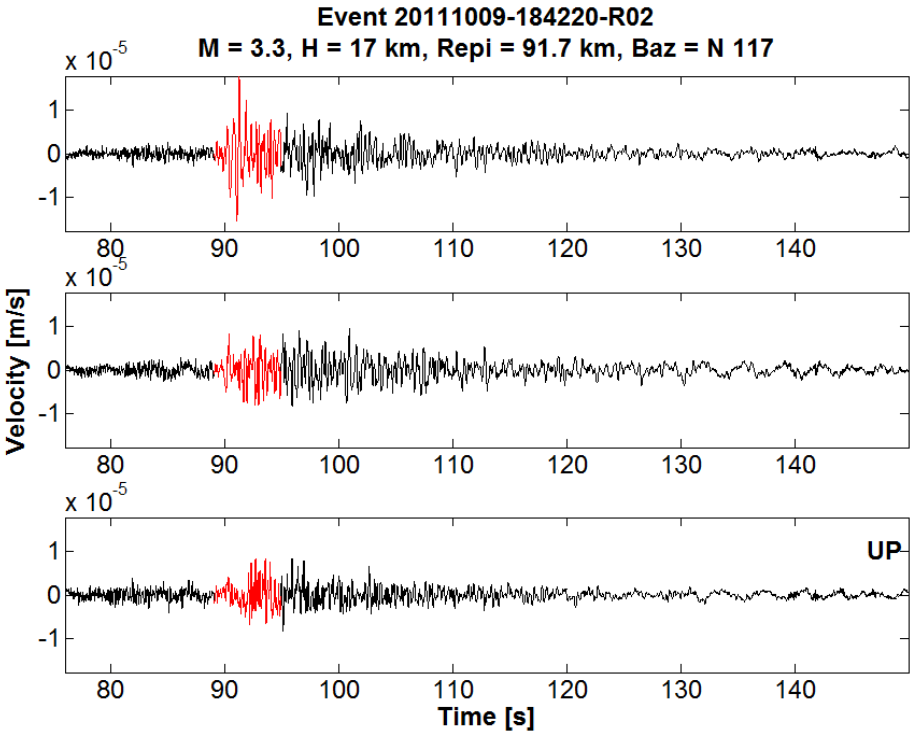
Event 20111009-184220-R02
M = 3.3, H = 17 km, Repi = 91.7 km, Baz = N 117
x 10-5
1
0
-1
80
90
100
110
120
130
140
Velocity [m/s]
UP
Time [s]

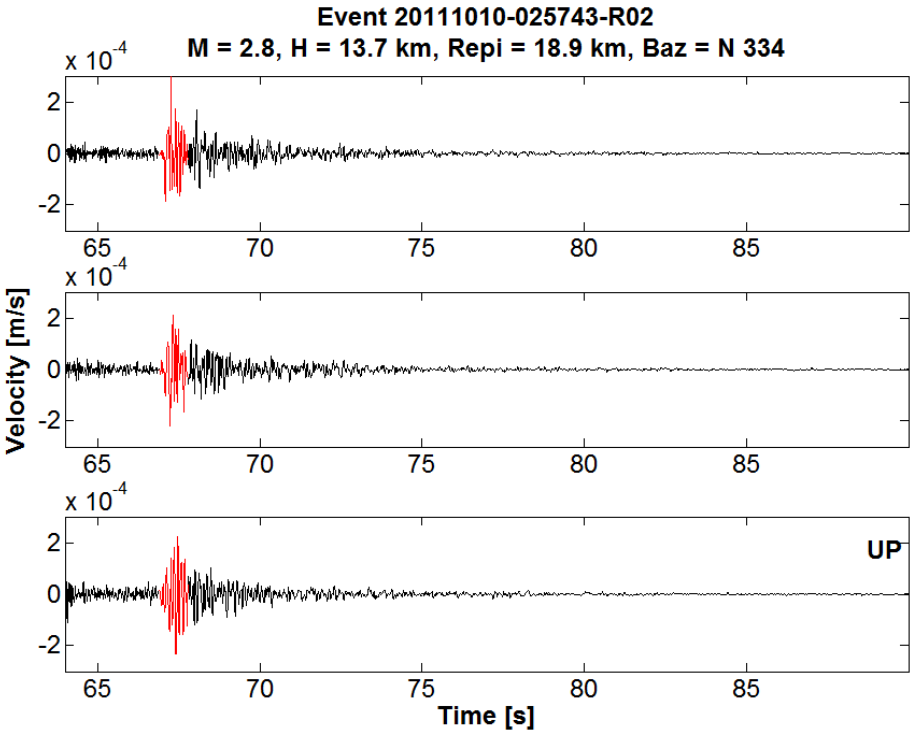
Event 20111010-025743-R02
M = 2.8, H = 13.7 km, Repi = 18.9 km, Baz = N 334
x 10^-4
2
0
-2
65
70
75
80
85
Velocity [m/s]
UP
Time [s]

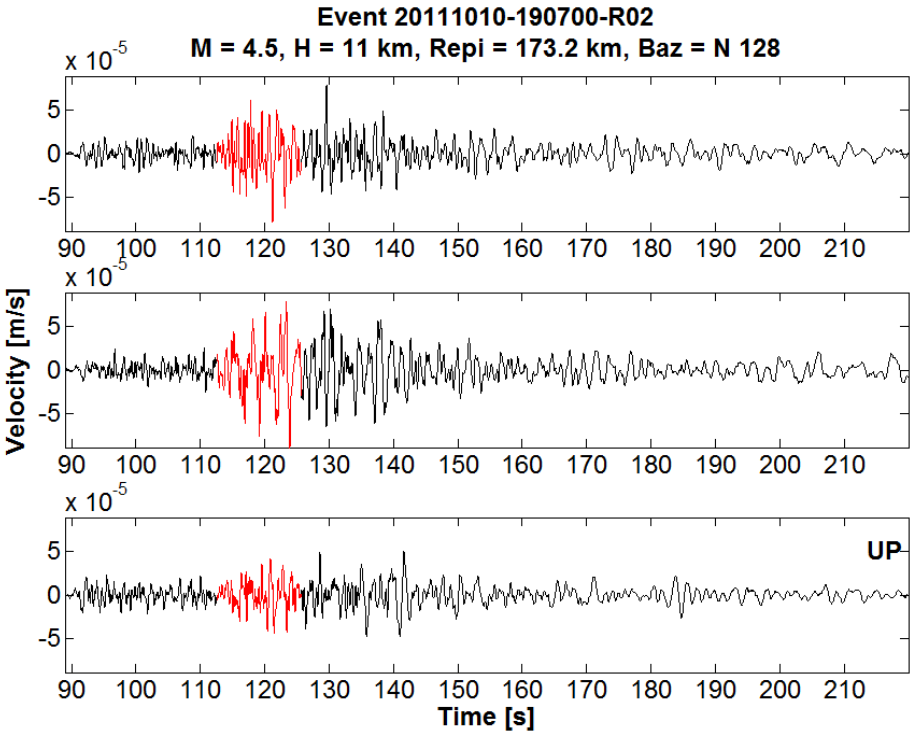
Event 20111010-190700-R02
M = 4.5, H = 11 km, Repi = 173.2 km, Baz = N 128
x 10^-5
5
0
-5
90
100
110
120
130
140
150
160
170
180
190
200
210
Velocity [m/s]
UP
Time [s]

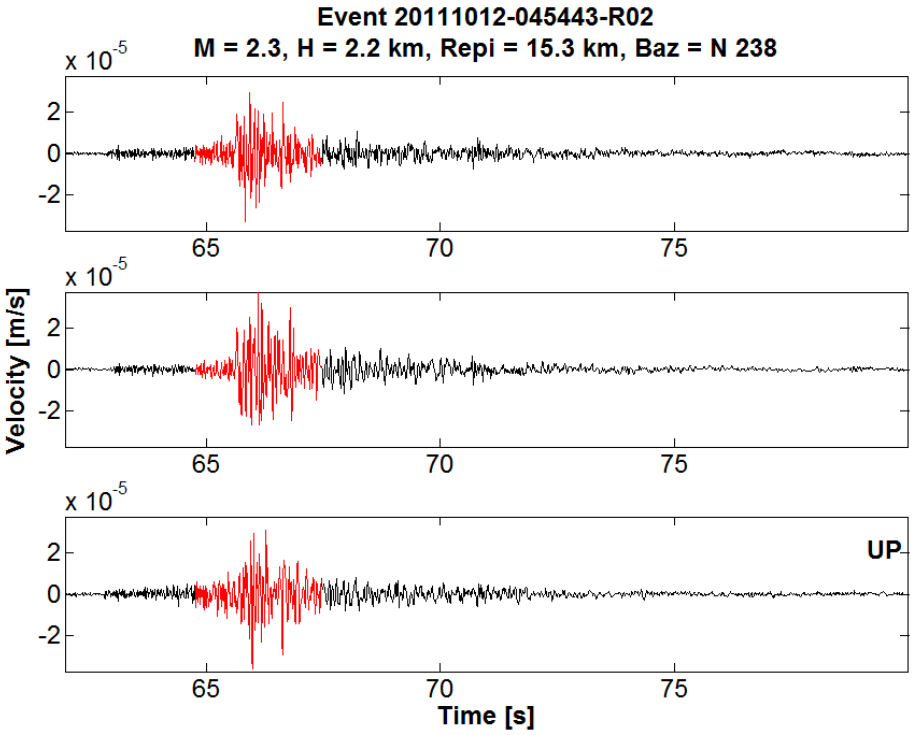
Event 20111012-045443-R02
M = 2.3, H = 2.2 km, Repi = 15.3 km, Baz = N 238
x 10-5
2
0
-2
65
70
75
Velocity [m/s]
UP
Time [s]

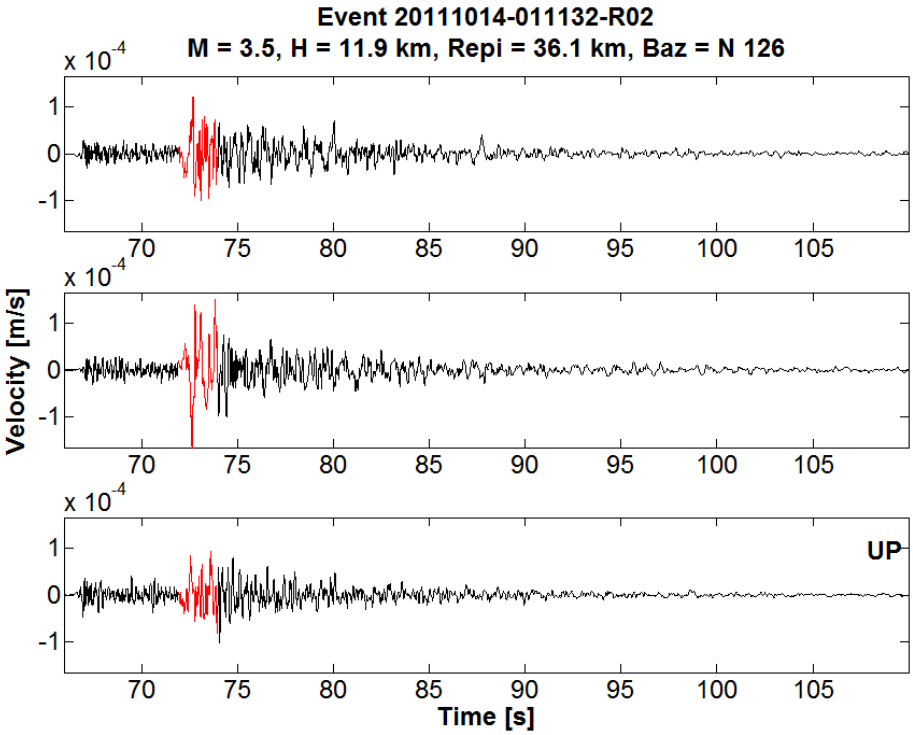
Event 20111014-011132-R02
M = 3.5, H = 11.9 km, Repi = 36.1 km, Baz = N 126
x 10-4
1
0
-1
70
75
80
85
90
95
100
105
Velocity [m/s]
UP
Time [s]

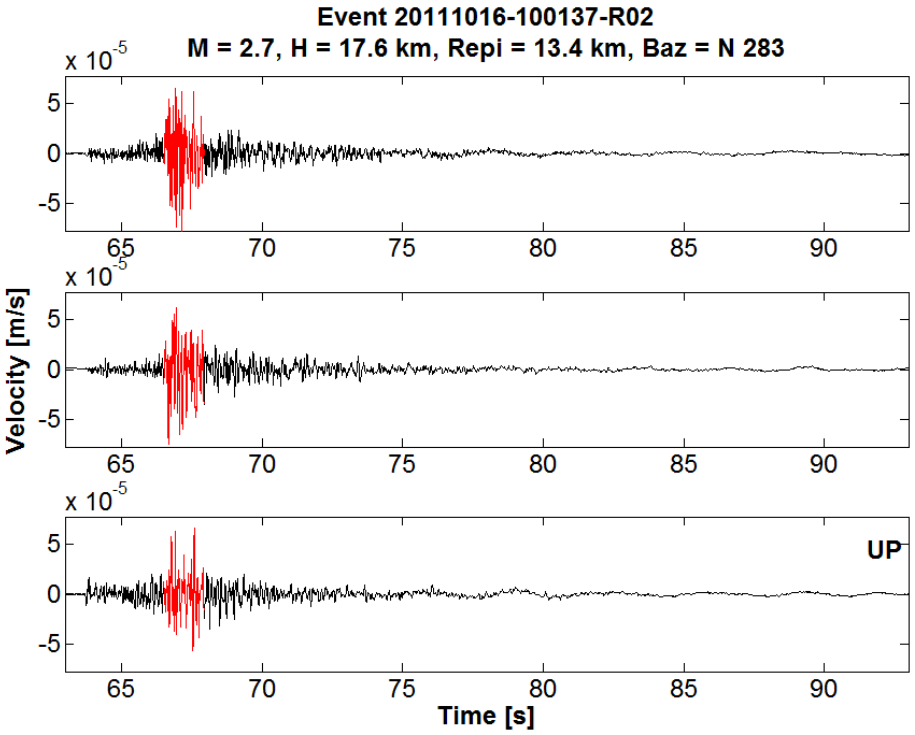
Event 20111016-100137-R02
M = 2.7, H = 17.6 km, Repi = 13.4 km, Baz = N 283
x 10^-5
Velocity [m/s]
UP
Time [s]

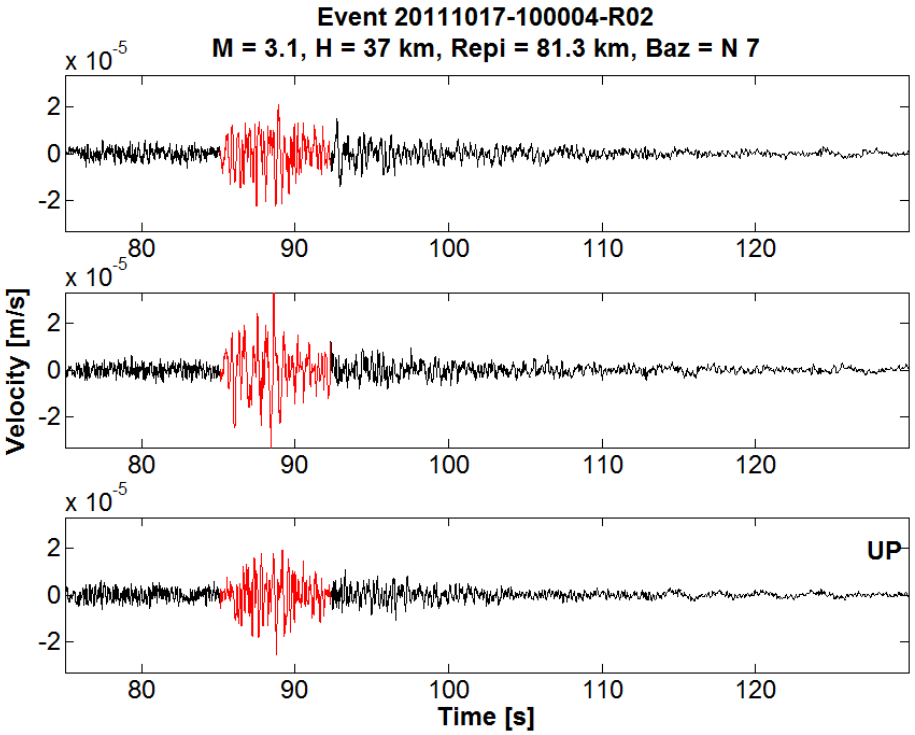
Event 20111017-100004-R02
M = 3.1, H = 37 km, Repi = 81.3 km, Baz = N 7
x 10^-5
Velocity [m/s]
UP
Time [s]

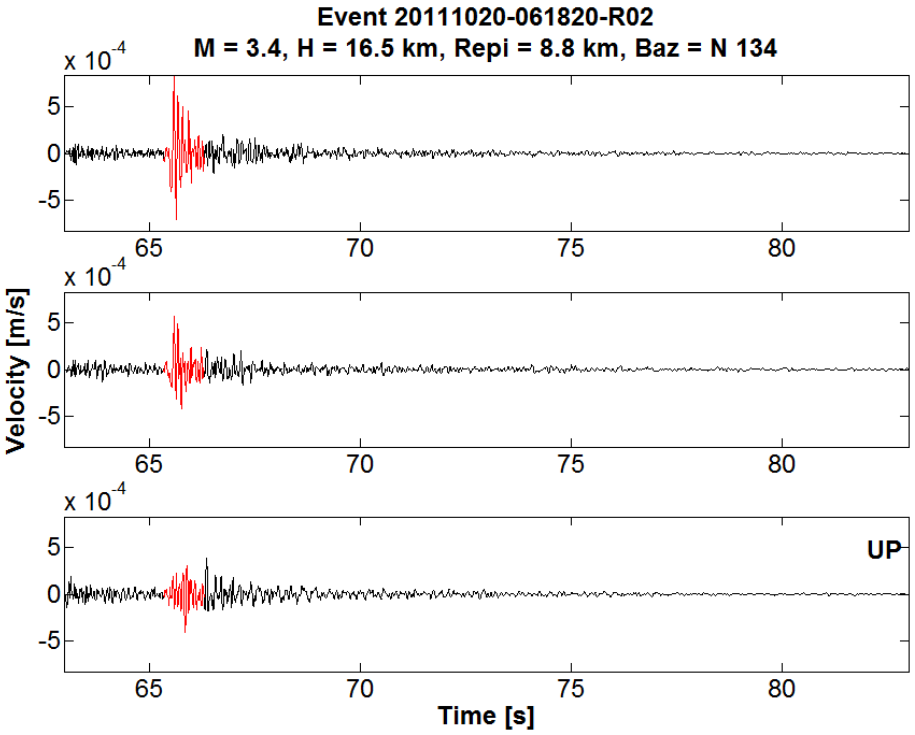
Event 20111020-061820-R02
M = 3.4, H = 16.5 km, Repi = 8.8 km, Baz = N 134
x 10^-4
5
0
-5
65
70
75
80
Velocity [m/s]
UP
Time [s]

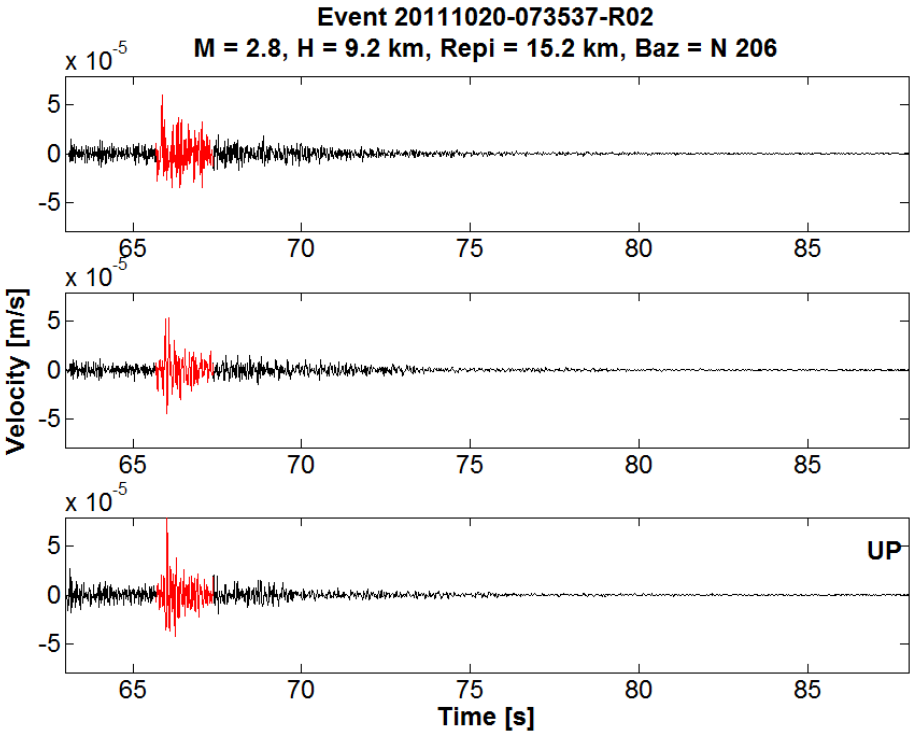
Event 20111020-073537-R02
M = 2.8, H = 9.2 km, Repi = 15.2 km, Baz = N 206
x 10^-5
5
0
-5
65
70
75
80
85
Velocity [m/s]
UP
Time [s]

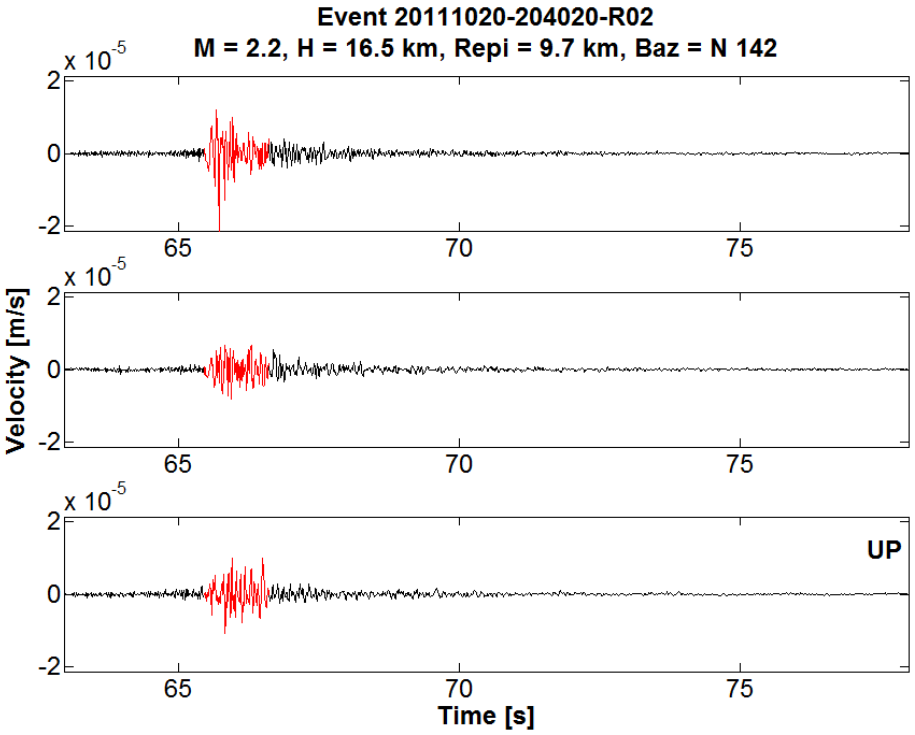
Event 20111020-204020-R02
M = 2.2, H = 16.5 km, Repi = 9.7 km, Baz = N 142
x 10-5
2
0
-2
65
70
75
Velocity [m/s]
UP
Time [s]

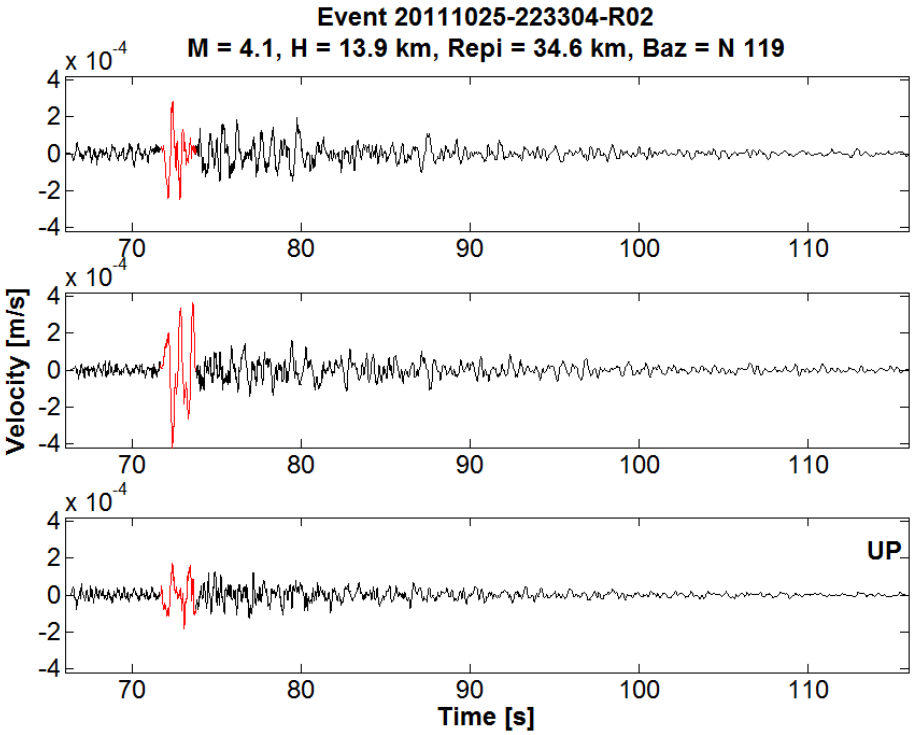
Event 20111025-223304-R02
M = 4.1, H = 13.9 km, Repi = 34.6 km, Baz = N 119
x 10-4
4
2
0
-2
-4
70
80
90
100
110
Velocity [m/s]
UP
Time [s]

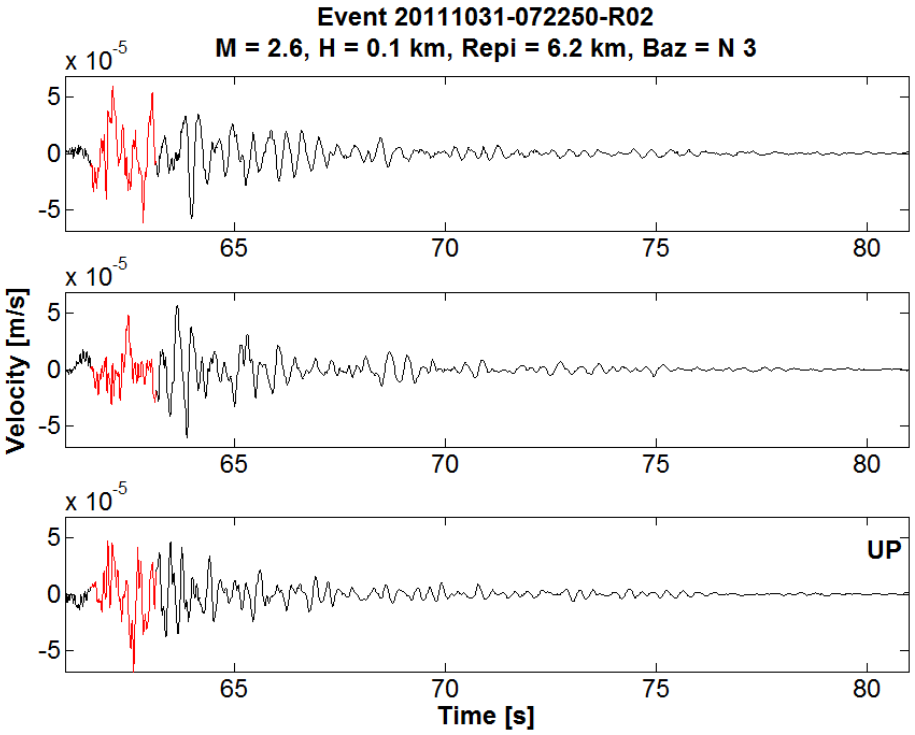
Event 20111031-072250-R02
M = 2.6, H = 0.1 km, Repi = 6.2 km, Baz = N 3
x 10^-5
5
0
-5
65
70
75
80
Velocity [m/s]
UP
Time [s]

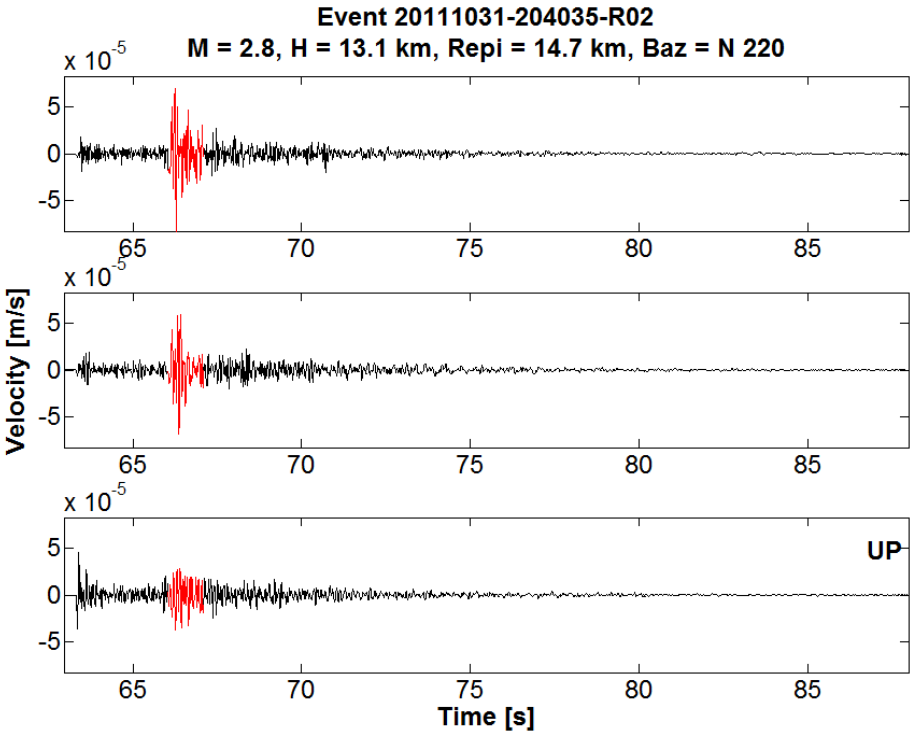
Event 20111031-204035-R02
M = 2.8, H = 13.1 km, Repi = 14.7 km, Baz = N 220
x 10^-5
5
0
-5
65
70
75
80
85
Velocity [m/s]
UP
Time [s]

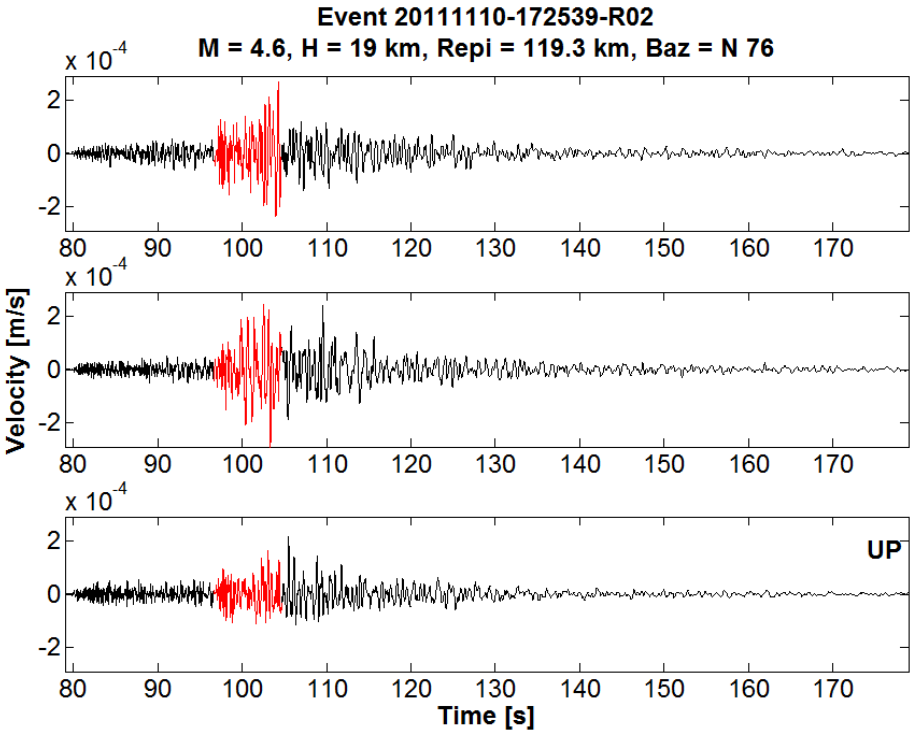
Event 20111110-172539-R02
M = 4.6, H = 19 km, Repi = 119.3 km, Baz = N 76
x 10^-4
Velocity [m/s]
UP
Time [s]

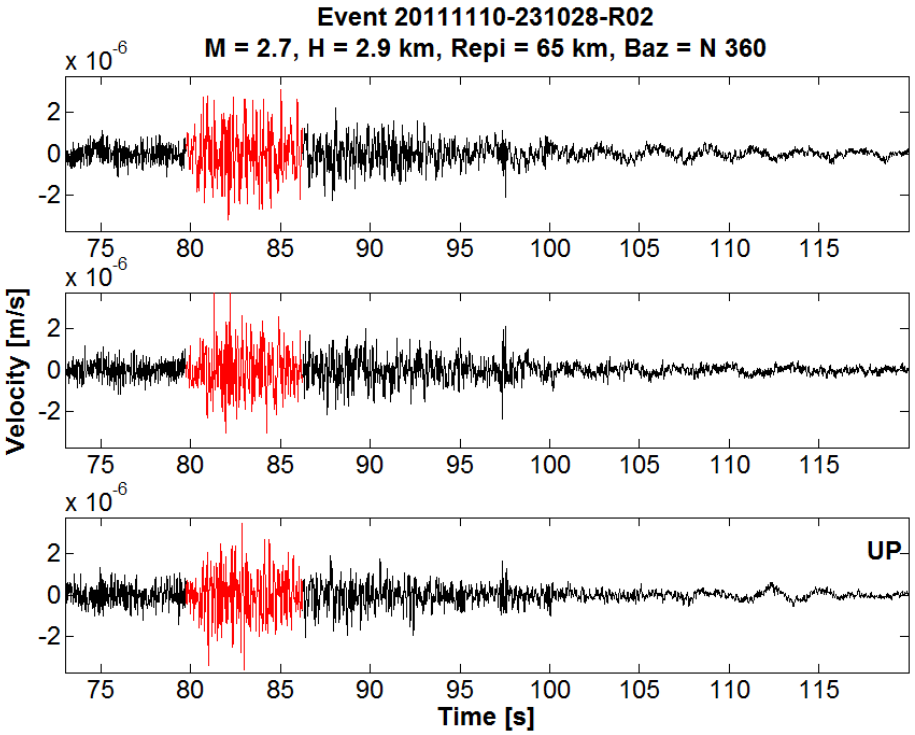
Event 20111110-231028-R02
M = 2.7, H = 2.9 km, Repi = 65 km, Baz = N 360
x 10^-6
Velocity [m/s]
UP
Time [s]

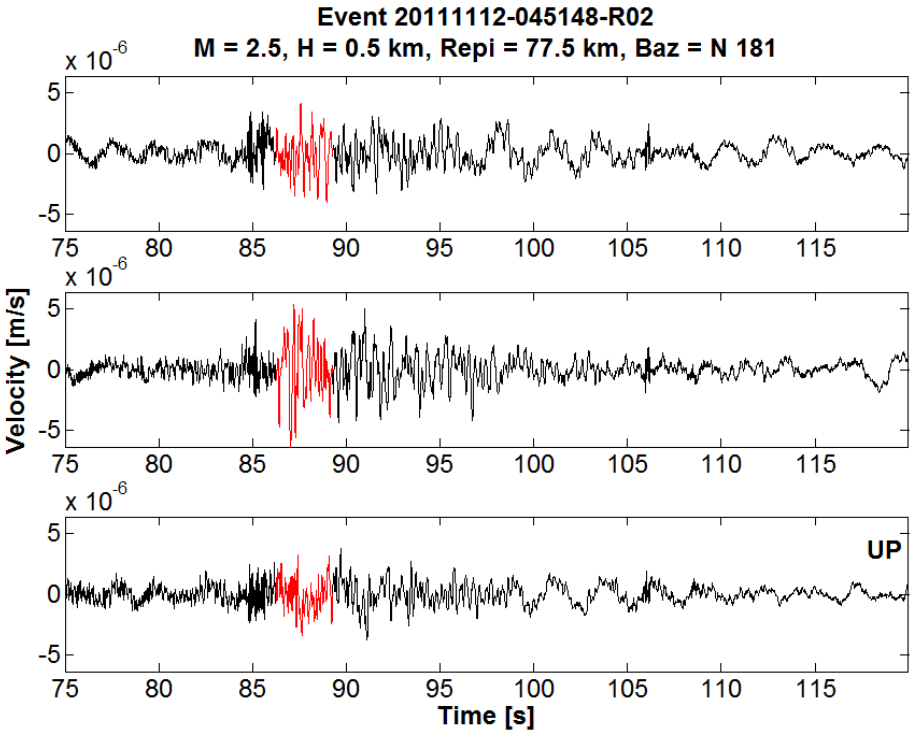
Event 20111112-045148-R02
M = 2.5, H = 0.5 km, Repi = 77.5 km, Baz = N 181
x 10^-6
Velocity [m/s]
UP
Time [s]

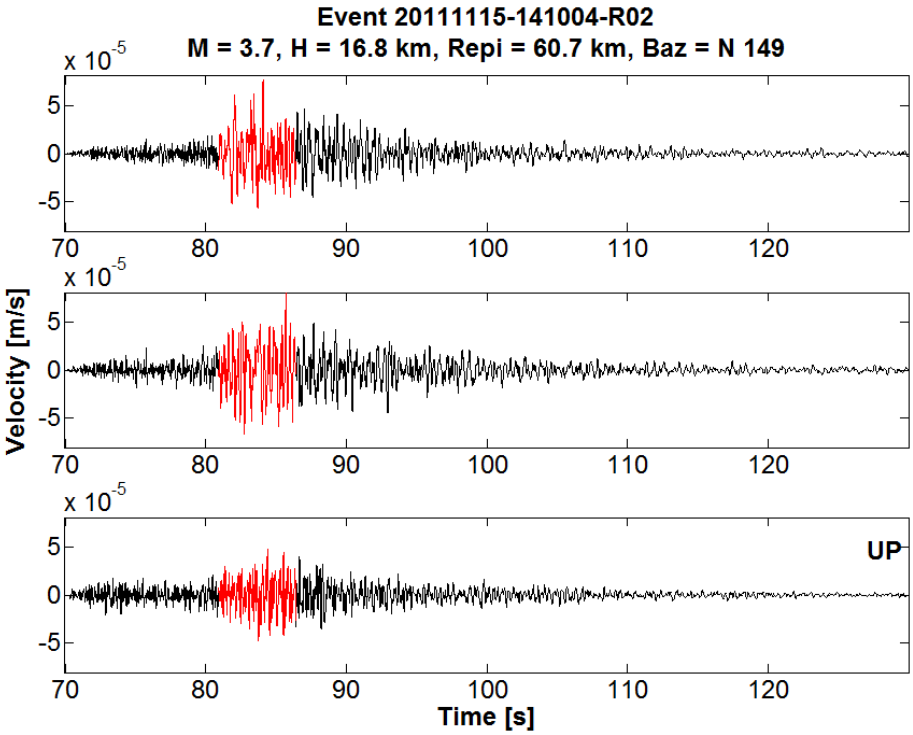
Event 20111115-141004-R02
M = 3.7, H = 16.8 km, Repi = 60.7 km, Baz = N 149
x 10^-5
Velocity [m/s]
UP
Time [s]

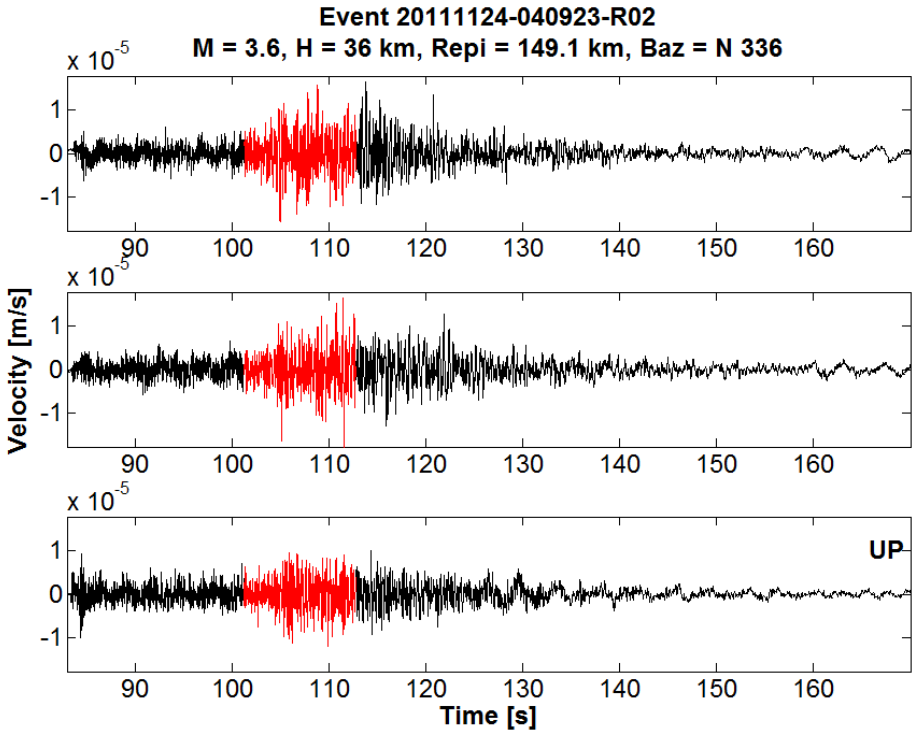
Event 20111124-040923-R02
M = 3.6, H = 36 km, Repi = 149.1 km, Baz = N 336
x 10^-5
Velocity [m/s]
UP
Time [s]

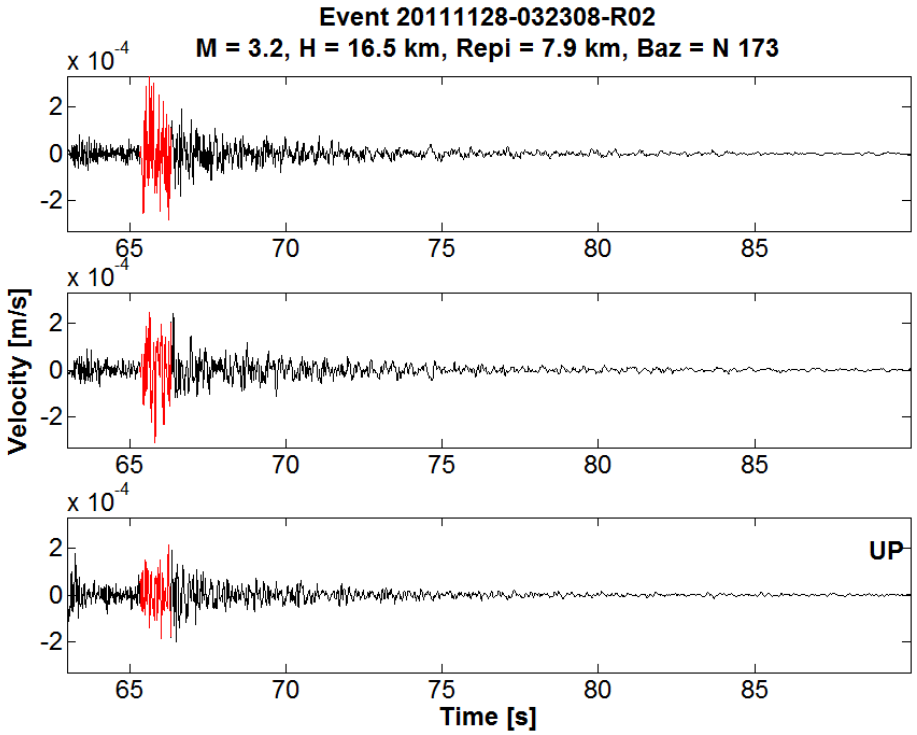
Event 20111128-032308-R02
M = 3.2, H = 16.5 km, Repi = 7.9 km, Baz = N 173
x 10^-4
Velocity [m/s]
UP
Time [s]

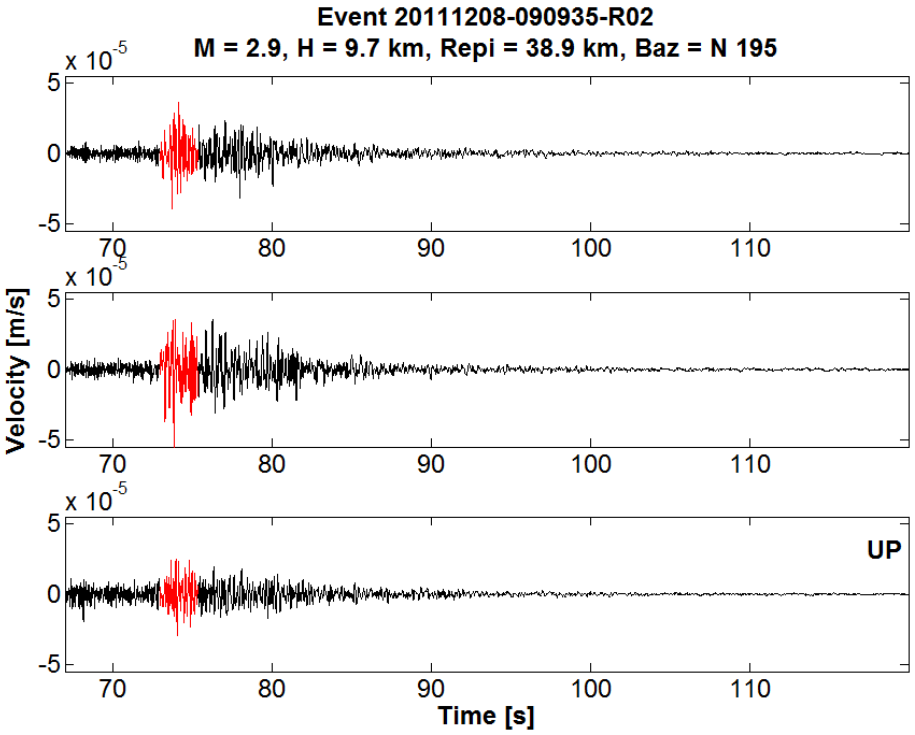
Event 20111208-090935-R02
M = 2.9, H = 9.7 km, Repi = 38.9 km, Baz = N 195
x 10^-5
5
0
-5
70
80
90
100
110
Velocity [m/s]
UP
Time [s]

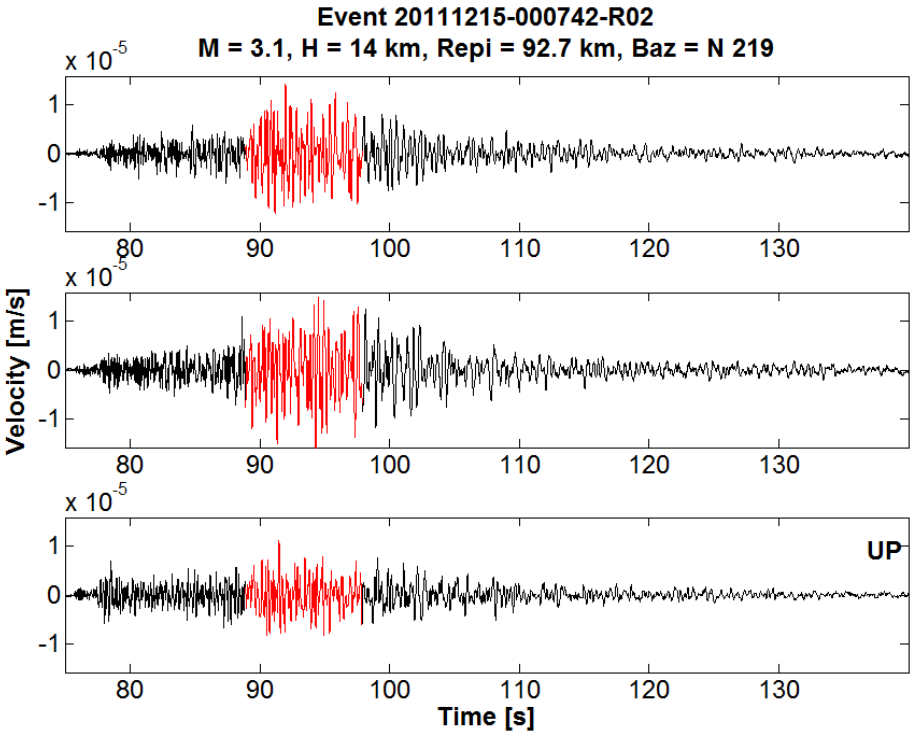
Event 20111215-000742-R02
M = 3.1, H = 14 km, Repi = 92.7 km, Baz = N 219
x 10^-5
1
0
-1
80
90
100
110
120
130
Velocity [m/s]
UP
Time [s]

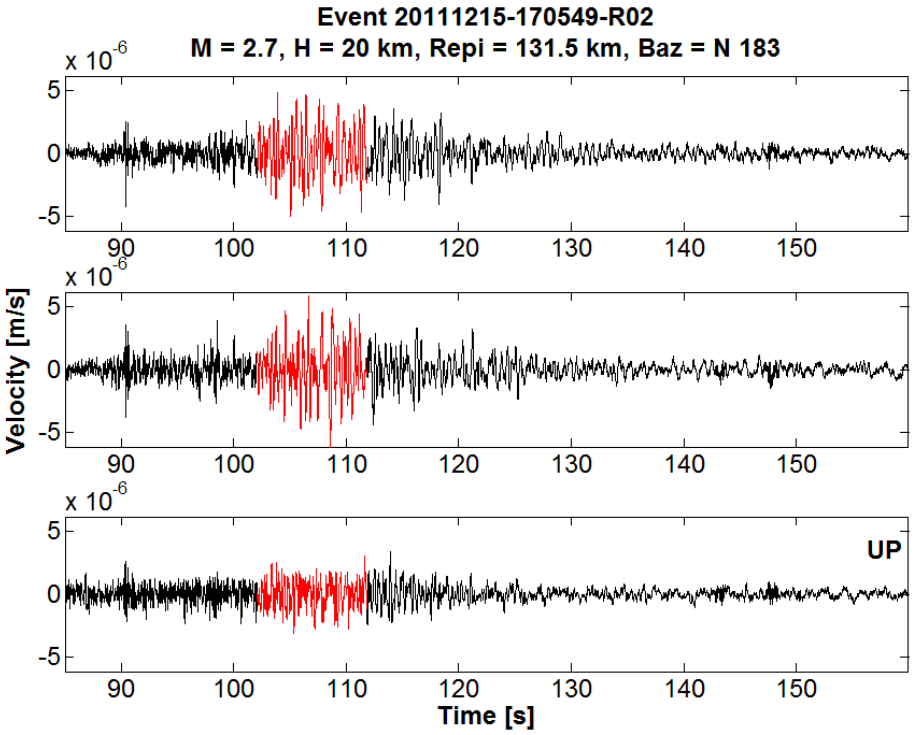
Event 20111215-170549-R02
M = 2.7, H = 20 km, Repi = 131.5 km, Baz = N 183
x 10-6
5
0
-5
90
100
110
120
130
140
150
Velocity [m/s]
UP
Time [s]

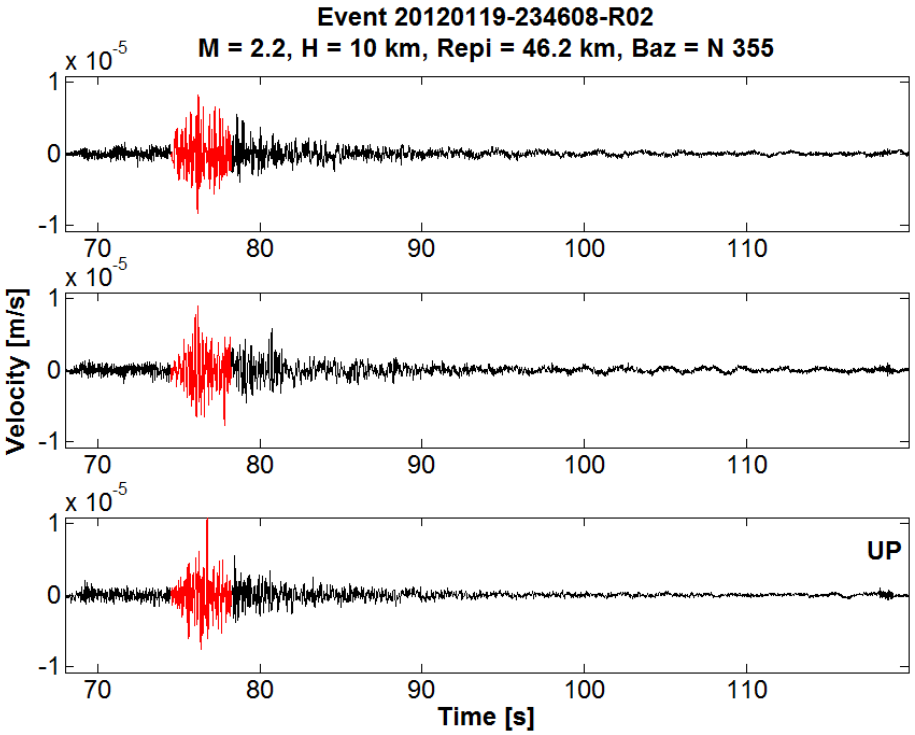
Event 20120119-234608-R02
M = 2.2, H = 10 km, Repi = 46.2 km, Baz = N 355
x 10-5
1
0
-1
70
80
90
100
110
Velocity [m/s]
UP
Time [s]

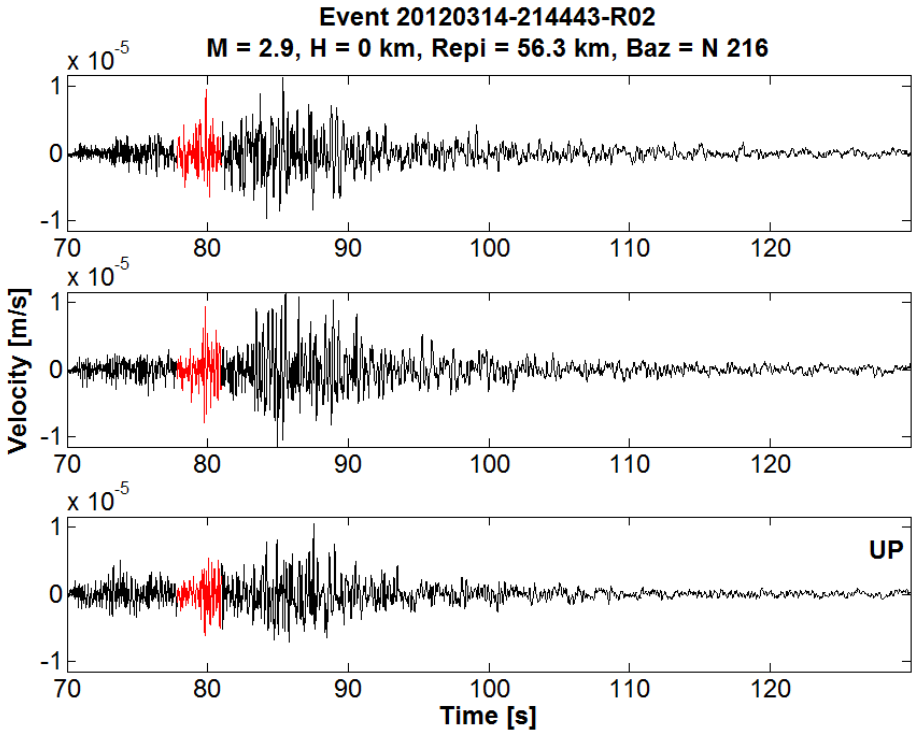
Event 20120314-214443-R02
M = 2.9, H = 0 km, Repi = 56.3 km, Baz = N 216
x 10^-5
Velocity [m/s]
UP
Time [s]

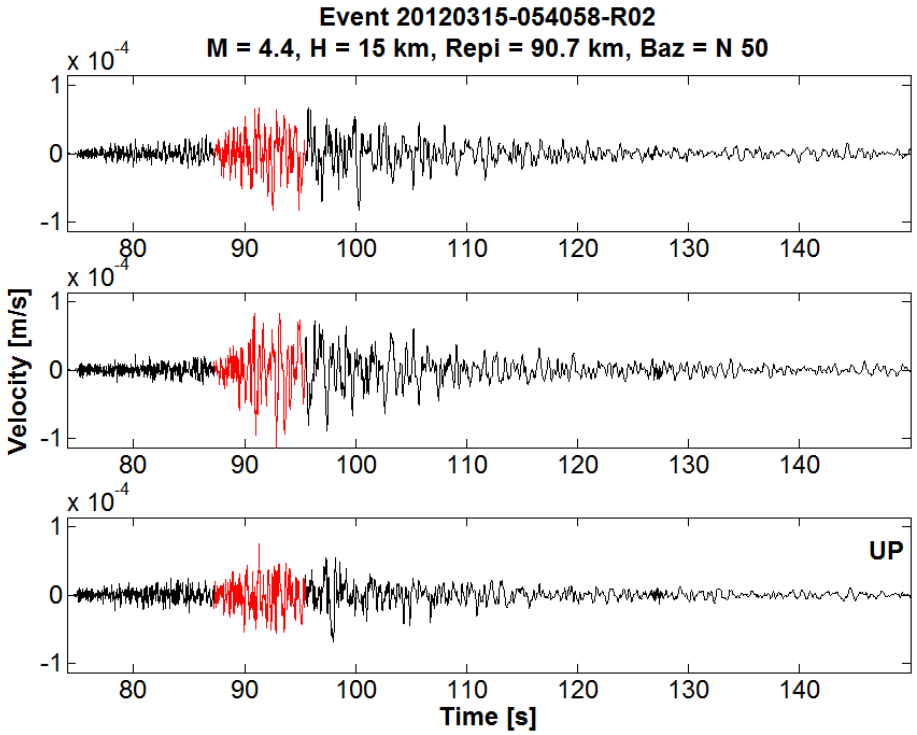
Event 20120315-054058-R02
M = 4.4, H = 15 km, Repi = 90.7 km, Baz = N 50
x 10^-4
Velocity [m/s]
UP
Time [s]

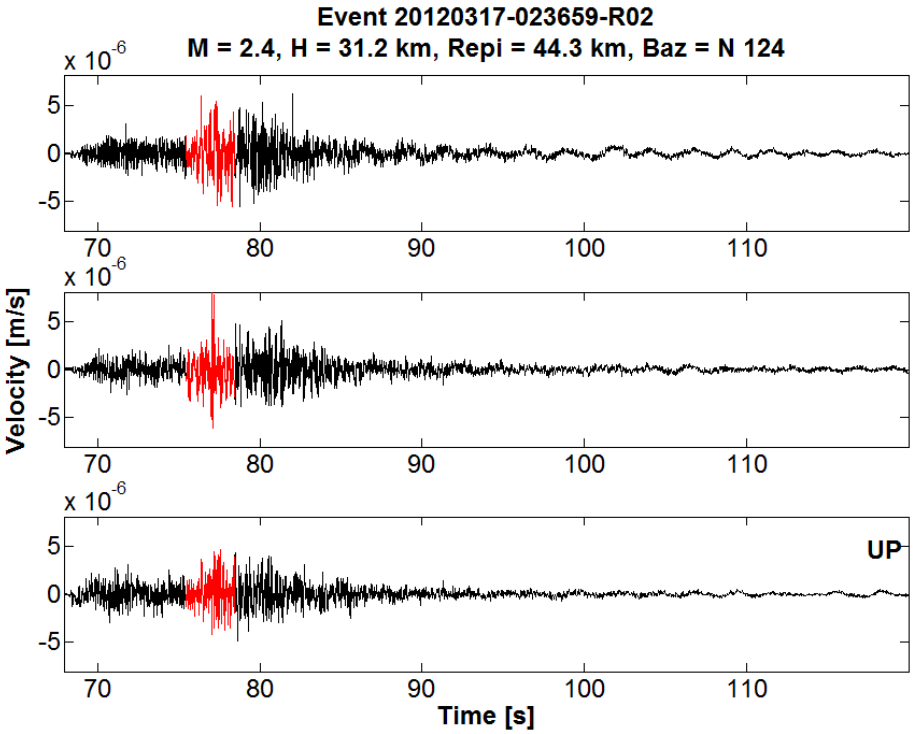
Event 20120317-023659-R02
M = 2.4, H = 31.2 km, Repi = 44.3 km, Baz = N 124
x 10-6
5
0
-5
70
80
90
100
110
Velocity [m/s]
UP
Time [s]

Appendix J

Interstation distance and angles for Array A

The station separation (interstation) distance and interstation angle for each pair of stations (total 210 pairs) at Array A are given. The interstation distance and angles have been used to group the coherency estimates in Chapter 4. The station names in the first row refer to the first station in a pair and in the first column refer to the second station of that pair.

J.1 Station separation distances (m) for the pairs of stations at Array A

Stations	A00	A01	A02	A03	A04	A05	A06	A07	A08	A09	A10	A11	A12	A13	A14	A15	A16	A17	A18	A19	A20
A00	-	-	-	-	-	-	-	-	-	-	-	-	-	-	-	-	-	-	-	-	-
A01	4.8	-	-	-	-	-	-	-	-	-	-	-	-	-	-	-	-	-	-	-	-
A02	5.1	5.7	-	-	-	-	-	-	-	-	-	-	-	-	-	-	-	-	-	-	-
A03	5.2	9.6	6.3	-	-	-	-	-	-	-	-	-	-	-	-	-	-	-	-	-	-
A04	5.1	9.5	9.7	5.9	-	-	-	-	-	-	-	-	-	-	-	-	-	-	-	-	-
A05	5.0	5.8	9.6	9.7	6.0	-	-	-	-	-	-	-	-	-	-	-	-	-	-	-	-
A06	14.8	10.0	13.9	19.3	19.2	14.2	-	-	-	-	-	-	-	-	-	-	-	-	-	-	-
A07	15.1	14.3	10.0	14.6	19.5	19.3	17.3	-	-	-	-	-	-	-	-	-	-	-	-	-	-
A08	15.2	19.3	14.5	10.0	14.4	19.5	28.5	18.0	-	-	-	-	-	-	-	-	-	-	-	-	-
A09	15.0	19.1	19.4	14.1	9.9	14.2	28.4	28.7	17.8	-	-	-	-	-	-	-	-	-	-	-	-
A10	15.1	14.4	19.4	19.4	14.3	10.0	17.9	28.7	28.7	17.4	-	-	-	-	-	-	-	-	-	-	-
A11	39.8	34.9	38.4	44.1	44.0	38.5	24.9	37.6	52.7	52.6	38.2	-	-	-	-	-	-	-	-	-	-
A12	40.2	39.0	35.2	39.1	44.4	44.4	38.2	25.2	38.4	53.2	53.3	46.9	-	-	-	-	-	-	-	-	-
A13	39.9	43.9	38.8	34.7	38.6	44.1	52.6	38.3	24.8	38.1	52.7	75.8	47.3	-	-	-	-	-	-	-	-
A14	40.2	44.2	44.4	38.8	35.1	38.9	52.9	53.3	38.4	25.2	37.9	76.0	76.6	47.2	-	-	-	-	-	-	-
A15	40.0	38.8	44.1	44.2	38.7	35.0	38.4	52.9	53.0	37.9	24.9	47.3	76.4	75.8	46.6	-	-	-	-	-	-
A16	79.9	75.1	78.3	84.2	84.2	78.6	65.1	76.1	92.5	92.5	77.1	40.2	76.9	114.4	115.0	78.5	-	-	-	-	-
A17	79.9	78.5	74.8	78.7	84.1	84.0	76.3	64.8	76.7	92.6	92.6	76.9	39.7	78.0	115.1	114.6	92.2	-	-	-	-
A18	81.0	84.9	79.7	75.8	79.5	85.1	93.3	77.8	65.8	77.8	93.5	115.4	78.4	41.1	78.9	115.6	152.5	95.1	-	-	-
A19	80.1	84.0	84.3	78.5	75.0	78.6	92.5	92.9	76.9	65.1	76.4	114.6	115.2	77.9	39.9	77.0	152.3	152.6	95.3	-	-
A20	79.8	78.5	83.9	83.9	78.4	74.8	76.9	92.4	92.4	76.3	64.7	78.0	115.0	114.3	76.7	39.8	95.6	151.9	152.7	92.8	-

J.2 Interstation angles (deg) for the pairs of stations at Array A

Stations	A00	A01	A02	A03	A04	A05	A06	A07	A08	A09	A10	A11	A12	A13	A14	A15	A16	A17	A18	A19	A20
A00	-	-	-	-	-	-	-	-	-	-	-	-	-	-	-	-	-	-	-	-	-
A01	39.2	-	-	-	-	-	-	-	-	-	-	-	-	-	-	-	-	-	-	-	-
A02	328.7	275.7	-	-	-	-	-	-	-	-	-	-	-	-	-	-	-	-	-	-	-
A03	253.4	236.9	201.9	-	-	-	-	-	-	-	-	-	-	-	-	-	-	-	-	-	-
A04	183.7	201.0	166.3	127.9	-	-	-	-	-	-	-	-	-	-	-	-	-	-	-	-	-
A05	111.1	163.5	130.0	92.0	57.0	-	-	-	-	-	-	-	-	-	-	-	-	-	-	-	-
A06	38.7	38.4	58.6	47.4	29.9	18.8	-	-	-	-	-	-	-	-	-	-	-	-	-	-	-
A07	328.2	309.5	327.9	348.2	336.9	319.2	274.1	-	-	-	-	-	-	-	-	-	-	-	-	-	-
A08	255.4	246.8	235.9	256.4	275.0	264.1	237.2	202.0	-	-	-	-	-	-	-	-	-	-	-	-	-
A09	182.8	191.5	174.4	162.6	182.4	202.5	200.6	165.5	128.7	-	-	-	-	-	-	-	-	-	-	-	-
A10	112.3	130.9	121.2	102.6	92.5	112.8	164.8	130.2	93.8	57.8	-	-	-	-	-	-	-	-	-	-	-
A11	39.1	39.1	46.2	42.9	35.2	31.9	39.3	61.3	48.9	29.4	16.9	-	-	-	-	-	-	-	-	-	-
A12	327.4	320.6	327.2	334.7	331.3	323.5	305.8	326.9	349.4	336.8	318.0	273.7	-	-	-	-	-	-	-	-	-
A13	255.1	251.4	247.9	255.4	262.3	259.0	245.5	233.0	255.0	277.1	265.1	237.1	200.9	-	-	-	-	-	-	-	-
A14	182.8	186.5	179.2	175.6	182.7	189.9	192.3	173.6	160.7	182.8	204.8	200.9	165.1	129.2	-	-	-	-	-	-	-
A15	111.8	118.6	115.7	107.6	104.6	111.9	133.5	121.5	102.0	89.8	111.5	165.2	129.6	93.5	57.1	-	-	-	-	-	-
A16	38.4	38.3	41.8	40.4	36.4	34.9	38.3	49.1	44.0	33.0	27.6	37.7	68.0	50.4	26.7	9.2	-	-	-	-	-
A17	327.9	324.6	327.9	331.5	329.9	325.9	317.3	327.8	338.8	333.2	322.5	298.6	328.5	357.2	339.4	316.0	273.1	-	-	-	-
A18	255.4	253.5	251.9	255.6	258.9	257.4	249.9	244.7	255.4	266.0	261.0	243.6	226.2	255.7	284.5	267.3	237.0	202.2	-	-	-
A19	182.8	184.8	180.9	179.2	182.7	186.3	188.2	177.5	172.0	182.8	193.5	194.7	171.1	153.6	182.8	212.2	200.6	165.4	128.7	-	-
A20	111.9	115.3	114.0	109.7	108.4	111.9	122.5	117.4	106.3	101.2	111.8	141.1	123.6	99.8	82.3	112.0	165.2	129.9	93.5	57.2	-

Appendix K

Sensitivity of lagged coherency to duration of time window

Sensitivity of estimated lagged coherency to duration of selected time window (event no. 46 (Appendix F)) for separation distances 40 m and 80 m are given here. The plots represent the estimated coherency (EW component) between A00 and the stations on the 40m- and 80m-radius circles of the Array A. The array geometry, velocity time series of the event and the results for separation distance of 15 m are given in Figure 4.17.

K.1 For the pairs at station separation distance 40 m

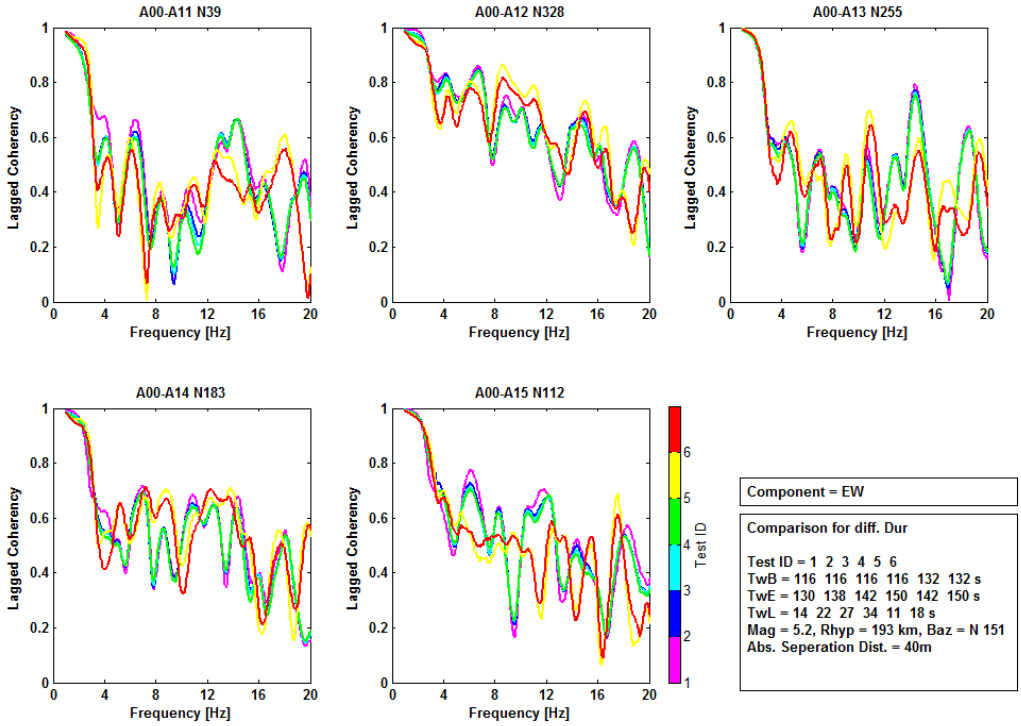

K.2 For the pairs at station separation distance 80 m

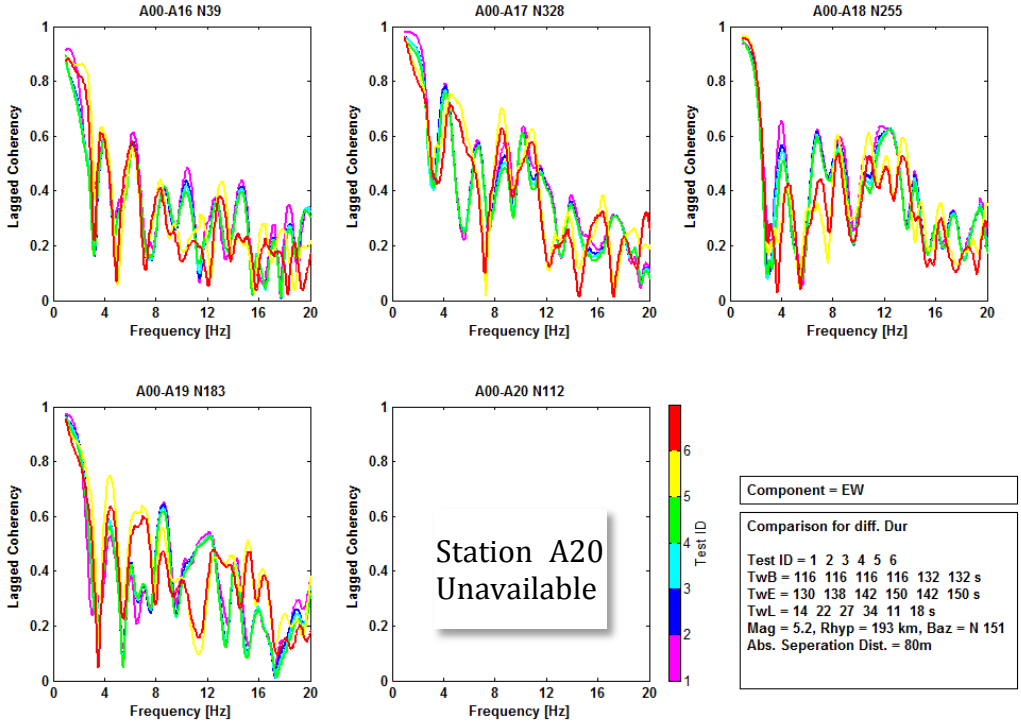

Appendix L

Additional results from coherency analyses

Some additional results from the coherency analysis in Chapter 4 are given here.

L.1 Distribution of ATANH coherency:
Distribution of ATANH coherency estimates of 46 events, from the manually selected strong-motion (most energetic, S-wave dominated) time window, for three components, EW, NS and Z, are given here. The distribution is shown at four interstation distances and for five groups of frequencies, 1-2, 2-4, 4-8, 8-16 and 16-20 Hz.

(a) Frequency 1-2 Hz

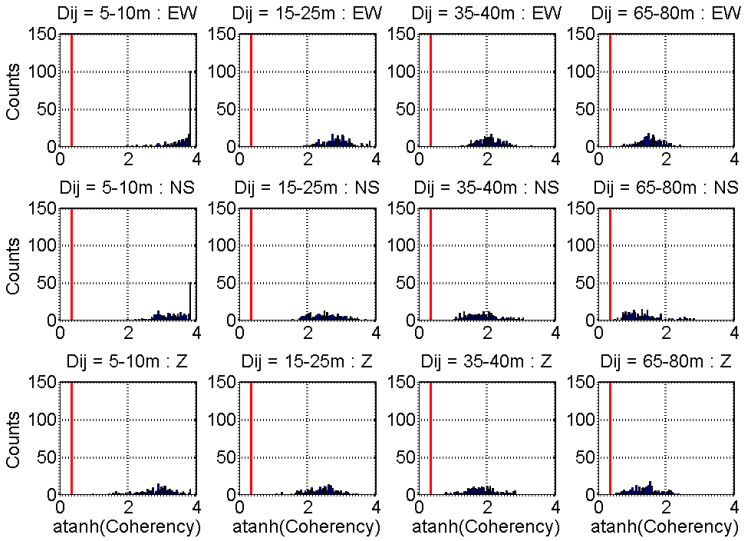

(b) Frequency 2-4 Hz

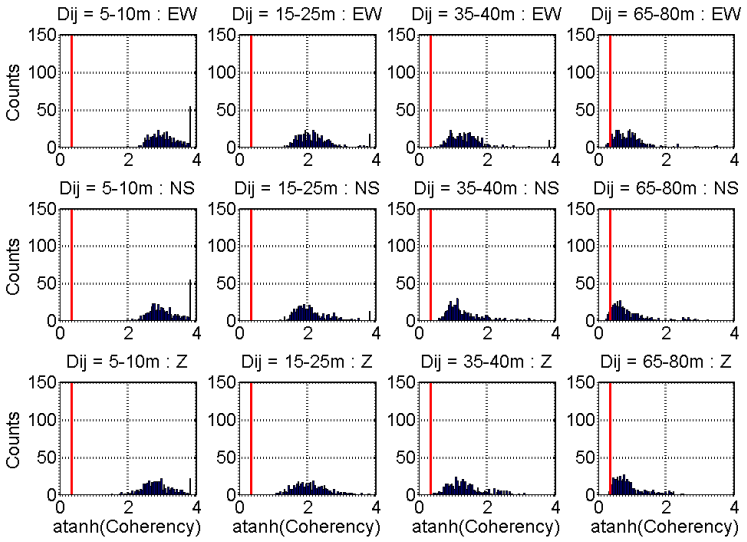

(c) Frequency 4-8 Hz

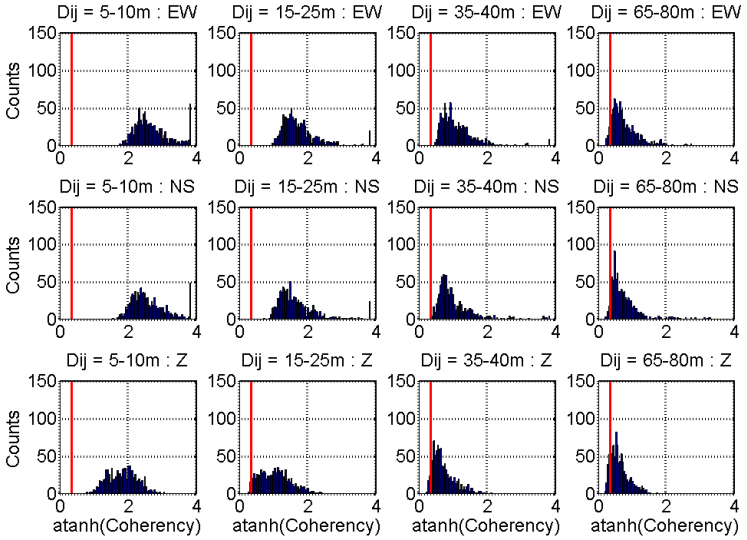

(d) Frequency 8-16 Hz

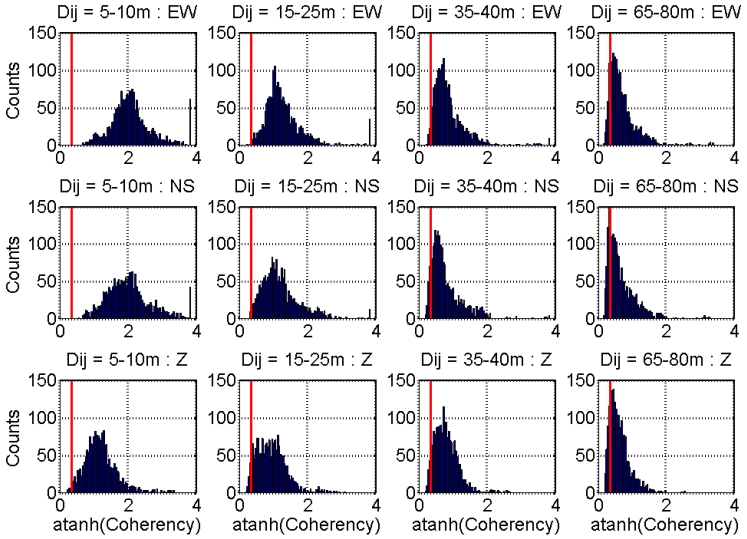

(e) Frequency 16-25 Hz

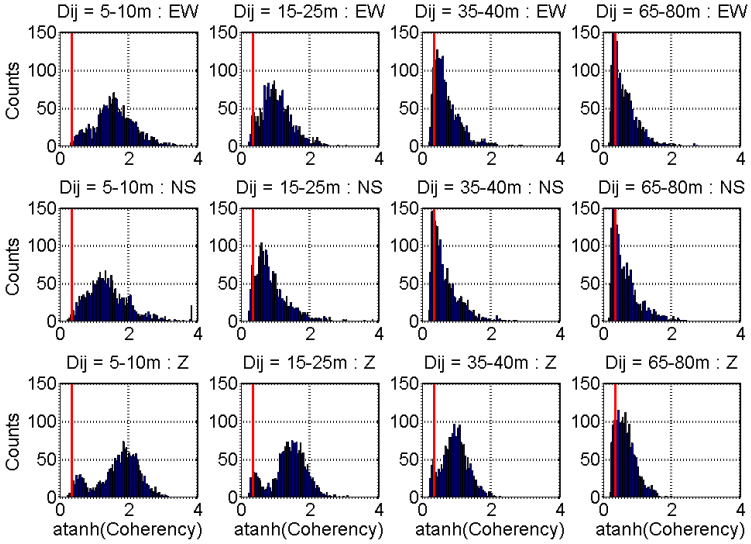

L.2 Variation of ATANH coherency from different time-window selection approaches

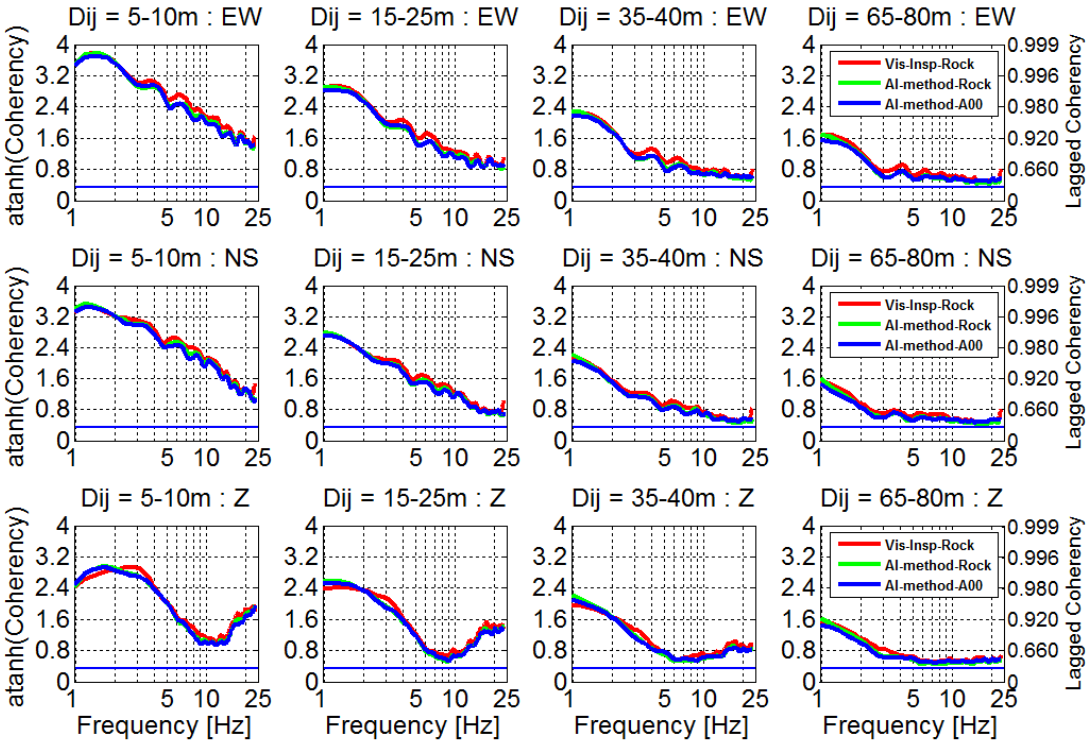

L.3 ATANH coherency (AI-based time-windows selection – rock station)

(a) Median Estimates

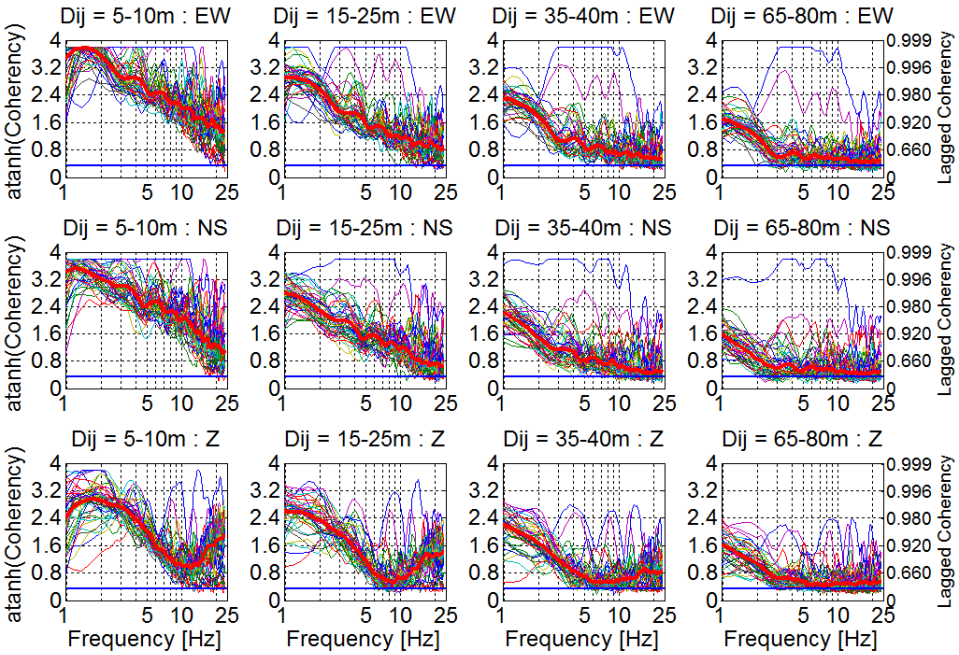

(b) Residual

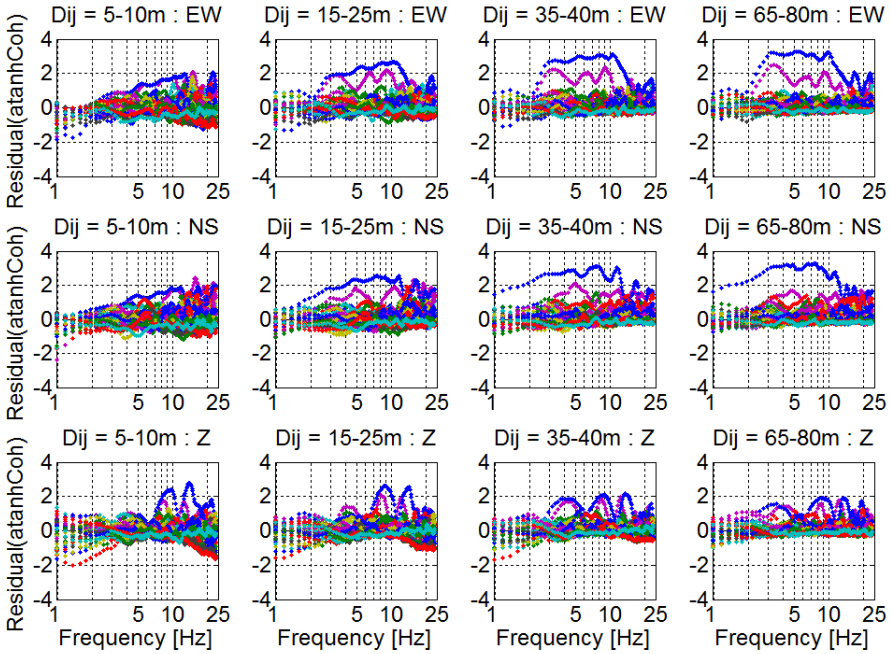

L.4 ATANH coherency (AI-based time-windows selection – A00 station)

(a) Median Estimates

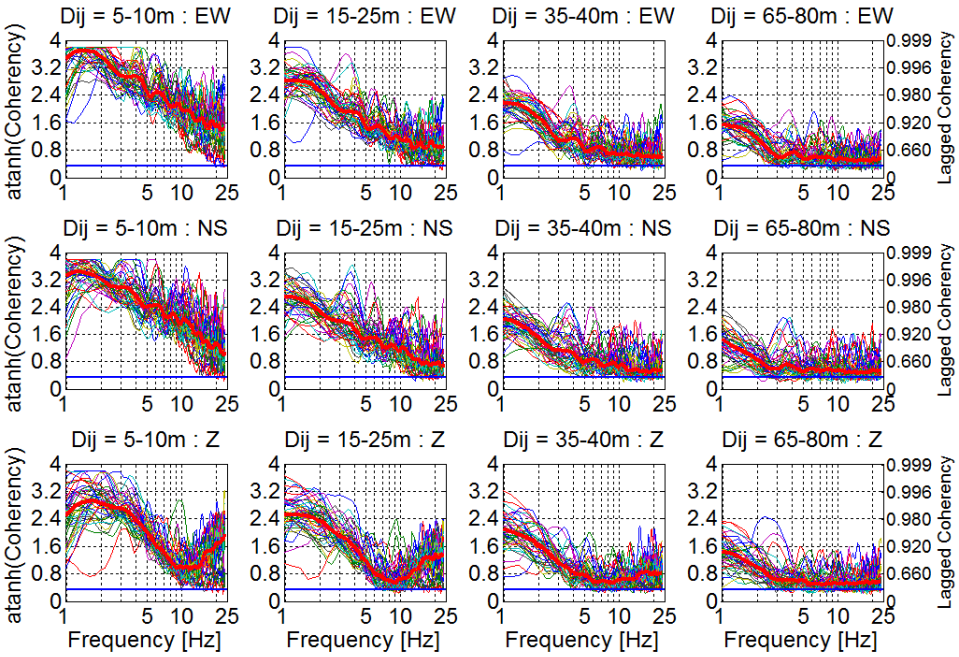

(b) Residuals

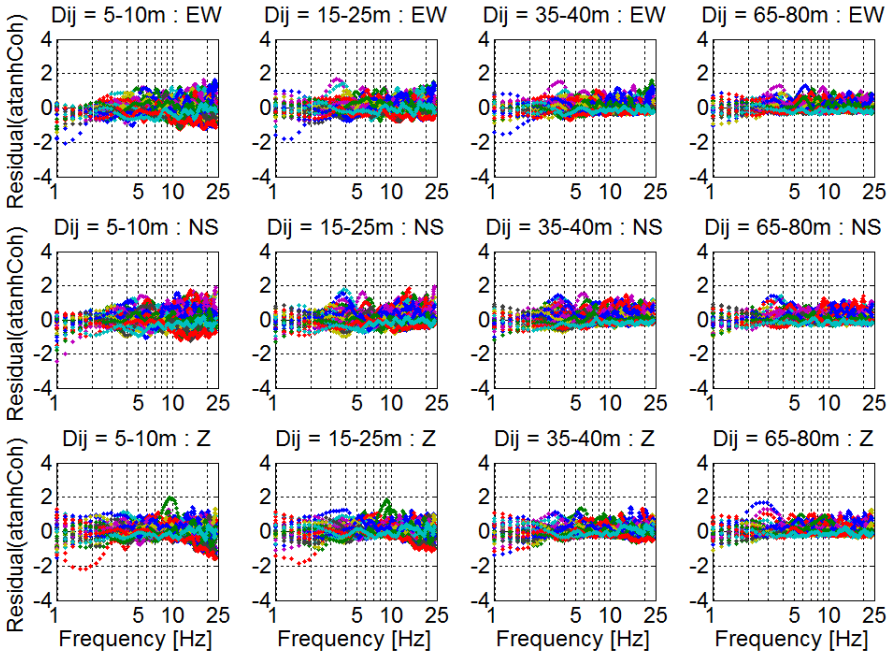

L.5 ATANH coherency (most energetic time window from S-wave onset): valley-axis oriented horizontal components

(a) Median Estimates

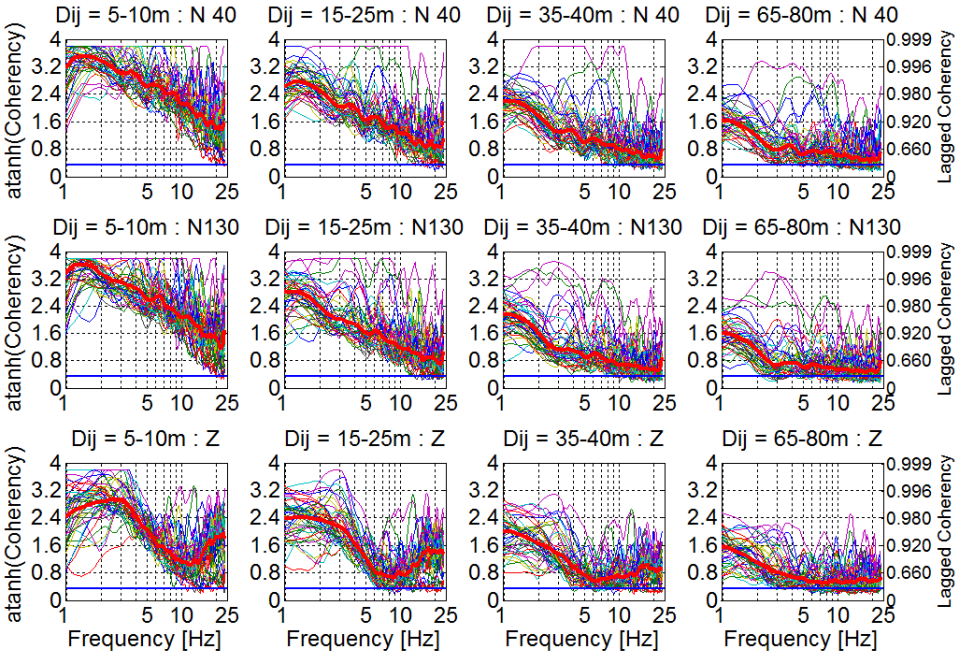

(b) Residuals

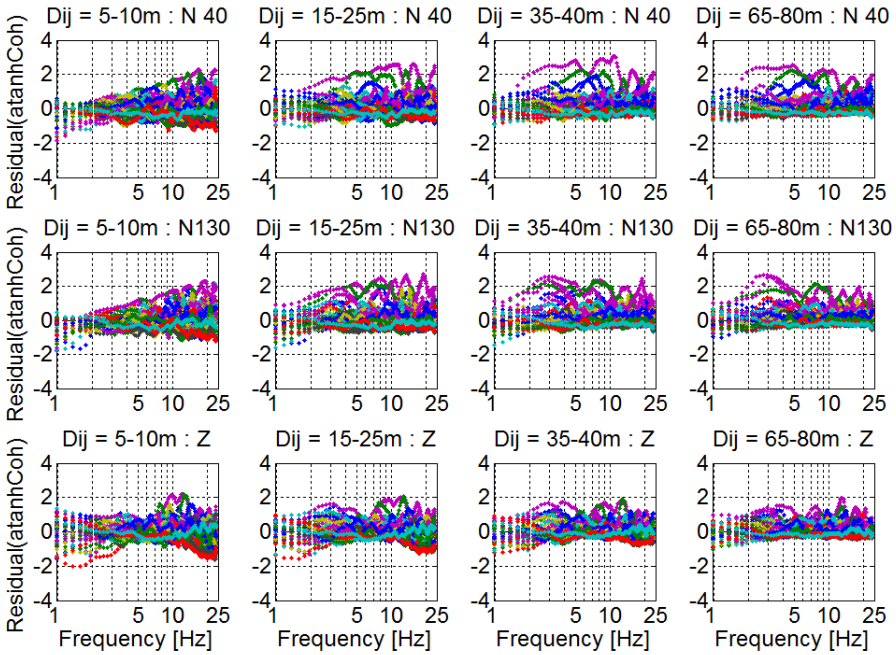

L.6 ATANH coherency (most energetic time window from S-wave onset): back-azimuth oriented horizontal components

(a) Median Estimates

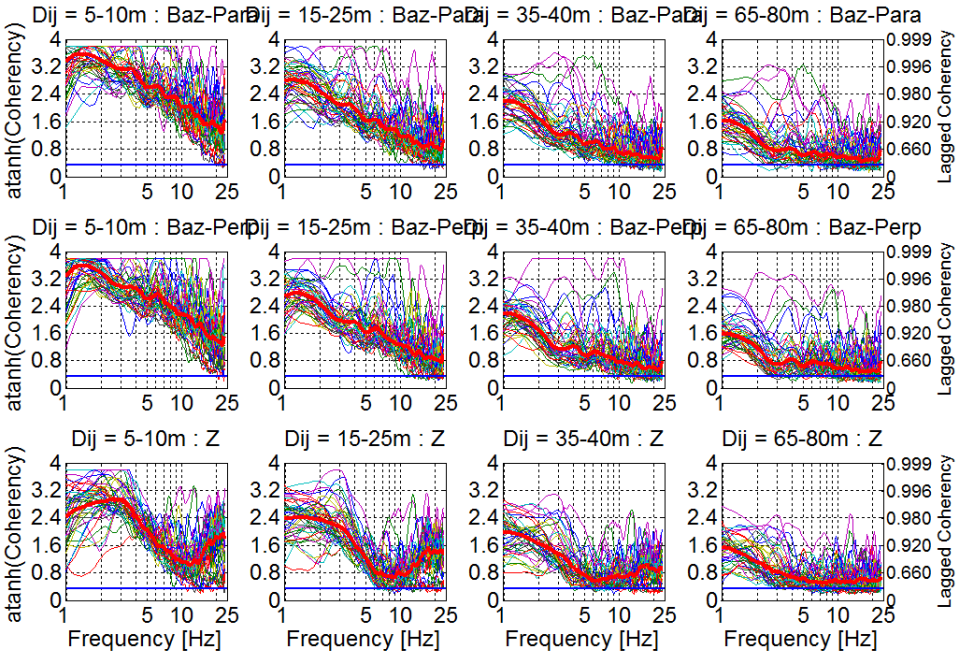

(b) Residuals

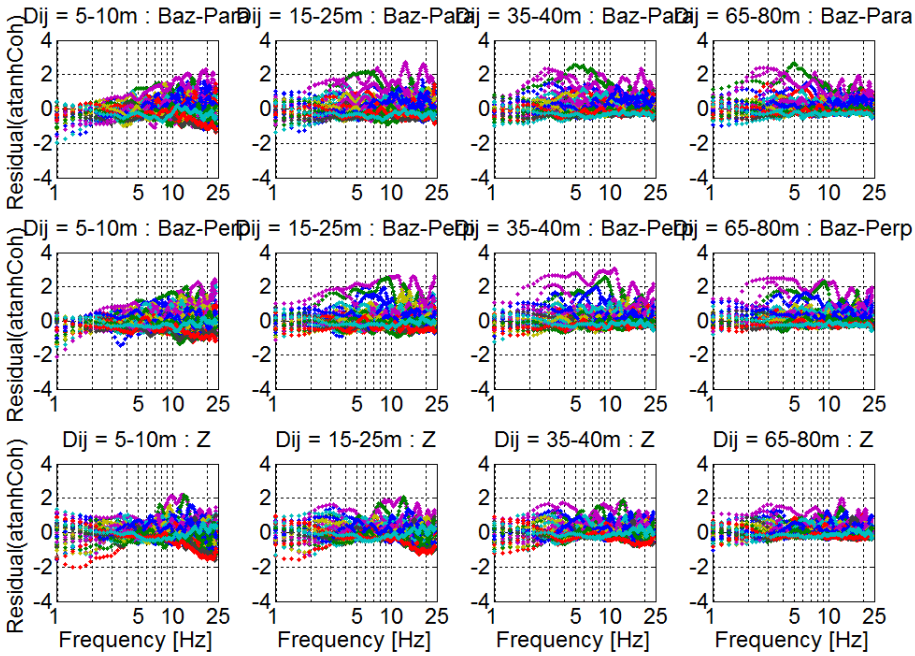

(c) Pairs grouped at five array-branch directions

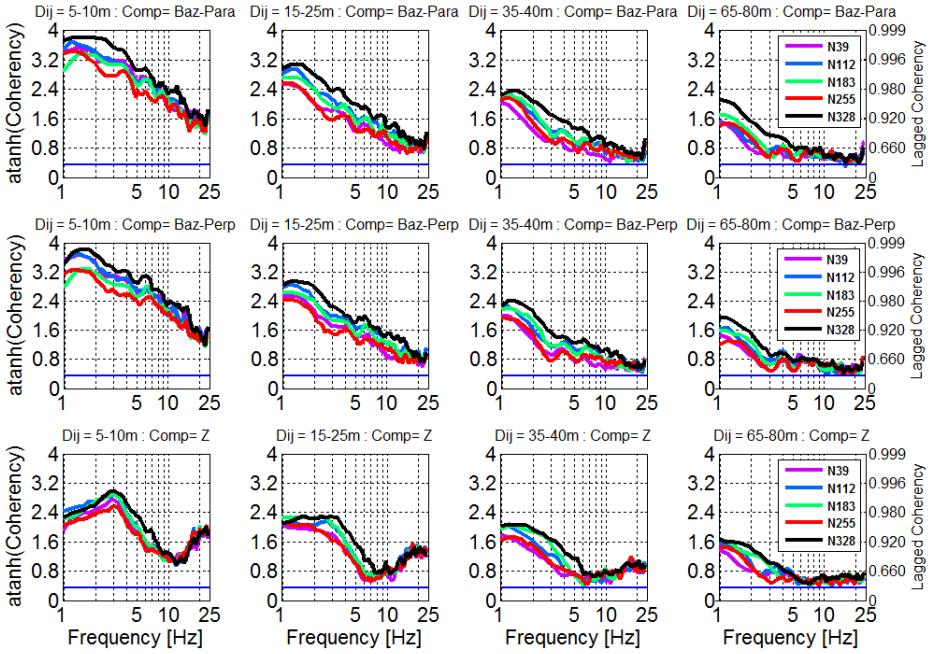

(d) Pairs grouped at five valley-parallel and –perpendicular directions

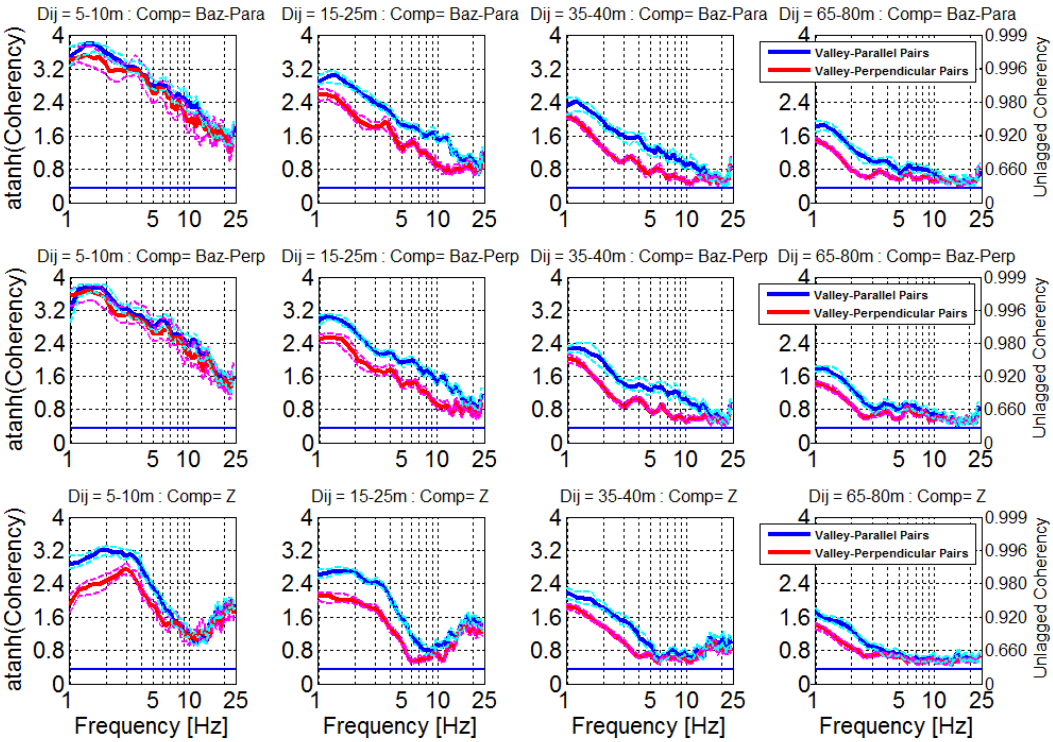

L.7 'Unlagged coherency': most energetic time window from S-wave onset

(a) Median Estimates

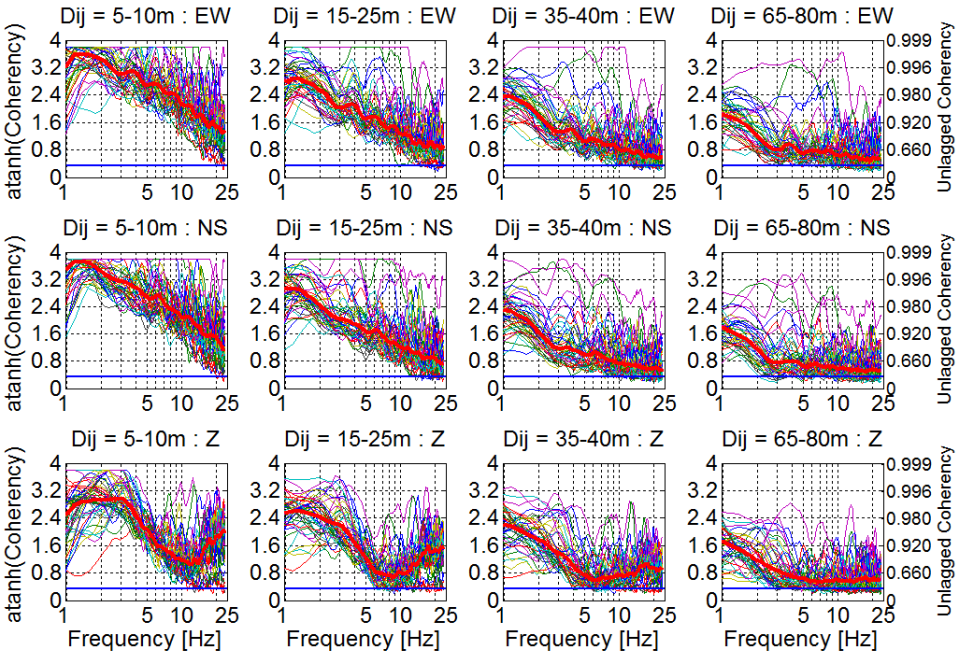

(b) Residuals

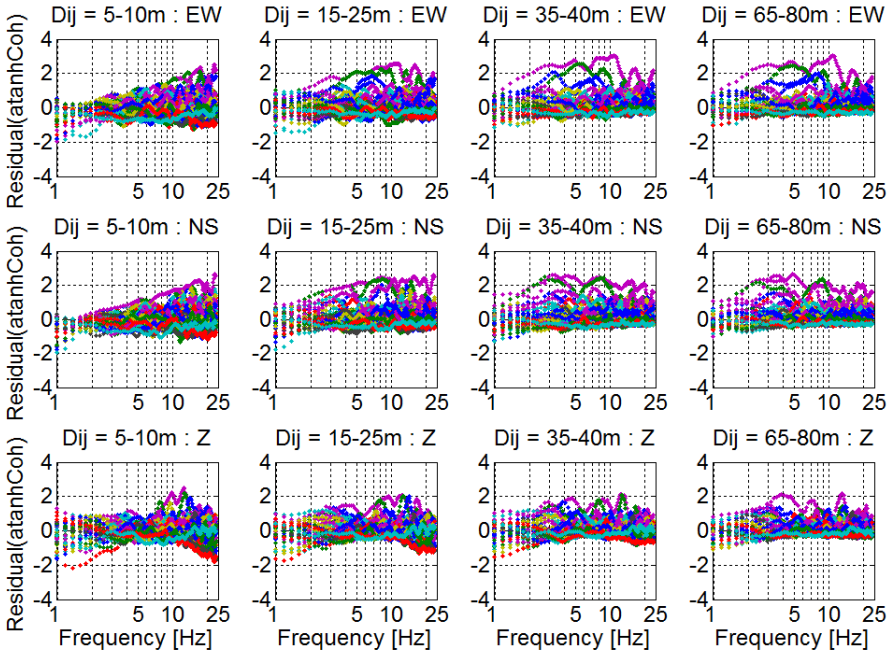

L.8 Median and residual 'unlagged coherency': coda-wave window

(a) Median Estimates

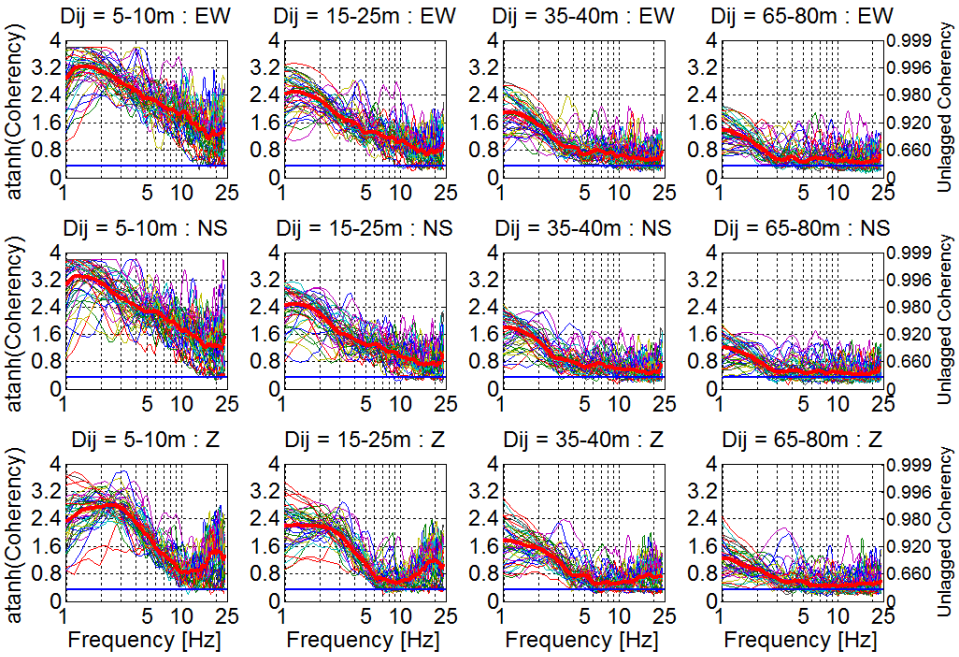

(a) Residuals